SCHOLARLY PUBLICATIONS

A CURRENT AWARENESS BULLETIN
OF RESEARCH OUTPUT

@DTU

(69th Edition)

SEPTEMBER, 2018

BY: CENTRAL LIBRARY

DELHI TECHNOLOGICAL UNIVERSITY
(FORMERLY *DELHI COLLEGE OF ENGINEERING)*
GOVT. OF N.C.T. OF DELHI
SHAHBAD DAULATPUR, MAIN BAWANA ROAD
DELHI 110042

PREFACE

This is the **Sixty Ninth** Issue of Current Awareness Bulletin started by Delhi Technological University, Central Library. The aim of the bulletin is to compile, preserve and disseminate information published by the faculty, students and alumni for mutual benefits. The bulletin also aims to propagate the intellectual contribution of Delhi Technological University (DTU) as a whole to the academia.

The bulletin contains information resources available in the internet in the form of articles, reports, presentations published in international journals, websites, etc. by the faculty and students of DTU. The publications of faculty and student which are not covered in this bulletin may be because of the reason that the full text either was not accessible or could not be searched by the search engine used by the library for this purpose.

The learned faculty and students are requested to provide their uncovered publications to the library either through email or in CD, etc. to make the bulletin more comprehensive.

This issue contains the information published during **September, 2018**. The arrangement of the contents is alphabetical. The full text of the article which is either subscribed by the university or available in the web is provided in this bulletin.

Central Library

CONTENTS

1. A Generalized Power-Flow Model of VSC Based Hybrid AC-DC Systems Integrated with Offshore Wind Farms, ***6.1.Shagufta Khan*** and ***3.Suman Bhowmick***, Electrical, DTU

2. A review of state-of-the-art techniques for abnormal human activity recognition, ***6.Chhavi Dhiman*** [a] and ***3.Dinesh Kumar Vishwakarma*** [b], [a]Electronics and Communication and Information Technology, DTU

3. An extensive analysis of search-based techniques for predicting defective classes, ***3.Ruchika Malhotra***, Computer Science, DTU

4. Challenges & Physical Insights Into the Designof Fin-Based SCRs and a Novel Fin-SCR for Efficient On-Chip ESD Protection, ***7.1.Milova Paul***, B. Sampath Kumar , Christian Russ, Harald Gossner, and Mayank Shrivastava, Electronics, DTU

5. Corona based node distribution scheme targeting energy balancing in wireless sensor networks for the sensors having limited sensing range, ***3.1.Richa Mishra***, Vivekanand Jha, Rajeev K. Tripathi and Ajay K. Sharma, Computer Science, DTU

6. Degradation of AY36 using TiO2-UV Photocatalytic System, Palak, Shivani Chauhan, Krishan Kumar and ***3.A.K. Haritash***, Environmental, DTU

7. Design and Analysis of a Cross V-shaped Nanoantenna for Visible Region, ***6.Shanu Kumar***, ***6.Pooja Chauhan*** and ***3.Ajeet Kumar***, Applied Physics, DTU

8. DETERMINING PLURIPOTENCY OF A CELL BY AN IN SILICO METHOD, ***6.Abhishek Saini***, ***3.Jai Gopal Sharma*** and Vimal Kishor Singh, Biotechnology, DTU

9. Distinguishing different classes of entanglement of three-qubit pure states, Chandan Datta, ***6.Satyabrata Adhikari***, Arpan Das and Pankaj Agrawal, Physics, DTU

10. Effect of Fiber Content on Thermal Behavior and Viscoelastic Properties of PALF/Epoxy and COIR/Epoxy Composites, ***6.Mohit Mittal*** and ***3.Rajiv Chaudhary***, Mechanical, Production, and Industrial, DTU

11. Energy-Exergetic performance and parametric evaluation of Haylent liquefaction system using different gasses system, ***3.R.S. Mishra*** and ***6.Devender Kumar***, Mechanical, Production and Automobile, DTU

12. Global Financial Crisis and Price Risk Management in Gold Futures Market-Evidences from Indian & US Markets, Narinder Pal Singh and ***3.Archana Singh***, DSM, DTU

13. Honeycomb photonic crystal as a zero index metamaterial, ***6.Nishant Shankhwar***, ***3.Yogita Kalra*** and ***3.Ravindra Kumar Sinha***, Applied Physics, DTU

14. Matrix Games with Interval-Valued 2-Tuple Linguistic Information, ***6.Anjali Singh*** and ***3.Anjana Gupta***, Applied Mathematics, DTU

15. Methods for improving thermal performances of vapour compression refrigeration systems using ecofriendly refrigerant in the expander, ***3.R.S. Mishra***, Mech & Prod, DTU

16. Modeling of variable speed compressor vapour compression refrigeration system using ecofriendly refrigerants and nano refrigerants and water cooled condenser-evaporator with experimental validation, ***3.Radhey Shyam Mishra***, Mech, Prod, & Indu, DTU

17. Near Field Enhancement in a Hollow Flower Shaped Nanoantenna, ***6.Parul Goyal***, ***6.Nishant Shankhwar*** and ***3.Yogita Kalra***, Applied Physics, DTU

18. Numerical Investigation of Short-Channel Effects in Negative Capacitance MFIS and MFMIS Transistors: Subthreshold Behavior, ***8.1.Girish Pahwa***, Amit Agarwal, and Yogesh Singh Chauhan, Electronics and Communication, DTU

19. On the Minimum Perceptual Temporal Video Sampling Rate and its Application to Adaptive Frame Skipping, Christoph Bachhuber, ***8.1.Amit Bhardwaj***, Rastin Pries and Eckehard Steinbach, Electronics and Communications, DTU

20. Performance parametric analysis of retrofitted Gas turbine cycle using STIG and Evaporative cooling techniques, ***3.R.S. Mishra*** and ***6.Shyam Agarwal***, Mechanical & Production, DTU

21. Rectangular Core Dispersion Engineered Photonic Crystal Fiber for Supercontinuum Generation, ***6.Pooja Chauhan***, ***3.Ajeet Kumar***, ***3.Yogita Kalra*** and Than Singh Saini, Applied Physics, DTU

22. Selection of Traceable Technology in Food Supply Chain, Mr Shahbaz Khan, Mr Mohd Imran Khan, Dr Abid Haleem and ***3.Mr Mohd Shuaib***, Mechanical, DTU

23. Selection of warehouse location for a global supply chain: A case study, Rajesh Kr Singh, ***8.Nikhil Chaudhary*** and ***8.Nikhil Saxena***, Production, DTU

24. Significant improvement in morphological, dielectric, ferroelectric and piezoelectric characteristics of Ba0.9Sr0.1Ti0.9Zr0.1O3– BaNb2O6 nanocomposites, ***3.Aditya Jain***, ***3.Amrish K. Panwar*** and A. K. Jha, Applied Physics, DTU

25. Slow Light Generation in Decagonal Liquid Core Photonic Crystal Fiber, ***6.Rahul Kumar***, ***6.Pooja Chauhan*** and ***3.Ajeet Kumar***, Applied Physics, DTU

26. Structure, magnetism and electrical transport in epitaxial La0.23Pr0.41Ca0.36MnO3 thin films: Consequences of film thickness, ***6.Sandeep Singh***, ***3.P. K. Tyagi*** and H. K. Singh, Applied Physics, DTU

27. Thermal optimization of three stage vapour compression cascade refrigeration system using entropy generation principle for reducing global warming and ozone depletion using ecofriendly refrigerants, ***3.R.S. Mishra***, Mechanical, Production, Industrial and Automobiles, DTU

28. Thermodynamic (energy-exergy) analysis of hydrogen liquefaction system, ***3.R.S. Mishra*** and ***6.Devendra Kumar***, Mechanical, Production & Industrial and Automobiles, DTU

29. Thermodynamic (energy-exergy) analysis to improve its efficiencies of multiple stage vapour compression refrigeration systems, ***3.Radhey Shyam Mishra***, Mechanical, Production, Industrial & Automobiles, DTU

30. Thermodynamic analysis of modified rankine cycle used for power generation, ***3.R.S. Mishra*** and ***6.Manish Kumar***, Mechanical, DTU

31. Thermodynamic analysis of solar integrated waste heat recovery systems for power generation industry using eco-friendly fluids, ***3.R.S. Mishra*** and Kaushalendra Kumar Dubey, Mechanical & Production, DTU

32. Thermodynamic performance of modified collin cryonic system using energy-exergy analysis for liquefaction of helium gas, ***3.S. Mishra*** and ***6.Devendra Kumar***, Mechanical, Production & Industrial and Automobiles, DTU

33. Thermodynamic performance of vapour compression refrigeration systems using HFO refrigerants for replacing HFC refrigerants, ***3.R.S. Mishra***, Mechanical & Production, DTU

34. Ultralow-power dielectric-modulated nanogap-embedded sub-20-nm TGRC-MOSFET for biosensing applications, ***6.Ajay Kumar***[1], ***3.M. M. Tripathi***[1] and ***3.Rishu Chaujar***[2], [1]Electrical and [2]Applied Physics, DTU

1. *Chancellor*

2. *Pro Vice Chancellor* ***2.1.*** *Ex Pro Vice Chancellor*

3. *Faculty* ***3.1.*** *Ex Faculty*

4. *Teaching-cum-Research Fellow* ***4.1.****Asst. Librarian*

5. *Alumni*

6. *Research Scholar* ***6.1.*** *Ex Research Scholar*

7. *PG Scholar* ***7.1.*** *Ex PG Scholar*

8. *Undergraduate Student* ***8.1.*** *Ex Undergraduate Student*

This article has been accepted for publication in a future issue of this journal, but has not been fully edited. Content may change prior to final publication. Citation information: DOI 10.1109/TSTE.2018.2870914, IEEE Transactions on Sustainable Energy

A Generalized Power-Flow Model of VSC Based Hybrid AC-DC Systems Integrated with Offshore Wind Farms

Shagufta Khan, *Member, IEEE* and Suman Bhowmick

***Abstract*— This paper presents a unified power-flow model of AC power systems incorporating voltage-sourced converter (VSC) based multi-terminal high voltage direct current (MTDC) grids. Offshore wind farms (OWFs) are appropriately interfaced with the MTDC grid(s). Pulse-width modulation (PWM) control is employed for the VSCs. In the proposed model, the VSC modulation indices are considered as unknowns. The proposed model employs realistic grid control strategies like nonlinear distributed DC voltage control. The power-flow solution is carried out using the Newton-Raphson (NR) method. The convergence properties of the proposed algorithm are investigated vis-à-vis varying terminal end active and reactive power specifications of the VSCs and the rectifying power injections of the OWFs, in light of different MTDC control strategies employed. Corresponding to nonlinear DC voltage droop control, five different operating points are considered to observe the sharing of power among the DC terminals with changes in the operating point specifications. The results validate the model.**

***Index Terms*—** MTDC grid, Newton power-flow, OWFs, VSC

I. Introduction

Due to the ever increasing demand of electrical energy and environmental concerns, both the industry and the academia have been focusing on the harnessing of remotely located renewable energy sources, particularly the aggregation and integration of offshore renewable energy sources [1]-[8]. In order to integrate such remotely located energy sources with the AC grid, VSC based MTDC grids have been proposed over conventional HVDC which can connect different offshore stations at the same voltage or at different voltages.

VSC based MTDC grids present a feasible option for asynchronous power transmission. Contrary to conventional HVDC, VSC-HVDC technology employing IGBTs with PWM control technique enables independent control of active and reactive power, reversible power flow without the change of voltage polarity, asynchronous decoupling from AC grids and the use of compact and inexpensive AC filters [1]-[9]. Moreover, remotely located offshore wind farm stations at the same voltage or at different voltages can be easily integrated with the MTDC grid, as and when the need arises. A meshed MTDC grid linking offshore wind farms and three asynchronous AC grids of the European Network Transmission System Operators for Electricity (ENTSO-E) is being envisaged in the North Sea region [8], [9].

In a MTDC grid, the VSCs can be connected in a back-to-back (BTB) or a point-to-point (PTP) disposition, depending on whether they are placed nearby or are at distant locations, respectively [10]. PTP is the most widely used configuration among all the MTDC systems installed worldwide, wherein DC links or cables are used to connect the DC terminals.

For proper MTDC operation, DC voltage control is an essential requirement. In this respect, several DC voltage control techniques have been envisaged. Among these, DC slack bus control (familiar as master-slave control) and distributed voltage droop control have been the more popular ones.

In DC slack bus control [10]-[15], the voltage of one DC terminal is maintained constant. It is known as the DC slack bus and it sustains the power balance of the DC grid. The main disadvantage of this control scheme is the DC grid instability following a failure of the master converter.

The above problem can be tackled by ensuring that individual converters take part in the DC voltage regulation scheme by adjusting their active power flow in response to changes in the DC voltage. This is known as DC voltage droop control [16]-[25].

DC voltage droop control comprises both linear and nonlinear voltage droop characteristics [23], [25]-[27]. Among the linear ones, Voltage-Power (V-P) and Voltage-Current (V-I) droops have been the two most popular and widely used strategies for DC voltage droop control. Among the nonlinear ones, Voltage Margin, V-P droop with power dead-band and V-P droop with voltage limits are some of the more widely used characteristics.

For planning, operation and control of integrated AC-MTDC systems, their power-flow models are required. [23], [28]- [33] present some comprehensive power-flow models of integrated AC-DC systems. [23] presents an AC-DC power flow model incorporating linear and nonlinear DC voltage droop control. Power flow models of hybrid AC-DC systems incorporating offshore wind farms have been presented in [28]-[29]. [30] - [32] present optimal power flow models of VSC based hybrid AC-DC systems. A sequential power flow model of hybrid AC-DC systems employing DC master-slave control has been presented in [33]. However, most of the current research works do not address the following issues:

1. Development of a unified power-flow model of integrated AC-MTDC grids incorporating OWFs and employing DC voltage droop control. In this regards,

1949-3029 (c) 2018 IEEE. Personal use is permitted, but republication/redistribution requires IEEE permission. See http://www.ieee.org/publications_standards/publications/rights/index.html for more information.

This article has been accepted for publication in a future issue of this journal, but has not been fully edited. Content may change prior to final publication. Citation information: DOI 10.1109/TSTE.2018.2870914, IEEE Transactions on Sustainable Energy

though, [23] have presented a sequential counterpart of the above.

2. The VSC modulation index 'm' is not considered as an unknown. For VSC applications, 'm' is a crucial parameter. Typically, $0 < m \leq 1$. [5] has reported some of the factors that put a cap on the lower and upper bounds of 'm'.

This paper presents a unified power flow model of a hybrid AC-MTDC system integrated with OWFs. The power-flow equations are solved using the Newton-Raphson (NR) method. Unlike sequential models like [23], the proposed algorithm is faster, has a convergence which is quadratic and is independent of the operating conditions and/or the control strategy employed. As against most of the research works published in this area, 'm' is considered as an unknown and can be obtained directly, from the power-flow solution. Putting a cap on the upper bounds of 'm' and V_{DC} takes care of the Q-limit of the converter. Realistic MTDC grid control strategies like nonlinear DC voltage droop control have been implemented in the proposed model. In addition, the proposed model also includes the converter losses.

The remainder of this paper is extended as follows: In section II, the modeling of hybrid AC-MTDC systems integrated with OWFs, is presented. DC voltage droop control is discussed in section III. Section IV details the Newton power-flow equations of AC-MTDC systems employing DC voltage droop control. The case studies and results are presented in section V. Section VI presents the conclusions.

II. Modeling of AC-MTDC Systems Integrated with Offshore Wind Farms

Fig. 1 shows an AC power system network comprising 'n' buses, integrated with a 'q' terminal MTDC grid. The integration of the MTDC grid with the AC network takes place at 'p' AC buses ($p \leq q$) through 'p' VSCs. Converter transformers are used to interconnect the VSCs with their AC terminal buses. Further, offshore wind farms (OWFs) are appropriately interfaced at '$(q-p)$' terminals of the MTDC grid. For generalization, it is assumed that the AC buses connected to the 'p' VSCs are numbered as 'i', '$(i+1)$' and so on, up to '$(i+p-1)$'. On their DC sides, the 'p' VSCs follow a PTP connection. Fig. 2 shows the equivalent circuit for the network shown in Fig. 1.

In Fig. 2, 'p' fundamental frequency, positive sequence voltage sources pertaining to the 'p' VSCs are shown. Now, let R_{sha} and X_{sha} be the resistance and the leakage reactance of the a^{th} $(1 \leq a \leq p)$ converter transformer, respectively. Also, let $\boldsymbol{y_{sha}} = 1/\boldsymbol{Z_{sha}}$, where $\boldsymbol{Z_{sha}} = R_{sha} + jX_{sha}$. Therefore, from Fig. 2, the current in the link (not shown) connecting the a^{th} VSC and its AC terminal bus is

$$\boldsymbol{I_{sha}} = \boldsymbol{y_{sha}}\,(\boldsymbol{V_{sha}} - \boldsymbol{V_{i+a-1}}) \tag{1}$$

In Eqn. (1), $\boldsymbol{V_{sha}}$ is the voltage phasor pertaining to the a^{th} VSC. Also, in Eqn. (1), $\boldsymbol{V_{sha}} = V_{sha} \angle \theta_{sha} = m_a\, c\, V_{DCa} \angle \theta_{sha}$ where 'm_a' is the VSC modulation index. The constant 'c' is representative of the VSC architecture [4].

Now, from Fig. 1, it is shown that, the a^{th} $(1 \leq a \leq p)$ VSC is connected to the AC terminal bus '$(i+a-1)$' whose voltage is represented by the phasor $\boldsymbol{V_{i+a-1}} = V_{i+a-1} \angle \theta_{i+a-1}$.
Accordingly, from Fig. 2, using Eqn. (1) and manipulating, the net current injection at the AC terminal bus '$(i+a-1)$' can be represented as

$$\mathbf{I_{i+a-1}} = \sum_{k=1}^{n} \mathbf{Y_{(i+a-1)k}}\,\mathbf{V_k} \;-\; \mathbf{y_{sha}}\mathbf{V_{sha}} \tag{2}$$

where $\mathbf{Y_{(i+a-1)(i+a-1)}} = \mathbf{Y^{old}_{(i+a-1)(i+a-1)}} + \mathbf{y_{sha}}$ and

$\boldsymbol{Y^{old}_{(i+a-1)(i+a-1)}} = \boldsymbol{y_{(i+a-1)0}} + \sum_{k=1,\, k\neq i+a-1}^{n} \boldsymbol{y_{(i+a-1)k}}$ are the new and old values of the self admittance of bus '$(i+a-1)$' with the a^{th} VSC connected and without any VSC, respectively.
'$\boldsymbol{y_{(i+a-1)0}}$' accounts for the shunt capacitances of all the transmission lines connected to bus '$(i+a-1)$'.

Using Eqn. (2), it can be shown that the net active and reactive power injections at the AC bus '$(i+a-1)$' are

$$P_{i+a-1} = \sum_{k=1}^{n} V_{i+a-1}\, V_k\, Y_{(i+a-1)k}\, cos\,\left[\theta_{i+a-1} - \theta_k - \Phi_{(i+a-1)\,k}\right] - m_a\, c\; V_{DCa}\, V_{i+a-1}\; y_{sha}\, cos\,(\theta_{i+a-1} - \theta_{sha} - \phi_{sha}) \tag{3}$$

$$Q_{i+a-1} = \sum_{k=1}^{n} V_{i+a-1}\, V_k\, Y_{(i+a-1\,k}\, sin\,\left[\theta_{i+a-1} - \theta_k - \Phi_{(i+a-1)\,k}\right] - m_a\, c\; V_{DCa}\, V_{i+a-1}\; y_{sha}\, sin(\theta_{i+a-1} - \theta_{sha} - \phi_{sha}) \tag{4}$$

where 'ϕ_{sha}' is the phase angle of $\boldsymbol{y_{sha}}$.
In a similar manner, from Fig. 2, it can be shown that the line active and reactive power flows pertaining to the a^{th} VSC are

$$P_{sha} = m_a\, c\, V_{DCa}\, V_{i+a-1}\; y_{sha}\; cos\,\left(\theta_{i+a-1} - \theta_{sha} - \phi_{sha}\right) - V^2_{i+a-1}\, y_{sha}\, cos\,\phi_{sha} \tag{5}$$

$$Q_{sha} = m_a\, c\, V_{DCa}\, V_{i+a-1}\, y_{sha}\, \sin(\,\theta_{i+a-1} - \theta_{sha} - \Phi_{sha}) + V^2_{i+a-1} y_{sha}\, sin\Phi_{sha} \tag{6}$$

Again from Fig. 2, in the MTDC grid, the net injected current at the u^{th} $(1 \leq u \leq q)$ DC node is given as

$$I_{DCu} = \sum_{v=1}^{q} Y_{DCuv}\; V_{DCv} \tag{7}$$

where $Y_{DCuv} = -\frac{1}{R_{DCuv}}$, where '$R_{DCuv}$' is the resistance of the interconnection between DC buses 'u' and 'v'.
Now, for the a^{th} VSC, the converter losses [13], [24], [27] are

$$P_{lossa} = a_1 + b_1\, I_{sha} + c_1\, I^2_{sha} \tag{8}$$

where, 'a_1' indicates the VSC losses at no load, 'b_1' and 'c_1' are constants representative of the linear and quadratic dependency of the VSC losses on the converter current magnitude ('I_{sha}'), respectively.
Also, from Fig. 2, by virtue of the power balance at its AC and DC sides,

1949-3029 (c) 2018 IEEE. Personal use is permitted, but republication/redistribution requires IEEE permission. See http://www.ieee.org/publications_standards/publications/rights/index.html for more information.

This article has been accepted for publication in a future issue of this journal, but has not been fully edited. Content may change prior to final publication. Citation information: DOI 10.1109/TSTE.2018.2870914, IEEE Transactions on Sustainable Energy

$$\sum_{v=1}^{q} V_{DCa} I_{DCa} + Re(\boldsymbol{V_{sha}\, I_{sha}^{*}}) = -P_{lossa}$$

Substituting Eqns. (1), (7) and (8) in the above equation, we get, for the a^{th} VSC,

$$\sum_{v=1}^{q} V_{DCa} I_{DCa} + P_{lossa} + (m_a c\, V_{DCa})^2\; y_{sha}\; cos\phi_{sha} - m_a\; c\; V_{DCa}\, V_{i+a-1}\, y_{sha}\; cos\;(\theta_{sha} - \theta_{i+a-1} - \phi_{sha}) = 0$$

$$\text{or, } f_{1a} = 0 \qquad \forall\, a,\;\; 1 \le a \le p \tag{9}$$

Thus, *'p'* independent equations are obtained.
Now, in the AC-MTDC system (Fig. 2) with *'p'* VSCs, it is important to note that not more than *'(p-1)'* line active power flows Eqn. (5) can be specified. It is assumed that VSC '1' is used for DC voltage control while the other '$(p\text{-}1)$' VSCs (VSCs '2' to 'p') control the line active power flows. With DC voltage droop control, usually, the average voltage 'V_{DCav}' of all the *'q'* DC terminals is maintained constant [23]. Hence,

$$V_{DCav}^{sp} - V_{DCav}^{cal} = 0 \quad \forall\, a,\;\; 1 \le a \le q \tag{10}$$

where $V_{DCav} = (\sum_{v=1}^{q} V_{DCv})/q$ and

$$P_{sha}^{sp} - P_{sha}^{cal} = 0 \qquad \forall a, \quad 2 \le a \le p \tag{11}$$

Now, all the 'p' VSCs line control their line reactive power flows. Hence,

$$Q_{sha}^{sp} - Q_{sha}^{cal} = 0 \qquad \forall a, \quad 1 \le a \le p \tag{12}$$

Thus, we get *'(2p-1)'* independent equations.
Also, the rectified power injections of the '$(q-p)$' OWFs can be written as

$$P_{DCWFb}^{sp} - P_{DCWFb}^{cal} = 0 \qquad \forall b, \quad 1 \le b \le q-p \tag{13}$$

where $P_{DCWFb}^{cal} = \sum_{v=1}^{q} V_{DCb}\, Y_{DCuv}\; V_{DCv}$

$$\forall\; b,\; v, \quad 1 \le b \le q-p, \quad 1 \le v \le q$$

In Eqn. (10), 'V_{DCav}^{sp}' and 'V_{DCav}^{cal}' represent the specified and the calculated value of 'V_{DCav}'. This notation also holds good for Eqns. (11) - (13).

III. DC VOLTAGE DROOP CONTROL IN MTDC SYSTEMS

As already discussed in Section I, for DC voltage control, MTDC systems employ both classical methods like DC slack bus control (master-slave control) and modern ones like DC voltage droop control [14]-[27]. In the latter, both linear and nonlinear DC voltage droop characteristics can be realized, which are elaborated below.

A. Voltage-Power (V-P) Droop

If the a^{th} VSC follows a linear V-P droop characteristic, its rectifying power can be expressed as

$$P_{DCa} = R_a(V_{DCa}^{*} - V_{DCa}) + P_{DCa}^{*} \tag{14}$$

where *'V_{DCa}^{*}'* and *'P_{DCa}^{*}'* represent the DC voltage and power references of its droop characteristic and *'R_a'* is the droop control gain.

B. Voltage-Current (V-I) Droop

If the a^{th} VSC follows a linear V-I droop characteristic, the net DC current injection at its terminal can be expressed as

$$I_{DCa} = R_a(V_{DCa}^{*} - V_{DCa}) + I_{DCa}^{*} \tag{15}$$

In Eqn. (15), *'I_{DCa}^{*}'* and *'V_{DCa}^{*}'* are the DC current and voltage references of its droop line and *'R_a'* is the droop control gain. Thus, the rectifying power of the VSC can be expressed as

$$P_{DCa} = V_{DCa}\,[R_a(V_{DCa}^{*} - V_{DCa}) + I_{DCa}^{*}] \tag{16}$$

Fig. 3 depicts the linear V-P and V-I droop characteristics for any arbitrary VSC *'a'*.

C. Voltage-Power (V-P) Droop with dead-band

In practical DC grids, the droop characteristic is a combination of multiple linear or nonlinear functions of the DC voltage. Fig. 4 shows the nonlinear voltage droop characteristic of the a^{th} VSC with dead-band and voltage limits, for which, the converter power (P_{DCa}) can be expressed as

$$\begin{aligned}
P_{DCa} &= R_{a\,max}\,(V_{DCa\,max} - V_{DCa}) + \left[R_a\left(V_{DCa\,high}^{*} - V_{DCa\,max}\right) + P_{DCa}^{*}\right] \quad for\;\; V_{DCa} \ge V_{DCa\,max} \\
&= R_a\left(V_{DCa\,high}^{*} - V_{DCa}\right) + P_{DCa}^{*} \quad for\;\; V_{DCa\,high}^{*} < V_{DCa} < V_{DCa\,max} \\
&= 0.\left(V_{DCa\,high}^{*} - V_{DCa}\right) + P_{DCa}^{*} \quad for\; V_{DCa\,low}^{*} \le\; V_{DCa} \le V_{DCa\,high}^{*} \\
&= R_a\,(V_{DCa\,low}^{*} - V_{DCa}) + P_{DCa}^{*} \quad for\; V_{DCa\,min} < V_{DCa} < V_{DCa\,low}^{*} \\
&= R_{a\,max}(V_{DCa\,min} - V_{DCa}) + [R_a\,(V_{DCa\,low}^{*} - V_{DCa\,min}) + P_{DCa}^{*}] \quad for\; V_{DCa} \le V_{DCa\,min}
\end{aligned} \tag{17}$$

In this control scheme, the droop control gains can be specified according to the ratings of the converters to share the additional power.

D. DC voltage margin control

In this mode of DC voltage control, the VSC regulates the DC voltage as long as its DC power is within the minimum and maximum power limits. The V-P characteristic corresponding to this scheme is shown in Fig. 5.

1949-3029 (c) 2018 IEEE. Personal use is permitted, but republication/redistribution requires IEEE permission. See http://www.ieee.org/publications_standards/publications/rights/index.html for more information.

This article has been accepted for publication in a future issue of this journal, but has not been fully edited. Content may change prior to final publication. Citation information: DOI 10.1109/TSTE.2018.2870914, IEEE Transactions on Sustainable Energy

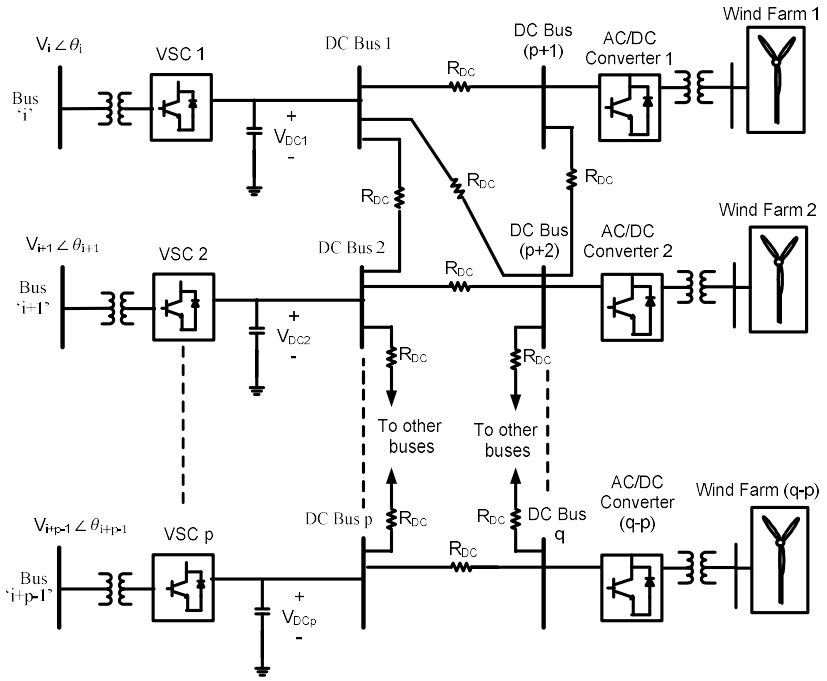


Fig. 1. Schematic diagram of AC-MTDC system with offshore wind farms

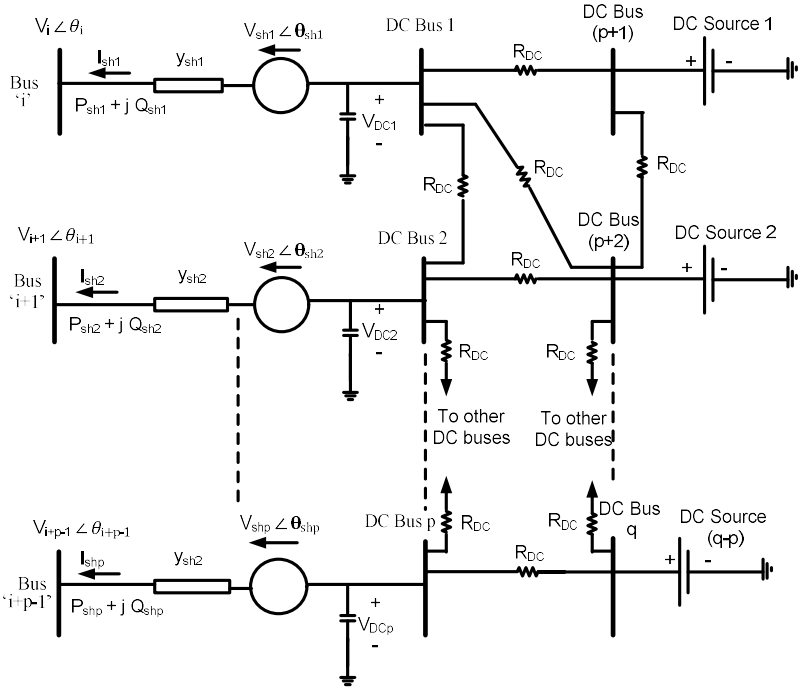


Fig. 2. Equivalent circuit of AC-MTDC system with offshore wind farms

1949-3029 (c) 2018 IEEE. Personal use is permitted, but republication/redistribution requires IEEE permission. See http://www.ieee.org/publications_standards/publications/rights/index.html for more information.

This article has been accepted for publication in a future issue of this journal, but has not been fully edited. Content may change prior to final publication. Citation information: DOI 10.1109/TSTE.2018.2870914, IEEE Transactions on Sustainable Energy

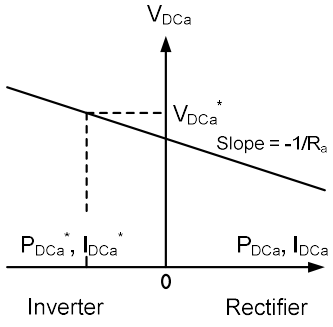


Fig. 3: Linear voltage droop characteristics of the a[th] VSC

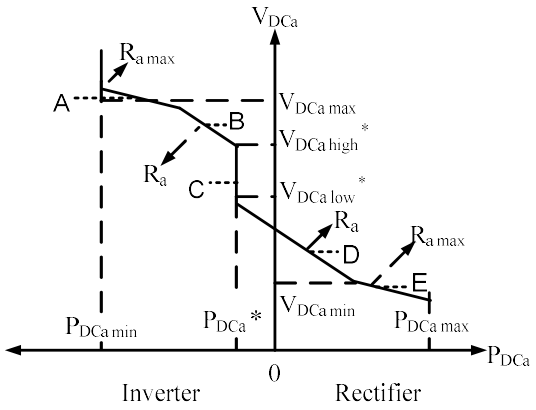


Fig. 4: Nonlinear Voltage Droop Characteristic of the *a[th]* VSC

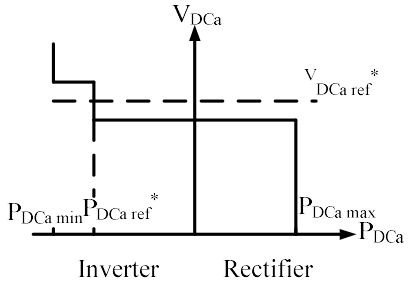


Fig. 5. Voltage Margin Characteristic of the *a[th]* VSC

IV. Newton Power-Flow Equations of AC-MTDC Systems Employing DC Voltage Droop Control

In the AC-MTDC system shown in Fig. 1 and 2, let us assume that there are *'g'* generators connected at the first *'g'* buses of the *'n'* bus AC system with bus 1 being the slack bus. Let us also assume that for the MTDC grid, all the *'p'* VSCs employ linear V-P droop control (Eqn. (14)). While VSC 1 controls the average voltage *'V_{DCav}'* of all the *'p'* DC terminals, the other '(*p-1*)' VSCs control their line active power flows. All the *'p'* VSCs control their line reactive power flows. Then the unified AC-MTDC power-flow problem is of the form

Compute $\boldsymbol{\theta}, \boldsymbol{V}, \boldsymbol{X}$ Specified $\boldsymbol{P}, \boldsymbol{Q}, \boldsymbol{R}$
where

$$\boldsymbol{\theta} = [\theta_2 \dots \theta_n]^T,\ \boldsymbol{V} = [V_{g+1} \dots V_n]^T,\ \boldsymbol{\theta_{sh}} = \left[\theta_{sh1} \dots \theta_{shp}\right]^T,$$

$$\boldsymbol{m} = \left[m_1 \dots m_p\right]^T,\ \boldsymbol{V_{DC}} = \left[V_{DC} \ \dots V_{DCq}\right]^T,$$

$$\boldsymbol{X} = [\boldsymbol{\theta}_{\boldsymbol{sh}}^{\boldsymbol{T}}\ \boldsymbol{m}^{\boldsymbol{T}}\ \boldsymbol{V}_{\boldsymbol{DC}}^{\boldsymbol{T}}]^{\boldsymbol{T}}$$

$$\boldsymbol{P} = [P_2 \dots P_n]^T,\ \boldsymbol{Q} = [Q_{g+1} \dots Q_n]^T,\ \boldsymbol{P_{sh}} = [P_{sh2} \dots P_{shp}],$$

$$\boldsymbol{Q_{sh}} = [Q_{sh1} \dots Q_{shp}],\ \boldsymbol{f_1} = [f_{11} \dots f_{1p}],$$

$$\boldsymbol{P_{DCWF}} = [\ P_{DCWF1} \dots . . P_{DCWF(q-p)}\ ]$$

$$\boldsymbol{R} = [\boldsymbol{P_{sh}}\ \boldsymbol{Q_{sh}}\ V_{DCav}\ \boldsymbol{f_1}\ \boldsymbol{P_{DCWF}}]^T$$

and *'$\boldsymbol{P_{DCWF}}$'* represents the vector of rectified wind farm power injections.
The unified AC-MTDC power-flow equations are solved using the Newton-Raphson (NR) method. The NR power flow equation is

$$\boldsymbol{J}\left[\Delta\boldsymbol{\theta}^{\boldsymbol{T}}\ \Delta\boldsymbol{V}^{\boldsymbol{T}}\ \Delta\boldsymbol{\theta_{sh}}^{\boldsymbol{T}}\ \Delta\boldsymbol{m}^{\boldsymbol{T}}\ \Delta\boldsymbol{V_{DC}}^{\boldsymbol{T}}\right]^{\boldsymbol{T}} = [\Delta\boldsymbol{P}^{\boldsymbol{T}}\ \Delta\boldsymbol{Q}^{\boldsymbol{T}}\ \Delta\boldsymbol{R}^{\boldsymbol{T}}]^{\boldsymbol{T}} \qquad (18)$$

where **J** is the power-flow Jacobian, *'$\Delta\boldsymbol{P}$'*, *'$\Delta\boldsymbol{Q}$'* and *'$\Delta\boldsymbol{R}$'* are the mismatch vectors while $\Delta\boldsymbol{\theta}$, $\Delta\boldsymbol{V}$, $\Delta\boldsymbol{\theta_{sh}}$, $\Delta\boldsymbol{m}$ and $\Delta\boldsymbol{V_{DC}}$ represent the correction vectors.

It may be noted that if a VSC operates in the PV control mode (instead of PQ), the voltage magnitude of its AC terminal bus will be a specified quantity instead of the line reactive power and the Jacobian matrix *'**J**'* will be appropriately modified.

Subsequent to *'V_{DCa}' ($1 \le a \le p$)* being obtained from the AC-MTDC power-flow Eqn. (18), *'P_{DCa}' ($1 \le a \le p$)* is computed. Thereafter, the DC voltage *('V_{DCa}^*')* and power *('P_{DCa}^*')* references of the *'p'* VSC droop lines can be computed using the *'p'* droop equations (Eqn. (14)).
Fig. 6 depicts the flow chart of the AC-MTDC power-flow using the NR algorithm.

V. Case Studies and Results

For validation of the proposed model, a number of case studies were carried out in the IEEE 300-bus test system [34] integrated with a MTDC grid. OWFs are appropriately interfaced with the MTDC grid. The terminal end line active and reactive power specifications of the VSCs, the MTDC control strategy adopted and the rectified power injections of the OWFs are all varied to observe their effects on the convergence features of the proposed technique. All the case studies were implemented in MATLAB. The value of *'c'* for all VSCs was uniformly chosen as $\frac{1}{2\sqrt{2}}$ [4].

Also, for all the VSC coupling transformers, $R_{sha} = 0.001$ p.u. and $X_{sha} = 0.1$ p.u. $(\forall\ a,\ 1 \le a \le p)$. For interconnections between DC terminals, $R_{DCuv} = 0.05$ p.u. $(\forall\ u, v,\ 1 \le u \le q,\ 1 \le v \le q,\ u \ne v)$, throughout the

1949-3029 (c) 2018 IEEE. Personal use is permitted, but republication/redistribution requires IEEE permission. See http://www.ieee.org/publications_standards/publications/rights/index.html for more information.

This article has been accepted for publication in a future issue of this journal, but has not been fully edited. Content may change prior to final publication. Citation information: DOI 10.1109/TSTE.2018.2870914, IEEE Transactions on Sustainable Energy

paper [22]. The converter loss constants 'a_1', 'b_1' and 'c_1' are chosen as 0.011, 0.003 and 0.0043, respectively [24]. In all occurrences, a termination error tolerance of 10^{-10} p.u. was selected. '*IN*' and '*PT*' denote the iteration number and the processing time in seconds, pertaining to a 1.99 GHz Dell PC. In all the results given in Tables I-IV, values of bus voltages, currents, active and reactive powers and droop control gains are denoted in p.u. while phase angles are denoted in degrees.

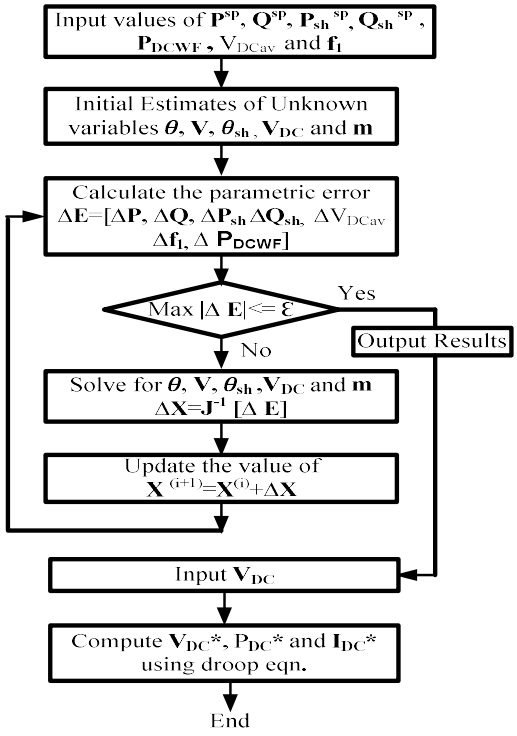


Fig. 6: Flow chart of the AC-MTDC power-flow using NR method

Study 1: DC voltage droop control (linear)

In this study, at first, a base case power flow (without any MTDC grid) was carried out. The results are shown in row 1 of Table 1. Subsequently, a five terminal MTDC grid ($q = 5$) is integrated with the IEEE-300 bus system at AC buses 266, 270 and 292 through VSCs '1', '2' and '3', respectively. While VSCs '1' and '2' follow linear V-P droops, VSC '3' follows a linear V-I droop. Two OWFs ('OWF 1' and 'OWF 2') are appropriately interfaced with the DC grid at terminals 4 and 5, respectively. Their rectifying power injections are P_{DCWF1} = 0.4 p.u. and P_{DC} = 0.5 p.u, respectively. The droop control gains of VSCs 1, 2 and 3 are set to 20, 15 and 10, respectively [19], [21], [23]. The specified quantities are shown in the third row and first column of Table I. The AC-MTDC power-flow (Eqn. (18)) solution is shown in the third row (columns 2-3) of Table I.

From Table I, it can be observed that '*IN*' in the proposed AC-MTDC power-flow model with linear DC voltage droop control remains same as that in the base case power-flow. However, '*PT*' increases than that in the base case as the number of unknowns involved in the AC-MTDC model is more.

TABLE I
AC-MTDC POWER-FLOW WITH LINEAR DC VOLTAGE DROOP CONTROL

<table>
<tr><td colspan="4">Base case power-flow (IN=6 and PT=0.56);
$\boldsymbol{V_{266}} = 1.011\angle -11.24; \boldsymbol{V_{270}} = 1.011\angle -11.32;$
$\boldsymbol{V_{292}} = 1\angle -18.74$</td></tr>
<tr><td colspan="4">Power flow of AC-MTDC system with OWFs
(VSCs connected to AC buses 266, 270 and 292)</td></tr>
<tr><td colspan="2" rowspan="2">Specified quantities</td><td colspan="2">Solution</td></tr>
<tr><td>AC buses</td><td>VSCs</td></tr>
<tr><td>V_{DCav}</td><td>3.0</td><td rowspan="7">$\theta_{266} = -8.338$;
$\theta_{270} = -8.201$;
$\theta_{292} = -5.391$;
$V_{266} = 1.0222$;
$V_{270} = 1.0231$;
$V_{292} = 1.00$;
$P_{sh1} = -0.2423$;</td><td rowspan="5">$\theta_{sh1} = -9.653$; $\theta_{sh2} = -4.976$;
$\theta_{sh3} = -2.5644$;
$V_{DC1} = 3.0008$; $V_{DC2} = 2.9979$;
$V_{DC3} = 2.9983$;
$V_{DC4} = 3.0013$; $V_{DC5} = 3.0017$;
$m_1 = 0.9819$; $m_2 = 0.9812$;
$m_3 = 0.9544$;</td></tr>
<tr><td>Q_{sh1}</td><td>0.2</td></tr>
<tr><td>Q_{sh2}</td><td>0.15</td></tr>
<tr><td>Q_{sh3}</td><td>0.1</td></tr>
<tr><td>P_{sh2}</td><td>0.6</td></tr>
<tr><td>P_{sh3}</td><td>0.5</td></tr>
<tr><td colspan="2" rowspan="2">Rectifying power of offshore wind farms
P_{DCWF1} =0.4;
P_{DCWF2} = 0.5;</td><td>Converter loss (%)
P_{loss} = 1.23;
P_{loss2} = 1.44;
P_{loss3} = 1.36;</td></tr>
<tr><td colspan="2">IN=6; PT=1.00;</td></tr>
<tr><td colspan="4">Computation of references V_{DC}^*, P_{DC}^* and I_{DC}^* from droop equations</td></tr>
<tr><td colspan="4">VSC 1: $R_1 = 20$ (V-P droop); $V_{DC1}^* = 2.9868$; $P_{DC1}^* = 0.5093$;
VSC 2: $R_2 = 15$ (V-P droop); $V_{DC2}^* = 2.9837$; $P_{DC2}^* = -0.4017$;
VSC 3: $R_3 = 10$ (V-I droop); $V_{DC3}^* = 2.9847$; $I_{DC3}^* = -0.0359$;</td></tr>
<tr><td colspan="4">IN=4; PT=0.07;</td></tr>
</table>

After obtaining the 'q' (here q=5) DC terminal voltages from the AC-MTDC power-flow, the DC voltage, power and current references for the linear V-P and V-I droop lines of the 'p' VSCs (here p=3) are obtained from a DC power-flow using the 'p' droop equations given by Eqns. (14) and (16) along with '(q-p)' rectified OWF power injection equations given by Eqn. (13). The results are shown in the last two rows of Table I.

Subsequently, the rectifying power 'P_{DCWF2}' of OWF '2' (connected to DC terminal 5) is gradually varied while that of OWF 1 (connected to DC terminal 4) is maintained constant at 0.4 p.u. The droop control gains of the VSCs are maintained identical to those in the study of Table I. The variation of the VSC DC side voltages ('V_{DC1}', 'V_{DC2}' and 'V_{DC3}') with 'P_{DCWF2}' is shown in Fig. 7.

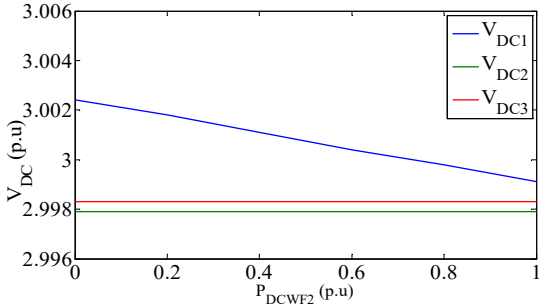


Fig. 7. Variation of the VSC DC side voltages with P_{DCWF2}

Fig. 8 shows the variation of the number of iterations '*IN*' with 'P_{DCWF2}'. It is also observed that unlike [23], '*IN*' is

1949-3029 (c) 2018 IEEE. Personal use is permitted, but republication/redistribution requires IEEE permission. See http://www.ieee.org/publications_standards/publications/rights/index.html for more information.

This article has been accepted for publication in a future issue of this journal, but has not been fully edited. Content may change prior to final publication. Citation information: DOI 10.1109/TSTE.2018.2870914, IEEE Transactions on Sustainable Energy

independent of P_{DCWF2} and remains same as that in the base case power-flow case. This exhibits the robustness of the proposed algorithm.

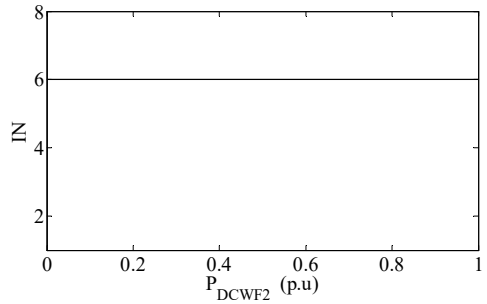


Fig. 8: Variation of *'IN'* with P_{DCWF}

Study 2: DC voltage droop control (nonlinear)

This study is similar to the study carried out in Table I. However, VSC '1' now employs a nonlinear V-P droop characteristic with dead-band and voltage limits (Fig. 4), while VSCs '2' and '3' operate on linear V-P and V-I droop controls, respectively. The droop control gains are kept identical to the study of Table I. The terminal end active and reactive power specifications of all the three VSCs are changed, along with the rectified power injections of the two OWFs.

At first, the AC-MTDC power flow (Eqn. (18)) is carried out. The solution is shown in row 3 and columns 2-3 of Table II. From the power flow solution, it is observed that VSC 1 operates at point *'A'* of the characteristic shown in Fig. 4.

After the AC-MTDC power-flow, the reference values of the droop lines of the three VSCs are computed by using three droop equations and two OWF power injections. The droop equations correspond to Eqns. (17), (14) and (16) for VSCs '1', '2' and '3', respectively while the OWF power injection equations correspond to Eqn. (13). The results are shown in the last two rows of Table II.

Subsequently, VSC '1' is made to operate at different operating points of its non-linear droop characteristic (Fig. 4) by varying the rectifying power of the OWFs. The power flow solution and the corresponding operating points (on the droop characteristic shown in Fig. 4) are shown in Table III.

Finally, another study is carried out on the same AC-MTDC system. In this study, VSCs '1' and '3' again employ linear V-P and V-I droop controls, respectively, while VSC '2' is operated in the DC voltage margin control mode (Fig. 5). The droop control gains of the three VSCs 1 and VSC 3 are maintained identical to those in Table I. The droop control gain of VSC '2' is set to a value of 1000 for voltage margin control. The corresponding maximum and minimum DC power thresholds are set to 1.0 and -1.0 p.u, respectively. The power flow solution is shown in the third row (columns 2-3) of Table IV.

After the AC-MTDC power-flow, the DC voltage, power and current references for the VSC droop lines are again obtained using the three droop equations given in Eqns. (14), (17) and (16) for VSCs '1', '2' and '3', respectively, along with the two rectified OWF power injection equations given by Eqn. (13). The results are shown in the last two rows of Table IV.

TABLE II
AC-MTDC POWER-FLOW WITH NONLINEAR DC VOLTAGE DROOP CONTROL WITH DEAD-BAND AND VOLTAGE LIMITS

<table>
<tr><td colspan="4">Power flow of AC-MTDC system with OWFs
(VSCs connected to AC buses 266, 270 and 292)</td></tr>
<tr><td colspan="2" rowspan="2">Given quantities</td><td colspan="2">Solution</td></tr>
<tr><td>AC buses</td><td>VSCs</td></tr>
<tr><td>V_{DCav}</td><td>3.0</td><td rowspan="7">$\theta_{266} = -10.75$;
$\theta_{270} = -10.57$;
$\theta_{292} = -1.658$;
$V_{266} = 1.0142$;
$V_{270} = 1.0152$;
$V_{292} = 1.00$;</td><td rowspan="2">$\theta_{sh1} = -17.1116$; $\theta_{sh2} = -7.822$;
$\theta_{sh3} = 2.8812$;
$V_{DC} = 3.0038$; $V_{DC2} = 2.9983$;
$V_{DC3} = 2.9973$;
$V_{DC4} = 3.0003$; $V_{DC5} = 3.0003$;
$m_1 = 0.9682$; $m_2 = 0.9667$;
$m_3 = 0.9531$;</td></tr>
<tr><td>Q_{sh1}</td><td>0.09</td></tr>
<tr><td>Q_{sh2}</td><td>0.08</td><td rowspan="5">Converter loss (%)
$P_{loss} = 2$;
$P_{loss2} = 1.36$;
$P_{loss3} = 1.62$;</td></tr>
<tr><td>Q_{sh3}</td><td>0.06</td></tr>
<tr><td>P_{sh2}</td><td>0.5</td></tr>
<tr><td>P_{sh3}</td><td>0.8</td></tr>
<tr><td colspan="2" rowspan="2">Rectifying power of offshore wind farms
P_{DCWF1} =0.1;
P_{DCWF2} =0.1;</td><td colspan="2">*IN*=6; *PT*=1.005;</td></tr>
<tr><td colspan="4">Computation of references V_{DC}^*, P_{DC}^* and I_{DC}^* from droop equations</td></tr>
<tr><td colspan="4">VSC 1: $R_1 = 20$ (Nonlinear V-P droop with dead band); $R_{1\,max} = 30$
V_{DCmax} = 3.0037; $V_{DChigh}^* = 3.0026$; V_{DClow}^* = 3.002; V_{DCmin} = 3;
$V_{DC1}^* = 2.9981$; $P_{DC1}^* = 1.2473$;
VSC 2: $R_2 = 15$ (V-P droop); $V_{DC2}^* = 2.9919$; $P_{DC2}^* = -0.5952$;
VSC 3: $R_3 = 10$ (V-I droop); $V_{DC3}^* = 2.9917$; $I_{DC3}^* = -0.2171$;</td></tr>
<tr><td colspan="4">*IN=4; PT=0.07;*</td></tr>
</table>

TABLE III
POWER FLOW SOLUTIONS AT DIFFERENT OPERATING POINTS ON NONLINEAR DROOP CHARACTERISTIC OF VSC '1'

P_{DCWF1} (p.u)	P_{DCWF2} (p.u)	V_{DC1} (p.u)	θ_{sh1} (deg.)	Operating point
0.1	0.1	3.0038	−17.1116	*A*
0.1	0.4	3.0028	−14.3843	*B*
0.3	0.4	3.0021	−12.5804	*C*
0.5	0.4	3.0014	−10.7891	*D*
0.6	0.8	2.9998	−6.3697	*E*

TABLE IV
AC-MTDC POWER-FLOW WITH NONLINEAR DC VOLTAGE MARGIN CONTROL

<table>
<tr><td colspan="4">Power flow of AC-MTDC system with OWFs
(VSCs connected to AC buses 266, 270 and 292)</td></tr>
<tr><td colspan="2" rowspan="2">Given quantities</td><td colspan="2">Solution</td></tr>
<tr><td>AC buses</td><td>VSCs</td></tr>
<tr><td>V_{DCav}</td><td>3.0</td><td rowspan="7">$\theta_{266} = -6.669$;
$\theta_{270} = -6.490$;
$\theta_{292} = 2.3832$;
$V_{266} = 1.0209$;
$V_{270} = 1.0217$;
$V_{292} = 1.00$;</td><td rowspan="2">$\theta_{sh1} = -6.3697$; $\theta_{sh2} = -3.7741$;
$\theta_{sh3} = 6.923$; $m_1 = 0.9710$;
$m_2 = 0.9727$; $m_3 = 0.9531$;
$V_{DC1} = 2.9998$; $V_{DC2} = 2.9983$;
$V_{DC3} = 2.9973$;
$V_{DC4} = 3.0020$; $V_{DC5} = 3.0027$;</td></tr>
<tr><td>Q_{sh1}</td><td>0.09</td></tr>
<tr><td>Q_{sh2}</td><td>0.08</td><td rowspan="5">Converter loss (%)
$P_{loss} = 1.14$;
$P_{loss2} = 1.35$;
$P_{loss3} = 1.62$;</td></tr>
<tr><td>Q_{sh3}</td><td>0.06</td></tr>
<tr><td>P_{sh2}</td><td>0.5</td></tr>
<tr><td>P_{sh3}</td><td>0.8</td></tr>
<tr><td colspan="2" rowspan="2">Rectifying power of offshore wind farms
P_{DCWF1} =0.6;
P_{DCWF2} =0.8;</td><td colspan="2">*IN*=6; *PT*=1.003;</td></tr>
<tr><td colspan="4">Computation of references V_{DC}^*, P_{DC}^* and I_{DC}^* from droop equations</td></tr>
<tr><td colspan="4">VSC 1: $R_1 = 20$ (V-P droop); $V_{DC1}^* = 2.992$; $P_{DC1}^* = 0.089$;
VSC 2: $R_2 = 1000$ (Voltage margin); P_{DCmin} = - 1; P_{DCmax} = 1;
$V_{DC2}^* = 2.9933$; $P_{DC2}^* = 0.5$;
VSC 3: $R_3 = 10$ (V-I droop); $V_{DC3}^* = 2.9897$; $I_{DC3}^* = -0.1968$;</td></tr>
<tr><td colspan="4">*IN*=4; *PT*=0.07;</td></tr>
</table>

1949-3029 (c) 2018 IEEE. Personal use is permitted, but republication/redistribution requires IEEE permission. See http://www.ieee.org/publications_standards/publications/rights/index.html for more information.

This article has been accepted for publication in a future issue of this journal, but has not been fully edited. Content may change prior to final publication. Citation information: DOI 10.1109/TSTE.2018.2870914, IEEE Transactions on Sustainable Energy

From Tables I-II and IV, it is observed that the number of iterations 'IN' is independent of the operating point specifications and the MTDC control strategy employed. This once again validates the robustness of the proposed technique.

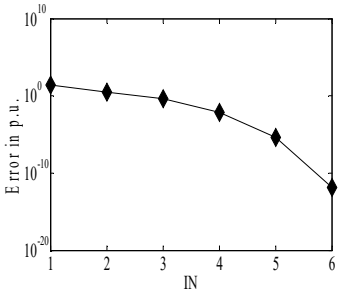


Fig. 9. Convergence characteristic of the base case power-flow

The convergence characteristics of the base case power-flow (first row of Table I) and the AC-MTDC power-flow (Table II) using nonlinear DC voltage droop control (with dead-bands and voltage limits) are shown in Figures 9 and 10, respectively. The convergence characteristics with linear voltage droop and DC voltage margin control, although similar, could not be accommodated due to page limitations.

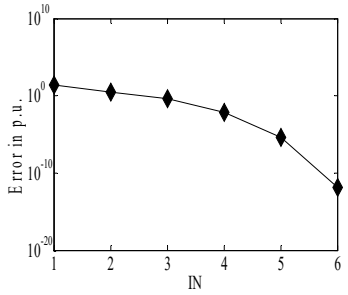


Fig. 10. Convergence characteristic of the AC-MTDC power-flow with nonlinear voltage droop control with dead-band and voltage limits

From Figures 9 and 10, it is observed that unlike [23], the unified NR power-flow algorithm possesses a quadratic convergence characteristic which is independent of the operating point specifications and the MTDC control strategy employed. This validates the proposed technique. Table VI compares the convergence features of the proposed model vis-à-vis some of the existing ones. From Table VI, it can be observed that as compared to an error tolerance of 10^{-8} p.u in a 29-bus test system in [23], the proposed algorithm has a lesser 'PT' with an error tolerance of 10^{-10} p.u in the IEEE 300-bus test system.

Table VI
A COMPARISON OF CONVERGENCE FEATURES WITH EXISTING AC-MTDC POWER-FLOW MODELS

Ref No.	Tolerance (p.u)	No. of buses		*IN*	*PT*
		AC	DC		
[23]	10^{-8}	29	5	Min:3 Max:15	Min:0.37 Max:1.98
[13]	10^{-6}	9	4	6	0.2
		32	4	7	0.45
Proposed Model	10^{-10}	300	NIL	6	Min:0.56 (base case)
			5	6	Max: 1.005 (nonlinear droop)

VI. CONCLUSIONS

In this paper, a unified power-flow model of VSC based hybrid AC-MTDC systems integrated with offshore wind farms (OWFs) has been presented. The power-flow solution is obtained using the Newton-Raphson method. Both the modulation indices and the DC side voltages of the VSCs are obtained directly from the power-flow solution. VSC losses have been included in the model. The performance of the proposed technique is investigated by integrating OWFs with MTDC grids incorporated within the IEEE 300-bus test network. The MTDC grids employ DC voltage droop control. Both linear and nonlinear voltage droop control techniques have been employed. Corresponding to the nonlinear DC voltage droop characteristic with dead-band and voltage limits, five different operating points have been considered. From the case studies, it is observed that the proposed algorithm displays quadratic convergence features independent of the MTDC control strategy and the operating point specifications. A comparison of all the case studies with existing works is also presented.

REFERENCES

[1] J. Arrillaga, Y. H. Liu and N.R Watson, *Flexible Power Transmission: The HVDC Options*, The Atrium, Southern Gate, Chichester, West Sussex PO19 8SQ, England, John Wiley & Sons Ltd, 2007.

[2] V. K. Sood, HVDC and FACTS Controllers – Applications of Static Converters in Power Systems, Kluwer, 2004.

[3] E. Acha, V.G Agelidis, O Anaya Lara and T.J.E. Miller, "*Power Electronic Control in Electrical Systems*", Newnes, Butterworth, 2002.

[4] K.R Padiyar, Multi-terminal and Multi-Infeed DC system in *HVDC Power Transmission Systems*, 2nd ed., New Age International Publishers, 2012.

[5] A. Yazdani and R. Iravani, Voltage-Sourced Converters in Power Systems: Modeling, Control and Applications, Wiley-IEEE Press, 2010.

[6] N. Flourentzou, V.G. Agelidis and G.D. Demetriades, "VSC-Based HVDC power Transmission Systems: An Overview", *IEEE Trans., Power Electronics,* vol. 24, nO. 3, pp. 592-602, March 2009.

[7] Gunnar Asplund, "Application of HVDC Light to Power System Enhancement", *Proc. IEEE PES Winter Meeting, January 2000.*

[8] J. Blau, "Europe Plans a North Sea Grid", *IEEE Spectrum,* pp. 12-13, March 2010.

[9] Temesgen M. Haileselassie, Kjetil Uhlen, "Power System Security in a Meshed North Sea HVDC Grid," *IEEE Proc., Invited Paper,* vol. 101, no. 4, pp. 978-990, April 2013.

[10] X.P. Zhang, "Multi-terminal Voltage-Sourced Converter-based HVDC Models for Power Flow Analysis," *IEEE Trans. Power Syst.,* vol. 19, no. 4 , pp. 1877-1884, Nov. 2004.

[11] C. Angeles-Camacho, O.L Tortelli, E. Acha, and C.R Fuerte-Esquivel, "Inclusion of a High Voltage DC Voltage Source Converter Model in a Newton Raphson Power Flow Algorithm," *Proc. Inst. Elect. Eng., Gen., Transm., Distrib.,* vol 150, no. 6, pp. 691-696, Nov. 2003.

[12] S. Khan and S. Bhowmick, "A Novel Power Flow Model of Multi-terminal VSC HVDC Systems," *Electric Power Systems Research,* vol., 133, no. pp. 219-227, Jan. 2016.

[13] M. Baradar and M. Ghandhari, "A Multi-Option Unified Power Flow Approach for Hybrid AC/DC Grids Incorporating Multi-Terminal VSC-HVDC," *IEEE Trans. Power Syst.,* vol. 28, no. 3, pp. 2376-2383, Aug. 2013.

[14] L. Gengyin, Z.Ming, H. Jie, L. Guangkai, and L. Haifeng, "Power flow calculation of power systems incorporating VSC-HVDC," in *Proc. Int. Conf. Power System Technology (PowerCon)*, Nov. 2004, vol. 2, pp. 1562–1566.

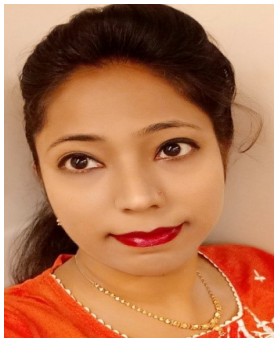
[15] E. Acha, Behzad Kazemtabrizi and Luis M. Castro, "A New VSC HVDC Model for Power Flows Using the Newton Raphson Method," *IEEE Trans. Power Syst*., vol. 28, no. 3, pp. 2602-2612, Aug. 2013.

[16] C. Dierckxsens, "VSC MTDC Systems with Distributed slack bus," Master's thesis, Katholieke Univ., Leuven., Belgium, 2010.

1949-3029 (c) 2018 IEEE. Personal use is permitted, but republication/redistribution requires IEEE permission. See http://www.ieee.org/publications_standards/publications/rights/index.html for more information.

This article has been accepted for publication in a future issue of this journal, but has not been fully edited. Content may change prior to final publication. Citation information: DOI 10.1109/TSTE.2018.2870914, IEEE Transactions on Sustainable Energy

[17] N.R. Chaudhuri, B. Chaudhuri, R. Majumder and Amirnaser, "Autonomous Power Sharing" in Multiterminal Direct Current Grids Modelling Analysis and Control*, first* ed. New Jersey: Wiley IEEE Press, 2014.
[18] K. Rouzbehi, A. Miranian, J.I Candela, A. Luna and P. Rodriguez, "A Generalised Voltage Droop Strategy for Control of Muti-terminal DC Grids," *IEEE Trans. Industry Applications* vol. 51, no. 1, pp. 607-618, Feb. 2015.
[19] A. S. A. Khalik, A. M. Massoud, A. A. Elserougi and S. Ahmed, "Optimum Power Transmission Based Droop Control Design for Multi-terminal HVDC of Offshore Wind Farms," *IEEE Trans. Power Systems,* vol. 28, no. 3, pp. 3401-3409, Aug. 2013.
[20] O. G. Bellmunt, J.Liang, J. Ekanayake and N. Jenkins, "Voltage Current Characteristics of Multi-terminal HVDC VSC for Offshore Wind Farms," *EPSR (ELSEVIER)* vol. 81, no. 2, pp. 440-450, Feb. 2011.
[21] X. Zhao and K. Li, "Droop Setting Design for Multi-terminal HVDC Grids Considering Voltage Deviation Impacts," *EPSR JOURNAL (ELSEVIER)* vol. 123, pp. 67-75, Feb. 2015.
[22] J. Beerten, D. V. Hertem and R. Belmans, "VSC MTDC Systems with a Distributed DC Voltage Control- A Power Flow Approach," *IEEE Trondheim Power Tech*, pp. 1-6, 2011.
[23] W. Wang and M. Barnes, "Power Flow Algorithms for Multi-Terminal VSC-HVDC with Droop Control," *IEEE Trans. Power Systems,* vol. 29 no. *4,* pp. 1721-1730, July 2014.
[24] Cao, J., Du, W., Wang, H.F., "Minimization of Transmission Loss in Meshed AC/DC Grids with VSC-MTDC Networks," *IEEE Trans. Power Systems*, vol. 28, no. 3, pp. 3047-3055, Aug. 2013.
[25] T. M. Haileselassie and K. Uhlem, "Impact of DC Line Voltage Drops on Power Flow of MTDC Using Droop Control," *IEEE Trans. Power Systems,* vol. 27, no. 3, pp. 1441-1448, Aug. 2012.
[26] C. Dierckxsens, K. Srivastava, M. Reza, S. Cole, J. Beerten and R. Belmans, "A Distributed DC Voltage Control Method for VSC MTDC Systems," *EPSR ELSEVIER Journal*, vol. 82, no. 1, pp. 54-58, Jan. 2012.
[27] G. Daelemans, "VSC HVDC in Meshed Networks", Master's Thesis, Katholieke Universiteit Leuven, Belgium, 2008.
[28] L. Xu, B.W. Williams, and L. Yao, "Multi-terminal DC Transmission Systems for Connecting Large Offshore Wind Farms," *IEEE Proc. PES General Meeting- Conversion and Delivery of Electrical Energy,* 21st Century, pp. 1-7, July 2008.
[29] R. da Silva, R. Teodorescu and Rodriguez, "Power Delivery in MTDC Transmission System for Offshore Wind Power Applications," *IEEE Proc. PES ISGT Europe,* pp. 1-8, Oct. 2010.
[30] K. Rouzbehi, A. Miranian, A. Luna and P. Rodriguez, "DC Voltage and Power Sharing in Multi-terminal DC Grids based on Optimal DC Power Flow and Voltage Droop Strategy," *IEEE Journal of Emerging and Selected Topics in Power Electronics*, vol. 2, no. 4, pp. 1171-1180, 2014.
[31] A. Martinez, C. Esquivel, H. Perez and E. Acha, "Modelling of VSC-Based HVDC Systems for a Newton Raphson OPF Algorithm," *IEEE Trans. Power Syst.*, vol. 22, no. 4, pp. 1794-1799, Nov. 2007.
[32] J. Cao and H.F. Wang, "An improved Corrective Security Constrained OPF for Meshed AC/DC Grids With Multi-Terminal VSC-HVDC," *IEEE Trans. Power Systems,* vol. 31, no. 1, pp. 1-11, Jan. 2016.
[33] J. Beerten, S.Cole and Ronnie Belmans, "Generalised Steady State VSC MTDC Model for Sequential AC/DC Power Flow Algorithms," *IEEE Trans. Power Systems,* vol. 27, no. 2, pp. 821-829, May 2012.
[34] http://www.ee.washington.edu/research/pstca.



Shagufta Khan received the Ph.D degree in Electrical Engineering from Delhi Technological University, Delhi, India.
She is presently associated with Galgotias University, Gr. Noida, UP, India, as Assistant Professor in the School of Electrical and Electronics Engineering. Her research interests are power systems and renewable energy.



Suman Bhowmick, B.E., M.E., Ph.D., is a Professor in the Department of Electrical Engineering, Delhi Technological University, Delhi, India. He has more than 25 years of experience in the power sector and the academia. His research interests include Power Systems in general, FACTS and VSC-HVDC.

1949-3029 (c) 2018 IEEE. Personal use is permitted, but republication/redistribution requires IEEE permission. See http://www.ieee.org/publications_standards/publications/rights/index.html for more information.

Engineering Applications of Artificial Intelligence 77 (2019) 21–45

Contents lists available at ScienceDirect

Engineering Applications of Artificial Intelligence

journal homepage: www.elsevier.com/locate/engappai

A review of state-of-the-art techniques for abnormal human activity recognition

Chhavi Dhiman [a], Dinesh Kumar Vishwakarma [b,*]

[a] Department of Electronics and Communication Engineering, Delhi Technological University, Delhi, 110042, India
[b] Department of Information Technology, Delhi Technological University, Delhi, 110042, India

ARTICLE INFO

Keywords:
Two-dimensional anomaly detection
Three-dimensional anomaly detection
Crowd anomaly
Skeleton based fall detection
Ambient Assistive Living

ABSTRACT

The concept of intelligent visual identification of abnormal human activity has raised the standards of surveillance systems, situation cognizance, homeland safety and smart environments. However, abnormal human activity is highly diverse in itself due to the aspects such as (a) the fundamental definition of anomaly (b) feature representation of an anomaly, (c) its application, and henceforth (d) the dataset. This paper aims to summarize various existing abnormal human activity recognition (AbHAR) handcrafted and deep approaches with the variation of the type of information available such as two-dimensional or three-dimensional data. Features play a vital role in an excellent performance of an AbHAR system. The proposed literature provides feature designs of abnormal human activity recognition in a video with respect to the context or application such as fall detection, Ambient Assistive Living (AAL), homeland security, surveillance or crowd analysis using RGB, depth and skeletal evidence. The key contributions and limitations of every feature design technique, under each category: 2D and 3D AbHAR, in respective contexts are tabulated that will provide insight of various abnormal action detection approaches. Finally, the paper outlines newly added datasets for AbHAR by the researchers with added complexities for method validations.

1. Introduction

Abnormal Human Action Recognition (AbHAR) through visual data and sensor data has appealed, tremendous attention in the computer vision community. It is because of its gigantic potential in wide spectrum of areas i.e. Ambient Assistive Living (AAL) (Ismail et al., 2015; Dragone et al., 2015; Andò et al., 2015; Rafferty et al., 2017; Zolfaghari and Keyvanpour, 2016), and healthcare of elderly people (Zhao et al., 2014; Cardile et al., 2010), Intelligent Video surveillance systems (Hsieh et al., 2015; Li et al., 2014a; Coşar et al., 2017; Ben and Zagrouba, 2018), human–computer interfaces (HCI) (Mosquera et al., 2017; Zhu et al., 2017; Feng et al., 2016; Roudposhti et al., 2017; Liu et al., 2014), sports (Zhu et al., 2009; Shih, 2017; Stein et al., 2016), event analysis, robotics (Chien et al., 2005), intrusion detection system (Yu et al., 2016; Aburomman and Reaz, 2016), content-based video analysis (Song and Fan, 2006; Kulkarni et al., 2015), multimedia semantic annotation and indexing (Chou et al., 2017) etc. Abnormal Human Activity Recognition and Anomaly detection are used interchangeably which refers to non-conforming patterns in a given data. Abnormalities are the rarely occurring activities that are different from others. The accuracy and efficiency of the abnormal HAR system depend on the features representing the actions. A robust and highly discriminative feature representation (Vishwakarma et al., 2015b, a, 2016a; Aggarwal and Vishwakarma, 2016) of the action can lead to better recognition results under various challenges i.e. lighting conditions, cluttered background, partial or complete occlusion, crowded scenes, different viewpoint of the camera, size, shape, appearance and complexity of human actions. Such challenges have always pushed forth the researchers to explore new dimensions of the solution from vision-based to sensors based Surveillance Systems integrating multiple features, over the years. Various algorithms (Singh et al., 2016; Chathuramali et al., 2014; Nguyen et al., 2016; Panahi and Ghods, 2018) have been developed keeping different challenging scenarios in mind by the researchers, but one thing remains common that action is defined by two attributes: motion magnitude and motion orientation.

Anomaly detection has been surveyed and reviewed in number of articles, as well as books highlighting various techniques/methods (classification, clustering, nearest neighbor, statistical (Hodge and Austin, 2004), information theoretic and spectral-based techniques) to perform the detection more effectively under different constraints and also various applications such as cyber intrusion detection (Synder, 2001),

* Corresponding author.
E-mail addresses: chhavi1990delhi@gmail.com (C. Dhiman), dvishwakarma@gmail.com (D.K. Vishwakarma).

https://doi.org/10.1016/j.engappai.2018.08.014
Received 6 July 2017; Received in revised form 12 June 2018; Accepted 27 August 2018
0952-1976/© 2018 Elsevier Ltd. All rights reserved.

fraud detection (Chen and Gangopadhyay, 2016), medical anomaly detection, industrial damage detection, image processing, textual anomaly detection (Gorai et al., 2016), sensors networks. This survey focuses on the latest methodologies marking their impacts on the performance of a robust Abnormal HAR system based on two-dimensional (intensity) and three-dimensional (depth/skeleton) input by covering a wide range of applications from a single person based application-AAL, fall detection to multi-persons based application-crowd analysis.

Motivation: The European Statistical Office reported that by 2060, the ratio of young and old person will be 1:1 in the EU (EC, 2012). In addition to it, World Health Organization (World Health Organization, 2008) mentioned that injuries due to fall will shoot up by 100% by 2030. Henceforth, the smart home is drawing a lot of considerations by many researchers (Zolfaghari and Keyvanpour, 2016; Li et al., 2015a; Rashidi and Mihailidis, 2013) to support peoples' health. Technological inventions and development play a significant role in extending support to them through assistive and autonomous care facilities, preferably based on a low-cost setup that can be set up at homes or care centers. Nowadays, depth images have taken over intensity images. Firstly, because they are illumination invariant and can provide a 3D model of the scene. Secondly, with depth images segmentation, background subtraction, and motion estimation, silhouette extraction has been significantly simplified and robust by advancement in depth sensor hardware i.e. time-of-flight (TOF) cameras, low-cost structures light sensor (Microsoft Kinect). Availability of three-dimensional data (depth or skeleton) has opened a different direction for abnormal Human action recognition. Therefore, various real-time depth and skeleton based fall detection systems (Ma et al., 2014; Akagunduz et al., 2016; Zhang et al., 2012; Diraco et al., 2010) are evolving considering the affordable range of the common user and various challenges. In addition to this, deep architectures (Hammerla and Plotz, 2015) have also foot-stepped in the field of computer vision and are used for automatic assessment of Parkinson's disease, AAL applications and many more. The work includes both two-dimensional and three-dimensional AbHAR systems, in which, research is progressing rapidly. The significant contributions of the papers are as follows:

- A structured overview of Abnormal Human Activity Recognition (AbHAR) is provided through the comprehensive survey. Broadly, it covers abnormal human activity recognition i.e. handcrafted-2D and 3D AbHAR based on RGB, depth and skeleton evidence and deep single person and multiple person based methodologies as illustrated in the taxonomy, (Fig. 3).
- A 2D AbHAR state-of-arts for a single person and a multiple persons AbHAR systems have been presented, which target smart home surveillance and also any unusual behavior at a public place (crowd).
- A 3D AbHAR system state-of-arts have been reviewed and presented the depth based, and skeleton based abnormal activity recognition system designs have significant applications in elderly healthcare and AALs, ADL, and fall detection.
- The literature is updated with the application of recent advances of deep neural networks in the field of abnormal human action recognition, Section 3.3 by analyzing the challenges present.
- A systematic arrangement of discussed 2D and 3D features extraction methods have been discussed and well analyzed in Tables 1 and 2 and 4–7 by highlighting their key contributions and limitations.

Organization of our survey is as follows. Section 2, provides a panoramic summary of the related state-of-the-art survey works in the area of abnormal human action recognition followed by paper count analysis per year. It will help the reader to get an overview of key contributions of previous surveys done. Section 3, discusses the outlined taxonomy for categorizing anomaly detection techniques evolved from 2006 to 2018. Every aspect for a robust and real-time abnormal human action recognition system are closely discussed and analyzed in Section 4. Section 5, outlines recently introduced publicly available datasets used for abnormal activity recognition in the mentioned works. Finally, in Section 6, peculiar observations and possible directions are highlighted, that need to further explore for research in the field of AbHAR.

2. Earlier state-of-the-arts surveys

A Reliable and Intelligent Abnormal Behavior Surveillance Systems are the need of the hour to mitigate the effects of abnormal/ undesired activities in public place, health-care organizations and smart homes and other security threats. Therefore, tracking and identifying objects and human motion in surveillance videos, trailed by automatic encapsulation of the content has turn out to be a hot topic of research (Gowsikhaa et al., 2014). Fig. 1 illustrates statistical compilation of some papers on abnormal activity recognition, reviewed in our survey from each category that has evolved over the period 2006 to present. It is clearly evident from the literature that research has increased rapidly in the field of AbHAR (RGB, depth, and skeleton based) in last few years. A Few surveys (Rashidi and Mihailidis, 2013; Chaaraoui et al., 2012) are identified, discussing about computer vision solutions for elderly health care, home surveillance and AAL. Rashidi and Mihailidis (2013) talked about Ambient-Assisted Living tools and techniques for older adults from types of wearable and ambient sensors to vision sensors. Chaaraoui et al. (2012) highlighted the challenges of sensor technologies, limited assistive robot technologies and social security and privacy issues of AAL systems to make it widely acceptable among the users. Whereas, in Li et al. (2015a) the focus is brought to IoT, wearable devices, cloud computing, advanced robotics, sensor networks based assistive living products to discern the wider frontiers of AAL for healthcare, rehabilitation and assistive living. Some surveys (Chen and Wei, 2013; Presti and Cascia, 2016; Edwards et al., 2016; Synnott et al., 2015) conferred about depth imagery based human motion analysis, 3D some skeleton based human action classification and introduced new datasets for handling complex interactions and smart home activities respectively. A broad survey (Popoola and Wan, 2012) of video-based anomaly detection has brought forward diversified work much more in-depth. It defined the characteristics of an anomaly and context-based anomaly which may not be an anomaly in another frame of reference and discussed various scene behavior modeling methods, considering behavior abstraction. Probability of occlusion is relatively less in uncrowded scenes, therefore tracking based approach (Piciarelli and Foresti, 2011) is suitable for action pattern mining in uncrowded videos. However, in crowded scenes pixel level or frame level anomaly detection should be preferred to handle occlusion.

Over the year's behavior modeling focus has shifted from rule-based methods to probability-based statistical methods, being superior in robustness and scalability. But the real challenge still lies in making the system free from human interventions and minimizing false alarm (positive/negative) rate. For which global and local features have proved to be highly descriptive and discriminative in nature to encode the behavior. In addition to it, trajectory, speed, and direction, optical flow, object-based abstraction methods are also used for complete abstraction of the scene behavior. Whereas, for high dimensional behavior modeling, learning with Generative Topic Model framework (Popoola and Wan, 2012) generate more robust sparse spatial–temporal interest points than and can determine eloquent activities from co-occurrence of visual words automatically. Such complex scene models are validated with UMN dataset (Detection of unusual crowd activity dataset, 2006), web dataset (Web Dataset, 2009), UCSD (UCSD Anomaly Detection Dataset, 2013), CAVIAR (CAVIAR Test Case, 2005), PETS dataset (Patino et al., 2016), which are grouped based on the scene density i.e. single person, sparse, relatively dense. From the literature (Turaga et al., 2008), it is notified that graphical models (i.e. dynamic Bayes net, propagation nets, Petri nets), syntactic (i.e. context-free grammars, attribute grammar and stochastic CFG), and knowledge-based approaches (i.e. ontologies, logic rules, constraint satisfaction) are

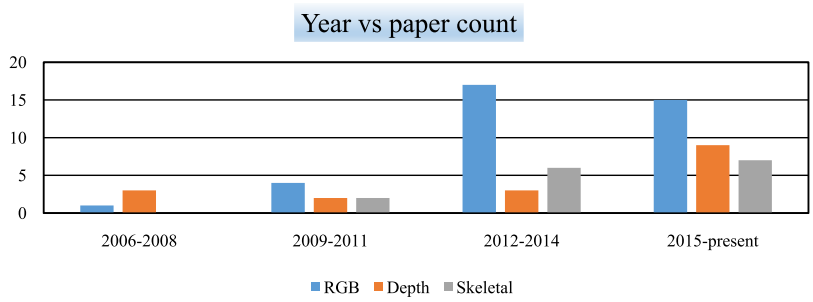


Fig. 1. The graph demonstrates the number of papers reported in this survey on AbHAR from 2006–present.

preferred to model complex scenes, the inherent structure and semantics of complex activities and provide higher level representation for activity recognition. Whereas, Chandola et al. (2009) covered wide application areas of anomaly detection i.e. anomaly detection in scripts, sensor network, image processing, medical and communal health anomaly detection, fraud detection, network intrusion detection.

Fall (Aslan et al., 2017) is one of the major unusual events occurring at any public or private place that needs to be identified well in time and help should be extended according to the severity of fall (child/older person). A comprehensive survey (Mubashir et al., 2013) is laid out describing various existing approaches for fall detection dividing them into three categories such as wearable device, ambient device, and vision-based approaches. Wearable and ambient device based methodologies are scenario dependent whereas vision-based approaches are generalized, which induce no intrusion to the person under surveillance.

In vision-based approaches (Nguyen et al., 2016; Panahi and Ghods, 2018; Rougier et al., 2011b; Jansen and Deklerck, 2006) spatiotemporal details, shape deformation features, posture information and inactivity information after fall, and 3D head position have been used enormously over the years to design an efficient real-time fall detection system with standard computing platforms, and low-cost cameras but a wide area is still untouched that deals with the robustness of the system. Recently in Chen and Wei (2013), an overview of various available depth sensors and their benefits over conventional cameras are stated. It is noticed that the growing research area is addressing human action recognition as normal or abnormal and focusing on depth based body part detection and pose estimation, body pose modeling, and space–time evidences. Synnott et al. (2015) discussed the need for simulated sensor data generated in the field of behavior analysis algorithm/models/data-driven learning approaches/classification mechanisms. All the pose oriented datasets introduced between 2009 and 2015 are reviewed in the survey (Edwards et al., 2016). A new dataset CONVERSE representing Complex Conversational Interactions between two individuals via 3D poses in the survey has opened more possibilities for Abnormal Human activity Recognition (AbHAR). This dataset caters real-world challenging scenarios incorporating frequent primitive actions, interactions, and motion over a period of time. It is clearly evident that in this decade, it is the vantage point for posed based 3D abnormal human activity recognition in research where enormous information is available Presti and Cascia (2016) discussed different aspects of data pre-processing, publically available benchmarks, and commonly used accuracy measurements along with feature representation and 3D Skeleton based action classification at length. In the year 2013 three kinds of literature (Thida et al., 2013; Jo et al., 2013; Kok et al., 2016) were presented which laid out three different perspectives of crowd analysis. Thida et al. (2013) emphasized macroscopic and microscopic modeling with crowd event detection. Jo et al. (2013) highlighted physic based approaches for the crowd and group analysis in computer vision whereas, Kok et al. (2016) discussed state-of-the-art methods from the physics and biologically inspired perspective for crowd activity analysis as shown in Fig. 2.

Li et al. (2015b) have drawn a general structure of crowd scene analysis. According to which, crowd activity can be recognized via holistic approach or object-based approach. Initially, authors (Zitouni et al., 2016) talked about various motion representation methods in crowd scenes- flow-based features, spatiotemporal features and trajectory based features and motion pattern segmentation techniques — Flow Field Model-based segmentation, correspondence-based clustering, and probability-based model clustering. The recent work by Tripathi et al. (2018) defined four aspects of crowd analysis with recent advances of CNN architectures, as Crowd counting and density estimation, Crowd motion detection, Crowd tracking, Crowd behavior understanding and their benefits over traditional methods (Loy et al., 2013; Hassner et al., 2012). The work addresses the fact that three steps must be followed to analyze crowd behavior with real-time challenges i.e. crowd modeling, crowd monitoring and crowd management it deals with all the strategic decision-making to control the crowd by maintaining social i to optimize operational efficiency.

3. Abnormal human activity recognition methods

Abnormal Human Activity Recognition (AbHAR) methods can be broadly categorized into Two-Dimensional AbHAR systems and Three-Dimensional AbHAR systems on the basic type of input fed to the system. The detailed classification of AbHAR system is shown in Fig. 3. A two-dimensional AbHAR system is fed with 2D silhouettes for single person AbHAR in the majority of mentioned approaches. Whereas, three-dimensional AbHAR systems are fed with depth silhouettes and skeleton structures of the person for AbHAR. Both kinds of approaches have their own set of applications and benefits. A detailed description of feature representation of the abnormal human activity is mentioned in Sections 3.1 and 3.2 with an analytical discussion in Section 3.3.

3.1. Two-Dimensional AbHAR

The RGB intensity and object detection (spatial information) are some elementary observations of an image. A significant amount of research has been done by researchers using 2D RGB/intensity/spatial information of an image for normal and abnormal HAR systems. In this section, 2D-AbHAR approaches are broadly categorized as single person AbHAR and Multiple Persons AbHAR. The former one is further grouped as silhouette based, Spatio-temporal based approaches and some miscellaneous techniques on the bases of their significant contributions in understanding the single person action recognition. Multiple Persons AbHAR methods are summarized as Spatio-temporal approaches, sparse representations based approaches and some miscellaneous ones. In each category different types of feature representations of action are discussed to provide a brief understanding of existing methods.

3.1.1. Single person AbHAR

One of the major application of Single Person AbHAR is in Ambient Assistance Living (AAL), home monitoring where a single person is under surveillance for abnormal activity recognition. Therefore, in this section, we have included single person AbHAR methodologies supporting elderly health care issues and AAL (Li et al., 2015a). Table 1 briefs

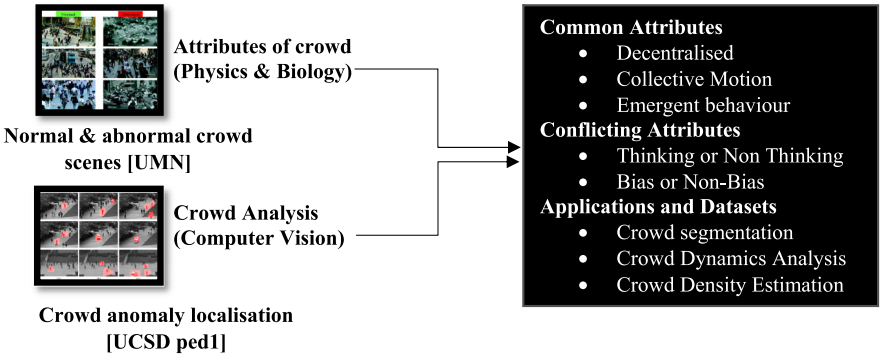


Fig. 2. Crowd Analysis (Kok et al., 2016).

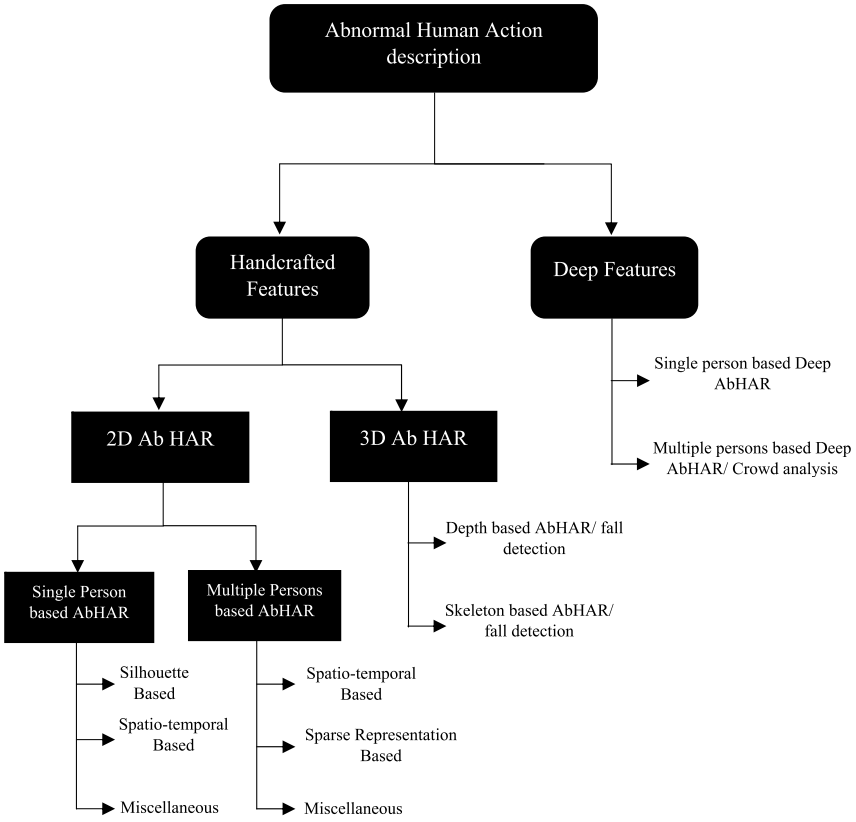


Fig. 3. Taxonomy of Abnormal Human Activity Recognition (AbHAR).

about various approaches based on two-dimensional fundamentals for single person activity recognition. It highlights the scene representation and feature extraction techniques with individual's key elements and limitations for a better understanding of the method.

It can be observed from Table 1that LOTAR framework (Riboni et al., 2016) offers a stronger feature representation platform for AAL application which analyzes both short term and long term anomalies by collecting data from multiple sensors i.e. temperature, pressure & RFID sensors along with vision sensors. For experimentation, the framework is employed in the real patient home, which needs to be extended to multiple individuals for realistic results. And in work (Huang et al., 2014), the habit of the person is studied and analyzed for the first time by fusing ISUS (Intelligent space for understanding and service) and multi-camera positioning algorithm. Single Person, AbHAR approaches are discussed in detail by categorizing them as silhouette based, spatiotemporal based and some miscellaneous approaches, below.

3.1.1.1. Silhouette-based approaches. Robustness of any AbHAR method depends on how efficiently action evidence in an image are extracted as a feature. R-Transform has been used frequently (Khan and Sohn, 2013, 2011) to target elderly health care issues and providing a highly practical solution to it. Khan and Sohn (2011) took into account six possible unusual activities (i) faint (ii) backward fall (iii) forward fall (iv) vomit (v) chest pain and (vi) a headache (see Fig. 5). It integrated R-Transform with Kernel Discriminant Analysis (KDA) to minimize interclass similarity of different activity postures as binary silhouette maintaining individual's privacy.

Khan and Sohn (2013) designed a two-level hierarchical anomalous human activity recognition system to increase the recognition rate for intra-class activities, particularly for falling forward-vomiting postures and falling backward-fainting postures. The first level performs KDA on the R-Transform of binary silhouettes. In the second level, a k-mean clustering algorithm is applied to make groups of similar postures and four state HMM classifier in training and recognition of the activities

Table 1
Scene representation & feature abstraction techniques for two-dimensional single person abnormal human activity recognition (AbHAR) approaches.

Scene representation & feature abstraction techniques	Year	Ref.	Key contributions	Limitations
HMM + SVM	2010	Hung et al. (2010)	Inexpensive sensor network	Collect data from RFID-based sensor network
Separable linear filter (spatiotemporal feature) +Topic HMM	2011	Zhu and Liu (2011a)	Efficient extraction of variable length action sequences and construct highly descriptive features.	THMM is sensitive to the noise of Spatio-temporal words.
R-Transform and Kernel Discriminant Analysis	2013, 2011	Khan and Sohn (2013) and Khan and Sohn (2011)	Scale and translational invariant and reduced intraclass false recognition rate (FRR)	Binary silhouettes used create ambiguities in discerning the certain postures in case of self-occlusion (front-view)
Jerk based Inactivity Magnitude (JIM) feature	2014	Candás et al. (2014)	An autonomous framework that makes no assumptions about the activity data distribution	The experiment needs to be performed with more users under different conditions.
Key points' duration histogram	2014	Huang et al. (2014)	multi-camera positioning algorithm advances the positioning accuracy	The method can be applied in the intelligent space where the elderly lives regularly
Shape Model based on OMEGA equation	2016	Al-Nawash et al. (2016)	automatic real-time video-based surveillance system with simultaneous tracking, semantic scene learning, and abnormality detection ability in an academic environment	The complexity of the algorithm is not discussed
LOTAR framework	2016	Riboni et al. (2016)	Detects both Short term and Long term anomalies	Heavily depends on indicator models developed by cognitive neuroscience experts.

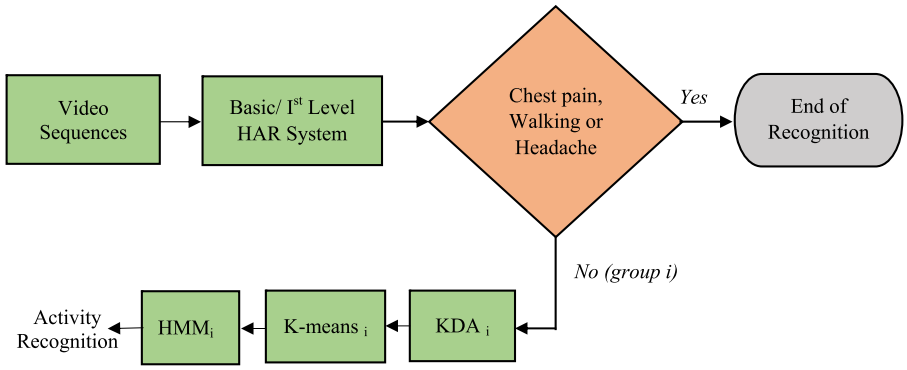


Fig. 4. Block diagram of hierarchical HAR system.

(see in Fig. 4). This hierarchical approach has increased the average recognition rate of similar activities to 97.1% in a confined environment which needs to be extended with real-time abnormal activity dataset augmented with noise. Binary silhouette fails to describe the posture in case of self-occlusion, this limitation can be removed using depth silhouettes . Early detection of short-term or long-term abnormal behavior of the person under AAL (Ambient Assistive Living) is emerging as a promising field of abnormal activity recognition. With the help of medical models, provided by cognitive neuroscience researchers a FABER hybrid technique is presented (Riboni et al., 2015) which focuses on abnormal activity routines to identify symptoms of mild cognitive impairment (MCI) at a fine-grained level with the assimilation of supervised learning and symbolic reasoning i.e. problems with memory, language, thinking, and judgment which is a significant information for early detection of MCI.

Generally, the camera or sensor-based monitoring systems (Crispim Junior et al., 2012) in the closed environment have the limitation of individual privacy. The approaches which monitor low-level behavioral indicators such as walking speed steps taken, they fail to acquire fine-grained depiction of the action during execution of Instrumental Activities of Daily Living (IADL). Some approaches (Sacco et al., 2012) require high implementation cost and cannot be applied

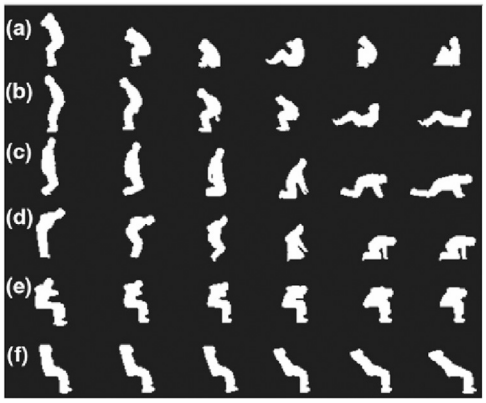


Fig. 5. Selected postures for the six abnormal activities: (a) fainting, (b) falling backward, (c) falling forward, (d) vomiting, (e) chest pain, and (f) a headache (Khan and Sohn, 2013).

for a long-term basis. For long-term abnormal behavior recognition, Riboni et al. (2016) developed a LOTAR framework (see Fig. 6) which

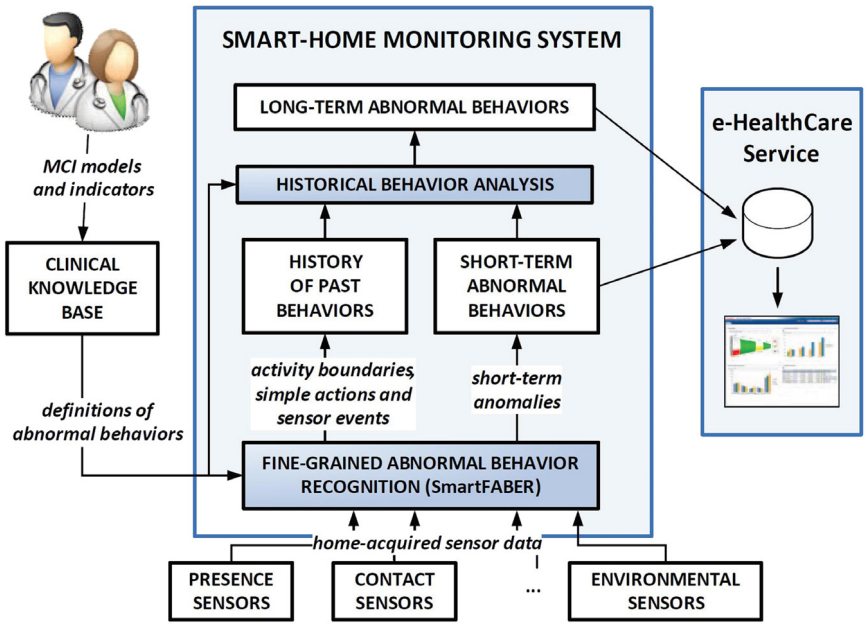


Fig. 6. The LOTAR framework to recognize long-term abnormal behaviors (Riboni et al., 2016).

is a hybrid behavior analysis system integrated with knowledge-based and data mining based machine learning techniques. It acquires data from non-intrusive sensors set up in the patient's home preserving the individual's privacy and fine-grained process statistics vital for long-term abnormal behavior recognition.

3.1.1.2. Spatio-temporal based approaches. It has been seen that spatiotemporal representation (Vishwakarma and Singh, 2016; Diba and Gool, 2016; Guo et al., 2008; Li et al., 2015c) is used abundantly to describe the actions in a video sequence for normal/abnormal human action recognition. Li et al. (2015c), utilised spatiotemporal contextual details for anomaly detection and localization from captured video volumes.

An unsupervised statistical learning structure is developed which excavates global activity patterns and local salient behavior patterns using clustering and sparse coding respectively along with multiple scale analysis to detect and localize the anomalous region efficiently. However, during this process, codebook and dictionary learning algorithm must update them for new input videos to cater a practical solution in real-time applications. Phase Spectrum of Quaternion Fourier Transform (PQFT) (Guo et al., 2008) is identified as a potential solution for the spatiotemporal Salience Detection in videos frames. It has been demonstrated experimentally that PQFT works with less computational complexity, being robust to noise and faster than existing methods i.e. spectral Residue (SR), Phase Spectrum of Fourier Transform (PFT), Neuromorphic Vision Toolbox (NVT), and Saliency Toolbox (SBT). Addition of motion cue with PQFT further strengthens the representation of spatiotemporal saliency in videos in the presence of white-colored noise. However, if the noise is similar to salient object, the approach fails to detect the saliency. PQFT cannot detect the closure patterns of the image, which humans can identify very quickly in an image. Vishwakarma et al. (2016b) defined an activity recognition framework using shape and motion orientation of the object as baseline features. In which spatial edge distribution of gradients and texture based segmentation technique are used to extract binary silhouette. However, the work needs to be evaluated with more complex and real-life environment to provide the solution for real-life applications.

3.1.1.3. Miscellaneous. Nowadays the existing methods (classification based, clustering based and statistical methods) for abnormal human behavior detection are facing the challenge of making the system independent of human arbitrations. Candás et al. (2014) made an attempt technique to detect human behavior abnormality autonomously, without making any assumption using Jerk based Inactivity Magnitude (JIM) feature. However, the experimental work needs to be extended for more users and under different conditions. Huang et al. (2014) utilised intelligent space for understanding and user service (ISUS) for abnormal habit recognition problem, for the first time, with multi-camera positioning algorithm to locate the person using the concept of distribution of time spent at different duration histogram of key points in the intelligent system under surveillance for the entire day that makes the habit recognition task simpler. However, the application of this model is limited to ISUS environment to monitor the habit of the elder people, which may not be under affordable range of an individual. There is a need to develop low-cost fall detector (Miguel et al., 2017) for smart homes based on artificial vision algorithms that can be available in affordable range to the common man.

3.1.2. Multiple persons AbHAR

Multiple Persons AbHAR is a generalized case of Crowd Activity analysis, which are used interchangeably in this review. It is a novel area of interest in computer vision which will potentially advance to new application domain such as automatic detection of riots or chaotic acts in crowd and localization of the abnormal areas in scenes for high resolution investigation. Occlusions and ambiguities in crowded scenes with complex activities and scene semantics are some of the challenges needs to be addressed for crowd activity analysis. It is systematically studied in the field of transportation and communal security. But the level of complexity is very high to define the complete crowd activity with the help of a feature. There are two approaches to analyze the crowd activity (1) identify group activity patterns — abnormal activity localization (Antic and Ommer, 2015; Fagette et al., 2014) (2) represent an individual's behavior in the crowd i.e. trajectory-based approach (Chathuramali et al., 2014), and shape dynamics based approach (Vaswani et al., 2005). Table 2outlines various approaches for multiple persons AbHAR specifying feature abstraction methods with their key elements of the approaches and their limitations.

It is observed from Table 2 that the optical flow based motion descriptions — SOF (Chathuramali et al., 2014), MHOF (Cong et al., 2013), HNF (HOG + HOF) (Zhao et al., 2015), Histogram of Maximal Optical Flow Projection (HMOFP) (Li et al., 2016), extract meaningful statistics

Table 2
Scene representation & feature abstraction techniques for two-dimensional multiple persons abnormal human activity recognition (AbHAR) approaches.

Scene representation & feature abstraction techniques	Year	Ref.	Key elements	Limitations
Trajectory Sparse Reconstruction Analysis	2012	Li et al. (2012)	Number of control points and weight factors, makes the method flexible to adapt to the complicated shape of curves.	Performance is highly sensitive to control point parameters of the trajectory.
Spatio-temporal volume construction	2013	Roshtkhari and Levine (2013)	Robust to spatial and temporal scale variations under varying brightness conditions.	Fails to detect an anomaly in sudden variations in dynamic backgrounds
Silhouettes and Optic Flow-based Features (SOF) +Dense Trajectory-based Features (DTF)	2014	Chathuramali et al. (2014)	Adaptive to dynamic background	The complexity of DTF descriptor generation is high
Laplacian Eigen-map (LE)	2013	Eng et al. (2013)	Local probabilistic model allows to detect abnormalities in both local and global contexts	pixel-level abnormality localization is responsible for high computation cost
Dynamic Patch Grouping(DPG) +Multilayer Histogram of Optical Flow (MHOF) Edge Orientation Histogram (EOH)	2013	Cong et al. (2013)	DPG adaptively cluster similar patches and process only foreground region which makes it computationally efficient	DPG performance reduces with increase in the size of patch and noise in the frame.
A mixture of dynamic textures (MDT) models	2014	Li et al. (2014b)	Spatial and temporal scores at multiple scales ensure global uniformity of anomaly decision	Occlusion is not discussed
Dominant sets	2014	Alvar et al. (2014)	sparse representation	A sudden change in direction and speed are responsible for FP error
Laplacian Sparse Representation (LSR) of spatiotemporal HNF (HOG + HOF) feature	2015	Zhao et al. (2015)	LSR is responsible for minimum feature quantization error	Computational time involved in feature generation is not discussed
Histogram of Maximal Optical Flow Projection (HMOFP) descriptor	2016	Li et al. (2016)	K-SVD is used for dictionary optimization	User-defined threshold τ controls the abnormal event detection
ICA-based linear representation model-(off-line long-term sparse representation (LTSR) and on-line short-term sparse representation (STSR))	2016	Wang et al. (2017b)	High computational efficiency due to selective visual attention analysis	Needs better saliency detection method.
Region Association Graph (RAG)	2017	Dogra et al. (2015)	Movement patterns-trajectories	Manual classification of trajectories is required for supervised training (HMM)

to describe densely crowded scenes. The trajectory-based methods — Region Association Graph (RAG) (Dogra et al., 2015), Dense Trajectory-based Features (DTF) (Chathuramali et al., 2014; Li et al., 2012) can easily handle the complexity of shapes but involves high computational cost. Recently Saini et al. (2017) extended the concept of RAG by defining a high-level non-overlapping block based scene representation using raw object trajectories for video scene segmentation. As far as real-time applicability of the method is concerned, ICA-based linear representation model (Wang et al., 2017b) is implemented in a real-time scenario with high computational efficiency due to selective visual attention analysis using both long term and short term sparse representation of crowded scenes. Multiple persons AbHAR based approaches are discussed in detail by categorizing them as Spatio-temporal based approaches, sparse representation based approaches, and miscellaneous ones.

3.1.2.1. Spatio-temporal based approaches. Effective encryption of complex details of the dynamic background and multiple variations of foreground in crowded or public place demands both spatial and temporal information (Zhan et al., 2016) of the scenes. In the work (Mehran et al., 2009) dynamics of a crowd is represented using social force model without tracking the objects. Where moving particles are considered as individuals whose new positions are measured with space–time average of optical flow. And Force Flow is observed for each pixel of every frame and arbitrarily selected spatiotemporal volumes of Force Flow are used to design the ordinary activity/ behavior of the crowd. In this work, bag of words methodology is used for classification of frames as normal/abnormal. Escape panic scenarios of UMN dataset (Detection of unusual crowd activity dataset, 0000), a challenging and interesting crowd videos datasets from the web (Web Dataset, 2009) are used for validation of this scheme. To overcome unstable foreground excavation, crowd distribution is defined with the concept of particle entropy (Gu et al., 2014) integrated with GMM. Eng et al. (2013) used the concept of Laplacian Eigen-map (LE) to detect and localize the abnormality in the video scene robustly. It represents the local regions and edges in frame as nodes of a graph. And the nodes are assigned with weights by considering the relation of local regions on the basis of joint similarity in feature, space and time domain. Since the dynamics of the crowd changes instantaneously, therefore, less computation time to perform the task in real life crowded scenes is one of the key issues, which is difficult to achieve in graph-based approaches. In one of the studies (Wang et al., 2017b) the author aims to detect and localize the abnormal act in crowd using the concept of visual attention analysis. The presented approach used two sparse coding strategies: Off-line long-term sparse representation and online short-term sparse representation, for spatiotemporal feature extraction. Dense Trajectory-based features (DTF) (Chathuramali et al., 2014) can handle dynamics of the background with near to perfect accuracy however, DTF fail when both normal and abnormal actions occur in the same frame and require high performance hardware. DTF–SOF descriptors are used to train SVM lending small time complexity. A recent work (Saini et al., 2017) highlighted the importance of complete scene understanding along with motion detection by defining block based scene representation. It extracted high-level features from object trajectories using non-overlapping block-based representation of surveillance scene. And Hidden Markov Model (HMM) learned the parameters that describes the dynamics of a given surveillance scene. Anomaly detection can also be formulated either as an outlier detection

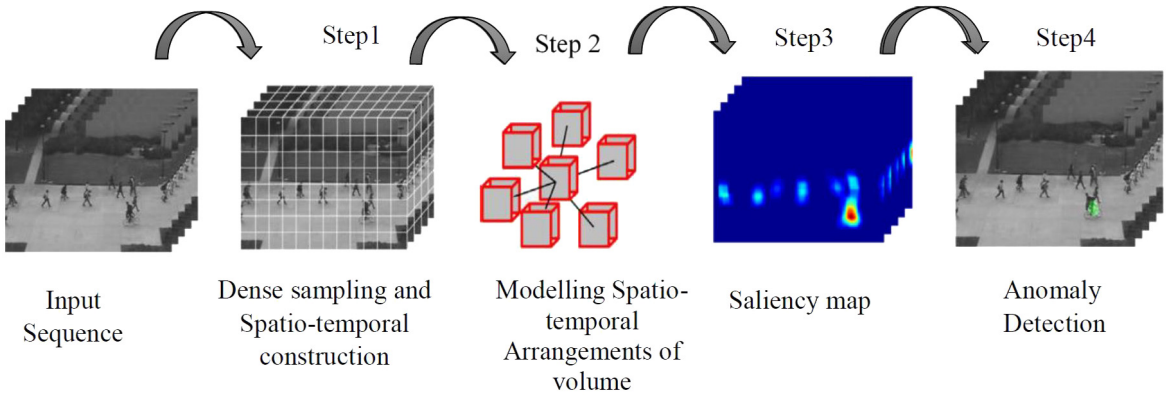


Fig. 7. An on-line, real-time learning method for detecting anomalies in videos using Spatio-temporal compositions (Roshtkhari and Levine, 2013).

process or as a reconstruction process (Roshtkhari and Levine, 2013). At different spatial and temporal scales, spatiotemporal compositions of the video volume are created and analogous spatiotemporal volumes are clustered. It helped to detect anomaly without background subtraction and tracking, as shown in Fig. 7. This framework performs well even in the concurrent occurrence of normal and doubtful events in the video. Zhu and Liu (2011b) used spatiotemporal interest point to give a compact representation to human actions and similar human actions patterns are grouped using Topic Hidden Markov Model (HMM: based on HMM and LDA) clustering technique. The presented THMM clustering approach offers smaller computational complexity. However, spatial and temporal arrangements of local features can provide fine details to develop compact video representation. Another work (Roshtkhari and Levine, 2013), segregated the video into three components: background, dominant activities and rare activities (bicyclist in walking pedestrians) and learn the video events for every pixel without supervision using closely built hierarchical codebook of spatiotemporal video volume (STVs), Fig. 8. The major advantage of this method is that it is adaptive to variable background conditions and illuminations and requires less number of initialization frames (200 frames compared to 6400 frames). But it fails to learn long time behaviors. Li et al. (2014b) utilised crowd dynamics as well as crowd appearance in the video jointly using mixture of dynamic textures (MDT) models. These texture models account for designing center-surrounded discriminant saliency detector and normal behavior model which produces spatial saliency score and temporal saliency score respectively at different scales. Here, multiscale scores strongly support capabilities of a conditional random field.

(CRF) that assures reliability of the abnormality decision globally. In addition to this, authors presented an anomaly detection dataset to address complex scenes of pedestrian crowds i.e. stochastic motion, complex occlusions, and entity interactions. It offers both frame-level and pixel-level ground truth, and also a protocol for anomaly detection algorithms authentication. Antic and Ommer (2011) presented a probabilistic model to detect abnormality in a video which consists irregular objects and sequence of activities. The task becomes more challenging when sufficient abnormal activities-training data is not available. In this model, while video parsing, a hypothesis layout is obtained that jointly describes the scene (foreground) instead of detecting individual hypothesis. This work is extended by the authors in Antic and Ommer (2015) in which their goal of video parsing is to determine a set of necessary normal spatiotemporal object hypotheses that mutually describe foreground of a video supporting normal training samples. Further, MAP inference in graphical method is explored for abnormality localization efficiently using it as a convex optimization problem (UCSD ped1, ped2) dataset. Abnormal event detection is formulated as a matching problem being more robust than statistic model-based methods, particularly for small training dataset. Cong et al. (2013) outlined region-based descriptor called "*Motion Context*", by incorporating both motion — the Multilayer Histogram of Optical Flow (MHOF) and appearance — Edge Orientation Histogram (EOH), evidence of the spatiotemporal video segments. Han et al. (2016) looks for latent action patterns among crowd activities using the concept of visual attention mechanism with spatiotemporal saliency-based representation and divide them in significant groups using affinity matrix based N-cut.

3.1.2.2. Sparse Representation based approaches. Sparse models provide unique discrimination ability to the descriptors which has made sparse representation a popular approach for abnormal behavior detection. Li et al. (2016) defined Histogram of Maximal Optical Flow Projection (HMOFP) descriptor and used it for dictionary optimization and computing 'l1' norm of sparse reconstruction coefficient (SRC) for crowd anomaly detection in the test frame. The combination of spatiotemporal features and its Laplacian Sparse representation is reported in Zhao et al. (2015) to identify a normalized combinational vector HNF (HOG + HOF), as shown in Fig. 9.

It is made more descriptive with minimized feature quantization error, by Laplacian sparse representation and maximum pooling. It is noted that the presented approach detects both global and local abnormal activities with 93% accuracy for UMN dataset (Detection of unusual crowd activity dataset, 0000). Whereas, for trajectory sparse reconstruction analysis (SRA) (Li et al., 2012) control point features of cubic B-spline curves are extracted from sequence of normal actions trajectory to build a normal dictionary set. In testing phase of abnormal event detection, sparse linear reconstruction coefficients and residuals help to decide normal or abnormal event. However, one of the limitations of this approach is that its performance is highly sensitive to the control point parameters of the trajectory. The recent work (Liu et al., 2017) observed the crowd motion using a double sparse representation with a dynamic dictionary updating mechanism that increases the size of dictionary dynamically for a small set of training samples. Dominant Set (DS) has emerged as a powerful technique to detect any abnormal behavior in an unsupervised framework (Alvar et al., 2014) that provide a locally adaptive boundary to represent the unknown data points sparsely. Experimentally, it is identified that Dominant Sets produce smallest overall error rate in comparison to other clustering algorithms i.e. KNN, a mixture of Gaussians, fuzzy k-means.

3.1.2.3. Miscellaneous. In a group activity, the shape of the objects deforms continuously. Co-occurrence statistics and dynamic Bayesian networks are used for group activity modeling which fails when objects are large in an activity. This problem can be avoided by treating interacting objects as point objects or landmarks. Kendall's shape theory proved to be valuable to represent shape deformations of a discrete landmark in Vaswani et al. (2005). A continuous-state Hidden Markov Model is defined for each landmark shape dynamics in an activity. Where, for each landmark, scaled Euclidean motion parameters, and corresponding shape, together, are used to describe the hidden state vector of the HMM. The conceptualization of the use of shape and its dynamics for abnormal activity detection makes it translation, in-plane rotation or sensor zoom invariant.

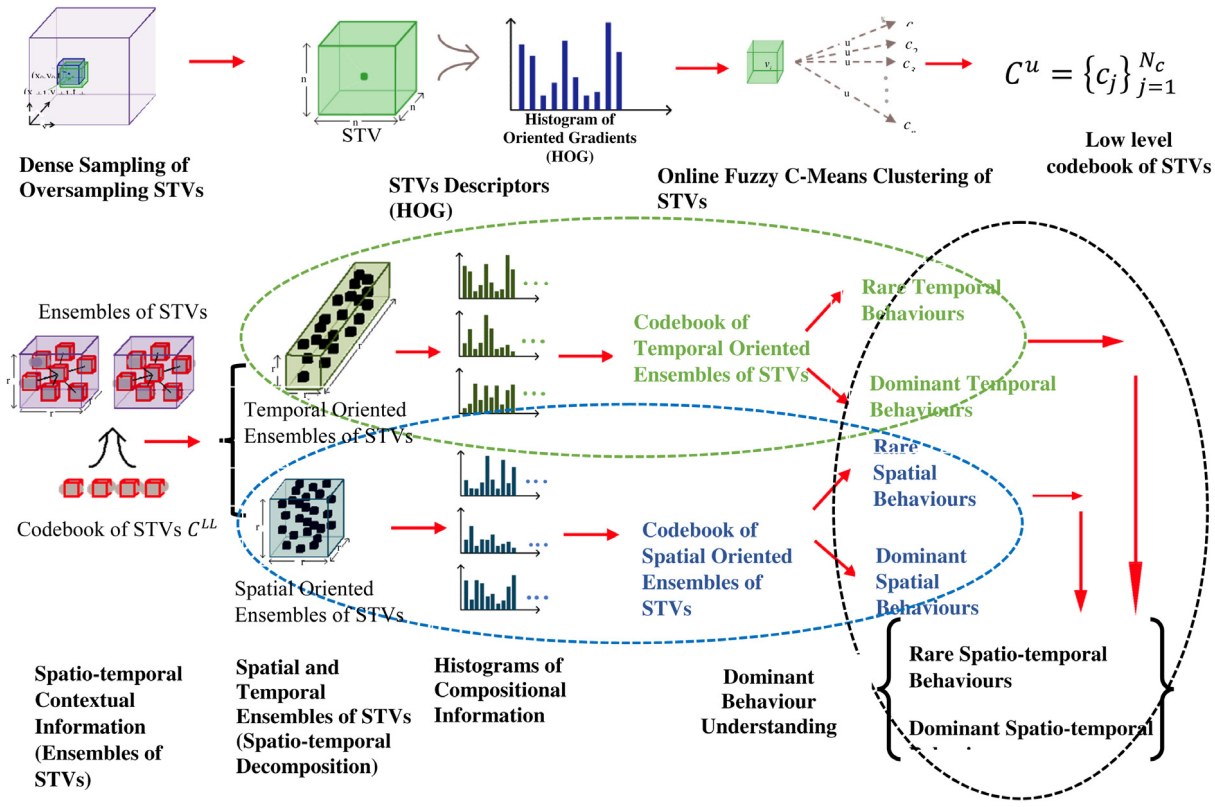


Fig. 8. Algorithm Overview: Online Dominant and Anomalous Behavior Detection in Videos (Roshtkhari and Levine, 2013).

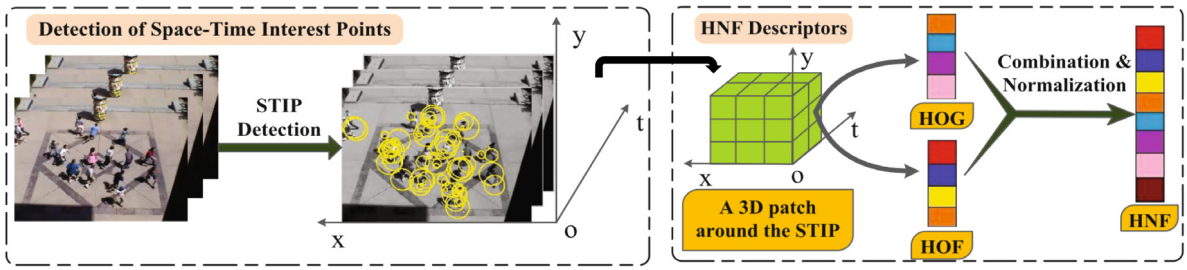


Fig. 9. Extraction of discriminative spatiotemporal features (Zhao et al., 2015).

In Hu et al. (2013) an unsupervised semiparametric statistical method is used to examine the (crowded) video with windows of adjustable shape and size for abnormal activity detection. The time complexity involved in the window scanning stage over the video is resolved with a fast two round scanning algorithm to advance the efficiency of the algorithm. People behavior can be defined as set of individual activities and group interactive behavior. And native motion details i.e. speed and direction, are sufficient to represent individual activity. However, for group interactive behavior interactive motion between neighbors information is required. In Cho and Kang (2014), a hybrid agent system is designed which comprises static and dynamic agents for efficient inspection of the corresponding individual and interactive behaviors in a crowded scene represented by a bag of words. Another unsupervised context-aware approach (Leach et al., 2014) targeted elusive anomalies in a behaviorally heterogeneous surveillance scene. Social context and scene context are used in conjunction for thorough activity analysis. Social contextual evidence supports anomaly propagation in a social network assuring better anomaly detection rate. Detection and localization of dense crowd in a scene is accomplished in Fagette et al. (2014) without any context-awareness in an unsupervised manner by multi-scale texture analysis. For which, firstly, three types of features are mined at different scales of the observation to design a high-dimensional multiscale feature vector for every pixel of the image. While binary classification (crowd or background) diffusion distance is preferred over traditional Euclidean distance to know the length and the density of the path between the data points. To reduce time and volume of computation complexity concept of coarse-graining is investigated using a quad-tree.

In Guo et al. (2016), authors follow pixel-wise approach, Weighted Quaternion Discrete Cosine Transform (QDCT) to find anomaly saliency map. The limitation of this approach is that QDCT cannot exploit information for long-term events. In Stephens and Bros (2016) specific human activities in a video are identified and distinguished by medium-term movement flow using streaklines model. Where each streakline is constructed by multiple optical flow vectors that keep a track of local movements in the scene. In Zhang et al. (2016), authors defined Locality Sensitive Hashing Filters (LSHF) which filter out abnormal activities by hashing regular activities into multiple feature buckets. To enhance the efficiency of anomaly detection in the video Particle Swarm Optimization (PSO) method is employed. Further, dynamic scene variations in the video, are updated to this framework by an online updating procedure.

Table 3
Evaluation of wearable devices and vision system (Rougier et al., 2011b) performance for fall detection.

	Wearable device	2D vision system	3D vision system
Lack of Significate movement	+ +	+ +	+ +
Lying position	+	+	+ +
Lying on the ground	–	+	+ +
Vertical speed	+ +	+	+ +
Impact shock	+ +	–	+
Body shape change	–	+	+ +

+ +: excellent performance.
+: satisfactory performance.

3.2. Three-dimensional AbHAR

Multi-dimensional data processing always produce more accurate and precise results in comparison to one-dimensional data processing. This fact has always attracted researchers towards 3D, 4D data. In recent years, due to the gigantic popularity of Microsoft depth sensors, the research work on abnormal Human Activity using depth information has proliferated. A number of new datasets (Fothergill et al., 2012; Escalera et al., 2014, 2013) have provided researchers enormous opportunities to create novel designs and test them on a bigger set of sequences. We can generate depth details of the image and also skeletal view with each joint position in three coordinate system. Some interesting applications are developed using depth and skeleton representation of an image.

3.2.1. Depth based AbHAR

Depth images not only simplifies and fasten up the low-level image processing but also delivers better processing outcomes in terms of background subtraction, object motion detection, and localization. In the following series various popular depth based approaches are discussed and summarized in Table 4 highlighting the key contributions and limitations of these methodologies with year of publication. From where it is identified that depth-silhouette based statistics such as height to width ratio, centroid, and silhouette shape deformations, are used very commonly to extract features of the person under motion. Human motion and shape variation features (Rougier et al., 2011b; Nguyen et al., 2016) can handle realistic challenges such as occlusion, different viewpoints etc.

Vision-based AAL solutions (Chaaraoui et al., 2012) are the best examples of depth based anomaly detection which assists the elderly while performing their daily living activities using depth information. A significant amount of work (Tran et al., 2014; Rashidi and Mihailidis, 2013) has been done to produce depth based AAL solutions. Jyothilakshmi et al. (2016) extended the Ambient concept Assistance of the patient through the application of Smart Ward System (SWS) using Kinect sensor camera. In existing patient assistance systems in hospitals, the patient is provided with a remote control to fine-tune the bed and to call a nurse for assistance. Many hospitals are not equipped with this automation system due to the expenses involved, and conventional gesture recognition systems are wearable sensors' dependent. The concept of Smart Ward System empowers the hospital workforce to emphasize majorly on patients with the facility of collection of data at the bedside and remove the chances of duplication and double-handling, i.e. security issues over data storage in the cloud. In Uddina et al. (2011); Triantafyllou et al. (2016), HMM model is used with depth features to develop a real-time solution which generates a warning alarm for the person walking in a room which can be extended to various home activities in the drawing room, living room, and kitchen. ICA helps to extract local features of human gait depth silhouette rather than PCA. Whereas in Uddin et al. (2014) Local Directional Patterns (LDPs) are used to extract local features from depth silhouette producing superior gait recognition rate using HMM model. The edge responses extracted via LDP are calculated in eight directions using Kirsch edge masks. To handle the problem of dehydration, RGB-D data is used (Tham et al., 2014) to monitor drinking activities at home with the help of Dynamic Time Warping (DTW) concept.

Fall (Mohamed et al., 2014) is one of the most frequently identified unusual events. Various methodologies have been presented for fall detection, highlighting this major health concern. Few studies presented that falls are the foremost reason for elder persons', disabled people or overweight/obese peoples' hospitalization. An extensive survey on fall detection is made in Yu (2008) which focused on identifying principles and approaches to existing work and literature. It classified the fall detection technologies into three categories: *wearable device, ambient device, and vision-based approaches,* as shown in Fig. 10. It is notified most wearable devices are cost-effective and easy to use, but they may not be very appealing to the wearers, in addition to this wearable device based approach is prone to the high rate of false alarm. Ambient device-based approaches commonly use pressure, vibration, acoustic sensors, and stabile-meters which need to be positioned in a permanent space to gather facts about the person in their operative range. Thus these sensors have limited range of usage and are noise sensitive due to environmental factors. The vision-based approach has an overhead over others that it is not intrusive to the person under monitoring in comparison to wearable devices and ambiance devices. They can be divided into three sub-categories: *Inactivity Analysis (IA), Shape Change Analysis (SCA), and Head Motion Analysis (HMA)*. Table 3gives an overall summary of wearable devices and 2D & 3D vision-based systems for fall detection. It also shows the circumstances where wearable and 2D & 3D vision-based system performances, are good and bad. The 3D vision system can detect fall with maximum accuracy between two with any combination of fall features such as lack of significant movement, lying position, lying on the ground, vertical speed, impact shock and body shape change.

3.2.1.1. Depth based fall detection. The concept of inactive period strengthens the severity of fall. Lying on the ground being inactive for longer duration is a consequence of strong fall. Fall detection cannot be made from one instance information, but discriminative features need to be analyzed for the entire duration of fall and also after the fall. The confirmation of inactivity is highly context dependent. The exact location of the person, time and duration of inactivity collectively gives wise decision such as staying in bed for long duration is not an alarming event but staying long on the floor after a fall will lead to an alarm. Hence contextual information helps to reduce the false alarming rate. Therefore, Jansen and Deklerck (2006) learnt about contextual details of the fall by quantifying the area of the body on the floor and 3D orientation of fall to understand the inactive duration of a person during and after fall. In daily activities, human body possesses various quick movements which may lead to false large motion identification. Therefore in Nguyen et al. (2016) center of mass of human 2D silhouette is quantified to observe overall motion (magnitude and orientation) of the object, with the help of image moments, along with human shape feature. It reduces the impact of sudden movements on fall detection. In addition to this, MHI (motion history image) provides exact location and trajectory of motion in the video sequence. However, 2D silhouette extraction approach needs to be improved to reduce false detection rate.

Human body posture is also used as a key element for fall detection by set of researchers (Ma et al., 2014; Akagunduz et al., 2016; Rougier et al., 2011b; Yu et al., 2013; Yao et al., 2017; Rougier et al., 2011a). Yu et al. (2013) represented human body posture with the centroid

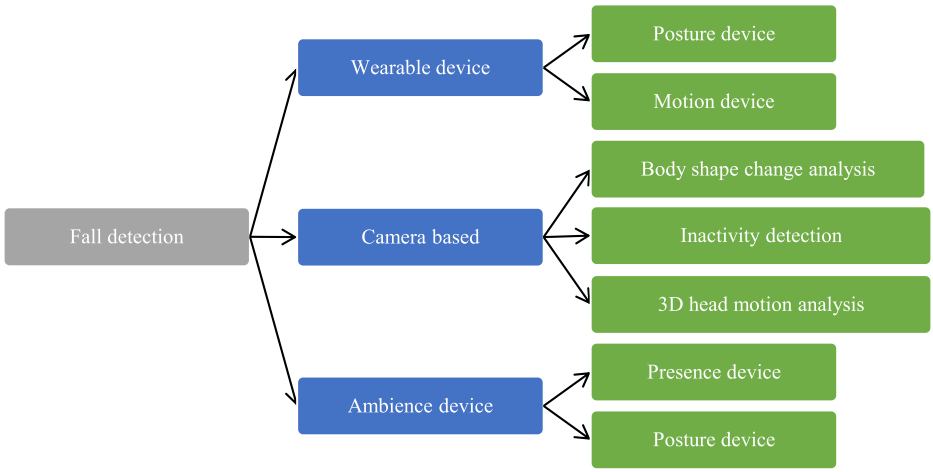


Fig. 10. An ordered structure of fall detection methods for elderly and patients (Yu, 2008).

Table 4
Feature extraction and representation techniques for three-dimensional-depth based fall detection techniques.

Method	Year	Technique involved	Performance	Dataset	Challenges	limitations
Yu et al.	2013	Online One-Class Support Vector Machine (OCSVM)	Accuracy-100%	The self-recorded dataset in a real home environment of elderly people	Handles occlusion well	Tested for a single dataset
Goudelis et al.	2015	History Triple features	Accuracy — 100% (both)	Le2i Fall Detection dataset, UR fall dataset	handles common visual distortions, camera placement variations and noise	Does not support real-time fall recognition
Nguyen et al.	2016	body width-to-height ratio, the angle between body and horizontal plane	Precision — 93.25%	Lie2 Fall detection dataset	Handles shadow, light reflection, complex, textured background, and view variations	suitable foreground segmentation technique required
Jansen and Deklerck	2006	context model defined after fall using area of the body and 3D orientation of fall	–	Synthetically generated fall sequences	–	Human interventions are required
Rougier et al.	2011b	full Procrustes distance and mean matching cost as shape deformation measures	Accuracy-99.6%	Self-recorded dataset (Fig. 11)	occlusion, use of the object, putting off clothes, different viewpoints	–
Yang et al.	2016	Position and orientation analysis	–	The self-recorded dataset in a real home environment of elderly people	Detects fall accurately when the fall orientation is aligned with the optical axis of the vision sensor	Require adaptive thresholds for fall detection
Panahi and Ghods	2018	The distance of the person's centroid to the floor	Sensitivity-100% Specificity –97.5%	The self-recorded dataset in the real home environment	Videos are recorded in different rooms and decorations, with different people, and in different lighting conditions.	the application of the Kinect v2 strongly depends on the distance to the target and the incidence angle of the sunlight
Yao et al.	2017	Person's torso angle and centroid height	97.5%	Self-recorded Kinect based dataset	High discriminating power between Fall- and fall-like events	Depends on threshold values for fall detection
Rougier et al.	2011a	human centroid height relative to the ground and 3D person velocity	98.7%	Self-recorded Kinect based dataset	Occlusion	suitable foreground segmentation technique required
Ma et al.	2014	Bag of Curvature Scale space (BoCSS)	86.83%, 97.2%	SDUFall Dataset, MultiCam dataset	–	Time cost is high
Akagunduz et al.	2016	Silhouette Orientation volume (SOV)	91.89%, 100%, 89.63%	SDUFall Dataset. Weizmann Dataset, six-class action recognition dataset	Scale invariant	–

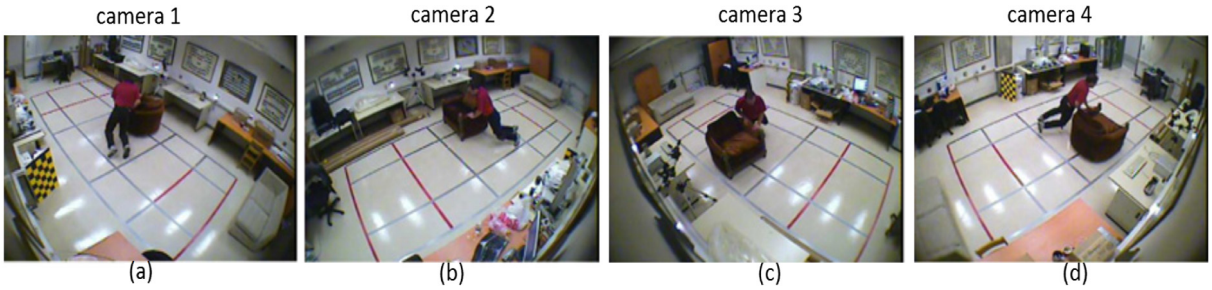


Fig. 11. A same person fall activity viewed from different viewpoints (Rougier et al., 2011b).



Fig. 12. Other examples considered in Rougier et al. (2011b) (a) Forward fall (b) sitting down (c) crouching down (d)–(e),(g) fall (loss of balance) (f) putting off a coat (h) fall from sofa (i) housekeeping (j) backward fall (k) occlusion (l) carrying a box.

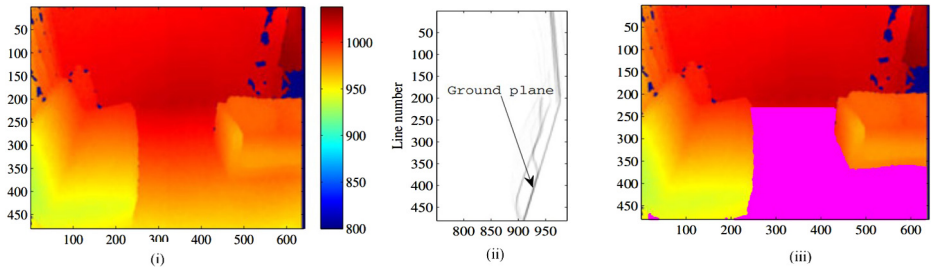


Fig. 13a. Ground Plane detection (i) depth image (ii) V-Disparity image (iii) ground plane segmentation (in magenta) (Rougier et al., 2011a). (For interpretation of the references to color in this figure legend, the reader is referred to the web version of this article.)

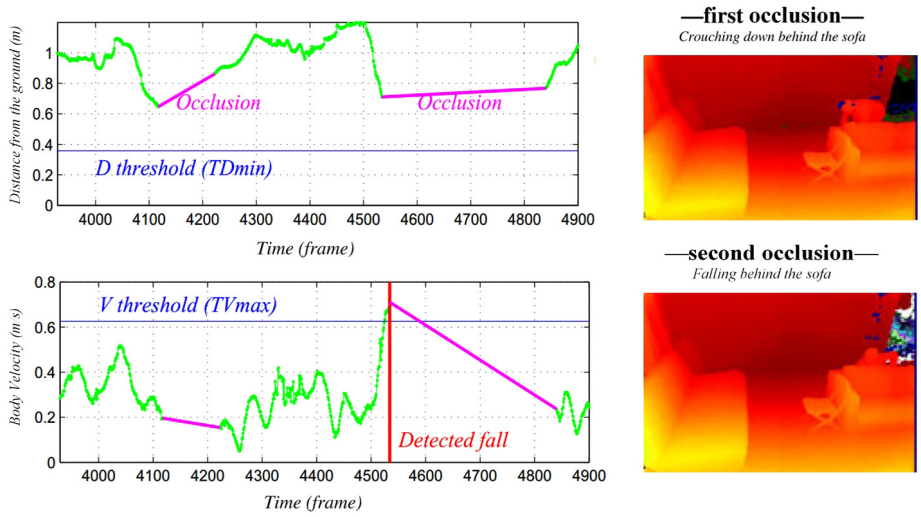


Fig. 13b. Distance from the ground and body velocity curves (left) obtained for occluded events (right). The fall is correctly detected with a high body velocity (Rougier et al., 2011a).

position of the body, ellipse feature and shape structure feature. They have defined two rules to reduce false alarm rate, which is as follows:- *First rule*: area ratio (AR) between the area of MEI frames and area of the current frame's foreground region compute the magnitude of motion. AR will be larger for fall activity than walking, sitting or bending. Fall will not be reported for a small value of AR, even though the system detects abnormal postures. *Second rule*: a fall is declared only if any abnormal posture occurs for a longer period than a threshold; it reduces false alarms (i.e. occasional bends, tying shoes) to an acceptable range. In spite of the excellent fall detection accuracy, the method demands human interventions for manual segmentation and video clip selection. Another approach (Rougier et al., 2011b) measured human shape deformation during fall using full Procrustes distance and mean matching cost as deformation measures. Realistic scenarios like occlusion, use of the object, putting off clothes, different viewpoints are addressed by authors in their dataset as shown in Figs. 11 and 12**.** Yao et al., (2017) introduced Human Torso Motion Model (HTMM) which can discriminate fall and fall-like activities such as bending and crouching down with 97.5% accuracy by observing changing rates of torso angle and the centroid height. Since the existing RGB-D action datasets i.e. CAD-60/120 do not provide fall sequences, ADL and fall sequences are recorded for experimentation. However, the method is dependent on threshold values which used with hit and trial approach to optimize the result, which needs to be identified every time for a new dataset. Rougier et al. (2011a) computed human centroid height relative to the ground and 3D person velocity. 3D person velocity helps the system to make fine discrimination between crouching down behind the sofa from fall behind the sofa — look alike cases as shown in Fig. 13b**.** Here, 3D velocity is preferred over 2D velocity of a person during fall because 2D velocity is generally very high near the camera for normal walking activity resulting misclassification between a fall and a walk. Detection of the ground plane for human centroid height computation relative to ground in depth images, accomplished using V Disparity histogram, is shown in Fig. 13a. It is observed that height (Gasparrini et al., 2014) and height velocity (Yang et al., 2015) based approaches fail to distinguish fall and fall-like actions and whereas bounding box width to height ratio based (Nguyen et al., 2016; Rougier et al., 2011a) and HTMM (Yao et al., 2017) based fall detection model has **the** higher discrimination power of fall and fall-like actions.

Ma et al. (2014) represented the actions by a bag of words model (BoCSS) using distinctive Curvature Scale Space (CSS) features of depth silhouette for fall detection, whereas Akagunduz et al. (2016) integrated orientation scale space (OSS) and morphological scale space of a curve to form robust Silhouette Orientation volume (SOV) global scale invariant descriptor to represent actions. However, these approaches have high computational cost.

Some researchers came up with fusion of sensor (accelerometer, floor sensor) and visual depth data to develop an improved human fall detection system which has improved the performance of the fall detection. Toreyin et al. (2006) integrated sound impact of falling person with height to width ratio of the bounding box on a person under falling condition to discriminate a fall from a normal sitting in the floor action. Zerrouki et al. (Zerrouki et al., 2016) used the concept of Univariate Statistical monitoring method Exponentially Weighted Moving Average (EWMA) control scheme to detect potential fall integrating accelerometric data and depth data with low computational cost. Though such fusions produce impressive outcome but this detection is dependent on sensor and its periphery which may not be in the comfort zone of the user. Therefore, the purpose of making the fall detection system non-intrusive to the user is defeated.

3.2.2. Skeleton based AbHAR

Skeleton representation of human body provides incisive details of the human posture in compact form which has definitely resolved the problem of need of effective segmentation technique to extract 2D silhouettes and simplifies the height centroid computation (Rougier et al., 2011a) from depth silhouettes. This has encouraged researchers to develop real-time applications using skeleton modality making the computation process faster, simpler and more effective. Nar et al. (2016) designed an effective real-time ATM intelligent monitoring system to recognize abnormal postures prevailing stronger security in the ATM i.e. fiddling with the camera, aggressive posture, and peeping. The work used angles between different bones as useful features to compute the optimum value of weights for computing probability of the current pose of the person under surveillance being abnormal. The computation of angle between joints (x, y, z) becomes quite simple and fast and more accurate with 3D skeleton coordinates. Hendryli and Fanany (2016) addressed the issue of automatic detection of abnormal activities of students in examination hall that generates warning to exam proctors if any doubtful activity is detected (Cheating activity). For this purpose, MCMCLDA (Multi-class Markov Chain Latent Dirichlet Allocation) framework is designed that access arm joints and head location as interest points directly from skeleton representation without considering irrelevant ones resulting better accuracy and higher computational speed than Harris3D detector. Nowadays, health professionals and researchers have also shifted their attention to Human gait analysis (Aggarwal and Vishwakarma, 2016). Because human gait not only helps to know different traits of a person but also variation in the human

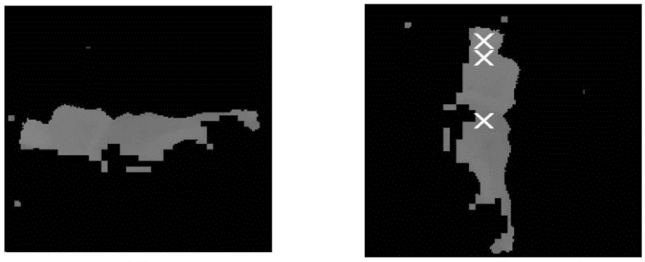


Fig. 14. An example of rotation. (a) Before rotation. (b) After rotation, the head, neck and hip center joints can be extracted correctly (Bian et al., 2012c).

gait from normal frame may be correlated with neurological diseases. Chaaraoui et al. (2015) developed generic machine learning framework (Bag- of-Key-Poses) using joint motion history feature i.e. 3D location of skeletal joints and motion cues. To handle complex behaviors both low and high-level multi-scale motion cues are extracted in Paiement et al. (2014). However, skeleton data acquired with a Kinect sensor likely to suffer from relatively large amount of noise, and also contain outliers, especially in case of partial occlusion. Therefore, the work incorporates diffusion maps to filter the outliers. Jalal et al. (2014), tried to develop a design continuous surveillance and daily activity recognition in indoor environments (i.e., smart homes, smart office and smart hospitals) turning the space into a smart living space. It also failed to handle complex activities and partial occlusion of the body while generating skeleton joints and resulting in noise.

3.2.2.1. Skeletal based Fall Detection. Research in abnormal activity recognition is receiving dynamically increasing attention, encouraged by the speedy growth of information (Khan and Hoey, 2017), intelligent video systems, and communication technologies. Medical consequences of a fall mainly depend on the response and rescue time. Hence, an accurate automatic fall detector (Bian et al., 2012a) is an essential element for an older adult living to expedite and improve the medical care provided to this group. Skeletal representation of a person is proving its strength by enhancing the performances of fall detection systems and many other abnormal activities in daily routine. Table 5 outlines various skeleton based AbHAR approaches. It is visible from here that trajectory of joints (Rougier et al., 2006; Bian et al., 2012b; Nizam et al., 2016) and Joint Motion History (JMH) (Chaaraoui et al., 2015) based action description is simple and very effective having high temporal efficiency and appreciable view and illumination invariance property for skeleton-based abnormal human action detection.

However, the distance between silhouette center and the floor (Rougier et al., 2011a) or shape deformation concept based fall detection work is not able to discriminate the initiative action and fall accident well i.e. fall in bed and fall in the floor without defining normal inactivity zones, a person is sleeping on the sofa or bed and falls down to the floor. 3D human skeleton joins distance from the floor and joins hitting velocity, joint position and its height from the ground (Bian et al., 2012b; Nizam et al., 2016) collectively elicit robust results by discriminating a fall from slowly lying down on the floor and other similar cases. While falling, human's body orientation changes dramatically which leads to poor tracking of joints. Therefore in Bian et al. (2012c) the author initially corrected the trunk orientation (from hip point to neck) of the person before applying a fast Randomized Decision Forest (RDF) algorithm for human skeleton extraction which has improved the accuracy of fall detection rate as shown in Fig. 14. The presented work is able to detect minor fall like falling from the sofa when our half body (legs) is still on the sofa by simultaneously tracking head, which silhouette center-based approach fails to identify. A view independent statistical method (Zhang et al., 2012) takes a decision based on the information how human behave in last few frames after falling. It defined a feature set $f = [f_1, f_2, f_3, f_4, f_5]$, where f_1 is duration of fall, f_2 is total head drop, f_3 is the maximum speed of fall, f_4 is the smallest head height, f_5 is the fraction of frames where head has a smaller height than in the previous frame. The five features are combined using the Bayesian network. But few false alarms are received for a person lying on the floor and a person jumping on the bed. Diraco et al. (2010) used distance of 3D centroid from floor plane as threshold to confirm high performance in terms of consistency and competence on a large real dataset which uses Bayesian segmentation to detect moving regions. It also introduced 3D Geodesic Distance Map-Based Posture Recognition (3dGDMPR) system prototype, Fig. 15. Occluded leg is used as a test case and overlapping region postures are detected and interpolated as mentioned in Fig. 16.

3.3. Deep features based action description

It is observed that over the passage of time the concept of feature engineering is evolving from 2D features to 3D features in order to improve the action representation. However, complexity involved in designing handcrafted features is very high which is one of the key reasons to shift the features from shallow region to deep that has brought the practical applicability of the action recognition algorithms at another level of excellence by empowering the knowledge of deep learning to the recognition systems. Though the concept of deep learning and architectures (Koohzadi and Charkari, 2017) was existing since 1980s but could not perform up to the mark due to lack of sufficient datasets and computational resources. In 1998, LeNet (Lecun et al., 1998) came up as the first real-world successful application of CNN for handwritten digit recognition. However, in successive years, various deeper architectures have been reported in Russakovsky et al. (2014) and are being used in different application areas such as computer vision (Herath et al., 2017; Paul et al., 2013; Taylor et al., 2010), speech recognition (Vesperini et al., 2018), brain–computer interaction (Cecotti and Graser, 2010) and natural language processing (Yin et al., 2017) with the availability of large datasets and hardware resources. Deep models learn a hierarchy of features by constructing high-level features from low-level ones. CNN is a type of deep model which is made up of neurons and learnable weights and biases which were initially applied on 2D images for visual object segmentation (Iannizzotto et al., 2005) and recognition (Wang et al., 2018; Uddin et al., 2017) tasks. And later, many researchers experimented CNN with videos by considering video frames as still images to recognize action in each frame. However, this approach was limited to learn only spatial information. Some authors (Ji et al., 2013) tried to incorporate temporal information by expanding the 2D CNN to 3D CNN. 3D CNN applies 3D convolution in CNN convolution layers by using 3D kernel to multiple contiguous frames stacked together to encode the motion information with spatial one. In subsequent years, the work is further extended by bringing the concept multi-stream CNNs (Simonyan and Zisserman, 2014) based action recognition, which has fortified feature description of an action to a higher level by making the deep recognition system to analyze not just raw images at a time but multiple set of inputs such as: RGB image, optical flow (Simonyan and Zisserman, 2014), dynamic images (Jing et al., 2017), and depth images (Liua et al., 2016). On the other hand, long short term memory (LSTM) (Liu et al., 2018) has emerged as one of the most popular unsupervised models that learns temporal arrangements of frames and predict time series data.

3.3.1. Single person based abnormal human action recognition

As far as application of deep architectures in the area of abnormal human action recognition for AAL and smart homes, is concerned, a limited work has been carried out yet. It is the need of an hour to apply deeper architectures to develop stronger algorithms (Zhang et al., 2017) for single person specific abnormal actions recognition applications i.e. AAL, smart homes. The generalized deep frameworks for human action recognition are summarized in Table 3 and single person based abnormal human action recognition work is discussed below.

Table 5
Feature extraction and representation techniques for three-dimensional-skeleton based abnormal human activity recognition (AbHAR).

Feature representation for depth based anomaly detection	Key Contribution	Limitations	Year	Ref.
Joint Motion History Feature (JMH) + Bag Of Key Poses	high temporal efficiency	Multi-scale feature extraction technique is required to handle complex human activities	2015	Chaaraoui et al. (2015)
The angle between different bones, the 3D trajectory of head motion, Human joints height, joint positions and falling velocity	The velocity of joints a stronger classifier than distance variations.	Adaptive thresholds need to be used to handle individual differences	2014 2012 2016 2006	Tran et al. (2014) Nar et al. (2016) and Rougier et al. (2006) Bian et al. (2012b) and Nizam et al. (2016)
Dynamic Time Warping	Illumination invariant	Manual segmentation of drinking video needs to be replaced by automatic segmentation procedure	2014	Tham et al. (2014)
Multi-class Markov Chain LDA Based on MODEC (Multimodal Decomposable Models) Features	MODEC interest point detection is faster than Harris3D	Incapable of distinguishing elbow and wrist when the object wears clothes with indistinguishable colors	2016	Hendryli and Fanany (2016)
Trunk orientation correction and Randomized Decision Forest (RDF)	Trunk orientation correction improves the accuracy of fall detection.	Time involved in trunk correction per frame not discussed	2012	Bian et al. (2012c)
Depth comparison feature (DCF) a+ RDF	DCF is extracted pixel wise	Computation cost is high for large datasets	2018	Abobakr et al. (2017)
Bayesian Network with Statistical parameters	Viewpoint invariant and user independent		2012 2010	Zhang et al. (2012) and Diraco et al. (2010)
PCA (20 skeleton joints) +HMM	human posture sequence modeling	Non-availability of the large-sized dataset	2013	Dai et al. (2013)
3D trajectory of head joints	Illumination invariant of the lights and perform well in dark room	Head occlusion case not discussed	2015	Bian et al. (2015)

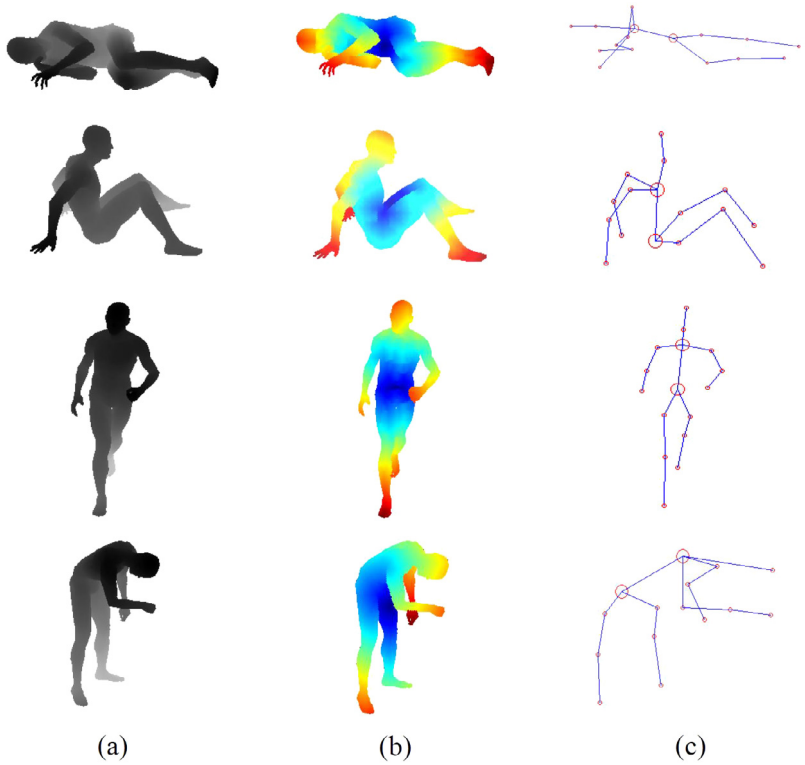


Fig. 15. Four main postures examined in Diraco et al. (2010): lie, sit, stand and bend. (a) Depth map (b) Geodesic distance map and (c) skeleton. Upper and lower nodes of the skeleton Reeb Graph are encircled with red circle.

The common signs of dementia (Alzheimer, Parkinson's disease) can be acknowledged by behavioral variations such as disturbance in sleep, difficulty in walking and fail to complete tasks. Such variations can be identified in early stages by monitoring the elderly person in smart homes which may prove to be more beneficial than medical diagnosis. However, availability of the real world data of dementia patients is a big challenge for non-medical diagnosis of the patient. Therefore, Arifoglu and Bouchachia (2017) introduced an approach to generate synthetic data to represent behavior of dementia patients and addressed the problem of abnormal behavior detection for elderly

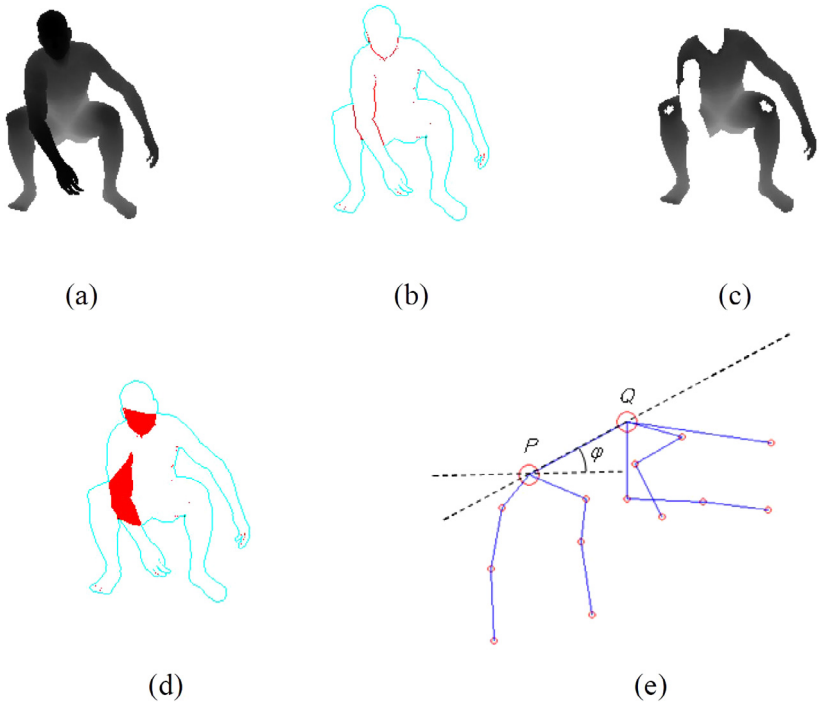


Fig. 16. Detection and interpolation of overlapped regions (a) the arm occludes a leg (b) Laplacian operator detect occluded bounds (c) and level sets of the height function (depth map) detect inbound region (d) interpolation is performed to obtain a connected mesh (e) body spine orientation is approximated by the orientation φ of the PQ segment in the body skeleton (Diraco et al., 2010).

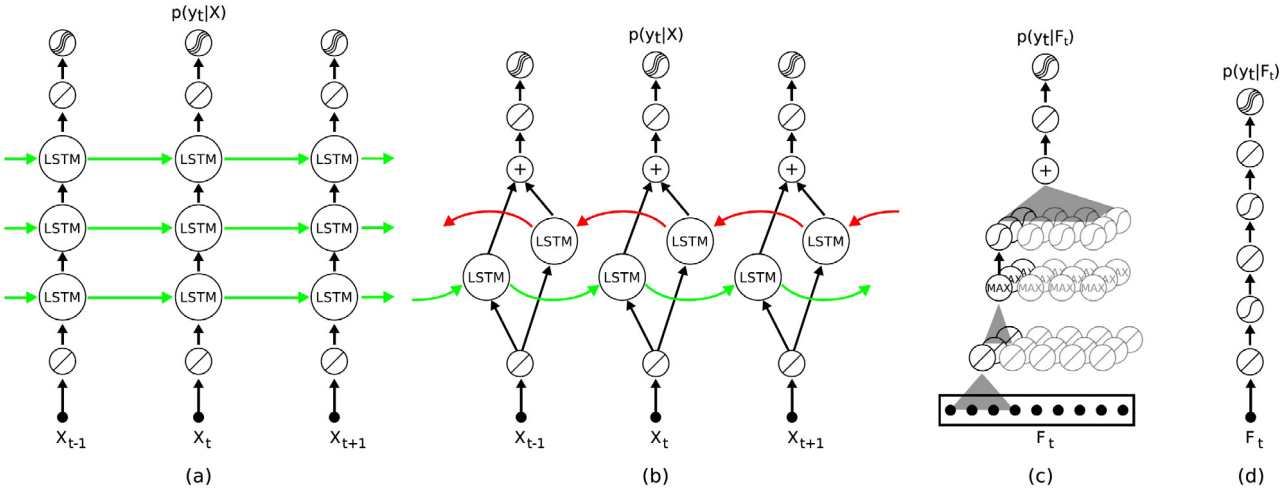


Fig. 17. (a) LSTM network hidden layers containing LSTM cells and a final Softmax layer at the top. (b) bi-directional LSTM network with two parallel tracks in both future direction (green) and to the past (red). (c) Convolutional networks that contain layers of convolutions and max-pooling, followed by fully-connected layers and a Softmax group. (d) Fully connected feed-forward network with hidden (ReLU) layers (Hammerla et al., 2016). (For interpretation of the references to color in this figure legend, the reader is referred to the web version of this article.)

people with dementia using three variants of Recurrent Neural Networks (RNNs)- Vanilla RNNs (VRNN), Long Short-Term RNNs (LSTM) and Gated Recurrent Unit RNNs (GRU), see Fig. 17. Recently, Park et al. (2018) analyzed the sequence of actions recorded in ambient intelligent environment i.e. smart home and city with multiple sensors by introducing the concept of Residual-Recurrent Neural Network (Residual-RNN). The extensive experiments assert that the proposed model (in Fig. 18) performs better than LSTM and Gated Recurrent Units (GRU) in respect of recognition accuracy. However, GRU performs slightly better in terms of computational speed. In another work by Hammerla et al. (2016), LSTM, bi-directional LSTM, and convolutional networks are used to detect abnormal actions of the patient under surveillance using movement data acquired from wearable sensors.

Considering the fact that deep models are outperforming existing state-of-arts (Zhang et al., 2018a, b; Hou et al., 2018) in almost all the fields being used such as face recognition, handwriting detection (Tolosana et al., 2018), audio signal processing, a variety of plans are discovered that use pre-trained, fully-connected networks for automatic assessment of Parkinson's Disease (Hammerla and Plotz, 2015), replace emission models i.e. GMM, random forest (RF) in Hidden Markov Models (HMMs) with Deep Neural Networks (DNN) (Zhang et al., 2015; Alsheikh et al., 2016) ; and design a mobile audio sensing

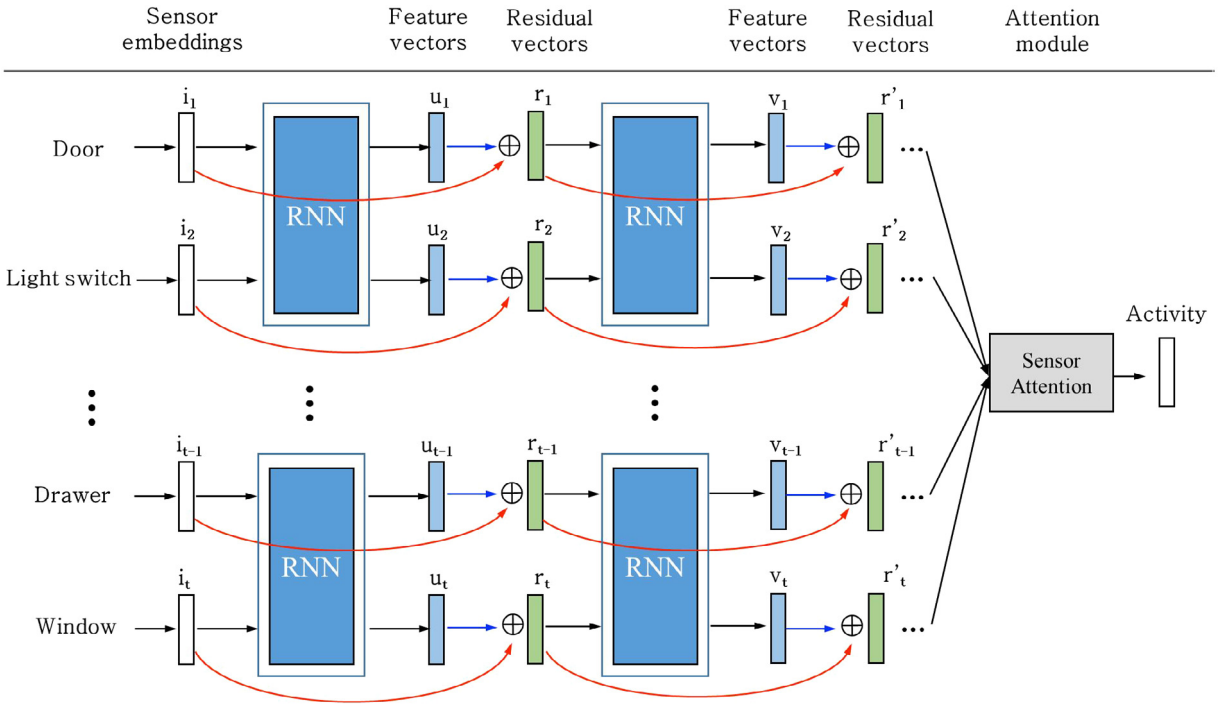


Fig. 18. Residual-RNN structure for activity recognition in smart homes (Park et al., 2018).

framework using DNNs (Lane et al., 2015). These works (Hammerla and Plotz, 2015; Zhang et al., 2015; Alsheikh et al., 2016) are restricted to the accelerometer and wearable sensor data, that is very scarcely available and labeled. It limits the application of the methods in real-world scenarios where vision sensors are used profoundly.

3.3.2. *Multiple persons based abnormal event detection*

Evolution of abnormal event detection approaches in crowded scenes from shallow to deep is reported in a recent survey (Tripathi et al., 2018) which has emphasized on four attributes of the crowd to be considered for crowd analysis:-crowd counting, crowd motion detection, crowd tracking, and crowd behavior understanding. Crowd analysis is one of the demanding issues in public domain**.** And deep learning models i.e. variants of CNN, LSTM, autoencoders, RNN are providing improved solutions (Sindagi and Patel, 2018) compared with hand-crafted features for real-life challenges in crowded scenes like occlusion, cluttered background etc.

In the work (Vignesh et al., 2017) the property of LSTM network to learn the long-term dependence between the frames is fused with CNN features to recognize the unusual event in videos. Here, the LSTM network possess two layers — 1×1024 LSTM layer followed by 1×512 bi-directional layer. This set of arrangement of layers overcomes the limitation of standard recurrent neural networks for inflexible size of input data and also that the forthcoming input cannot be obtained from the current state. Whereas, bi-directional LSTM has forward and a backward LSTMs operational in reverse time that combine the significant features of past and future. Though, the approach produces impressive results for ARENA dataset but the experimental work deals with only one type of activity. In Medel and Savakis (2016), author introduced the concept of Conv-LSTM to model and predict video sequences. Conv-LSTM layers are memory insensitive which makes training testing phase slow. In real-world scenario, the probability of abnormal event occurrence is lesser than a normal event. 3D ConvNet fails in the absence of abnormal events and loosely supervised datasets, in spite of being able to discriminate normal and abnormal events. Chong and Tay (2017) proposed a spatiotemporal end-to-end model for anomaly detection in videos or crowded scene. Which performs well even in the absence of abnormal events in video samples. It has a CNN based spatial feature extractor and a temporal encoder–decoder which collectively learns the temporal patterns of the input volume. To understand the crowd scenes Shao et al. (2016) developed a spatiotemporal CNN named as Slicing SCC (S-CNN) which decompose the 3D volume (x, y, t) input video into 2D spatial (x, y) and 3D temporal slices (x, y), (x, t), and (y, t) by exploiting selectiveness of spatial filters. The semantic feature maps claims that such kind of slicing helps to discard background clutter of scene and select only the people under action. In addition to this, in a recent work (Li and Chuah, 2018) defined a robust and efficient human activity recognition framework (ReHAR) that combined optical flow and CNN based image feature extractor with global average pooling layer which is fed to stack of two LSTM networks to predict the group activities of Basketball dataset and UCF sports action dataset. Global average pooling layer and stack of two LSTM structures helps to perform the task faster supporting real time action recognition.

The development of generalized deep learning architectures for human action recognition is summarized in Table 6. Which indicates that various modalities-RGB, depth, skeleton, optical flow, MSDI, and dynamic images are integrated to enhance the performance of the system by the researchers. Each set of representation has its benefit over another such as dynamic images (Jing et al., 2017) and optical flow (Hana et al., 2018) both provide motion representation, however, from the aspect of time of computation and storage capacity dynamic images offer a more compact representation of motion in a video sequence than optical flow. Set of researchers (Liu et al., 2018; Amir et al., 2016; Song et al., 2016; Ding et al., 2016) have exploited view-invariant and succinct property of skeletons for deep action recognition models and observed impressive performance. However, the real-time applicability of such algorithms is still an important issue from the point of single person surveillance. As listed in Table 7, it can be seen that only a little work is carried out on the problem of single person abnormal human action recognition using the benefits of deep architectures, which needs to be focused seriously, considering the need of better healthcare services, smart homes, and AAL. The work which is listed is also based on wearable sensor data. Sometimes wearing the sensors is not a pleasant experience and if the person forgets to

Table 6
Generalized deep approaches for human action recognition.

Method	Year	Technique		Dataset (Accuracy)	Modality
Simonyan and Zisserman	2014	Two stream CNN	Spatial and temporal streams	UCF-101(88%), HMDB51 (59.4%)	RGB + optical flow
Diba and Gool	2016		Appearance and motion streams	UCF101 (90.2%)	RGB
Hana et al.	2018		Spatial and temporal streams	UCF101 (95.1%), KTH (93.1%)	RGB + optical flow
Jing et al.	2017	Three stream CNN	Appearance, short-term temporal and long-term temporal streams	UCF-101(88.6%), HMDB51 (57.9%)	RGB + optical flow + Dynamic images
Wang et al.	2017a		spatial, local temporal and global temporal streams	UCF-101(93.4%), HMDB51 (68.3%), Hollywood2 (74.6%), YouTube (83.8%)	single frame + optical flow + Motion Stacked Difference Image (MSDI)
Liua et al.	2016	$3D^2CNN$		MSR Action-3D (98.14%) and UTKinect-Action3D (95.5%)	Depth image + skeleton
Ji et al.	2013	3D CNN		KTH (90.2%)	RGB
Ijjina and Chalavadi	2017	MEI and MHI based Temporal Templates for RGBD 2D ConvNet features		MIVIA action (93.37%), NATOPS gesture (86.52%), SBU Kinect interaction (90.98%), and Weizmann dataset (100%)	RGB + Depth
Bilen et al.	2016	Dynamic Image Network (2D CNN)		HMDB51 (65.9%) and UCF101 (91.5%)	RGB
Wang et al.	2015a	Trajectory-Pooled Deep-Convolution Descriptor (TDD) + iDT		HMDB51 (65.9%) and UCF101 (91.5%)	RGB
Shao et al.	2016	S-CNN	2D CNN + 1D Temporal pooling	WWW crowd video dataset (62.55%)	RGB
Amir et al.	2016	Spatiotemporal LSTM (Tree Traversal) with Trust Gates		NTU RGB+D Dataset (77.7%) SBU Interaction Dataset (93.3%) UT-Kinect Dataset (97.0%) Berkeley MHAD (100%)	skeleton
Song et al.	2016	Deep LSTM with Spatio-Temporal Attention Model		NTU RGB+D Dataset (81.2%) SBU Interaction Dataset (91.51%)	skeleton
Ding et al.	2016	Profile HMM		MSRAction3D (86.4%), UTKinect-Action (91.7%), and UCF Kinect (97.6%) Dataset	skeleton
Liu et al.	2018	Global context aware attention LSTM network		UT-Kinect Action (99%), NTU RGB+D (84%) , SYSU-3D (79.1%), SBU-Kinect (94.6%) dataset	skeleton

wear the sensors, the actions of the person cannot be observed through the recognition system. However, it should be acknowledged that deep models have enhanced the performance of crowd analysis systems by handling the real-life challenges which are reducing the barrier of scene complexity for an excellent analysis of crowd activities.

Development and establishment of deeper architectures do involve some set of challenges such as a small set of training data, computational resources etc. Deep learning based neural networks cannot produce a realistic performance with small training datasets. Therefore, rigorous data augmentation techniques (Tran et al., 2017; Hanab et al., 2018) (i.e. cropping, rotating, and flipping input images) are utilised to analyze to small dataset samples for human action recognition. The work (Aquino et al., 2017) introduced 'Only augmented' and 'Balanced augmented,' two augmentation strategies and their effect on CNN architectures which is pointing the upgraded performance of CNNs. Transfer learning (Cook et al., 2013; Sargano et al., 2017) is another good approach to handle limited data samples for a specific application without involving considerable training time from scratch and large dataset by transferring the learned knowledge in one set of use to another.

The work (Hammerla and Plotz, 2015; Zhang et al., 2015; Alsheikh et al., 2016) performed in the direction to improve performance of smart homes, elderly people is majorly sensor based which is limited to a small set of data samples. If, we apply transfer learning techniques on visual datasets for abnormal action recognition and use LSTMs, RNNs to analyze temporal details involved, it can improve the image of single person abnormal human recognition.

Table 7
Single and multiple person based deeper abnormal human action recognition approaches.

Method	Year	Varient of CNN		Dataset (Accuracy)	Short-comings
A. **Single Person based Deep Abnormal HAR methods**					
Hammerla et al.	2016	Bi-directional-LSTM-S		Ubicom — Daphnet Gait dataset (DG) (F1-score-0.868)	The analysis is based on Wearable sensors' movement data
Arifoglu and Bouchachia	2017	Variants of RNN-Vanilla RNNs (VRNN), Long Short-Term RNNs (LSTM) and Gated Recurrent Unit RNNs (GRU)		Artificially generated dementia specific abnormal samples (96.7%)	A small set of sensor-based dataset
Park et al.	2018	Residual-RNN		MIT dataset (90.85%)	The absence of vision sensors in the smart and small dataset
B. **Multiple Persons based Deep Abnormal HAR methods**					
Karpathy et al.	2014	Two stream CNN	Context stream (low resolution image) and Fovea Stream (high resolution image)	Sports-1M (80.2%) and UCF101 (65.4%)	Weekly annotated data samples
Chong and Tay	2017	Autoencoders		Avenue (80.3%), UCSD Ped1 (89.1%)and Ped2 (87.4%), Subway entrance(84.7%) and exit (94%)datasets-AUC	Performance is sensitive to view variations.
Medel and Savakis	2016	Conv-LSTM		UCSD Ped1 (85.1%), Ped2 (92.3%), Avenue (85.1%), Subway Enter (81.57%) and Exit (65.9%)Datasets-Precision	–
Vignesh et al.	2017	CNN-LSTM-SVM-TA		ARENA Dataset (96.4%)	Model is evaluated for only one type of abnormal event
Hinami et al.	2017	Multi-task Fast R-CNN		Avenue (89.8%) and UCSD Ped2 (92.2%)- AUC	Fast R-CNN must be trained with richly annotated image datasets
Ravanbakhsh et al.	2017	Generative Adversarial Nets		UCSD Ped1 (97.4%, Ped2 (93.5%) and UMN dataset (99%)	–
Ravanbakhsh et al.	2016	Plug- and Play CNN		UCSD Ped1 (95.7%), Ped2 (88.4%) UMN (98%) dataset	–
Li and Chuah	2018	CNN-LSTM single frame		NCAA Basketball Dataset (94%) and the UCF Sports Action Dataset (92.8%).	Optical flow needs to be extracted manually

4. Discussion

For vision-based human action recognition systems as normal or abnormal in a different set of applications-AAL, smart homes, crowd analysis etc., a compact representation of the action videos needs to be defined considering the discrimination ability of the description along with time and computational complexity. The paper has covered three types of approaches to representing the actions for abnormal human recognition application specifically-2D AbHAR, 3D AbHAR and deep recognition systems for abnormal activities.

During the survey it is observed that every approach has certain limitations. Therefore the selection of the action description method must be application specific always. For RGB images/video sequences abnormal action detection and recognition can be categorized as a single person based and multiple person based approaches. It is noticed that for single person based AbHAR, silhouette and spatiotemporal based approaches became quite popular. In Khan and Sohn (2011) R-Transform is applied on silhouettes and KDA is applied to improve the discrimination ability of the descriptor. However, the system is evaluated for the hypothetical dataset. And (Sacco et al., 2012) demands high implementation cost and cannot perform the long-term real-time analysis. Whereas real-time dataset. However, LOTAR framework (Riboni et al., 2016) is developed for real-time abnormal human behavior detection at an early stage. However, this approach depends on multiple sensors other than vision sensor-camera. The integration of sensors and simultaneous acquisition and analysis of different sensors data become another challenge in real time. For abnormal behavior recognition with multiple persons spatiotemporal details (Roshtkhari and Levine, 2013; Roshtkhari and Levine, 2013) provide significant aspects of the abnormal crowd behavior. Sparseness (Chathuramali et al., 2014) of extracted features also play a major role in the accurate detection of the abnormal crowd behavior such as stampede.

For indoor activities where depth cameras can be fixed, skeleton and depth generation of a person is possible. It is witnessed during the survey that in closed environment single person based abnormal actions are analyzed keeping in mind the smart homes, elderly health care, and fall detection applications. From the performance point of view full Procrustes distance (Rougier et al., 2011b), OCSVM (Yu et al., 2013), History Triple Factor (HTF) (Goudelis et al., 2015), BoCSS (Ma et al., 2014) methods recognize the fall efficiently while handling occlusion, view variations quite well. However, (Ma et al., 2014; Goudelis et al., 2015) involve high computation cost not supporting real-time fall detection and (Yu et al., 2013) is evaluated only for one type of fall dataset.

The developed single person deep abnormal behavior recognition methods (Hammerla et al., 2016; Arifoglu and Bouchachia, 2017; Park

et al., 2018) utilised variants of RNN-Vanilla RNNs (VRNN), Long Short-Term RNNs (LSTM) and Gated Recurrent Unit RNNs (GRU) and Residual-RNN architectures to understand long-term details. However, no vision based single person deep abnormal behavior recognition model has been developed yet due to non-availability of sufficiently large abnormal datasets for deep networks driven by millions of data. Whereas for multiple person based AbHAR, a significant number of datasets are now available which is one of the major reasons that ample experiments have been performed using the combinations of CNNs and LSTMs (Vignesh et al., 2017; Medel and Savakis, 2016; Li and Chuah, 2018; Hinami et al., 2017; Ravanbakhsh et al., 2016), Generative Adversarial Nets (Ravanbakhsh et al., 2017) to define the deep model. However, some of the frameworks are trained with loosely annotated data, and some are not able to achieve real-time computational efficiency and accuracy.

5. Datasets

With the evolution of new technologies, there has been a tremendous rise in the number and also variations in publicly available datasets for experimentation. Recently introduced 3D AbHAR and AAL Datasets are summarized in Table 8 specifying the methodologies used in the introducing paper, accuracy, precision and recall obtained and set of challenges addressed by these datasets. Commonly used datasets for crowd activity analysis are UMN dataset (Detection of unusual crowd activity dataset, 2006) UCSD-ped1, ped2 dataset (UCSD Anomaly Detection Dataset, 2013),PETS dataset (Patino et al., 2016), web videos (Web Dataset, 2009), subway surveillance dataset, the boat-sea, boat-river, traffic-Belleview and airport-wrong-direction datasets (Anomalous Behavior Data Set, 2018). Recently a new dataset HIT-JUT (Han et al., 2016) is introduced for crowd activity detection which includes fight, shoot, and escape scenarios. It is captured in crowded indoor scenes with 15 people shot from two different views using two cameras. Saini et al. (2017) defined anomalies as Type-I and Type-II and their mathematical definitions. According to Type-I anomaly target resides within a region for a long duration of time. And in Type-II anomaly a target switches between two or more regions for a sustained duration. The above mentioned datasets (Akagunduz et al., 2016; Web Dataset, 2009; Diraco et al., 2010; Patino et al., 2016; Han et al., 2016; Anomalous Behavior Data Set, 2018) only exhibit Type-I anomaly. The In-House dataset introduced in the work (Saini et al., 2017) includes both Type-I and Type-II anomalies and provides wider set of anomaly situations. The dataset is recorded for 70 min using a static camera (25 FPS) hosted on top of a building, to capture public movement on a busy working day. The camera supports both HD as well as SD quality video recording. The video frames are prepossessed to 640 × 480. Whereas for single person Abnormal Human Action Recognition from 2011 to 2014 very less number of datasets were publicly available. In Khan and Sohn (2013, 2011), 2D-silhouette based abnormal dataset is introduced that considers six abnormal activities: forward fall, backward fall, chest pain, faint, vomit, and headache, stored in audio video interleave (AVI) format. The activities are executed by six persons (4 males, 2 females) by repeating ten sequences for each activity. There are 150 silhouettes for each activity and 900 silhouettes for each person performing the activities. Later, in the concern of ADL and elderly health care, good number of AbHAR 3D datasets are reported i.e. CAD60, CAD-120, TST fall detection dataset, UR fall detection, SisFall dataset, Le2i datasets.

CAD-60 (Cippitelli et al., 2016), CAD-120 are two popular datasets designed for home monitoring. CAD-120 includes 120 RGBD video sequences with 10-high level activities such as *making cereal, taking medicine, stacking objects, unstacking objects, microwaving food, Picking objects, cleaning objects, taking food, arranging objects, having a meal and* 12 object affordance labels: *reachable, movable, pourable, pour to, containable, drinkable, openable, placeable, closable, scrubbable, scrubber, stationary*. To provide Activity of daily living (ADL) and fall solutions TST Fall detection dataset v2 (Gasparrini et al., 2015) offers different variations of fall : forward fall, backward fall, side fall, fall ending up sitting and daily activities such as walk back and forth, sit on a chair, walk and grasp object from the floor, lying down . The dataset has been collected using Microsoft Kinect v2 and IMU (Inertial Measurement Unit) manufactured by Shimmer Research and simulated by 11 volunteers. The database contains 264 different actions for a total no. of 46 k skeleton samples and 230 k acceleration values. These actions are stored as depth frames, skeleton joints in-depth, time information helpful for synchronization and two raw acceleration streams, provided by SHIMMER devices constrained to the waist and right wrist of the volunteer. UR fall detection (Kwolek, 2014) dataset contains 70 (30 falls + 40 activities of daily living) sequences. Fall events are chronicled with two Microsoft Kinect cameras and corresponding accelerometric data. ADL events are recorded with only one device (camera 0) and accelerometer. Sensor data was collected using PS Move (60 Hz) and x-IMU (256 Hz) devices. On the basis of a survey (Sucerquia et al., 2017), exact pre and post falling situation are identified with the help of three questions (i) which activity the person was performing when the fall happened? (ii) Reason for fall? A sliding, a faint, a trip, other? (iii) In which orientation did the fall happen and what part of the body received the impact? SisFall dataset, selected Lateral fall/Fall forward/fall backward while walking caused by a slip/trip or falling asleep or while getting up/sitting down, vertical fall while fainting after surveying. In total it includes 15 types of falls and 19 ADL activities. Le2i robust fall detection dataset (Nguyen et al., 2016) has 221 videos (320 × 240 pixels at 25 fps) of different living environments with various daily activities. These video sequences includes real-world challenges such as shadow and light reflection, complex textured background, actors wear different colored clothes.

6. Conclusion and future directions

The literature has covered rapid development of feature designing strategies, from hand-crafted features to deep features, for video sequences to support a real-time, robust and computationally efficient abnormal human activity recognition framework depending on the context of application such as fall detection, Ambient Assistive Living (AAL), homeland security, surveillance or crowd analysis. The feature designing approach also change with dimension of input in the application i.e. RGB, depth and skeleton. In past few years, due to the diffusion of infrared sensor (Microsoft Kinect), abnormal human activity recognition using depth and skeleton sequences has proliferated. But the use of Kinect sensor is limited to confined region, therefore experiments are performed using depth sensors only for fall detection, AAL and smart home applications for abnormal human action recognition. Depth and skeleton representation provide view and illumination invariance, which are observed as a very serious issue in crowd or public scenes where the background changes dynamically with illumination variations in open areas. For multiple persons based abnormal human activities RGB images are used. Deep features based abnormal human action description which has surpassed the performance of hand-crafted features due to the ability of learning the video scenes dynamically but demands high computational resources.

The paper also incorporated through study of the publicly available dataset in the field of fall detection, AAL and abnormal human action recognition to outline the scope of experiments. As far as AbHAR datasets are concerned, many Kinect-based 3D datasets — pose based human activity datasets : *MoCap* (Subtle Walking From CMU Mocap Dataset, 2018) , MHAD (Teleimmersion Lab, 2018) , MSRAction3D dataset (MSR ACtion 3D Dataset, 0000) ; human interaction datasets :*G3Di* (Bloom et al., 2014) , K3Hi (K3HI Kinect-based 3D Human Interaction Dataset, 2018) , CONVERSE (Edwards et al., 2016), In-HOUSE Dataset (Saini et al., 2017), Fu Kinect Fall Dataset (Aslan et al., 2017) are being generated but the type of dataset stipulating the abnormal actions specifically, identified very few (Nguyen et al., 2016; Khan and Sohn, 2013, 2011; Han et al., 2016; Gasparrini et al., 2015; Sucerquia et al., 2017).

Table 8
3D AbHAR and AAL datasets summary.

Dataset	Method	Year	Accuracy	Precision	Recall	resolution	challenges
CAD-60	Key pose extraction and association using clustering algorithm (Cippitelli et al., 2016)	2016	–	93.9%	93.5%	640 × 480	Illumination Invariant
	Neural integration pose motion features (Parisi et al., 2015)	2015		91.9%	90.2%		
	Pose Kinetic energy (Shan and Akella, 2014)	2014		93.8%	94.5%		
CAD-120	Conditional Random Field (CRF) (Koppula and Saxena, 2013)	2013	93.5%	95.0%	93.3%	640 × 480	
	Latent graphical structure (Hu et al., 2014)	2014	87.0%	89.2%	83.1%		
TST fall detection v2	Fusion of Kinect sensor and joint acceleration matrix (Gasparrini et al., 2015)	2015	99%	–	–	512 × 424	–
UR Fall detection	Hough Transform on V-disparity values of images	2014	99.67%	–	–	640 × 480	View-invariant
Le2i dataset	Feature Set — MHI based motion magnitude and orientation measure with human shape variations	2016	–	93%	100%	320 × 240 (25 fps)	• shadow • light reflection, • complex textured background, • actors wear different colored clothes
In-HOUSE Dataset	Non-overlapping block-based surveillance scene segmentation (Saini et al., 2017)	2015	83%	100%	83%	640 × 480	Demonstrates both Type-I and Type II anomaly
Fu Kinect Fall Dataset	coded regions on nested circles (Aslan et al., 2017)	2017	97.92% (max)	–	–	–	View invariance

In future, abnormal human action recognition systems need to address specific issues to bring abnormal action recognition methodologies to a real-time platform within the affordable range of the common users that will foster the security level to a higher level in the day-to-day routine of the common user.

- During the survey, it was witnessed that a few handcrafted (Al-Nawash et al., 2016; Roshtkhari and Levine, 2013; Wang et al., 2017b; Uddina et al., 2011; Yang et al., 2016; Triantafyllou et al., 2016; Yu et al., 2013) and deep features (Li and Chuah, 2018) based recognition systems' performances cannot be maintained near to real-time performances due to non-availability of large-sized real-time dataset samples for validation. That limits not only the generalizability of the systems but also robustness. Human skeletons provide view invariance to the action, but the availability of abnormal actions from a different view is still a big challenge. The work (Diraco et al., 2010) also depend on artificially generated data which does not reflect real-life challenges. Therefore, some meaningful datasets must be developed to represent abnormal actions in different scenarios-office, home, the coffee shop.
- Researchers are working on developing deep architectures from primary CNN to RCNN, RNN, auto-encoders. However, availability of deep architectures (Wang et al., 2015b) based efficient and deeper abnormal action recognition system with required computational resources to the common man is a serious the future concern.
- Though three dimensional data have enhanced the performance of recognition systems yet computational complexity is always high while using three-dimensional data. Therefore, first challenge lies in transferring the knowledge of three-dimensional data as depth or skeleton based feature descriptor to a real-time AbHAR systems with improved true detection rate and less computational complexity.

Acknowledgments

The authors would like to acknowledge the support of the Biometric Research Laboratory, Department of Information Technology, Delhi Technological University, New Delhi, India.

References

Abobakr, A., Hossny, M., Nahavandi, S., 2017. A skeleton-free fall detection system from depth images using random Decision Forest. IEEE Syst. J. 1–12.
Aburomman, A.A., Reaz, M.B.I., 2016. Ensemble of binary SVM classifiers based on PCA and LDA feature extraction for intrusion detection. In: Advanced Information Management, Communicates, Electronic and Automation Control Conference (IMCEC). IEEE, Xi'an, China.
Aggarwal, H., Vishwakarma, D.K., 2016. Covariate conscious approach for Gait recognition based upon Zernike moment invariants. IEEE Trans. Cognitive Develop. Syst. PP (99), 1-1.
Akagunduz, E., Aslan, M., Sengur, A., Wang, H., Ince, M., 2016. Silhouette orientation volumes for efficient fall detection in depth videos. IEEE J. Biomed. Health Inform. PP (99), 2168–2194.
Al-Nawash, M., Al-Hazaimeh, O.M., Mohamad, S., 2016. A novel framework for intelligent surveillance system based on abnormal human activity detection in academic environments. Neural Comput. Appl. 28 (1), 565–572.
Alsheikh, M.A., Seleim, A.A.S., Niyato, D., Doyle, L., Lin, S., Tan, H.P., Deep activity recognition models with triaxial accelerometers, CoRR, arXiv:abs/1511.04664, 2016.
Alvar, M., Torsello, A., Miralles, A.S., Armingol, J.M., 2014. Abnormal behavior detection using dominant sets. Mach. Vis. Appl. 25 (5), 1351–1368.
Amir, J.L., Xu, S.D., Wang, G., 2016. Spatio-temporal LSTM with trust gates for 3D human action recognition. In: European Conference on Computer Vision (ECCV), Amsterdam, The Netherland.
Andò, B., Baglio, S., Lombardo, C.O., Marletta, V., 2015. An event polarized paradigm for ADL detection in AAL context. IEEE Trans. Instrum. Meas. 64 (7), 1814–1825.
Anomalous Behavior Data Set, [Online]. Available: http://vision.eecs.yorku.ca/research/anomalous-behaviour-data/. (Accessed 16 May 2018).
Antic, B., Ommer, B., 2011. Video parsing for abnormality detection. In: 13th International Conference on Computer Vision, Barcelona.
Antic, B., Ommer, B., Spatio-temporal video parsing for abnormality detection, arXiv, arXiv:abs/1502.06235, 2015, pp. 1–15.
Aquino, N.M.R., Gutosk, M., Hattori, L.T., Lopes, H.S., 2017. The effect of data augmentation on the performance of convolutional neural networks. In: Brazilian Society of Computational Intelligence, Niterói, Rio de Janeiro.
Arifoglu, D., Bouchachia, A., 2017. Activity recognition and abnormal behaviour detection with recurrent neural networks. In: International Conference on Mobile Systems and Pervasive Computing, Leuven, Belgium.

Aslan, M., Akbulut, Y., Sengor, A., CevdetInce, M., 2017. Skeleton based efficient fall detection. J. Faculty Eng. Architecture Gazi Univ. 32 (4), 1025–1034.
Ben, A.M., Zagrouba, E., 2018. Abnormal behavior recognition for intelligent video surveillance. Expert Syst. Appl. 91, 480–491.
Bian, Z., Chau, L.P., Thalmann, N.M., 2012a. Fall detection based on skeleton extraction. In: International Conference on Virtual-Reality Continuum and its Applications in Industry, Singapore.
Bian, Z.P., Chau, L.P., Thalmann, N.M., 2012b. A depth video approach for fall detection based on human joins height and falling velocity. In: Proceedings of International Conference on Computer Animation and Social Agents, Singapore.
Bian, Z.P., Chau, L.P., Thalmann, N.M., 2012. Fall detection based on skeleton extraction. In: 11th International Conference on Virtual-Reality Continuum and its Applications in Industry, Singapore.
Bian, Z.P., Hou, J., Chau, L.P., Thalmann, N.M., 2015. Fall detection based on body part trackingusing a depth camera. IEEE J. Biomed. Health Inform. 19 (2), 430–439.
Bilen, H., Fernando, B., Gavves, E., Vedaldi, A., Gould, S., 2016. Dynamic image networks for action recognition. In: CVPR, Las Vegas.
Bloom, V., Argyriou, V., Makris, D., 2014. G3Di: A gaming interaction dataset with a real time detection and evaluation framework. In: Workshop at the European Conference on Computer Vision. Cham.
Candás, J.L.C., Peláez, V., López, G., Fernández, M.Á., Álvarez, E., Díaz, G., 2014. An automatic data mining method to detect abnormal humanbehaviour using physical activity measurements. Pervasive Mob. Comput. 15, 228–241.
Cardile, F., Iannizzotto, G., Rosa, F.L., 2010. A vision-based system for elderly patients monitoring. In: 3rd International Conference on Human System Interaction, Rzeszow.
CAVIAR test case scenarios, 2005. http://homepages.inf.ed.ac.uk/rbf/CAVIAR/.
Cecotti, H., Graser, A., 2010. Convolutional neural networks for P300 detection with application to brain-computer interfaces. IEEE Trans. Pattern Anal. Mach. Intell. 33 (3), 433–445.
Chaaraoui, A.A., Padilla-López, J.R., Flórez-Revuelta, F., 2015. Abnormal gait detection with RGB-D devices. In: 11th IEEE International Conference and Workshops on Automatic Face and Gesture Recognition (FG), Ljubljana, Slovenia.
Chaaraoui, A.A., Pérez, P.C., Revuelta, F.F., 2012. A review on vision techniques applied to human behaviour analysis for ambient-assisted living. Expert Syst. Appl. 39 (12), 10873–10888.
Chandola, V., Banerjee, A., Kumar, V., 2009. Anomaly detection : a survey. ACM Comput. Surv. 41 (3).
Chathuramali, K.G.M., Ramasinghe, S., Rodrigo, R., 2014. Abnormal activity recognition using spatio-temporal features. In: 7th International Conference of Information and Automation of Sustainablilty, Colombo.
Chen, S., Gangopadhyay, A., 2016. Health care fraud detection with community detection algorithms. In: IEEE International Conference on Smart Computing (SMARTCOMP), St. Louis, MO.
Chen, L., Wei, J.F., H., 2013. A survey on human motion analysis using depth imagery. Pattern Recognit. Lett. 34, 1995–2006.
Chien, T.L., Su, K.L., Guo, J.H., 2005. The multiple interface security robot - WFSR-II. In: IEEE International Safety, Security and Rescue Rototics, Workshop, Kobe, Japan.
Cho, S.H., Kang, H.B., 2014. Abnormal behavior detection using hybrid agents in crowded scenes. Pattern Recognit. Lett. 54, 64–70.
Chong, Y.S., Tay, Y.H., 2017. Abnormal event detection in videos using spatiotemporal autoencoder. In: International Symposium on Neural Networks, Japan.
Chou, C.L., Chen, H.T., Lee, S.Y., 2017. Multimodal video-to-near-scene annotation. IEEE Trans. Multimed. 19 (2), 354–366.
Cippitelli, E., Gasparrini, S., Gambi, E., 2016. Ahuman activity recognition system using skeleton data from RGBD sensors. Comput. Intell. Neurosci. 2016, 1–14.
Coşar, S., Donatiello, G., Bogo, V., Garate, C., Alvares, L.O., Brémond, F., 2017. Toward abnormal trajectory and event detection in video surveillance. IEEE Trans. Circuit Syst. Video Technol. 27 (3), 683–695.
Cong, Y., Yuan, J., Tang, Y., 2013. Video anomaly search in crowded scenes via spatio-temporal motion context. IEEE Trans. Inform. Forensics Secur. 8 (10), 1590–1599.
Cook, D.J., Feuz, K.D., Krishnan, N.C., 2013. Transfer learning for activity recognition: a survey. Knowledge Inform. Syst. 36 (3), 537–556.
Crispim Junior, C.F., Joumier, V., Hsu, Y.L., Chung, P.C., Dechamps, A., Pai, M.C., Robert, P., Bremond, F., 2012. Alzheimer's patient activity assessment using different sensors. Gerontechnology 11 (2), 266–267.
Dai, X., Wu, M., Davidson, B., Mahoor, M., Zhang, J., 2013. Image-based fall detection with human posture sequence modelling. In: IEEE International Conference on Healthcare Informatics, Philadelphia, USA.
Detection of unusual crowd activity dataset, 2006. http://mha.cs.umn.edu/proj_events.shtml#crowd.
Diba, A., Gool, L.V., 2016. Efficient two-stream motion and appearance 3D CNNs for video classification. In: European Conference on Computer Vision, ECCV, Amsterdam, The Netherlands.
Ding, W., Liu, K., Fu, X., Cheng, F., 2016. Profile HMMs for skeleton-based human action recogniti. Signal Process., Image Commun. 42, 109–119.
Diraco, G., Leone, A., Siciliano, P., 2010. An active vision system for fall detection and posture recognition in elderly healthcare. In: Design, Automation & Test in Europe Conference & Exhibition, Dresden.
Dogra, D.P., Reddy, R., Subramanyam, K., Ahmed, A., Bhaskar, H., 2015. Scene representation and anomalous activity detection using weighted region associated graph. In: 10th International Conference on Computer Vision Theory and Applications, Berlin, Germany.
Dragone, M., Amato, G., Bacciu, D., Chessa, S., Coleman, S., Rocco, M.D., Gallicchio, C., Gennaro, C., Lozano, H., Maguire, L., McGinnity, M., Micheli, A., O'Hare, M.P., G., Renteria, A., Saffiotti, A., Vairo, C., Vance, P., 2015. A cognitive robotic ecology approach to self-configuring and evolving AAL systems. Eng. Appl. Artif. Intell. 45, 269–280.
EC, 2012. Active ageing special eurobarometer 378, tech. rep. DG COMM "Research and Speechwriting" Unit, European Comission. In: Conducted by TNS Opinion & Social at the request of Directorate-General for Employment, Social Affairs and Inclusion.
Edwards, M., Deng, J., Xie, X., 2016. From Pose to Activity : Surveying datasets and introducing CONVERSE. Comput. Vis. Image Underst. 144, 73–105.
Eng, H.L., Thida, M., Remagnino, P., 2013. Laplacian eigenmap with temporal constraints for local abnormality detection in crowded scenes. IEEE Trans. Cybern. 43 (6), 2147–2156.
Escalera, S., Baro, X., Gonzalez, J., Bautista, A.M., Madadi, M., Reyes, M., Ponce-Lopez, V., Escalante, J.H., Shotton, J., Guyon, I., 2014. Chalearn looking at people challenge 2014: Dataset. In: Computer Vision - ECCV 2014 Workshop, Zurich, Switzerland.
Escalera, S., Gonzàlez, J., Baró, X., Reyes, M., Lopes, O., Guyon, I., Athitsos, V., Escalante, H.J., 2013. Multi-modal gesture recognition challenge 2013: Dataset. In: International Conference on Multimodal Interaction, Sydney, Australia.
Fagette, A., Courty, N., Racoceanu, D., Dufour, J.Y., 2014. Unsupervised dense crowd detection by multiscale texture analysis. Pattern Recognit. Lett. 44, 126–133.
Feng, B., He, F., Wang, X., Wu, Y., Wang, H., Yi, S., Liu, W., 2016. Depth-projection-map-based bag of contour fragments for robust hand Gesture Recognition. IEEE Trans. Hum.-Mach. Syst. PP (99), 1–13.
Fothergill, S., Mentis, H., Kohli, P., Nowozin, S., 2012. Instructing people for training gestural interactive systems. In: Conference on Human Factors in Computing Systems, Austin, Texas.
Gasparrini, S., Cippitelli, E., Gambi, E., Spinsan, S., Wahslen, J., Orhan, I., Lindh, T., 2015. Proposal and experimental evaluation of fall detection solution based on wearable and depth data fusion. In: ICT Innovations, Advances in Intelligent Systems and Computing. Cham.
Gasparrini, S., Cippitelli, .E., Spinsante, S., Gambi, E., 2014. A depth-based fall detection system using a Kinect sensor. Sensors 14 (2), 2756–2775.
Gorai, A., Pal, R., Gupta, P., 2016. Document fraud detection by ink analysis using texture features and histogram matching. In: International Joint Conference on Neural Networks (IJCNN), Vancouver, BC.
Goudelis, G., Tsatiris, G., Karpouzis, K., Kollias, S., 2015. Fall detection using History Triple Features. In: Proceedings of the 8th ACM International Conference on PErvasive Technologies Related to Assistive Environments, Corfu, Greece.
Gowsikhaa, D., Abirami, S., Baskaran, R., 2014. Automated human behavior analysis from surveillance. Artif. Intell. Rev. 42 (5), 747–765.
Gu, X., Cui, J., Zhu, Q., 2014. Abnormal crowd behavior detection by using the particle entropy. Int. J. Light Electron Opt. 125 (14), 3428–3433.
Guo, C., Ma, Q., Zhang, L., 2008. Spatio-temporal saliency detection using phase spectrum of quaternion Fourier transform. In: IEEE Conference on Computer Vision and Pattern Recognition (CVPR), Anchorage, Alaska.
Guo, H., Wu, X., Cai, S., Li, N., Cheng, J., Chen, Y.L., 2016. Quaternion discrete cosine transformation signature analysis in crowd scenes for abnormal event detection. Neurocomputing 204, 106–115.
Hammerla, N., Halloran, S., Pltz, T., 2016. Deep, convolutional, and recurrent models for human activity recognition using wearables. In: International Joint Conference on Artificial Intelligence, New York.
Hammerla, N.Y., Plotz, T., 2015. Let's (not) stick together: pairwise similarity biases cross-validation in activity recognition. In: ACM International Joint Conference on Pervasive and Ubiquitous Computing (UbiComp), Umeda, Osaka, Japan.
Han, T., Yao, H., Sun, X., Zhao, S., Zhang, Y., 2016. Unsupervised discovery of crowd activities by saliency-based clustering. Neurocomputing 171, 347–361.
Hana, Y., Zhanga, P., Zhuob, T., Huangc, W., Zhang, Y., 2018. Going deeper with two-stream ConvNets for action recognition in video surveillance. Pattern Recognit. Lett. 107, 83–90.
Hanab, D., Liua, Q., Fan, W., 2018. A new image classification method using CNN transfer learning and web data augmentation. Expert Syst. Appl. 95 (1), 43–56.
Hassner, T., Itcher, Y., Gross, O.K., 2012. Violent flows: Real-time detection of violent crowd behavior. In: IEEE Computer Society Conference on Computer Vision and Pattern Recognition Workshops, Providence, RI.
Hendryli, J., Fanany, M.I., 2016. Classifying abnormal activities in exam using multi-class Markov chain LDA based on MODEC features. In: Fourth International Conference on Information and Communication Technologies, Bandung, Indonesia.
Herath, S., Harandi, M., Porikli, F., 2017. Going deeper into action recognition: a survey. Image Vis. Comput. 60, 4–21.
Hinami, R., Mei, T., Satoh, S., 2017. Joint detection and recounting of abnormal events by learning deep generic knowledge. In: ICCV, Venice Italy.
Hodge, V.J., Austin, J., 2004. A survey of outlier detection methodologies. Artif. Intell. Rev. 22 (2), 85–126.
Hou, J.C., Wang, S.S., Lai, Y.H., Tsao, Y., Chang, H.W., Wang, H.M., 2018. Audio-visual speech enhancement using multimodal deep convolutional neural networks. IEEE Trans. Emerg. Top. Comput. Intell. 2 (2), 117–128.

Hsieh, J.W., Chuang, C.H., Alghyali, S., Chiang, H.F., Chiang, C.H., 2015. Abnormal scene change detection from a moving camera using bag of patches and spider web map. IEEE Sens. J. 15 (5), 2866–2881.

Hu, N., Englebienne, G., Lou, Z., Kröse, B., 2014. Learning latent structure for activity recognition. In: IEEE International Conference on Robotics and Automation, Hong Kong.

Hu, Y., Zhang, Y., Davis, L., 2013. Unsupervised abnormal crowd activity detection using semiparametric scan statistic. In: Computer Vision and Pattern Recognition Workshop, Portland, Oregon.

Huang, B., Tian, G., Wu, H., Zhou, F., 2014. A method of abnormal habits recognition in intelligent space. Eng. Appl. Artif. Intell. 29, 125–133.

Hung, Y.X., Chiang, C.Y., Hsu, S.J., Chan, C.T., 2010. Abnormality detection for improving elder's daily life independent. In: International Conference on Smart Homes and Health Telematics, Korea.

Iannizzotto, G., Lanzafame, P., Rosa, F.L., 2005. A CNN-based framework for 2D still-image segmentation. In: International Workshop on Computer Architecture for Machine Perception, Palermo, Italy.

Ijjina, E.P., Chalavadi, K.M., 2017. Human action recognition in RGB-D videos using motion sequence information and deep learning. Pattern Recognit. 72, 504–516.

Ismail, S.J., Rahman, M.A.A., Mazlan, S.A., Zamzuri, H., 2015. Human gesture recognition using a low cost stereo vision in rehab activities. In: IEEE International Symposium on Robotics and Intelligent Sensors (IRIS), Langkawi.

Jalal, A., Kamal, S., Kim, D., 2014. A depth video sensor-based life-logging human activity recognition system for elderly care in smart indoor environment. J. Sensors 14 (7), 11735–11759.

Jansen, B., Deklerck, R., 2006. Context aware inactivity recognition for visual fall detection. In: Pervasive Health Conference and Workshops. IEEE, Innsbruck.

Ji, S., Xu, W., Yang, M., Yu, K., 2013. 3D convolutional neural networks for human action recognition. IEEE Trans. Pattern Anal. Mach. Intell. 35 (1), 221–231.

Jing, L., Ye, Y., Yang, X., Tian, Y., 2017. 3D convolutional neural network with multi-model framework for action recognition. In: International Conference on Image Processing (ICIP), Beijing, China.

Jo, H., Chug, K., Sethi, R.J., 2013. A review of physics-based methods for group and crowd analysis in computer vision. J. Postdr. Res. Postdr Aff. 1 (1), 4–7.

Jyothilakshmi, P., Rekha, K.R., Nataraj, K.R., 2016. Patient assistance system in a super speciality hospital using a kinect sensor camera. In: International Conference on Electrical, Electronics, and Optimization Techniques, Chennai.

Karpathy, A., Toderici, G., Shetty, S., Leung, T., Sukthanka, R., Fei-Fei, L., 2014. Large-scale video classification with convolutional neural networks In: Computer Vision and Pattern Recognition, Columbus, Ohio.

Khan, S.S., Hoey, J., 2017. Review of fall detection techniques: a data availability perspective. Med. Eng. Phys. 39, 12–22.

Khan, Z.A., Sohn, W., 2011. Abnormal human activity recognition system based on R-transform and kernel discriminant technique for elederly home care. IEEE Trans. Consum. Electron. 57 (4), 1843–1850.

Khan, Z.A., Sohn, W., 2013. A hierarchical abnormal human activity recognition system based on R-transform and kernel discriminant analysis for elderly health care. Computing 95 (2), 109–127.

Kok, V.J., Li, M.K., Chan, C.S., 2016. Crowd behavior analysis: a review where physics meets biology. Neurocomputing 177, 342–362.

Koohzadi, M., Charkari, N.M., 2017. Survey on deep learning methods in human action recognition. IET Comput. Vis. 11 (8), 623–632.

Koppula, H.S., Saxena, A., 2013. Learning spatio-temporal structure from RGB-D videos for human activity detection and anticipation. In: 30 th International Conference on Machine Learning, Atlanta, USA.

Kulkarni, P., Patil, B., Joglekar, B., 2015. An effective content based video analysis and retrieval using pattern indexing techniques. In: International Conference on Industrial Instrumentation and Control (ICIC), Pune.

Kwolek, M.K.B., 2014. Human fall detection on embedded platform using depth maps and wireless accelerometer. Comput. Methods Programs Biomed. 117 (3), 489–501.

K3HI: Kinect-based 3D Human Interaction Dataset, [Online] Available: http://www.lmars.whu.edu.cn/prof_web/zhuxinyan/DataSetPublish/dataset.html. (Accessed 16 May 2018).

Lane, N.D., Georgiev, P., Qendro, L., 2015. Deepear: robust smartphone audio sensing in unconstrained acoustic environments using deep learning. In: ACM International Joint Conference on Pervasive and Ubiquitous Computing (UbiComp), Umeda, Osaka, Japan.

Leach, M.J., Sparks, E., Robertson, N.M., 2014. Contextual anomaly detection in crowded surveillance scenes. Pattern Recognit. Lett. 44, 71–79.

Lecun, Y., Bottou, L., Bengio, Y., Haffner, P., 1998. Gradient-based learning applied to document recognition. Proc. IEEE.

Li, X., Chuah, M.C., 2018. ReHAR: Robust and Efficient Human Activity Recognition, in IEEE Winter Conference on Applications of Computer Vision, Lake Tahoe.

Li, C., Han, Z., Ye, Q., Jiao, J., 2012. Visual abnormal behavior detection based on trajectory sparse reconstruction analysis. Neurocomputing 119, 94–100.

Li, Y., Li, X., Jia, L., 2014a. Abnormal crowd behavior detection based on optical flow and dynamic threshold. In: Proceeding of the 11th World Congress on Intelligent Control and Automation, Shenyang, China.

Li, R., Lua, B., Maier, K.D.M., 2015a. Cognitive assisted living ambient system: a survey. Digit. Commun. Netw. 1 (4), 229–252.

Li, W., Mahadevan, V., Vasconcelos, N., 2014b. Anomaly detection and localization in crowded scenes. IEEE Trans. Pattern Anal. Mach. Intell. 36 (1), 18–32.

Li, A., Miao, Z., Cen, Y., Liang, Q., 2016. Abnormal event detection based on sparse reconstruction in crowded scenes. In IEEE International Conference on Acoustics, Speech and Signal Processing (ICASSP), Shanghai.

Li, H.C.T., Wang, M., Ni, B., Hong, R., Yan, S., 2015b. Crowd scene analysis : a survey. IEEE Trans. Circuits Syst. Video Technol. 25 (3), 1–20.

Li, N., Wu, X., Xu, D., Guo, u., Feng, W., 2015c. Spatio-temporal context analysis within video volumes for anomalous-event detection and localization. Neurocomputing 155, 309–319.

Liu, W., Fan, Y., Lei, T., Zhang, Z., 2014. Human gesture recognition using orientation segmentation feature on random rorest. In: IEEE China Summit & International Conference on Signal and Information Processing (ChinaSIP), Xi'an.

Liu, P., Tao, Y., Zhao, W., Tang, X., 2017. Surveillance scene segmentation based on trajectory classification using supervised learning. Neurocomputing 269, 3–12.

Liu, J., Wang, G., Duan, L.Y., Abdiyeva, K., Kot, A.C., 2018. Skeleton-based human action recognition with global context-aware attention LSTM networks. IEEE Trans. Image Process. 27 (4), 1586–1599.

Liua, Z., Zhangb, C., Tian, Y., 2016. 3D-based deep convolutional neural network for action recognition with depth sequences. Image Vis. Comput. 55 (2), 93–100.

Loy, C.C., Chen, K., Gong, S., Tao, X., 2013. Crowd counting and profiling: methodology and evaluation. In: Modeling, Simulation and Visual Analysis of Crowds. In: The International Series in Video Computing, vol. 11, Springer, New York, NY, pp. 347–382.

Zolfaghari, S., Keyvanpour, M.R., 2016. SARF: Smart activity recognition framework in Ambient Assisted Living. In: Federated Conference on Computer Science and Information Systems (FedCSIS), Gdansk.

Ma, X., Wang, H., Xue, B., Zhou, M., Ji, B., Li, Y., 2014. Depth-based human fall detection via shape features and improved extreme learning machine. IEEE J. Biomed. Health Inform. 18 (6), 1915–1922.

Medel, J., Savakis, A., 2016. Anomaly detection using predictive convolutional long short-term memory units, arXiv:1612.00390v2 [cs.CV].

Mehran, R., Oyama, A., Shah, M., 2009. Abnormal crowd behavior detection using social force model. In: IEEE Conference on Computer Vision and Pattern Recognition, Miami, FL.

Miguel, K.d., Brunete, A., Hernan, M., 2017. Home camera-based fall detection system for the elderly. Sensors (Basel) 17 (12).

Mohamed, O., Choi, H.J., Iraqi, Y., 2014. Fall detection systems for elderly care: A survey. In: International Conference on New Technologies, Mobility and Security (NTMS), Dubai, United Arab Emirates.

Mosquera, J.H., Loaiz, H., Nope, S.E., Restrepo, A.D., 2017. Identifying facial gestures to emulate a mouse: navigation application on Facebook. IEEE Latin Amer. Trans. 15 (1), 121–128.

MSR action 3D dataset, [Online]. Available: http://www.uow.edu.au/~wanqing/#Datasets.

Mubashir, M., Shao, L., Seed, L., 2013. A survey on fall detection : principles and approaches. Neurocomputing 100, 144–152.

Nar, R., Singal, A., Kumar, P., 2016. Abnormal activity detection for bank ATM surveillance. In: International Conference on Advances in Computing, Communications and Informatics, Jaipur, India.

Nguyen, V.A., Le, T.H., Nguyen, T.T., 2016. Single camera based fall detection using motion and human shape features. In: 7th International Symposium on Information and Communication Technology, Hochiminh city, Vietnam.

Nizam, Y., Mohd, M.N.H., Mohd, H., Jamil, M.M.A., 2016. Development of human fall detection system using joint height, joint velocity and joint position from depth maps. J. Telecommun. Electron. Comput. Eng. 8 (6), 125–131.

Paiement, A., Tao, L., Camplani, M., Hannuna, S., Damen, D., Mirmehdi, M., 2014. Online quality assessment of human motion from skeleton data. In: Proceedings of the British Machine Vision Conference, Nottingham.

Panahi, L., Ghods, V., 2018. Human fall detection using machine vision techniques on RGB–D images. Biomed. Signal Process. Control 44, 146–153.

Parisi, G.I., Weber, C., Werm, S., 2015. Self-organizing neural integration of pose-motion features for human action recognition. Front. Neurorobot. 9 (3), 1–14.

Park, J., Jang, K., Yang, S.B., 2018. Deep neural networks for activity recognition with multi-sensor data in a smart home. In: IEEE World Forum on Internet of Things (WF-IoT), Singapore.

Patino, L., Cane, T., Vallee, A., Ferryman, J., 2016. PETS 2016: Dataset and challenge. In: CVPR, Las Vegas, NV, USA.

Paul, M., Haque, S., Chakraborty, S., 2013. Human detection in surveillance videos and its applications - a review. EURASIP J. Adv. Signal Process. 1.

Piciarelli, C., Foresti, G.L., 2011. Surveillance-oriented event detection in video streams. IEEE Intell. Syst. 26 (3), 32–41.

Popoola, O.P., Wan, K., 2012. Video-based abnormal human behavior recognition—a review. IEEE Trans. Syst. Man Cybern. 42 (6), 865–878.

Presti, L.L., Cascia, M.L., 2016. 3D skeleton based human action classification : A survey. Pattern Recognit. 53, 130–147.

Rafferty, J., Nugent, C.D., Liu, J., Chen, L., 2017. From activity recognition to intention recognition for assisted living within smart homes. IEEE Trans. Hum.-Mach. Syst. PP (99), 1–12.

Rashidi, P., Mihailidis, A., 2013. A survey on ambient-assisted living tools for older adults. IEEE J. Biomed. Health Inform. 17 (3), 579–590.
Ravanbakhsh, M., Nabi, M., Mousavi, H., Sangineto, E., Sebe, N., 2016. Plug-and-play Cnn for crowd motion, arXiv:1610.00307.
Ravanbakhsh, M., Nabi, M., Sangineto, E., Marcenaro, L., Regazzoni, C., Sebe, N., 2017. Abnormal event detection in videos using generative adversarial nets. In: IEEE International Conference on Image Processing (ICIP), Beijing, China.
Riboni, D., Bettini, C., Civitarese, G., Janjua, Z.H., Helaoui, R., 2015. Fine-grained recognition of abnormal behaviors for early detection of mild cognitive impairment. In: IEEE International Conference on Pervasive Computing and Communications, St. Louis, USA.
Riboni, D., Civitarese, G., Bettini, C., 2016. Analysis of long-term abnormal behaviors for early detection of cognitive decline. In: IEEE International Workshop on PervAsive Technologies and care systems for sustainable Aging-in-place, Sydney.
Roshtkhari, M.J., Levine, M.D., 2013. Online dominant and anomalous behaviour detection in videos, In: Conference on Computer Vision and Pattern Recognition (CVPR), Portland, Oregon.
Roshtkhari, M.J., Levine, M.D., 2013. An on-line real-time learning method for detecting anomalies in videos using spatio-temporal compositions. Comput. Vis. Image Underst. 117 (10), 1436–1452.
Roudposhti, K.K., Dias, J., Peixoto, P., Metsis, V., Nunes, U., 2017. A multilevel body motion-based human activity analysis methodology. IEEE Trans. Cogn. Develop. Syst. 9 (1), 16–29.
Rougier, C., Auvinet, E., Rousseau, J., Mignotte, M., Meunier, J., 2011a. Fall detection from depth map video sequences. In: International Conference on Smart Homes and Health Telematics, Montreal.
Rougier, C., Meunier, J., St-Arnaud, A., Rousseau, J., 2006. Monocular 3D head tracking to detect falls of elderly people. In: IEEE International Conference on Engineering in Medicine and Biology Society, New York.
Rougier, C., Meunier, J., St-Arnaud, A., Rousseau, J., 2011b. Robust video surveillance for fall detection based on human shape deformation. IEEE Trans. Circuit. Syst. Video Technol. 21 (5), 611–622.
Russakovsky, O., Deng, J., Su, H., Krause, J., Satheesh, S., Ma, S., Huang, Z., Karpathy, A., Khosla, A., Bernstein, M., Berg, A.C., Fei, F.L., 2014. ImageNet large scale visual recognition challenge. Int. J. Comput. Vis. 115 (3), 211–252.
Sacco, G., Joumier, V., Darmon, N., Dechamps, A., Derreumaux, A., Lee, J.H., Piano, J., Bordone, N., Konig, A., Teboul, B., Davi, R., Guerin, O., Bremond, F., Robert, P., 2012. Detection of activities of daily living impairment in Alzheimer's disease and mild cognitive impairment using information and communication technology. Clin. Interv. Aging 7, 539–547.
Saini, R., Sk, A.A., Dogra, D.P., Roy, P.P., 2017. Surveillance scene segmentation based on trajectory classification using supervised learning. In: Proceedings of International Conference on Computer Vision and Image Processing, Roorke.
Sargano, A.B., Wang, X., Angelov, P., Habib, Z., 2017. Human action recognition using transfer learning with deep representations. In International Joint Conference on Neural Networks (IJCNN), Anchorage, AK, USA.
Shan, J., Akella, S., 2014. 3D human action segmentation and recognition using pose kinetic energy. In: IEEE Workshop on Advanced Robotics and its Social Impacts, Evanston, Illinois, USA.
Shao, J., Loy, C.C., Kang, K., Wang, X., 2016. Slicing convolutional neural network for crowd video understanding. In: IEEE Conference on Computer Vision and Pattern Recognition, Las Vegas, NV, USA.
Shih, H.C., 2017. A survey on content-aware video analysis for sports. IEEE Trans. Circuits Syst. Video Technol. PP (99), 1-1.
Simonyan, K., Zisserman, A., 2014. Two-stream convolutional networks for action recognition in videos. In: Advances in Neural Information Processing Systems (NIPS), Montreal; Canada.
Sindagi, V.A., Patel, V.M., 2018. A survey of recent advances in CNN-based single image crowd counting and density estimation. Pattern Recognit. Lett. 107, 3–16.
Singh, K., Vishwakarma, D.K., Walia, G.S., Kapoor, R., 2016. Contrast enhancement via texture region based histogram equalization. J. Modern Opt. 63 (15), 1444–1450.
Song, X., Fan, G., 2006. Joint key-frame extraction and object segmentation for content-based video analysis. IEEE Trans. Circuits Syst. Video Technol. 16 (7), 904–914.
Song, S., Lan, C., Xing, J., Zen, W., Liu, J., 2016. An end-to-end spatio-temporal attention model for human action recognition from skeleton data, CoRR, arXiv:1611.06067.
Stein, M., Janetzko, H., Lamprecht, A., Seebacher, D., Schreck, T., Keim, D., Grossniklaus, M., 2016. From game events to team tactics: Visual analysis of dangerous situations in multi-match data. In: International Conference on Technology and Innovation in Sports, Health and Wellbeing (TISHW), Vila Real.
Stephens, K., Bros, A.G., Grouping multi-vector streaklines for human activity identification. In: IEEE 12th Image, Video, and Multidimensional Signal Processing Workshop, Bordeaux, 2016.
Subtle Walking From CMU Mocap Dataset, [Online]. Available: http://users.eecs.northwestern.edu/~jwa368/my_data.html. (Accessed 16 May 2018).
Sucerquia, A., López, J.D., Vargas-Boni, J.F., 2017. SisFall: a fall and movement dataset. Sensors 17 (198), 1–14.
Synder, D., 2001. Online Intrusion Detection Using Sequences of System Calls. (MS thesis), Department of Computer Science, Florida State University.
Synnott, J., Nugent, C., Jeffers, P., 2015. Simulation of smart home activity datasets. Sensors 15 (6), 14162–14179.
Taylor, G.W., Fergus, R., LeCun, Y., Breg, C., 2010. Convolutional Learning of Spatio-temporal Features, In: ECCV, Greece.
Teleimmersion Lab, [Online]. Available: http://tele-immersion.citris-uc.org/berkeley_mhad/. (Accessed 16 May 2018).
Tham, J.S., Chang, Y.C., Fauzi, M.F.A., 2014. Automatic identification of drinking activities at home using depth. In: International Conference on Control, Automation and Information Sciences, Gwangju, Korea.
Thida, M., Yong, Y.L., Pérez, P.C., Eng, H.l., Remagnino, P., 2013. A literature review on video analytics of crowded scenes. In: Intelligent Multimedia Surveillance: Current trends and research. Springer, Berlin Heidelberg, pp. 17–36.
Tolosana, R., Rodriguez, R.V., Fierrez, J., Garcia, J.O., 2018. Exploring recurrent neural networks for on-line handwritten Signature Biometrics. IEEE Access 6, 5128–5138.
Toreyin, B.U., Dedeoglu, Y., Cetin, A.E., 2006. HMM based falling person detection using both audio and video. In: Signal Processing and Communications Applications, Antalya.
Tran, T.T.H., Le, T.L., Morel, J., 2014. An analysis on human fall detection using skeleton from Microsoft kinect. In: International Conference on Communication and Electronics (ICCE), Danang, Vietnam.
Tran, T., Pham, T., Carneiro, G., Palm, L., Reid, I., 2017. A Bayesian data augmentation approach for learning deep models. In: Neural Information Processing Systems (NIPS), Long Beach California.
Triantafyllou, D., Krinidis, S., Ioannidis, D., Metaxa, I.N., Ziazios, C., Tzovaras, D., 2016. A real-time fall detection system for maintenance activities in indoor environments. IFAC-PapersOnLine 49 (28), 286–290.
Tripathi, G., Singh, K., Vishwakarma, D.K., 2018. Convolutional neural networks for crowd behaviour analysis: a survey. Vis. Comput. PP, 1–24.
Turaga, P., Chellappa, R., Subrahmanian, V.S., Udrea, O., 2008. Machine recognition of human activities: a survey. IEEE Trans. Circuits Syst. Video Technol. 18 (11), 1473–1488.
UCSD Anomaly Detection Dataset, 2013. http://svcl.ucsd.edu/projects/anomaly/dataset.htm.
Uddin, M.Z., haksar, W., Torresen, J., 2017. Facial expression recognition using salient features and convolutional neural network. IEEE Access 5.
Uddin, M.Z., Kim, J.T., Kim, T.S., 2014. Depth video-based gait recognition for smart home using local directional pattern features and hidden markov model. Indoor Built Environ. 23 (1), 133–140.
Uddina, M.Z., Kim, T.S., Kim, J.T., 2011. Video-based indoor human gait recognition using depth imaging and hidden markov model : a smart system for smart home. Indoor Built Environ. 20 (1), 120–128.
Vaswani, N., Chowdhury, A.K.R., Chellappa, R., 2005. Shape activity: a continuous-state HMM for moving/deforming shapes with application to abnormal activity detection. IEEE Trans. Image Process. 14 (10), 1603–1616.
Vesperini, F., Vecchiotti, P., Principi, E., Squartini, S., Piazza, F., 2018. Localizing speakers in multiple rooms by using deep neural networks. Comput. Speech Lang. 49, 83–106.
Vignesh, K., Yadav, G., Sethi, A., 2017. Abnormal event detection on BMTT-PETS 2017 surveillance challenge. In: CVPR, Honolulu, Hawaii.
Vishwakarma, D.K., Dhiman, A., Maheshwari, R., 2015a. Human motion analysis by fusion of silhouette orientation and shape features. In: 3rd International Conference on Recent Trends in Computing (ICRTC), Ghaziabad, India.
Vishwakarma, D.K., Kapoor, R., Dhiman, A., 2016a. A proposed unified framework for the recognition of human activity by exploiting the characteristics of action dynamics. Robot. Auton. Syst. 77, 25–38.
Vishwakarma, D.K., Kapoor, R., Dhiman, A., 2016b. Unified framework for human activity recognition: An approach using spatial edge distribution and R-transform. AEU-Int. J. Electron. Commun. 70 (5), 341–353.
Vishwakarma, D.K., Rawat, P., Kapoor, R., 2015b. Human activity recognition using gabor wavelet transform and ridgelet transform. In 3rd International Conference on Recent Trends in Computing (ICRTC), Ghaziabad, India.
Vishwakarma, D.K., Singh, K., 2016. Human activity recognition based on spatial distribution of gradients at sub-levels of average energy silhouette images. IEEE Trans. Cogn. Develop. Syst. 9 (4), 316–327.
Wang, L., Ge, L., Li, R., Fang, Y., 2017a. Three-stream CNNs for action recognition. Pattern Recognit. Lett. 92 (1), 33–40.
Wang, L., Qiao, Y., Tang, X., 2015. Action recognition with trajectory-pooled deep-convolutional descriptors. In: CVPR, Boston, MA, USA.
Wang, L., Xiong, Y., Wang, Z., Qiao, Y., 2015. Towards good practices for very deep two-stream ConvNets, CoRR, arXiv:abs/1507.02159.
Wang, L., Xu, Y., Cheng, J., Xia, H., Yin, J., 2018. Human action recognition by learning spatio-temporal features with deep neural network. IEEE Access 6, 17913–17922.
Wang, C., Yao, H., Sun, X., 2017b. Anomaly detection based on spatio-temporal sparse representation and visual attention analysis. Multimedia Tools Appl. 76 (5), 6263–6279.
Web Dataset: Abnormal/Normal Crowds, 2009. Available from http://crcv.ucf.edu/projects/Abnormal_Crowd/Normal_Abnormal_Crowd.zip.
World Health Organization (WHO), 2008. Global report on falls prevention in older age, Geneva.
Yang, L., Ren, Y., Hu, H., Tian, B., 2015. New fast fall detection method based on spatio-temporal context tracking of head by using depth images. Sensors 15, 23004–23019.
Yang, L., Ren, Y., Zhang, W., 2016. 3D depth image analysis for indoor fall detection of elderly people. Digit. Commun. Netw. 2, 24–34.

Yao, L., Min and. K. Lu, W., 2017. A new approach to fall detection based on the human torso motion model. Appl. Sci. 7.
Yin, W., Kann, K., Yu, M., Schütz, H., Comparative Study of CNN and RNN for Natural Language Processing, 2017. arXiv:1702.01923.
Yu, X., 2008. Approaches and principles of fall detection for elderly and patient. In: 10th International Conference on E-health Networking, Applications and Services, Singapore.
Yu, S.J., Koh, P., Kwon, H., Kim, D.S., Kim, H.K., 2016. Hurst parameter based anomaly detection for intrusion detection system. In: IEEE International Conference on Computer and Information Technology (CIT), Nadi.
Yu, M., Yu, Y., Rhuma, A., Mohsen, S., Naqvi, R., Wang, L., Chambers, J.A., 2013. An online one class support vector machine-based person specific fall detection system for monitoring an elderly individual in a room environment. IEEE J. Biomed. Health Inform. 17 (6), 1002–1014.
Zerrouki, N., Harrou, F., Sun, Y., Houacine, A., 2016. Accelerometer and camera-based strategy for improved human fall detection. J. Med. Syst. 40 (12), 1–6.
Zhan, Y., Lu, H., Zhang, L., Ruan, X., 2016. Combining motion and appearance cues for anomaly detection. Pattern Recognit. 51, 443–452.
Zhang, Z., Liu, W., Metsis, V., Athitsos, V., 2012. A viewpoint-independent statistical method for fall detection. In: 21st International Conference on Pattern Recognition, Tsukuba.
Zhang, Y., Lu, H., Zhang, L., Ruan, X., Sakai, S., 2016. Video anomaly detection based on locality sensitive hashing filters. Pattern Recognit. 59, 302–311.
Zhang, Z., Ma, X., Song, R., Ron, X., Tian, X., Tian, G., Li, Y., 2017. Deep learning based human action recognition: A survey, in Chinese Automation Congress (CAC), Jinan, China.
Zhang, Y., Shang, K., Wang, J., Li, N., Zhang, M.M., 2018a. Patch strategy for deep face recognition. IET Image Process. 12 (5), 819–825.
Zhang, L., Wu, X., Luo, D., 2015. Human activity recognition with HMM-DNN model. In: International Conference on Cognitive Informatics & Cognitive Computing, Beijing, China.
Zhang, X.Y., Yin, F., Zhang, Y.M., Liu, C.L., Bengio, Y., 2018b. Drawing and recognizing chinese characters with recurrent neural network. IEEE Trans. Pattern Anal. Mach. Intell. 40 (4), 849–862.
Zhao, X., Naguib, A.M., Lee, S., 2014. Kinect based calling gesture recognition for taking order service. In: 23rd IEEE International Symposium on Robot and Human Interactive Communication, Edinburgh, Scotland, UK.
Zhao, Y., Qiao, Y., Yang, J., Kasabov, N., 2015. Abnormal activity detection using spatio-temporal feature and laplacian sparse representation. In: International Conference on Neural Information Processing, Switzerland.
Zhu, X., Liu, Z., 2011a. Human behavior clustering for anomaly detection. Front. Comput. Sci. 5 (3), 279–289.
Zhu, X., Liu, Z., 2011b. Human behavior clustering for anomaly detection. Front. Comput. Sci. China 5 (3), 279–289.
Zhu, G., Xu, C., Huang, Q., Rui, Y., Jiang, S., Gao, W., Yao, H., 2009. Event tactic analysis based on broadcast sports video. IEEE Trans. Multimed. 11 (1), 49–67.
Zhu, G., Zhang, L., Shen, P., Song, J., 2017. Multimodal gesture recognition using 3D convolution and convolutional LSTM. IEEE Access PP (99), 1-1.
Zitouni, M.S., Bhaskar, H., Dias, J., Al-Mualla, M., 2016. Advances and trends in visual crowd analysis: a systematic survey. Neurocomputing 186, 139–159.



Ms. Chhavi Dhiman received B.Tech. from Indira Gandhi Technical University for Women, New Delhi, India in 2011, and M.Tech. from Delhi Technological University, New Delhi, India in year 2014. She is currently working towards the Ph.D. degree in the Bio-Metric Research Laboratory, Delhi Technological University, New Delhi. Her current research interest includes deep learning, pattern recognition, human abnormal action identification and classification.



Dinesh Kumar Vishwakarma received the B.Tech. degree from Dr. Ram Manohar Lohia Avadh University, Faizabad, India in 2002, the M.Tech. degree from the Motilal Nehru National Institute of Technology, Allahabad, India in 2005, and the Ph.D. degree from Delhi Technological University, New Delhi, India, in 2016. He is currently an Associate Professor with the Department of Information Technology, Delhi Technological University, New Delhi, India. His current research interests include Human–Computer Interaction, Machine Learning, Deep Learning, Pattern Recognition, Computer Vision, Human Action and Activity Recognition, Sentiment Analysis, Spam Analysis, and Fake News Analysis. He is also reviewer of various journals of IEEE/IET, Springer, and Elsevier.

Computers and Electrical Engineering 71 (2018) 611–626

Contents lists available at ScienceDirect

Computers and Electrical Engineering

journal homepage: www.elsevier.com/locate/compeleceng

An extensive analysis of search-based techniques for predicting defective classes☆

Ruchika Malhotra

Discipline of Software Engineering, Department of Computer Science & Engineering, Delhi Technological University, Delhi, India

ARTICLE INFO

Article history:
Received 2 June 2017
Revised 28 August 2018
Accepted 28 August 2018

Keywords:
Defect prediction
Object-oriented metrics
Search-based techniques
Hybridized techniques
Empirical validation

ABSTRACT

In spite of constant planning, effective documentation and proper implementation of a software during its life cycle, many defects still occur. Various empirical studies have found that prediction models developed using software metrics can be used to predict these defects. Researchers have advocated the use of search-based techniques and their hybridized versions in literature for developing software quality prediction models. This study conducts an extensive comparison of 20 search-based techniques, 16 hybridized techniques and 17 machine-learning techniques amongst each other, to develop software defect prediction models using 17 data sets. The comparison framework used in the study is efficient as it (i) deals with the stochastic nature of the techniques (ii) provides a fair comparison amongst the techniques (iii) promotes repeatability of the study and (iv) statistically validates the results. The results of the study indicate promising ability of search-based techniques and their hybridized versions for predicting defective classes.

© 2018 Elsevier Ltd. All rights reserved.

1. Introduction

In today's era, software industries have touched new heights with ever-increasing demands for new applications based on upcoming and cutting-edge technologies. The complexity and restrictions under which the software is developed are increasing, thus, it is becoming difficult to produce a defect-free software. Occurrence of defects in a software will lead to increase in development time, maintenance costs and customer dissatisfaction. Hence, software testing and verification activities along with debugging process should be used to remove defects from a software. However, software testing is very costly in terms of time and resources, therefore, software should be analyzed quantitatively to predict where the errors are likely to occur. Prediction of software defects in the early phases of software development serves as a guiding tool to build better quality software at reduced costs [1]. This is important as the cost to rectify errors increases exponentially as they propagate to later stages of a software product. According to literature studies, software metrics are effective predictors in determining defective portions of a software [2]. The early detection of defects in the life cycle of a software product can enable testing experts to focus their resources on defect-prone areas of the software under development. This would enable the development of a software with fewer defects.

Over the years, there has been a surge of studies in defect prediction which use Machine Learning (ML) techniques [2]. In the last decade, apart from ML techniques, the use of Search-Based Techniques (SBT) have gained importance for developing effective defect prediction models [3]. SBT use metaheuristic search with the aim to provide an optimal or near-optimal

☆ Reviews processed and approved for publication by the Editor-in-Chief.

E-mail address: ruchikamalhotra@dtu.ac.in

https://doi.org/10.1016/j.compeleceng.2018.08.017
0045-7906/© 2018 Elsevier Ltd. All rights reserved.

solution amongst a large search space of possible solutions for the problem under consideration. The fitness function of a SBT is used to compute the quality of solutions and can be easily represented in the form of performance measures in case of software quality predictive modeling [4]. Apart from SBT, their hybridized versions should also be explored in the predictive modeling domain. The HyBridized Techniques (HBT) combine the advantages of both SBT and ML techniques into a single technique. The use of such techniques may provide an improvement in the performance of the developed predicted models. Hence, this work evaluates the capabilities of these three categories of techniques. It is important to compare their capabilities as it would guide the software community in the effective selection of modeling techniques for developing predictive models which determine defective portions of a software product.

It has been noted in the literature, that previous comparison of classification techniques is often done in an improper manner, leading to inappropriate conclusions and worthless results. However, a fair comparison should be carried out. For example, *Technique X* scored better than *Technique Y*, but, *Technique X* running time is smaller whilst *Technique Y*. To really show that *Technique Y* outperforms *Technique X, Technique X* should be allowed to run up to the time *Technique Y* runs (or to consume an equal number of fitness evaluations). Keeping this in view, this work conducts a fair comparison by assuring that all compared meta-heuristics techniques used proper parameter settings that do not allow certain meta-heuristics to consume more fitness evaluations or run longer. Further, to deal with the stochastic nature of SBT and their hybridized versions the study performed multiple runs to reduce result bias. In addition, to deal with the imbalanced nature of the data sets, appropriate performance measures were used. Moreover, statistical tests were conducted to verify the superiority of specific techniques. A recent review on the application of SBT in software quality predictive modeling domain pointed out that 62% of the investigated studies did not perform any statistical validation of the obtained results [2]. Thus, there is an urgent need for such a comparative study to yield generalizable results which are widely accepted since previous studies have not suitably addressed concerns such as “fair comparison” or “rigorous statistical validation of results”. Moreover, the study assesses 46 modeling techniques for developing effective defect prediction models on 17 datasets. Thus, the results obtained would be “generalizable” and would aid in “efficient selection of a technique” for developing defect prediction models.

Hence, the major contributions of the study are as follows:

1. Use of various techniques and data sets for extensive comparison: The study compares and assesses 10 ML techniques, 20 SBT and 16 HBT for predicting defective classes using Object-Oriented (OO) metrics. The results are validated on 17 data sets obtained from Promise data repository [4] so that well-formed and generalized conclusions can be derived.
2. Use of fair comparison amongst techniques: This study ensures appropriate run time for each technique in order to perform unbiased comparison amongst the investigated techniques.
3. Use of appropriate performance measures: The unbalanced nature of the data sets is dealt with using appropriate performance measures i.e. G-mean and Balance. These performance measures are advocated by Kubat and Matwin [5] and Menzies et al. [6] to assess and analyze the prediction models that are constructed using imbalanced data sets.
4. Use of multiple runs to deal with the stochastic nature of SBT: In order to deal with the non-deterministic nature of the SBT and their hybridized versions, researchers advocate the use of multiple runs. In this work, the author utilizes thirty runs for each technique for development of defect prediction models.
5. Use of statistical tests to verify whether the techniques are statistically different than each other: Demšar [7] advocated the use of statistical tests for comparing and assessing the predictive capability of the compared techniques. This work uses Friedman test for statistically determining the superiority of one technique over the other and Nemenyi test for determining significance of techniques when compared pairwise. Kendall’s coefficient of concordance is also reported.

As already discussed, it is important to ascertain a relevant category of technique which is appropriate for developing predictive models for ascertaining defective classes in a software. Thus, this study provides an extensive comparison by validating a wide number of techniques belonging to three specific categories to determine their effectiveness in developing software defect prediction models. The following Research Questions (RQ) are formed in order to achieve the above main contributions.

RQ1: What is the comparative performance of ML techniques, SBT and HBT for developing predictive models for identifying defective classes in a software?

RQ2: Which is the best or the worst technique for defect prediction using OO metrics? Which techniques are significantly better as compared to the other techniques?

The results of the study point out that the defect prediction models developed using SBT and HBT perform well when compared to ML techniques with respect to G-mean and Balance values. While a SBT which is based on Genetic Programming (GP) named Bojarczuk yielded the best G-mean values, the best Balance values were exhibited by an HBT named Decision Trees with Genetic Algorithms (DT-GA). The worst G-mean and Balance values were exhibited by an ML technique (Partial Decision Trees (PART)). Thus, researchers and practitioners should evaluate the use of SBT and their hybridized versions for developing defect prediction models.

The evidence gathered from this study will guide the practitioners and researchers in the selection of an efficient technique for defect prediction. The results of the study will allow developers and managers to plan and allocate the testing and inspection resources in a better fashion. The defective classes of a software may be given a larger percentage of testing

and maintenance resources so that stringent testing and maintenance activities can be performed. This would provide better quality software products at reasonable costs.

The remainder of the study is organized as follows: Section 2 summarizes the related work that focuses on defect prediction using SBT and HBT. In Section 3, the research components are presented and Section 4 presents the experimental design of the study. Section 5 presents the results that provide the answers to the RQs. Section 6 provides a discussion of results and Section 7 summarizes the threats to empirical validity. Finally, in Section 7 the conclusions and future work of the research is presented.

2. Related work

The ML techniques, SBT and HBT have been widely used for various applications [8]. Some of the interesting applications of these techniques include unmanned aerial systems specifically mission critical planning, ground control operators modeling behavior and malware detection.

The details on these studies can be found in a recent systematic review conducted in [2] that focuses on the use of ML techniques for defect prediction.

A number of studies in literature have successfully used SBT for predicting defect-prone modules/classes. A study by Carvalho et al. [9] analyzed the effectiveness of Multi-Objective Particle Swarm Optimization (MOPSO) on industrial data sets for predicting defective modules/classes by optimizing both the sensitivity and the specificity of individual solutions. Catal and Diri [10] explored several artificial immune system algorithms for predicting defective classes on industrial data sets. The capability of Ant Colony Optimization (ACO) technique for defect prediction was analyzed by Vandercruys et al. [11] by statistically comparing the performance of the model developed by ACO with several other ML techniques. A study by Singh et al. [12] validated the effectiveness of gene expression programming, while Liu et al. [13] used genetic programming for developing defect prediction models. Pendharkar [14] proposed two hybrid techniques that combined exhaustive search and simulated annealing respectively, with probabilistic neural networks for effective learning of software defect prediction models. Another hybrid technique, which was a combination of Genetic Algorithm (GA) with support vector machine (SVM) was successfully used by Di Martino et al. [15] and Sarro et al. [16] for predicting defect prone classes.

Yu [17] proposed the use of evolutionary programming integrated with asymmetric weight least square SVM, which depicted promising results for ascertaining defective modules. Rodriguez et al. [18] successfully used evolutionary decision rules subgroup discovery algorithm on several industrial data sets for predicting defective modules. Canfora et al. [19] used the NSGA-II algorithm along with logistic regression technique on several widely used open source data sets for developing defect prediction models. Jin & Jin [20] assessed the capability of three HBT for developing prediction models to identify defective classes. Arar & Ayan [21] assessed the capability of two SBT and one HBT and compared the performance of these techniques with three ML algorithms. A recent study by Hosseini et al. [22] used nearest-neighbor filter which was embedded in a GA for selecting training data for cross project defect prediction. Xia et al. [23] developed cross-project defect prediction models using GA and logistic regression.

Although, the studies mentioned above use SBT and HBT for analyzing the relationship between OO metrics and defect prediction, but they have evaluated only few of these techniques. To the best of the author's knowledge, there is no study till date that extensively analyzes and compares 20 SBT and 16 HBT for defect prediction. These techniques are also compared with 10 ML techniques. Another issue which needs to be addressed while comparing various techniques is the statistical evaluation of the obtained results., There are few studies which evaluate the statistical significance of the obtained results. To incorporate statistical comparison, this study will evaluate the results using Friedman test. The study also reports the effect size and performs post-hoc analysis (Nemenyi test). As discussed in Section 1, another important issue is "fair comparison" amongst techniques. The current study attempts to perform fair comparison amongst the investigated techniques. It may also be noted that the framework used in this work is complete and repeatable. Therefore, the study can be easily replicated in the future and the framework can be used for effective comparison amongst various classification techniques.

3. Empirical research components

This section describes the datasets, independent and dependent variables, performance evaluation measures, the validation method and the statistical tests used in the study.

3.1. Data sets

The results of the work are validated using 17 data sets obtained from Promise data repository [4]. The systems have been developed using Java programming language and can be easily downloaded from the Promise repository. The datasets were collected by Jureczko and Madeyski [24] using two tools, namely: CKJM and BugInfo. Each dataset consists of 19 commonly used OO metrics collected using CKJM, an open source tool. The definition of these metrics is given in the next section. The BugInfo tool was used to identify whether a commit, extracted from the source code repository was a bug fix or not. This was done by regular expression matching. The regular expressions were formulated using bug fixes commented guidelines. These guidelines were the ones which were used in the source code repositories such as Git and SVN. The 17 datasets were chosen as a) they were open-source and easily available which enhances the replicability of the study, b) they belong to

Table 1
Summary of data sets.

Data set	#Cls.	# Defc.	% Defc.	LOC	Data set name	#Classes	# Defc.	% Defc.	LOC
Ant	745	166	22.28	208,653	**Log4j**	135	34	25.19	21,549
Arc	234	27	11.54	31,342	**Lucene**	340	203	59.71	102,859
Berek	43	16	37.21	32,320	**Nieruchomosci**	27	10	37.04	4754
Camel	965	188	19.48	113,055	**Zuzel**	29	13	44.83	
Ckjm	10	5	50	1469	**Redaktor**	176	27	15.34	59,280
Elearning	64	5	7.81	3639	**Serapion**	45	10	22.22	10,505
Intercafe	27	4	14.81	11,322	**Workflow**	39	20	51.28	4125
Ivy	352	40	11.36	87,769	**Wspo**	18	12	66.67	5685
Kalkulator	27	6	22.22	4022					

Table 2
Independent variables used in the study.

Metrics	Full form	Description
amc	Average method complexity	Estimates the average method size for a specific class.
ca	Afferent couplings	Counts the number of external classes dependent on a given class.
cam	Cohesion amongst classes	Estimates the cohesion among methods of a class by analysing their list of parameters.
lcom	Lack of cohesion in methods	Based on the pairs of methods that do not have any common attribute usage.
cbm	Coupling between methods	Counts the number of methods (new or redefined) to which all the methods that are inherited are coupled.
cbo	Coupling between objects	Counts the number of methods of a given class access methods of other class.
ce	Efferent couplings	Counts the number of classes called by a specific class.
rfc	Response for a class	Counts the number of methods (external and internal) in a class.
dit	Depth of inheritance tree	Counts the number of maximum levels from a given class to the root node.
noc	Number of children	Calculates the number of direct subclasses of a given class.
ic	Inheritance coupling	Counts the number of parent classes on which a given class is dependent.
avg_cc	Average McCabe	Computes average cyclomatic complexity given by McCabe's in a class.
max_cc	Maximum McCabe	Calculates the maximum cyclomatic complexity (McCabe's) in a given class.
mfa	Measure of functional abstraction	Counts the number of methods accessible by methods of a class plus the number of methods inherited by a class.
moa	Measure of aggregation	Counts the number of user defined data types in a class.
npm	Number of public methods	Counts the number of public methods in a given class.
dam	Data access methods	Calculates the ratio of number of private (protected) attributes in a class to the total number of attributes.
loc	Lines of code	Counts the lines of code in a class.
wmc	weighted methods per class	Counts the number of methods weighted by their complexity in the class.

different domains which increases the generalizability of the study and c) they contain varying number of defective classes (7–60%) so that the capability of the investigated techniques is assessed properly with different ratio of defective classes. The characteristics of the 17 data sets are summarized in terms of number of classes (#Cls.), number of defective classes (#Defc.), percentage of defective classes (%Defc.) and Lines of Code (LOC) in Table 1.

3.2. Independent and dependent variables

The independent variables are the 19 OO metrics given by Chidamber & Kemerer [25], Henderson-Sellers metrics [26], Martin's metrics [27] and QMOOD metrics suite (Bansiya and Davis [28]). The list of metrics is presented in Table 2. The binary dependent variable used in the study is defect proneness that has two values {yes, no}, where yes specifies that a class was found defective and no specifies that a class was not defective. The aim of this experiment is to develop defect prediction models using ML, SBT and HBT and assess the capability of each category of techniques.

3.3. Performance evaluation measures

The positive and negative samples are represented by defective and non-defective classes in the context of this study. The performance of the defect prediction models is evaluated using evaluation measures based on the following measures:

TP: number of correctly predicted defective classes; FP: number of incorrectly predicted defective classes; TN: number of correctly predicted non-defective classes and FN: number of incorrectly predicted non-defective classes

The study compares the predictive performance of 46 techniques using G-mean and Balance measures. It is essential to deal with the imbalanced nature of the data sets. The use of G-mean has been advocated by Kubat and Matwin [5]. G-mean is an improvement over the traditional performance measure accuracy. Hence, it is a frequently used performance evaluation measure that provides the information about how the predicted model balances between positive and negative classes (defective and non-defective classes in this context).

G-mean calculates the geometric mean of sensitivity (the ratio of correctly predicted defective classes to the total number of defective classes (Sen.)) and specificity (the ratio of correctly predicted non-defective classes to the total number of non-defective classes). The formula for calculating G-mean is given as follows:

$$G-mean = \sqrt{\frac{TP}{TP+FP} \times \frac{TN}{TN+FN}} \tag{1}$$

However, another performance measure used for handling imbalanced data sets is Balance, which is defined as the normalized Euclidean distance from the optimum point on the Receiver Operating Characteristic (ROC) curve, i.e. (0,1) to (PF, sensitivity) [6]. Balance is based on ROC curve and is thus a threshold independent measure.

$$Balance = 1 - \sqrt{\frac{\left(0 - \frac{PF}{100}\right)^2 + \left(1 - \frac{sen}{100}\right)^2}{2}} \; where\, PF \; = FN/FN + TN^{*}100 \tag{2}$$

3.4. Validation methods used and multiple runs

The performance of the techniques is validated using the commonly used k-fold cross validation method. The value of k is 10 for medium and large-sized datasets and one for small sized datasets (<50 number of samples). In k-fold cross validation method, the dataset is divided into k parts. Nine parts are used as training set and one part is used as validation set and the process the repeated k times. When k = 1 the method is often known as leave-one-out cross validation. In leave-one-out cross validation method, only one data point is used for validation in each iteration.

The models are developed using 30 iterations for each technique and the median values are reported. This reduces the validation bias [9]. Since SBT are non-deterministic in nature, at least 10 iterations should be performed while using these techniques. A recent review on the application of SBT for developed software quality prediction models pointed out that 38% of defect prediction studies which used multiple runs for encountering the stochastic nature of SBT used 30 runs [3]. Thus, this study uses 30 runs as was done by a number of studies in literature [9,19,20,22].

3.5. Statistical tests used

It is important to strengthen the conclusions by statistically inferring the results obtained from the predictive models. Demšar [7] has recommended the use of Friedman, a non-parametric test that is based on the ranks of the performance of the predicted models [29]. The null hypothesis, Ho, of Friedman test is that there is no difference in the performance of techniques when evaluated using G-mean and Balance measures. The alternative hypothesis, H1, is that the performance of the techniques is statistically different.

The study reports Kendall's coefficient of concordance to determine the effect size of Friedman test. The post-hoc analysis is carried using Nemenyi test. The test is based on the ranks obtained from the Friedman test and involves computation of Critical Distance (CD) [7]. If the difference between mean ranks of a pair of classification techniques obtained from the Friedman test is greater than the CD value, then the difference is said to be significant. The critical distance is calculated using the following formula,

$$CD = q_{\alpha}\sqrt{\frac{t(t+1)}{6d}} \tag{3}$$

Here q_{α} corresponds to a statistic for studentized range, which is divided by $\sqrt{2}$, d represents the number of data sets and t represents the number of classification techniques.

4. Experimental design

This extensive experiment aims to compare and assess several ML, SBT and HBT techniques over 17 datasets. The aim is to analyze the predictive performance of techniques that have not yet been explored in the literature. A detailed description of well-known ML techniques can be found in [1]; however, specific reference to unexplored/less unknown techniques is provided. Table 3 summarizes the description of each classification technique used in this study. These techniques have been simulated using the KEEL tool [30].

The parameters of the techniques should be carefully tuned so that overfitting is avoided. While comparing various techniques, one should perform a fair comparison. The vertical approach for fair comparison involves running all the algorithms for at least the same amount of CPU time or fitness evaluations/iterations. For example, Technique X obtains a G-mean value of 0.72 on a specific dataset. In similar experimental settings, Technique Y obtained a G-mean value of 0.78 on the same dataset. But, Technique X took 60 s of running time, while the running time of Technique Y was 300 s To really show that Technique Y outperforms Technique X, Technique X should have been allowed to run also for 300 s so that equal or more number of fitness evaluations are performed. The running time for a specific technique can be increased by altering the internal parameters of a given technique (increasing the population size or the number of generations/iterations). In order to perform a fair and meaningful comparison, several additional experiments were performed by altering the internal

Table 3
Summary of classification techniques used in this study.

Technique	Description
Machine Learning Techniques	
Batch Nested Generalized Exemplar (BNGE), Exemplar-Aided Constructor of Hyperrectangles (EACH), Rule Induction from a Set of Exemplars (RISE)	BNGE, EACH & RISE are instance based learning algorithms which use a batch version of Nested Generalized Exemplar, uses Euclidean distance and rule induction algorithms respectively for efficient classification.
C4.5, Classification & Regression Trees (CART), Partial Decision Trees (PART), PrUning and BuiLding Integrated in Classification (PUBLIC)	C4.5 is a decision tree algorithm that uses information entropy. CART is a recursive binary decision tree algorithm. PART creates partial decision trees by combining C4.5 and RIPPER. PUBLIC trees combine both the pruning as well as the building phase.
ChiRW (Fuzzy Rule Learning Model by the Chi et al. approach with rule weights), Rule Induction with Optimal Neighborhood Algorithm (Riona)	ChiRW is a technique for rule learning with rule weights. Riona is a combined approach of nearest neighbor technique along with rule induction.
Simple Learner with Iterative Pruning to Produce Error Reduction (Slipper)	This is a boosting algorithm in which a weak learner divides the training set into two, one which is used for rule learning and the other which is used for pruning.
Search-based Techniques	
Bioinformatics-oriented hierarchical evolutionary learning (BioHEL), CO-Evolutionary Rule Extractor (CORE)	BioHEL uses a GA where the population consists of classification rules. CORE uses two co-evolving populations for obtaining rules and set of rules.
CHC Adaptative Search for Instance Selection (CHC), Generational Genetic Algorithm for Instance Selection (GGA), Population-Based Incremental Learning (PBIL), Steady-State Genetic Algorithm for Instance Selection (SGA)	All these algorithms are instance selection algorithms that are evolutionary in nature. CHC uses cataclysmic mutation to balance exploitation and exploration. GGA uses a number of generations and PBIL maintains statistics in order to decide where to sample next. SGA chooses specific parents for steady GA.
Constricted Particle Swarm Optimization (CPSO), Linear Decreasing Weight PSO (LDWPSO) and Real Encoding PSO (REPSO)	CPSO and LDWPSO are variants of Particle swarm optimization (PSO) techniques which use constriction factor or linear decreasing weight for algorithm's convergence. REPSO uses a population of prediction rules.
Bojarczuk GP (Bojarczuk), Falco GP method (Falco_GP), Tan-GP method (Tan-GP)	Bojarczuk uses a GP method with a number of syntactic constraints. Falco_GP uses a population of trees for representing classification rules. Tan-GP memorizes all previously seen good rules.
GA based Classifier System with Adaptive Discretization Intervals (GA-ADI), GA based Classifier System with Intervalar Rules (GA-Int)	GA-ADI uses a decision list like structure where rules are formulated with simultaneous discretization of constant width. GA-Int uses intervals for rule representation.
Incremental Learning with GA (ILGA), GA for solving problem MAX-F (OlexGA), Supervised Inductive Algorithm (SIA)	ILGA uses a GA with an incremental approach Olex-GA uses more than one rule for representing an individual. SIA uses a GA to learn rules which are attribute based.
Supervised Classifier System (UCS), X-Classifier System (XCS), Memetic Pittsburgh Learning Classifier System (MPLCS)	UCS uses a niche-based algorithm along with supervised learning while XCS uses reinforcement learning. MPLCS is a genetic based classifier that combines a number of local search algorithms.
Hybridized Techniques	
Decision Tree- Genetic Algorithm (DT-GA), Oblique Decision Tree with Evolutionary Learning (DT-Oblique), Tree Analysis with Randomly Generated and Evolved Trees (Target)	DT-GA uses C4.5 for rules identification in large disjuncts and a GA for rules identification in small disjuncts. DT-Oblique uses an evolutionary algorithm in order to find an optimum split for a decision tree. Target uses GA for a non-greedy decision tree.
Genetic Algorithm with MSE estimation, clustered crossover and fast smart mutation (GA_MSE), Intelligent Genetic Algorithm for Edition (IGA)	GA_MSE selects training patterns for performance improvement in K-nearest neighbor algorithm while IGA uses an intelligent crossover operation for improvising nearest neighbor.
Genetic based Fuzzy Adaboost (GFS-AB), Genetic Fuzzy Learning with Logitboost (GFS-LB), Logitboost with Single Winner Inference (GFS-MaxLB)	The algorithms use boosting techniques, namely Logitboost and Adaboost along with GA to find effective fuzzy rules where the sum of votes is accounted for decision. GFS-MaxLB uses a "single winner" approach rather than summing the votes.
Fuzzy rule approach based on a genetic cooperative-competitive learning (GFS-GCCL), Fuzzy Learning based on GP (GFS-GP), Fuzzy Learning based on GP Grammar Operators (GFS-GPG), Fuzzy Learning based on GP Grammar Operators and Simulated Annealing (GFS-SP)	GFS-GP and GFS-GCCL uses GP for classification through fuzzy rules, GFS-GPG uses grammar-based GP for finding effective fuzzy rule sets and GFS-SP uses a simulated annealing method in order to ascertain the structure of fuzzy rules in grammar-based GP.
Hierarchical Decision Rules (HIDER), Neural Network Evolutionary Programming (NNEP)	HIDER and NNEP use evolutionary algorithms to generate hierarchical rules or to optimize the weight and structure of neural networks respectively.
Steady-State GA for Extracting Fuzzy Classification Rules from Data (SGERD), Structural Learning Algorithm in a Vague Environment with Feature Selection (SLAVE)	Both algorithms extract fuzzy rules using GA's. SGERD uses GA with non-random selection and SLAVE uses an iterative GA.

parameters of a technique appropriately to increase the running time. However, it was found that the performance of the SBT and their hybridized versions did not improve or rather decreased in several cases. Thus, by increasing the number of fitness evaluations also, better solutions could not be found. Therefore, the default parameter settings of the techniques have been adapted as they are chosen with good reason by the respective authors who propose the algorithm. Ramirez et al. [31] emphasize that the characteristics internal to the algorithm are extremely crucial so that an efficient decisive outcome can be obtained. Thus, an extensive study that evaluates a number of techniques may have to deal with various corresponding fitness functions or internal characteristics, which are specific to a technique to achieve best results [32]. The details of the fitness functions and parameter settings of techniques are provided in Appendix A to promote the repeatability and replicability of the study.

5. Experiment results

In this section, the results of the empirical comparison are reported and the answers to the RQ's (Section 1) are provided.

5.1. RQ1: what is the comparative performance of ML techniques, SBT and HBT for developing predictive models for identifying defective classes in a software?

The performance of the techniques is assessed by evaluating the performance (G-mean and Balance values) of the corresponding defect prediction models developed using them. The median G-mean and Balance values with regard to all the 17 data sets over 30 runs are presented in Tables 4–6. Techniques yielding G-mean values greater than 0.7 and/or Balance greater than 70 are shown in boldface. A value of "-" indicates that the performance metric is not defined for the particular scenario. The defect prediction models have been validated using cross validation methods (as discussed in Section 3.4).

The following observations were made from Table 4 with respect to ML techniques for defect prediction:

- The G-mean values of the C4.5 technique range from 0.33 to 0.89, the G-mean values of the CART technique range from 0.23 to 0.91 and the G-mean values of the Slipper technique range from 0.24 to 0.88. Similarly, the Balance values of C4.5 technique ranged from 12.01 to 94.34, for CART technique they ranged from 12.01–91.16 and the Balance values of Slipper technique ranged from 21.43 to 86.39.
- The PART technique showed the worst performance with median G-mean values zero in certain datasets, followed by the PUBLIC technique. A similar trend was observed regarding the Balance values. The best ML technique with respect to G-mean values was the Slipper technique followed by the RISE technique and the C4.5 technique. It may be noted that the C4.5 technique depicts the best Balance values amongst the investigated ML techniques followed by the CART technique.

The following observations were made with respect to SBT for defect prediction (Table 5):

- The Bojarczuk technique exhibited the highest G-mean values for four data sets. It's G-mean values ranged from 0.47 to 0.86. Most of the G-mean values of the Bojarczuk technique are greater than 0.7 that shows that the Bojarczuk technique is a good classifier for defective classes. The Balance values exhibited by the Bojarczuk technique ranged from 37.49 to 75.72.
- The ILGA technique depicted the best Balance values amongst the investigated SBT in five datasets. The majority of Balance values depicted by the ILGA technique ranged from 29.12 to 90.36 indicating its effectiveness in developing defect prediction models. However, in certain datasets (Elearning, Intercafe and Wspo) the G-mean values of the ILGA technique was 0.00.
- The Balance values obtained by the GA-Int technique ranged from 21.29 to 84.59 and that for the MPLCS technique varied from 18.55 to 83.33. The Tan-GP technique exhibited Balance values in the range 39.02–80.55. The G-mean values for the GA-Int technique range from 0.27 to 0.85. The majority of G-mean values of the MPLCS technique range from 0.34 to 0.86 and G-mean values for the Tan-GP technique range from 0.37 to 0.78.

As can be seen from the table, most of the SBT performed reasonably with respect to G-mean values except REPSO and CORE techniques that showed low G-mean values for all the datasets. However, both these techniques exhibited exceptional Balance values in certain data sets. The Balance values obtained by the REPSO technique on Camel and Intercafe datasets were 86.28 and 91.84 respectively. Similarly, the CORE technique obtained exceptional Balance values on Log4j (79.60) and Nieruchomosci (89.39) datasets.

The following observations were made with respect to HBT techniques for defect prediction (Table 6):

- The DT-GA and the DT-Oblique techniques exhibited good Balance values. Apart from Redaktor dataset, the Balance values exhibited by the DT-GA technique ranged from 36.54 to 94.34 and those obtained by the DT-Oblique technique ranged from 31.66 to 82.06. The G-mean values of these two techniques were also acceptable (DT-GA:0.40 to 0.86, DT-Oblique:0.41 to 0.87).
- The GFS-GP technique exhibited G-mean values in the range 0.13–0.78 and Balance values in the range 8.29 to 97.68. The majority of G-mean values obtained by the GFS-SP technique were in the range 0.37–0.80 and Balance values in the range 14.14–83.96.
- It may be noted that the HBT techniques show comparable performance with regard to ML techniques using G-mean values. However, their performance with respect to Balance values is superior than the ML techniques as well as the SBT.

Fig. 1 shows the comparison of ML, SBT and HBT for developing defect prediction models with respect to mean G-mean values obtained on all the datasets. Few ML techniques such as C4.5, CART and Slipper show good G-mean values, but PART and PUBLIC techniques show very low values of G-mean. Most of the SBT except REPSO show comparable results. Similarly, most of the HBT except GFS-GCCL show comparable results. Fig. 2 depicts the comparison amongst the three investigated categories of techniques with respect to mean Balance values. Amongst the ML techniques, again PART and PUBLIC techniques depicted poor Balance values. Amongst the HBT, DT-GA, GFS-SP and GFS-GP depicted good mean Balance values. The highest mean Balance values obtained by the SBT were comparable to that of HBT. Hence, it can be seen that the average G-mean and Balance values of the SBT and HBT are slightly better or comparable to the G-mean and Balance values

Table 4
Validation results of 10 ML techniques using G-mean & balance values over 30 runs.

G-mean values

Technique	Ant	Arc	Berek	Camel	Ckjm	Elea	Inter	Ivy	Kal.	Log4j	Lucene	Nier	Zuzel	Reda	Sera	Wor	Wspo
BNGE	0.65	0.27	**0.92**	0.36	0.49	0.00	0.00	0.44	0.45	0.69	0.59	0.62	**0.70**	0.68	0.53	**0.72**	0.00
C45	0.65	0.56	**0.86**	0.48	0.60	0.62	**0.71**	0.41	0.44	0.59	0.66	0.64	**0.72**	0.66	0.63	0.53	0.33
CART	**0.73**	0.46	**0.91**	0.23	0.40	0.62	0.69	0.30	0.35	0.58	0.57	0.68	**0.75**	0.66	0.62	0.56	0.53
ChiRW	0.49	0.34	**0.87**	0.22	0.00	0.00	0.00	0.43	0.35	0.52	0.67	0.00	**0.80**	0.69	0.00	0.51	0.00
EACH	0.52	0.68	**0.72**	0.41	0.00	0.44	0.00	0.61	0.40	0.41	0.47	0.41	0.48	0.65	0.31	0.55	–
PART	0.08	0.00	0.00	0.00	0.00	0.00	0.00	0.00	–	0.00	0.65	0.31	0.43	0.00	0.00	0.36	0.33
PUBLIC	**0.72**	0.46	**0.86**	0.00	0.00	0.00	0.00	0.00	0.00	**0.70**	0.60	0.31	0.60	0.57	0.00	0.22	0.00
Riona	0.66	0.27	**0.92**	0.22	0.00	0.57	0.50	0.41	0.37	0.68	0.56	0.59	**0.72**	0.66	0.68	0.54	–
RISE	**0.72**	0.43	**0.88**	**0.62**	0.49	0.42	0.00	0.55	0.51	0.66	0.67	0.75	**0.72**	**0.80**	0.41	0.68	0.00
Slipper	0.61	0.49	**0.88**	0.46	**0.80**	0.43	0.69	0.46	0.44	0.64	0.66	0.65	**0.76**	0.7	0.60	0.64	0.24

Balance values

Technique	Ant	Arc	Berek	Camel	Ckjm	Elea	Inter	Ivy	Kal.	Log4j	Lucene	Nier	Zuzel	Reda	Sera	Wor	Wspo
BNGE	69.96	48.9	**93.09**	57.50	50.00	29.07	–	60.14	44.78	65.98	63.39	62.94	64.96	14.94	14.99	54.06	9.45
C45	67.04	64.16	**83.30**	56.22	60.00	57.42	**94.34**	52.34	**70.12**	66.52	65.21	67.61	46.31	12.01	33.16	56.34	38.35
CART	**72.56**	51.13	**87.88**	63.96	40.00	57.42	**75.70**	39.26	**91.16**	57.92	58.77	67.19	41.87	12.01	34.43	48.51	54.25
ChiRW	**77.41**	58.89	**86.26**	68.81	20.94	29.16	29.04	**77.81**	**94.95**	64.42	65.55	28.85	34.51	19.44	15.02	21.52	15.02
EACH	47.00	43.47	**79.89**	43.40	0.00	46.76	–	41.17	41.19	**71.67**	59.27	50.39	27.83	45.94	6.36	38.04	–
PART	50.31	–	–	–	16.61	–	–	–	–	–	63.70	56.43	20.88	0.00	0.00	81.98	38.35
PUBLIC	**72.93**	61.34	**83.30**	27.96	0.00	–	–	28.83	–	63.29	58.70	56.43	17.76	7.86	0.00	92.01	0.00
Riona	67.46	44.44	**93.09**	48.68	0.00	66.35	**91.84**	63.98	58.98	59.51	60.80	58.98	46.31	12.01	24.55	46.01	–
RISE	59.10	38.43	**86.39**	51.81	50.00	36.94	28.31	47.96	**70.12**	57.85	67.34	**70.99**	46.31	31.76	22.49	62.78	6.87
Slipper	63.93	50.36	**86.39**	53.89	**80.00**	43.23	**75.70**	53.28	58.22	61.70	67.14	63.32	50.95	23.33	21.43	56.57	29.92

Table 5
Validation results of 20 SBT using G-mean & balance values over 30 runs.

G-mean values

Technique	Ant	Arc	Berek	Camel	Ckjm	Elea	Inter	Ivy	Kal.	Log4j	Lucene	Nier	Zuzel	Reda	Sera	Wor	Wspo
BioHEL	0.64	0.61	**0.79**	0.49	0.40	0.00	0.00	0.43	0.45	0.56	0.66	0.00	**0.79**	**0.70**	0.42	0.64	0.47
Bojarczuk	**0.75**	0.62	**0.70**	0.57	0.69	**0.72**	0.47	**0.76**	0.50	**0.77**	0.64	**0.70**	**0.75**	0.67	**0.86**	0.66	**0.75**
CHC	0.59	0.19	**0.86**	0.29	0.00	0.00	0.00	0.49	0.43	0.59	0.59	0.57	**0.73**	0.66	0.55	0.54	0.37
CORE	0.4	0.42	**0.80**	0.13	0.28	0.00	0.00	0.22	0.26	0.48	0.53	**0.84**	0.62	0.00	0.43	0.44	0.00
CPSO	0.58	0.40	0.59	0.23	0.00	0.61	0.61	0.45	0.41	0.55	0.59	**0.70**	**0.78**	0.52	0.52	0.59	0.58
Falco_GP	0.46	0.33	0.68	0.13	0.40	0.00	0.00	0.22	0.30	0.50	0.51	0.53	0.54	0.00	0.31	0.55	0.17
GA_ADI	0.62	0.50	**0.78**	0.36	0.40	0.00	0.49	0.41	0.42	0.62	0.67	0.62	0.68	0.66	0.39	0.54	0.37
GA_Int	0.61	0.42	**0.85**	0.27	0.49	0.44	0.49	0.53	0.38	0.63	0.64	0.59	0.66	0.65	0.59	0.63	0.31
GGA	0.57	0.27	**0.90**	0.29	0.00	0.00	0.00	0.47	0.41	0.59	0.65	**0.70**	**0.75**	0.63	0.53	0.62	0.33
ILGA	0.53	0.44	**0.87**	0.10	0.35	0.00	0.00	0.40	0.24	0.61	0.45	0.60	**0.89**	0.61	0.46	**0.70**	0.00
LDWPSO	0.66	0.51	0.66	0.25	0.63	0.58	0.64	0.52	0.39	0.69	0.47	0.64	0.56	0.27	0.37	0.64	**0.82**
MPLCS	0.66	0.46	**0.86**	0.34	0.57	0.00	0.47	0.41	0.41	0.65	0.64	**0.76**	**0.73**	0.62	0.42	0.66	0.53
OlexGA	0.67	0.61	0.66	0.42	0.69	0.59	0.00	0.00	0.45	**0.70**	0.41	0.69	0.52	**0.70**	0.00	0.46	0.12
PBIL	0.62	0.19	**0.90**	0.33	0.00	0.00	0.00	0.52	0.46	0.57	0.62	0.68	**0.73**	0.66	**0.71**	0.54	0.24
REPSO	0.15	0.00	0.67	0.07	0.40	0.00	0.50	0.00	0.31	0.30	0.24	**0.71**	0.34	0.19	0.44	0.43	0.17
SGA	0.57	0.33	**0.85**	0.34	0.00	0.00	0.00	0.41	0.43	0.60	0.64	0.57	**0.71**	0.65	**0.70**	0.59	0.26
SIA	0.52	0.45	**0.86**	0.36	0.49	0.00	0.50	0.56	0.40	0.49	0.65	**0.76**	**0.75**	**0.73**	0.43	0.67	0.00
TAN-GP	0.74	0.66	**0.78**	0.60	0.69	0.59	0.47	**0.72**	0.48	**0.73**	0.68	0.64	**0.72**	**0.71**	**0.75**	0.51	0.37
UCS	0.64	0.38	**0.86**	0.50	0.40	0.44	0.00	0.49	0.48	0.58	0.68	**0.77**	**0.76**	0.63	0.41	0.61	0.33
XCS	0.62	0.33	**0.87**	0.42	0.29	0.00	0.00	0.51	0.46	0.69	0.67	0.64	**0.79**	**0.71**	0.32	0.56	0.42

Balance values

Technique	Ant	Arc	Berek	Camel	Ckjm	Elea	Inter	Ivy	Kal.	Log4j	Lucene	Nier	Zuzel	Reda	Sera	Wor	Wspo
BioHEL	59.97	53.26	**87.14**	48.16	40.00	29.05	28.39	49.01	62.57	55.61	67.08	22.9	**75.72**	22.19	18.55	39.71	47.30
Bojarczuk	62.51	41.90	66.78	45.90	**70.54**	48.50	46.17	54.62	63.23	62.22	62.67	67.32	**75.72**	37.49	45.10	42.18	**73.65**
CHC	**73.41**	46.37	**83.30**	57.01	0.00	–	–	60.90	**73.65**	**70.08**	61.48	63.01	32.36	9.63	3.87	51.18	47.30
CORE	69.87	58.16	**79.45**	53.74	29.04	–	–	52.22	27.28	**79.60**	56.72	**89.39**	63.13	0.00	12.56	23.00	11.61
CPSO	55.00	40.99	**73.15**	47.71	16.61	52.72	46.45	45.59	–	49.49	61.48	67.32	36.17	22.45	41.54	45.75	59.59
Falco_GP	**71.44**	63.87	**77.78**	53.74	40.00	29.07	–	63.81	61.92	**70.82**	56.87	54.19	41.67	6.23	6.36	17.66	17.66
GA_ADI	**70.88**	64.07	**80.55**	**70.70**	50.00	29.06	63.64	54.79	**70.12**	66.20	67.32	62.94	42.18	12.01	25.27	51.18	47.30
GA_Int	**72.17**	50.87	**84.59**	57.20	50.00	52.63	63.64	60.25	68.88	59.86	63.84	68.96	53.26	21.29	26.65	62.08	31.28
GGA	**70.06**	52.23	**89.73**	54.29	0.00	29.07	–	68.38	**80.06**	66.52	64.20	**71.67**	41.87	15.04	14.99	48.31	38.35
ILGA	**74.43**	**72.72**	**90.18**	50.99	36.58	29.12	–	**87.96**	**90.36**	**78.05**	60.98	56.42	55.03	11.13	9.22	52.04	10.42
LDWPSO	61.01	40.65	66.65	47.27	**73.48**	42.01	52.38	50.10	27.43	64.04	55.77	67.61	27.52	11.04	28.26	45.37	**71.72**
MPLCS	**71.25**	59.03	**83.30**	57.43	61.61	29.04	46.17	57.83	**70.12**	68.87	62.84	**75.39**	54.45	19.22	18.55	53.85	54.25
OlexGA	56.00	48.27	64.28	44.38	**70.54**	44.87	28.31	–	48.95	65.98	47.25	65.98	58.45	36.01	0.00	43.65	12.40
PBIL	**71.26**	42.86	**89.73**	55.66	0.00	29.06	–	**71.82**	**80.06**	66.76	63.17	67.19	32.36	12.01	6.04	51.18	29.92
REPSO	65.95	28.81	**73.84**	**86.28**	40.00	–	**91.84**	28.83	61.92	**75.66**	66.23	**83.93**	20.24	0.33	8.29	**71.78**	18.25
SGA	65.79	55.17	**84.59**	52.89	0.00	–	–	63.98	**70.12**	**74.26**	63.29	63.01	37.80	17.50	14.72	51.07	39.89
SIA	63.85	47.26	**83.30**	49.22	50.00	29.03	**91.84**	62.87	**80.06**	61.55	63.51	**75.39**	41.87	29.54	12.56	48.04	9.45
TAN-GP	59.27	45.48	**80.55**	47.59	**70.54**	44.87	46.17	48.64	41.19	61.45	67.62	67.61	46.31	39.02	39.58	43.53	47.30
UCS	69.62	54.42	**83.30**	61.89	40.00	52.63	28.31	60.90	58.22	**72.94**	66.26	**86.53**	50.95	16.60	22.49	53.75	38.35
XCS	69.83	45.09	**87.91**	60.77	29.04	29.03	28.63	60.99	52.21	66.31	66.20	**77.36**	28.47	19.48	21.76	36.28	49.20

Table 6
Validation results of 16 HBT using G-mean & balance values over 30 runs.

G-mean values Technique	Ant	Arc	Berek	Camel	Ckjm	Elea	Inter	Ivy	Kal.	Log4j	Lucene	Nier	Zuzel	Reda	Sera	Wor	Wspo
DT-GA	0.67	0.54	**0.86**	0.45	0.40	0.62	**0.71**	0.49	0.44	0.66	**0.70**	0.59	0.69	0.62	0.60	0.50	**0.75**
DT-Oblique	0.61	0.45	**0.87**	0.58	0.57	0.59	0.69	0.50	0.48	0.63	0.67	0.68	**0.76**	0.68	0.64	0.59	0.41
GA_MSE	0.61	0.51	**0.73**	0.49	0.00	0.42	0.00	0.55	0.47	0.40	0.60	**0.70**	0.58	0.68	0.46	0.35	–
GFS-AB	0.37	0.19	0.65	0.22	0.00	0.00	0.00	0.49	0.41	0.37	0.21	0.00	**0.73**	0.38	0.64	0.52	0.46
GFS-GCCL	0.19	0.00	**0.74**	0.00	0.58	0.00	0.00	0.52	0.00	0.35	0.41	0.46	**0.71**	0.00	0.31	0.59	0.00
GFS-GP	0.52	0.27	**0.71**	0.13	0.60	**0.77**	**0.71**	0.59	0.31	0.59	0.45	**0.76**	**0.78**	0.66	0.44	0.59	0.37
GFS-GPG	0.38	0.19	**0.74**	0.15	0.60	0.44	**0.71**	0.38	0.33	0.47	0.40	0.49	**0.73**	0.63	0.31	0.64	0.29
GFS-LB	0.55	0.42	**0.76**	0.42	0.28	0.00	0.00	0.38	0.45	0.51	0.65	0.39	0.69	**0.71**	0.31	0.51	0.47
GFS-MaxLB	0.49	0.27	0.54	0.20	0.00	0.00	0.00	0.49	0.42	0.46	0.32	0.00	0.60	0.58	0.43	0.48	0.50
GFS-SP	0.60	0.47	**0.80**	0.26	0.35	0.00	0.69	0.41	0.37	0.68	0.56	0.68	**0.82**	0.53	0.60	0.42	**0.75**
Hider	0.55	0.27	**0.92**	0.22	0.00	0.00	0.45	0.31	0.36	0.47	0.63	0.63	0.60	0.60	0.63	**0.72**	0.24
IGA	0.62	0.25	0.39	0.35	0.00	0.43	0.48	0.60	**0.58**	0.51	0.67	0.57	0.51	0.59	–	0.53	–
NNEP	0.63	0.50	**0.75**	0.36	0.35	0.60	0.00	0.46	0.43	0.68	0.66	0.55	**0.76**	0.65	0.57	0.64	0.46
SGERD	0.29	0.19	**0.77**	0.00	0.61	0.00	0.00	0.27	0.00	0.35	0.44	0.31	**0.71**	0.47	0.45	0.49	0.00
SLAVE	0.56	0.46	**0.77**	0.24	0.40	0.00	0.00	0.47	0.36	0.68	0.55	0.62	0.68	0.69	0.60	0.52	0.34
Target	0.55	0.00	**0.86**	0.00	0.57	0.00	0.48	0.00	0.00	0.51	0.59	0.56	0.66	0.38	0.62	0.58	0.26

Balance values Technique	Ant	Arc	Berek	Camel	Ckjm	Elea	Inter	Ivy	Kal.	Log4j	Lucene	Nier	Zuzel	Reda	Sera	Wor	Wspo
DT-GA	69.62	66.44	**83.30**	55.24	40.00	57.42	**94.34**	62.41	**70.12**	**73.79**	67.32	58.98	50.00	19.22	36.54	58.93	**73.65**
DT-Oblique	58.68	43.98	**82.06**	54.66	61.61	44.87	**75.70**	46.96	68.88	63.66	66.38	67.19	50.95	28.05	31.66	51.07	43.46
GA_MSE	57.21	44.59	**75.06**	47.32	0.00	36.94	27.74	53.08	23.40	42.26	59.18	67.32	45.41	29.11	30.48	34.65	–
GFS-AB	64.10	52.19	**79.78**	54.91	–	–	28.46	44.75	**88.69**	55.51	50.60	24.24	32.36	8.55	40.37	**77.28**	43.85
GFS-GCCL	**81.64**	–	**83.42**	27.95	**76.43**	–	–	64.10	**86.40**	**84.23**	62.58	68.08	37.80	0.00	6.36	42.66	15.02
GFS-GP	**74.87**	63.82	69.08	**77.69**	60.00	**97.68**	**94.34**	66.52	**91.16**	66.52	53.08	**75.39**	36.17	9.63	8.29	51.07	47.30
GFS-GPG	**80.07**	42.86	**83.42**	66.79	60.00	46.76	**94.34**	58.97	**93.85**	63.62	50.35	56.84	32.36	11.29	10.24	39.71	31.02
GFS-LB	64.87	50.87	**81.94**	66.46	29.04	29.05	28.39	52.31	**73.65**	61.69	63.34	45.71	29.04	19.45	10.24	43.53	47.30
GFS-MaxLB	69.44	63.82	**70.42**	56.91	16.61	–	28.46	44.75	**88.69**	59.45	51.46	–	17.76	22.15	15.89	41.04	47.30
GFS-SP	**70.84**	**70.95**	**83.96**	63.60	37.91	29.07	**75.70**	59.62	**73.65**	**74.87**	59.34	67.19	40.83	14.14	36.54	**82.10**	67.61
Hider	66.31	56.88	**85.86**	48.68	0.00	–	42.62	46.43	27.28	61.42	62.64	62.64	17.76	8.42	33.16	54.06	29.92
IGA	63.94	32.74	48.59	44.37	0.00	43.23	52.04	53.55	27.28	52.61	66.38	63.01	44.77	31.80	–	56.34	–
NNEP	**74.39**	61.74	78.41	67.00	37.91	46.83	28.39	57.69	58.22	68.41	66.07	58.18	25.17	20.17	30.05	50.99	51.23
SGERD	**76.41**	**92.01**	**82.56**	27.97	63.18	29.14	–	**92.48**	62.38	**78.63**	57.17	46.83	37.80	4.23	2.74	55.19	4.44
SLAVE	**74.95**	61.34	**77.31**	60.79	40.00	–	28.46	77.30	**91.16**	**74.87**	58.26	62.94	42.18	12.78	21.43	52.43	35.13

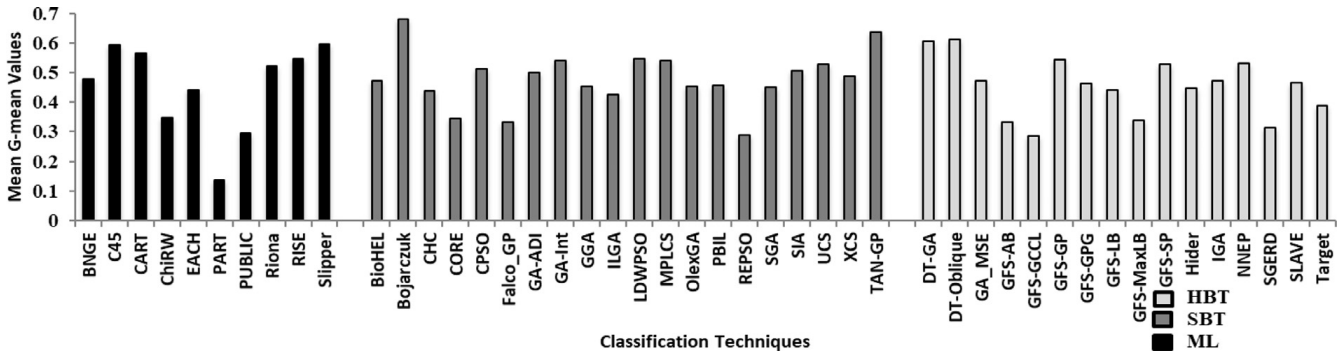


Fig. 1. Comparison of classification techniques using mean g-mean values.

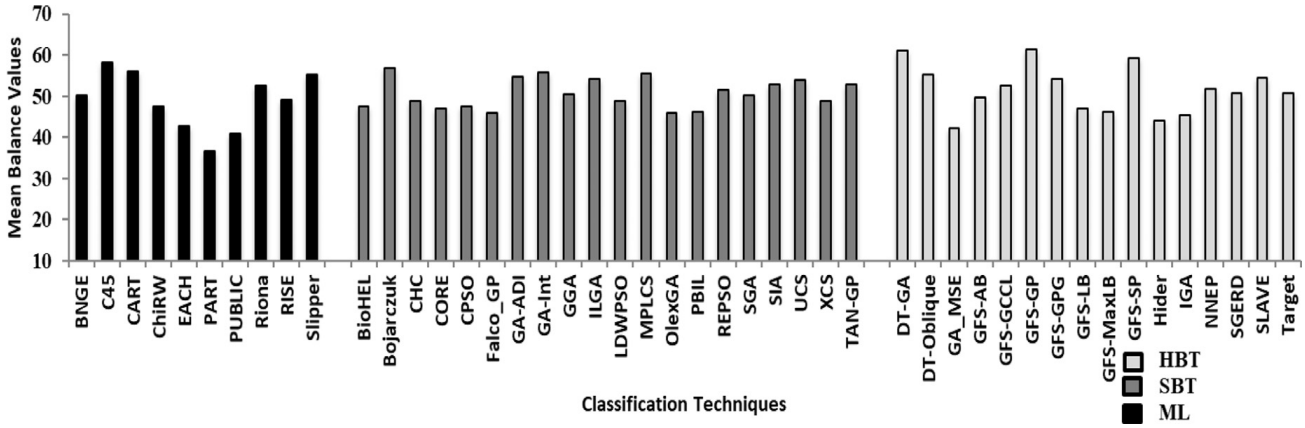


Fig. 2. Comparison of classification techniques using mean balance values.

of ML techniques. Thus, the predictive performance of SBT and HBT are comparable for development of defect prediction models.

The study also performed cost-benefit analysis of the defect prediction models developed using 46 techniques in order to evaluate the cost effectiveness of the proposed models. The gain in effort is computed according to the formula provided by [32],

$$Effort\ \text{Gain} = \text{RTL} - \text{DML}/\text{RTL}^{*}100 \tag{4}$$

Here, RTL represents the LOC that needs to be tested when Random Testing (RT) is performed. DML corresponds the LOC that needs to be tested when a Defect prediction Model (DM) is employed. It is basically the reduction in cost due to use of the DM. The SBT and HBT show 30–60% effort gain for developing defect prediction models. The Bojarczuk and Tan-GP technique show 60% effort gain and is higher than those obtained by the ML techniques (Slipper). Hence, it is shown that the use of SBT and HBT for developing defect prediction models reduces the project cost.

The predictive capability of the classification techniques is analysed by evaluating the G-mean and Balance performance measures of the developed defect prediction models. The results indicate that the SBT and the HBT show comparable performance to that of the ML techniques. The performance of SBT and HBT were even better than ML techniques in some cases.

5.2. RQ2: which is the best and the worst technique for defect prediction using OO metrics? Which techniques are significantly better as compared to the other techniques?

In order to statistically verify the superiority of one technique over the other, the Friedman test was conducted at significance level of 0.05 with respect to G-mean and Balance values. The Friedman test evaluates the hypothesis that the techniques are statistically different than each other by computing the mean ranks over 17 datasets. The degree of freedom is 45 as the number of classification techniques evaluated in the study is 46. The obtained Friedman ranks using G-mean and Balance values (median of 30 runs) over all the 17 datasets are depicted in Table 7 (in parenthesis). The obtained p-value ($p < 0.001$) after application of both the Friedman tests indicates that the results are significant.

The results in Table 7 depict that the Bojarczuk and the Tan-GP techniques are best for developing defect prediction models according to G-mean values. Both these techniques are based on the GP method. The use of GP is advantageous in classification because of a) its flexible representation of the solution, b) its non-parametric nature which does not need prior

Table 7
Results of Friedman test.

Results using median G-mean values			Results using median balance values		
Bojarczuk (38.8)	**GFS-GP** (26.9)	**IGA** (20.26)	**DT-GA** (34.1)	**GGA** (26.3)	**CPSO** (19.9)
Tan-GP (36.8)	**GA-Int** (26.4)	**GFS-GPG** (18.5)	**GFS-SP** (31.9)	**Tan-GP** (26.1)	**LDWPSO** (19.8)
DTOblique (35.3)	**GA-ADI** (25.3)	**EACH** (18.4)	**C4.5** (31.2)	**XCS** (25.6)	**Falco_GP** (19.0)
Slipper (33.6)	**GFS-SP** (25.3)	**ChiRW** (18.4)	**GA-Int** (31.0)	**BNGE** (25.2)	**CORE** (18.9)
RISE (33.1)	**PBIL** (25.0)	**Target** (17.1)	**MPLCS** (30.6)	**SIA** (24.9)	**GFS-AB** (18.4)
DT-GA (32.1)	**CPSO** (24.6)	**GFS-AB** (15.2)	**GFS-GP** (30.1)	**GFS-GPG** (24.6)	**Target** (18.2)
C4.5 (31.81)	**OlexGA** (24.3)	**PUBLIC** (14.9)	**UCS** (29.9)	**RISE** (23.3)	**Hider** (18.1)
UCS (29.9)	**Riona** (24.3)	**CORE** (13.9)	**GA-ADI** (29.1)	**PBIL** (22.9)	**OlexGA** (18.0)
CART (29.5)	**GGA** (24.2)	**GFS-MaxLB** (13.9)	**CART** (28.7)	**Riona** (22.8)	**GFS-MaxLB** (17.9)
XCS (29.2)	**SLAVE** (22.7)	**GFS-GCCL** (12.6)	**Slipper** (28.5)	**SGA** (22.7)	**IGA** (17.8)
NNEP (28.9)	**GA_MSE**(22.7)	**Falco_GP** (11.9)	**ILGA** (27.2)	**SGERD** (22.6)	**GA_MSE**(16.0)
MPLCS (28.8)	**CHC** (22.2)	**SGERD** (11.7)	**NNEP** (27.2)	**BioHEL** (22.4)	**PUBLIC** (13.6)
BioHEL (27.9)	**SGA** (22.2)	**REPSO** (11.6)	**DT-Oblique** (27.1)	**GFS-GCCL** (22.1)	**EACH** (13.6)
SIA (27.9)	**GFS-LB** (20.7)	**PART** (7.3)	**SLAVE** (27.1)	**REPSO** (21.9)	**PART** (9.3)
LDWPSO (27.3)	**ILGA** (20.4)		**ChiRW** (26.8)	**CHC** (21.3)	
BNGE (26.9)	**Hider** (20.4)		**Bojarczuk** (26.5)	**GFS-LB** (20.7)	

information about data distribution, c) its capability of discovering data trends by detecting unknown data relationships, and d) its robust nature. Furthermore, grammar-guided GP is an extension of GP that aids in increasing the flexibility and expressiveness of extracted knowledge with the help of context-free grammar [33]. Bojarczuk-GP and Tan-GP are grammar-guided GP algorithms which were found efficient in determining defective classes. The Bojarczuk algorithm, apart from generating effective classification rules also focuses on the comprehensibility of the obtained classification rules by minimizing the size of the generated rules, making it an efficient classifier.

According to Table 7, the DT-GA and the GFS-SP technique obtained the best ranks with Balance values. Both these techniques belong to HBT category and thus they depict favourable results as they combine the advantages of two base techniques. The DT-GA technique is a combination of decision trees and GA. The presence of decision trees indicates the incorporation of competent pruning procedure and the presence of GA indicates effective global search process which avoids local optima [32]. GFS-SP is a combination of grammar-based GP with simulated annealing. Models developed using GFS-SP depict good capability for determining defective classes as grammar-guided GP algorithms are effective. A similar result can be noted from the Friedman results using G-mean values (Bojarczuk and Tan-GP techniques showed good performance). Thus, grammar-based GP techniques exhibit effective prediction capability. The performance of PART (an ML technique) is worst, according to G-mean as well as Balance values.

In order to determine the effect size, the study also determined Kendall's coefficient using both G-mean and Balance values. The Kendall's coefficient (W) was computed as 0.308 for G-mean values (moderate effect size) and 0.166 (low effect size) using Balance values. As the results of Friedman test were statistically significant, post hoc analysis was conducted to perform pairwise comparisons using the Nemenyi test ($\alpha = 0.05$). The CD (as explained in Section 3.5) is computed and is checked against the difference in ranks for each pair of techniques obtained from the Friedman test. The computed value of CD is 20.11 and 63 pairs of classification techniques are significantly different from each other when evaluated using G-mean ranks. Amongst these pairs, the Bojarczuk technique was found to be significantly better than 10 other techniques and the Tan-GP technique was found to be significantly better than 8 other techniques. It was found that 9 pairs of classification techniques were found significantly different from each other using Balance ranks. Amongst these pairs, the DT-GA technique was found significantly better than three other techniques. Hence, the results show that few pairs of techniques are statistically different.

The results of the study were compared with two recent literature studies (Arar and Ayan [21] and Hosseini et al. [22]) and the methods proposed by them i.e. Artificial Neural Network with Artificial Bee Colony proposed by [21] and Genetic Instance Selection with Naïve Bayes proposed by [22]. It should be noted that we could only compare our results with those studies which used G-mean or Balance as a performance measure and developed software defect prediction models. Table 8 depicts the comparison, which states the method proposed by the literature study, its performance and the comparison with this study. According to the results in Table 8, the methods investigated in this study are comparable and even better in certain cases to the methods proposed by the literature studies.

The Bojarczuk and Tan-*GP techniques significantly outperform other techniques when evaluated using Friedman test on G-mean values. The Bojarczuk technique yielded improved G-mean values in majority of the cases by increasing G-mean values by 0.01 to 0.56. The DT-GA and GFS-SP techniques are better than other investigated techniques when assessed using Friedman test on Balance values. There was improvement in Balance values by 2 to 57 in majority of the datasets when the DT-GA technique was used for developing defect prediction models. The PART technique is the worst technique for predicting defective classes. There were few pairs of techniques which were found significantly different from each other using Nemenyi test. The Bojarczuk technique was found to be statistically better than ten other*

techniques using Nemenyi test on G-mean values while the DT-GA technique was found statistically better than three other techniques when evaluated using Nemenyi test on Balance values.

6. Discussion of results

The results of the study indicate the effectiveness of SBT and HBT for developing software defect prediction models. A recent study in the area of software change prediction, which is a related area of defect prediction also encourages the use of HBT [32]. The study supports the use of HBT as they provide a combined approach which incorporates the strengths of both a SBT and an ML technique. This is indicated by the results of Friedman test on Balance values. Both DT-GA and GFS-SP are hybridized versions of competent SBT and ML techniques. Furthermore, the effectiveness of grammar-based GP techniques (Bojarczuk, Tan-GP and GFS-SP) was observed due to their flexibility, robustness and ease of representation. They exhibited top ranks amongst G-mean and Balance values. On the contrary, PART, an ML technique depicted the worst ranks both using G-mean as well as Balance. A possible reason for its poor performance could be due to its inability to perform global optimization as it uses divide and conquer methodology. Though, other successful ML techniques such as C4.5 and RIPPER operate in two stages: creation of an initial rule set and pruning or adjustment of these initial rules, PART simplifies the process by building rules on the instances and removing instances that match a specific rule. PART generates further rules only for the unmatched instances in the training set. Though, some of the datasets used in the study are imbalanced in nature, but the use of stable performance measures (G-mean and Balance) yields reliable results.

As indicated in Section 5.2, there were few pairs of techniques which were found statistically better using Nemenyi test. This indicates that SBT and HBT in general depict good results, the choice of a specific SBT/HBT is not very crucial. This fact can also be supported by the Friedman ranks shown in Table 7. The Friedman ranks using G-mean and Balance were quite different but ten of the top-15 techniques were either SBT or HBT.

The contribution of this study is significant as it evaluates a number of not commonly used techniques on a wide array of data sets for developing software defect prediction models. Furthermore, the comparison performed in the study is extensive with regard to use of statistical tests, number of techniques evaluated and the number of datasets used from different domains and with different ratios of defective classes.

7. Empirical validity threats

In this section, we analyze the possible threats to validity of the study. The datasets have been extracted from the Promise data repository and use popular OO metrics. These steps reduce the threat to construct validity. Though selection of classification techniques can contribute towards selection bias, but we have reduced this biasness by selecting a wide variety of classification techniques from ML, SBT and HBT categories.

Conclusion validity threats are concerned with the accuracy and the statistical validity of the conclusions. This threat is reduced by a) using nonparametric statistical tests and appropriate significance value b) conducting post-hoc analysis and c) by using multiple runs and cross-validation method. The study uses default parameter settings of the KEEL tool. However, this choice was made after executing several experiments for performing “fair comparison”. Thus, a possible threat that proper tuning of internal parameter settings may provide better results has been reduced as several repeated experiments with different internal parameter settings were performed. The study uses k-fold cross-validation. However, a recent study has advocated the use of out-of-sample bootstrap validation. This is a possible limitation of the study.

The external validity threats are concerned with the applicability and generalizability of the results. In this study, this threat is reduced by using 17 data sets. The datasets of the study have been developed by a group of professionals and

Table 8
Comparison with literature studies.

Literature study	Method of literature study	Performance of literature study	Comparison remarks
Arar and Ayan [21]	Artificial Neural Network combined with Artificial Bee Colony (HBT)	Defect prediction models were developed on 5 unbalanced datasets. The Balance values were obtained in the range 64–79.	Of the investigated SBT and HBT, 7 exhibited comparable results on majority of the investigated datasets. These 7 techniques along with the range of Balance values on majority of the datasets is DT-GA (62–94), GFS-GP (60–97), GFS-SP (60–84), Bojarczuk (62–75), GA-ADI (63–81), GA-Int (60–72) and REPSO (61–92).
Hosseini et al. [22]	Genetic Instance Selection with Naïve Bayes	Models were developed on 41 datasets and the mean G-mean value reported by the study on all the datasets was 0.453.	12 SBT and 9 HBT, investigated in this study depict better mean G-mean values than [22]. However, it may be noted that there is a difference in the definition of G-mean performance measure in this study. The current study reports G-mean as a geometric mean sensitivity and specificity while [22] report the geometric mean of sensitivity and precision.

not student programmers. The study clearly states and describes the classification techniques along with their fitness values and parameter settings. This promotes the repeatability and replicability of the study. However, the datasets used have been developed using Java programming language and hence may not be applicable to datasets obtained from other software developed using other languages such as C++. The results are applicable to similar domain software systems.

8. Conclusions and future work

The study has successfully evaluated 46 classification techniques, which belong to three categories viz. search-based techniques, hybridized techniques and Machine Learning, for developing defect prediction models. The experiments were carried out using 17 open-source datasets with a proper framework for comparison. The framework dealt with the stochastic nature of the search-based techniques and the hybridized techniques by conducting multiple runs, used appropriate parameter settings for the investigated techniques and evaluated the statistical significance of results which were obtained using stable performance measures (G-mean and Balance).

In order to perform fair comparison amongst two techniques, several experiments were conducted by varying the parameter settings of the search-based techniques and the hybridized techniques. These experiments aimed at increasing the run time of a technique by varying internal parameters such as size of population, number of generations or iterations. However, it was found that default parameter settings were suitable as any change in them to increase the running time of hybridized techniques or search-based techniques decreased their performance measure values.

The results of the study confirm the effectiveness of search-based techniques and the hybridized techniques for developing software defect prediction models. The genetic programming based search based techniques, Bojarczuk and Tan-GP, exhibited the best performance for predicting defective classes using G-mean. The hybridized technique, DT-GA yielded the best results using Balance values.

The study's results can be used by software testers for proper allocation of testing and verification resources as the classes which are predicted as defective should be allocated more resources. Researchers and practitioners can use the study's results for selecting an appropriate classification technique for developing defect prediction models. In future, the investigated classification techniques may be evaluated on datasets of other programming languages such as C# and Kotlin. Furthermore, the capability of search-based techniques and their hybridized versions for predicting defect severity may be investigated.

Appendix A

Algorithm	Fitness and parameter settings
BioHEL	*Fitness:* A principal commonly termed as Minimum Description Length (MDL) is employed to evaluate the fitness. *Parameters:* PS: 500; Mp: 0.6; Cp: 0.6; NG: 100; MDL weight relation factor: 0.9.
Bojarczuk	*Fitness* = Specificity * Sensitivity * Simplicity, Where Simplicity = (MNodes – 0.5*NNodes −0.5)/(MNodes −1); NNodes → current no. of nodes; MNodes → maximum no. allowed nodes. *Parameters:* PS: 200; NG: 200; Copy probability: 0.01.
CHC	*Fitness* = α. Classification Rate + (1-α). $\frac{100(K-S)}{S}$,where K → training set instances; S → subset of K. *Parameters:* PS: 50; NG: 10,000; DF: Euclidean.
CORE	*Fitness* = n/(n + FP) * Sensitivity (1 + Specificity), where n → No. of training set instances. *Parameters:* PS: 100; Co-population size: 50; No. of co-populations: 15; Cp: 1.0; Mp: 0.1.
CPSO	*Fitness* = Specificity * Sensitivity. *Parameters:* Constriction Coefficient: 0.83; Weights Upper limit: 1.05; No. of Particles: 25; Convergence Platform Width: 35; Convergence Radius: 0.1.
DTGA	*Fitness:* Same as CPSO. *Parameters:* PS: 200; NG: 50; Small disjunct: 10.
DTOblique	*Fitness* = $\frac{K_L}{K}\frac{K_R}{K}(\sum_{i=1}^{p}\frac{L_i}{K_L}-\frac{R_i}{K_R})^2$; Where K_L & K_R → no. of instances on left & right tree split; K → total no. of instances; L_i & R_i → no. of instances of class i on the left and right of the tree split. *Parameters:* NG: 25.
Falco_GP	*Fitness* = (K – f_c) + αf_s , where K → no. training set instances; f_c → difference between actual no. of instances for which the rule provides a clear classification and the no. of instances for which the rule classifies incorrectly; f_s → sum of no. of nodes in the tree and the tree depth. *Parameters:* PS: 200; NG: 200; Maximum derivation size: 10; Mp: 0.1; Copy probability: 0.01; $\alpha = 0.9$.
GA_MSE	*Fitness* = $\frac{1}{KC}\sum_{k=1}^{K}\sum_{i=1}^{C}(a_k[i]-d_n[i])^2$, Where K → no. of patterns; C → no. of outputs; $a_k[i]$ → *i*th output for the *k*th pattern; $d_n[i]$ → *i*th desired output for the *k*th pattern. *Parameters:* PS: 100; NG: 100; DF: Euclidean.
GA_ADI	*Fitness* = (Accuracy)^2. *Parameters:* No. of intervals for discretization: 4, 5, 6, 7, 8, 10, 15, 20, 25; NG: 500.
GA_Int	*Fitness:* Same as BioHEL. *Parameters:* No. of Iterations: 500; Size penalty min rules: 4.
GFS-AB	*Fitness:* For a fuzzy rule, the fitness is the weighted difference between all instances belonging to class c_i (positive) and all instances not belonging to class c_i (negative). *Parameters:* No. of labels: 3; No. of rules: 8.
GFS-GCCL	Fitness of i^{th} rule is the no. of correctly classified training patterns by the rule. *Parameters:* PS: 100; No. of labels: 5; NG: 10,000; Cp: 1.0; Mp: 0.1.
GGA	*Fitness:* Same as CHC. *Parameters:* Cp: 0.6; PS: 51; NG: 10,000; DF: Euclidean.
GFS-GP	The fitness function minimizes both the classification error along with complex representation of the linguistic description. *Parameters:* PS: 30; No. of labels: 3; No. of rules: 8; NG: 10,000; Mp: 0.01.

(*continued on next page*)

Algorithm	Fitness and parameter settings
GFS-SP	*Fitness:* Same as GFS-GP. *Parameters:* No. of labels: 3; No. of rules: 8; NG: 10,000; Mp: 0.5.
GFS-GPG	*Fitness:* Same as GFS-GP. *Parameters:* PS: 30; No. of labels: 3; No. of rules: 8; NG: 10,000; Mp: 0.01.
GFS-LB	The fitness function is the square of the error obtained by comparing the logistic transform of the actual output by the classifier and the desired output. *Parameters:* No. of rules: 25; No. of labels: 3.
GFS-MaxLB	Fitness $(P^1, \ldots, P^N) = D_{ik} - (\Sigma_j\ H(x_i j).\ P^j(x_i).W^j{}_k)^2$ Where N → no. of membership functions (P); $H(x_i,j)$ is taken as 1 if rule j wins when input x is classified, otherwise it is assumed as 0; $W^j{}_k$ → rule weights and D_{ik} → dependent variable. *Parameters:* No. of rules: 8; No. of labels: 3.
HIDER	Rule r Fitness = 2 (N − C.Error (r)) + G(r) + Cov (r), N → no. of examples; C. error → misclassified instance; G(r) → no. of correctly classified examples; cov → part of search space covered by a rule r. *Parameters:* PS: 100; NG: 100; Mp: 0.5; Cross percent: 80.
IGA	The fitness maximizes the accuracy of classification and minimizes the size of feature set as well as an reference set. *Parameters:* PS: 10; NG: 10,000; DF: Euclidean.
ILGA	*Fitness*: Instances that can be correctly classified (in percentage) by the rule set. *Parameters:* Mp: 0.01; Cp: 1.0; PS: 200; No. of rules: 30.
LDWPSO	*Fitness:* Same as CPSO. *Parameters:* Weights upper limit: 2.05; Convergence platform width: 30; Constriction coefficient: 0.73.
MPLCS	*Fitness:* Same as BioHEL. *Parameters:* No. of iterations: 750; Cp: 0.1; Size of Penalty Rules: 4.
NNEP	*Fitness* = 1/ (1 + Hessian matrix for Error function). *Parameters:* NG: 200; No. of Hidden Nodes: 6.
OlexGA	*Fitness* = (2* Precision * Sensitivity) / (Precision + Sensitivity). *Parameters:* PS: 500; No. of features: 50; Cp: 1.0; Elitism rate: 0.2; Mp: 0.001; NG: 200.
PBIL	*Fitness:* Same as CHC. *Parameters:* PS: 50; Mp: 0.02; Learning rate: 0.1; DF: Euclidean; NG: 10,000.
REPSO	*Fitness* = (w1 * Precision * Sensitivity) + (w2 * (1-(CA-1)/AC)); where CA → conditions in the rule antecedent and AC → decision attributes. *Parameters:* Cognitive learning rate: 2; Social learning rate: 2; Constriction factor: 1.
SGA	*Fitness:* Same as CHC. *Parameters:* PS: 50; NG: 10,000; DF: Euclidean.
SGERD	The fitness function balances the generality as well as the specificity of the rule. *Parameters:* NG: 10; No. of rules:7.
SIA	Fitness of rule r = (C-αn + βg)/ Csize Where C → examples which rule r classifies correctly; n → examples which are misclassified by r; Csize → total weight of examples; g → value between 0 & 1. *Parameters:* No. of iterations: 200.
SLAVE	Fitness of a rule is the product of consistency and completeness. *Parameters:* PS: 100; No. of iterations: 500; Mp: 0.01; No. of labels: 5.
TAN-GP	*Fitness* = $\frac{TP}{TP+w_1.FN} * \frac{TN}{TN+w_2.FP}$ Parameters: PS: 150; NG: 100; Mp: 0.1; Support: 0.03; $w_1 = 0.7$; $w_2 = 0.8$.
Target	The fitness function is Bayesian Information Criterion. *Parameters:* Probability of splitting a node: 0.5; NG: 100.
UCS	*Fitness* = (Total correct classifications/ Total no. of rule matches)^v; where v is a constant. *Parameters:* No. of explores: 100,000; Cp: 0.8; Mp: 0.04; PS: 6,400.
XCS	Fitness is computed as the inverse of error. The error is ascertained by comparing the classifier's prediction and the environment's reward. *Parameters:* No. of explores: 1,00,000; Cp: 0.8; Mp: 0.04; PS: 6,400; Type of Selection: Roulette Wheel Selection.

ML Technique Parameter Settings
C4.5: Confidence: 0.25; No. of leaf instances: 2. **CART:** Maximum Depth: 90. **ChiRW:** No. of labels: 3. **EACH:** Feature adjustment rate: 0.2. **PART:** Item sets per leaf: 2; Confidence: 0.25. **PUBLIC:** No. of nodes between prune: 25. **Riona:** Maximum no. of nearest neighbour: 200. **Slipper:** Confidence: 0.25; Probability of growth and pruning: 0.66.
Mp: Mutation probability; Cp: Crossover probability; PS: Size of population; NG: No. of generations, DS: Distance Function; no.: Number

References

[1] Malhotra R. Empirical research in software engineering: concepts, analysis, and applications. USA: CRC Press; 2015.
[2] Malhotra R. A systematic review of machine learning techniques for software fault prediction. Appl Soft Comput 2015 Feb 1;27:504–18.
[3] Malhotra R, Khanna M, Raje RR. On the application of techniques for software engineering predictive modeling: a systematic review and future directions. Swarm Evolut Comput 2017 Feb 1;32:85–109.
[4] Menzies T, Krishna R, Pryor D. The promise repository of empirical software engineering data [Online], Available: http://openscience.us/repo.
[5] Kubat M, Matwin S. Addressing the curse of imbalanced training sets: one-sided selection. In: ICML, July 8; 1997. p. 179–86.
[6] Menzies T, Greenwald J, Frank A. Data mining static code attributes to learn defect predictors. IEEE Trans Software Eng 2007;33(January (1)):2–13.
[7] Demšar J. Statistical comparisons of classifiers over multiple data sets. J Mach Learn Res 2006;7(Jan):1–30.
[8] Malhotra R. An empirical framework for defect prediction using machine learning techniques with Android software. Appl Soft Comput 2016;49(Dec):1034–50.
[9] De Carvalho AB, Pozo A, Vergilio SR. A symbolic fault-prediction model based on multiobjective particle swarm optimization. J Syst Software 2010;83(May (5)):868–82.
[10] Catal C, Diri B, Ozumut B. An artificial immune system approach for fault prediction in object-oriented software. In: Dependability of computer systems, 2007. DepCoS-RELCOMEX'07. 2nd international conference on, June 14. IEEE; 2007. p. 238–45.
[11] Vandecruys O, Martens D, Baesens B, Mues C, De Backer M, Haesen R. Mining software repositories for comprehensible software fault prediction models. J Syst Software 2008;81(May (5)):823–39.
[12] Singh Y, Kaur A, Malhotra R. Prediction of software quality model using gene expression programming. In: International conference on product-focused software process improvement, June 15. Berlin, Heidelberg: Springer; 2009. p. 43–58.
[13] Liu Y, Khoshgoftaar TM, Seliya N. Evolutionary optimization of software quality modeling with multiple repositories. IEEE Trans Software Eng 2010;36(November (6)):852–64.
[14] Pendharkar PC. Exhaustive and heuristic search approaches for learning a software defect prediction model. Eng Appl Artif Intell 2010;23(February (1)):34–40.
[15] Di Martino S, Ferrucci F, Gravino C, Sarro F. A genetic algorithm to configure support vector machines for predicting fault-prone components. In: International conference on product focused software process improvement, June 20. Berlin, Heidelberg: Springer; 2011. p. 247–61.
[16] Sarro F, Di Martino S, Ferrucci F, Gravino C. A further analysis on the use of genetic algorithm to configure support vector machines for inter-release fault prediction. In: Proceedings of the 27th annual ACM symposium on applied computing, March 26. ACM; 2012. p. 1215–20.
[17] Yu L. An evolutionary programming based asymmetric weighted least squares support vector machine ensemble learning methodology for software repository mining. Inf Sci 2012 May 15;191:31–46.
[18] Rodríguez D, Ruiz R, Riquelme JC, Aguilarâ€"Ruiz JS. Searching for rules to detect defective modules: a subgroup discovery approach. Inf Sci 2012;191(May):14–30.

[19] Canfora G, De Lucia A, Di Penta M, Oliveto R, Panichella A, Panichella S. In: Multi-objective cross-project defect prediction. InSoftware testing, verification and validation (ICST), 2013 IEEE sixth international conference on, March 18. IEEE; 2013. p. 252–61.
[20] Jin C, Jin SW. Prediction approach of software fault-proneness based on hybrid artificial neural network and quantum particle swarm optimization. Appl Soft Comput 2015;35(October):717–25.
[21] ÖF Arar, K Ayan. Software defect prediction using cost-sensitive neural network. Appl Soft Comput 2015;33(August):263–77.
[22] Hosseini S, Turhan B, Mäntylä M. A benchmark study on the effectiveness of search-based data selection and feature selection for cross project defect prediction. Inf Software Technol 2017(June).
[23] Xia X, Lo D, Pan SJ, Nagappan N, Wang X. Hydra: massively compositional model for cross-project defect prediction. IEEE Trans Software Eng 2016;42(October (10)):977–98.
[24] Jureczko M, Madeyski L. Towards identifying software project clusters with regard to defect prediction. In: Proceedings of the 6th international conference on predictive models in software engineering. ACM; 2010. p. 9.
[25] Chidamber SR, Kemerer CF. A metrics suite for object oriented design. IEEE Trans Software Eng 1994;20(June (6)):476–93.
[26] Henderson-Sellers B. Object-oriented metrics: measures of complexity. Upper Saddle River, NJ, USA: Prentice-Hall, Inc.; 1996.
[27] Martin RC. Object oriented design quality metrics: an analysis of dependencies. Rep Object Anal Design 1995;2(September (3)):1–8.
[28] Bansiya J, Davis CG. A hierarchical model for object-oriented design quality assessment. IEEE Trans Software Eng 2002;28(January (1)):4–17.
[29] Friedman M. The use of ranks to avoid the assumption of normality implicit in the analysis of variance. J Am Stat Assoc 1937;32(December (200)):675–701.
[30] Alcalá-Fdez J, Sanchez L, Garcia S, del Jesus MJ, Ventura S, Garrell JM, Otero J, Romero C, Bacardit J, Rivas VM, Fernández JC. KEEL: a software tool to assess evolutionary algorithms for data mining problems. Soft Comput 2009;13(February (3)):307–18.
[31] Ramírez A, Romero JR, Ventura S. A comparative study of many-objective evolutionary algorithms for the discovery of software architectures. Emp Software Eng 2016;21(December (6)):2546–600.
[32] Malhotra R, Khanna M. An exploratory study for software change prediction in object-oriented systems using hybridized techniques. Autom Software Eng 2017;24(September (3)):673–717.
[33] Cano A, Luna JM, Zafra A, Ventura S. A classification module for genetic programming algorithms in JCLEC. J Mach Learn Res 2015;16(January (1)):491–4.

Ruchika Malhotra is Associate Professor at the Delhi Technological University, Delhi, India. She has completed her Post-doctoral research in Indiana University Purdue University Indianapolis USA. She has received IBM Faculty Award 2013. Her h-index is 23 (Google Scholar). She is the author of book "Empirical Research in Software Engineering" published by CRC press. She has published more than 160 research papers in international journals and conferences.

This article has been accepted for inclusion in a future issue of this journal. Content is final as presented, with the exception of pagination.

Challenges & Physical Insights Into the Design of Fin-Based SCRs and a Novel Fin-SCR for Efficient On-Chip ESD Protection

Milova Paul, *Student Member, IEEE*, B. Sampath Kumar, Christian Russ, Harald Gossner, *Senior Member, IEEE*, and Mayank Shrivastava, *Senior Member, IEEE*

***Abstract*— This paper presents the detailed physical insights into the silicon-controlled rectifier (SCR) phenomena in planar equivalent Fin SCR devices. The complexity and roadblocks for SCR triggering in FinFET technology are explored. Implication of contact silicidation on Fin SCR turn-ON is discussed in detail. Device design approaches are discussed for efficient Fin-enabled SCRs. In this direction, a novel contact engineering scheme in Fin technology is disclosed for improved SCR action. Moreover, a novel Fin SCR is presented, which offers area-efficient electrostatic discharge current carrying capability.**

***Index Terms*— Electrostatic discharge (ESD), FinFET, on chip, silicon-controlled rectifier (SCR).**

I. Introduction

IT HAS been over seven years since FinFET-based commercial products were first announced by semiconductor industry. The tremendous pace of CMOS scaling and projected short-channel performance requirements pushed FinFETs to get into the mainstream, which are structurally designed to have an efficient channel control to reduce the OFF-state leakage [1] with least foot print and maximum ON-current per unit area. While FinFETs enjoy lower silicon footprint, these devices, however, become increasingly vulnerable toward overvoltage, self-heating, and electrostatic discharge (ESD) stress due to poorer heat dissipation when compared to its planar counterpart. Having such a technology at disposal, designing wide variety of ESD protection devices has become a major concern [2]–[5]. Reduced ESD design window for FinFET and beyond FinFET technology have posed further difficulty in developing ESD protection elements in FinFET technology [6]–[12], causing Fin-based ICs to be increasingly susceptible to ESD events [13]–[16]. This is one of the reasons why FinFET technology is mostly filling the high-performance computing and digital baseband-like product needs, to begin with. Developing a system-on-chip is still a long shot, attributed to missing variety of ESD protection devices, beside high-voltage capability.

Silicon-controlled rectifiers (SCRs) have widely been used as an efficient ESD protection device for low-voltage applications, owing to their low parasitic loading effects, relatively smaller device footprint area, lower holding voltage, and faster turn-ON [18]–[27]. With the principle of regenerative positive feedback under ESD, such as high current injection event, SCR stands as a desirable ESD protection element when compared to ggnMOS or diodes. While often the fundamental concepts for device designs are borrowed from its previous nodes, adapting the planar-like conventional SCR design approach for FinFET technology presents numerous design challenges [28], [29]. It was reported that SCR device designs from planar counterparts could not be borrowed successfully for the Fin-based SCR devices due to the lack of reproducible SCR-like action [29].

In this paper, fundamental roadblock and physical phenomena associated with Fin-based SCR designs have been studied using 3-D device TCAD. Furthermore, Section II presents the physical insights into the missing SCR action in FinFET technology. With the corresponding findings, Section III discusses the design challenges and engineering approaches toward efficient SCR mechanism. Having explored the physical insights of fin-based bottlenecks and techniques to redesign conventional Fin SCR (CFSCR), a novel dual-Fin SCR (DFSCR) is introduced in Section IV, as an efficient ESD protection element, which provides an area efficient solution with a well-distributed current conduction mechanism. Finally, Section V concludes the new findings and proposed design rules for an efficient SCR for FinFET technology.

Manuscript received June 18, 2018; revised August 16, 2018; accepted September 6, 2018. The work of M. Paul, B. S. Kumar, and M. Shrivastava was supported by the Department of Science and Technology, Government of India, India, through the IMPacting Research INnovation and Technology Program. The review of this paper was arranged by Editor E. Rosenbaum. *(Corresponding author: Milova Paul.)*

M. Paul, B. S. Kumar, and M. Shrivastava are with the Advance Nanoelectronic Device Research Group, Department of Electronic Systems Engineering, Indian Institute of Science, Bengaluru 560012, India (e-mail: milova@iisc.ac.in; mayank@iisc.ac.in).

C. Russ was with Intel Deutschland GmbH, 85579 Neubiberg, Germany. He is now with Infineon Technologies AG, 85579 Neubiberg, Germany.

H. Gossner is with Intel Deutschland GmbH, 85579 Neubiberg, Germany.

Color versions of one or more of the figures in this paper are available online at http://ieeexplore.ieee.org.

Digital Object Identifier 10.1109/TED.2018.2869630

0018-9383 © 2018 IEEE. Personal use is permitted, but republication/redistribution requires IEEE permission.
See http://www.ieee.org/publications_standards/publications/rights/index.html for more information.

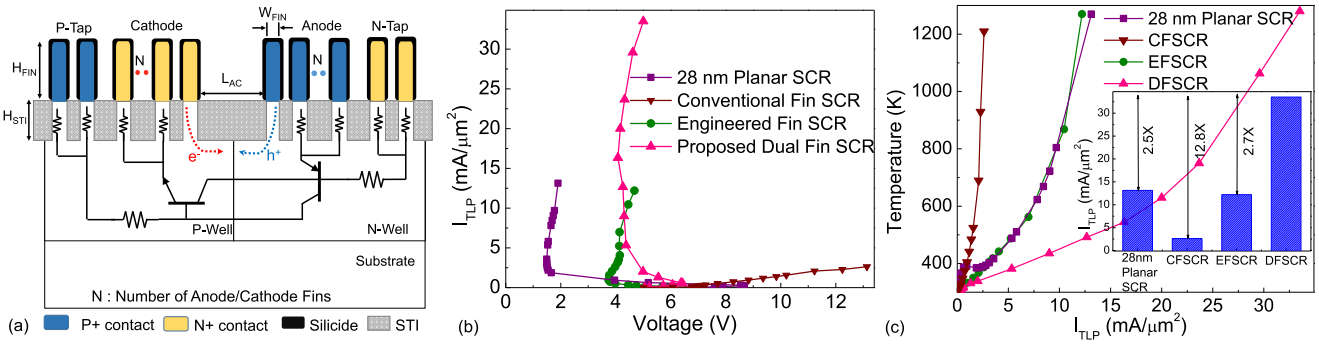


Fig. 1. (a) Planar equivalent of CFSCR. (b) TLP I–V characteristics of CFSCR, EFSCR, and proposed DFSCR. (c) Self-Heating: Lattice temperature versus I_{TLP} of CFSCR, EFSCR, and proposed DFSCR, extracted using 3-D TCAD simulations. Inset of (c) compares the ESD robustness (It2) of the CFSCR with the proposed DFSCR and EFSCR, respectively [17].

II. FinFET SCRs: A Brief Outlook

On account of a low holding voltage (V_{Hold}), high failure current (It2) and an excellent ON-resistance (R_{ON}), SCR devices serve as an efficient ESD protection element. However, the translation of this planar-based SCR ESD protection concept to FinFET technology presents many design-specific challenges, which alters the ESD relevant metrics of the SCR, such as snapback, low V_{Hold}, desirable It2, and R_{ON}. Fig. 1(a) illustrates the schematic of the planar equivalent CFSCR with the anode, cathode, and n/p triggering taps/fins. The n+ or p+ fins are fully silicided at the fin surface and are used to contact the n-/p-wells (base–collector taps) with the respective emitters. Throughout this paper, the number of fins used in n/p tap region is designed, such that the number of N/P tap fins to anode/cathode fins (N) ratio is 0.6. This ratio is considered to mimic the approximate length ratio of n/p tap to anode/cathode length of that of planar SCR, to have a conservative comparison. This design is also compared with a 28-nm technology equivalent planar SCR device, an engineered Fin SCR (EFSCR) device, and a newly proposed DFSCR device. The idea behind EFSCR and DFSCR architectures are revealed in later sections. It is worth highlighting that Transmission Line Pulse (TLP) I–V characteristics of various SCR devices explored in this paper have been extracted using 3-D device TCAD simulations [30]. The TCAD simulation deck for SCR is well-calibrated with experimental FinFET results [31] using appropriate fin aspect ratio and TCAD models, as explained in our earlier works [32], [33]. To account for self-heating effects under ESD stress condition, thermal boundary conditions are taken into consideration, as reported in [34], beside incorporating thermal resistance equivalent to back-end metal interconnect and interlayer dielectric. State-of-the-art TLP I–V extraction methodology was used with 100-ns pulsewidth with increasing amplitude after each pulse with a rise time of 10 ns. An averaging window of 60–80 ns was adopted to extract the individual I–V points in the TLP I–V curve. The failure criteria (It2) for all the devices were considered with a conservative estimate of temperature exceeding 1200 K. This is in accordance with an earlier failure analysis work on FinFETs [3]. For all investigations, H_{FIN}, H_{STI}, and W_{FIN} were considered to be 42, 70, and 8 nm, respectively.

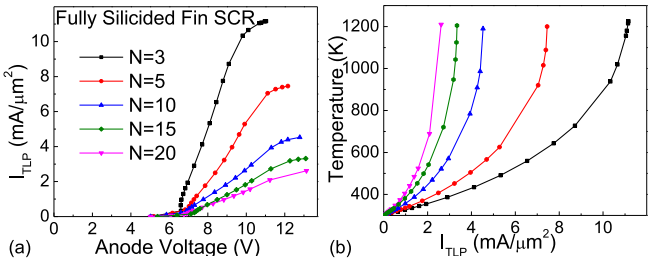


Fig. 2. (a) TLP I–V characteristics and (b) lattice temperature versus I_{TLP} characteristics of fully silicided CFSCR as a function of number of anode/cathode Fins (N).

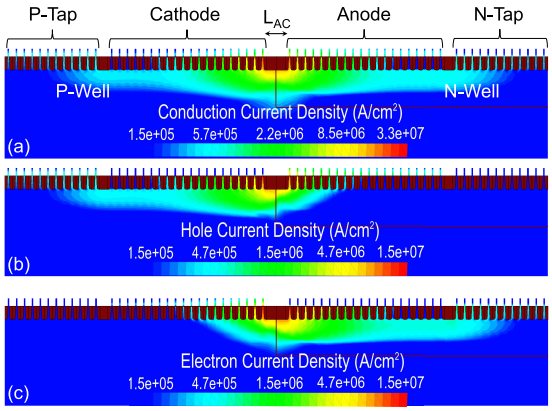


Fig. 3. (a) Total current density, (b) hole current density, and (c) electron current density across a fully silicided CFSCR, extracted at 50% of It2 [17].

The anode/cathode/tap doping was chosen as 1×10^{21} cm^{-3}; however, the p-/n-well doping was selected to be 5×10^{18} cm^{-3}. To encapsulate the real-time heat dissipation, an equivalent thermal resistance of 1-μm copper metal was defined over the anode/cathode/tap terminals. All the characteristics were extracted considering negligible contact resistance due to the degenerate doping of the anode/cathode/tap regions. Adding external contact resistance at the terminals affects the R_{ON} of the device without inducing significant effect on the intrinsic device parasitics.

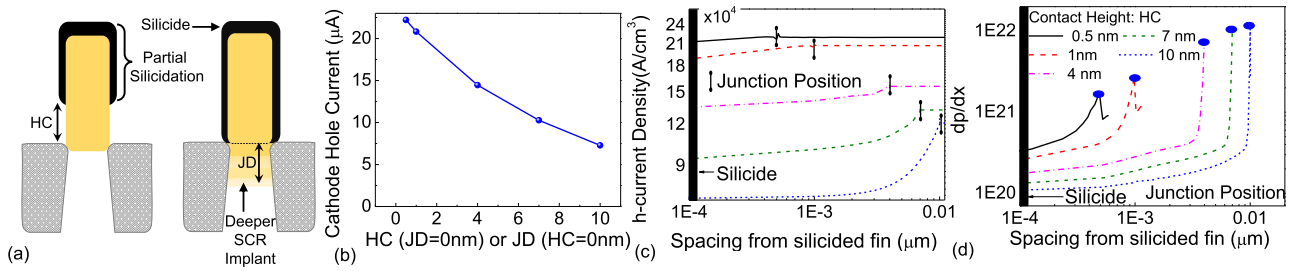


Fig. 4. (a) Fin schematic depicting contact and junction engineering schemes. CFSCR has HC = JD = 0 nm [see Fig. 1(a)]. (b) Cathode (or emitter) hole current versus HC or JD. (c) Hole current density and (d) hole density gradient (dp/dx) as a function of spacing from the silicided fin.

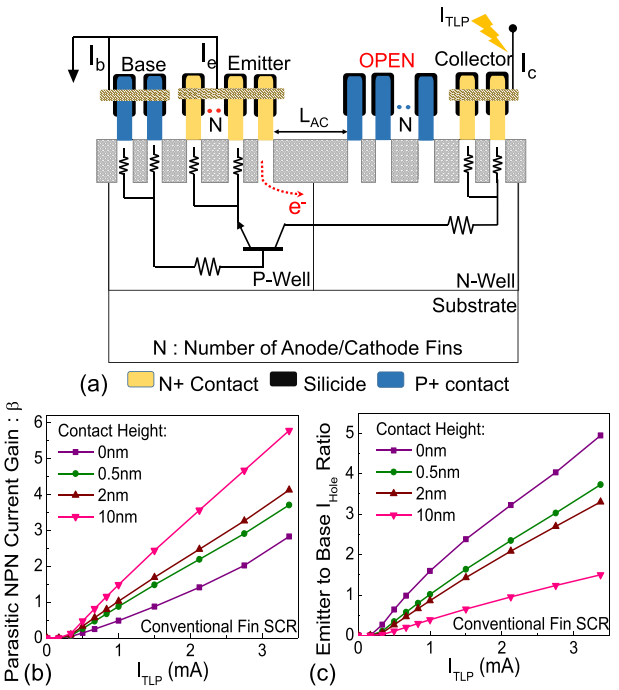


Fig. 5. (a) Cross-sectional view depicting the parasitic n-p-n device of the planar equivalent Fin SCR. (b) Current gain (β) as a function of injected collector current. (c) Emitter-to-base hole current ratio as a function of pulsed collector current.

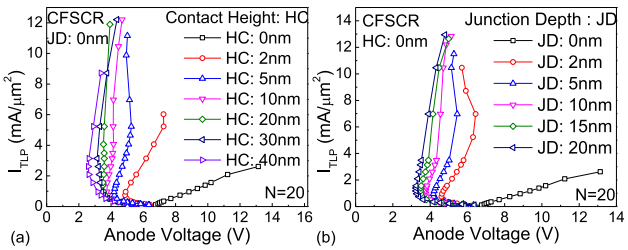


Fig. 6. TLP I–V characteristics of CFSCR with varying (a) HC (JD = 0) and (b) JD (HC = 0). Here, the number of anode/cathode fins, $N = 20$.

Fig. 1(b) depicts the simulated TLP I–V characteristics of various SCR designs, briefly mentioned earlier. It depicts absence of regenerative snapback in the CFSCR, which reveals a missing SCR action leading to higher holding voltage and a very low It2. In order to demonstrate a fair comparison

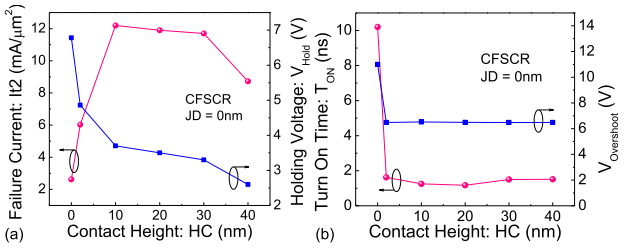


Fig. 7. (a) Failure current (It2) and holding voltage (V_{Hold}) and (b) turn-ON time (T_{ON}) and voltage overshoot ($V_{Overshoot}$) as a function of spacing between contact silicidation and base–emitter junction (HC) for JD = 0 nm. These trends were extracted at an injected stress current equivalent to 90% of the respective It2.

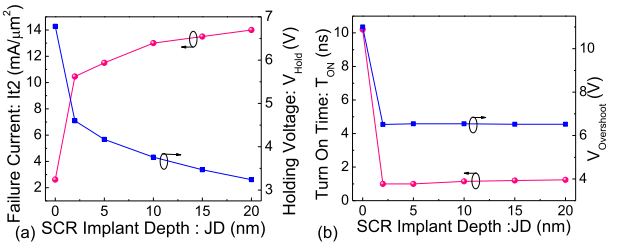


Fig. 8. (a) Failure current (It2) and holding voltage (V_{Hold}) and (b) turn-ON time (T_{ON}) and voltage overshoot ($V_{Overshoot}$) as a function of diffusion depth below active Fin (JD) for HC = 0 nm. These trends were extracted at injected stress current equivalent to 90% of the respective It2.

between 2-D (planar) and 3-D nature of the various SCR designs, the stress currents are normalized per unit layout area. The following sections present the underlying phenomena leading to the missing SCR action in conventional-/planar-based Fin topology and ways to mitigate Fin-based SCR design challenges. The corresponding findings are used to reengineer the CFSCR design and propose a novel DFSCR design [see Fig. 1(b)], providing a 13× improvement in layout efficiency in terms of failure current per unit area, beside significant improvement in holding voltage and ON-resistance of these SCR devices.

III. Fin SCRs: Design Challenges and Engineering

As discussed earlier, the CFSCR does not exhibit an SCR action (or first snapback), as depicted in Fig. 1(b), which is further elaborated in Fig. 2, as a function of number of

This article has been accepted for inclusion in a future issue of this journal. Content is final as presented, with the exception of pagination.

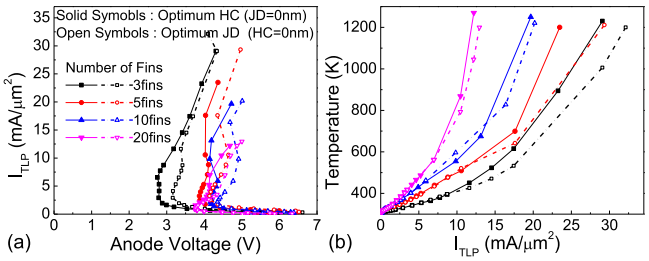


Fig. 9. (a) TLP I–V characteristics and (b) lattice temperature versus I_{TLP} characteristics of partially silicided Fin SCR device for both optimum HC and optimum JD, as a function of number of anode/cathode fins (N).

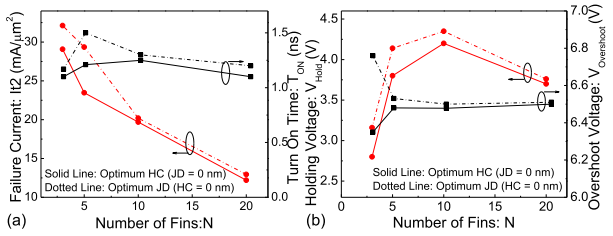


Fig. 10. (a) Failure current (It2) and turn-ON time (T_{ON}) and (b) holding voltage (V_{Hold}) and voltage overshoot ($V_{Overshoot}$) as a function of number of fins (N) for partially silicided Fin SCR device.

anode/cathode fins (N). Fig. 2 demonstrates the TLP I–V characteristics of CFSCR with increasing N, and it can be seen that, as N increases, the It2 per unit area lowers, and it does not affect the SCR action. The possible explanation for this is the weak parasitic bipolar, which can be attributed to an increased emitter resistance due to the Fin shape or increased carrier recombination in the base region due to relatively higher doping in FinFET's n-/p-wells. However, detailed TCAD analysis revealed that none of these were responsible for the missing SCR action or weaker bipolar action in CFSCRs. Fig. 3(a) shows the total conduction current density for CFSCR (considering $N = 20$), where the major current carrying regions are anode and cathode terminals, which is consistent with the traditional understanding of current transport across SCR device [20]. Fig. 3(b) and (c) depicts the respective minority carrier current conduction (electron and hole) across CFSCR. It has been found that unlike in planar SCRs, a significant portion of minority carrier current flows through the respective cathode/anode contacts, which are the emitter contacts of the Fin SCR, i.e., a significant hole current through the cathode contact and an electron current through the anode contact. This minority hole (electron) conduction through the parasitic n-p-n (p-n-p) emitter contact is expected to dominate through p (n)-Tap to trigger the SCR. The weaker bipolar action in CFSCR can then be explained due to the significant loss of minority carriers through the emitter contacts. The high minority carrier conduction through emitter contacts is due to fully silicided nature of Fins, which is elaborated in Fig. 4. Fig. 4(a) shows single-Fin schematic, depicting parameters contact height (HC) or junction depth (JD) to study the impact of spacing between silicided portion of the Fin and base–emitter junction. The HC is defined as the height from the base of the fin, above which the fin is fully silicided. This refers

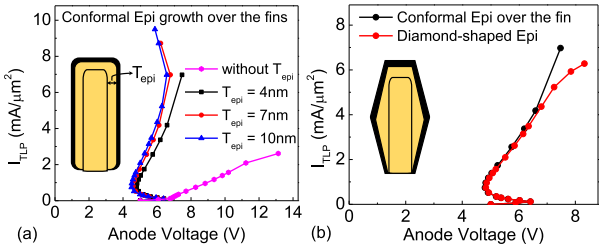


Fig. 11. (a) TLP I–V characteristics of CFSCR with the incorporation of a conformal epitaxial silicon layer over the fins (shown in inset) as a function of epi layer thickness (T_{epi}). (b) TLP I–V characteristics of CFSCR with conformal and diamond-shaped epi-growth over the fins (shown in inset).

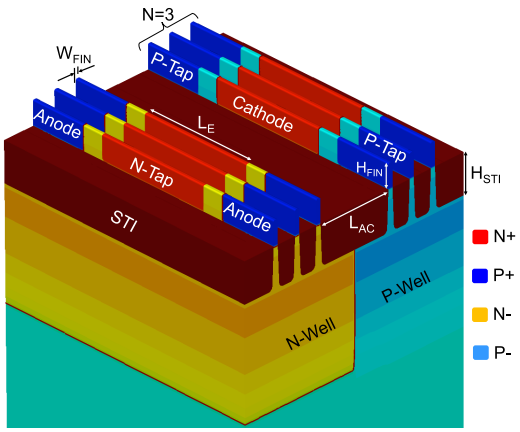


Fig. 12. 3-D architectural view of the proposed DFSCR design. The active Fin regions consist of anode/cathode and n-/p-taps, which forms a junction or contact with the respective n-/p-wells [17].

to contact silicidation from the base of the fin up to a desired height. The JD can be defined as the diffusion depth of the emitters, beneath the active region of the fin. In case of conventional (fully silicided) Fin SCR, HC = 0 and JD = 0, Fig. 4(b) depicts the gradual reduction in minority carrier conduction through the emitter contact, as HC was increased from 0 to 10 nm (keeping JD = 0 nm) or when JD was increased from 0 to 10 nm (keeping HC = 0 nm). This is plotted as a decrease in the minority hole current through the emitter cathode contact for the n-p-n parasitic bipolar. This is attributed to the minority carrier diffusion current [see Fig. 4(c)], which is a strong function of the minority carrier gradient between junction and the contact as

$$J_P = q.D_p \frac{dp}{dx}. \tag{1}$$

In theory, for HC = JD = 0, $dx \to 0$ and, hence, $dp/dx \to \infty$. Extrapolating this to the situation when contact was placed next to the vertical junction in case of fully silicided Fin, it resulted in significantly higher carrier gradient [see Fig. 4(d)] and minority carrier conduction through emitter (anode/cathode) contacts. This can also be observed from Fig. 4(b), which depicted highest minority hole current through the cathode (or emitter) for HC = 0 and JD = 0. This can be relaxed by keeping the silicided region away from the junction, either by increasing HC or by increasing JD, which is found

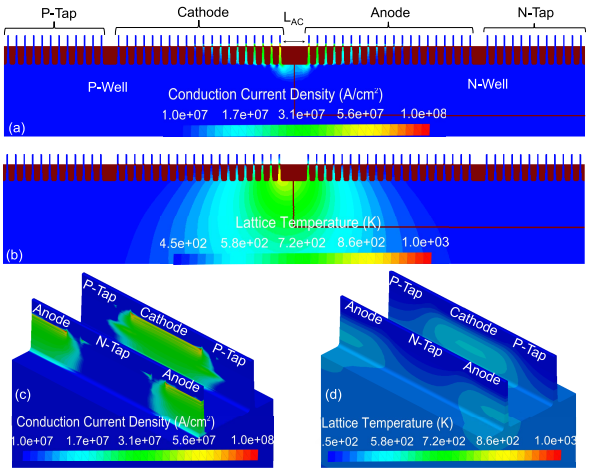


Fig. 13. Conduction current density and lattice temperature profiles of (a) and (b) CFSCR and (c) and (d) DFSCR, respectively, extracted for $I_{TLP} = 2.3$ mA/μm^2.

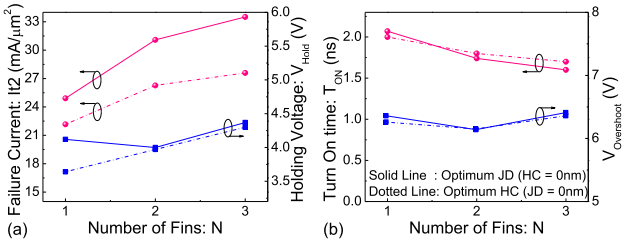


Fig. 14. (a) Failure current (It2) and holding voltage (V_{Hold}) and (b) turn-ON time (T_{ON}) and voltage overshoot ($V_{Overshoot}$) as a function of number of Fins (N) over the n-/p-wells in DFSCR. These trends were extracted using 3-D TCAD simulation at injected stress current equivalent to 90% of the respective It2.

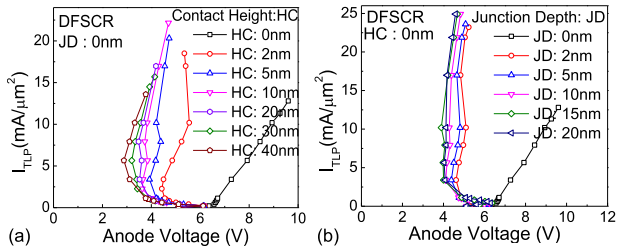


Fig. 15. TLP I–V characteristics of DFSCR with varying (a) HC (JD = 0) and (b) JD (HC = 0). Here, the number of anode/cathode fins, $N = 1$.

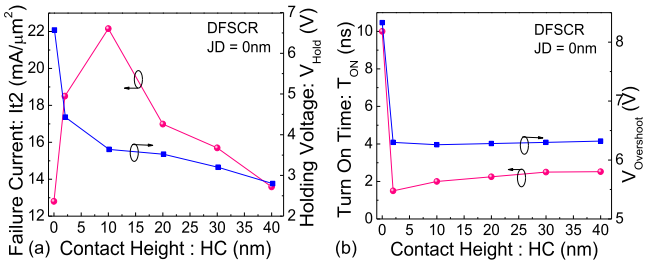


Fig. 16. (a) Failure current (It2) and holding voltage (V_{Hold}) and (b) turn-ON time (T_{ON}) and voltage overshoot ($V_{Overshoot}$) as a function of HC in DFSCR.

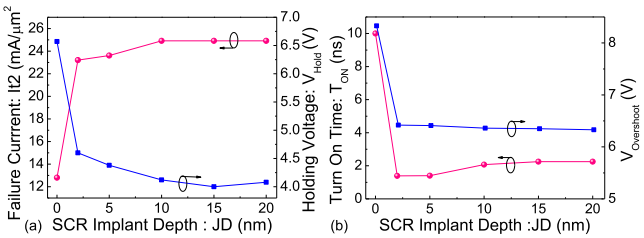


Fig. 17. (a) Failure current (It2) and holding voltage (V_{Hold}) and (b) turn-ON time (T_{ON}) and voltage overshoot ($V_{Overshoot}$) as a function of JD in DFSCR.

to improve the parasitic bipolar action. Similar improvement in bipolar efficiency for planar nMOS devices was earlier experimentally validated with thin S/D salicides [16]. Fig. 5(a) depicts a scheme using which, the efficiency of the parasitic n-p-n bipolar was studied, where the anode contact was left open, the p-tap and cathode were grounded and the n-tap was stressed. It can be observed that as the spacing between silicided portion of the Fin and base-emitter junction was increased, the bipolar gain (β) was found to increase [see Fig. 5(b)], which is attributed to the reduced emitter-to-base hole current ratio [see Fig. 5(c)]. This results in an efficient SCR action, which manifests as a deep snapback in the TLP I–V characteristics, further illustrated in Fig. 6, where an SCR action is clearly visible for HC $>$ 2 nm or JD $>$ 2 nm. Similar improvement in the parasitic bipolar efficiency with the increase in HC was observed for dc simulations, as well. An important point to highlight here is that the SCR action (or efficient bipolar action) for FinFET technology can be improved by separating the contact (or silicide) from the junction by either lifting the silicide up from the base of the fin (increasing HC) or by diffusing the emitter deeper (increasing JD).

Figs. 7 and 8 further depict the impact of contact separation from the junction by increasing HC and JD, respectively, on the ESD figure-of-merit parameters of SCR device, such as It2, V_{Hold}, turn-ON time (T_{ON}), and overshoot voltage ($V_{Overshoot}$). The trends were extracted for injected stress current equivalent to 90% of the respective It2. As HC or JD was increased, SCR's failure current and turn-ON time were found to improve by an order of magnitude. Similarly, holding voltage and voltage overshoot was found to scale by a factor of 3 and 2, respectively, [V_{Hold} drops from 7 to 3 V, and $V_{Overshoot}$ drops from 11 to 6.5 V in Fig. 8]. It should be noted that normalized It2 per layout area drops and then saturates after an optimum value of HC or JD = 10 nm. This is attributed to the increased thermal resistance between S/D Fins and contact with increase in HC and/or JD, which enhances the lattice heating and resulting device failure. Given that most of the thermal energy from FinFET channel is taken away by the Back End of Line metallization via S/D contacts [35], any change in contact scheme is prone to affect the self-heating behavior of the FinFET devices. With increasing HC or JC, the silicided region is moved away from hot spot, which adds to the thermal resistance mentioned. Therefore, from Figs. 7 and 8, it can be stated that the CFSCR can be engineered

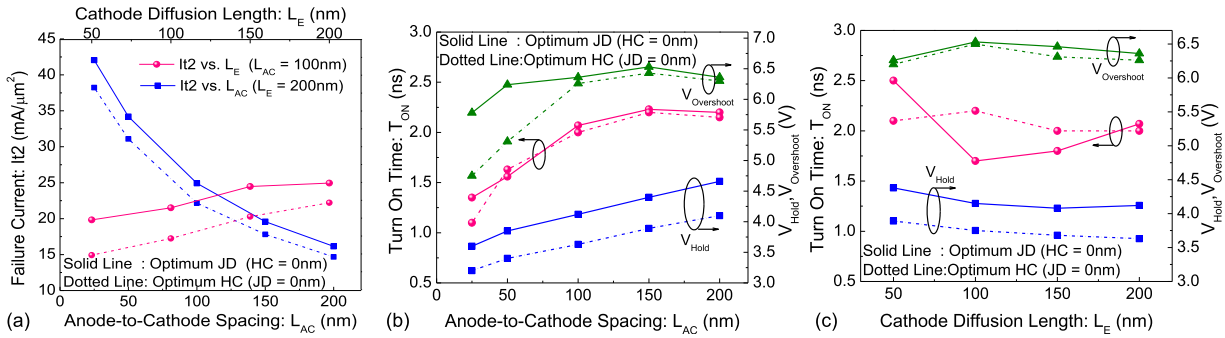


Fig. 18. (a) Failure current (It2), holding voltage (V_{Hold}), turn-ON time (T_{ON}) and voltage overshoot ($V_{Overshoot}$) as a function of (b) anode-to-cathode spacing (L_{ac}) and (c) anode/cathode diffusion length (L_E), as shown in Fig. 12, depicting improved design scalability for DFSCR. The respective trends were extracted using 3-D TCAD simulation at an injected stress current equivalent to 90% of the respective It2.

with HC = 10 nm (keeping JD = 0 nm) or JD = 10 nm (keeping HC = 0 nm) to offer optimum performance as an SCR ESD protection device, which is termed as EFSCR device in this paper. This value for the optimum HC and JD shall be used in the subsequent investigations too.

Fig. 9 demonstrates the TLP characteristics for the EFSCR with HC = 10 nm (JD = 0 nm) and with JD = 10 nm (HC = 0 nm), as a function of number of anode/cathode fins (N). With the contact and junction engineering scheme, an efficient SCR action is evident from deep snapback in the TLP I–V graph. It is also worth highlighting that the EFSCR exhibits reduced failure current per layout area with the increase in the number of anode/cathode fins. This is because It2 per unit device width does not increase linearly with increasing number of anode/cathode Fins, which is due to nonuniform current contributions from anode/cathode Fins. Fins that are close to well junction contribute to higher SCR current, which falls as one moves away from well junction. Attributed to this reduced current contribution while moving away from junction, It2 per unit area falls beyond an optimum value of 3 Fins. This trend is found to be similar to the CFSCR devices, as depicted in Fig. 2. Fig. 10 further illustrates the effect of the number of anode/cathode fins on the ESD relevant metrics for the partially silicided Fin-SCR. It can be observed that the turn-ON time and the overshoot characteristics do not get affected with the increase in the number of anode/cathode fins. However, the holding voltage (V_{Hold}) reaches a peak at $N = 10$ and is seen to roll off at higher values of N. With the increase in the number of fins, the current density drops, and hence, it requires an increased number of minority carriers to sustain the bipolar action, which leads to an increase in V_{Hold}. Furthermore, as the number of fins is increased, the emitter junction area increases, which improves the emitter injection efficiency and allows the bipolar action to be maintained even at slightly lower holding voltages. Hence, the number of anode/cathode Fins in FinFET SCRs can be used as a design knob to tune the holding voltage, as per the design requirement.

To summarize, so far we have shown that for efficient SCR action in FinFET-based ESD protection devices, the efficiency of the parasitic bipolar needs to be improved, which is achieved by separating the contact silicide and the drain-well junction. This was found to mitigate the minority carrier

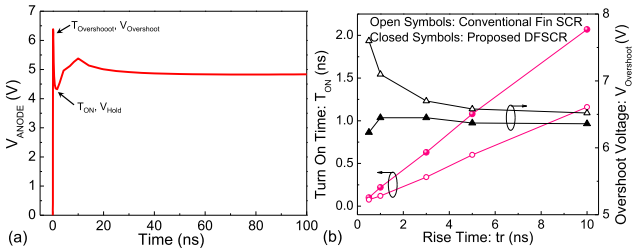


Fig. 19. (a) Anode voltage versus stress time for DFSCR, depicting the extraction of T_{ON}. (b) Transient figure-of-merit comparison (T_{ON} and $V_{Overshoot}$) of EFSCR and DFSCR as a function of pulse rise time, extracted for optimum JD. These trends were extracted using 3-D TCAD simulation at an injected stress current equivalent to 90% of the respective It2.

loss through the emitter contacts, which can be achieved by either increasing HC (i.e., moving silicide region vertically) or increasing JD (pushing the anode/cathode regions deeper into the n-/p-wells). Fig. 11 proposes and depicts another approach to disjoint the p-n junction from the silicide by incorporating an epitaxial layer over the fins before the metal silicidation process. With the epitaxial growth over the fins, the contact silicidation at the base of the fin may not be present. This phenomena act as a raised contact metallization case. The epitaxial layer can be a conformal growth all over the fins, leading to a rectangular epitaxy profile or a diamond-like epitaxy over the fins. Fig. 11(a) depicts the TLP I–V characteristics of the CFSCR with increasing thickness of a conformal epitaxial layer of silicon (with thickness T_{epi}) all over the active-fin region. As depicted, the SCR action is improved with increasing epi thickness, attributed to the physics explained earlier while increasing JD or HC. Fig. 11(b) presents the TLP I–V comparison of CFSCR with conformal and diamond-shaped epitaxy over the fins. It is worth highlighting that no significant change is observed in the TLP characteristics, which demonstrates the independence of the behavior of the parasitic bipolar with the shape of the epitaxial growth over the fins.

IV. Novel Dual Fin SCR

The previous section demonstrated the physical insights and ways to overcome the challenges associated in designing efficient FinFET SCR ESD protection devices. This section presents a novel DFSCR design to further improve the layout

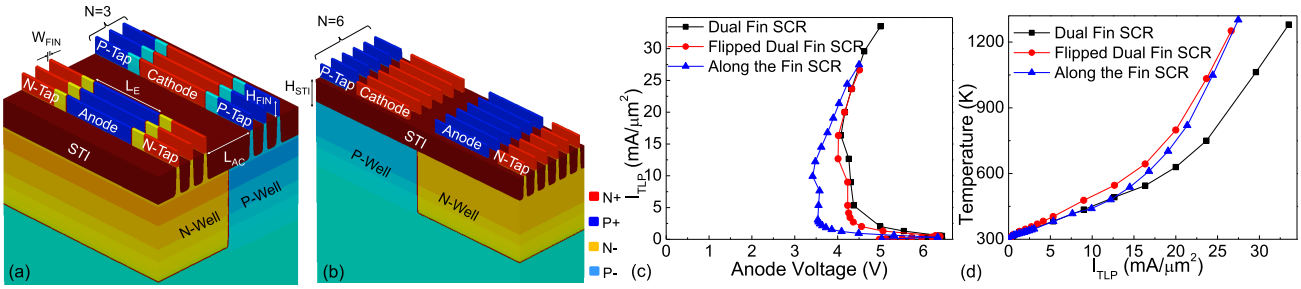


Fig. 20. 3-D architectural view of (a) Flipped DFSCR with adjacent anode/cathode regions, (b) along the Fin-SCR, where the anode/cathode and tap regions are placed on the same group of fins, and (c) and (d) TLP I–V and lattice temperature versus I_{TLP} characteristics of DFSCR, Flipped version of DFSCR (or nondiagonal DFSCR), and along the Fin SCR, respectively.

efficiency of these protection elements. Fig. 12 depicts the proposed DFSCR design, which consists of two groups of fins separately placed in n- and p-wells. Here, each group may have one or more number of Fins (N). n-/p-taps are placed on both the sides of anode/cathode. Note that the anode and cathode diffusions are intentionally placed diagonal to each other. This permits uniform current spreading and, therefore, lowers the current density for a given absolute anode-to-cathode current, which further helps in relaxing the heat dissipation across the device and improves failure current per unit area [Fig. 1(b) and (c)] [17]. This is also depicted in Fig. 13, which shows relaxed lattice temperature for DFSCR, as compared to the CFSCR architecture. The proposed DFSCR device can easily be used in cell-based geometry to minimize its overall footprint.

Fig. 14 plots the ESD relevant parameters for SCR device for DFSCR as a function of number of anode/cathode fins (N). It shows that increasing number of Fins in a given group improves the overall area efficiency of the device without sacrificing the turn-ON or holding voltage characteristics. Comparing with the optimum EFSCR [see Figs. 7 and 8], the proposed DFSCR device offers 3× higher It2 per unit area. The same concept for separating the contact from the junction by increasing HC or JD can be implied in DFSCR. Fig. 15 summarizes the TLP I–V results for DFSCR with increasing HC and JD. As discussed in the previous section, with the increase in the contact and junction separation, the bipolar efficiency improves, leading to a snapback in the I–V characteristics. This is attributed to the reduction in the minority carrier current through the emitter regions. Figs. 16 and 17 depict the variation of the ESD figure-of-merit parameters with HC and JD, respectively. Similar to EFSCR, the proposed DFSCR also exhibits improved SCR action when HC and JD were increased above 2 nm, which validates the design challenges and proposed solutions in the previous section. However, unlike EFSCR, DFSCR with optimum JD exhibits higher failure threshold than the same with optimum HC, which validates the presence of efficient current spreading in the proposed device compared to planar equivalent design.

Fig. 18 illustrates the design scalability of the proposed DFSCR. Fig. 18(a) shows 20% improvement in failure current per unit area when cathode diffusion length (L_E) was increased by 4×. This can be achieved without sacrificing transient performance, as depicted in Fig. 18(c). By scaling the anode-to-cathode spacing (L_{ac}) by 4×, It2 per unit area was found to improve by 3× with 25% reduction in holding voltage, 25% reduction in voltage overshoot, and 2× faster turn-ON. This was found to achieve without sacrificing the OFF-state leakage. Similar design feasibility was missing in the conventional designs. The transient performance metrics of the EFSCR and DFSCR are compared as a function of pulse rise time, for optimum JD, as depicted in Fig. 19. Here, the turn-ON time (T_{ON}) is extracted as the time when the voltage achieves a minimum holding state [see Fig. 19(a)]. DFSCR offers lower voltage overshoot at shorter rise times (tr < 2 ns, emulating the vf-TLP conditions), without compromising with the turn-ON time, when compared to EFSCR. This is attributed to the smaller design foot print area (lower capacitance) and improved current-spreading characteristics in the proposed DFSCR. Similar trends were also observed for optimum HC design too. This affirms an area efficient ESD robustness of DFSCR when compared to EFSCR.

So far, the planar SCR is compared with the Fin-based SCR (EFSCR and DFSCR), where DFSCR depicts relaxed lattice temperatures and higher ESD robustness. An obvious question regarding this is whether the It2 improvement is due to the diagonal placement of anode/cathode in DFSCR or some other phenomenon. To quantify this, the TLP results with diagonally placed anode/cathode contacts (see Fig. 12) are compared with a Flipped version of DFSCR with anode/cathode regions facing toward each other [see Fig. 20(a)] and an "Along the Fin-SCR," where the anode/cathode and the tap regions are all placed along the same group of fins [see Fig. 20(b)]. The TLP I–V and lattice temperature comparison of these variants plotted in Fig. 20(c) and (d) clearly depict that while a diagonal placement offers similar I–V characteristics as other variants, the It2 for the case of diagonal DFSCR is 20% higher than the other design architectures, attributed to relaxed self-heating, depicted in Fig. 20(d). This difference is ascribed to the way the majority current carrying regions are placed in the device. In the Flipped DFSCR, the anode/cathode diffusions are placed adjacent to each other; however, in the diagonal configuration, the current effectively spreads across the entire active device, thereby relaxing the lattice heating, which eventually leads to increased ESD robustness of DFSCR.

V. Conclusion

In this paper, we revealed physical insights into the missing SCR action in planar equivalent CFSCR devices. The fundamental reason for the weak parasitic bipolar and missing SCR

action was found to be the excess minority carrier conduction through the anode/cathode contacts in CFSCR device. This was attributed to the fully silicided nature of the Fins, which gives rise to minority carrier diffusion current through parasitic bipolar's emitter–base junction. This was avoided by: 1) pushing the silicided region away from the junction by introducing partial silicidation (HC) or 2) pushing the junction away from the silicided portion by introducing an SCR implant (JD). The same can also be achieved by incorporating an epitaxial layer of silicon grown over the emitter contacts. This resumed the SCR action with significantly improved performance. Finally, the novel DFSCR design is proposed, which allows uniform current spreading, better design scalability, and relaxed heat dissipation across the device. Attributed to this, the proposed design offers 3× higher failure current per unit area and 35% lower voltage overshoot without compromising with turn-ON time when compared to EFSCR device. This efficient diagonal anode/cathode placement in DFSCR accounts for 20% increase in It2 when compared to other nondiagonal Flipped DFSCR and along the Fin-SCR variants.

REFERENCES

[1] D. Hisamoto *et al.*, "FinFET—A self-aligned double-gate MOSFET scalable to 20 nm," *IEEE Trans. Electron Devices*, vol. 47, no. 12, pp. 2320–2325, Dec. 2000.

[2] D. Linten, G. Hellings, S. H. Chen, and G. Groeseneken, "ESD in FinFET technologies: Past learning and emerging challenges," in *Proc. IEEE Int. Rel. Phys. Symp. (IRPS)*, Apr. 2013, pp. 2B.5.1–2B.5.8.

[3] H. Gossner *et al.*, "Unique ESD failure mechanism in a MuGFET technology," in *IEDM Tech. Dig.*, Dec. 2006, pp. 1–4.

[4] S. H. Chen, G. Hellings, S. Thijs, D. Linten, M. Scholz, and G. Groeseneken, "Exploring ESD challenges in sub-20-nm bulk FinFET CMOS technology nodes," in *Proc. 35th Elect. Overstress/Electrostatic Discharge Symp.*, Sep. 2013, pp. 1–8.

[5] A. Griffoni *et al.*, "Next generation bulk FinFET devices and their benefits for ESD robustness," in *Proc. 31st EOS/ESD Symp.*, Aug. 2009, pp. 1–10.

[6] J. Guan, Y. Wang, S. Hao, Y. Zheng, and X. Jin, "A novel high holding voltage dual-direction SCR with embedded structure for HV ESD protection," *IEEE Electron Device Lett.*, vol. 38, no. 12, pp. 1716–1719, Dec. 2017.

[7] F. A. Altolaguirre and M. D. Ker, "Low-leakage bidirectional SCR with symmetrical trigger circuit for ESD protection in 40-nm CMOS process," *IEEE Trans. Device Mater. Rel.*, vol. 16, no. 4, pp. 549–555, Dec. 2016.

[8] C. Y. Lin, Y. H. Wu, and M. D. Ker, "Low-leakage and low-trigger-voltage SCR device for ESD protection in 28-nm high-k metal gate CMOS process," *IEEE Electron Device Lett.*, vol. 37, no. 11, pp. 1387–1390, Nov. 2016.

[9] D. Alvarez, M. Wendel, and A. Stuffer, "ESD failure caused by parasitic SCR in an overvoltage tolerant I/O," in *Proc. 37th Elect. Overstress/Electrostatic Discharge Symp. (EOS/ESD)*, Sep. 2015, pp. 1–9.

[10] Y. Li, J. Li, and R. Gauthier, "Junction engineering for SOI SCR triggering and performance improvement," in *Proc. 36th Elect. Overstress/Electrostatic Discharge Symp. (EOS/ESD)*, Sep. 2014, pp. 1–8.

[11] Z. Wang, R.-C. Sun, J. J. Liou, and D.-G. Liu, "Optimized pMOS-triggered bidirectional SCR for low-voltage ESD protection applications," *IEEE Trans. Electron Devices*, vol. 61, no. 7, pp. 2588–2594, May 2014.

[12] J. Li, J. Di Sarro, Y. Li, and R. Gauthier, "Investigation of SOI SCR triggering and current sustaining under DC and TLP conditions," in *Proc. 35th Elect. Overstress/Electrostatic Discharge Symp.*, Sep. 2013, pp. 1–6.

[13] V. A. Vashchenko, P. Lindorfer, and P. Hopper, "Implementation of high VT turn-on in low-voltage SCR devices," in *Proc. Elect. Overstress/Electrostatic Discharge Symp.*, Sep. 2005, pp. 1–6.

[14] J. A. Salcedo, J. J. Liou, Z. Liu, and J. E. Vinson, "TCAD methodology for design of SCR devices for electrostatic discharge (ESD) applications," *IEEE Trans. Electron Devices*, vol. 54, no. 4, pp. 822–832, Apr. 2007.

[15] Z. Liu, J. J. Liou, and J. Vinson, "Novel silicon-controlled rectifier (SCR) for high-voltage electrostatic discharge (ESD) applications," *IEEE Electron Device Lett.*, vol. 29, no. 7, pp. 753–755, Jul. 2008.

[16] A. Amerasekera, V. McNeil, and M. Rodder, "Correlating drain junction scaling, salicide thickness, and lateral NPN behavior, with the ESD/EOS performance of a 0.25 μm CMOS process," in *IEDM Tech. Dig.*, Dec. 1996, pp. 893–896.

[17] M. Paul, B. S. Kumar, C. Russ, H. Gossner, and M. Shrivastava, "FinFET SCR: Design challenges and novel fin SCR approaches for on-chip ESD protection," in *Proc. 39th Elect. Overstress/Electrostatic Discharge Symp. (EOS/ESD)*, Sep. 2017, pp. 1–6.

[18] T. H. Chang, Y. Y. Hsu, T. C. Tsai, J. C. Tseng, J. W. Lee, and M. H. Song, "High-k metal gate-bounded silicon controlled rectifier for ESD protection," in *Proc. Elect. Overstress/Electrostatic Discharge Symp.*, Sep. 2012, pp. 1–7.

[19] M.-D. Ker and K. C. Hsu, "Overview of on-chip electrostatic discharge protection design with SCR-based devices in CMOS integrated circuits," *IEEE Trans. Device Mater. Rel.*, vol. 5, no. 2, pp. 235–249, Jun. 2005.

[20] K. Esmark *et al.*, "Transient behavior of SCRS during ESD pulses," in *Proc. IEEE Int. Rel. Phys. Symp.*, Apr. 2008, pp. 247–253.

[21] J. Di Sarro, K. Chatty, R. Gauthier, and E. Rosenbaum, "Study of design factors affecting turn-on time of silicon controlled rectifiers (SCRS) in 90 and 65 nm bulk CMOS technologies," in *Proc. IEEE Int. Rel. Phys. Symp.*, Mar. 2006, pp. 163–168.

[22] Z. Wang and J. J. Liou, "Evaluation of geometry layout and metal pattern to optimize ESD performance of silicon controlled rectifier (SCR)," in *Proc. IEEE Int. Rel. Phys. Symp.*, Jun. 2014, pp. EL.2.1–EL.2.4.

[23] R. Mertens and E. Rosenbaum, "Separating SCR and trigger circuit related overshoot in SCR-based ESD protection circuits," in *Proc. EOS/ESD Symp.*, Sep. 2013, pp. 1–8.

[24] Y. C. Huang and M. D. Ker, "A latchup-immune and robust SCR device for ESD protection in 0.25 μm 5-V CMOS process," *IEEE Electron Device Lett.*, vol. 34, no. 5, pp. 674–676, May 2013.

[25] J. Li, J. Di Sarro, and R. Gauthier, "Design and optimization of SCR devices for on-chip ESD protection in advanced SOI CMOS technologies," in *Proc. Elect. Overstress/Electrostatic Discharge Symp.*, Sep. 2012, pp. 1–7.

[26] C. T. Wang, T. H. Tang, and K. C. Su, "Latch-up free ESD protection design with SCR structure in advanced CMOS technology," in *Proc. IEEE Int. Rel. Phys. Symp. (IRPS)*, Apr. 2011, pp. 4C.3.1–4C.3.4.

[27] O. Marichal, G. Wybo, B. V. Camp, P. Vanysacker, and B. Keppens, "SCR based ESD protection in nanometer SOI technologies," in *Proc. Elect. Overstress/Electrostatic Discharge Symp.*, Sep. 2005, pp. 1–8.

[28] C. T. Dai *et al.*, "Latchup in bulk FinFET technology," in *Proc. IEEE Int. Rel. Phys. Symp. (IRPS)*, Apr. 2017, pp. EL-1.1–EL-1.3.

[29] L. W. Chu, Y. F. Chang, Y. T. Su, K. J. Chen, M. H. Song, and J. W. Lee, "FinFET SCR structure optimization for high-speed serial links ESD protection," in *Proc. IEEE Int. Rel. Phys. Symp. (IRPS)*, Apr. 2016, pp. 6A-1-1–6A-1-6.

[30] *TCAD Sentaurus Device User's Manual*, Synopsys, Mountain View, CA, USA, 2016.

[31] S. Natarajan *et al.*, "A 14 nm logic technology featuring 2nd-generation FinFET, air-gapped interconnects, self-aligned double patterning and a 0.0588 μm^2 SRAM cell size," in *IEDM Tech. Dig.*, Dec. 2014, pp. 3.7.1–3.7.3.

[32] M. Paul, B. S. Kumar, H. Gossner, and M. Shrivastava, "Contact and junction engineering in bulk FinFET technology for improved ESD/latch-up performance with design trade-offs and its implications on hot carrier reliability," in *Proc. IEEE Int. Rel. Phys. Symp. (IRPS)*, Mar. 2018, pp. 3E.3-1–3E.3-6.

[33] M. Shrivastava *et al.*, "Toward system on chip (SoC) development using FinFET technology: Challenges, solutions, process co-development & optimization guidelines," *IEEE Trans. Electron Devices*, vol. 58, no. 6, pp. 1597–1607, Jun. 2011.

[34] M. Shrivastava *et al.*, "Physical insight toward heat transport and an improved electrothermal modeling framework for FinFET architectures," *IEEE Trans. Electron Devices*, vol. 59, no. 5, pp. 1353–1363, May 2012.

[35] M. Shrivastava *et al.*, "On the thermal failure in nanoscale devices: Insight towards heat transport including critical BEOL and design guidelines for robust thermal management & EOS/ESD reliability," in *Proc. IEEE Int. Rel. Phys. Symp. (IRPS)*, Apr. 2011, pp. 3F.3.1–3F.3.5.

This article has been accepted for inclusion in a future issue of this journal. Content is final as presented, with the exception of pagination.

Milova Paul (S'18) received the M.Tech. degree from Delhi Technological University, Delhi, India, in 2014. She is currently pursuing the Ph.D. degree in electronic engineering with the Indian Institute of Science, Bangalore, India.

She is currently with the Advanced Nano-electronic Devices and Circuits Research Group, Indian Institute of Science. Her current research interests include the ESD/HCI exploration of advanced CMOS and FinFET technologies.

B. Sampath Kumar received the M.Tech. degree from the Visvesvaraya National Institute of Technology, Nagpur, India, in 2013. He is currently pursuing the Ph.D. degree in electronic engineering with the Indian Institute of Science, Bangalore, India.

He is currently with the Advanced Nano-electronic Devices and Circuits Research Group, Indian Institute of Science.

Christian Russ received the M.S. and Ph.D. degrees in electrical engineering from the Technical University of Munich, Munich, Germany, in 1991 and 1999, respectively.

Since 2017, he has been with Infineon Technologies AG, Neubiberg, Germany, as a Principal Engineer, for ESD solutions in automotive sensor technologies. He has published over 75 conference and journal publications and holds over 70 patents in his field.

Harald Gossner (M'07–SM'11) received the Diploma degree in physics from the Ludwig Maximilian University of Munich, Munich, Germany, in 1990, and the Ph.D. degree in electrical engineering from Bundeswehr University Munich, Neubiberg, Germany, in 1995.

He is currently a Senior Principal Engineer with Intel Deutschland GmbH, Neubiberg. He has authored and co-authored over 130 technical papers and two books in the field of ESD and device physics.

Mayank Shrivastava (S'09–M'10–SM'16) received the Ph.D. degree from IIT Bombay, Mumbai, India.

He held positions at Infineon Technologies, Munich, Germany, Infineon Technologies, East Fishkill, NY, USA, IBM Microelectronics, Burlington, VT, USA, Intel Mobile Communications, Hopewell Junction, NY, USA, and Intel Mobile Communications GmbH, Munich, from 2010 to 2013. He joined the Indian Institute of Science, Bengaluru, India, in 2013, as a Faculty Member.

Wireless Networks
https://doi.org/10.1007/s11276-018-1834-9

Corona based node distribution scheme targeting energy balancing in wireless sensor networks for the sensors having limited sensing range

Richa Mishra[1] · Vivekanand Jha[2] · Rajeev K. Tripathi[1] · Ajay K. Sharma[1]

© Springer Science+Business Media, LLC, part of Springer Nature 2018

Abstract
Wireless sensor networks are equipped with sensor nodes having limited battery as energy source. These sensor nodes have to maintain the desirable coverage of the network to ensure the periodical communication of the sensed data to the base station. Therefore, lifetime of sensor nodes and the energy efficient network coverage are the two major issues that needs to be addressed. Effective placement of wireless sensor nodes is of paramount importance as the lifetime of the network depends upon it. In this work, a corona based energy balanced node deployment scheme for sensors with a limited sensing range is proposed in which the nodes are distributed in accordance with a probability density function (PDF). Optimal number of nodes in each corona is determined using the proposed PDF. Performance of the scheme is evaluated in terms of coverage, energy balance and network lifetime through simulation. The intrinsic characteristic of the proposed PDF has been derived. It is noticed that the node distribution through the proposed scheme not only provides better coverage in each layer but also minimizes both the energy-hole and the coverage-hole problems in the deployment field while maintaining longevity of the sensor network.

Keywords Wireless sensor network · Probability density function · Cumulative density function

1 Introduction

Wireless sensor networks (WSNs) are self-organizing, large-scale networks that are a wireless association of large number of tiny sensor nodes (SNs). These SNs have low battery power, limited storage capacity and low processing speed. These WSNs are being applied in numerous applications such as health monitoring [1], surveillance [2], temperature monitoring [3], forest [4, 5], battlefield [6], earthquake monitoring [7] and many others. In these applications, the SNs are deployed to operate independently in unattended/attended environments. These SNs sense the data from the surrounding areas and communicate the sensed data to the base station (BS) through multi-hop or single-hop transmission. In WSNs, energy conservation of each node is of utmost importance and also a major challenge. Therefore, the battery of these nodes should be used intelligently to prolong the life of the WSN.

The position of SNs have tremendous impact on the performance of the WSNs. The choice of the node deployment scheme depends upon the metrics such as connectivity of the network [8], full area coverage [9] and remains unchanged throughout the lifetime of the network. A significant problem receiving large consideration recently is the coverage along with connectivity problem [8]. This emphasizes on how effectively the wireless sensors monitor the physical surroundings and also communicate the sensed data to the BS. The area covered by a sensor node is known as its sensing area. When two SNs lie

✉ Richa Mishra
richas.phoenix@gmail.com

Vivekanand Jha
vivekanandjha@igdtuw.ac.in

Rajeev K. Tripathi
rajivtripathi@nitdelhi.ac.in

Ajay K. Sharma
sharmaajayk@nitj.ac.in

[1] National Institute of Technology, Delhi, India

[2] Indira Gandhi Delhi Technical University for Women, Delhi, India

Published online: 12 September 2018

within the transmission range of each other and can communicate, it can be said that the two nodes are connected. The sensing and communication domain of a SNs are closely related [10]. Therefore, these two parameters are essentially considered in the deployment of SNs in the WSN. Each sensor node dessipates energy in sensing and communicating the data to the BS. Therefore, energy is the most important constraint in WSN. Deployment of SNs and location of the BS has a vital role in increasing the life of the WSN [11, 12]. It is well proven in the literature [13] that multi-hop communication is more energy efficient in terms of lifetime [14, 15] of the network as compared to direct communication. In the case of multi-hop communication the energy depletion rate of nodes placed near the BS is higher as compared to the distant nodes. Energy-hole [16] can be created if the nodes near the BS die out early as compared to the distant nodes. Many researches have been carried out in this area and non-uniform node deployment [12, 16, 17] is considered to be the best strategy to eliminate energy-hole issue. In this type of node deployment maximum numbers of nodes are placed towards the BS and decreases as the distance from the BS increases. These deployed nodes can handle the traffic flow and avoid the energy-hole in WSNs.

In this paper, a non-uniform corona based energy balanced node distribution (ND) scheme is proposed that contributes to better coverage and an energy-efficient communication even when SNs are limited in sensing range[3].

The paper is organized as follows: Sect. 2 discusses the existing literature survey regarding various node deployment schemes. The problem is described in Sect. 3. The energy model is discussed in Sect. 4. Section 5 presents the description of the proposed scheme. Section 6 discusses the EEAGTACO [18] protocol. In Sect. 7, the performance of the proposed scheme is evaluated quantitatively and qualitatively. Finally, Sect. 8 concludes the work done in this paper.

2 Related work

Conserving energy has been fundamental issue in WSNs. Many research have been reported in order to avoid energy-hole problem and maximizing the network lifetime in WSNs. Isabel and Falco in their work [14] discuss about the lifetime of WSN in detail. Here, the authors present the lifetime as a measure of the number of alive nodes, coverage, connectivity, both the connectivity and the coverage and many others. Various parameters that affects the lifetime of WSN are also discussed in their work.

Amini et al. [19] propose a DBS protocol that divides the area into equal sized segments. Different clustering mechanism were applied to each area in order to reduce the energy consumption by SNs, thereby, increasing the lifetime of the network. Yetgin et al. [15] discuss various techniques that maximizes the lifetime of the network. They are namely: optimal node deployment, routing, data co-relation and many others. We propose a corona based node deployment scheme that not only balances the energy across the network but also provides better coverage and connectivity in WSN thereby maximizes the network lifetime. Hence, the literature is surveyed regarding deployment schemes, network connectivity and coverage in WSN. Rahman et al. [20] classify the deployment scheme into two: non-corona and corona based strategies. The non corona based strategies are distinguished into random Gaussian and random uniform. Here, random means the nodes are dropped by helicopter and uniform means that the nodes density is uniform across the network in deployment field. The authors in [21] use random deployment strategy to deploy SNs. Additional SNs were deployed to achieve maximum coverage. The drawback is the decreased lifetime due to unbalanced energy consumption in the network. In [22], the authors present a mathematical calculation based on which the number of nodes in each corona is placed. Hence, the density of the nodes is decided based on the communication range of each sensor. This approach creates an energy-hole problem in the innermost corona. Similarly, in [23, 24] the authors propose the node deployment scheme with the objective to achieve full coverage with minimum number of SNs. In [25], the authors propose a node deployment scheme that uses the minimum number of nodes and provides full coverage of the network field. However, such an approach cannot be realized in some application such as battle field and habitat monitoring. Halder et al. in their work [26] propose a PDF that derives its intrinsic characteristic such as CDF, expectation and covariance. The authors divide the square region into number of concentric circles. SNs are deployed in accordance with the proposed PDF and is randomly distributed within each annuli. Also, in the considered architecture the number of nodes had decreased as the area had increased.

The work PDFND [27] is an extension of [26]. Here, the questions such as how many number of nodes should be deployed per unit area to accomplish balanced energy consumption in WSN to enhance network lifetime has been answered. Performance has been evaluated by qualitative and quantitative techniques. In [28] the authors demonstrated that the node distribution through Gaussian distribution (GD) was not energy balanced. Further, the authors identified standard deviation as most important parameter for energy balancing. Finally, a node deployment strategy is proposed using customized GD scheme. The authors prove that for a given network, balanced energy

consumption across WSN takes place when SNs are distributed through the customized GD. In this architecture the area of each annulus keeps on increasing and the number of nodes keeps decreasing.

Bhardwaj et al. in their work [29], observed that single-hop transmission to BS consumes more energy compared to multi-hop transmission mechanism. Here, the authors have proposed the optimal size of hop and derived an upperbound in lifetime. Similar work was reported in [30], where the authors argued that equal sized multi-hop transmission was more efficient compared to direct transmission. However, the authors did not prove that equal-sized multi-hop was an optimal criteria. In [31], the network architecture consists of concentric disks with the BS situated at the center. Here, the authors propose a hybrid of single and multi-hop transmissions where the ratio of these two is not equal in a disk. Yuan et al. [13] propose a node distribution scheme to avoid energy-hole problem. Here, the SNs were distributed depending upon the distance from the BS. In this scheme, the energy consumption rate is relatively faster leading to shortening of network lifetime. Chatterjee and Das [9] propose a node distribution strategy to avoid energy-hole in WSN. Here, two types of nodes namely; data originator and data router were considered. Data originators collected the data from the environment and router routes the data to the next hop. This led to increase in network lifetime and reduction in network traffic. Liao et al. [32] proposed a sweep based strategy to balance the energy consumed by the SNs. Liu [33] propose a scheme that adjusts the transmission range of SNs based on inter-nodal distance to maximize WSN lifetime. Ramos et al. [34] introduced the guidelines regarding the node distribution scheme. They showed that the proposed method could increase the network lifetime as well as avoid the energy-hole problem. Ferng et al. [35] in their work, considered a special case in which all the coronas were having uniform width except for the outermost corona.

SNs in WSN may fail to provide the sensed data to BS due to the following reasons namely; depletion of the battery power, poor deployment schemes, physical damage. The failure of the SNs can affect the connectivity amongst the SNs and also to the BS. Our paper provides connectivity among the SNs from one corona to the next intermediate corona. Node failure in any corona may lead to partitioned network due to loss in connectivity in a WSN. Severals researchers have proposed various solution for the recovery from the partitioned network. Younis et al. [36] classify the connectivity restoration into three types. In first, the disjoint partition is connected by replacing the failed nodes by the existing SNs. In second, authors introduce the group of relay nodes to establish the connectivity in a WSN. In third, large number of SNs are deployed to establish k-connectivity [37] to tolerate node failures in WSN. However, the authors do not discuss about achieving the coverage in WSN. In [38], the authors propose a recovery process by moving the relay nodes towards the BS. The communication is established only when all the relay nodes come within the range of each other in order to establish connectivity. Here, the minimum number of relay nodes is obtained using Steiner tree for the disjoint partitioned network. Similar work has been proposed [8]. Here, the authors propose a different optimization technique to calculate the number of relay nodes needed for the restoration of the connectivity in a WSN. Here, the authors do not discuss about the coverage. In [39], the authors propose coverage-aware connectivity method to restore the connectivity along with the coverage of the network. In this method, if a node fails then one of its neighbor is brought to its position to reassure the connectivity and coverage. Wu et al. [40] propose an energy efficient routing scheme called BRIT for sensor nodes distributed in underground tunnel and compare the performance with AODV using various parameters. In [41], the authors analyze the energy consumption and data relay models for their considered architecture. Using the analysis the authors propose ENS-PD algorithm that uses the optimal energy and also prolongs the life of the network. Jha et al. [42] in their work propose a constant area based network architecture. Here the field was partitioned into a number of coronas with the BS positioned at the center. The number of node distribution was non-uniform i.e., the number of nodes distributed kept decreasing in each corona as one moved away from the center. This node distribution may not provide suitable coverage in limited sensing range nodes.

We aim to extend our work discussed in [18]. In this work an energy efficient protocol based on Game Theoretic approach and Ant Colony Optimization (EEAGTACO) was proposed. Here, coalitions amongst SNs were formed based on the coverage and the degree of co-relation in the sensed data throughout the network. In the afore-said work, only the coalition was optimized while the node distribution scheme was yet to be done. Also it was discussed that the EEAGTACO could be used in real life applications such as monitoring the temperature. In such application, the SNs have limited sensing capabilities. In view of this, we propose a corona based node distribution scheme that balances the uniform energy consumption across the network, provides better coverage and connectivity as well as elongates the lifetime of the network even when the SNs have limited sensing capabilities. The main contributions

of this paper are: (1) The PDF is proposed and designed on the basis of node density that controls network lifetime. (2) The energy balanced node deployment algorithm is developed based on the PDF and (3) The performance of the proposed scheme is analysed qualitatively and quantitatively. In qualitative analysis, the intrinsic parameters of the proposed PDF such as CDF and expectations has been derived. Theoretical analysis of energy balancing in WSN is also presented in this section. In quantitative analysis, we compare the proposed ND strategy with other strategies through simulation to substantiate the performance of the algorithm.

3 Problem description

In the literature review section discussed above, the researchers have considered the corona based network architecture wherein the width of each corona is kept uniform. In this architecture, the deployment area is divided into a number of concentric coronas with the BS situated at the center. The width of each corona is kept constant and it is equal to the radius (R) of the innermost corona. Hence, the area of each corona starting from the BS increases in arithmetic progression with the common difference of $2\pi R^2$. In the past various researchers have focused on the approach to avoid the occurrence of energy-hole and coverage-hole in uniform width corona based network architecture. In order to achieve energy efficient WSN, the nodes are distributed in such a way that the node density is inversely proportional to the area of each corona. To avoid the occurrence of energy-holes in the network a non-uniform node distribution is most commonly applied such that the maximum numbers of SNs are deployed in the innermost corona near the BS and thereafter it decreases towards the outer coronas. This type of ND proves to be useful in avoiding the energy-hole problem in WSN. However, for a particular sensing range the number of SNs required to cover the successive coronas should increase from inner corona to outer corona to avoid occurrence of coverage holes. This is because the area of each corona increases in the uniform width corona based network architecture. Hence for avoiding energy-hole, the node density should decrease from inner to outer coronas whereas for avoiding coverage-holes the node density should increase from inner to outer coronas. One important observation is that, these constraints share an inverse relationship with each other with respect to node density. In all these existing approaches it is common that on one hand node density decreases while on other hand the area of each corona increases. Hence, the amalgamation of both the non-uniform ND and the coronas having uniform width may not provide a suitable choice to avoid both the energy and the coverage hole across the network. Therefore, in this paper we have proposed a ND scheme that considers decreasing width corona based network architecture. In this, when SNs are non-uniformly deployed in decreasing width corona based network architecture, the sensing coverage of the deployed sensor nodes overlap more towards outer coronas as shown in Fig. 1. This brings down the requirements of SNs to be deployed in the outer corona and it also offers better coverage.

The objective of this paper is to propose a non-uniform ND for decreasing width corona based architecture with a constraint of SNs having limited sensing capabilities. An example of SNs having limited sensing capability is well explained in literature [3]. In the proposed varying width corona based network architecture, the deployment area is divided in such a way that the area of each corona decreases as one moves towards the boundary. This type of network architecture for ND can provide better coverage, avoid the occurrence of energy-hole and also balance the energy consumption across the network. Limited sensing range is shown in Fig. 2. Here, R_s and R_c are the sensing and communication range of a SN respectively and S_1 and S_2 are two SNs overlapping an area P_0. Sensing range is the area sensed by a SN and communication range is the transmission range of a SN.

4 Energy model

The first order radio model similar to [43] has been used in this work. The first energy model consists of a transmitter and a receiver. Here, two kinds of signal loss are used namely; multipath and free space signal loss. When the distance d between the transmitter and the receiver is greater then the threshold d_0, multipath (mp) signal loss is used while if the distance d between the transmitter and the receptor is less then the threshold d_0 free space (fs) signal loss is used. The threshold d_0 is given by

$$d_0 = \sqrt{\frac{E_{fs}}{E_{mp}}} \tag{1}$$

The multipath and free space signal loss is given by

$$E_{amp} = \begin{cases} E_{fs}.d^2, & \text{if } \mathrm{d} < \mathrm{d}_0 \\ E_{mp}.d^4, & \text{if } \mathrm{d} \geq \mathrm{d}_0 \end{cases} \tag{2}$$

Here, E_{amp}, E_{fs} and E_{mp} are the energy used in transmission of fs or mp signal loss, energy consumed in fs signal loss and energy consumed in mp loss respectively. The energy used in transmitting k-bit of data at a distance d is given by

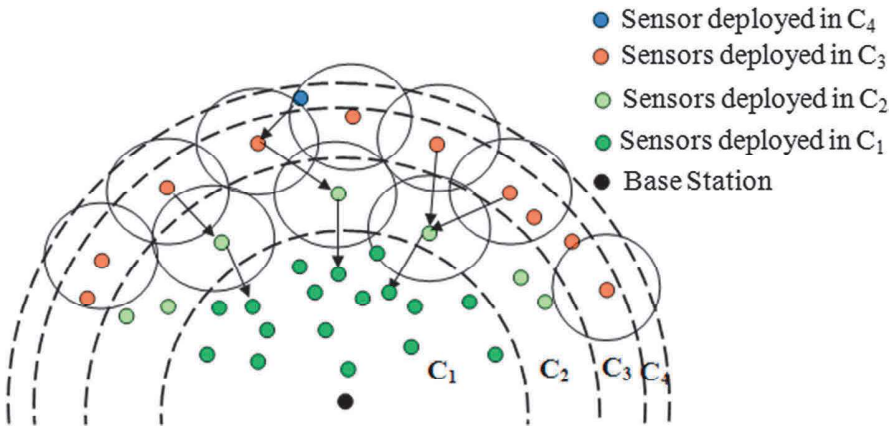


Fig. 1 Sensing overlap in decreasing width network architecture

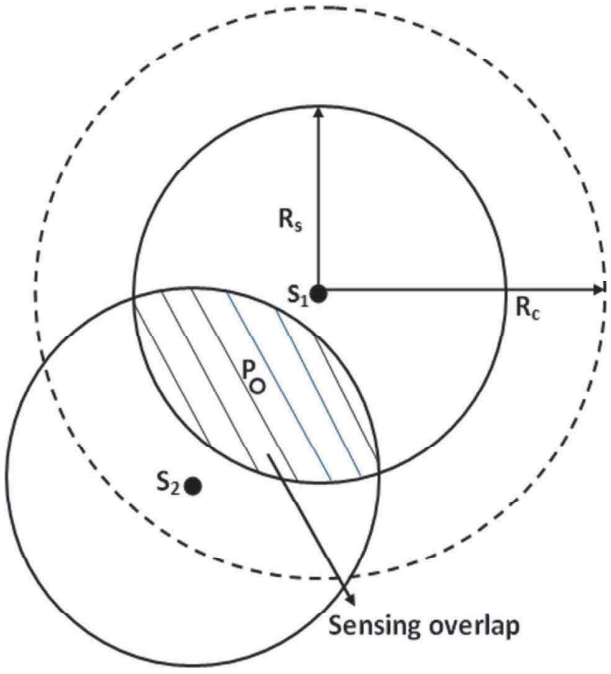


Fig. 2 Communication range greater then sensing range

$$E_{tx}(k,d) = E_{tx_{elec}}(k) + E_{tx_{amp}}(k,d) \tag{3}$$

Here, E_{tx}, $E_{tx_{elec}}$ and $E_{tx_{amp}}$ are the energy consumed during transmission of k bits at a distance d, energy consumed by circuitry and the energy consumed in amplification of k-bit data at a distance d. Using Eqs. (2) and (3), the overall energy used up in transmission is given as

$$E_{tx}(k,d) = \begin{cases} kE_{tx_{elec}} + kE_{fs}d^2, & \text{if } d < d_0 \\ kE_{tx_{elec}} + kE_{mp}d^4, & \text{if } d \geq d_0 \end{cases} \tag{4}$$

Energy consumed in receiving k-bit data is given by

$$E_{rx}(k) = E_{rx_{elec}}(k) = kE_{elec} \tag{5}$$

Here, E_{elec} is the energy required in receiving one-bit data.

5 Proposed solution

The paper proposes a PDF that disseminates sensors with varying densities in the considered deployment/network field to effectively address the problem described in Sect. 3. The deployment field considered is as shown in Fig. 3(a) with the BS situated at the center. The deployment field is divided into a number of concentric circles (NConC). In this division, the innermost corona has the largest area and it decreases in the successive coronas of the deployment field. This kind of division [44] aims to provide better coverage in the network as the maximum number of SNs are deployed in the largest area. Node distribution scheme is proposed based on the designed PDF. Finally, the SNs are disseminated through the proposed node deployment algorithm that distributes the SNs non-uniformly in each corona with the objective of better coverage and elimination of energy-hole thereby, prolonging the life of the network.

5.1 The network model

Considered deployment field is assumed to be square shaped having an area of $M \times M$ units square with BS positioned towards the center of the field as shown in Fig. 3(a). The network field is divided into for equal sized triangles namely; ΔAOB, ΔAOD, ΔBOC and ΔCOD. Initially, the centroid of any triangle can be used in determining the radius of the first corona (C_1). Next, considering C_1 (the centroid of ΔAOB as the new vertex, new ΔAC_1B is formed whose centroid C_2 determines the radius of the next consecutive circle. Same procedure is repeated and the radius of corresponding circles is determined as $R_1, R_2, R_3, \ldots, R_L$ as shown in Fig. 3(a).

The radius of each annulus and the number of layers the network should be divided is discussed in detail in [44] and are given as follows:

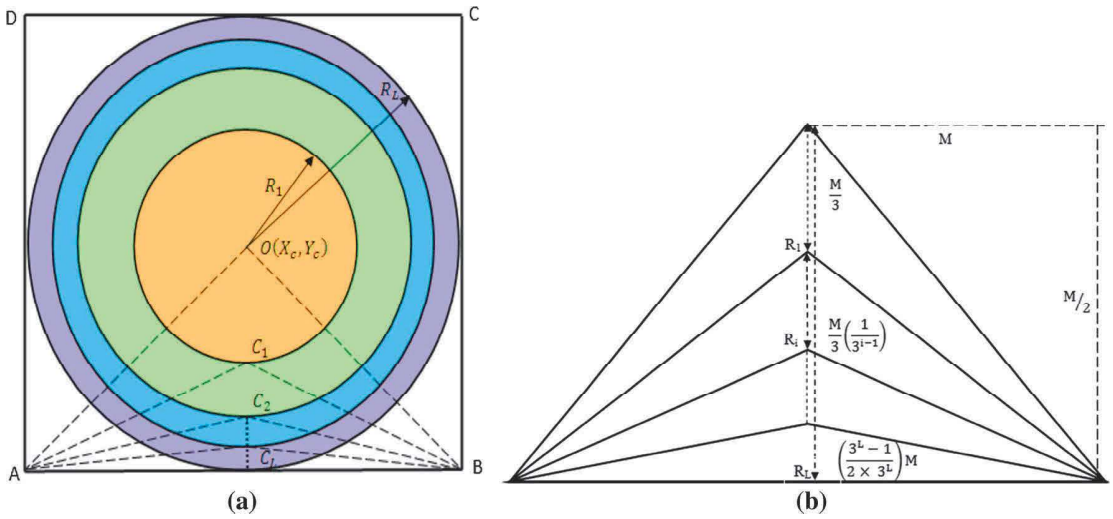


Fig. 3 Network architecture. **a** Proposed network architecture. **b** Successive radii creation

Using the geometrical properties, the distance of ith centroid from the center O is calculated as given by

$$R_i = \frac{(3^i - 1)}{2.3^i} M \tag{6}$$

where M and R_i are the length of the side and the radius of the ith concentric circle respectively. Therefore, the total area covered by the ith circle is given as

$$A_i = \pi\left(R_i^2 - R_{i-1}^2\right) = \left(\frac{3^i - 2}{3^{2i}}\right)\pi M^2 \tag{7}$$

The detailed description of the division of the deployment field is shown in Fig. 3(b). Here, the number of regions/layers (L) depends on the sensing range (R_s) of a node and the side (M) of the field. Two SNs are known to be redundant [45] if they sense the same area by more then 50% of their total sensing area. Also the two SNs are placed at their optimal positions if their sensing boundaries touch each other. The aforesaid conditions for redundancy (the area covered by two SNs overlap) and optimal placement of SNs are used to find the number of layers in the network. Let the euclidean distance between any two SNs be represented by $|S_1 - S_2|$ then, the situation to bypass the redundancy between these SNs can be expressed by $\frac{R_s}{2} \leq |S_1 - S_2|$. The condition for the optimally placement of SNs can be expressed as $|S_1 - S_2| \leq 2R_s$. Therefore, the placement of the SNs can be expressed by $\frac{R_s}{2} \leq |S_1 - S_2| \leq 2 \times R_s$. Assuming the position of the two SNs are located in adjacent centroid then the above relation can be given as $\frac{R_s}{2} \leq (R_L - R_{L-1}) \leq 2 \times R_s$. Hence according to the principle of optimality the equation can be rewritten and is given by,

$$\frac{3^L}{2} \leq \frac{M}{R_s} < 2 \times 3^L \tag{8}$$

The sensing range of a node is used only to restrict any further divisions of the network.

5.2 Analysis of network lifetime

In EEAGTACO [18] protocol as discussed in Sect. 6, all the nodes form singleton coalition, given the quality service specification (QSS) parameter as $q = 1$. Here singleton coalition refers to coalition having single SN. Therefore in worst case the number of the representative SNs is the same as the total number of SNs distributed in the network. Hence, the analysis has been done on the total number of SNs which is the same as the number of representative SNs in the network and is as discussed below:

Mathematically the lifetime [14, 15] of the ith node can be defined as the ratio of the initial energy of the ith node to its energy consumption rate and is given by

$$LT_i = \frac{E_o}{ECR_i} \tag{9}$$

Here, E_o and ECR_i are the initial energy and energy consumption rate of ith node in the network respectively. Similarly lifetime of jth layer can be obtained by

$$LT_j = \frac{E_o \times T_j}{ECR_j \times T_j} \tag{10}$$

Here, T_j is total number of SNs in jth layer. Therefore, from Eq. (10), it can be said that the lifetime of one layer is same as the lifetime of one node.

Definition 1 Network lifetime is defined as the duration from the beginning of the network till all the SNs in any

corona die out such that an energy-hole is created in the network.

Definition 2 Node density [46] is defined as the ratio of the number of SNs distributed in a corona and the area of that corona.

Data transmission rate (*DTR*) of the *i*th node in the *j*th layer can be defined as the ratio of the data generated in the *i*th layer to the node density in that layer and is mathematically given by

$$DTR_j = \frac{\alpha \times A_j}{\gamma_j \times A_j} = \frac{\alpha}{\gamma_j} \tag{11}$$

Here, α, A_j and γ_j are the data generation rate of a node, area and node density of the *j*th layer respectively. Since the SNs in the *j*th layer transmit their own data along with the data received from $(j+1)$th layer to the BS or to the next consecutive layer towards the BS, the average DTR of $(j+1)$th layer towards a node in the *j*th layer is given by

$$DTR_{avg} = \frac{\alpha \gamma_{j+1} A_{j+1}}{\gamma_j A_j} \tag{12}$$

Here, DTR_{avg}, γ_{j+1} and A_{j+1} are the average DTR, the node density and the area of $(j+1)$th layer respectively.

The node from a layer forward data to the next consecutive layer nearing sink using greedy routing policy [47]. We assume Q-switch [16] routing to forward the data from the outer layer to its inner consecutive layer.

The average data transmission rate of $(j+1)$th layer is similar to as given in Eq. (12) and is given as $DTR_{j+1} = \frac{\alpha \gamma_{j+1} A_{j+1}}{\gamma_j A_j}$. Therefore, the total data forwarded by a node in the *j*th layer is the sum of the average data transmitted by all the consecutive layers farther away and can be written as

$$DTR_{Total} = \frac{\alpha \sum_{h=j+1}^{L} \gamma_h A_h}{\gamma_j A_j} \tag{13}$$

Here, L, DTR_{Total} are overall number of layers (NoL), the total data relayed by the outer consecutive layers to its inner successive layer respectively. Using Eqs. (11) and (13), the DTR of each node in the *j*th layer can obtained by,

$$DTR_j = \begin{cases} \frac{\alpha}{\gamma_j} + \frac{\alpha \sum_{h=j+1}^{L} \gamma_h A_h}{\gamma_j A_j}, & \text{for j} = 1, 2, \ldots, (\text{L} - 1) \\ \frac{\alpha}{\gamma_L}, & \text{for j} = \text{L} \end{cases} \tag{14}$$

The first component $\frac{\alpha}{\gamma_j}$ is the SNs' own data to be transmitted and the second component $\frac{\alpha \sum_{h=j+1}^{L} \gamma_h A_h}{\gamma_j A_j}$ is the sum of all the data of the farther consecutive layers to be transmitted to the innermost layer.

The energy required to transmit SNs' own data is given by

$$E_i = \frac{\alpha}{\gamma_j} \times E_{tx} \tag{15}$$

Here, E_i and E_{tx} is the total energy consumed by the *i*th node and the energy needed to transmit one-bit data respectively. Similarly, the energy needed to transmit the total relayed data from the farther consecutive layers is given by

$$E_{relayeddata} = \left[\frac{\alpha \sum_{h=j+1}^{L} \gamma_h A_h}{\gamma_j A_j} \right] \times E_{tx} \tag{16}$$

Here, $E_{relayeddata}$ is the total energy consumed to forward all the data from the outer consecutive layers. The energy consumed by each node in *j*th layer is computed using the Eqs. (15) and (16) and is given by

$$ECR_j^{tx} = \begin{cases} \left[\frac{\alpha}{\gamma_j} + \frac{\alpha \sum_{h=j+1}^{L} \gamma_h A_h}{\gamma_j A_j} \right] \times E_{tx}, & \text{for j} = 1, 2, \ldots, (\text{L} - 1) \\ \frac{\alpha}{\gamma_L} \times E_{tx}, & \text{for j} = \text{L} \end{cases} \tag{17}$$

where ECR_j^{tx} is the energy consumed in transmission by the layer *j*. Similarly, energy consumed in receiving the data from farther consecutive layers is given by

$$ECR_j^{rx} = \left[\frac{\alpha \sum_{h=j+1}^{L} \gamma_h A_h}{\gamma_j A_j} \right] \times E_{rx} \tag{18}$$

Here, E_{rx} is energy used in receiving data per bit. ECR_j^{rx} is the energy consumed in reception of data by the *j*th layer. Total energy consumed by the *i*th node is given by

$$ECR_i = ECR_i^{tx} + ECR_i^{rx} \tag{19}$$

Here, ECR_i^{tx}, ECR_i^{rx} and ECR_i are the energy consumed in transmission, the energy consumed in reception and the total energy consumed by a node i in the layer j respectively. Therefore, the total energy consumed by the SNs in *j*th layer is given by

$$ECR_j = \begin{cases} ECR_j^{tx} + ECR_j^{rx}, & \text{for j} = 1, 2, \ldots, (\text{L} - 1) \\ ECR_L^{tx}, & \text{for j} = \text{L} \end{cases} \tag{20}$$

Energy balancing is a situation in which all the SNs in the network use up their energy around like time. Therefore, in order to obtain an energy balanced network the following condition has to be satisfied.

$$ECR_j = ECR_{j+1} = ECR_{j+2} = \ldots = ECR_{j+L} \tag{21}$$

Substituting Eqs. (17) and (18) for the layer j and $j+1$ in the above equation we get

$$\begin{aligned}\frac{\alpha}{\gamma_j}E_{tx} + \left[\frac{\alpha\sum_{h=j+1}^{L}\gamma_h A_h}{\gamma_j A_j}\right]E_{tx} + E_{rx} \\ = \frac{\alpha}{\gamma_{j+1}}E_{tx} + \left[\frac{\alpha\sum_{h=j+2}^{L}\gamma_h A_h}{\gamma_{j+1}A_{j+1}}\right]E_{tx} + E_{rx}\end{aligned} \tag{22}$$

On simplifying Eq. (22) we get Eq. (23) and is given by

$$\gamma_j = \gamma_{j+1}\frac{\left[\alpha E_{tx} + (E_{tx}+E_{rx})\left(\frac{\alpha\sum_{h=j+1}^{L}\gamma_h A_h}{A_j}\right)\right]}{\left[\alpha E_{tx} + (E_{tx}+E_{rx})\left(\frac{\alpha\sum_{h=j+2}^{L}\gamma_h A_h}{A_{j+1}}\right)\right]} \tag{23}$$

The above equation implies that the ratio of node density depends upon two successive layers and the total number of layers. Node density is more towards the BS and decreases in layers further away from BS i.e., $\gamma_j > \gamma_{j+1} > \gamma_{j+2} > \ldots > \gamma_N$. When the SNs are distributed according to the said equation, it can be assumed that the SNs in the network deplete their energy at the same time. Now, as the lifetime of a node is defined as $\frac{E_o}{ECR_i}$ where E_o is the initial energy of ith node and ECR_i is the energy dissipation rate of the ith node in the network, replacing ECR_i in denominator in Eq. (9), we get

$$LT_j = \frac{E_o}{ECR_j^{tx} + ECR_j^{rx}} \tag{24}$$

Here, LT_j is the network lifetime of jth layer. Using Eqs. (17), (18), (20) and also substituting the value of A_i in the above equation, the lifetime of the network can be calculated as given by Eq. (25).

$$LT_j = \begin{cases} \dfrac{E_o\gamma_j\left(\frac{3^j-2}{3^{2j}}\right)}{\alpha E_{tx}\left(\frac{3^j-2}{3^{2j}}\right) + \psi\sum_{h=j+1}^{L}\alpha\gamma_h\left(\frac{3^h-2}{3^{2h}}\right)}, & \text{for j} = 1,2,\ldots,(\text{L}-1) \\ \dfrac{E_o\gamma_L}{E_{tx}\alpha}, & \text{for j} = \text{L} \end{cases} \tag{25}$$

5.3 Proposed probability density function

The probability density function of a point $P(x, y)$ lying between the annulus $(i-1)$ and i is given by

$$f(x,y;M,R,i) = \frac{\beta\times(3^i-2)}{3^{2i-2}\times i} \;\forall\; {R_{i-1}}^2 < x^2+y^2 \le {R_i}^2 \tag{26}$$

The mathematical domain considered in this paper is similar to [44], is divided into L concentric circles centred at (0, 0), each having radius $R_i = \left(\frac{3^i-1}{2\times 3^i}\right)\times M$ where M and i are the side of the square field, i is the radius of the ith circle and β is a constant which is given by

$$\beta = \frac{1}{i\times\pi\left(\frac{M}{3}\right)^2\sum_{i=1}^{L}\left(\frac{3^i-2}{3^{2i-2}}\right)^2}$$

Theorem 1 *The value of the constant is given by* β

$$\beta = \frac{1}{\pi\times\left(\frac{M}{3}\right)^2\times\left\{1+\frac{1}{2}\left(\frac{7}{9}\right)^2+\cdots+\frac{1}{L^2}\left(\frac{3^L-2}{3^{2L-2}}\right)^2\right\}} \tag{27}$$

Theorem 2 *If two random discrete variables V and U follow a proposed PDF with parameters i and L, then the CDF of V and U is given as*

$$\begin{aligned}F[V\le x, U\le y] = \pi\beta\left(\frac{M}{3}\right)^2\left[\sum_{j=1}^{i}\left[\frac{1}{j}\left(\frac{3^j-2}{3^{2j-2}}\right)^2\right]\right. \\ \left.+\left[\frac{1}{i}\left(\frac{3^\eta-2}{3^{2\eta-2}}\right)^2-\frac{1}{i}\left(\frac{3^i-2}{3^{2i-2}}\right)^2\right]\right]\end{aligned}$$

where (x, y) *such that* $0\le x^2+y^2\le {R_\eta}^2$, *where* $i\le\eta\le i+1$.

Theorem 3 *If two discrete random variables V and U follow the proposed PDF with parameters l and i than the expectation of V and U is given as*

$$E[XY] = \beta 4\left(\frac{M}{3}\right)^2\sum_{i=1}^{L}\left[\frac{81}{4i3^i}+\frac{5103}{2i3^{3i}}-\frac{91}{3^{2i}}\right]$$

The proof of Theorems 1, 2, 3 and also the summary of notations used in this paper is presented in the "Appendix" of the paper.

5.4 PDF based node distribution scheme (PDFNDS)

The proposed PDF is discrete in nature. The objective here is to map the proposed PDF on the layered network architecture as follows: i represents the layer number in both the proposed PDF and layered network field where $i = 1, 2, \ldots, L$. Relationship between the radius of the concentric circle and communication radius is $R_1 \le R_c$. The distribution of the sensor node across the network is non-uniform i.e., the number of SNs distributed are maximum near the BS and keeps decreasing as one moves towards the outer annuli. The SNs can be distributed in any inaccessible geographical area [27] through an unmanned helicopter [48–50] in a controlled manner.

The PDF at any point $P(x, y)$ lying between the annulus $(i-1)$ and i is given as $\frac{\beta(3^i-2)}{3^{2i-2}\times i}$ where $i = 1, 2, \ldots, L$. The probability of the number of SNs deployed within an annulus i is given as $\frac{\beta(3^i-2)}{3^{2i-2}\times i} \times A_i$ where A_i is the area of the ith layer. The area of the ith layer is given as $\pi\left(\frac{M}{3}\right)^2\left(\frac{3^i-2}{3^{2i-2}}\right)$. The value of constant β is given as

$$\beta = \left[\pi \times \left(\frac{M}{3}\right)^2 \times \left\{\sum_{i=1}^{L} \frac{1}{i}\left(\frac{3^i-2}{3^{2i-2}}\right)^2\right\}\right]^{-1}$$

[*as given in Eq.* (27)]

By replacing A_i, the probability (p_i) of deploying SNs at layer i is given as

$$p_i = \frac{\beta\pi}{i}\left(\frac{3^i-2}{3^{2i-2}}\right)^2\left(\frac{M}{3}\right)^2 \qquad [\textit{as given in Equation}\ (47)]$$

The total number of SNs T_i deployed in the ith layer is given by

$$T_i = p_i \times N_{Total} \tag{28}$$

Here, N_{Total} are the total number of SNs in the deployment field. The node deployment algorithm is given in Algorithm 1.

Table 1 Nodes dissemination

Layers (L_i)	L_1	L_2	L_3	L_4
Probability (p_i)	0.74	0.226	0.023	0.0023
Node distribution (T_i)	224	68	7	1

the layers away from the BS. This kind of deployment is expected to achieve balanced energy consumption, better degree of coverage with each node having limited sensing range thereby, eliminating coverage hole along with the energy efficient node deployment scheme.

6 Node distribution through PDFNDS in EEAGTACO protocol

Implementation of energy efficient approach using game theory and ant colony optimization (EEAGTACO) consists of following phases:

6.1 Node deployment phase

In this phase, the area of the deployment field is divided into coronas as discussed in Sect. 5. The SNs are then distributed in each corona through PDFNDS scheme as discussed in Algorithm 1.

Algorithm 1 Node Deployment

Input : Area $M \times M$, Center (X_c, Y_c), Sensing Radius (R_s), Total number of SNs (N_{Total}), Sensing radius R_s
Output :Nodes to be disseminated in each corona
Calculate L from the Equation (8);
for $i = 1$ to L **do**
  Calculate β using Equation (27);
  Calculate p_i from the Equation (49);
  Calculate T_i using Equation (28);
end for

Example Consider a network dimension/area as 100×100 units with $N_{Total} = 250$ and the sensing radius as $R_s = 5$ units is deployed using the proposed node density function based node deployment scheme. The maximum number of layers 'L' as obtained using Eq. (8) and 'β' is obtained using Eq. (27) are 4 and 0.00021435 respectively. The probability of the number of SNs deployed in first layer is obtained by replacing i, β, M by 1, 0.00021435 and 250 respectively in Eq. (28). Similarly the probability of the number of SNs to be distributed in the other layers is calculated. The probability of the total number of SNs distributed in the 4-layered network is presented in Table 1. It is observed that the node is distributed according to the designed PDF. As per the design of the PDF, more number of SNs are distributed towards the BS and it decreases in

6.2 Initialization phase

In this phase, the parameters of the SNs such as communication range (R_c), initial energy (E_0), pheromone evaporation rate (ρ), pheromone density of the SNs, negotiation constant (λ), Quality of Service Specification (QSS) (q) and total number of SNs (N_{Total}) are initialized.

6.3 Coalition formation phase

In this phase, coalitions are formed within each corona. All the SNs participate in the formation of coalition. The

coalition initially starts with the formation of singleton coalition. Every node is singleton coalition and declare its partial solution. Singleton coalition is denoted as $s(b, rep)$. Here b is coalition having w SNs in it and rep is the representative node of the coalition. Representative node is the node that communicates with the representative of its sucessive corona on the behalf of its coalition. All the neighbours of the partial coalitions are discovered and stored for further computation. The size of coalition is extended using ant colony optimization (ACO) [51, 52] technique. All the edges in $s \in \{S\}$, where S is the set of coalitions are identified i.e., $e \in \{E\}$ where E is set all the edge. Now, each edge is chosen probabilistically using the equation given by

$$P(e) = \frac{\tau(e).\eta}{\sum_{Available\ Edges} \tau(e).\eta} \tag{29}$$

Here, η is inversely dependent on the distance between the two SNs and τ is evaporation rate of the pheromone. Ant packet is now sent to every $e \in \{E\}$ to discover its next hop neighbour. A negotiation operation is performed between a single node belonging to a coalition $S(b, rep_j)$ and its next hop neighbour $(S(k, rep_j))$. Negotiation operation is performed using utility function computed by

$$U(e_k, b_i) = (|\bar{\sigma} - \sigma|) - \bar{o}.f(d(b_i, e_k), q) \tag{30}$$

Here, σ, $\bar{\sigma}$ and $\bar{o}$ is the standard deviation of the energies of the coalition, the standard deviation calculated after the neighbour node b is added to the coalition and the offset respectively. The $\bar{o}$ is directly proportional to the average residual energy and is calculated by

$$\bar{o} = \lambda * average(E_{Res}) \tag{31}$$

Here, λ is a negotiation constant. The utility function manages two factors; the first component $(|\bar{\sigma} - \sigma|) - \bar{o}$ adds SNs with diverse level of residual energies and the second component $f(d(b_i, e_k), q)$ governs the size of coalition. Here, q is QSS and is defined by the user such as $q = 0.7$ (70% data accuracy). In case of 100 % accurate data i.e., when $q = 1$, all the SNs are singleton coalition. Let X_i and X_c be the data reported by two SNs say, b_i and b_j, then the dissimilarity metric [53] $d(b_i, e_k)$ is given by

$$d(b_i, e_k) = |\frac{X_i - X_c}{X_c}| \tag{32}$$

Here, $d(b_i, e_k)$ reports the data measured between node b_i and the node which initially started the formation of coalition, let it be denoted by b_c. Accuracy function q is defined by QSS. The data sensed by the SNs using the dissimilarity function should satisfy the Eq. (32). The accuracy function is also called q rule [53] and is given by

$$f(d(b_i, e_k, q) = \begin{cases} 1 - d(b_i, e_k), & d(b_i, e_k) \leq 1 - q \\ -1, & d(b_i, e_k) > 1 - q \end{cases} \tag{33}$$

The value $U(e_k, b_i)$ should be greater then zero i.e., $U(e_k, b_i) > 0$ for the negotiation to be successful. If the negotiation is successful than the ants mark it with pheromone. The pheromone density is computed by

$$\tau_\phi(b_i, e_k) = 1 - \frac{\rho}{e^\iota} * \tau_\phi \tag{34}$$

Here, $\tau_\phi(b_i, e_k)$, ρ, ι and τ_ϕ is the pheromone value associated with the edge joining the edge node e to the neighbour node b, the evaporation rate, the transmission delay of the packet, and the initial pheromone value respectively. Once all the neighbours are discovered, the partial solution is now ready for an optimization phase.

Optimization phase The partial solution and the pheromone deposited (obtained by previous phase) serve as an input to this phase. In this phase, an overall quantity of the pheromone deposited in each coalition is computed. If the pheromone deposited in a coalition is greater then an average value of the pheromone then such a node is selected and added to the optimized coalition. Once a node is part of any optimized coalition it cannot be part of any other optimized coalition.

Association phase In this phase, one node with the highest residual energy from each optimized coalition is elected as a representative node. The representative node from the outer corona sends data to the representative node of its successive inner corona and so on till the message is transmitted to the BS.

7 Results

In this section, the performance analysis of the proposed node deployment scheme is analysed using qualitative and quantitative techniques. Both the qualitative and quantitative analysis is presented here.

7.1 Qualitative analysis

In this sub-section, the theoretic analysis of the balanced energy consumption across the network is evaluated.

7.1.1 Energy balancing

The energy balancing aims to balance the energy consumption of each layer so that the network lifetime of each layer can be maximized. In WSN, the energy balancing is achieved when all the SNs end up their energy at the same time. Similarly, in layered architecture, the energy

balancing is achieved when all SNs in all the layers exhaust their energy at the same time. Nodes deployed in the farthest layer transmit their data to the next consecutive layer towards the BS.

The energy required to transmit the data using Eq. (35) is given as

$$E_{tx}(k,d) = E_{tx_{elec}}\, k + k\, E_{tx_{amp}}(R_c^2) \tag{35}$$

The above equation can be rewritten as

$$E_{tx}(k,d) = k\, E_{Tx} \tag{36}$$

Here, $E_{tx} = E_{tx_{elec}}\, k + k\, E_{tx_{amp}}(R_c^2)$. Similarly, energy required to receive k-bit data is given by

$$E_{rx}(k) = k\, E_{rx_{elec}} = kE_{rx} \tag{37}$$

Here, $E_{rx} = E_{rx_{elec}}$. Energy consumed by the last layer in transmitting its data is given by

$$ECR_L = E_{tx} \times \alpha \times A_L \tag{38}$$

Here, $\alpha \times A_L$ is data to be transmitted by layer L. Rest of the layers transmit their own sensed data and received data from their outer layers. Therefore, energy consumed by layers other than the outer layer is given by

$$ECR_j = E_{tx} \times \alpha \times A_j + \left[(E_{tx} + E_{rx}) \sum_{j=i+1}^{L} (\alpha \times A_j)\right] \tag{39}$$

To achieve the condition for energy balancing the following condition must be satisfied.

$$\frac{T_1 \times E_o}{ECR_1} = \frac{T_2 \times E_o}{ECR_2} = \cdots = \frac{T_i \times E_o}{ECR_i} \tag{40}$$

Here, T_1 and E_o are the number of SNs in the innermost layer and the initial energy of the SNs respectively. From the above Equation, the condition for the balance energy is given as

$$\frac{ECR_i}{T_i} = \frac{ECR_{i+1}}{T_{i+1}} \tag{41}$$

Using Eqs. (39) and (41), we get

$$\frac{T_i}{T_{i+1}} = \frac{E_{tx} \times \alpha \times A_i + \left[(E_{tx} + E_{rx}) \sum_{j=i}^{L} (\alpha \times A_j)\right]}{E_{tx} \times \alpha \times A_{i+1} + \left[(E_{tx} + E_{rx}) \sum_{j=i+1}^{L} (\alpha \times A_j)\right]} \tag{42}$$

Substituting A_i by $\left(\frac{3^i-2}{3^{2i}}\right)\pi M^2$ and by dropping α, we get

$$\frac{T_i}{T_{i+1}} = \frac{E_{tx} \times \alpha \times \left(\frac{3^i-2}{3^{2i}}\right)\pi M^2 + \left[(E_{tx} + E_{rx}) \sum_{j=i}^{L} \left(\alpha \times \left(\frac{3^j-2}{3^{2j}}\right)\pi M^2\right)\right]}{E_{tx} \times \alpha \times \left(\frac{3^{i+1}-2}{3^{2i+2}}\right)\pi M^2 + \left[(E_{tx} + E_{rx}) \sum_{j=i+1}^{L} \left(\alpha \times \left(\frac{3^j-2}{3^{2j}}\right)\pi M^2\right)\right]} \tag{43}$$

Simplifying the above equation, we obtain

$$\frac{T_i}{T_{i+1}} = \frac{E_{tx} \times \left(\frac{3^i-2}{3^{2i}}\right) + \left[(E_{tx} + E_{rx}) \sum_{j=i}^{L} \left(\frac{3^j-2}{3^{2j}}\right)\right]}{E_{tx} \times \left(\frac{3^{i+1}-2}{3^{2i+2}}\right) + \left[(E_{tx} + E_{rx}) \sum_{j=i+1}^{L} \left(\frac{3^j-2}{3^{2j}}\right)\right]} \tag{44}$$

By using the proposed PDF discussed in Sect. 5, the LHS of the above expression can be written as

$$\frac{T_i}{T_{i+1}} = \frac{(3^i-2)^2 3^{4i+2}(i+1)}{(3^{i+1}-2)^2 3^{4i-2} i} \tag{45}$$

Equating the above Eqs. (44) and (45), we get

$$\frac{E_{tx} \times \left(\frac{3^i-2}{3^{2i}}\right) + \left[(E_{tx} + E_{rx}) \sum_{j=i}^{L} \left(\frac{3^j-2}{3^{2j}}\right)\right]}{E_{tx} \times \left(\frac{3^{i+1}-2}{3^{2i+2}}\right) + \left[(E_{tx} + E_{rx}) \sum_{j=i+1}^{L} \left(\frac{3^j-2}{3^{2j}}\right)\right]} = \frac{(3^i-2)^2 3^{4i+2}(i+1)}{(3^{i+1}-2)^2 3^{4i-2} i} \tag{46}$$

Assuming E_{tx} and E_{rx} as constant in the above equation, we get $LHS \simeq RHS$. Hence, the objective of energy balancing is fulfilled with the proposed node distribution deployed using the proposed scheme.

7.2 Quantitative analysis

Simulation parameters and its meaning is as given in Table 2. We have used MATLAB for simulations. The SNs are assumed to be static. The performance of the proposed probability density function based node distribution scheme (PDFNDS) is compared to the node distribution as given in PDFND [27] and EEAGTACO protocol [18].

7.2.1 Analysis of PDFNDS

Analysis of the proposed node distribution scheme has been carried out in Fig. 4(a). Here, the number of SNs distributed is plotted against the number of layers. It can be seen that with the total SNs $N_{Total} = 50$, a total of 39 SNs are deployed in *layer*-1 and it keeps decreasing in the outer successive layers as one moves towards the boundary in $3 - layer$ network. Similar is the case with $N_{Total} = 100$, $N_{Total} = 150$, $N_{Total} = 200$ and $N_{Total} = 250$. In the

Table 2 Simulation parameter and its meaning

Parameter symbol	Meaning	Value
Area (M)	Deployment area	100–300 square units
Nodes (T_{Total})	Sensor SNs to be deployed	100–300
E_o	Initial energy	0.01 units
R_s	Sensing range	4–8 units

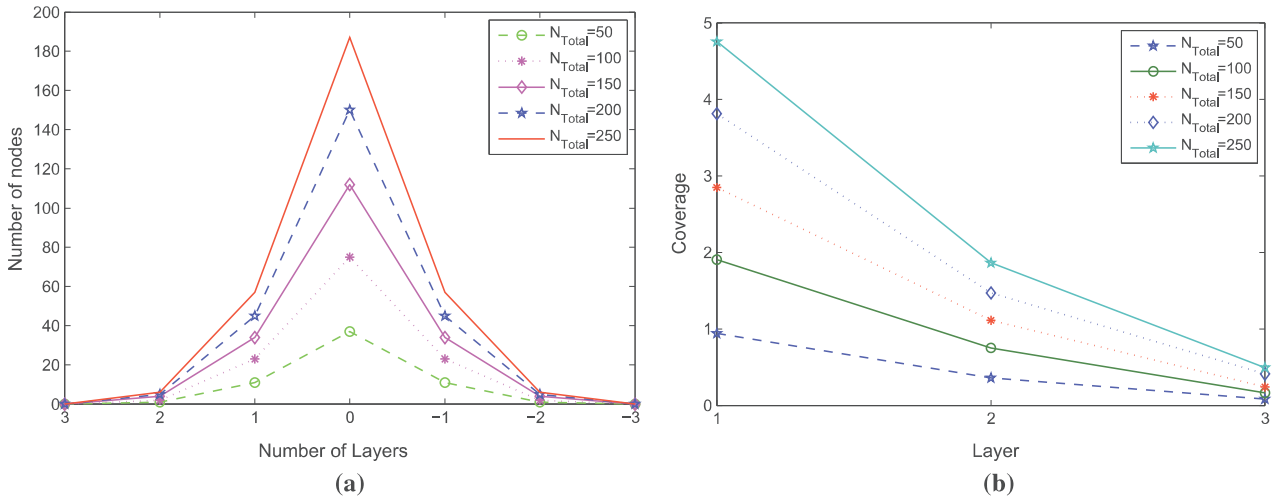


Fig. 4 Analysis of PDFNDS. **a** Node distribution through PDFNDS. **b** Coverage achieves using PDFNDS

proposed scheme, the node distribution is directly proportional to the deployment area.

Coverage analysis of the node distribution through PDFNDS is carried out using the definition given below.

Definition 3 The coverage density of *i*th layer is defined as the sensing area of the SNs multiplied by the number of SNs deployed per unit area in that layer.

Therefore using the above definition of coverage we get $L^i_{Coverage} = \frac{T_i \times \pi \times R_S^2}{A_i}$. Substituting A_i in the above equation of coverage as given above we get $\frac{T_i \times \pi \times R_S^2}{\frac{3^i-2}{3^{2i}} \times \pi M^2} = \frac{3^{2i} \times T_i \times R_S^2}{M^2 \times (3^i-2)}$. Here, $L^i_{Coverage}$ is the coverage obtained in *i*th layer. In Fig. 4(b) coverage obtained is plotted against the number of layers. It is observed that when the SNs are distributed through PDFNDS scheme, 1-coverage [54] is achieved with $N_{Total} = 50$ while *k*-coverage is achieved with $N_{Total} = 100$, $N_{Total} = 150$, $N_{Total} = 200$ and $N_{Total} = 250$ in case of layer−1. A gradual decrease in the curve towards layer−3 is noticed in the figure. This is because the distribution of SNs is dependent on the area of each layer. In other words, as the area of each successive annulus decreases as one moves towards the boundary so does the distribution of SNs. Therefore, higher coverage density is achieved in the layer innermost layer and it keeps decreasing a one progresses towards the boundary. Similar and predictable behaviour is noticed for all the considered cases when $N_{Total} = 50$, $N_{Total} = 100$, $N_{Total} = 150$, $N_{Total} = 200$ and $N_{Total} = 250$.

Coverage obtained in various layers in 4-layered network architecture with varying sensing range (R_s) is shown in Fig. 5. The nodes having different sensing range such as $R_s = 4, R_s = 5, R_s = 6$, $R_s = 7$ and $R_s = 8$, are distributed using the proposed scheme and their coverage in various layers is examined. It is noticed that when the SNs are equipped with $R_s = 4$ the coverage density obtained in *layer*-1 is 2.1 and it keeps decreasing in successive outer annuli i.e., *layer*-2, 3 respectively. Similar is the case with $R_s = 5, 6, 7$ and 8. Therefore, it can be said that higher the sensing range of the node, higher is the coverage density achieved in the network.

7.2.2 Comparison of proposed scheme with the existing scheme

Proposed node distribution scheme is compared with the node distribution scheme discussed in PDFND [27].

Area covered, node density achieved and number of SNs distributed is plotted on y-axis while number of layers is plotted on x-axis is shown in Fig. 6. In the proposed scheme (PDFNDS), the area covered by *layer*-1 is maximum while it decreases as one approaches towards the

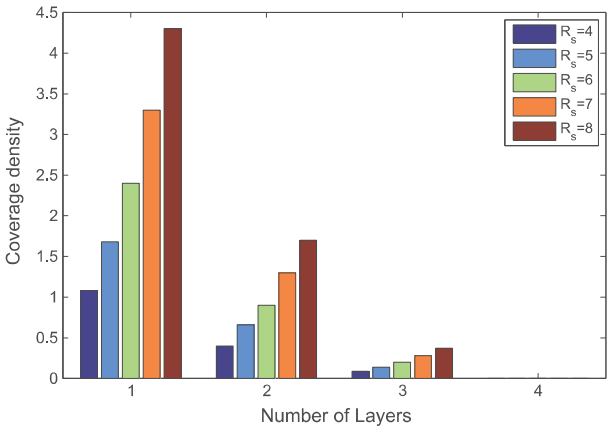


Fig. 5 Coverage obtained with varying sensing range of nodes

boundary of the deployment field. Also, the maximum number of SNs are deployed towards the BS and it decreases as one moves towards the boundary of the deployment field. It can be verified from the figure that the maximum area is covered by *layer*-1 and also maximum number of SNs are distributed in this area. Also the coverage density achieved through the PDFNDS is approximately 20 units. Similar is the case with other 2 layers namely; *layer*-2 and *layer*-3. Area covered by *layer*-3 is smaller as compared to *layer*-1 and 2. The number of SN distribution is directly proportional to the deployment area, hence the number of SNs distributed is lesser as compared to other layers. It can be verified from the Fig. 6(a). Node distribution through the PDFND is shown in Fig. 6(b). In this scheme, the area is divided in such a way that the larger area is towards the boundary and it decreases in geometric progression. Also, the number of SNs distributed is inversely proportional to the deployment area i.e., maximum number of SNs are distributed in *layer*-1 when compared to the node distribution in *layer*-2 and *layer*-3 as observed from the figure. The maximum number of SNs are deployed in *layer*-1 therefore, maximum coverage density is obtained in *layer*-1 when compared to the other cases. Comparing the two node distribution schemes, it can be said that the proposed scheme offers better coverage density in larger area.

The lifetime of the EEAGTACO protocol is analyzed in the Fig. 7(a). Here, the number of dead SNs for each round is plotted. It is observed from the figure that the node distribution through PDFNDS improves the performance of EEAGTACO protocol. The representative SNs from each coalitions in the outer corona send the data to the representative node to its consecutive inner corona on behalf of its coalition members. This node distribution scheme reduces the number of transmissions thereby increases the lifetime of the network. The figure for the number of representative SNs in each round is shown in Fig. 7(b). The gradual curve is noticed when the SNs are distributed through PDFPDS whereas a steep curve is noticed in case of EEAGTACO protocol. It can be seen from the figure that the performance of EEAGTACO protocol is increased when the SNs are distributed through PDFNDS scheme.

Finally, the lifetime of the network in terms of balanced energy consumption is analyzed in the Fig. 8. Here, the number of dead SNs in plotted against the number of rounds for PDFNDS and PDFND. A steep curve is noticed when the SNs are distributed though PDFND while a gradual curve is obtained when the SNs are distributed through PDFNDS respectively. The SNs deployed through

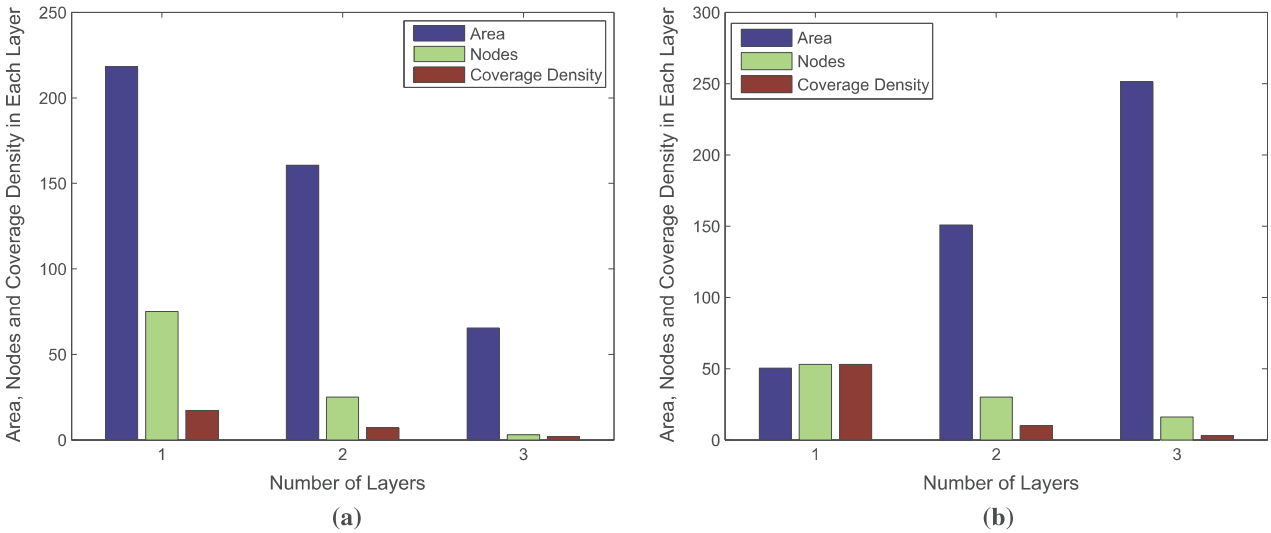


Fig. 6 Comparision of node distribution schemes. **a** Node distribution through PDFNDS. **b** Node distribution through PDFND

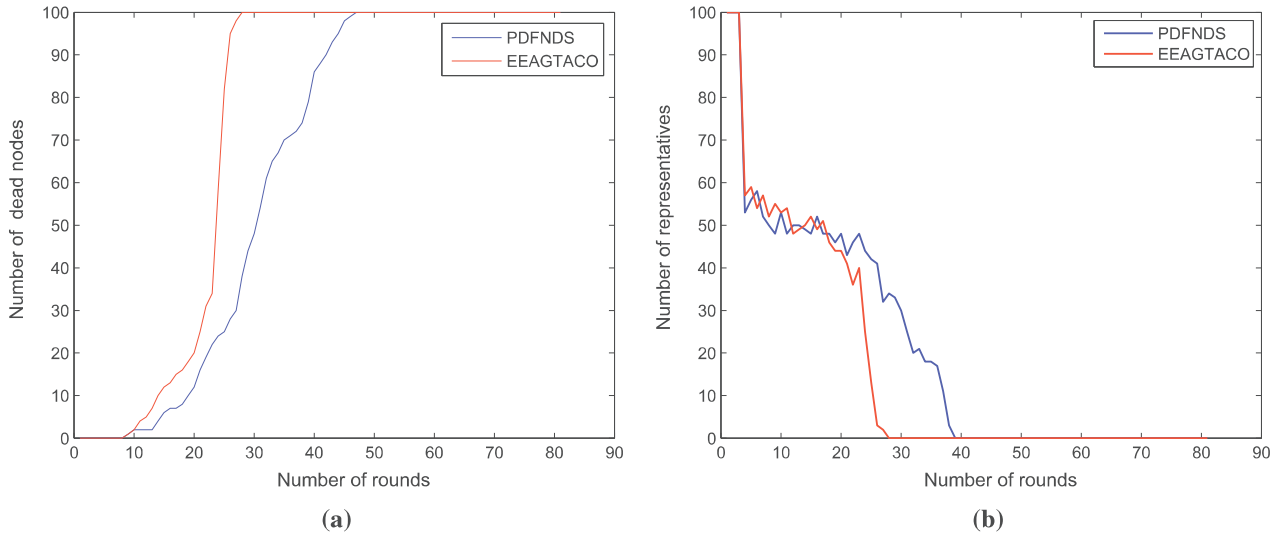


Fig. 7 Comparision of lifetime and number of repersentativs. **a** Comparision of Lifetime. **b** Number of representatives in each round

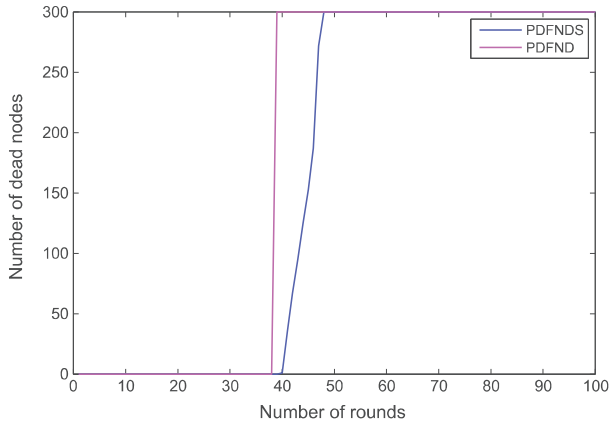


Fig. 8 Comparision of lifetime for balanced energy consumption

the PDFNDS increases the lifetime of the network when compared with the node distribution through PDFND. The gradual decay in number of SNs in case of PDFNDS is due to the proposed mathematical model for the area division and inter-layer communication from the outermost to the innermost layer. With parameter $R_s = 4$, the deployment area is divided into 13 layers. Number of layers is obtained using the relation $\frac{M}{2\times R_s}$ where M is the side of the deployment field and R_s is the sensing range of the node. The SNs are then distributed using their proposed scheme. With $N_{Total} = 300$, the number of SNs distributed in each layer is 117, 66, 36, 22, 15, 11, 8, 6, 5, 4, 4, 3 and 3. It can be seen that the SNs distributed in last layers is equal. The SNs distributed in the inner layers have to receive the data coming from the outer layer, generate its own data and finally aggregate the total data to forward it to the next consecutive layer. Due to this, more number of SNs should be distributed in the inner layers. But in case of PDFND, the energy-hole is created in *layer*2-1. Due to to this the network is partitioned into two sub-networks. Similar problem occurs in *layer*-10. Therefore, there are three partitions in the network in this case. It can be concluded that when the SNs are distributed using PDFND, the energy-hole is created when the SNs have smaller sensing range. This leads to decrease in the lifetime of the network using our definition of lifetime. In the case of PDFNDS, the SNs are distributed in such a way that energy-hole is eliminated, thereby maintaining the connectivity. This increases the network lifetime as shown in Fig. 8.

8 Conclusion

Corona based energy balanced node distribution scheme employing PDF for WSNs is proposed. The considered WSN field in the proposed work is divided into a number of coronas with BS positioned at the center of the deployment field. The area of each corona keeps decreasing as one move away from the BS towards the boundary of the deployment field. The corona based energy balanced node distribution in accordance with the designed PDF is then proposed. The objective of the proposed scheme is to provide energy balancing in each corona, eliminate energy-hole and minimize coverage-hole problems in the WSN field. The performance of the proposed scheme is compared with the existing techniques and analysed qualitatively. It is observed that the scheme not only balances the energy across the network but also minimized and eliminates coverage and energy-hole problems. The proposed

scheme is especially designed for the applications in which sensors have limited sensing range.

Appendix

Summary of notations used in the paper is given below (Table 3):

The proof of Theorem 1 is as given below:

Let p_i denote the probability of a point (x, y) lying between the annulus i and $(i-1)$. From the proposed probability density function, the probability p_i is given by

$$p_i = \frac{\beta \times (3^i - 2)}{i \times 3^{2i-2}} \iint f(x,y)\, dx\, dy \tag{47}$$

Here, $\iint f(x,y)dxdy$ is the domain area. The considered domain area is circular and is given as

$$\iint f(x,y)\, dx\, dy = \pi \times \left(\frac{M}{3}\right)^2 \times \left(\frac{3^i - 2}{3^{2i-2}}\right) \tag{48}$$

By the fundamental law of probability,

$$\sum_{i=1}^{L} p_i = 1 \; or \; \frac{\beta \times (3^i - 2)}{i \times 3^{2i-2}} \times \pi \times \left(\frac{M}{3}\right)^2 \times \left(\frac{3^i - 2}{3^{2i-2}}\right) = 1$$

Substituting Eq. (48) in Eq. (47),

Table 3 Table of notations

Notation	Meaning
E_{tx}	Energy consumed during transmission
E_{rx}	Energy consumed in reception
$O(X_c, Y_c)$	Center of the network domain
R_i	Radius of the ith corona
$M \times M$	Area of the network domain in square units
L	Number of layer
C_i	ith corona of the network domain
α	Data generartion rate
γ	Node density
ECR	Energy consumption rate
DTR	Data transmission rate
E_o	Initial energy of nodes
T_j	Total nodes in jth layer
A_j	Area of jth layer
β	A constant
p_i	Probability of nodes in ith layer
N_{Total}	Total number of nodes to be deployed
R_c	Communication range of a node
R_s	Sensing range of a node

$$p_i = \frac{\beta \times (3^i - 2)}{i \times 3^{2i-2}} \times \pi \times \left(\frac{M}{3}\right)^2 \times \left(\frac{3^i - 2}{3^{2i-2}}\right) \tag{49}$$

Simplifying the above equation using the fundamental law of probability we get,

$$\beta = \frac{1}{\pi \times \left(\frac{M}{3}\right)^2 \times \left\{1 + \frac{1}{2}\left(\frac{7}{9}\right)^2 + \cdots + \frac{1}{L^2}\left(\frac{3^L-2}{3^{2L-2}}\right)^2\right\}}$$

The proof of Theorem 2 is as given below:

The probability of discrete random variable X and Y for any value within a range i is given as

$$\pi\beta\left(\frac{M}{3}\right)^2 \sum_{j=1}^{i} \frac{1}{j}\left(\frac{3^j - 2}{3^{2j-2}}\right)^2 \tag{50}$$

The probability of the variable X and Y between domain area A_i and A_η such that $\eta > i$ is given as

$$\frac{\beta}{i}\left[A_\eta - A_i\right] \tag{51}$$

Substituting value of A_i and A_η in the above equation we get

$$\frac{\beta}{i}\left[\pi\left(\frac{M}{3}\right)^2\left(\frac{3^\eta - 2}{3^{2\eta-2}}\right)^2 - \pi\left(\frac{M}{3}\right)^2\left(\frac{3^i - 2}{3^{2i-2}}\right)^2\right] \tag{52}$$

Simplifying the above equation we get

$$\pi\left(\frac{M}{3}\right)^2 \frac{\beta}{i}\left[\left(\frac{3^\eta - 2}{3^{2\eta-2}}\right)^2 - \left(\frac{3^i - 2}{3^{2i-2}}\right)^2\right] \tag{53}$$

The CDF of X and Y using Eqs. (50) and (53) is obtained as

$$F[X \le x, Y \le y] = \pi\beta\left(\frac{M}{3}\right)^2 \left[\sum_{j=1}^{i}\left[\frac{1}{j}\left(\frac{3^j - 2}{3^{2j-2}}\right)^2\right] + \left[\frac{1}{i}\left(\frac{3^\eta - 2}{3^{2\eta-2}}\right)^2 - \frac{1}{i}\left(\frac{3^i - 2}{3^{2i-2}}\right)^2\right]\right]$$

The proof of the Theorem 3 as as given below:

Expectations of two random variables X and Y is given as

$$E[XY] = E_1[XY] + E_1[XY] + \cdots + E_L[XY] = \sum_{i=1}^{L} E_i[XY] \tag{54}$$

Here, $E_i[XY]$ is the expectation of X and Y in domain i. Now,

$$E_i[XY] = \iint f(xy)\; x\; y\; dy\; dx \tag{55}$$

$$E_i[XY] = \frac{\beta}{i} \iint x\; y\; dy\; dx \tag{56}$$

$$E_i[XY] = \frac{4\beta}{i}\left[\int_{x=0}^{x=R_{i-1}} x\left(\int_{y=\sqrt{R^2_{i-1}-x^2}}^{y=\sqrt{R^2_1-x^2}} y\,dy\right)dx + \int_{x=R_{i-1}}^{x=R_i} x\left(\int_{y=0}^{y=\sqrt{R^2_1-x^2}} y\,dy\right)dx\right] \tag{57}$$

Simplifying the above equation we get,

$$E_i[XY] = \beta\left(\frac{M}{3}\right)^4\left[\frac{81}{4i3^i} + \frac{5103}{2i3^{3i}} - \frac{91}{3^{2i}}\right] \tag{58}$$

Substituting the above equation in Eq. (54), we get

$$E[XY] = \beta 4\left(\frac{M}{3}\right)^2\sum_{i=1}^{L}\left[\frac{81}{4i3^i} + \frac{5103}{2i3^{3i}} - \frac{91}{3^{2i}}\right]$$

References

1. Biagetti, G., Crippa, P., Falaschetti, L., Orcioni, S., & Turchetti, C. (2016). Wireless surface electromyograph and electrocardiograph system on 802.15.4. *IEEE Transactions on Consumer Electronics*, *62*(3), 258–266.
2. Mishra, R., Kumar, P., Chaudhury, S., & Indu, S. (2013).Monitoring a large surveillance space through distributed facematching. In *2013 fourth national conference on computer vision, pattern recognition, image processing and graphics(NCVPRIPG)* (pp. 1–5). December 2013.
3. Mathew, J., Hauser, C., Stoll, P., Kenel, C., Polyzos, D., Havermann, D., et al. (2017). Integrating fiber fabry-perot cavity sensor into 3-d printed metal components for extreme high-temperature monitoring applications. *IEEE Sensors Journal*, *17*(13), 4107–4114.
4. Tanenbaum, A. S., Gamage, C., & Crispo, B. (2006). Taking sensor networks from the lab to the jungle. *Computer*, *39*(8), 98–100.
5. Meng, S., Kashyap, S. R., Venkatramani, C., & Liu, L. (2012). Resource-aware application state monitoring. *IEEE Transactions on Parallel and Distributed Systems*, *23*(12), 2315–2329.
6. Dempsey, T., Sahin, G., Morton, Y. T., & Hopper, C. M. (2009). Intelligent sensing and classification in ad hoc networks: A case study. *IEEE Aerospace and Electronic Systems Magazine*, *24*(8), 23–30.
7. Lin, S. C., Alshehri, A. A., Wang, P., & Akyildiz, I. F. (2017). Magnetic induction-based localization in randomly deployed wireless underground sensor networks. *IEEE Internet of Things Journal*, *4*(5), 1454–1465.
8. Joshi, Y. K., & Younis, M. (2016). Restoring connectivity in a resource constrained WSN. *Journal of Network and Computer Applications*, *66*, 151–165.
9. Chatterjee, P., & Das, N. (2014). Coverage constrained non-uniform node deployment in wireless sensor networks for load balancing. In *2014 applications and innovations in mobile computing (AIMoC)* (pp. 126–132). February 2014.
10. Zhu, Chuan, Zheng, Chunlin, Shu, Lei, & Han, Guangjie. (2012). Review: A survey on coverage and connectivity issues in wireless sensor networks. *Journal of Network and Computer Applications*, *35*(2), 619–632.
11. Anastasi, Giuseppe, Conti, Marco, Di Francesco, Mario, & Passarella, Andrea. (2009). Energy conservation in wireless sensor networks: A survey. *Ad Hoc Networks*, *7*(3), 537–568.
12. Liu, A., Jin, X., Cui, G., & Chen, Z. (2013). Deployment guidelines for achieving maximum lifetime and avoiding energy holes in sensor network. *Information Sciences*, *230*, 197–226. (Mobile and Internet Services in Ubiquitous and Pervasive Computing Environments.).
13. Yuan, J., Ling, Q., Yan, J., Zhang, W., & Gu, H. (2011). A novel non-uniform node distribution strategy for wireless sensor networks. In *2011 Chinese control and decision conference (CCDC)* (pp. 3737–3741). May 2011.
14. Dietrich, I., & Dressler, F. (2009). On the lifetime of wireless sensor networks. *ACM Transactions on Sensor Networks*, *5*(1), 5:1–5:39.
15. Yetgin, H., Cheung, K. T. K., El-Hajjar, M., & Hanzo, L. H. (2017). A survey of network lifetime maximization techniques in wireless sensor networks. *IEEE Communications Surveys Tutorials*, *19*(2), 828–854. (Secondquarter 2017).
16. Wu, X., Chen, G., & Das, S. K. (2008). Avoiding energy holes in wireless sensor networks with nonuniform node distribution. *IEEE Transactions on Parallel and Distributed Systems*, *19*(5), 710–720.
17. Lian, J., Naik, K., & Agnew, G. B. (2006). Data capacity improvement of wireless sensor networks using non-uniform sensor distribution. *International Journal of Distributed Sensor Networks*, *2*(2), 121–145.
18. Mishra, R., Jha, V., Tripathi, R. K., & Sharma, A. K. (2017). Energy efficient approach in wireless sensor networks using game theoretic approach and ant colony optimization. *Wireless Personal Communications*, *95*(3), 3333–3355.
19. Amini, N., Fazeli, M., Miremadi, S. G.,&Manzuri, M. T. (2007). Distance-based segmentation: An energy-efficient clustering hierarchy for wireless microsensor networks. In *Fifth annual conference on communication networks and services research (CNSR'07)* (pp. 18–25). May 2007.
20. Rahman, A. U., Alharby, A., Hasbullah, H., & Almuzaini, K. (2016). Corona based deployment strategies in wireless sensor network. *Journal of Network and Computer applications*, *64*(C), 176–193.
21. Ishizuka, M., & Aida, M. (2004). Performance study of node placement in sensor networks. In *24th international conference on distributed computing systems workshops, 2004. Proceedings* (pp. 598–603). March 2004.
22. Rahman, I. A. A. U., Al-Shomrani, M. M., & Hasbullah, H. (2015). Two echelon architecture using relay node placement in wireless sensor network. *Journal of Applied Sciences*, *5*, 214–222.
23. Ammari, H. M., & Das, S. (2010). A study of k-coverage and measures of connectivity in 3D wireless sensor networks. *IEEE Transactions on Computers*, *59*(2), 243–257.
24. Gupta, H. P., & Rao, S. V. (2016). Demand-based coverage and connectivity-preserving routing in wireless sensor networks. *IEEE Systems Journal*, *10*(4), 1380–1389.
25. Zaidi, S. A. R., Hafeez, M., Khayam, S. A., Mclernon, D. C., Ghogho, M., & Kim, K. (2009). On minimum cost coverage in wireless sensor networks. In *2009 43rd annual conference on information sciences and systems*, (pp. 213–218). March 2009.
26. Halder, S., Ghosal, A., Chaudhuri, A., & DasBit, S. (2011). *A probability density function for energy-balanced lifetime-enhancing node deployment in WSN* (pp. 472–487). Berlin: Springer.
27. Halder, S., & DasBit, S. (2014). Design of a probability density function targeting energy-efficient node deployment in wireless

sensor networks. *IEEE Transactions on Network and Service Management*, *11*(2), 204–219.
28. Halder, S., & Ghosal, A. (2014). Is sensordeployment using Gaussian distribution energy balanced? In*2014 IEEE 11th consumer communications and networking conference (CCNC)* (pp. 721–728). January 2014.
29. Bhardwaj, M., Garnett, T., & Chandrakasan, A. P. (2001).Upper bounds on the lifetime of sensor networks. In *ICC2001. IEEE international conference on communications. Conference record (Cat. No. 01CH37240)* (Vol. 3, pp. 785–790).
30. Mhatre, V., & Rosenberg, C. (2004). Design guidelines for wireless sensor networks: Communication, clustering and aggregation. *Ad Hoc Networks*, *2*(1), 45–63.
31. Efthymiou, C., Nikoletseas, S., & Rolim, J. (2004). Energy balanced data propagation in wireless sensor networks. In *18th international parallel and distributed processing symposium, 2004. Proceedings.* (p. 225). April 2004.
32. Liao, Wen-Hwa, Kuai, Ssu-Chi, & Lin, Mon-Shin. (2015). An energy-efficient sensor deployment scheme for wireless sensor networks using ant colony optimization algorithm. *Wireless Personal Communications*, *82*(4), 2135–2153.
33. Liu, X. (2015). An optimal-distance-based transmission strategy for lifetime maximization of wireless sensor networks. *IEEE Sensors Journal*, *15*(6), 3484–3491.
34. Ramos, H. S., Boukerche, A., Oliveira, A. L., Frery, A. C., Oliveira, E. M., & Loureiro, A. A. (2016). On the deployment of large-scale wireless sensor networks considering the energy hole problem. *Computer Networks*, *110*, 154–167.
35. Ferng, H. W., Hadiputro, M., & Kurniawan, A. (2011). Design of novel node distribution strategies in corona-based wireless sensor networks. *IEEE Transactions on Mobile Computing*, *10*(9), 1297–1311.
36. Younis, M., Senturk, I. F., Akkaya, K., Lee, S., & Senel, F. (2014). Topology management techniques for tolerating node failures in wireless sensor networks: A survey. *Computer Networks*, *58*, 254–283.
37. Han, X., Cao, X., Lloyd, E. L., & Shen, C. C. (2010). Fault-tolerant relay node placement in heterogeneous wireless sensor networks. *IEEE Transactions on Mobile Computing*, *9*(5), 643–656.
38. Lee, S., & Younis, M. (2010). Recovery from multiple simultaneous failures in wireless sensor networks using minimum Steiner tree. *Journal of Parallel and Distributed Computing*, *70*(5), 525–536.
39. Tamboli, N., & Younis, M. (2009). Coverage-aware connectivity restoration in mobile sensor networks. In *2009 IEEE international conference on communications* (pp. 1–5). June 2009.
40. Wu, D., Li, R., & Bao, L. (2008). A holistic routing protocol design in underground wireless sensor networks. In *2008 The 4th international conference on mobile ad-hoc and sensor networks* (pp. 187–194). December 2008.
41. Luo, J., Di, W., Pan, C., & Zha, J. (2015). Optimal energy strategy for node selection and data relay in WSN-based IoT. *Mobile Networks and Applications*, *20*(2), 169–180.
42. Jha, V., Verma, S., Prakash, N., & Gupta, G. (2018). Corona based optimal node deployment distribution in wireless sensor networks. *Wireless Personal Communications*, *102*, 325–354.
43. Heinzelman, W. R., Chandrakasan, A., & Balakrishnan, H. (2000). Energy-efficient communication protocol for wireless microsensor networks. In *Proceedings of the 33rd annual Hawaii international conference on system sciences* (Vol. 2, pp. 10). January 2000.
44. Mishra, R., Jha, V., Tripathi, R. K., & Sharma, A. K. (2018). Design of probability density function targeting energy efficient network for coalition based wsns. *Wireless Personal Communications*, *99*(2), 651–680.
45. Bhattacharjee, M., & Gupta, S. (2014). Determining redundant nodes in a location unaware wireless sensor network. In *2014 IEEE international conference on advanced communications, control and computing technologies* (pp. 858–862) May 2014.
46. Li, J., & Mohapatra, P. (2007). Analytical modeling and mitigation techniques for the energy hole problem in sensor networks. *Pervasive and Mobile Computing*, *3*(3), 233–254.
47. Xian, Q., & Long, Y. (2016). An enhanced greedy perimeter stateless routing algorithm for wireless sensor network. In *2016 IEEE international conference of online analysis and computing science (ICOACS)* (pp. 181–184). May 2016.
48. Bernard, M., Kondak, K., Maza, I., & Ollero, A. (2011). Autonomous transportation and deployment with aerial robots for search and rescue missions. *Journal of Field Robotics*, *28*(6), 914–931.
49. Song, W. Z., Huang, R., Xu, M., Shirazi, B., & LaHusen, R. (2010). Design and deployment of sensor network for real-time high-fidelity volcano monitoring. *IEEE Transactions on Parallel and Distributed Systems*, *21*(11), 1658–1674.
50. Mathisen, S. H., Grindheim, V., & Johansen, T. A. (2017). Approach methods for autonomous precision aerial drop from a small unmanned aerial vehicle. *IFAC-PapersOnLine*, *50*(1), 3566–3573. (20th IFACWorld Congress).
51. Kyriakopoulos, C. A., Papadimitriou, G. I., Nicopolitidis, P., & Varvarigos, E. (2016). Energy-efficient lightpath establishment in backbone optical networks based on ant colony optimization. *Journal of Lightwave Technology*, *34*(23), 5534–5541.
52. Dorigo, M., & Stützle, T. (2004). *Ant colony optimization*. Scituate: Bradford Company.
53. Voulkidis, A. C., Anastasopoulos, M. P., & Cottis, P. G. (2013). Energy efficiency in wireless sensor networks: A game-theoretic approach based on coalition formation. *ACM Transactions on Sensor Networks*, *9*(4), 43:1–43:27.
54. Huang, C.-F., & Tseng, Y.-C. (2005). The coverage problem in a wireless sensor network. *Mobile Networks and Applications*, *10*(4), 519–528.



Richa Mishra is currently working as an Assistant Professor in the Department of Computer Science and Engineering in National Institute of Technology Delhi, Delhi, India. She has received B.E. degree from Shivaji University Kolhapur, India and M.E. degree from University of Mumbai, India in the year 2008. She has completed her Ph.D. from National Institute of Technology Delhi, Delhi, India in the year 2018. She has served 5 years as an Assistant Professor in Guru Gobind Singh Indraprastha University (GGSIPU) and Delhi Technological University (Formerly known as Delhi College of Engineering), India. Her current area of interest includes designing energy efficient protocols in wireless sensor networks.



Vivekanand Jha received the B.Tech. degree in Computer Science & Information Technology (CSIT) from I.E.T Bareilly, Rohilkhand University, U.P, India, in 2001 and the M.Tech. degree in Information Technology from Indian Institute of Information Technology, Gwalior, India, in 2006. He is working as Assistant Professor in Department of Computer Science & Engineering at Indira Gandhi Delhi Technical University for Women, Delhi, India from 2007. His research interests include wireless sensor networks, Algorithm Design, and Cloud Computing.



Rajeev K. Tripathi received Ph.D. degree from Indian Institute of Technology, Kanpur, India. He is currently working as an Assistant Professor in Electronics and Communication Engineering at National Institute of Technology, Delhi, India. His current area of interest includes clustering algorithms for Wireless Sensor Networks.



Ajay K. Sharma is working as Director at National Institute of Technology (An Institute of National Importance), Ministry of Human Resource Development, Government of India, New Delhi since October 2013. He received his B.E. in Electronics and Electrical Communication Engineering from Punjab University Chandigarh, India in 1986, M.S. in Electronics and Control from Birla Institute of Technology (BITS), Pilani in the year 1994 and Ph.D. in Electronics Communication and Computer Engineering in the year 1999. His Ph.D. thesis was on "Studies on Broadband Optical Communication Systems and Networks". After serving various organizations from 1986 to 1995, he has joined National Institute of Technology (Erstwhile Regional Engineering College) Jalandhar as Assistant Professor in the Department of Electronics and Communication Engineering in the year 1996. From November 2001, he has worked as Professor in the ECE department and thereafter he has worked as Professor in Computer Science & Engineering from 2007 to 2013 in the same institute. His major areas of interest are broadband optical wireless communication systems and networks, dispersion compensation, fiber nonlinearities, optical soliton transmission, WDM systems and networks, Radio-over-Fiber (RoF) and wireless sensor networks and computer communication. He has published 290 research papers in the International/National Journals/Conferences and 12 books. He has supervised 22 Ph.D. and 52 M.Tech. theses. He has completed two R&D projects funded by Government of India and one project is ongoing. He was associated to implement the World Bank project of 209 Million for TEQIP-I programme of the institute. He has been appointed as member of technical Committee on Telecom under International Association of Science and Technology Development (IASTD) Canada for the term 2004–2007 and he is Life Member of Optical Society of America, USA, (LM ID-361253), Computer Society of India, Mumbai, India, (LM-Associate: 01099298), Advanced Computing & Communications Society, Indian Institute of Science, Bangalore, India, (L284M1100306), SPIE, USA, (ID: 619838), Indian Society for Technical Education (I.S.T.E.), New Delhi, India, (LM-11724), Fellow The Institution of Electronics and Telecommunication Engineers (IETE), (F-224647).

——ONLINE FIRST(NOT Peer-Reviewed)——

Title ： Degradation of AY36 using TiO2-UV photocatalytic system

Author：Palak Palak 1

Institute/Affiliation：1 Department of Environmental Science & Engineering, Guru Jambheshwar University of Science & Technology, Hisar, Haryana (125001) India

Received：2018-02-04

Accepted：2018-09-05

Process：1、First trial(Field and check) ✓

2、Peer review ☐

3、Editing and three trials ☐

4、Published online ☐

EnPress Publisher, LLC. United States

EnPress Publisher

Degradation of AY36 using TiO_2-UV Photocatalytic System

Palak[1], Shivani Chauhan[1], Krishan Kumar[2], A.K. Haritash[3]*
[1]Department of Environmental Science & Engineering, Guru Jambheshwar University of Science & Technology, Hisar, Haryana (125001) India
[2]Department of Chemistry, Vaish College, Bhiwani, Haryana (127021) India
[3]Department of Environmental Engineering, Delhi Technological University, Bawana Road, Shahbad Daulatpur, Delhi(110042) India

ABSTRACT

This studyinvestigates the efficacy of photocatalytic degradation process using TiO_2-UV configuration for treatment of waste water containing textile dye Acid Yellow 36 (AY36).Acid Yellow 36 dye was degraded using catalyst TiO_2 in analkaline medium of pH8.0.A dose of 0.25g of TiO_2 was used for 88.4% degradation of initial concentration of 20mg/l AY36 dye in 28 hrs. The effect of parameters such as pH, initial dye concentration, amount of TiO_2used, and exposure to UV light/irradiation on degradation of AY36 was investigated.Further it was observed that suspended TiO_2 in dye solution shows more effective results towards dye degradation, than embedded TiO_2 in the form of alginate beads. The study concluded that photocatalytic degradation is a potential tool for degradation of azo dyes.

Keywords: TiO_2; acid yellow 36; advanced oxidation process (AOPs); photocatalysis

1. Introduction

Dyes are important raw material for industries like paper, pulp, leather,textile etc. Azo dyes have excellent coloring properties like yellow to orange so they are used in almost every industry. These dyes have colouring properties because of the presence of a chemical azo group.Other industries where dyes are used are tinting and inks,paints adhesive, polymers etc.(Sharma et. al., 2016).Effluents from different industries are the main source of contamination of water as they contain different fractions of residuals of dye. Azo dyes are highly resistant in nature;they are even resistant to heat temperature and weather condition.

Azo dye; R-N=N-R’

Where, R and R’ can be either alkyl or aryl. The N=N is an azo group, which is only responsible for the colour of the dye and the only reason for its recalcitrant nature. It is hard to degrade dye by any biological means so chemical methods need to be applied for breakdown of double bond which turns coloured solution to colourless (Mahmoud *et al.*, 2009).Industrial outlets contains huge amount of an azo dye residues which are toxic in nature and cause harmful effects on ecosystem. Dyes are not only harmful to plants and water organisms, but also show harmful Impact on human beings. There is ample evidence of the harmful effects of dyes. These are

14701 Myford Road, Suite B-1, Tustin, CA 92780, United States
Tel：+1 (949) 299 0192
Email：contact@enpress-publisher.com

highly mutagenic and carcinogenic in nature and hence causing cancer and other dreadful disease. These are continuously being released to the environment from industries which impart ecotoxicity in aquatic ecosystems (Ratna & Padhi, 2012). Since dyes are readily dissolved in water, they interfere with the photosynthetic activity of water organisms,and disturb the food chain of aquatic ecosystem by reducing visibility of zooplanktons. Textile dyes also cause allergies, respiratory diseases and dermatitis, irritation of skin and eyes etc.Considering the harmful effects of dyes on environment, it is important to explore an effective method for its degradation.

There are various methods of dye degradation but one of the more efficient accelerated processes is advanced oxidation process. It is a chemical treatment which reduces organic impurities of water by oxidising them to simpler forms (Haritash *et al.*, 2015). The hydroxyl radicals are produced during the process with the help of primary oxidants (H_2O_2, ozone) or energy sources (UV lights) or catalyst (TiO_2). These components must be precised, properly configured, and used for the study. AOPs are mainly used for non-degradable and toxic products which include photocatalysis (Barka *et al.*, 2010), Fenton oxidation (Haritash *et al.*, 2016), Photofenton, ozonolysis, and ultrasonication in standalone mode or combination of two.Photocatalysis processis the acceleration of photoreaction in presence of catalyst like TiO_2 or ZnO etc.The most widely used semiconductor catalyst in photo-induced process is TiO_2 which is activated by UV light(Saggioro *et al.*, 2011).TiO_2 is also known as heterogeneous catalyst. It is chemically and biologically inert, stable, relatively easy to produce and reuse, cheap, environment friendly, have stable electrical properties, and efficiently catalyse reactions. It exists in four mineral state anatase, rutile, brookite and TiO_2(B) (Akpan & Hameed,2009). It is versatile in nature and has various application areas like paints, varnishes, paper, plastics, solar cells, glass, electrical conductors, food colouring agents etc. It is also used in immobilised form of beads and acts as an opacifier in powdered form.It is widely used as a white pigment due to its sticky nature and having very high refractive index. TiO_2 is being used in the photocatalysis process because of the following factors - inexpensive, easily available, wavelength selective, and accelerated by UV light. Photocatalytic reactions take place at room temperature and the formation of intermediate products is avoided.UV light is absorbed by TiO_2, making ground state electrons jump to excited state forming an electron hole pair. This creates a void or energy gap between lower vacant conduction band and upper filled valence band. Hydroxyl ions are generated by this process. When photons with greater or equal energy to 3.4eV is adsorbed by TiO_2, an electron is excited from valence band to conduction band; charge carriers (OH radicals) are generated and leave a positive hole in the valence band, this photo generated electron hole pair is known as excitons.

There are various operating parameters which play a vital role in the photocatalytic degradation (Shrivastava, 2012).Onesuch parameter is amount of catalyst used. Greater the amount of catalyst used more will be the rate of degradation (Akpan & Hameed, 2009).

The mechanism of photocatalytic degradation can be described by following steps:

- Absorption of photons by TiO_2 and productions of electron- hole pairs.
- Oxygen ion absorption.
- Neutralisation of OH radicals by photon holes.
- Reaction of organic pollutant with OH radical.

  The first step of the reaction is carried out by photons with the energy higher than the band gap of TiO_2 i.e. 3.2eV (Sima & Hasal,2013).

2. Materials and methods

The AY36 is an azo dye with complex chemical structure, recalcitrant nature, and reported eco-toxicity. The dye was obtained from Vishnu chemicals, Ankleshwar, Gujarat having 85% minimum assay. Titanium dioxide (99% AR Grade) was obtained from High Purity Laboratory Chemicals Pvt. Ltd., Mumbai. All the experiments were performed in triplicates using Grade 1 ultrapure water.

A stock solution of 1000ppm (0.5mg/500ml) of AY36 was prepared for degradation experiments. The 20mg/l solution of dye was prepared by diluting the stock solution. A standard curve of AY36 was plotted in concentration range of 5-20 mg/L with regular interval of 5mg/L The absorption spectrum for absorbance (400-700nm) of AY36 against wavelength reported 434nm as the wavelength of maximum absorption.The pH was adjusted at 8.0 with the help of HCl (1N) and NaOH (1N) solutions. The experiment was conducted using 150ml of the dye solution in conical flask.The solution was continuously stirred using magnetic stirrer at 150 rpm in the UV chamber fitted with three (03) lamps (λ – 254 nm) of capacity of 30W each.The photo-catalytic degradation of AY36 was studied at an initial dye concentration of 20mg/L withTiO_2 as catalyst under UV light. A volume of 10 ml was extracted from the flask placed in a UV light and the absorbance was monitored first at interval of 15 minutes for first one hour; 30 minutes for next one hour; and then at regular interval of two (02) hours .The extracted sample was centrifuged at 5000rpm for 20minutes to separate TiO_2 particles from the solution. A blank without dosing of TiO_2 was also run to compensate for the photo-degradation. The concentration was obtained observing the absorbance at 434nm over Labtronics make LT-290 model spectrophotometer. The percentage degradation of AY36 was calculated using formula given below

$$\text{Percentage degradation } \% = ((C_i - C_f)/C_i)*100$$

Where, C_i is the initial concentration of dye, and C_f is the final concentration of dye.

3. Results and discussion

Based on the results obtained, it was observed that photoctalytic process could degrade AY36 dye. The concentration of AY36 went on decreasing with time. It decreased from initial concentration (Ci) of 22.6 mg/l to 20.4 mg/l in first one hour.Later, the rate of degradation reduced but the degradation progressed slowly; and residual concentration of AY36 stabilised at around 2.2 mg/l after a period of 32 hours (Fig. 1). Further degradation of AY36 was not observed, and it was concluded that

Photocatalytic degradation of AY36 has an overall efficiency of about 90%. The reduced rate of degradation in later phase may be ascribed to reduction in initial dye concentration with time. The Photocatalytic degradation of AY36 might be following first order rate kinetics which is dependent over initial concentration of reactants viz. AY36 in the present study. In order to confirm it, the rate of degradation (mg/h) was calculated using the following relation

$$\text{Rate of reaction (K) (mg/h)} = (C_i - C_f)/(t_i - t_f)$$

Where, Ci is initial concentration of AY36; C_f is the final concentration; t_i is initial time; and t_f is the final time during an interval of degradation. The rate of degradation was maximum during 15 to 30 minutes (@ 2.6 mg/h) followed by the rate of 2.2 mg/h during 30 minutes to one hour. Later, the rate of degradation went on decreasing with time (Table 1) and it stabilised at 0.1 mg/h after a period of 32 hours with an overall decolourisation efficiency of 90.3%.

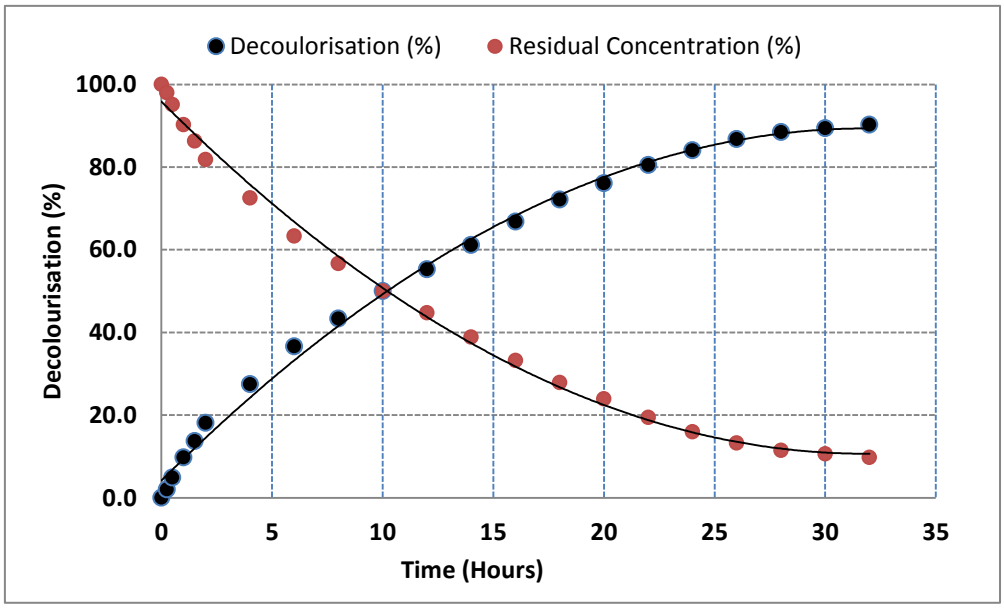


Figure 1. Degradation profile of AY36 during photocatalytic treatment

S. No.	Time (hours)	Concentration (mg/l)	Decolourisation (%)	Rate of decolourisation (mg/hour)
1	0	22.6	0.0	0.0
2	0.25	22.2	2.0	1.8
3	0.5	21.5	4.9	2.6
4	1	20.4	9.8	2.2
5	1.5	19.5	13.7	1.8
6	2	18.5	18.2	2.0

14701 Myford Road, Suite B-1, Tustin, CA 92780, United States
Tel: +1 (949) 299 0192
Email: contact@enpress-publisher.com

7	4	16.4	27.4	1.1
8	6	14.3	36.6	1.0
9	8	12.8	43.4	0.8
10	10	11.3	50.0	0.8
11	12	10.1	55.3	0.6
12	14	8.8	61.2	0.7
13	16	7.5	66.8	0.6
14	18	6.3	72.1	0.6
15	20	5.4	76.1	0.5
16	22	4.4	80.5	0.5
17	24	3.6	84.1	0.4
18	26	3.0	86.7	0.3
19	28	2.6	88.5	0.2
20	30	2.4	89.4	0.1
21	32	2.2	90.3	0.1

Table 1. Percent decolourisation and rate of degradation of AY36 in the present study

4. Conclusion

Based on results obtained in the present study, Photocatalytic degradation was observed to be an effective process for decolourisation of azo dyes like AY36. The TiO2-UV system can be used for the treatment textile industry wastewater containing toxic azo dyes. Optimisation of parameters regulating photocatalysis may be done to improve efficiency of the process to treat the industrial effluents to the level of compliance.

References

1. Akpan UG., Hameed BH. Parameters affecting the photocatalytic degradation of dyes using TiO2-based photocatalysts: A review. Journal of Hazardous Materials 2009; 170: 520-529.
2. Barka N, Samir Q, Assabbane A, *et al.* Photocatalytic degradation of an azo reactive dye, Reactive Yellow 84, in water using an industrial titanium dioxide coated media. Arabian Journal of Chemistry 2010; 3: 279-283.
3. Haritash AK., Deepika VM., Shan V. Degradation of Acid Yellow 36(AY36) dye using Fenton's Process. International Journal of Environmental Sciences 2016; 6(6): 1061-1067.
4. Haritash AK., Sharma A, Verma M. Photocatalytic degradation of Acid Orange 7 (AO7) dye using TiO2. International Journal of Engineering Research and Technology 2015; 4: 34-36.
5. Mahmoud MA., Poncheri A, Badr Y, *et al.* Photocatalytic degradation of methyl red blue. South African Journal of Science 2009; 105: 299-303.
6. Ratna B, Padhi S. Pollution due to synthetic dyes toxicity and carcinogenicity studies and remediation. International Journal of Environmental Sciences 2012; 3(3): 940-955.
7. Saggioro EM., Oliveira AS., Pavesi T, *et al.* Use of titanium dioxide

photocatalysis on the remediation of model textile wastewaters containing azo dyes. Molecules 2011; 16: 10370-10386.

8. Sharma A, Verma M, Haritash AK. Degradation of toxic azo dye (AO7) using Fenton's process. Advances in Environmental Research 2016; 5(3): 189-200.
9. Shrivastava VS. Photocatalytic degradation of Methylene blue dye and Chromium metal from wastewater using nanocrystalline TiO2 Semiconductor. Archives of Applied Science Research 2012; 4(3): 1244-1254.
10. Sima J, Hasal P. Photocatalytic Degradation of Textile dyes in a TiO2/UV System. Chemical Engineering Transactions 2013; 32: 79-84.

Design and Analysis of a Cross V-shaped Nanoantenna for Visible Region

Shanu Kumar[1], Pooja Chauhan, Ajeet Kumar[1]*

Advanced Photonics Simulation Research Lab., Department of Applied Physics Delhi Technological University, Delhi-110 042, India
ajeetdph@gmail.com

Abstract: A cross V-shaped nanonoantenna has been designed using gold as material with gap of 10 nm. The scattering cross-section and the Electric field at the centre has been obtained with optical resonant wavelength of 530 nm which lies in visible range.
OCIS codes: (260.5740) resonance, (290.0290) scattering.

Introduction:

Optical nanoantenna are just analogous to microwave antenna but the region of operation of optical nanoantenna is in optical range and size of nanoantenna is in nanometre range [1]. Metals at optical region behaves at strong coupled plasma which can increase the efficiency of light matter interaction at nanoscale [2].

In this paper, a cross V-shaped nanoantenna has been designed using gold as a material as shown in Fig 1. The scattering cross section and Electric field in the feed gap have been computed using the finite element method [3]. The modelling and optimization of the nanoantenna have been done using COMSOL Multiphysics Software.

Design of Nano-antenna:

A cross V-shaped nanoantenna using gold as a material with length 'l = 500 nm' and Width 'w = 100 nm' and the feed gap between them is 10 nm as shown in Fig 1. Perfectly matched layer (PML) of thickness 50[nm] is used. The most important property of PML is that it absorbs reflection coming out from the incident material and thus do not interfere with the incoming radiation wave which distinguishes it from the ordinary non-PML material.

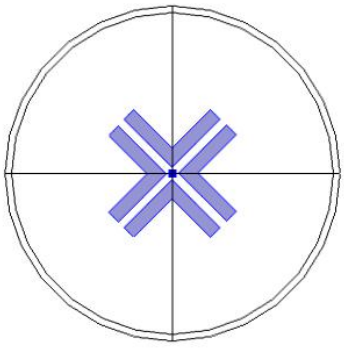


Fig 1: Design of cross V- shape nanoantenna

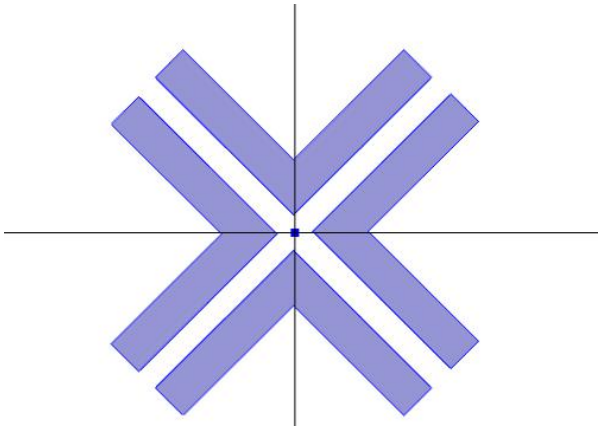


Fig 2: Zoomed in view with feed gap of 10 [nm]

Simulated results:

An input power is made incident on the antenna and the field enhancement is observed in the feed gap region of the nanoantenna.The different parameters of nanoantenna like scattering cross section and Electric field in the centre feed gap at resonance wavelength have been analysed.

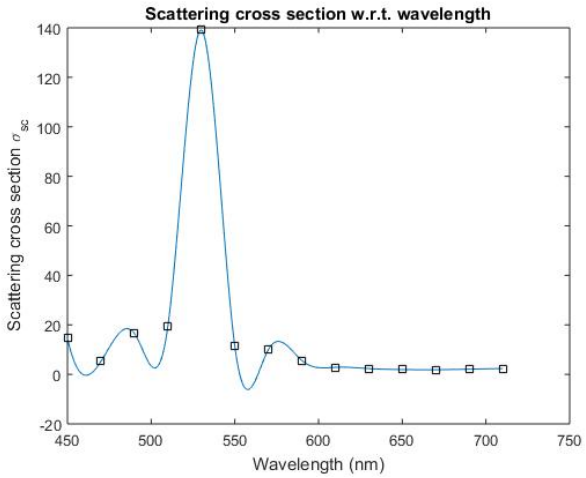


Fig 3: Variation of scattering cross section with wavelength

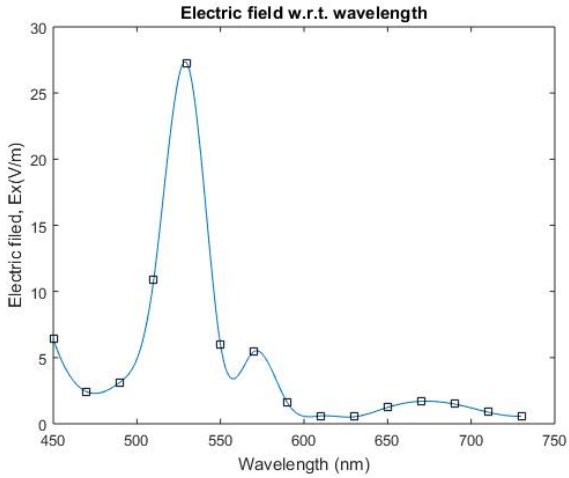


Fig 4: Variation of Electric field Ex with wavelength

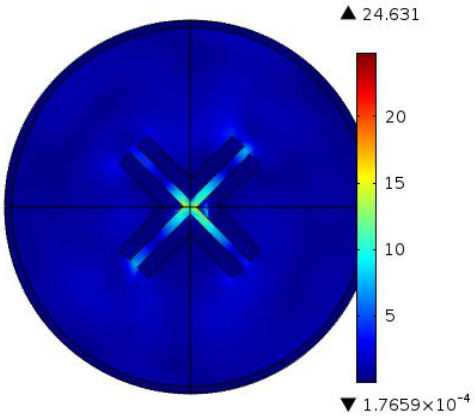


Fig 5: Electric field distribution in feed gap of nanoantenna

Conclusion

A cross V – shaped nanoantenna has been successfully designed and analysed. It has been observed that it has high scattering at resonant wavelength of 530 nm and Electric Peak at 530 nm.

References:

[1] Novotny, L., and B. Hecht. Principles of Nano-Optics. Cambridge: Cambridge University Press (2009).

[2] Bharadwaj, P., B. Deutsch, and L. Novotny. Optical antennas. Advances in Optics and Photonics (2009) 438-483

[3] Resonant optical antenna, "Physical Review Letters, vol. 102, no. 25,p.256801,Jun. 2009.

[4] N. J. Halas, "Connecting the dots: Reinventing optics for nanoscale dimensions," PNAS **106** (10), 3643 (2009).

[5] L. Novotny and N. van Hulst, "Antennas for light," Nature Photon. **5**, 83 (2011).

[6] K. B. Crozier, A. Sundaramurthy, G. S. Kino, and C. F. Quote, "Optical antennas: Resonators for local field enhancement," J. Appl. Phys. **94** (7), 4632 (2003).



Life Science Informatics Publications

Research Journal of Life Sciences, Bioinformatics, Pharmaceutical and Chemical Sciences

Journal Home page http://www.rjlbpcs.com/

RJLBPCS

ISSN 2454-6348

Original Research Article **DOI: 10.26479/2018.0404.09**

DETERMINING PLURIPOTENCY OF A CELL BY AN *IN SILICO* METHOD

Abhishek Saini[1], Jai Gopal Sharma[1], Vimal Kishor Singh[2*]

1. Department of Biotechnology, Delhi Technological University, Delhi, India.

2. Tissue Engineering and Regenerative Medicine Laboratory, Department of Biomedical Engineering, Amity School of Engineering and Technology, Amity University Haryana, India.

ABSTRACT: While working with stem cells one of the questions that bother the researcher is about their potency to reprogram. So, if the pluripotency of cells is known beforehand, it would be an added advantage. Bioinformatics approaches have a viable solution to such concerns saving a lot on time and energy. Stem cell isolation and utilizing them for regeneration is itself a very sophisticated and dynamic concept. Thus working with such cells statistical and probabilistic aspects would be in consideration to tackle the active state. Induced pluripotent stem cells were first described by Shinya Yamanaka[1], and since then the approach towards the regenerative field of medicine has seen tremendous changes. By utilizing the bioinformatics tools and resources, few research groups have demonstrated the level of pluripotency of the cells. All available methods have different approaches and have their own set of limitations. After thorough research on such tools, we have designed a novel tool for determining the pluripotency. Unlike existing methods, our method doesn't rely on particular cell type or specific file format to start with. It is a straightforward, quick and reliable way to check any cell's pluripotency. The information regarding the gene expression on the pluripotent stem cells has been gathered at one place and compared with test cell, all with the help of programming languages viz. R, JAVA. Since the identification of cell is based on their genetic expression, the output is robust and reliable. It would be a key player in the field of regenerative medicine where pluripotent stem cells are being utilized for drug development and gene therapy. Further, for gene therapy and ex-vivo generation of cells determining the pluripotency of the source cells would not only increase the efficiency of the overall procedure but reduce the time and capital investment.

KEYWORDS: iPSCs, ESCs, POU5F1, NANOG, Pluripotency.

© 2018 Life Science Informatics Publication All rights reserved

Peer review under responsibility of Life Science Informatics Publications

Corresponding Author: Dr. Vimal Kishor Singh* Ph.D.
Tissue Engineering and Regenerative Medicine Laboratory, Department of Biomedical Engineering, Amity School of Engineering and Technology (ASET), Amity University Haryana, Amity Education Valley, Gurgaon (Manesar), Haryana,India.
Email Address: vksingh@ggn.amity.edu

1. INTRODUCTION

Stem Cells are most promising in the regenerative field of medicine. With so many stem cells based therapies and protocols for ex-vivo generation of cells being developed throughout the globe. Several obstacles are faced by the researchers, and one of them is the determination of the pluripotency of any cell. As per definition, stem cells can be divided based on their potency viz. unipotent, multipotent, pluripotent and totipotent. A unipotent cell can only give rise to a single type of cell and self-renew, e.g., late erythroid precursor cells can give rise to only erythrocytes. A multipotent stem cell has a potential to differentiate into multiple cell types under given conditions, e.g., a Hematopoietic stem cell can differentiate to form red blood cells, platelets, macrophages or lymphocytes. Pluripotent stem cells have the potential to differentiate into any cells type of body. On the other hand, the totipotent stem cells can give rise to the whole organism as they have the potential to give rise to extraembryonic cells. The cell differentiation capacity to any of three cell lineages, i.e., Ectoderm, endoderm, Mesoderm is dependent upon the potency of that particular cell [2]. Pluripotency in embryonic stem cells is regulated by strict regulation of transcription factors and the epigenetic modifications [3], [4], [5], [6]. Besides transcription factors, cell surface markers, pathway-specific markers, and lectins, peptides markers also play a major role in regulating the pluripotency level of the cell [7]. Here, in this study we have used the bioinformatics tools, software and databases to overcome the situation of determining the pluripotency of any cell specially IPSCs. Initially, we have compared the already existing tools for the similar job, after analyzing the online tools we narrowed down on three commonly used tools viz. PluriTest, CellNet, and TertaScore. PluriTest is a DNA microarray-based tool in which researchers at Scripps have created a microarray database containing the genes expressing in embryonic stem cell and induced pluripotent stem cells. For determining the pluripotency of the given cell or cell line microarray file in *.idat (Raw intensity file) format, has to be created and uploaded on the website http://www.pluritest.org. Microsoft Silverlight is required to access the website, and the uploaded data is compared to the PluriTest microarray database. The results displayed show the information about pluripotency and probability of abnormalities if any in the stem cells [8]. Other two platforms uses Affymetrix generated .cel* file format. Cell Net is a network –biology based platform and claims to access the fidelity of cellular

© 2018 Life Science Informatics Publication All rights reserved

engineering more accurately. CellNet is available at (http://cellnet.hms.harvard.edu/) where .cel* format can be uploaded for analysis. A standalone version of the same is also available [9]. For characterization of pluripotent stem cells, teratoma formation is considered to be the standard gold assay. Teratoscore utilizes this property of pluripotent stem cells and distinguishes pluripotent stem cell derived Teratomas from malignant tumors and translates cell potency into a quantitative meas ure (http://benvenisty.huji.ac.il/teratoscore.php). It uses the gene expression data from all germ layers and extraembryonic tissues and represents the results in a scorecard form [10]. Therefore we begin our quest for a universal input file format, and after thorough research, we developed an input file in .txt* Text file format. The text file format is universally accepted and can easily be found for microarray analysis along with particular default formats. It also removes the dependence on specific file format like in case of other online tools. In-vitro identification and characterization of pluripotent stem cells include certain markers viz. cell surface markers, transcription factors, signal pathway related intracellular markers, enzymatic markers. Gene expression and genome-wide H3K4me3 and H3K27me3 expression are found to be much similar between ESCs and iPS cells. The reprogrammed iPSCs are found to be remarkably similar to naturally isolated pluripotent ESCs. In the following respects, thus confirming the identity, authenticity, and pluripotency of iPSCs to naturally isolated pluripotent stem cells, we came across some properties, which are commonly present in any IPSCs, and ESCs Telomeres, have ribonucleoprotein heterochromatin-like structure which is present at the ends of a chromosome that protect them from degradation as well as from being, detected as double-strand DNA breaks. Telomeres present in mammals is consist of tandem repeats of TTAGGG seq. and are involved in maintaining the sustainability of cell division, which is unrestricted by the maximum limit of ~50 cell divisions. Human ESCs shows high telomerase activity to maintain self-renewal and proliferation like properties. Similarly, IPSCs also shows high telomerase activity, and they show the expression of hTERT (human telomerase reverse transcriptase), which is a necessary component in the telomerase protein complex. IPSCs form Teratomas readily after nine weeks of their injection into immunodeficient mice. Teratomas are tumors consist of multiple lineages containing tissues, which are derived from the three germ layers; this is unlike other tumors, which typically are of only one cell type. Teratoma formation is also proving as a landmark test for the detection of pluripotency. Histones are compacting proteins that are structurally localized to DNA sequences that can affect their activity through various chromatin-related modifications. H3 histones which are associated with Nanog, Oct-3/4, and Sox2 were demethylated, which indicates that the expression of Oct-3/4, Nanog, and Sox2 [11], [12], [13], [14], [15], [16], [17].

© 2018 Life Science Informatics Publication All rights reserved

2. MATERIALS AND METHODS

There is a total of 175 genes known as marker genes present in any pluripotent cell [7]. To validate this conclusion, an interaction network of these marker genes was generated using STRING, and after filtering the results by score provided by string, top scorer genes were got fetched out. Next step was to create a method which can identify pluripotency level of any cell. So, for this microarray data files (Control sample) were collected from NCBI's GEO (Gene Expression Omnibus) and *analyzed the results* using GEO2R (a GEO tool). Then, gene expression data file for that particular dataset was downloaded. After the preprocessing step which includes Gene matching (Using JAVA) and data arrangement; quantile function was adopted to calculate the threshold for any cell to be pluripotent. This generated threshold is based upon the Log FC value (Fold Change value) of the particular gene. After getting threshold, another data for test sample was taken and again after repeating the same process (as done for control sample), after this the log FC value of test sample was checked. Now, our main concern is to check that at what level the cell contains pluripotency? Since the cells that pass the threshold could either be multipotent or totipotent, therefore, we have developed a JAVA program. This JAVA program is trained by giving it a particular range for particular key regulator gene in both of ESC and iPSC condition. The result of the program is divided into three categories viz. Highly Pluripotent, Partial pluripotent, Low Pluripotent. This approach is a novel work for pluripotency determination as it uses the text format input file and a new robust method has been developed using Bioinformatics as a tool [18], [19], [20], [21], [22], [23], [24].

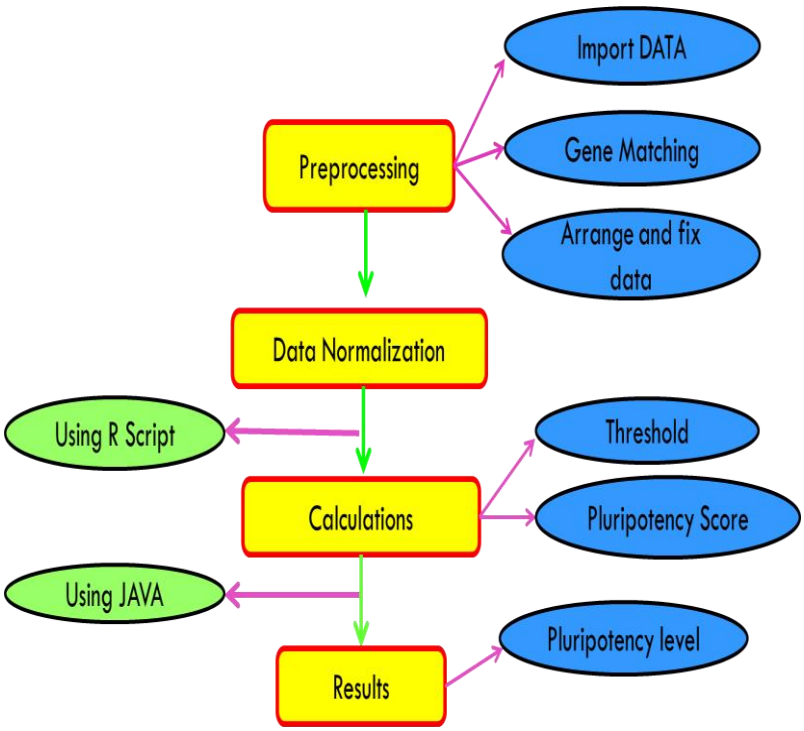


Fig.1: Defining various stages used in this method for finding pluripotency of any cell.

© 2018 Life Science Informatics Publication All rights reserved

3. RESULTS AND DISCUSSION

The list of marker genes present in any stem cell which decides the pluripotency level of an undifferentiated cell was created. These genes were isolated by using different techniques viz. MACS (Magnetic Cell Sorting Technique) and FCM (flow cytometry) technique which is one of the most effective cell isolating methods [7].

Table 1: List of 175 signature markers used for identifying Stem cells.

SUV39H1	SMAD1	LECTINS	KLF4	CD57	CD86	STELLA
SUV39H2	SMAD5	CD133	NANOG	CD58	CD87	TRA-2-54
EHMT2	SMAD8	CD96	REX1	CD59	CD88	CD45
EHMT1	SMAD4	CD34	UTF1	CD60	CD89	CD56
SETDB1	SMAD2	CD38	ZFX	CD61	CD90	CD85
RING1B	SMAD3	CD45	TBN	CD62	CD326	ECSA
EZH2	BETA CATENIN	CD46	FOXD3	CD63	CD9	TM4SF
EED	SSEA1	CD47	HMGA2	CD64	CD55	TRA-2-49
SUZ12	CD15	CD48	NAC1	CD65	CD59	OCT4
DICER1	SSEA3	CD49	GCNF	CD66	CD24	SOX2
DNMT1	SSEA4	CD50	NR6A1	CD67	CD44	CD54
DNMT3a	CD324	CD51	STAT3	CD68	SATA3	CD55
DNMT3b	CD90	DRAP27	LEF1	CD69	NCA1	CD83
DNMT3L	CD117	P24	TCF3	CD70	ALDH1	CD84
CXXC1	CD326	CKIT	SALL4	CD71	MUSASHI-1	DPPA3
BRG1	CD9	SCFR	FBXO15	CD72	LgR5	CD82
SMARCA4	CD29	THY-1	ECAT11	CD73	PSCA	CD53
SMARCA5	CD24	TRA-1-60	FLJ10884	CD74	DCAMKL-1	OCT3
SMARCB1	CD59	TRA-1-81	L1TD1	CD75	TIM3	MRP1
SMARCC1	CD133	FRIZZLED5	ECAT1	CD76	BRCA1	DPPA2
MBD3	CD32	SCF	ECAT9	CD77	SDF1	
HIR A	CD49F	C-KIT	GDF3	CD78	CXCR4	
DPPA5	CD96	TDGF-1	TGF Beta	CD79	PSCA	
ESG1	HAS	CRIPTO	TCF1	CD80	CD96	
DPPA4	PROTECTIN	POU5F1	CD52	CD81	CD44	

To validate our findings of marker genes, we create an interaction network of all these above genes to check whether they are interaction partners or not. This result assures us that the given marker

© 2018 Life Science Informatics Publication All rights reserved

genes are interacting partners of key regulatory genes, i.e., OCT-4, NANOG, SOX2, KLF4 and are showing great interaction score with each other, which confirms us the presence of all these genes in the pluripotent cell. STRING provided us with the nodes which are commonly interacting with most of the genes and are having highest scores, i.e., POU5F1, NANOG, KLF4, SOX2, SALL4, SMAD2, SMAD4, and DPPA4. Another network was plotted using the resultant common genes which we got from the parent network.

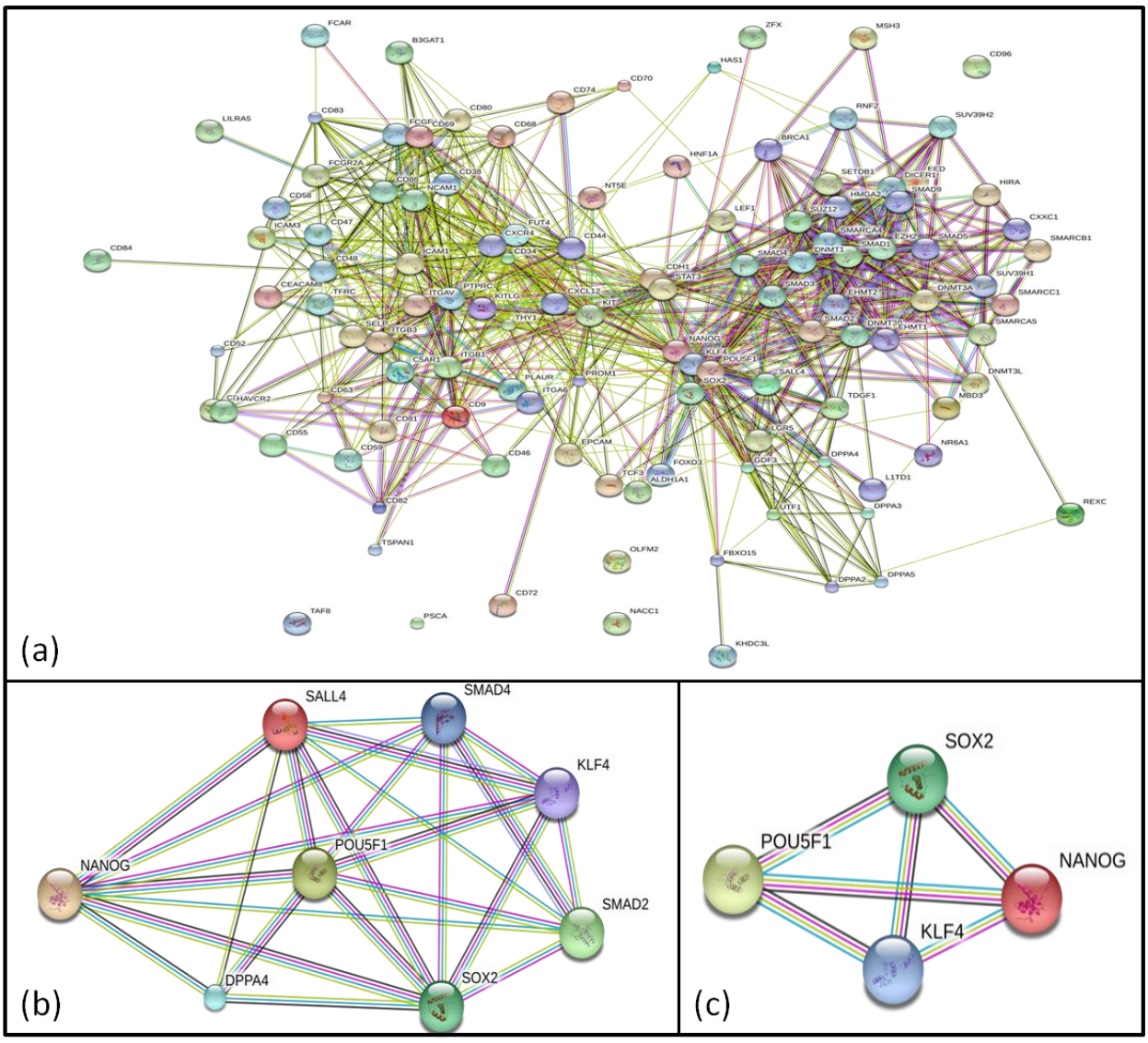


Fig.2: (a) Representation of Interaction network between various 175 Pluripotency Marker Genes identified by using STRING, each sphere (node) represents the particular gene. (b) A more specific STRING network is showing important genes responsible for pluripotency. (c) The final network with four key factors namely SOX2, NANOG, POU5F1, and KLF4.

We found that POU5F1, SOX2, NANOG, KLF4 are most commonly interacts. Thus an interaction network using STRING consisting of these four genes was plotted. Finally, genes with the most number of interactions and with highest no. of scores were obtained. By this we inference that the

© 2018 Life Science Informatics Publication All rights reserved

presence of these three genes and their expression values in microarray data could be the defining factor for the level of pluripotency in any cell. Now, our next step is to initially find out the state of any cell, i.e., whether it is pluripotent or not. For this, our first step is to determine the threshold for the genes of the cells. The cell has to pass this threshold before evaluating further. For this, we had taken Microarray data because this is the only way to check the expression value of the genes. The data we take is in TEXT file format, because of its availability. Firstly, the Microarray data containing Reference ID (Different for different types of analysis viz. "ILMN_xxxx" for Illumina analyzed data, "xxxx_s_at" for Affymetrix Data, "xxxxx" for Agilent Data), LogFC (Fold Change value showing Upregulation(+) and downregulation(-) of genes), Gene symbol etc. was downloaded for whole genome of human iPSC and ESC cell lines (GSE72078) from GEO datasets of National Centre for Biotechnology Information (NCBI) by analyzing with GEO2R (A GEO Tool available for visualization of Microarray data along with other relevant calculated statistical parameters). Now downloaded data was pasted into excel sheet with their respective gene expression values taken from series matrix file data. The data was then compared and matched with the expression values of available marker genes.

	N	O	P	Q	R	S	T	U	V	W	X
1	ID	GSM1854259	GSM1854260	GSM1854261	GSM1854262	GSM1854263	GSM1854264	GSM1854265	GSM1854266	GSM1854267	GSM1854268
2	ILMN_1801832	144.2388	156.737	147.6424	153.3328	166.7805	154.4627	157.0698	154.4065	156.8566	159.131
3	ILMN_1739810	172.5428	138.1559	159.8204	154.4375	153.6577	155.6567	183.7435	159.407	165.9471	175.239
4	ILMN_1654563	236.2552	210.4926	203.3152	216.7573	247.0767	203.9029	175.7356	202.5546	250.2343	196.815
5	ILMN_1801441	234.1016	195.04	196.5564	181.2354	201.2363	207.5756	213.9989	176.9021	196.6347	171.438
6	ILMN_1685709	2958.677	2873.692	2679.544	2810.01	2251.323	2741.401	2670.944	2362.221	2110.924	2609.41
7	ILMN_1710644	1150.73	1295.111	897.0232	991.2095	1004.035	1183.217	1218.794	1168.913	1068.282	1109.8
8	ILMN_1678215	186.1575	180.2909	202.7035	202.42	176.5194	192.3483	177.2236	179.3007	197.6062	200.246
9	ILMN_1795063	224.9271	185.7115	180.7282	178.4986	194.3223	207.4067	215.1077	191.1285	180.1656	191.809

(a)

	A	B	C	D	E	F	G	H	I	J	K	L	M	N
1	ID	Gene (20761)	GSM1854259	GSM1854260	GSM1854261	GSM1854262	GSM1854263	GSM1854264	GSM1854265	GSM1854266	GSM1854267	GSM1854268	GSM1854269	GSM1854270
2	ILMN_1801832	PRAC1	0.387405284	0.420973705	0.396546879	0.411830499	0.447949144	0.414865253	0.421867559	0.414714307	0.421294934	0.427404998	0.778046493	7.057100945
3	ILMN_1739810	RAI1	0.805181688	0.644713085	0.745811819	0.720692182	0.717053197	0.726381654	0.85745045	0.743882662	0.774402445	0.81776414	0.981175944	3.465490735
4	ILMN_1654563	EFNB1	0.844701539	0.752590517	0.726928603	0.774989185	0.883392487	0.729029852	0.62832112	0.72420917	0.8946821	0.703690079	0.923072028	3.41439332
5	ILMN_1801441	RFTN2	0.990015439	0.824823971	0.831236825	0.766444331	0.851028117	0.877837011	0.90500114	0.748118809	0.831567955	0.725014519	0.879301513	2.769610371
6	ILMN_1685709	TMEM125	1.224048607	1.188889051	1.10856714	1.162542862	0.931405754	1.1341583	1.105009193	0.977285903	0.873320603	1.079554145	0.950352239	0.264866204
7	ILMN_1710644	MARVELD3	1.10544626	1.244145552	0.861723377	0.95220324	0.964524029	1.136654825	1.170831793	1.122913719	1.026242769	1.066165371	1.057928776	0.291220289
8	ILMN_1678215	RHOJ	0.806467102	0.781051956	0.87814729	0.876919118	0.764713154	0.833286738	0.767763872	0.776762235	0.856064888	0.867504866	1.062662041	2.728656739
9	ILMN_1795063	ZADH2	0.989280349	0.816801255	0.794883572	0.785077286	0.854673504	0.91222166	0.946092403	0.840626448	0.79240913	0.843621641	0.940537883	2.483774869

(b)

$$\bullet \text{Mean} = \sum (xi) / ni$$

$$\text{Normalization} = \frac{\text{(Expression value of Gene in particular cell line)}}{\text{(Mean of exp. Values of same gene for all cell lines present in a single microarray text file)}}$$

Fig.3 (a) Table is showing Non-Normalized Microarray data (GSE72078) in excel sheet collected from GEO datasets. (b) Normalized microarray data (using Simple normalization function).

After this, we matched our 175 Marker genes with the existing list of NCBI and downloaded expression dataset's gene list by using JAVA program (specially designed for a finding of no. of

© 2018 Life Science Informatics Publication All rights reserved

marker genes present in the microarray data.

(a)

	A	B	C	D	E	F	G	H	I	J	K	L	M	N	O	P
1	ID_REF	Marker Genes	GSM1854259	GSM1854260	GSM1854261	GSM1854262	GSM1854263	GSM1854264	GSM1854265	GSM1854266	GSM1854267	GSM1854268	GSM1854269	GSM185427(	MEAN	log FC
2	ILMN_1738027	BRCA1	1.064204111	1.066910637	0.965772187	1.09517898	1.345089308	0.974611536	0.998565585	0.899985541	0.958697512	0.839551234	0.952575873	0.938728492	1.014649319	-0.12527768
3	ILMN_1805519	CD24	1.196464773	1.040636825	1.301754131	0.996958167	1.252667183	0.930427417	0.92839336	1.001318172	1.008611195	1.105111121	0.765862159	0.470571716	1.048018591	-0.59732382
4	ILMN_1694249	CD34	1.024213606	0.894395907	1.238996798	1.100989896	0.854721278	1.043513987	1.09149786	1.032396097	1.123224717	1.005482759	0.724232411	0.830974413	1.012151392	-0.2849001
5	ILMN_2233783	CD38	1.085565516	0.990348968	1.086241524	1.106629858	0.970284986	0.936206686	0.899269082	1.074289082	1.058622423	0.980541403	0.766270588	0.978924009	0.995842738	-0.12996308
6	ILMN_2348788	CD44	0.90048684	0.912958184	0.946984156	1.0087967	0.82863746	1.250788363	0.863549741	1.048655802	0.894837587	1.103556801	1.116497157	1.082234505	0.988704435	0.16475052
7	ILMN_2356991	CD47	0.968547352	1.285079635	1.020318057	0.993303393	1.103452372	1.034778726	1.095759716	0.810300124	1.098673082	1.069420079	0.930763114	0.797469831	1.037308696	-0.30976962
8	ILMN_2061043	CD48	0.877290148	0.936345764	0.844818449	0.859343886	0.870955979	0.847054783	0.875236121	1.162328315	1.255922436	1.224232326	1.011248911	1.093147276	0.978616102	0.18045392
9	ILMN_2208903	CD52	0.912569576	0.799117033	1.555364753	0.87609174	0.975012858	0.823189901	1.468912006	0.907738466	1.288711677	0.843155439	1.041305969	0.644354657	1.044651765	-0.26161893
10	ILMN_2413808	CD53	1.033037513	0.947970973	1.35117844	1.046216812	1.151531076	1.00063113	1.058095218	1.019360858	0.972766203	0.965203446	0.890587874	0.542934825	1.039689049	-0.41709316
11	ILMN_1800540	CD55	1.510996663	1.114243247	0.720050278	0.862982432	0.980763459	1.17947849	1.18971784	0.906015107	1.143500298	0.994915496	0.728662439	0.780489756	1.030120523	-0.38216103

Quantile function => Q (p) = (1 – f) Q (pi) + f Q (pi+1)

(b)

Threshold					
	0%	25%	50%	75%	100%
0.6193309	-2.8293789	-0.366737	0.350824	0.692554	5.249393

Fig.4 (a) Table is showing marker genes with reference IDs and their respective expression values in each cell line. Also, Calculated Mean and log FC values are shown. (b) The calculated Threshold value for detection of pluripotency using Quantile Normalization method through R script (Threshold = 0.6193309).

Total 68 Marker Genes are matched with the Genes of Microarray Data of GSE72078 cell lines. After normalization we took the data for prediction of Threshold using Quantile function through R Studio, this approach gives five different quantile calculated values including min. And max.; after taking the mean for these values, we got our Threshold, i.e., 0.62, which implies that if any cell passes this threshold, then it could say to be pluripotent. Now, the next step is to check the pluripotency status for a sample dataset (Test Sample). For this, we had taken a colon IPSC Cell line. The microarray data was downloaded for Colon IPSC's (GSE93228- Cell lines iPSC CRL1831 (induced pluripotent stem cells) derived from normal colon CRL1831 cells in 3D cell culture conditions and subjected to ionizing radiation doses) and then after arranging and preprocessing the data we check whether the cell lines are Stem cell lines or not. If they all are stem cell lines then we simply check their pluripotency score by taking the quantile normalization of their Log FC value, but if the data consist of both differentiated and undifferentiated cell lines then we have to take mean of each cell line's expression values and then match with the Threshold limit to check whether they are passing the set Threshold value or not. If the resultant score is less than the threshold, then that cell could be either Unipotent, totipotent, multipotent or differentiated somatic cell line.

© 2018 Life Science Informatics Publication All rights reserved

	ID	GENE_SYMBOL	GSM2448894	GSM2448895	GSM2448896
2	A_23_P34915	ATF3	0.07570648	0.14384651	0.08829689
3	A_23_P155890	NAA11	0.16908455	0.19882202	0.12617302
4	A_24_P246173	MYO9B	0.36398697	0.4689827	0.34682274
5	A_23_P146077	ZNF395	-0.020715714	-0.045152664	-0.020601273
6	A_32_P175739	HK2	0.25235748	0.37810516	0.20498085
7	A_33_P3419785	BNIP3	-0.0845108	-0.082969666	-0.05378151
8	A_33_P3350863	RETN	0.13268661	0.1523037	0.05083847
9	A_23_P214080	EGR1	0.3584175	0.5151024	0.41786766

(a)

	ID_REF	MATCHED GENES	GSM2448894	GSM2448895	GSM2448896	GSM2448897	GSM2448898	GSM2448899	MEAN	S.D.
2	A_23_P207400	BRCA1	1.38351364	1.376838746	0.38318811	0.386125862	1.44940836	1.020925282	1	0.499758794
3	A_23_P34676	CD24	0.744272163	1.607417099	0.894782913	1.011844222	0.592505176	2.29061474	1.190239386	0.641896483
4	A_23_P23829	CD34	-0.487966744	-0.064981111	0.228951986	-0.454359769	-0.21306606	0.714796164	-0.046104256	0.457115519
5	A_23_P167328	CD38	0.081032442	0.110366682	-0.048461156	0.63797343	-0.739991542	0.225116369	0.044339371	0.450460792
6	A_33_P3294509	CD44	0.101691245	0.504888381	0.508086052	0.356673482	-0.466319512	0.434216842	0.239872748	0.377196325
7	A_23_P35230	CD46	0.71376834	0.648747814	1.088147118	0.979391078	0.293287274	0.96256396	0.780984264	0.292074745
8	A_23_P6935	CD47	-0.759760354	-1.632580949	0.288360808	0.522507044	-0.612502401	-2.145987339	-0.723327198	1.043065612
9	A_32_P175934	CD48	0.037592248	0.105475673	-0.092192765	-0.156811571	0.701580185	-0.39111532	0.034088075	0.369822021

(b)

Fig.5: (a)Table Showing Test Sample consisting of GENE symbol with their expression values in respective cell lines of Colon IPSC (total 6 IPSC cell lines are taken after neglecting somatic cell lines data). (b)Table after matching our Marker genes with the Genes of Microarray Data of GSE93228 cell lines we obtained 71 matched entries by using JAVA developed program.

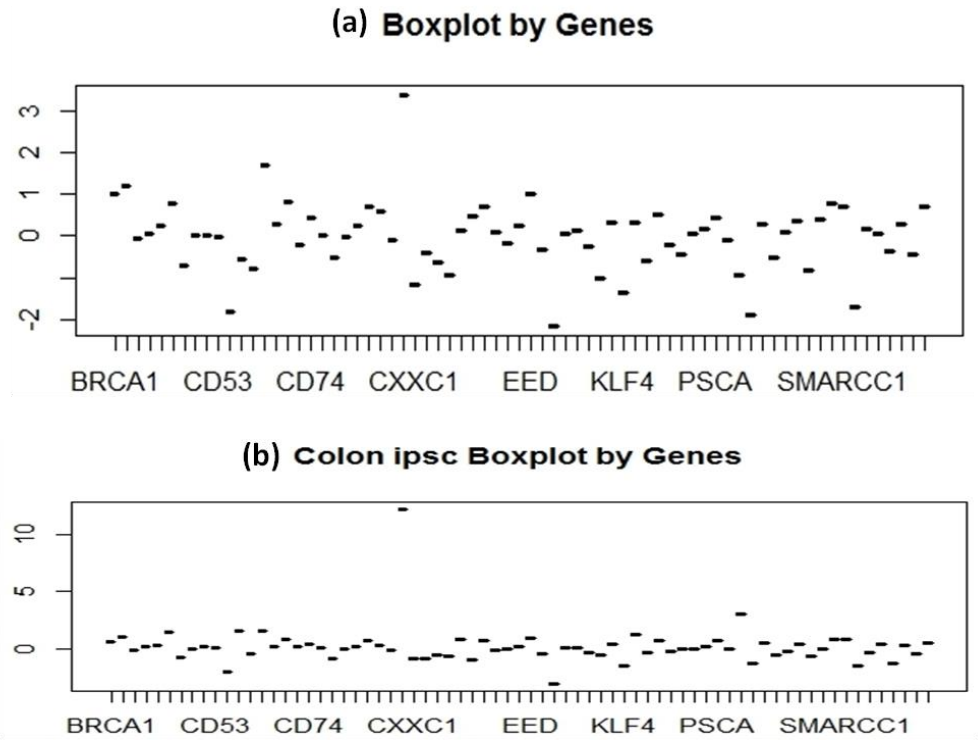


Fig.6: (a) Boxplot is showing non-normalized gene expression data of GSE93228, depicting discreteness of the values. (b) Boxplot showing Normalized gene expression values in a linear manner

© 2018 Life Science Informatics Publication All rights reserved

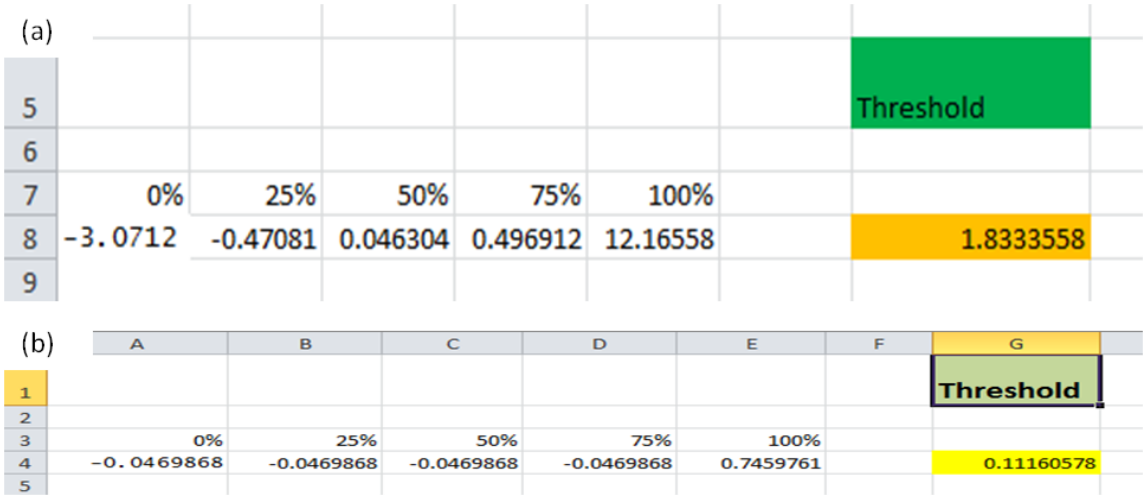


Fig.7: (a) The Pluripotency score is calculated again using R Script as earlier, and it passed the Threshold value. Hence we can say that the Cell line for Microarray data of GSE 93228 sample is pluripotent. (b)After the calculation of pluripotency score using Quantile function we deliberately checked mast cell data which could not pass the Threshold value.

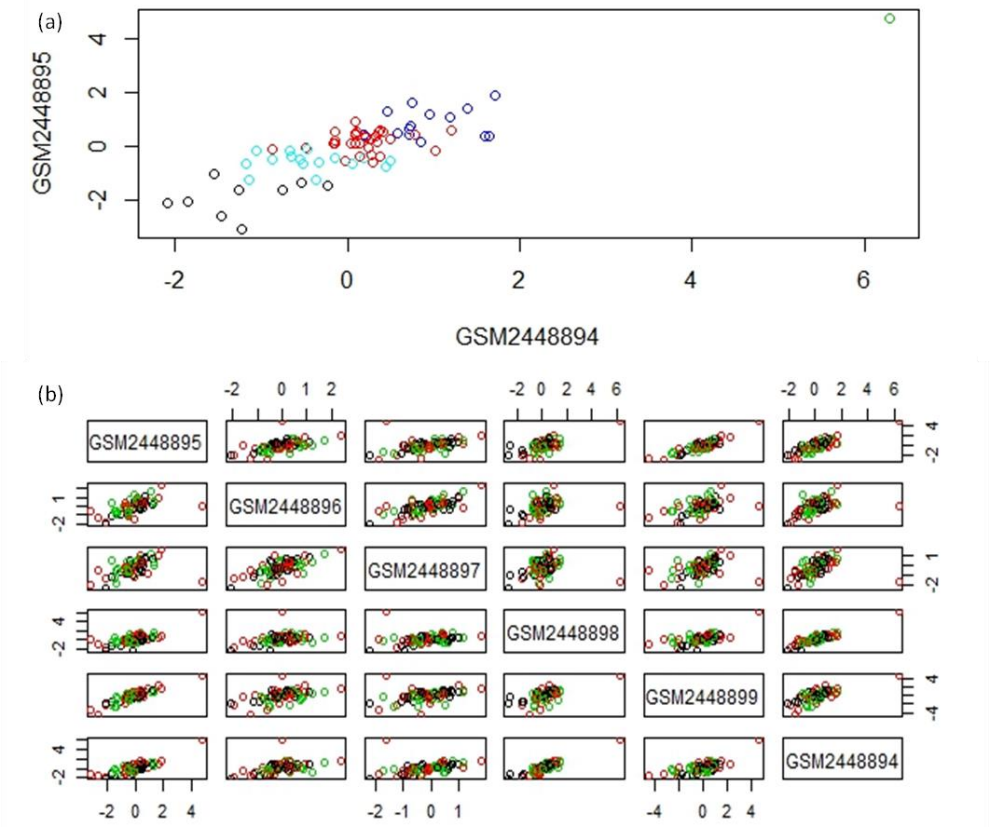


Fig.8: (a) Graph is showing clustered cell line from test sample by Gene expression data by using K-Means clustering through R Script for the development of Hierarchical clustering in Heatmap. (b)Figure showing K-Means clustered data of all six cell lines of test data sets created using R Script.

© 2018 Life Science Informatics Publication All rights reserved

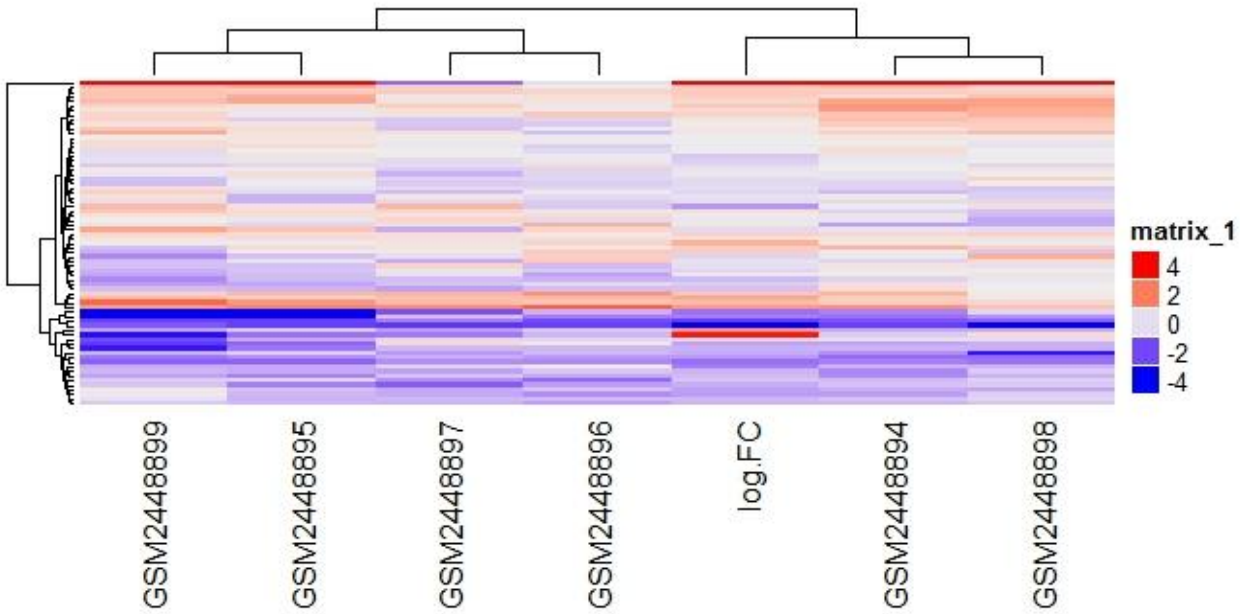


Fig.9: Heatmap Generated for all test sample's cell line's gene expression data using the R program.

After this, we analyze the level of Pluripotency using JAVA Program. For this, we initially set up a range parameter for all key regulator genes in three different ways viz.

1) Highly Pluripotent cells.

2) Partially Pluripotent cells.

3) Less Pluripotent cells.

Table 2	IPSC Range		ESC Range	
	Is Data Manually Normalized or Not			
	YES	NO	YES	NO
1)	5.0 to 9.0	-1.5 to 5.0	2.0 to 3.0	-0.25 to 2.0
2)	2.0 to 4.9	-2.0 to -1.51	1.5 to 1.9	-3.0 to -0.249
3)	-3.0 to 1.9	-3.0 to -2.1	1.2 to 1.49	-15.0 to -2.9

This Range is based upon the manually compared and calculated expression values of key regulators from Different samples (Microarray Samples) viz. (GSE72078, GSE76282, GSE42445, etc.) present in GEO datasets and depend upon the condition that either the data is pre-normalized or manually normalized. For both, the conditions the range is individually provided in each case of ESC as well as IPSC.

© 2018 Life Science Informatics Publication All rights reserved
Peer review under responsibility of Life Science Informatics Publications

Control sample (GSE72078) Pluripotency level determination:

Range: >=-3.0 to <=1.9
Range: GSM1854259
NANOG= 0.88792694
POU5F1= 0.94814897
SOX2= 1.6156561
Less Pluripotent Cell= GSM1854259
Range: >=-3.0 to <=1.9
Range: GSM1854260
NANOG= 0.87607163
POU5F1= 0.9470426
SOX2= 1.1104767
Less Pluripotent Cell= GSM1854260
Range: >=-3.0 to <=1.9
Range: GSM1854261
NANOG= 0.45721972
POU5F1= 0.79864424
SOX2= 0.9874374
Less Pluripotent Cell= GSM1854261
Range: >=-3.0 to <=1.9
Range: GSM1854262
NANOG= 0.70601815
POU5F1= 1.1790252
SOX2= 0.38984066
Less Pluripotent Cell= GSM1854262

Range: >=-3.0 to <=1.9
Range: GSM1854263
NANOG= 0.472952348
POU5F1= 1.056011706
SOX2= 1.505724634
Less Pluripotent Cell= GSM1854263
Range: >=-3.0 to <=1.9
Range: GSM1854264
NANOG= 1.0276734
POU5F1= 0.79453945
SOX2= 1.4517218
Less Pluripotent Cell= GSM1854264
Range: >=-3.0 to <=1.9
Range: GSM1854265
NANOG= 1.022949722
POU5F1= 1.046684461
SOX2= 1.192202724
Less Pluripotent Cell= GSM1854265
Range: >=-3.0 to <=1.9
Range: GSM1854266
NANOG= 1.0564212
POU5F1= 0.88678443
SOX2= 0.42901477
Less Pluripotent Cell= GSM1854266

Range: >=-3.0 to <=1.9
Range: GSM1854267
NANOG= 0.668517
POU5F1= 0.81713855
SOX2= 1.1758825
Less Pluripotent Cell= GSM1854267
Range: >=-3.0 to <=1.9
Range: GSM1854268
NANOG= 0.73580366
POU5F1= 0.9113936
SOX2= 0.42615175
Less Pluripotent Cell= GSM1854268
Range: >=-3.0 to <=1.9
Range: GSM1854269
NANOG= 1.5778602
POU5F1= 1.2110461
SOX2= 0.12783645
Less Pluripotent Cell= GSM1854269
Range: >=-3.0 to <=1.9
Range: GSM1854270
NANOG= 1.45287005
POU5F1= 1.2110461
SOX2= 1.522041676
Less Pluripotent Cell= GSM18542

Test Sample (GSE93228) Pluripotency level determination:

Range: >=-1.5 to <=5.0
Range: GSM2448894
NANOG= 0.053198583
POU5F1= 0.4979063
SOX2= -1.2365668
Highly Pluripotent Cell= GSM2448894
Range: >=-1.5 to <=5.0
Range: GSM2448895
NANOG= -0.661888992
POU5F1= 0.231759788
SOX2= -1.089963819
Highly Pluripotent Cell= GSM2448895

Range: >=-1.5 to <=5.0
Range: GSM2448896
NANOG= -0.089637
POU5F1= -0.07959507
SOX2= -0.59168214
Highly Pluripotent Cell= GSM2448896
Range: >=-1.5 to <=5.0
Range: GSM2448897
NANOG= -0.03093701
POU5F1= 0.239970536
SOX2= -1.397995012
Highly Pluripotent Cell= GSM2448897

Range: >=-1.5 to <=5.0
Range: GSM2448898
NANOG= 0.001854803
POU5F1= 0.20897053
SOX2= -0.087790065
Highly Pluripotent Cell= GSM2448898
Range: >=-1.5 to <=5.0
Range: GSM2448899
NANOG= -1.496865928
POU5F1= -0.03865551
SOX2= -1.2365668
Highly Pluripotent Cell= GSM2448899

Fig.10: Result for Pluripotency level determination through JAVA program

© 2018 Life Science Informatics Publication All rights reserved

For Pluripotency level determination we first took the control sample. Our program first checks whether the cell lines are IPSC or ESC. Then after confirming that the cell lines are for IPSC. It asked for whether the microarray data was manually normalized or not and then according to our entries for IPSC cell line with manually normalized data, the program took to consider the range for this condition and gave us the results that in which category or level the given sample is lying. In our control results show that the cells are least pluripotent in normalized IPSC range. Same is the case of test sample our program initially took the same step as done for control and then decides the level of pluripotency. Here, in our test sample, the condition came out for non manually normalized IPSC data and hence, we got the results for that condition range. We also took test sample datasets from different other arrays too like GSE92706 and GSE73330 which were found to be passed and failed respectively. For confirming our results, we cross-check our results with PLURITEST by taking the above IDs data in (.idat*) raw intensity file format, and after analyzing with PLURITEST, the result we got are surprisingly as same as ours. By, this we conclude that the method which we develop to test pluripotency using (.txt) text file format is worth to work with and giving favorable as well as satisfactory results. Here we have shown only results for GSE92706. The comparable results of tested sample with different approaches (i.e., using a text format and .idat format) are shown in figures. From our study, we found that the potency determination is a key factor of gene expression analysis and by considering only the gene effect we could determine various activities of cells including pluripotency. This in vitro approach is competing with other pre available online tools. Such tools are still dealing with some bugs as by considering the only limited number of files and with limited file format reliability. Also, their dependency on online servers are making them not 100% fit for potency determination, but in our case, the approach is working on the text file based logic of creating and arranging raw text file into matched and arranged file format concerning the gene expression values and Log FC. The level of pluripotency which we are calculating through JAVA determines us three levels, where each level gives us an idea about the potency of that particular cell to be differentiated into the basic three lineages. Highest level determines the potency of differentiating into all three lineages, whereas partial and low level determines us the differentiation into either two or one of the three lineages respectively. This approach gave us the way for determining the potency using computer programming language JAVA and statistical method based R Script, which was used in arranging data according to the matched marker genes and finally in the determination of Level of pluripotency using various ranges. Several graphs and plots viz. boxplots, clustering graphs, and heatmap were also developed using an R script. This approach will surely provide open access for identifying pluripotency and understanding the working and expression nature of various genes involved in reprogramming strategies.

© 2018 Life Science Informatics Publication All rights reserved

4. CONCLUSION

Microarray data proves beneficial in many regards. To get detailed info about any process related to protein or gene expression or their interaction we do need to take help from it. As in the above study, we found that to get pluripotency test of any cell sample. First, we have to access gene expression data of that particular cell. Followed by grabbing and arranging that data in a proper format, we will be able to fetch pluripotency data after checking whether the log FC value for that test sample either passing the threshold or not. Using this approach we are now in a state to tackle various problems associated with pre-existing online tools. We can make our tool based on this approach which will be free from various bugs that are present in existing tools; also we can identify which gene is devoting more in making any cell pluripotent. Through this approach, we can determine the pluripotency state of test cell regardless of any particular platform or any file format.

5. ACKNOWLEDGEMENT

We thank the honorable Vice Chancellor, Delhi Technological University, for providing essential support for carrying out the research.

6. CONFLICT OF INTEREST

The authors declare no conflict of interest.

REFERENCES

1. Takahashi K, Tanabe K, Ohnuki M, Narita M, Ichisaka T, Tomoda K, Yamanaka S. Induction of pluripotent stem cells from adult human fibroblasts by defined factors. cell. 2007 Nov 30;131(5):861-72.
2. Solter D. From teratocarcinomas to embryonic stem cells and beyond: a history of embryonic stem cell research. Nature Reviews Genetics. 2006 Apr;7(4):319.
3. Niwa H, Miyazaki JI, Smith AG. Quantitative expression of Oct-3/4 defines differentiation, dedifferentiation or self-renewal of ES cells. Nature genetics. 2000 Apr;24(4):372.
4. Mitsui K, Tokuzawa Y, Itoh H, Segawa K, Murakami M, Takahashi K, Maruyama M, Maeda M, Yamanaka S. The homeoprotein Nanog is required for maintenance of pluripotency in mouse epiblast and ES cells. cell. 2003 May 30;113(5):631-42.
5. Chambers I, Colby D, Robertson M, Nichols J, Lee S, Tweedie S, Smith A. Functional expression cloning of Nanog, a pluripotency sustaining factor in embryonic stem cells. Cell. 2003 May 30;113(5):643-55.
6. Boyer LA, Lee TI, Cole MF, Johnstone SE, Levine SS, Zucker JP, Guenther MG, Kumar RM, Murray HL, Jenner RG, Gifford DK. Core transcriptional regulatory circuitry in human embryonic stem cells. cell. 2005 Sep 23;122(6):947-56.
7. Zhao W, Ji X, Zhang F, Li L, Ma L. Embryonic stem cell markers. Molecules. 2012 May 25;17(6):6196-236.

© 2018 Life Science Informatics Publication All rights reserved

8. Müller FJ, Schuldt BM, Williams R, Mason D, Altun G, Papapetrou EP, Danner S, Goldmann JE, Herbst A, Schmidt NO, Aldenhoff JB. A bioinformatic assay for pluripotency in human cells. Nature methods. 2011 Mar 6;8(4):315.
9. Cahan P, Li H, Morris SA, Da Rocha EL, Daley GQ, Collins JJ. CellNet: network biology applied to stem cell engineering. Cell. 2014 Aug 14;158(4):903-15.
10. Avior Y, Biancotti JC, Benvenisty N. TeratoScore: assessing the differentiation potential of human pluripotent stem cells by quantitative expression analysis of teratomas. Stem cell reports. 2015 Jun 9;4(6):967-74.
11. Gokhale PJ, Andrews PW. The development of pluripotent stem cells. Current opinion in genetics & development. 2012 Oct 31;22(5):403-8.
12. Niwa H. How is pluripotency determined and maintained?. Development. 2007 Feb 15;134(4):635-46.
13. Singh VK, Kalsan M, Kumar N, Saini A, Chandra R. Induced pluripotent stem cells: applications in regenerative medicine, disease modeling, and drug discovery. Frontiers in cell and developmental biology. 2015 Feb 2;3:2.
14. Liu Y, Cheng D, Li Z, Gao X, Wang H. The gene expression profiles of induced pluripotent stem cells (iPSCs) generated by a non-integrating method are more similar to embryonic stem cells than those of iPSCs generated by an integrating method. Genetics and molecular biology. 2012;35(3):693-700.
15. Loh YH, Wu Q, Chew JL, Vega VB, Zhang W, Chen X, Bourque G, George J, Leong B, Liu J, Wong KY. The Oct4 and Nanog transcription network regulates pluripotency in mouse embryonic stem cells. Nature genetics. 2006 Apr;38(4):431.
16. Perez-Iratxeta C, Andrade-Navarro MA, Wren JD. Evolving research trends in bioinformatics. Briefings in Bioinformatics. 2006 Oct 31;8(2):88-95.
17. Tiemann U, Marthaler AG, Adachi K, Wu G, Fischedick GU, Araúzo-Bravo MJ, Schöler HR, Tapia N. Counteracting activities of OCT4 and KLF4 during reprogramming to pluripotency. Stem cell reports. 2014 Mar 11;2(3):351-65.
18. Zhao JH, Tan Q. Integrated analysis of genetic data with R. Human genomics. 2006 Dec;2(4):258.
19. Nestor MW, Noggle SA. Standardization of human stem cell pluripotency using bioinformatics. Stem cell research & therapy. 2013 Jun;4(2):37.
20. Babu PB, Krishnamoorthy P. Applications of Bioinformatics Tools in Stem Cell Research: An Update. Journal of Pharmacy Research Vol. 2012 Sep;5(9):4863-6.

© 2018 Life Science Informatics Publication All rights reserved

21. Dudoit S, Yang JY. Bioconductor R packages for exploratory analysis and normalization of cDNA microarray data. InThe analysis of gene expression data 2003 (pp. 73-101). Springer, New York, NY.
22. Som A, Harder C, Greber B, Siatkowski M, Paudel Y, Warsow G, Cap C, Schöler H, Fuellen G. The PluriNetWork: an electronic representation of the network underlying pluripotency in mouse, and its applications. PloS one. 2010 Dec 10;5(12):e15165.
23. Zhao W, Ji X, Zhang F, Li L, Ma L. Embryonic stem cell markers. Molecules. 2012 May 25;17(6):6196-236.
24. Huber W, Heydebreck AV, Vingron M. Analysis of microarray gene expression data. InHandbook of Statistical Genetics 2003 Jul. John Wiley & Sons, Ltd.

© 2018 Life Science Informatics Publication All rights reserved

Eur. Phys. J. D (2018) 72: 157
https://doi.org/10.1140/epjd/e2018-90199-2

THE EUROPEAN PHYSICAL JOURNAL D

Regular Article

Distinguishing different classes of entanglement of three-qubit pure states

Chandan Datta[1,2,a], Satyabrata Adhikari[3], Arpan Das[1,2], and Pankaj Agrawal[1,2]

[1] Institute of Physics, Sachivalaya Marg, Bhubaneswar 751005, Odisha, India
[2] Homi Bhabha National Institute, Training School Complex, Anushakti Nagar, Mumbai 400085, India
[3] Delhi Technological University, Shahbad Daulatpur, Main Bawana Road, Delhi 110042, India

Received 27 April 2018 / Received in final form 13 June 2018
Published online 13 September 2018
© EDP Sciences / Società Italiana di Fisica / Springer-Verlag GmbH Germany, part of Springer Nature, 2018

Abstract. Employing the Pauli matrices, we have constructed a set of operators, which can be used to distinguish six inequivalent classes of entanglement under stochastic local operation and classical communication (SLOCC) for three-qubit pure states. These operators have very simple structure and can be obtained from the Mermin's operator with suitable choice of directions. Moreover, these operators may be implemented in an experiment to distinguish the types of entanglement present in a state. We show that the measurement of only one operator is sufficient to distinguish GHZ class from rest of the classes. It is also shown that it is possible to detect and classify other classes by performing a small number of measurements. We also show how to construct such observables in any basis. We also consider a few mixed states to investigate the usefulness of our operators. Furthermore, we consider the teleportation scheme of Lee et al. [Phys. Rev. A **72**, 024302 (2005)] and show that the partial tangles and hence teleportation fidelity can be measured. We have also shown that these partial tangles can also be used to classify genuinely entangled state, biseparable state and separable state.

1 Introduction

Entanglement is one of the key features of quantum mechanics, which differentiates quantum world from the classical world. It is an essential resource for many information processing tasks, such as quantum cryptography [1], teleportation [2,3], super-dense coding [4,5] etc. Also from the foundational perspective of quantum mechanics, entanglement is unparalleled for its supreme importance. Therefore, its characterization and quantification is very important from both theoretical as well as experimental point of view.

A lot of research have been carried out to understand entanglement qualitatively and quantitatively. Quantification and characterization of entanglement is unambiguous for pure bipartite state, but not for the mixed states [6–8]. In the spirit of resource theory of entanglement [6,9], two entangled states are said to be equivalent if they can be obtained from each other with certainty with respect to local operation and classical communication (LOCC). Entanglement of any pure bipartite state is uniquely captured by the entropy of entanglement in the asymptotic limit [10]. But this is not true for mixed states. There is no unique quantification of entanglement for this case and a number of entanglement measures and monotones [7] have been constructed over the years. Situation gets worse for multipartite scenario, both for pure and mixed states. One can straightforwardly extend some of the entanglement measures and monotones constructed for bipartite systems to multipartite scenario, but there is no unique quantification of entanglement in multipartite scenario even for pure states. We can not even define a unique maximally entangled multipartite state and there are many inequivalent forms of entanglement in the asymptotic limit [11–14]. In this paper, we will restrict ourselves to the entanglement properties of a single copy of a pure multipartite state. For a single copy, two states are LOCC equivalent if and only if they are related by local unitary (LU) [14,15]. But in the single copy restriction, even two bipartite pure states are not typically related by LU. To evade this difficulty, the LOCC operation, through which the conversion of entangled states is considered is slightly loosened. One now considers the conversion of states through stochastic local operation and classical communication (SLOCC), i.e two entangled states are converted to each other by means of LOCC but with a non-vanishing probability of success [14]. Two states are now called SLOCC equivalent if they can be obtained from each other under SLOCC, otherwise they are SLOCC inequivalent. For three-qubit pure states all possible SLOCC inequivalent classes have been characterized [16]. There are six SLOCC inequivalent classes: separable, three bi-separable and two genuinely entangled

[a] e-mail: chandan@iopb.res.in

(GHZ and W). In general it is very difficult to characterize and distinguish different classes from each other. For three-qubit pure states analytical characterization is present in literature using local entropies and the concept of tangle [16]. But from an experimental point of view these are not realizable.

In this paper, we will be providing a feasible way to distinguish these six different classes of pure three-qubit states. In a very recent paper [17], a proposed set of Bell inequalities can distinguish separable, biseparable and genuine entanglement for pure three-qubit states by the pattern of violations of the Bell inequalities within the set. In another work, Zhao et al. [18] have provided the necessary and sufficient conditions to classify the separable, biseparable and genuine entangled state. But they did not succeed in distinguishing the GHZ-type and W-type states, which fall under the category of genuine entangled state. They have shown that measurement of seven observables are needed to classify and detect pure three-qubit entangled state.

In this work, we will not consider Bell inequalities but will construct operators, which can distinguish six classes of entanglement for pure three-qubit states. Firstly, we have related the tangle of the state with the expectation value of one operator, which consist of Pauli operators. This means that we may experimentally determine the value of the tangle. Non zero value of the tangle guarantees that the given three-qubit pure state is a GHZ-type state. Therefore, in our case only one operator is needed to differentiate between GHZ-type state and the other classes of three-qubit pure states. Measurement of three operators are needed to distinguish W-type state and biseparable/separable states. Measurement of four more operators are needed to classify biseparable and separable states. But Zhao et al. [18] have shown that measurement of seven operator is needed to classify the pure three-qubit state.

One can transform a given pure three-qubit state to the canonical form [19,20]. We have constructed the operators and proved our results using this form of an arbitrary state. In some experiments, the states are created in this canonical form [21], then our list of observables can be used without a change. But most of the time this is not the case, and a state is generated in a different basis. In such case, one can find another set of suitable observables by applying local unitary transformations on the given set of observables. We explicitly demonstrate this by considering two states in computational basis. This is possible because different sets of basis vectors are connected by unitary transformations. If we know the two sets, one can construct suitable unitary transformations. However, there is a drawback. Sometime, one has to know the state for constructing suitable unitary transformations, as they depend on the state parameters. Although our scheme is about distinguishing various SLOCC classes of pure states, we also examine the usefulness of our operators in the context of a few mixed states.

We also consider the teleportation scheme of Lee et al. [22]. They introduced the concept of partial tangle and related the fidelity of their teleportation scheme to these partial tangles. We relate these partial tangles to a set of observable quantities. By measuring these quantities, one can find out the values of partial tangles and the fidelity of the teleported state. In this way, the partial tangles can be also be used to classify genuinely entangled state, biseparable state and separable state.

We have organized the paper as follows. In Section 2, we have introduced the idea of tangle and its observable measure. In Section 3, the classification of different classes are done. Implementation of our scheme in any other basis has been discussed in Section 4. We have discussed the usefulness of our measurement observable for a few class of mixed states in Section 5. In Section 6, an experimental way of measuring fidelity for a teleportation scheme has been discussed using same kind of operators. Finally, we conclude in the last section.

2 Tangle and its observable measure

Tangle was first introduced in [23] in the context of distributed entanglement, to quantify the amount of three-way entanglement in a three-qubit state. For a pure state it can be interpreted as residual entanglement, which is not captured by two-way entanglement between the qubits. It was also shown to be an entanglement monotone [16]. The tangle is defined as

$$\tau = C^2_{A(BC)} - C^2_{AB} - C^2_{AC}, \tag{1}$$

where C_{AB} and C_{AC} denote the concurrence [24] of the entangled state between the qubits A and B and between the qubits A and C respectively. The concurrence $C_{A(BC)}$ refers to the entanglement of qubit A with the joint state of qubits B and C.

Any three-qubit pure state can be written in the canonical form [19,20],

$$|\psi\rangle = \lambda_0|000\rangle + \lambda_1 e^{i\theta}|100\rangle + \lambda_2|101\rangle + \lambda_3|110\rangle + \lambda_4|111\rangle, \tag{2}$$

where $\lambda_i \geqslant 0$, $\sum_i \lambda_i^2 = 1$, $\theta \in [0, \pi]$ and $\{|0\rangle, |1\rangle\}$ denote the basis of Alice's, Bob's and Charlie's Hilbert space. The tangle for the state $|\psi\rangle$ given in (2) is found to be

$$\tau_\psi = 4\lambda_0^2\lambda_4^2. \tag{3}$$

The tangle as given in (3) may be measured experimentally if we take the expectation value of the operator

$$O = 2(\sigma_x \otimes \sigma_x \otimes \sigma_x), \tag{4}$$

with respect to the state $|\psi\rangle$. The operator O given in (4) can be obtained by suitably choosing the unit vectors in Mermin operator, which is defined as [25,26]

$$\begin{aligned} B_M = {} & \hat{a}_1.\vec{\sigma} \otimes \hat{a}_2.\vec{\sigma} \otimes \hat{a}_3.\vec{\sigma} - \hat{a}_1.\vec{\sigma} \otimes \hat{b}_2.\vec{\sigma} \otimes \hat{b}_3.\vec{\sigma} \\ & - \hat{b}_1.\vec{\sigma} \otimes \hat{a}_2.\vec{\sigma} \otimes \hat{b}_3.\vec{\sigma} - \hat{b}_1.\vec{\sigma} \otimes \hat{b}_2.\vec{\sigma} \otimes \hat{a}_3.\vec{\sigma}, \end{aligned} \tag{5}$$

where $\hat{a}_j$, b_j $(j = 1, 2, 3)$ are the measurement direction for the jth party and $\vec{\sigma} = (\sigma_x, \sigma_y, \sigma_z)$ are the usual Pauli matrices. By choosing the unit vectors as $\hat{a}_1 = (1, 0, 0)$, $\hat{a}_2 = (1, 0, 0)$, $\hat{a}_3 = (1, 0, 0)$, $\hat{b}_1 = (-1, 0, 0)$, $\hat{b}_2 = (1, 0, 0)$

and $\hat{b}_3 = (1,0,0)$, we can construct the operator O. Therefore, the expectation value of the operator O in the state ψ is given by

$$\langle O\rangle_\psi = \langle\psi|O|\psi\rangle = 4\lambda_0\lambda_4 = 2\sqrt{\tau_\psi}. \tag{6}$$

Hence, from (6) it is clear that by measuring the expectation value of O, one can easily calculate the value of the tangle.

3 Classification of three-qubit pure states

In this section, we will show how to classify six different classes of three-qubit pure states. It is known that tangle is nonzero only for GHZ class [16]; it is zero for other five classes. So using (6) one can separate GHZ class from other five classes. Since it is not possible to distinguish zero tangle classes of three-qubit pure states with a single quantity τ_ψ, so we need to define other observables. To fulfill our aim, let us consider two quantities P and Q, which can be defined as

$$P = \langle\psi|O_1|\psi\rangle\langle\psi|O_2|\psi\rangle = \langle O_1\rangle_\psi\langle O_2\rangle_\psi, \tag{7}$$

and

$$Q = \langle O_1\rangle_\psi + \langle O_2\rangle_\psi + \langle O_3\rangle_\psi. \tag{8}$$

The operators O_1, O_2 and O_3 are given by

$$O_1 = 2(\sigma_x\otimes\sigma_x\otimes\sigma_z), \tag{9}$$
$$O_2 = 2(\sigma_x\otimes\sigma_z\otimes\sigma_x), \tag{10}$$

and

$$O_3 = 2(\sigma_z\otimes\sigma_x\otimes\sigma_x). \tag{11}$$

The operator O_1 given in (9) can be obtained from the Mermin operator (5) by choosing the unit vectors as $\hat{a}_1 = (1,0,0)$, $\hat{a}_2 = (1,0,0)$, $\hat{a}_3 = (0,0,1)$, $\hat{b}_1 = (-1,0,0)$, $\hat{b}_2 = (1,0,0)$ and $\hat{b}_3 = (0,0,1)$. One can find operator O_2 given in (10) by choosing the unit vectors as $\hat{a}_1 = (1,0,0)$, $\hat{a}_2 = (0,0,1)$, $\hat{a}_3 = (1,0,0)$, $\hat{b}_1 = (-1,0,0)$, $\hat{b}_2 = (0,0,1)$ and $\hat{b}_3 = (1,0,0)$. Similarly operator O_3 given in (11) can be obtained by choosing the unit vectors as $\hat{a}_1 = (0,0,1)$, $\hat{a}_2 = (1,0,0)$, $\hat{a}_3 = (1,0,0)$, $\hat{b}_1 = (0,0,-1)$, $\hat{b}_2 = (1,0,0)$ and $\hat{b}_3 = (1,0,0)$. The expectation value of the operators O_1, O_2 and O_3 with respect to the state $|\psi\rangle$ are as follows,

$$\begin{aligned}\langle O_1\rangle_\psi &= 4\lambda_0\lambda_3,\\ \langle O_2\rangle_\psi &= 4\lambda_0\lambda_2 \quad \text{and}\\ \langle O_3\rangle_\psi &= -4(\lambda_2\lambda_3 + \lambda_1\lambda_4\cos\theta).\end{aligned} \tag{12}$$

Therefore, using (12), we can obtain P and Q as

$$\begin{aligned}P &= 16\lambda_0^2\lambda_2\lambda_3 \quad \text{and}\\ Q &= 4\Big(\lambda_0\lambda_3 + \lambda_0\lambda_2 - (\lambda_2\lambda_3 + \lambda_1\lambda_4\cos\theta)\Big).\end{aligned} \tag{13}$$

We are now in a position to classify zero tangle three-qubit pure states based on the expectation values of the operators O_1,O_2,O_3 and the two quantities P and Q.

Theorem 1. *Any three-qubit state belongs to the W class if,*

$$\begin{aligned}&(i)\tau_\psi = 0,\\ &(ii)P \neq 0.\end{aligned} \tag{14}$$

Proof. Using parametrization (2), any three-qubit pure state, which is in W class can be written as [16,20],

$$|\psi\rangle_W = \lambda_0|000\rangle + \lambda_1|100\rangle + \lambda_2|101\rangle + \lambda_3|110\rangle. \tag{15}$$

As there is no λ_4, so from (3) it is clear that $\tau_{\psi_W} = 0$. From (13) one can find $P = 16\lambda_0^2\lambda_2\lambda_3 \neq 0$ and $Q = 4(\lambda_0\lambda_3 + \lambda_0\lambda_2 - \lambda_2\lambda_3) \neq 0$.

We will deduce the conditions by which it is possible to distinguish three biseparable classes.

Lemma 1. *Any three-qubit state is biseparable in* 1 *and* 23 *bipartition if*

$$\begin{aligned}&(i)\tau_\psi = 0,\\ &(ii)\langle O_1\rangle_\psi = 0,\\ &(iii)\langle O_2\rangle_\psi = 0 \quad \textit{and}\\ &(iv)\langle O_3\rangle_\psi \neq 0.\end{aligned} \tag{16}$$

Proof. Any pure three-qubit state which is biseparable in 1 and 23 bipartition, can be written as $|0\rangle(\alpha|00\rangle + \beta|11\rangle)$, upto some local unitary transformation [16]. Canonical form of three-qubit pure states as written in (2) will have the aforesaid biseparable form if all the λ_i's except λ_1 and λ_4 are zero. Hence, the state belonging to 1 and 23 bipartition can be written in terms of λ_i's as

$$|\psi\rangle_{1|23} = |1\rangle(\lambda_1|00\rangle + \lambda_4|11\rangle). \tag{17}$$

As $\lambda_0 = 0$, the tangle is zero for this class of state. From (12) we notice that, $\langle O_1\rangle_\psi = 0$, $\langle O_2\rangle_\psi = 0$ and $\langle O_3\rangle_\psi = -4\lambda_1\lambda_4$. Hence, $P = 0$ and $Q \neq 0$.

Lemma 2. *Any three-qubit state is biseparable in* 12 *and* 3 *bipartition if,*

$$\begin{aligned}&(i)\tau_\psi = 0,\\ &(ii)\langle O_1\rangle_\psi \neq 0,\\ &(iii)\langle O_2\rangle_\psi = 0 \quad \textit{and}\\ &(iv)\langle O_3\rangle_\psi = 0.\end{aligned} \tag{18}$$

Proof. The state, which belongs to 12 and 3 bipartition can be written as

$$|\psi\rangle_{12|3} = (\lambda_0|00\rangle + \lambda_3|11\rangle)|0\rangle. \tag{19}$$

The tangle is zero as $\lambda_4 = 0$. Using (12) we can infer that $\langle O_1\rangle_\psi = 4\lambda_0\lambda_3$, $\langle O_2\rangle_\psi = 0$ and $\langle O_3\rangle_\psi = 0$. Therefore, $P = 0$ and $Q \neq 0$.

Lemma 3. *Any three-qubit state is biseparable in* 13 *and* 2 *bipartition if*

$$\begin{aligned}&(i)\tau_\psi = 0,\\ &(ii)\langle O_1\rangle_\psi = 0,\\ &(iii)\langle O_2\rangle_\psi \neq 0 \quad \textit{and}\\ &(iv)\langle O_3\rangle_\psi = 0.\end{aligned} \tag{20}$$

Proof. The state belongs to 13 and 2 bipartition can be written as

$$|\psi\rangle_{13|2} = \lambda_0|000\rangle + \lambda_2|101\rangle. \tag{21}$$

The tangle is zero as $\lambda_4 = 0$. The expectation values of the operators O_1, O_2 and O_3 in this state are as follows $\langle O_1\rangle_\psi = 0$, $\langle O_2\rangle_\psi = 4\lambda_0\lambda_2$ and $\langle O_3\rangle_\psi = 0$. Therefore, $P = 0$ and $Q \neq 0$.

We can now use these lemmas to prove the following theorem.

Theorem 2. *Any three-qubit pure state is biseparable if,*

$$\begin{aligned}&(i)\tau_\psi = 0,\\ &(ii)P = 0 \quad \textit{and}\\ &(iii)Q \neq 0.\end{aligned} \tag{22}$$

Proof. From the above lemmas, it is clear that for a biseparable state, either $\langle O_1\rangle_\psi = 0$, or $\langle O_2\rangle_\psi = 0$. As P is the product of these two expectation values, therefore $P = 0$ for any biseparable three-qubit pure state. The quantity Q is the sum of the expectation values of the operators O_1, O_2 and O_3, and according to the above three lemmas, at least one is nonzero. Therefore $Q \neq 0$. This proves the theorem.

Theorem 3. *Any three-qubit state is separable if*

$$\begin{aligned}&(i)\tau_\psi = 0,\\ &(ii)P = 0 \quad \textit{and}\\ &(iii)Q = 0.\end{aligned} \tag{23}$$

Proof. Any separable three-qubit pure state can be written as $|0\rangle|0\rangle|0\rangle$, after applying some appropriate local unitary operation. For this state τ_ψ, P and Q all are zero. That completes our proof.

From the above theorems and lemmas we can classify all the classes of three-qubit pure states. Moreover, as these observables only contain Pauli matrices, they can be measured in experiments. We note that there is some arbitrariness in the definition of P. Above proofs will go through, even if we would have defined P as a product of the expectation values of operators "O_2 and O_3", or "O_1 and O_3", instead of operators "O_1 and O_2".

4 Local unitary equivalence with computational basis

One may now raise the question that entire analysis has been carried out by writing the state in the canonical form and the corresponding operators in the corresponding basis. So, if we are given a state in any other basis, will the analysis still hold? The fact, that any three qubit pure state can be written down in the canonical form is an existence proof that in principle one can always apply some local unitary operators to convert a state from any basis, in particular computational basis, to canonical-form basis and vice versa. We will now argue that these theorems will hold in any basis with suitably transformed operators. We have to find the particular local unitary operation that connect two sets of basis vectors and write those operator in that basis. Let us consider that we are given a three-qubit pure state : $|\psi\rangle = \sum_{i,j,k=0}^{1} t_{ijk}|ijk\rangle$ in computational basis. Now, given this state, we can in principle always transform it to the canonical form [27]. Only requirement is that one has to judiciously choose the local unitary operators. Following two examples will clarify this issue. Suppose, we have been given a state in computational basis:

$$|\psi\rangle_c = \frac{1}{2}(|000\rangle_c + |011\rangle_c + |100\rangle_c + |111\rangle_c), \tag{24}$$

where c represents that the state is in computational basis. Clearly the given state is not in canonical form. But it can be converted to one having the canonical form using local unitaries. For that we have to follow the prescription mentioned by Acín et al. in [27]. Doing the necessary calculations we have found that the unitary operators that have to act on the first, second and third qubits are, $U1 = \frac{1}{\sqrt{2}}\begin{pmatrix}-1 & 1\\ 1 & 1\end{pmatrix}$, $U2 = \begin{pmatrix}1 & 0\\ 0 & 1\end{pmatrix}$ and $U3 = \begin{pmatrix}1 & 0\\ 0 & 1\end{pmatrix}$. Then by applying the operator $U = U1 \otimes U2 \otimes U3$ on $|\psi\rangle_c$, we get the state in the canonical-form basis as

$$|\psi\rangle_a = \frac{1}{\sqrt{2}}(|100\rangle_a + |111\rangle_a), \tag{25}$$

where, a denotes that the state is in the canonical-form basis Now we can calculate the expectation values of those operators given in the previous sections. We will find that $\langle O\rangle_{\psi_a} = 0$, $\langle O_1\rangle_{\psi_a} = 0$, $\langle O_2\rangle_{\psi_a} = 0$ and $\langle O_3\rangle_{\psi_a} = -2$. So the state is biseparable in 1 and 23 bipartition. Now to verify this result in computational basis we have to rotate these observables by inverse of U. $U^{-1} = U^\dagger = U1 \otimes U2 \otimes U3 = U$. The transformed observables are $O_t = UOU^\dagger$, $O_{1t} = UO_1U^\dagger$, $O_{2t} = UO_2U^\dagger$ and $O_{3t} = UO_3U^\dagger$. If we calculate the expectation values of these operator on state $|\psi\rangle_c$, we find $\langle O_t\rangle_{\psi_c} = 0$, $\langle O_{1t}\rangle_{\psi_c} = 0$, $\langle O_{2t}\rangle_{\psi_c} = 0$ and $\langle O_{3t}\rangle_{\psi_c} = -2$. Hence, the state is $1|23$ biseparable.

Let us consider another state in computational basis :

$$|\phi\rangle_c = \frac{1}{\sqrt{3}}(e^{i\theta}|000\rangle_c + |011\rangle_c - |100\rangle_c). \tag{26}$$

To transform it in Acín's canonical form following local unitaries are required $U1 = \begin{pmatrix}0 & -1\\ 1 & 0\end{pmatrix}$, $U2 = \begin{pmatrix}1 & 0\\ 0 & 1\end{pmatrix}$ and $U3 = \begin{pmatrix}1 & 0\\ 0 & 1\end{pmatrix}$.

Hence, $U = U1 \otimes U2 \otimes U3$. Applying this operator to the state, we can get the final state as,

$$|\phi\rangle_a = \frac{1}{\sqrt{3}}(|000\rangle_a + e^{i\theta}|100\rangle_a + |111\rangle_a). \quad (27)$$

For this state, we find that $\langle O\rangle_{\phi_a} = \frac{4}{3}$, $\langle O_1\rangle_{\phi_a} = 0$, $\langle O_2\rangle_{\phi_a} = 0$ and $\langle O_3\rangle_{\phi_a} = -\frac{4\cos\theta}{3}$. So the state is in GHZ class. Now to get these results in computational basis we rotate these observables by $U^{-1} = U^{\dagger} = U1^{\dagger} \otimes U2 \otimes U3 = U_I$. Similarly, we transform these observables by U_I, as shown in previous example. Now we find that $\langle O_t\rangle_{\phi_c} = \frac{4}{3}$, $\langle O_{1t}\rangle_{\phi_c} = 0$, $\langle O_{2t}\rangle_{\phi_c} = 0$ and $\langle O_{3t}\rangle_{\phi_c} = -\frac{4\cos\theta}{3}$. Hence, the results are consistent. In the examples above, it was important to know the state to determine suitable unitary transformations.

5 Case of mixed states

The case of mixed states is more involved. There is no closed from of tangle. But one can find a lower bound on the tangle for a three-qubit mixed state. For a mixed state $C^2_{A(BC)} = 2(1 - \mathrm{Tr}\rho_A^2)$ is no longer valid. Here ρ_A is the density matrix of a subsystem of the three-qubit state ρ. Instead we have to consider the convex roof optimization of all the pure states as follows

$$C^2_{A(BC)}(\rho) = \inf_{p_i, |\psi_i\rangle} \sum_i p_i C^2_{A(BC)}(|\psi_i\rangle), \quad (28)$$

where $\rho = \sum_i p_i |\psi_i\rangle\langle\psi_i|$. But it is a formidable task. Instead of finding this, one can find a lower bound on $C^2_{A(BC)}(\rho)$ easily. It has been shown in [28] that this lower bound is given as – $C^2_{A(BC)}(\rho)|_{\mathrm{LB}} = 2(\mathrm{Tr}\rho^2 - \mathrm{Tr}\rho_A^2)$. By substituting this in the expression of tangle in equation (1), one can find the lower bound on tangle. However, this $\tau^{\mathrm{LB}}(\rho)$ is not always invariant under the permutation of A, B and C. Hence, for the case of mixed states, it is reasonable to use the average over all the permutations of A, B and C and calculate $\tau^{\mathrm{LB}}(\rho)$ as follows [28,29]

$$\bar{\tau}^{\mathrm{LB}} = \frac{1}{6} \sum_{\{ABC\}} \left(C^2_{A(BC)}|_{\mathrm{LB}} - C^2_{AB} - C^2_{AC} \right). \quad (29)$$

Let's take an example of a mixed state which is a mixture of a GHZ state and a W state

$$\rho = p|\mathrm{GHZ}\rangle\langle\mathrm{GHZ}| + (1 - \mathrm{p})|\mathrm{W}\rangle\langle\mathrm{W}|. \quad (30)$$

For this state we compare graphically our observable measure of tangle for pure state, i.e. $\frac{\langle O\rangle^2}{4}$ with the lower bound of tangle as given in equation (29).

As p increases, the state becomes more pure and the values of $(\bar{\tau}^{\mathrm{LB}})$ and $\frac{\langle O\rangle^2}{4}$ approach each other. In [29], Farías et al. considered a very interesting class of three-qubit mixed states which can be obtained as follows. First they prepare a two qubit Bell state $|\phi^+\rangle_{AB} = \frac{1}{\sqrt{2}}(|00\rangle + |11\rangle)$.

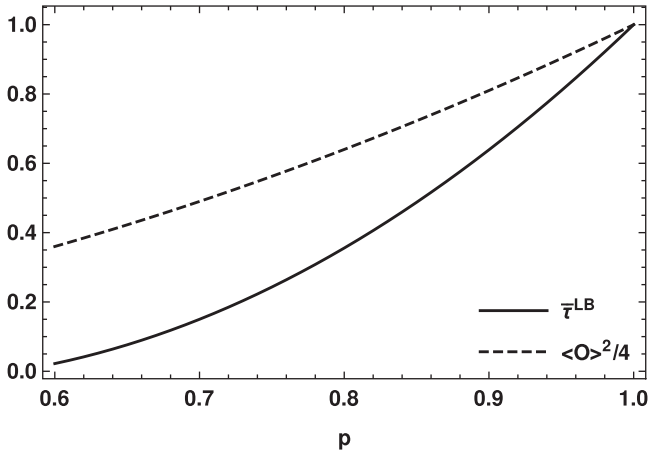


Fig. 1. Comparison between lower bound of tangle $(\bar{\tau}^{\mathrm{LB}})$ and $\frac{\langle O\rangle^2}{4}$ with the variation of p for the state given in equation (30).

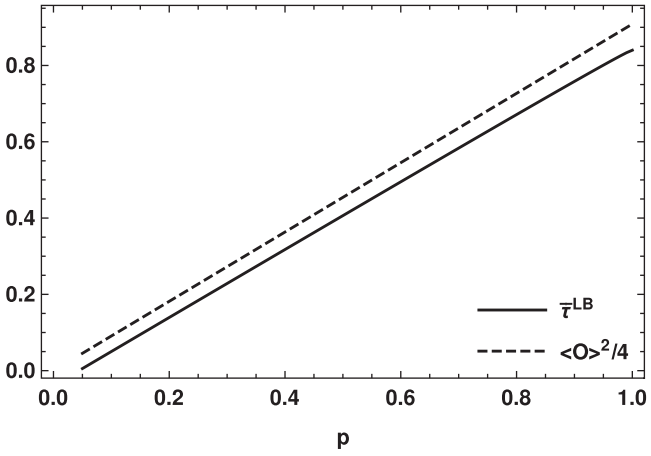


Fig. 2. Comparison between lower bound of tangle $(\bar{\tau}^{\mathrm{LB}})$ and $\frac{\langle O\rangle^2}{4}$ with the variation of p.

Then they let the second qubit interact with the environment. The interaction can be described by a phase damping channel

$$|0\rangle_B|0\rangle_E \to |0\rangle_B|0\rangle_E, \quad (31)$$
$$|1\rangle_B|0\rangle_E \to \sqrt{1-p}|1\rangle_B|0\rangle_E + \sqrt{p}|0\rangle_B|1\rangle_E, \quad (32)$$

where p is the channel parameter. This phase damping interaction prepares a tripartite state,

$$|\phi\rangle_{ABE} = \frac{1}{\sqrt{2}}(|000\rangle + \sqrt{1-p}|110\rangle + \sqrt{p}|111\rangle), \quad (33)$$

where initially the environment state is $|0\rangle$. In [29], authors experimentally prepared this kind of state with some purity. We can represent it by adding some white noise with $|\phi\rangle_{ABE}$ as

$$\rho = m|\phi\rangle_{ABE}\langle\phi| + \frac{1-m}{8}\mathbb{I}, \quad (34)$$

where $\mathbb{I}$ is the eight dimensional identity matrix. For purity equals to 0.92 or $m \approx 0.95$, we compare numerically our tangle measure for pure state, i.e., $\frac{\langle O\rangle^2}{4}$ with the lower bound of tangle. From the Figure 2, we see that $\frac{\langle O\rangle^2}{4}$, i.e., our measure of tangle is just above the value of lower bound of tangle. Similar results can be obtained for any other class of mixed state as well.

6 Experimental measure of fidelity for a teleportation scheme

In this section, we will discuss a teleportation scheme using a three-qubit pure state as studied earlier in [22]. The teleportation scheme is as follows: Let us consider a three-qubit pure entangled state shared by three parties i, j and k. We make an orthogonal measurement on the kth qubit and consider the joint state of the system i and j. Using this joint state as a resource state, one can teleport a single qubit state. The faithfulness of this teleportation scheme depends on the single qubit measurement on kth qubit and the compound state of the system i and j. In [22], authors introduced a new quantity called partial tangle, which is defined as,

$$\tau_{ij} = \sqrt{C^2_{i(jk)} - C^2_{ik}}, \quad i \neq j \neq k \quad \text{and} \quad i, j, k = 1, 2, 3. \tag{35}$$

The partial tangles for the state given in (2) are

$$\begin{aligned}
\tau_{12} &= 2\lambda_0\sqrt{\lambda_3^2 + \lambda_4^2},\\
\tau_{23} &= 2\sqrt{\lambda_0^2\lambda_4^2 + \lambda_1^2\lambda_4^2 + \lambda_2^2\lambda_3^2 - 2\lambda_1\lambda_2\lambda_3\lambda_4\cos\theta},\\
\tau_{31} &= 2\lambda_0\sqrt{\lambda_2^2 + \lambda_4^2}.
\end{aligned} \tag{36}$$

They showed that these partial tangles are related to singlet fraction f_k and maximum teleportation fidelity F_k. Here index k just indicates that the measurement is done on the kth qubit. The relation is as follows,

$$\tau_{ij} = 3F_k - 2 = 2f_k - 1. \tag{37}$$

We will now provide the explicit relationship between the partial tangles and the expectation value of the operators O, O_1, O_2, O_4 and O_5. The operators O_4 and O_5 will be defined in this section. Since partial tangle is related with singlet fraction and teleportation fidelity, we may measure the teleportation fidelity experimentally for the teleportation scheme given in [22].

Let us define two new operators as

$$\begin{aligned}
O_4 &= 2(\sigma_z \otimes \sigma_y \otimes \sigma_y),\\
O_5 &= 2(\sigma_z \otimes \sigma_y \otimes \sigma_x).
\end{aligned} \tag{38}$$

Operator O_4 given in (38) can be obtained from the Mermin operator (5) by choosing the unit vectors as $\hat{a}_1 = (0, 0, 1)$, $\hat{a}_2 = (0, 1, 0)$, $\hat{a}_3 = (0, 1, 0)$, $\hat{b}_1 = (0, 0, -1)$, $\hat{b}_2 = (0, 1, 0)$ and $\hat{b}_3 = (0, 1, 0)$. Similarly O_5 can be obtained by choosing the unit vectors as $\hat{a}_1 = (0, 0, 1)$, $\hat{a}_2 = (0, 1, 0)$, $\hat{a}_3 = (1, 0, 0)$, $\hat{b}_1 = (0, 0, -1)$, $\hat{b}_2 = (0, 1, 0)$ and $\hat{b}_3 = (1, 0, 0)$.

The expectation value of the above observables for the state in (2) are

$$\begin{aligned}
\langle O_4\rangle_\psi &= -4(\lambda_2\lambda_3 - \lambda_1\lambda_4\cos\theta),\\
\langle O_5\rangle_\psi &= 4\lambda_1\lambda_4\sin\theta.
\end{aligned} \tag{39}$$

After a few steps of calculation, we can show that,

$$\begin{aligned}
\tau_{12} &= \frac{1}{2}\sqrt{\langle O\rangle_\psi^2 + \langle O_1\rangle_\psi^2} = 3F_3 - 2,\\
\tau_{23} &= \frac{1}{2}\sqrt{\langle O\rangle_\psi^2 + \langle O_4\rangle_\psi^2 + \langle O_5\rangle_\psi^2} = 3F_1 - 2,\\
\tau_{31} &= \frac{1}{2}\sqrt{\langle O\rangle_\psi^2 + \langle O_2\rangle_\psi^2} = 3F_2 - 2.
\end{aligned} \tag{40}$$

We note that the operators O, O_1, O_2, O_4 and O_5 are observables and hence their expectation values are measurable quantities. Since the teleportation fidelities are related with some functions of these expectation values as shown in (40), so we can say that the teleportation fidelities for the teleportation scheme described in [22] may be measured experimentally.

From (39) and (40), we can draw following conclusions:

1. If all the partial tangles are equal to zero then the state is a separable one. This is because the expectation value of O_4 and O_5 are also zero for a separable state.
2. If at least one partial tangle is equal to zero, then the three-qubit state is a biseparable state.
3. If each partial tangle is not equal to zero then the state is a three-qubit genuine entangled state.

Lemma 4. *Any pure three-qubit genuinely entangled state is useful in the teleportation scheme of [22].*

Proof. Three-qubit genuinely entangled states consist of GHZ-class and W-class. We will prove the proposition by taking these two classes separately. The relation in (37) can be written as

$$F_k = \frac{2}{3} + \frac{\tau_{ij}}{3}. \tag{41}$$

Case-I: For GHZ-class states, $\tau_{ij} > 0$. This can be compared for If $\tau_{ij} > 0$, $F_k > \frac{2}{3}$ [30]. Therefore the resource state consisting of qubits i and j is suitable for teleportation. In this case, the partial tangle is nonzero and so $\langle O\rangle_\psi$ is also nonzero. Hence, from (40), it is clear that $\tau_{ij} > 0$. Therefore, F_k is always greater than $\frac{2}{3}$.

Case-II: For W-class states, $\tau_{ij} = 0$ and hence $\langle O\rangle_\psi = 0$. Therefore, for these class of states, equation (40) reduces to

$$\tau_{12} = \frac{1}{2}\langle O_1\rangle_\psi,$$
$$\tau_{23} = \frac{1}{2}\sqrt{\langle O_4\rangle_\psi^2 + \langle O_5\rangle_\psi^2},$$
$$\tau_{31} = \frac{1}{2}\langle O_2\rangle_\psi. \quad (42)$$

From (7) it can be seen that $4\tau_{12}\tau_{31} = P$. For W-class states, $\tau_{12} \neq 0$ and $\tau_{31} \neq 0$ as $P \neq 0$. Hence, F_3 and F_2 are greater than $\frac{2}{3}$. Thus it remains to see the remaining partial tangle τ_{23}, which is related with $\langle O_4\rangle_\psi$ and $\langle O_5\rangle_\psi$. From equation (13), for W-class states, λ_0, λ_2 and λ_3 can not be zero simultaneously. Equation (38) ensures that $\langle O_4\rangle_\psi$ is nonzero. Therefore, $\tau_{23} \neq 0$ and F_1 is greater than $\frac{2}{3}$. Thus for the teleportation scheme of [22], all states in W-class are useful for teleportation. This completes the proof.

7 Conclusion

We have constructed a set of operators, which can be used to distinguish six SLOCC inequivalent classes of entanglement present in pure three-qubit states. These operators contain only Pauli matrices and hence are easily implementable in experiments. So, it may possible to detect the type of entanglement present in a three-qubit pure state experimentally. Although we constructed theses operators in the canonical-form basis, a suitably transformed set of operators will work in any basis. In this sense, our results are independent of the choice of the basis. However, the construction of suitable transformations may require the knowledge about the state. We have also considered a few mixed states and showed graphically that our measure of tangle for pure states approaches minimum of the tangle as the state becomes more pure. In the one class of mixed states, that we considered, our measure of tangle is just above the lower bound on tangle. This is because the purity of the states is quite high. In another case, our measure of tangle approaches the lower bound, as the state becomes more pure. This shows that our measure of tangle works quite well for some classes of mixed state. Also we have shown that the operators defined here can be used to measure the fidelity of a teleportation scheme introduced in [22]. We believe that, there are other such applications, where we can use our operators effectively.

Note added in proofs. It has come to our notice that an experiment has been performed [32] based on the proposals in this paper.

Author contribution statement

All the authors contributed to the development and design of the problem. C. Datta and S. Adhikari did most of the calculation. Manuscript preparation has been done by all the authors.

References

1. N. Gisin, G. Ribordy, W. Tittel, H. Zbinden, Rev. Mod. Phys. **74**, 145 (2002)
2. C.H. Bennett, G. Brassard, C. Crepeau, R. Jozsa, A. Peres, W.K. Wootters, Phys. Rev. Lett. **70**, 1895 (1993)
3. D. Bouwmeester, J-W Pan, K. Mattle, M. Eibl, H. Weinfurter, A. Zeilinger, Nature **390**, 575 (1997)
4. C.H. Bennett, S.J. Wiesner, Phys. Rev. Lett. **69**, 2881 (1992)
5. A. Harrow, P. Hayden, D. Leung, Phys. Rev. Lett. **92**, 187901 (2004)
6. M.B. Plenio, S. Virmani, Quantum Inf. Comput. **7**, 1 (2007)
7. R. Horodecki, P. Horodecki, M. Horodecki, K. Horodecki, Rev. Mod. Phys. **81**, 865 (2009)
8. C. Datta, P. Agrawal, S.K. Choudhary, Phys. Rev. A **95**, 042323 (2017)
9. V. Vedral, M.B. Plenio, Phys. Rev. A **57**, 1619 (1998)
10. C.H. Bennett, H.J. Bernstein, S. Popescu, B. Schumacher, Phys. Rev. A **53**, 2046 (1996)
11. N. Linden, S. Popescu, B. Schumacher, M. Westmoreland, arXiv:quant-ph/9912039
12. G. Vidal, W. Dür, J.I. Cirac, Phys. Rev. Lett. **85**, 658 (2000)
13. S.Wu, Y. Zhang, Phys. Rev. A **63**, 012308 (2000)
14. C.H. Bennett, S. Popescu, D. Rohrlich, J.A. Smolin, A.V. Thapliyal, arXiv:quant-ph/9908073
15. G. Vidal, J. Mod. Opt. **47**, 355 (2000)
16. W. Dür, G. Vidal, J.I. Cirac, Phys. Rev. A **62**, 062314 (2000)
17. A. Das, C. Datta, P. Agrawal, Phys. Lett. A **381**, 3928 (2017)
18. M.-J. Zhao, T.-G. Zhang, X. Li-Jost, S.-M. Fei, Phys. Rev. A **87**, 012316 (2013)
19. A. Acín, A. Andrianov, E. Jané, R. Tarrach, J. Phys. A: Math. Gen. **34**, 6725 (2001)
20. A. Acín, D. Bruss, M. Lewenstein, A. Sanpera, Phys. Rev. Lett. **87**, 040401 (2001)
21. S. Dogra, K. Dorai, Arvind, Phys. Rev. A **91**, 022312 (2015)
22. S. Lee, J. Joo, J. Kim, Phys. Rev. A **72**, 024302 (2005)
23. V. Coffman, J. Kundu, W.K. Wootters, Phys. Rev. A **61**, 052306 (2000)
24. P. Rungta, V. Buzek, C.M. Caves, M. Hillery, G.J. Milburn, Phys. Rev. A **64**, 042315 (2001)
25. D.P. Chi, K. Jeong, T. Kim, K. Lee, S. Lee, Phys. Rev. A **81**, 044302 (2010)
26. S. Adhikari, A.S. Majumdar (2016), arXiv:1602.02619
27. A. Acín, A. Andrianov, L. Costa, E. Jané, J.I. Latorre, R. Tarrach, Phys. Rev. Lett. **85**, 1560 (2000)
28. F. Mintert, A. Buchleitner, Phys. Rev. Lett. **98**, 140505 (2007)
29. O.J. Farías, G.H. Aguilar, A.V. Hernández, P.H.S. Ribeiro, L. Davidovich, S.P. Walborn, Phys. Rev. Lett. **109**, 150403 (2012)
30. S. Popescu, Phys. Rev. Lett. **72**, 797 (1994)
31. S. Massar, S. Popescu, Phys. Rev. Lett. **74**, 1259 (1995)
32. A. Singh, H. Singh, K. Dorai, Arvind, arXiv:1804.09320 (2018)

Materials Research Express

ACCEPTED MANUSCRIPT

Effect of fiber content on thermal behavior and viscoelastic properties of PALF/Epoxy and COIR/Epoxy composites

To cite this article before publication: Mohit Mittal *et al* 2018 *Mater. Res. Express* in press https://doi.org/10.1088/2053-1591/aae274

Manuscript version: Accepted Manuscript

Accepted Manuscript is "the version of the article accepted for publication including all changes made as a result of the peer review process, and which may also include the addition to the article by IOP Publishing of a header, an article ID, a cover sheet and/or an 'Accepted Manuscript' watermark, but excluding any other editing, typesetting or other changes made by IOP Publishing and/or its licensors"

This Accepted Manuscript is **© 2018 IOP Publishing Ltd**.

During the embargo period (the 12 month period from the publication of the Version of Record of this article), the Accepted Manuscript is fully protected by copyright and cannot be reused or reposted elsewhere.
As the Version of Record of this article is going to be / has been published on a subscription basis, this Accepted Manuscript is available for reuse under a CC BY-NC-ND 3.0 licence after the 12 month embargo period.

After the embargo period, everyone is permitted to use copy and redistribute this article for non-commercial purposes only, provided that they adhere to all the terms of the licence https://creativecommons.org/licences/by-nc-nd/3.0

Although reasonable endeavours have been taken to obtain all necessary permissions from third parties to include their copyrighted content within this article, their full citation and copyright line may not be present in this Accepted Manuscript version. Before using any content from this article, please refer to the Version of Record on IOPscience once published for full citation and copyright details, as permissions will likely be required. All third party content is fully copyright protected, unless specifically stated otherwise in the figure caption in the Version of Record.

View the article online for updates and enhancements.

This content was downloaded from IP address 14.139.251.107 on 25/09/2018 at 10:50

Effect of Fiber Content on Thermal Behavior and Viscoelastic Properties of PALF/Epoxy and COIR/Epoxy Composites

Mohit Mittal [a,*], Rajiv Chaudhary [a]

[a] *Department of Mechanical, Production, and Industrial Engineering, Delhi Technological University, Delhi, 110042, India*

[*] Corresponding author. *E-mail address*: **mohit.30mittal@gmail.com**; Tel. +91-9971698741.

Abstract

The comprehensive cognition of the thermal and viscoelastic behavior of polymeric materials is highly significant in order to determine the structure-property relationship for various applications. The prime goal of this work was to study the effect of fiber content on the thermo-mechanical performance of fiber reinforced composites. In this regard, randomly oriented chopped fibers of length 20 mm with varying fiber volume content (17%, 23%, and 34%) were used as reinforcement in an epoxy polymer matrix for the development of a coir fiber-epoxy and pineapple leaf fiber-epoxy composites by hand lay-up technique. The results of thermogravimetric analysis (TGA) and dynamic mechanical thermal analysis (DMTA) showed that the increase in thermal stability, storage modulus (E'), loss modulus (E''), and glass transition temperature (T_g) of the matrix polymer with the incorporation of coir and pineapple leaf fiber. The neat epoxy matrix shows highest damping property while 34 vol.% fiber reinforced composites show the highest stiffness than the other samples. In all cases, the storage modulus was decreased with the increase of temperature. The reduction in E' over the temperature range of 45-80^{0}C corresponds to the phase transition. The optimum fiber volume content is 23% having the maximum thermal stability. The 23% coir and 34% pineapple leaf fiber reinforced composites have the lowest value of effectiveness coefficient 'C' obtained by the storage modulus analysis. The tan δ and loss modulus peak of polymer matrix was shifted to the higher temperature after the addition of reinforcing fiber, which indicates that the fibers play a major role to increase the stiffness of polymer composites by imposing the restriction in mobility of polymer chains.

Keywords: pineapple leaf fiber; coir fiber; epoxy matrix; thermal stability; dynamic mechanical thermal analysis (DMTA); polymer composites

Accepted Manuscript

1. Introduction

To develop a high-performance recyclable material based on the renewable resources is a challenge for researchers and technologist. In this context, natural fibers like banana, coir, sisal, hemp, kenaf, and pineapple leaf fiber have all obtained considerable attention from both academia and industry, due to their potential to grow the agricultural based economy and their environment-friendly and competitive mechanical properties compared to the synthetic fibers. Among these lignocellulosic materials, pineapple leaf fiber (PALF) and coconut husk fiber (COIR) are the most promising and potential candidates to be used as reinforcing fiber in a polymer matrix. This was attributed to the inexpensive, low density, abundantly availability, and less abrasive nature to processing equipment. The coir and pineapple leaf fiber can obtain from the husk of coconut fruit (*Cocos nucifera*) and from the leaves of pineapple fruit (*Ananas comosus*) by using the retting process respectively. According to the statistical database (2016) of "Food and Agriculture Organization" the total production of coconut and pineapple fruit in the whole world are 59 and 25.8 millions of tonnes respectively (Table 1) [1]. Therefore, the challenging job is to reduce their waste disposal in landfill areas by their efficient utilization for the development of a biomaterial. The inherent properties of natural fibers are mentioned in Table 2 and it clearly indicates that the pineapple leaf fiber (PALF) has favourable aspect ratio and higher tensile strength and modulus of elasticity as compared to the flax, jute, OPEFB, cotton, sisal, and oil palm mesocarp fiber. Furthermore, PALF has relatively lower density, diameter, and spiral angle which leads to the higher surface area and reinforcement effectiveness of PALF than others. In addition to PALF, the COIR fiber has largest value of microfibrillar angle which results that the impact energy absorbing power of COIR is higher than that of all above mentioned fibers. The tensile strength of coir is low but it has good resistance to microbial action and salt water damage. Due to their excellent mechanical properties, both types of fiber (PALF and COIR) have high potential to be used in structural applications. Inspite of their wide varieties of advantageous properties, NFRC's is far from easy selection in structural applications because of their hydrophilic nature, low thermal stability during processing, high variability in their properties, and poor interfacial adhesion with synthetic polymers. In past, a lot of researches have already been carried out on physical and chemical treatments of natural fibers to impart hydrophobicity and thermal stability. K. Panyasart et al. investigated the effect of chemical treatment (alkaline and silane) on the thermal stability of PALF/Polyamide 6 composites. The results showed the increase of main decomposition temperature by 25^0C and 30^0C after silane

Accepted Manuscript

and alkali treatment respectively [2]. A.N Nakagaito et al. studied the effect of MCF content on thermal expansion coefficient of MFC/PF composite and confirmed the decrease of CTE from 60 ppm/K (pure PF) to 10 ppm/K (at 40 wt% of MCF) [3]. Na Lu et al. reported the elevation in thermal stability of hemp fiber and hemp-PLA composites by alkaline treatment. It was attributed to the removal of less stable pectin, waxes, and hemicellulose after alkaline treatment [4]. Sergio et al. reported the general trend of NFRC weight loss in TGA analysis is the loss of moisture, hemicellulose degradation, and decomposition of α-cellulose, and lignin [5]. A. Rachini et al. reported the order of thermal stability of hemp fiber: NaOH treated fibers>silane-treated fibers>solvent extracted fibers (water/ethanol mixture, 20/80 v/v)> untreated hemp fibers [6]. S.H Lee et al. studied the effect of bamboo fiber loading on thermal stability of PLA polymer matrix, and have observed that the loading of bamboo fiber in PLA leads to the reduction in degradation temperature (more than 50^0C) [7]. L.B. Manfredi et al. compared the thermal stability of Jute/Modar composite with Jute/UP composite and confirmed the higher thermal stability of modar composites than the composites with a polyester matrix. It was due to the higher temperature resistance of modar matrix [8]. P.J Jandas et al. investigated the effect of banana fiber loading on thermal stability of PLA. The results showed the reduction in I_D (onset temperature) and M_D (maximum degradation temperature) by 15% and 16% respectively than virgin PLA [9]. M.S Teja et al. investigated the effect of SiC filler on thermal properties of Sisal/UPE composite and observed that the addition of SiC filler leads to the increment in thermal diffusivity, thermal conductivity, and thermal stability [10]. K. Zhang et al. reported the diminution in thermal stability of epoxy resin due to the loading of bamboo fiber [11]. M. Tajvidi et al. studied the thermal degradation of wood flour, kenaf fiber, newsprint, and rice hulls - polypropylene composites. The results revealed that the rice hulls composite decomposes at the lowest rate, wood flour, and kenaf fiber decompose at around the same temperature, and newsprint composite exhibits higher weight loss [12].

From the all above cited works, it can be concluded that the work on development and thermal characterization of PALF/Epoxy and COIR/Epoxy composites have not been addressed so far. Therefore, in this work we have fabricated the biocomposite material by the reinforcement of pineapple leaf fiber and coconut husk fiber in an epoxy based thermoset polymer. Further, this work also deals with the effect of fiber volume content on the thermo-mechanical properties of PALF/Epoxy and COIR/Epoxy composites. For this objective,

Accepted Manuscript

thermogravimetric analysis (TGA) and dynamic mechanical thermal analysis (DMTA) tests had been performed on fabricated composite samples.

Dynamic mechanical thermal analysis (DMTA) is a powerful technique in the development of composites aiming to establish a significant relationship between microscopic structure and thermo-mechanical properties. The comprehensive knowledge of viscoelastic properties such as stiffness and damping, thermal transition, melting & degradation, and crystallization is important for manufacturing a high-performance polymeric material. DMA method has enormous potential to analyze the elastic and viscous response of polymer composites over a range of temperature, frequency, and time [13]. The stiffness and damping of PMC's can be easily determined in terms of storage modulus (E' or G') and Tan δ. Nielson's proposed an equation to find out the damping of composites, based on the proportional contribution of a matrix.

$$\tan \delta_c = \tan \delta_m(1-V_f) \quad (1)$$

where $\tan \delta_c$ and $\tan \delta_m$ is the damping value of composite and matrix respectively, and V_f is the volume fraction of reinforcement. The damping behavior of composites is affected by the type of fiber and matrix resin, fiber/matrix adhesion, orientation of fiber in a matrix, fiber content and length, and void content [14-16]. B. Baghaei et al. investigated the effect of hemp and lyocell fibers on viscoelastic properties of PLA composites, and found that the storage modulus was increased and the peak of tan δ curve becomes smaller, which result the increment in stiffness of samples due to the effective stress transfer from matrix to fiber [17]. L.A Pothan et al. studied the effect of banana fiber content on dynamic modulus of epoxy composites and observed the maximum value of E' for the composites with 40% fiber content. It was attributed to the hydrodynamic effect of fiber, which leads to the restriction on molecular mobility and deformability [18]. M.J. John et al. reported the increase of loss modulus (E'') due to the incorporation of flax fiber in a polypropylene matrix. This was because of the higher molecular relaxation occurring at the interfacial region of the composite by increasing the flax fiber content [19]. MK Gupta et al. studied the dynamic mechanical properties of Jute/Epoxy composite and found the increase of storage modulus with increasing the fiber content up to 30% [20]. D. Shanmugam et al. reported the improvement in E' and T_g of Palmyra/jute reinforced hybrid polyester composite after the alkali treatment of fibers [21]. Y.S Song et al. examined the viscoelastic behavior of twill and plain woven hemp-PLA composites and observed the increment in storage and loss modulus in relation

Accepted Manuscript

with the volume fraction of fiber, but storage modulus was higher than loss modulus. The greatest impact strength was exhibited by twill hemp composites [22]. T.J Chung et al. studied the effect of acetylation on dynamic mechanical properties of Kenaf/PLA composite and observed the higher storage modulus of the acetylated kenaf-PLA composite than the untreated composite. It was attributed to good interfacial adhesion between fiber and matrix after acetylation [23]. M. Idicula et al. studied the effect of layering pattern on DMA of banana/sisal hybrid polyester composites. The authors observed the highest damping and stiffness of bi-layer and intimately mixed composites compared to others respectively [24]. J. Alexander et al. compared the dynamic viscoelastic behaviour of sisal/glass/epoxy with sisal/basalt/epoxy and basalt/sisal/glass/epoxy composites, and found the higher E' and E'' of sisal/basalt/epoxy than sisal/glass/epoxy and basalt/sisal/glass/epoxy composites [25]. Y. Nishitani et al. studied the DMA of surface treated hemp fiber-polyamide 1010 composites. The E' in high-temperature region decreases in the following order: HF/PA1010 (untreated)>HF-A/PA1010 (alkaline treated)>HF-A-Si/PA1010 (alkaline with silane treated)> HF-Si/PA1010 (Silane-treated) [26]. K.T.B Padal et al. investigated the effect of jute nanofiber content on dynamic mechanical properties of Jute/Epoxy composites and found the elevation in storage modulus with an increase of fiber content [27]. B. Asabe et al. have done the thermo-mechanical characterization of banana particulate reinforced PVC composite, and observed the loss of stiffness from 1.2 GPa to 0.9 GPa at 70^0C. This indicates the suitability of material up to 70^0C [28]. J. Alexander et al. investigated the viscoelastic properties of sisal/glass/epoxy, sisal/basalt/epoxy, and basalt/sisal/glass/epoxy composites, and observed that the sisal/basalt/epoxy has higher storage and loss modulus compared to other two composites. So, sisal/basalt hybrid epoxy composites can be used in aerospace applications [29]. Literature on DMA characterization of NFRC's is clearly depicts that the research on the effect of coir and pineapple leaf fiber volume content on viscoelastic properties of the COIR/Epoxy and PALF/Epoxy composites have not been investigated till now. Therefore, this work focuses on the experimental investigation of the influence of coir fiber and pineapple leaf fiber loading on the viscoelastic properties of the epoxy resin. The effect of frequency and temperature on the storage modulus (E'), loss modulus (E''), tan δ and glass transition temperature (T_g) is also reported.

Accepted Manuscript

Table 1. Total annual production of pineapple leaf fiber and coir fiber

Pineapple Production-2016		Coconut Production-2016	
Country	Millions of tonnes	Country	Millions of tonnes
Costa Rica	2.9	Indonesia	17.7
Brazil	2.7	Philippines	13.8
Philippines	2.6	India	11.1
Thailand	1.9	Brazil	2.6
India	1.9	Sri Lanka	2.5
Indonesia	1.3		
World	25.8	World	59.0

Table 2. Physical properties of natural fibers

Physical properties	Pineapple leaf fiber	Coir fiber	Flax	Jute	Oil Palm EFB	Cotton	Sisal	Oil Palm Mesocarp
Density (g/cm^3)	0.98	1.2	1.5	1.3-1.49	1.1-1.55	1.5-1.6	1.45	-
Cellulose (%)	70-82	32-43	71	61-71.5	65	85-90	66-78	60
Hemicellulose (%)	18.8	0.15-0.25	18.6-20.6	13.6-20.4	19	5.7	10-14	-
Lignin (%)	5-12.7	40-45	2.2	12-13	13.2		10-14	11
Pectin (%)	1.1	3-4	2.3	0.2	-	0-1	10	-
Moisture content (%)	11.8	8	8-12	12.5-13.7	-	7.85-8.5	10-22	-
Microfibrillar angle (deg)	14	30-49	5-10	8	42		10-22	46
Diameter (μm)	20-80	100-460	40-600	25-200	150-500	12-38	50-200	-
Tensile strength (MPa)	413-1627	131-220	345-1500	393-800	248	287-800	468-700	80
Young's modulus (GPa)	34.5-82.5	4-6	27.6	13-26.5	3.2	5.5-12.6	9.4-22	0.5
Elongation at break (%)	1.6	15-40	2.7-3.2	1.16-1.5	25	7-8	3-7	17

2. Experimental

2.1 Materials

Pineapple (*Ananas-comosus*) leaf fiber (PALF) and coconut (*Coco-nucifera*) husk fiber (COIR), of density 0.98 g/cm^3 and 1.2 g/cm^3 respectively, were procured from M/s Go Green Products, Chennai (India). The fibers were of the long form and cut into the optimum length of 20 mm by scissors. The primary reason to select the fiber length of 20 mm is it provides a high strength biocomposite material. Further increase of fiber length leads to the increment in void density and poor dispersion of fibers in the matrix resin (unpublished author work). The SEM micrographs of PALF and COIR are shown in Fig. 1. The medium viscosity epoxy

Accepted Manuscript

resin (LY 556) with hardener (HY 951) was used as a matrix resin, procured from M/s Sakshi Dies and Chemicals, Delhi (India). The important details of the matrix material are listed in Table 3. The epoxy thermoset as a polymer matrix was selected due to its excellent mechanical, chemical, and corrosion resistance properties.

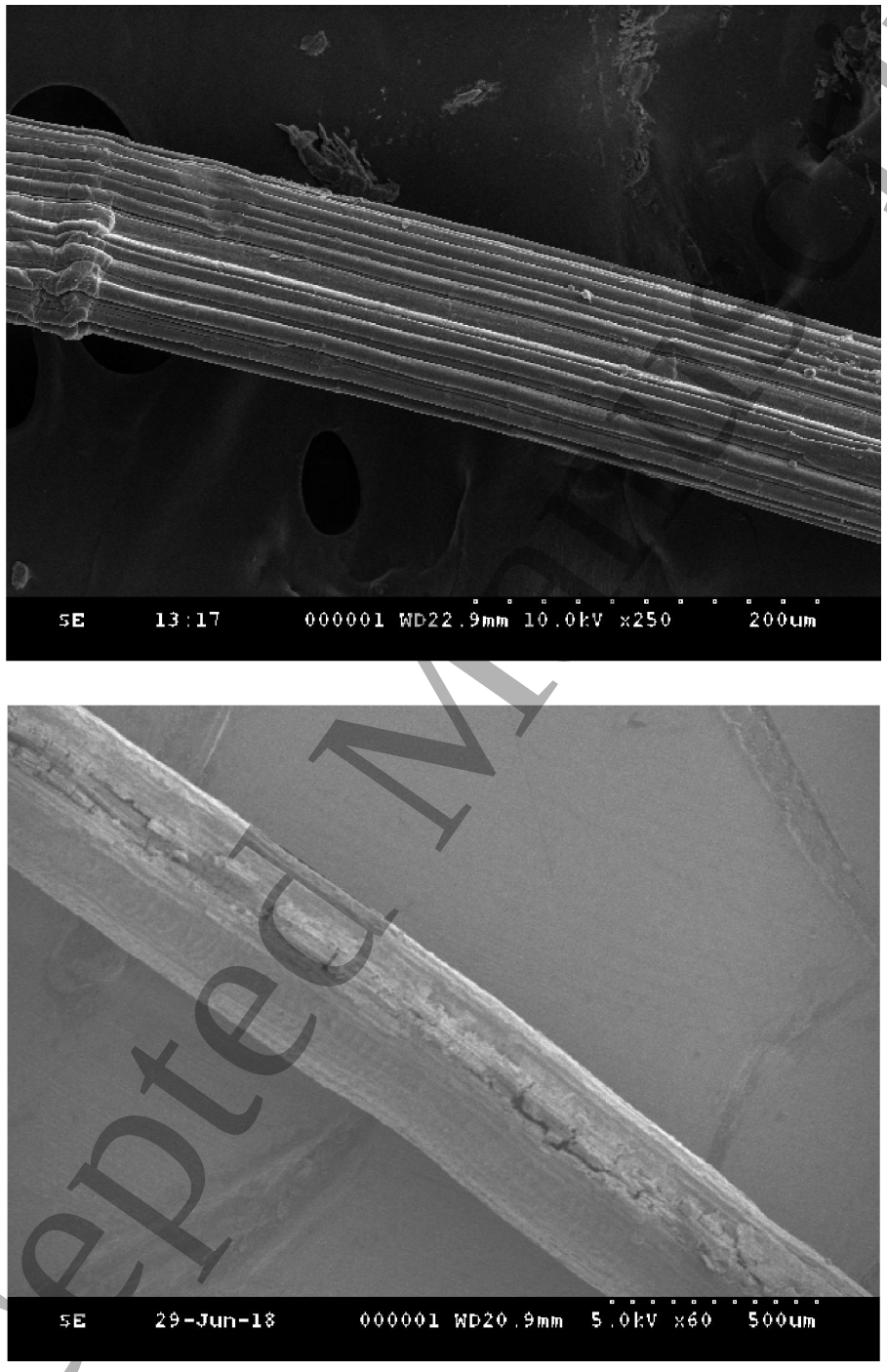


Fig. 1 SEM micrograph of pineapple leaf fiber (top) and coconut husk fiber (bottom)

Accepted Manuscript

Table 3. Details of the matrix material

Constituent Materials	Trade name	Chemical name	Density (g/cm^3)
Epoxy Resin	LY 556	Diglycidal ether bisphenol A (DGEBA)	1.16
Hardener	HY 951	Triethylenetetramine (TETA)	0.95

2.2 Fabrication of COIR/Epoxy and PALF/Epoxy composites

The chopped coir and pineapple leaf fibers of 20 mm length [Fig. 2 (a)-(b)] were used as reinforcement in an epoxy polymer matrix for fabrication the coir-epoxy and pineapple leaf fiber-epoxy composites by hand lay-up technique. The fibers were separated from pith, cleaned with distilled water, and dried in sunlight for 3 days to remove the entrapped water molecules prior to molding. The dried fibers with varying fiber volume (17%, 23%, and 34%) were thoroughly mixed with epoxy resin-hardener solution (2:1 by weight) to make the biocomposite sheets of dimensions 200 X 100 X 4 mm^3 [Fig. 3 (c)]. Table 4 records the designation and composition of the manufactured composites. The mold was made up of a toughened glass of 6 mm thickness, covered with Teflon sheet and surface of the mold was sprayed with releasing agent to avoid the sticking of polymer resin. The compounded material was poured into the mold [Fig. 3 (a)-(b)], closed the mold, and then pressed under 35 kg external loads for 24 hrs curing at room temperature. The DMA specimens of dimensions 30 X 10 X 2 mm^3 were cut from the molded sheet [Fig. 3(d)].

Table 4. Designation and composition of coir fiber-epoxy (CF-EP) and pineapple leaf fiber-epoxy (PF-EP) composites

Designation	Composition
EP	Epoxy (100 vol.%)
17 CF-EP	Epoxy (83 vol.%) + Coir fiber (17 vol.%)
17 PF-EP	Epoxy (83 vol.%) + Pineapple leaf fiber (17 vol.%)
23 CF-EP	Epoxy (77 vol.%) + Coir fiber (23 vol.%)
23 PF-EP	Epoxy (77 vol.%) + Pineapple leaf fiber (23 vol.%)
34 CF-EP	Epoxy (64 vol.%) + Coir fiber (34 vol.%)
34 PF-EP	Epoxy (64 vol.%) + Pineapple leaf fiber (34 vol.%)
34 CF-EP (1)	Epoxy (64 vol.%) + Coir fiber (34 vol.%) (frequency: 1 Hz)
34 CF-EP (5)	Epoxy (64 vol.%) + Coir fiber (34 vol.%) (frequency: 5 Hz)
34 PF-EP (1)	Epoxy (64 vol.%) + Pineapple leaf fiber (34 vol.%) (frequency: 1 Hz)
34 PF-EP (5)	Epoxy (64 vol.%) + Pineapple leaf fiber (34 vol.%) (frequency: 5 Hz)

Accepted Manuscript



(a) **(b)**

Fig. 2 (a) Short coir and (b) pineapple leaf fibers



(a) **(b)**



(c)

Accepted Manuscript



(d)

Fig. 3 (a) Glass mold with coir-epoxy compounded material (b) Glass mold with pineapple leaf fiber-epoxy compounded material (c) Coir/Epoxy and PALF/Epoxy biocomposite sheets (d) DMA specimens

2.3 Characterization of Materials

Thermogravimetric Analysis (TGA)

Thermal analysis of virgin epoxy, coir and pineapple leaf fibers, coir-epoxy, and pineapple leaf fiber-epoxy composites were carried out by using a thermogravimetric analyzer (Perkin Elmer, TGA 4000). The samples of mass 12 mg were evenly and uniformly distributed in the alumina crucible which was supported by a precision balance. The variation in mass of sample with respect to temperature and time was controlled, monitored and recorded using Perkin Elmer thermal software (Pyris). The temperature range was controlled from 25^0C to 700^0C at a heating rate of 10^0C/min under the high purity nitrogen (inert) atmosphere at a flow rate of 20 ml/min. The heating rate of 10^0C/min was selected for better resolution of transition. TGA of all the samples had done in Central Instrumentation Laboratory, DTU (Delhi).

Dynamic Mechanical Thermal Analysis (DMTA)

A dynamic mechanical thermal analyzer, installed in polymer testing laboratory, DTU (Delhi) was employed to study the effect of fiber content on viscoelastic properties of coir-epoxy and pineapple leaf fiber-epoxy composites in double cantilever mode over a temperature range of 25-140^0C. The test was performed at a heating rate of 3^0C/min. The effect of frequency on storage modulus (E'), tan δ, and glass transition temperature (T_g) was also studied at two different frequencies, namely 1 and 5 Hz.

Accepted Manuscript

3. Results and Discussion

3.1 Thermogravimetric Analysis

The thermal decomposition curves as a function of temperature for virgin epoxy, coir fiber, pineapple leaf fiber, and their composites were recorded in Fig. 4 and 5. All the samples show three steps of mass loss. The first step is the loss of absorbed moisture and volatile content in the range of 6-8.4 wt.%, up to 150^0C. The second and third decomposition step exists at 190-300^0C and 300-400^0C, corresponds to the loss of major constituents of natural fibers such as hemicellulose, cellulose, and lignin. Table 5 clearly shows that the decomposition temperature of virgin epoxy resin was increased, with the loading of coir and pineapple leaf fibers. The peak decomposition temperature (T_P) of the epoxy matrix was increased from 371.96^{0}C to 379.59, 386.03, and 377.45^{0}C, after the incorporation of 17, 23, and 34 vol.% of coir fiber content respectively. A similar result was also reported in the case of pineapple leaf fiber (Table 5). The maximum rate of thermal degradation (peak height in DTG curves) of epoxy resin was reduced by 14% and 12% after the loading of 34% coir and pineapple leaf fiber respectively. This was attributed to the higher restrictions in debonding of molecular chains. The TGA and DTG curves for coir and pineapple leaf fiber distinctly revealed their lower thermal stability as compared to the virgin epoxy and fiber-matrix composites. Table 5 also shows that the pineapple leaf fiber has higher thermal stability than coir fiber. It was due to the presence of more crystalline cellulose in PALF than COIR. Among all the fabricated composites, the composite containing 23% fiber volume content shows maximum thermal stability. It was due to the strong interfacial adhesion between fiber and matrix, less void content, and good wettability of fiber with a matrix resin. From Table 5, it was cleared that the major degradation of CF, PF, CF-EP, and PF-EP composites occur in the range of temperature 300-400^0C, was due to the decomposition of α-cellulose. Previous research works (Tajvidi et al. [30], Niu et al. [31], Yao et al. [32], El-Shekeil et al. [33]) were also concluded the same. Yang et al. reported that the presence of carbonyl group (C=O) in hemicellulose be the cause of its lower thermal stability than α-cellulose, and lignin [34]. Lignin was the most thermally stable component of natural fiber but it starts to decompose at a lower temperature (typically 160-175^0C) compared to cellulose. Mackay and Nassar reported the thermal stability of lignocellulosic fibers in the order: lignin>α-cellulose>hemicellulose [35]. According to Paiva et al. the decomposition of lignin occurred in a wider temperature range compared to cellulose and hemicellulose [36]. Table 6 shows that the residual mass (R_m) after 700 ^{0}C was increase with the increase of fiber content in an

Accepted Manuscript

epoxy matrix. The coir fiber has maximum residual mass (23.36%) at 700^{0}C. It was attributed to the presence of more lignin content in coir fiber.

Table 5. Thermal degradation temperature for virgin epoxy, coir fiber, pineapple leaf fiber, coir-epoxy, and pineapple leaf fiber-epoxy composites

Composites	$T_{5\%}$ (^{0}C) [1]	$T_{10\%}$ (^{0}C) [1]	$T_{30\%}$ (^{0}C) [1]	$T_{50\%}$ (^{0}C) [1]	T_P [2]	Peak height (%/min)	Peak width
EP	127.61	160.79	348.33	367.69	371.96	6.74	93.49
CF	69.85	239.12	293.55	335.83	302.56	4.85	121.48
17 CF-EP	132.42	201.16	358.13	380.79	379.59	6.24	101.69
23 CF-EP	134.19	229.2	362.82	384.48	386.03	6.5	101.53
34 CF-EP	131.37	209.08	356.37	382.08	377.45	5.79	104.94
PF	62.28	254.48	343.47	360.66	340.38	6.85	91.69
17 PF-EP	137.98	228.73	362.15	381.84	382.87	6.74	99.15
23 PF-EP	127.87	241.71	358.72	383.8	377.77	6.62	99.72
34 PF-EP	127.77	195.63	353.22	376.77	368.65	5.9	101.91

[1] Decomposition temperature of 5%, 10%, 30%, and 50% weight loss respectively; [2] Peak decomposition temperatures

Table 6. Weight loss and residual mass percentage for virgin epoxy, coir fiber, pineapple leaf fiber, coir-epoxy, and pineapple leaf fiber-epoxy composites

Composites	RT-150^{0}C	190-300^{0}C	300-400^{0}C	R_m (%)
EP	8.38	6.6	55.44	6.12
CF	7.39	24.56	29.85	23.36
17 CF-EP	6.75	5.36	49.98	10.11
23 CF-EP	6.57	4.56	49.39	10.12
34 CF-EP	6.65	5.82	47.36	10.56
PF	8.38	5.68	58.29	11.1
17 PF-EP	6.07	3.9	51.76	10.18
23 PF-EP	7.1	3.54	53.08	10.97
34 PF-EP	7.32	3.8	50.33	12.53

R_m= Residual mass at 700^{0}C

Accepted Manuscript

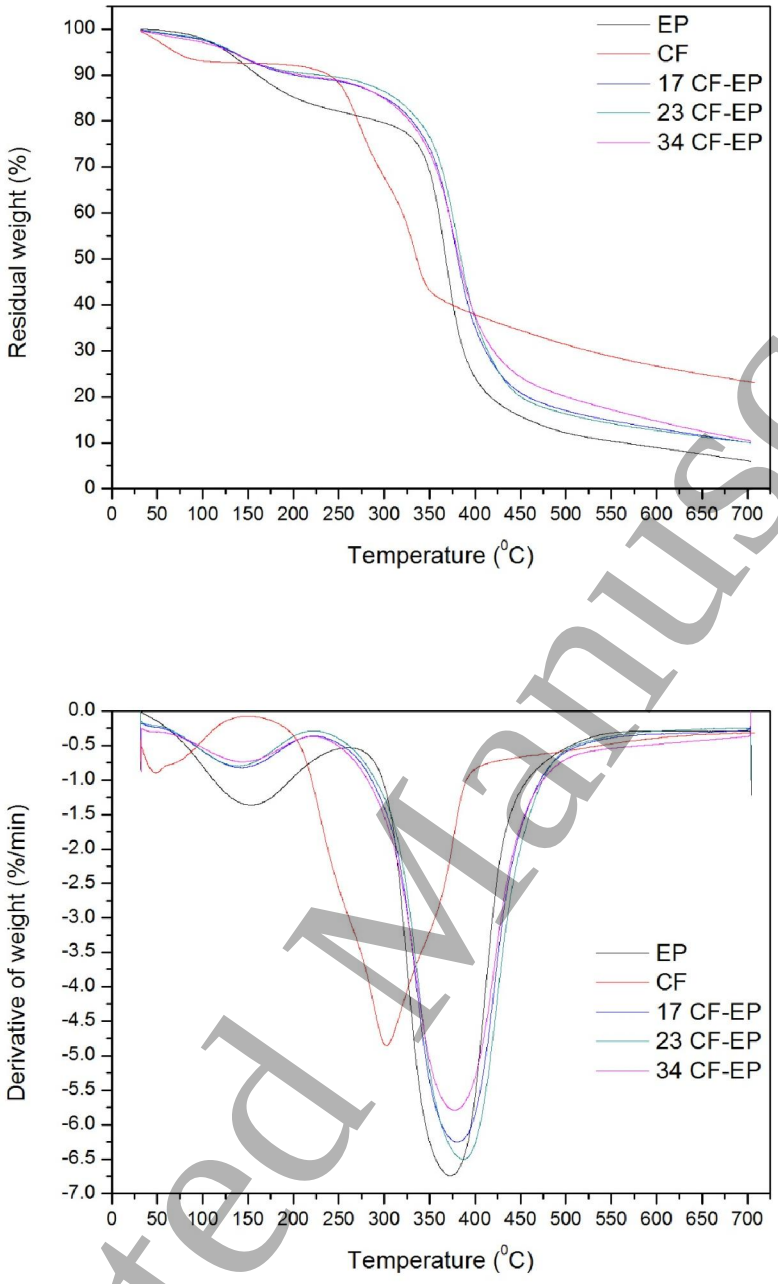


Fig. 4 TG (top) and DTG (bottom) curves of virgin epoxy, coir fiber, and coir fiber-epoxy composites

Accepted Manuscript

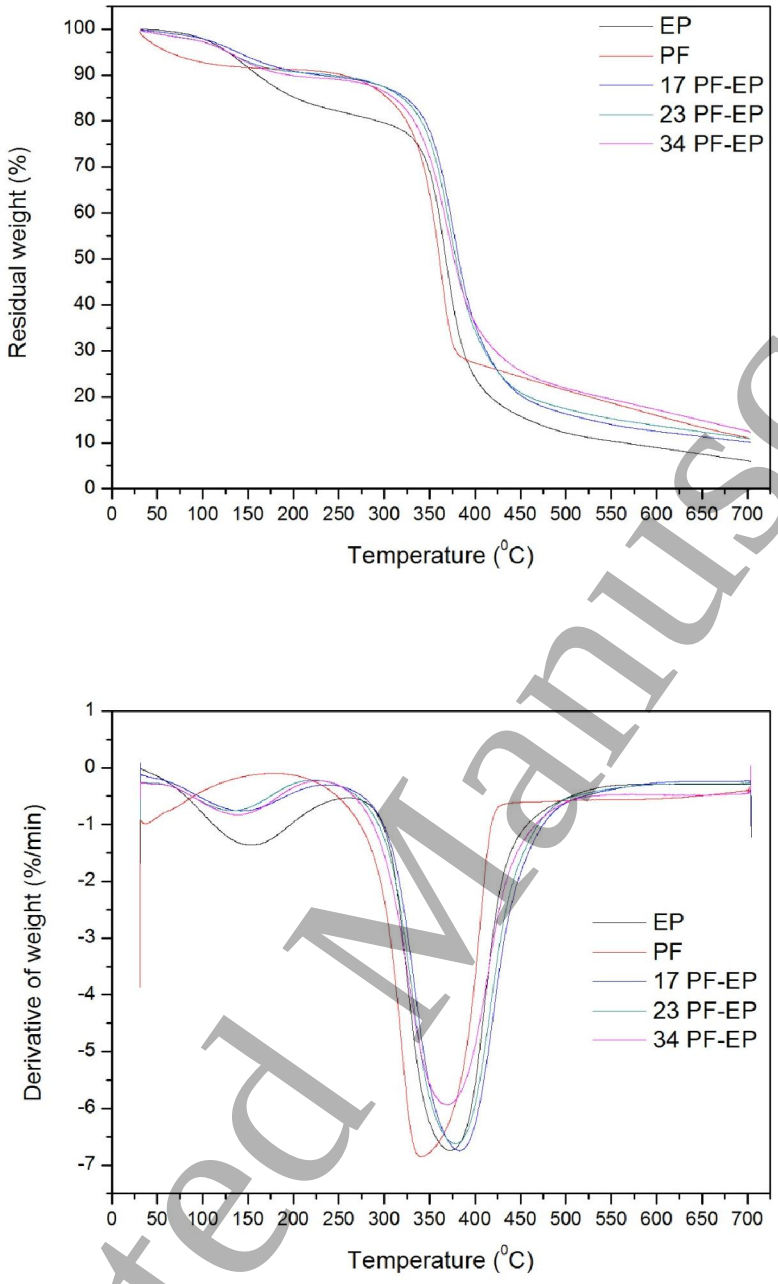


Fig. 5 TG (top) and DTG (bottom) curves of virgin epoxy, pineapple leaf fiber, and pineapple leaf fiber-epoxy composites

3.2 Dynamic Mechanical Thermal Analysis

The properties of fiber reinforced composites are depends on the characteristics of fiber and polymer, interfacial bond strength between them, and the aspect ratio, orientation, distribution, and volume content of the fiber. DMTA is one of the most significant and effective techniques to characterize the viscoelastic properties such as storage modulus, loss

Accepted Manuscript

modulus, and damping behavior of composites with respect to temperature, time, and frequency of oscillation.

Effect of fiber content on the storage modulus (E') of CF-EP and PF-EP composites

The stiffness of a composite material is mainly affected by the loading of reinforcing fibers. Fig. 6 and 7 shows the effect of fiber content with temperature on storage modulus (E') of the coir fiber-epoxy and pineapple leaf fiber-epoxy composites at a frequency of 1 Hz respectively. In both cases, the storage modulus of composite materials was found to be increased with an increase of fiber content over the entire temperature range. This was attributed to the hindrance in molecular mobility, the formation of more covalent bonds at the fiber-matrix interface, and the interference of molecular chains which results to slow down the stress relaxation process. Previous research works (Ornaghi et al. [37], Romanzini et al. [38], Obaid et al. [39], Idicula et al. [24]) were also reported the same effect. It was observed that the E' of neat polymer and polymer-based composites was reduced dramatically on passing through the dynamic glass transition temperature (T_g). From Table 7 and Figs. 6-7, we can conclude that the composites with 34 vol. % of fibers have the higher stiffness at room temperature or at high temperature compared to all other samples. This enormous increment in stiffness can be explained in terms of the higher fiber-matrix interfacial adhesion, rigidity of polymer chains, and restrictions to the deformability and viscous flow of the matrix. The storage modulus (E') of 17 PF-EP and 23 PF-EP composites had almost the same value. The modulus curves depict the higher E' values of all PF-EP composites than CF-EP composites. This was because of the stronger interfacial adhesion and high strength bonding between the pineapple leaf fibers and neighboring polymeric chains. The effectiveness of reinforcement to increase the stiffness of base polymer resin can be determined by a coefficient 'C' such as

$$C = \frac{{E'_G}/{E'_R}^{Composite}}{{E'_G}/{E'_R}^{Resin}} \quad (2)$$

where E'_G and E'_R are the storage modulus in the glassy and rubbery phase respectively. The higher value of C indicates the poor effectiveness of fiber to elevate the modulus. Usually, filled systems have lower C values as compared to the unfilled matrix polymer. Table 7 shows the calculated effectiveness coefficient 'C' (30-130^{0}C) for both types (CF-EP and PF-EP) of composites. The C value for 34 vol.% reinforced pineapple fiber composite is

Accepted Manuscript

minimum amongst all composites. The value of C is highly increased with the increase of PALF content from 17% to 23% in PF-EP composites. In coir fiber composites, the 23% fiber volume content is the most effective amount to reinforce epoxy matrix polymer. This high effectiveness of 23 CF-EP is in good agreement with their tensile strength data (unpublished author work).

Table 7. Values of effectiveness coefficient 'C', Tan δ peak height and width, glass transition temperature (T_g), loss modulus (E'') curves peak height, and E' values for coir fiber-epoxy and pineapple fiber-epoxy composites

Composites	C	Tan δ peak height	Tan δ peak width	T_g from Tan δ_{max} (^{0}C)	Log E'' Peak height (MPa)	T_g from E'' (^{0}C)	E' value (Pa) at 50^{0}C	E' value (Pa) at 70^{0}C
EP	-	0.82	19.84	52.95	8.79	47.1	2.092E + 09	1.524 E + 08
17 CF-EP	12.96	0.76	16.11	69.8	9.14	61.36	2.001E + 10	2.245E + 08
23 CF-EP	1.88	0.45	19.09	72.5	5.5	65.8	5.975E + 10	1.22E +09
34 CF-EP	2.38	0.41	23.33	63.5	9.15	54.5	7.356E +09	3.709E +09
17 PF-EP	1.15	0.69	18.43	63.72	9.02	54.38	5.037E +10	1.841E +09
23 PF-EP	39.58	0.73	19.08	62.9	9.2	52.17	4.715E +10	1.773E +09
34 PF-EP	0.66	0.53	17.22	66.1	9.58	60.08	1.196E +11	6.315E +09

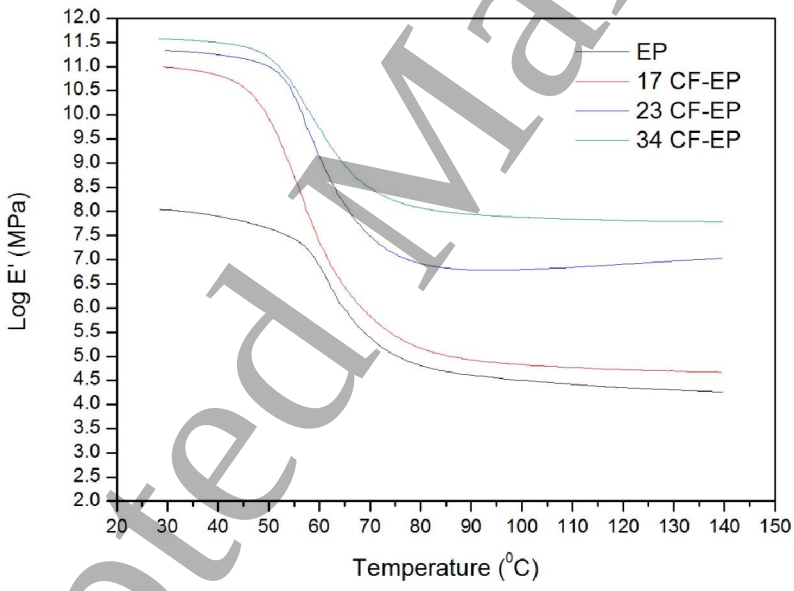


Fig. 6 Effect of fiber content with temperature on storage modulus of the coir fiber-epoxy composites at a frequency of 1 Hz

Accepted Manuscript

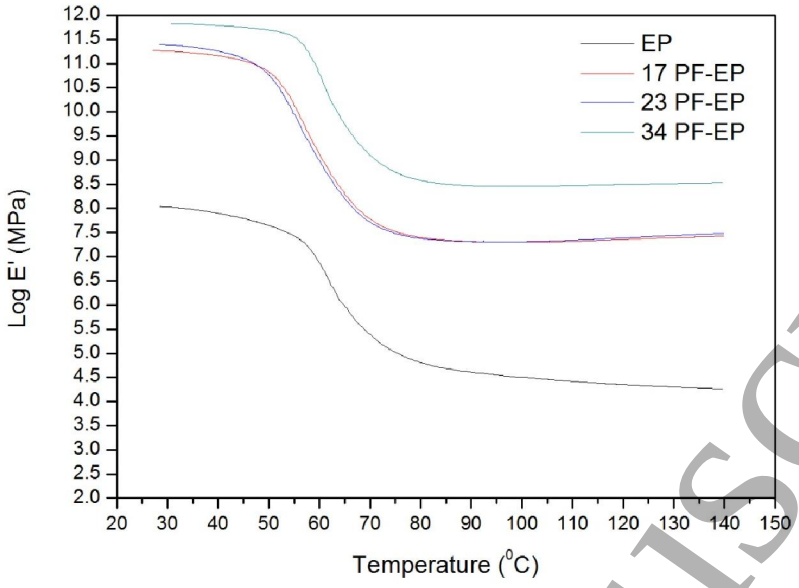


Fig. 7 Effect of fiber content with temperature on storage modulus of the pineapple leaf fiber-epoxy composites at a frequency of 1 Hz

Effect of fiber content on the loss factor (tan δ) of CF-EP and PF-EP composites

The variation of loss factor (tan δ) values with the fiber content and temperature for CF-EP and PF-EP composites at a frequency of 1 Hz are shown in Fig. 8 and 9 respectively. As seen in Fig. 8-9 and Table 7, the tan δ peak of the neat epoxy resin is lying at 52.95^0C (T_g). The temperature at which the tan δ curve shows a peak is called a dynamic glass transition temperature (T_g). It observed that the T_g value of the unfilled polymer was lowest as compared to the coir fiber reinforced and pineapple leaf fiber reinforced composites. This shift of tan δ peak to the higher temperature was because of the interphase interaction between the reinforcing filler and molecular chains. In the context of the glass transition temperature, the 23% and 34 vol.% are the optimum fiber content for coir fiber-epoxy and pineapple leaf fiber-epoxy composites respectively. The peak width and peak height values are also given in Table 7. As expected, the value of tan δ peak height was reduced after the incorporation of fiber in an epoxy resin. Amongst all samples, a shorter and wider peak was obtained in the case of 34 CF-EP. This was attributed to the better distribution of the fibers in matrix resin which leads to an inhibition of the relaxation process and the improvement in rigidity of polymeric chains. Fig. 8 clearly depicts that the peak height and width values for 23 CF-EP and 34 CF-EP composites was approximately the same, but the value of 'C' and T_g are more in favor in the case of 23 vol.% coir fiber reinforced composite. In PF-EP composites, the damping peak height was increased from 0.69 to 0.73, and T_g was decreased

Accepted Manuscript

from 63.72 to 62.9 ^{0}C, with the increase of fiber content from 17% to 23%. This may be due to the more interfacial area and large frictional forces which leads to more energy dissipation to overcome the friction. From Table 7, it can also be concluded that the COIR/Epoxy composites possess relatively higher value of T_g as compared to the PALF/Epoxy composites. This was because of the lesser cellulosic content and porous morphology of coir fiber than that of pineapple leaf fiber (shown in Table 2 and Fig. 1 respectively) which leads to the soundly interfacial adhesion and wetting of coir fiber with epoxy resin by capillary action.

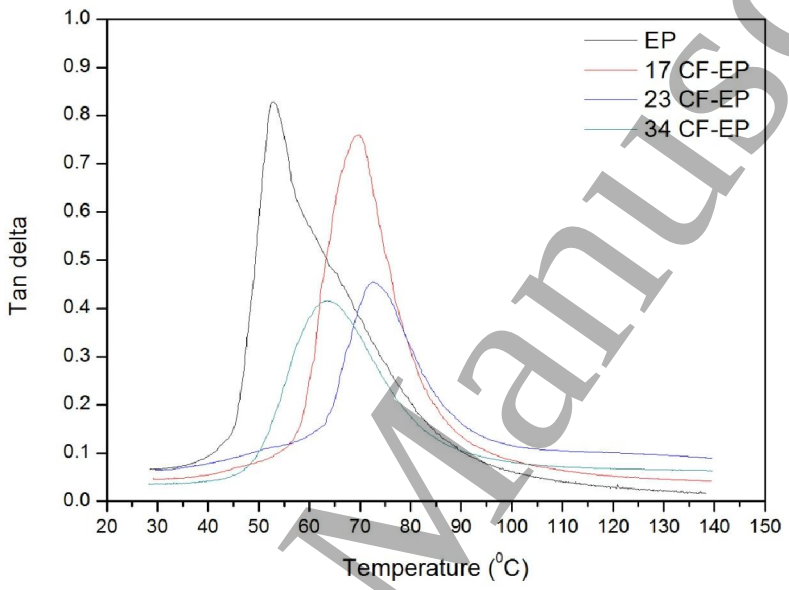


Fig. 8 Effect of fiber content with temperature on tan δ of the coir fiber-epoxy composites at a frequency of 1 Hz

Accepted Manuscript

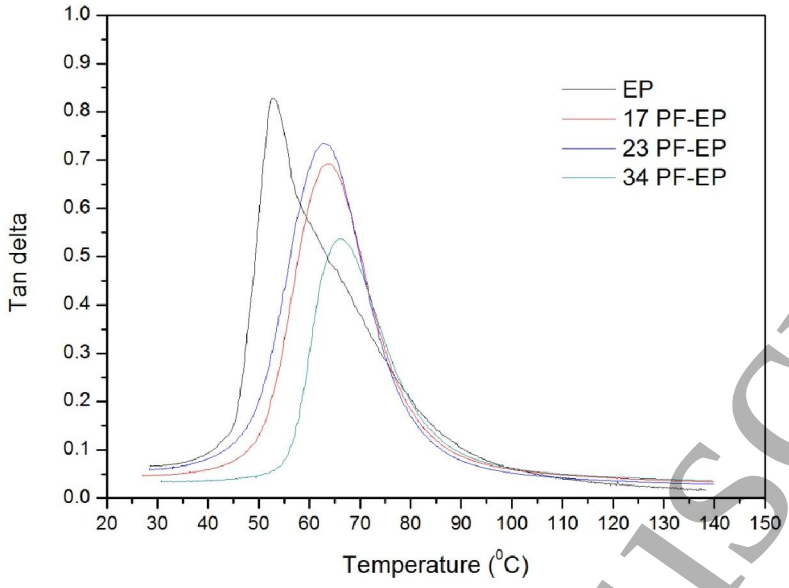


Fig. 9 Effect of fiber content with temperature on tan δ of the pineapple leaf fiber-epoxy composites at a frequency of 1 Hz

Effect of fiber content on the loss modulus (E'') of CF-EP and PF-EP composites

The effect of fiber content with temperature on the viscous response (loss modulus, E'') of CF-EP and PF-EP composites was recorded in Fig. 10 and 11 respectively. The temperature corresponding to the peak of E'' represents the T_g, at which the maximum energy dissipation occurred in the form of heat. The loss modulus (E'') peak height and T_g values are mentioned in Table 7. The elevation of peak height and the shifting of T_g to the higher temperature was observed with the increase of fiber content. This was because of the increment in the heterogeneity of polymer matrix, and recoverable viscoelastic deformation at higher concentration. All E'' curves attained a peak (maximum energy dissipation) and decreases at higher temperature (above T_g), due to the free molecular motion. It was observed from Figs. 10 and 11 that the effect of fibers is more prominent at the higher temperature (above T_g). From Table 8, it was cleared that the glass transition temperature (T_g) obtained from the peak of loss modulus (E'') curve was lower than that of damping factor (Tan δ) curve. The E'' value (MPa) of 34 vol.% is greater considerably than 17% and 23% fiber composites at a higher temperature. This result confirmed the higher activation energy required to mobile the polymer chains in case of 34% reinforced fiber-matrix composites.

Accepted Manuscript

Table 8. Comparison of T_g obtained from the Tan δ and loss modulus curve

Composites	T_g from Tan δ_{max} (^{0}C)	T_g from E'' (^{0}C)	Comment
EP	52.95	47.1	The glass transition temperature (T_g) is not a well defined temperature for thermodynamic phase transition. It depends on the experimental conditions (velocity or frequency used and cooling or heating rate). The T_g value obtained from E'' was lower (5-10^{0}C) than the value obtained from Tan δ_{max}. It can be defined by using the definition: Tan δ is defined as the ratio of loss modulus (E'') to storage modulus (E') which does not have the same maximum as E'' by itself. The glass transition is really a range of behavior where material softens.
17 CF-EP	69.8	61.36	
23 CF-EP	72.5	65.8	
34 CF-EP	63.5	54.5	
17 PF-EP	63.72	54.38	
23 PF-EP	62.9	52.17	
34 PF-EP	66.1	60.08	

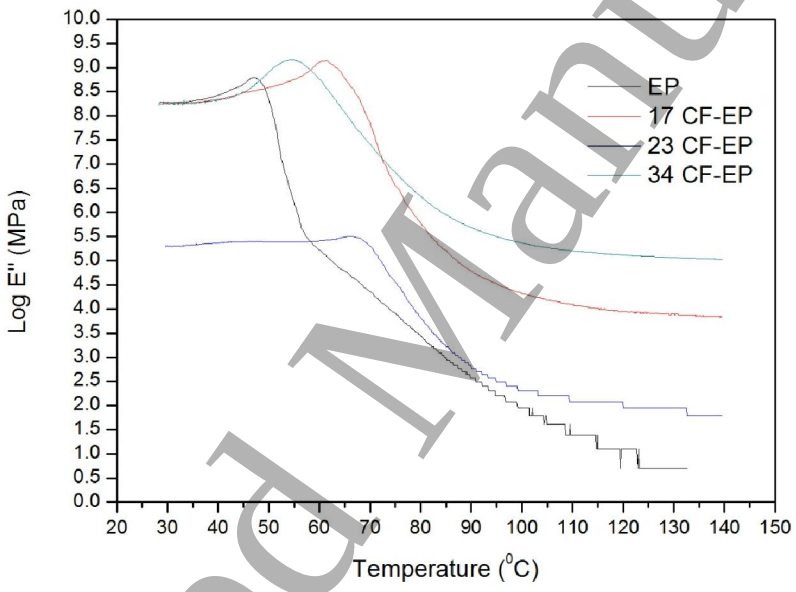


Fig. 10 Effect of fiber content with temperature on loss modulus of the coir fiber-epoxy composites at a frequency of 1 Hz

Accepted Manuscript

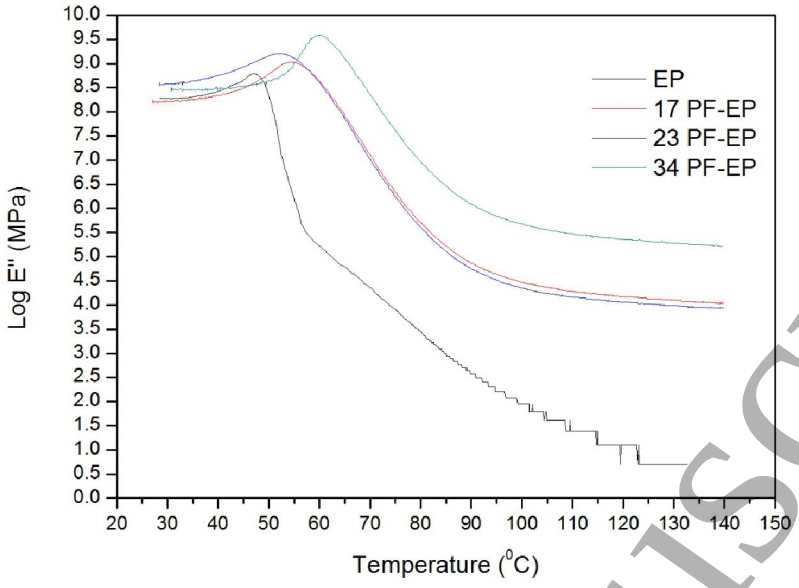


Fig. 11 Effect of fiber content with temperature on loss modulus of the pineapple leaf fiber-epoxy composites at a frequency of 1 Hz

Effect of frequency

In characterizing the viscoelastic behavior of a composite material, the frequency of oscillation plays a vital role. The stiffness and damping behavior of a material is a function of the frequency at which the load is applied. In this regard, the effect of a frequency with temperature on E' and tan δ of 34 CF-EP and 34 PF-EP are shown in Figs. 12-13 respectively. It can be observed that the value of the storage modulus (E') was reduced with the increase of oscillation frequency. Usually, the stiffness of a polymeric material is higher at high frequency (short time) than the lower frequency (large time). But, in this case, the reverse effect was observed. This surprising result may be due to the increased molecular-molecular interactions and entanglements of the polymeric chains over the time period. As seen in Table 9, we can report that the glass transition temperature and tan δ peak height of 34 CF-EP were increased, with the increase of frequency. This behavior confirmed the good damping power of manufactured composites at a higher frequency.

Table 9. Effect of frequency on glass transition temperature (T_g), tan δ peak and width values, and E' (storage modulus) of 34 vol.% fiber reinforced composites

Composites	T_g	Tan δ peak height	Tan δ peak width	E' value (Pa) at 50^0C	E' value (Pa) at 70^0C
34 CF-EP (1)	63.5	0.41	23.33	7.356E +09	3.709E +09
34 CF-EP (5)	70.8	0.58	22.61	3.164E +10	2.822E +09

Accepted Manuscript

34 PF-EP (1)	66.1	0.53	17.22	1.196E +11	6.315E +09
34 PF-EP (5)	64.8	0.55	23.28	8.167E +10	5.416E +09

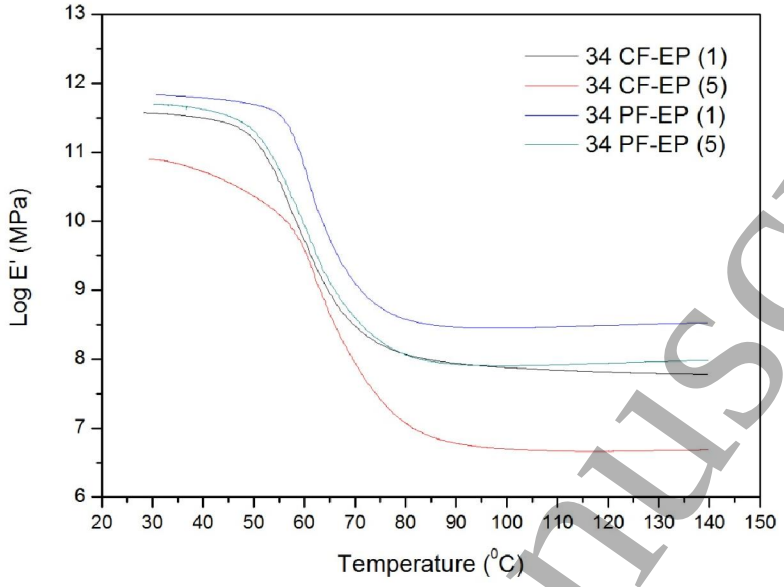


Fig. 12 Effect of frequency on storage modulus of the 34 CF-EP and 34 PF-EP composites as a function of temperature

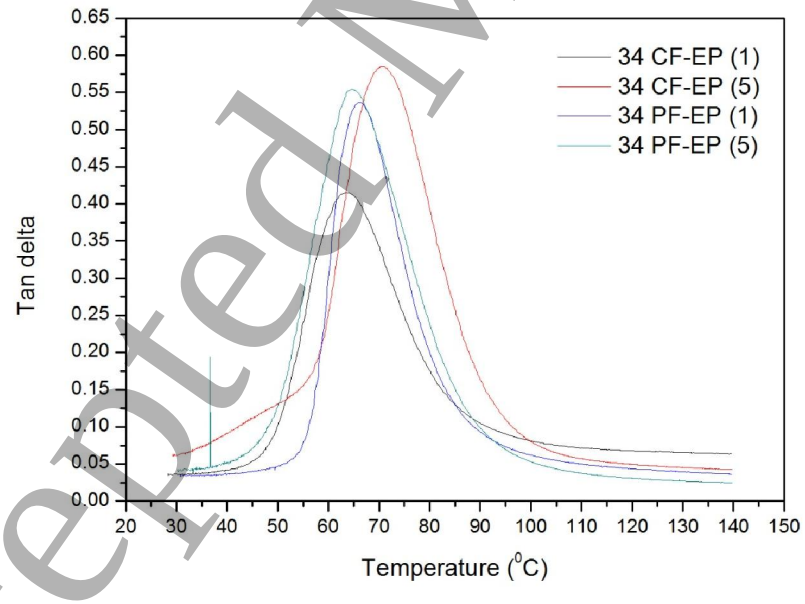


Fig. 13 Effect of frequency on loss factor (tan δ) of the 34 CF-EP and 34 PF-EP composites as a function of temperature

Accepted Manuscript

Cole-Cole Plot

In order to understand the structural/property relationship, the Cole-Cole plots are widely used. The effect of fiber content on the dielectric relaxation of a polymer can be analyzed by using the Cole-Cole plot. Fig. 14 and 15 depict the Cole-Cole plots of unfilled epoxy and filled epoxy system with coir fiber and pineapple leaf fiber respectively. The nature of the plot is an important tool to determine the homogeneity of the system. J. Ferry et al. reported that the homogenous polymeric systems should indicate a semicircular plot [13]. As seen in Figs. 14-15, where the log E'' values are plotted as a function of log E', the Cole-Cole plots for all the composites are imperfect circles. It was observed that the extent of plot imperfection was increased, with the increase of fiber content. Even, an unfilled epoxy polymer shows a large amount of heterogeneity. The 17 PF-EP and 23 PF-EP composites show the similar Cole-Cole plot. This result confirmed that both composites have almost the same degree of homogeneity.

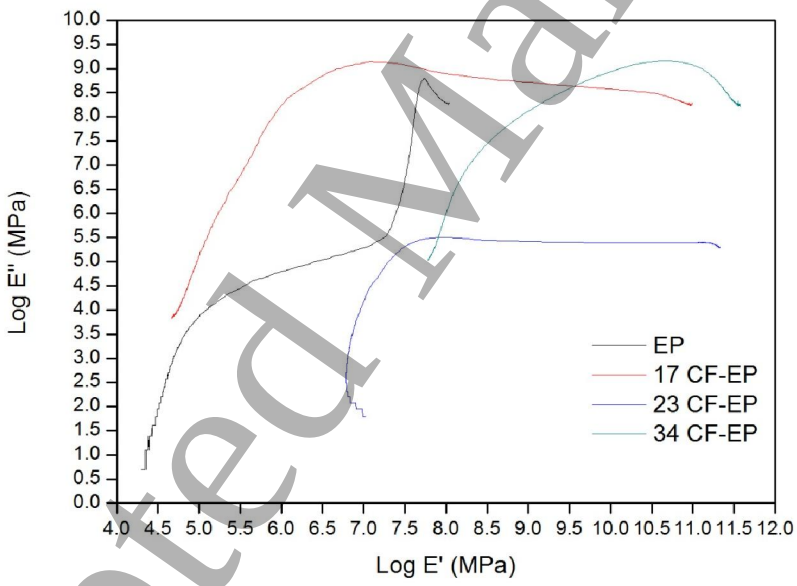


Fig. 14 Cole-Cole plots of the unfilled epoxy and filled epoxy with various fiber content of coir fiber

Accepted Manuscript

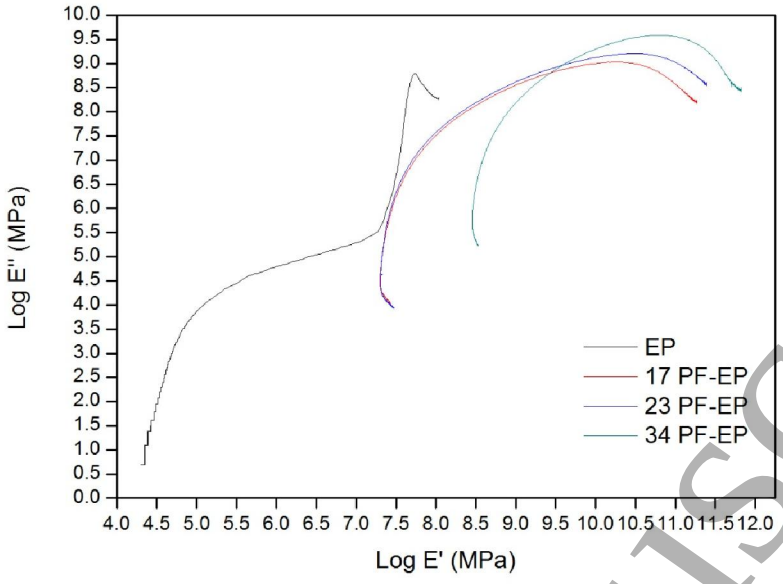


Fig. 15 Cole-Cole plots of the unfilled epoxy and filled epoxy with various fiber content of pineapple leaf fiber

4. Conclusions

The primary focus in this work was to study the effect of fiber content on the thermal stability and viscoelastic properties of epoxy composites. Based on this study the following conclusions can be made:

- The thermal stability, storage modulus (E'), loss modulus (E''), and glass transition temperature (T_g) of epoxy matrix polymer increases with the incorporation of coir and pineapple leaf fiber. This was attributed to the rigidity of polymer chains and higher restrictions in molecular mobility.
- In context to the thermal stability of coir-epoxy and pineapple-epoxy composites, the optimum fiber volume content is 23%. The main degradation temperature of epoxy polymer resin was increased by 16.79 ^{0}C and 23.14 ^{0}C after the loading with 23% coir and pineapple leaf fiber respectively.
- The order of thermal stability in coir fiber-epoxy and pineapple fiber-epoxy composites is: 23 CF-EP> 34 CF-EP> 17 CF-EP> EP> CF; 23 PF-EP> 34 PF-EP> 17 PF-EP> EP> PF respectively.
- The 23% coir and 34% pineapple leaf fiber reinforced composites have the lowest value of effectiveness coefficient 'C' obtained by the storage modulus analysis.

Accepted Manuscript

- The single tan δ peak (corresponds to the β relaxation) of the neat epoxy matrix was higher than the fiber reinforced composites. It indicates the good damping ability of polymer matrix. In case of composites, the tan δ peak height was reduced with the increase of fiber volume content.
- The reduction in storage modulus (E') of epoxy and epoxy-fiber composites over the temperature range 45-80 ^{0}C corresponds to the transition from the glassy phase to the rubbery phase.

Acknowledgments: The authors extend their gratitude to the Delhi Technological University, Delhi (India) for supporting this research work.

Conflicts of Interest: The authors declare no conflict of interest.

Funding: This research work received no specific grant from any funding agency in the public, commercial, and non profit sectors.

References

1. Statistical databases of "*Food and Agriculture Organization of the United Nations*", www.fao.org/statistics/databases/en/

2. Panyasart K, Chaiyut N, Amornsakchai T, and Santawitee O 2014 Effect of surface treatment on the properties of pineapple leaf fibers reinforced polyamide 6 composites *Energy Procedia* **56**: 406-413.

3. Nakagaito A N and Yano H 2008 The effect of fiber content on the mechanical and thermal expansion properties of biocomposites based on microfibrillated cellulose *Cellulose* **15**: 555-559.

4. Lu Na and Oza S 2013 Effect of surface treatment of hemp fibers on the thermal stability of Hemp-PLA composites *Adv. Mat. Res.* **651**: 499-504.

5. Sergio N M, Veronica C, and Rodriguez R J S 2012 The thermogravimetric behavior of natural fibers reinforced polymer composites *Mat. Sci. Eng.* **557**: 17-28.

6. Rachini A, Troedec M, Peyratout C, and Smith A 2008 Comparison of the thermal degradation of natural, alkali-treated, and silane-treated hemp fibers under air and an inert atmosphere *J. Appl. Polym. Sci.* **112**: 226-234.

Accepted Manuscript

7. Lee S H and Wang S 2006 Biodegradable polymers/bamboo fiber biocomposite with a bio-based coupling agent *Compos. Part A* **37**:80-91.

8. Manfredi L B, Rodriguez E S, Wladyka Przybylak M, and Vazquez A 2006 Thermal degradation and fire resistance of unsaturated polyester, modified acrylic resins and their composites with natural fibers *Polym. Degrad. Stab.* **91**: 255-261.

9. Jandas P J, Mohanty, S, Nayak, S K, and Srivastava H 2011 Effect of surface treatments of banana fiber on the mechanical, thermal, and biodegradability properties of PLA/Banana fiber biocomposites *Polym. Compos.* 1689-1700, doi: 10.1002/pc.

10. Teja M S, Ramana M V, Sriramulu D, and Rao C J 2016 Experimental investigation of mechanical and thermal properties of sisal fiber reinforced composite and effect of SiC filler material *IOP Conf. Ser. Mater. Sci. Eng.* **149**: 1-10.

11. Zhang K, Wang F, Liang W, Wang Z, Duan Z, Duan Z, and Yang B 2018 Thermal and mechanical properties of bamboo fiber reinforced epoxy composites *Polym.* **10**: 1-18.

12. Tajvidi M and Takemura A 2010 Thermal degradation of natural fiber reinforced polypropylene composites *J. Thermoplast. Compos. Mater.* **23**: 281-298.

13. Ferry J D 1980 Viscoelastic properties of polymers, *Wiley: NY.*

14. Ray D, Sarkar B K. Das S, and Rana A K 2002 Dynamic mechanical and thermal analysis of vinyl-ester resin matrix composites reinforced with untreated and alkali treated jute fibers *Compos. Sci. Technol.* **62**: 911-917.

15. Clark R L, Craven M D, and Kander R G 1990 Nylon 66/poly(vinyl pyrrolidone) reinforced composites: 2: Bulk mechanical properties and moisture effects *Compos. Part A* **30**: 37-48.

16. Mallarino S, Chailan J, and Vernet J L 2009 Interphase study in cyanate/glass fiber composites using thermomechanical analysis and micro-thermal analysis *Compos. Sci. Technol.* **69**: 28-32.

17. Baghaei B, Skrifvars M, Rissanes M, and Ramamoorthy S K 2014 Mechanical and thermal characterization of compression molded polylactic acid natural fiber

Accepted Manuscript

composites reinforced with hemp and lyocell fibers *J. Appl. Polym. Sci.* 1-10, doi: 10.1002/APP.40534.

18. Pothan L A, Oommen Z, and Thomas S 2003 Dynamic mechanical analysis of banana fiber reinforced polyester composites *Compos.Sci.Technol.* **63**: 283-293.

19. John M D and Anandjiwala R D Characterization of viscoelastic properties of flax reinforced polypropylene composites.

20. Gupta M K and Srivastava R K 2017 Mechanical, thermal, and dynamic mechanical analysis of jute fiber reinforced epoxy composite *Ind. J. Fib. Tex. Res.* **42**: 64-71.

21. Shanmugam D and Thiruchitrambalam M 2013 Static and dynamic mechanical properties of alkali treated unidirectional continuous Palmyra palm leaf stalk fiber/Jute fiber reinforced hybrid polyester composites *Mater. Des.* **97**: 533-542.

22. Song Y S, Lee J T, Sunji D, Kim M W, and Lee S H 2011 The viscoelastic and thermal behavior of woven hemp fiber reinforced polylactic acid composites *Compos. Part B* **43**: 856-860.

23. Chung T J, Park J W, Lee H J, Kwon H J, Kim H J, Lee Y K, and Yin Tze W 2018 The improvement of mechanical properties, thermal stability, and water absorption resistance of an eco-friendly PLA/Kenaf biocomposite using acetylation *Appl. Sci.* **8**: 1-13.

24. Idicula M, Malhotra S K, Joseph K, and Thomas S 2005 Effect of layering pattern on dynamic mechanical properties of randomly oriented short banana/sisal hybrid fiber reinforced polyesters composites *J. Appl. Polym. Sci.* **97**: 2168-2174.

25. Alexander J and Elphej S J 2017 Mechanical characterization of basalt based natural hybrid composites for aerospace applications *IOP Conf. Ser. Mater. Sci. Eng.* **197**: 1-8.

26. Nishitani Y, Yamanaka T, Kajiyama T, and Kitano T 2016 Thermal properties of hemp fiber reinforced plant derived polyamide biomass composites and their dynamic viscoelastic properties in the molten state *In-Tech* 53-79, doi: 10.5772/64215.

Accepted Manuscript

27. Padal K T B, Srikiran S, Nagendra P S 2014 Dynamic mechanical and thermal properties of jute nanofibre reinforced polymer composite *5th International & 26th All India Manufacturing Technology, Design, and Research Conference* **128**: 1-6.

28. Asabe B D 2016 Thermo-mechanical characterization of banana particulate reinforced PVC composite as piping material *J. King Saud Univ.* doi: 10.1016/j.jksues.2016.11.001.

29. Alexander J and Churchill E 2017 Mechanical characterization of basalt based natural hybrid composites for aerospace applications *IOP Conf. Ser. Mater. Sci. Eng.* doi: 10.1088/1757-899X/197/1/012008.

30. Tajvidi M and Takemura A 2008 Effect of fiber content and type, compatibilizer, and heating rate on thermogravimetric properties of natural fiber high-density polyethylene composites *Polym. Compo.* doi: 10.1002/pc.20682.

31. Niu P, Liu B, Wei X, Wang X, and Yang J 2011 Study on mechanical properties and thermal stability of polypropylene/hemp fiber composites *J. Reinf. Plast. Compo.* **30**: 36-44.

32. Yao F, Wu Q, Lei Y, Guo W, and Xu Y 2008 Thermal decomposition kinetics of natural fibers: Activation energy with dynamic thermogravimetric analysis *Polym. Degrad. Stab.* **93**: 90-98.

33. El-Shekeil Y A, Sapuan S M, Abdan K, and Zainudin E S 2012 Influence of fiber content on the mechanical and thermal properties of kenaf fiber reinforced thermoplastic polyurethane composites *Mater. Des.* **40**: 299-303.

34. Yang H, Yan R, Chen H, Lee D H, and Zheng C 2007 Characteristics of hemicellulose, cellulose, and lignin pyrolysis *Fuel* **86**(12): 1781-1788.

35. Nasar M N, and Mackay G D M 1984 Mechanism of thermal degradation of lignin *Wood Fib. Sci.* **16**(3): 441-453.

36. Paiva J M and Frollini E 2006 Unmodified and modified surface sisal fibers as reinforcement of phenolic and lignophenolic matrices composites: Thermal analysis of fibers and composites *Macromol. Mater. Eng.* **291**: 405-417.

Accepted Manuscript

37. Ornaghi H L, Bolner A S, Fiorio R, Zattera A J, and Amico S C 2010 Mechanical and dynamic mechanical analysis of hybrid composites molded by resin transfer molding *J. Appl. Polym. Sci.* **118**: 887-896.

38. Romanzini D, Lavoratti A, Ornaghi H, Amico S C, and Zattera A J 2013 Influence of fiber content on the mechanical and dynamic mechanical properties of glass/ramie polymer composites *Mater. Des.* **47**: 9-15.

39. Obaid N, Kortschot M T, and Sain M 2017 Understanding the stress relaxation behavior of polymers reinforced with short elastic fibers *Mater.* doi: 10.3390/ma10050472.

Accepted Manuscript

International Journal of Research in Engineering and Innovation (IJREI)
journal home page: http://www.ijrei.com
ISSN (Online): 2456-6934



Energy-Exergetic performance and parametric evaluation of Haylent liquefaction system using different gasses system

R.S. Mishra, Devender Kumar

Department of Mechanical, Production and Automobile Engineering, Delhi Technological University, Delhi, India

Abstract

The present studies concern on energy and exergy analyses of various cryogenics system up to their sub component level. A parametric study is conducted to investigate the effects of variation of various system input parameters such as pressure ratio, expander mass flow ratio, compressor output temperature on different performance parameters like COP , work input ,liquefaction rate ,specific heat and exergy. The numerical computations have been carried out for six system are study with six different gases for liquefaction like oxygen, argon, methane, fluorine, air and nitrogen respectively. Effect of different input gas also studies carefully and behavior of different gases in different system is concluded.
© 2017 ijrei.com. All rights reserved
Keywords: Energy-Exergetic Performance, Parametric Evaluation, Haylent liquefaction system

1. Introduction

Cryogenics has been an important area of refrigeration because of its application in industrial and commercial utilization, and many scientific and engineering researches are going on by using low temperature liquefied gases. Cryogenics isa branch of physics which deals with the achieving very low temperatures (below the 173 K.) and study their effects on matter .Cryogenic study presents broad goals for cryogenic support for various gas liquefaction systems. Due to industrial revolution, various issues like cost, efficiency and reliability are the challenges factors in employment of cryogenic support technology. In field of mechanical engineering we try to refine or improve the ability or quality of material to get in maximum use at maximum level at a reduce cost. In past many fantasticclaimhave been made as to the degree of improve performance achieved by employing cryogenics technology

In 1949 Helandt Davies in his research noticed that if the Claude system work on relative high pressure,e.g., approx. 200 bar for air liquefaction. The first heat exchanger in the system can eliminate; such modified system is extensively used in high-pressure liquefaction plant of air and known as high pressure modifiedClaude system or Haylent system. The problem of lubrication in expander is successfully eliminated in this modification. Use of light lubricant are quite suitable because, in the air-liquefaction system, the gas enters the expander at ambient temperature and leaves the expander at approximately 150 K (-190°F), so that light lubricants properties not much detroit. In high pressure Haylent system expander adjustment is also very crucial. All sub-component like compressor, expander, two heat exchangers with throttle valve and separator are arranged as shown in Figure .1.The block diagram completely define the working of system. The gas which has to be liquefied is fed in compressor at ambient condition like at 1.013 bar and 300 K .The gas is compressed up to their optimized pressure ratio selected on the basis of chosen gas. This compressed gas is further divided in two parts in perfect ratio for expander. One part of gas goes into expander while other part fed into the heat exchanger as a hot stream. Expander gives additional refrigeration effect in the system by giving additional cooling effect to the cold stream of gas into exchanger. After passing through the heat exchanger gas reached up to their critical temperature.

Corresponding author : R.S. Mishra
Email Id: rsmishradtu@gmail.com

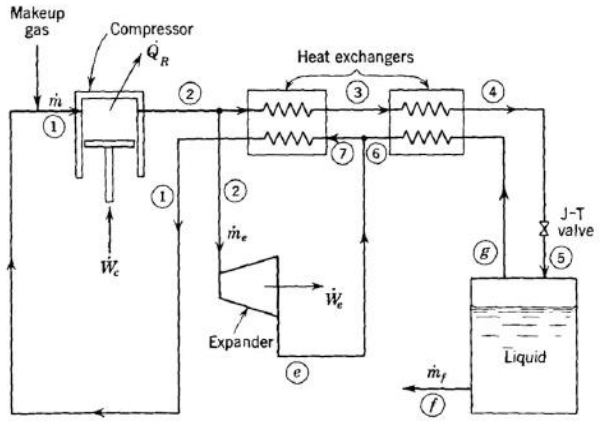


Figure 1: Schematic diagram of Haylent system

Now gas is passed through the J-T valve to get liquefy form of gas at the inlet pressure. The liquefy part is separate into the separator and gas part is recirculated back to the system via mixing with outlet of expander cooled gas. This mixed gas help into the exchanger to reduce the gas temperature up to their critical level via exchanging heat with hot stream. This cold stream after exchanging heat with hot stream add up with make gas to go again in cycle. The main difference in refrigeration and liquefier is that in refrigeration cycle the gas of system always constant while in liquefier the gas is continuously extracted as a liquefy part.

2. Literature Review and Research gap identified

R. Agrawal, D.W. Woodward,[1] carried out exergy analysis, for the efficient cryogenic nitrogen generators: Yasuki Kansha, et.al [2] , evaluated novel cryogenic air separation process based on self-heat recuperation. Gadhiraju Venkatarathnam [3], caried out simulation of cryogenic processes" using cryogenic mixed refrigeration Processes. R.L. Cornelissen, G.G. Hirs,[4] carried out energy-exergy analysis of cryogenic air separation,There is not enough literature available on second law performance on Haylent system. The thermodynamic analysis of Haylent system is presented here**.**

3. Thermal analysis of Haylent system

The work done by the compressor is given as

$$W_e = (m_e * h_2 - m_e * h_e) \quad (1)$$

$$W_c = \left(m * \left((h_2 - h_1)\right) - T_2 * (s_2 - s_1)\right) \quad (2)$$

$$W_{net} = W_c - W_e \quad (3)$$

$$Q = m * (h_2 - h_1) \quad (4)$$

$$y = \left(\frac{h_1 - h_2}{h_1 - h_f}\right) + r * \left(\frac{h_2 - h_e}{h_1 - h_f}\right) \quad (5)$$

$$y = \frac{m_f}{m} \quad (6)$$

$$Ed_{comp} = abs\begin{pmatrix} m * T_1 * (s_1 - s_2) - \\ \left(Q * \left(\frac{T_0}{T_1}\right)\right) \end{pmatrix} \quad (7)$$

$$Ed_{comp_{\%}} = \left(\frac{Ed_{comp}}{Ed_{Haylent}}\right) * 100 \quad (8)$$

$$x_f = 0 \quad (9)$$

$$x_g = 1 \quad (10)$$

$$r = 0.3 \quad (11)$$

$$r = \frac{m_e}{m} \quad (12)$$

$$\frac{W_{net}}{m} = z \quad (13)$$

$$\frac{W_{net}}{m_f} = t \quad (14)$$

$$COP = abs\left(\frac{h_1 - h_f}{W_{net}}\right) \quad (15)$$

$$Eta_{2nd_{\%}} = abs\left(\left(\frac{(h_f - h_1) - T_0 * (s_f - s_1)}{W_{net}} * m_f\right) * 100\right) \quad (16)$$

2.1 First Heat Exchanger (HX_1) analysis

$$TypeHX_{1\$} = 'counterflow'$$

$$epsilon_{HX1} = 0.85 \quad (17)$$

$$T_{h_i} = T_2 \quad (18)$$

$$T_{c_o} = T_8 \quad (19)$$

$$T_{h_o} = T_3 \quad (20)$$

$$T_{c_i} = T_7 \quad (21)$$

$$m_{dot_{h_{HX1}}} = m - m_e \quad (22)$$

$$m_{dot_{c_{HX1}}} = m - m_f \quad (23)$$

$$C_{dot_{h_{HX1}}} = m_{h_{HX1}} * cp_{hot_{fluid_{HX1}}} \quad (24)$$

$$C_{dot_{c_{HX1}}} = m_{c_{HX1}} * cp_{Cold_{fluid_{HX1}}} \quad (25)$$

$$q_{HX1} = C_{h_{HX1}} * \left(T_{h_i} - T_{h_o}\right) \quad (26)$$

$$q_{HX1} = C_{c_{HX1}} * \left(T_{c_o} - T_{c_i}\right) \quad (27)$$

$$q_{maxHX1} = C_{\min HX1} * \left(T_{h_i} - T_{c_i}\right) \quad (28)$$

$$epsilon_{HX1} = \frac{q_{HX1}}{q_{maxHX1}} \quad (29)$$

$$Ntu_{HX1} = \frac{G_{HX1}}{C_{minHX1}} \quad (30)$$

$$Ex_{in_{HX1}} = (m - m_e) * \left((h_2 - h_3) - \left(T_0 * (s_2 - s_3)\right)\right) \quad (31)$$

$$Ex_{out_{HX1}} = \left(m - m_f\right) * \left((h_7 - h_8) - \left(T_0 * (s_7 - s_8)\right)\right) \quad (32)$$

$$Ed_{HX1} = abs\left(\left(Ex_{in_{HX1}}\right) - \left(Ex_{out_{HX1}}\right)\right) \quad (33)$$

$$Ed_{HX1_{\%}} = \left(\frac{Ed_{HX1}}{Ed_{Haylent}}\right) * 100 \quad (34)$$

$$T_6 = T_7 \quad (35)$$

2.2 Second Heat Exchanger(HX_2) analysis

$$TypeHX_{2\$} = 'counterflow'$$

$$epsilon_{HX2} = 0.85 \quad (36)$$

$$m_{c_{HX2}} = m - m_f \quad (38)$$

$$C_{c_{HX2}} = m_{c_{HX2}} * cp_{Cold_{fluid_{HX2}}} \quad (39)$$

$$q_{HX2} = C_{h_{HX2}} * \left(T_3 - T_4\right) \quad (40)$$

$$q_{HX2} = C_{c_{HX2}} * \left(T_6 - T_g\right) \quad (41)$$

$$C_{minHX2} = \min\left(C_{h_{HX2}}, C_{c_{HX2}}\right) \quad (42)$$

$$q_{\max HX2} = C_{minHX2} * \left(T_3 - T_g\right) \quad (43)$$

$$epsilon_{HX2} = \frac{q_{HX2}}{q_{maxHX2}} \quad (44)$$

$$Ntu_HX2 = (G_HX2)/C\min_{HX2} \quad (45)$$

$$Ex_{in_{HX2}} = (m - m_e) * \Big((h_3 - h_4) - \big(T_0 * (s_3 - s_4)\big)\Big) \quad (46)$$

$$Ex_{out_{HX2}} = \big(m - m_f\big) * \Big(\big(h_g - h_6\big) - \big(T_0 * \big(s_g - s_6\big)\big)\Big) \quad (47)$$

$$Ed_{HX2} = abs\Big(\big(Ex_{in_{HX2}}\big) - \big(Ex_{out_{HX2}}\big)\Big) \quad (48)$$

$$Ed_{HX2_{\%}} = \left(\frac{Ed_{HX2}}{Ed_{Haylent}}\right) * 100 \quad (49)$$

"c) J-T Valve analysis"

$$h_4 = h_5 \quad (50)$$

$$Ex_{in_{Val}} = (h_4 - h_0) - T_0 * (s_4 - s_0)$$

$$Ex_{out_{val}} = (h_5 - h_0) - T_0 * (s_5 - s_0) \quad (51)$$

$$Ed_{val} = abs\big(Ex_{in_{Val}} - Ex_{out_{val}}\big) \quad (52)$$

$$Ed_{val_{\%}} = \left(\frac{Ed_{val}}{Ed_{Haylent}}\right) * 100 \quad (53)$$

"c) Sepeator analysis"

$$(m - m_e) * h_5 = m_f * h_f + \big(m - m_e - m_f\big) * h_g \quad (54)$$

$$Ed_{sep} = abs\left(T_0 * \left(\left(\frac{m_g * s_{g1} -}{\big(m_g + m_f\big) * s_5}\right) + \left(\frac{m_g * h_g - m_f * h_f}{T_0}\right)\right)\right) \quad (55)$$

$$Ed_{sep_{\%}} = \left(\frac{Ed_{sep}}{Ed_{Haylent}}\right) * 100 \quad (56)$$

$$m_g = \big(m - m_e - m_f\big) \quad (57)$$

$$s_{g1} = entropy\big(R\$, h = h_g, P = P_1\big) \quad (58)$$

$$Ed_{Haylent} = Ed_{comp} + Ed_{HX1} + Ed_{HX2} + Ed_{val} + Ed_{sep} \quad (59)$$

$$Ntu_{HX1} = HX\big(TypeHX_{1\$}, epsilon_{HX1}, C_{h_{HX1}}, C_{c_{HX1}}, \ 'Ntu'\big) \quad (60)$$

$$Ntu_{HX2} = HX\big(TypeHX_{2\$}, epsilon_{HX2}, C_{h_{HX2}}, C_{c_{HX2}}, \ 'Ntu'\big) \quad (61)$$

In Non ideal gas any variable can be defined by two other dependent variable on them:

$a_{non-ideal\ gas} = fx(b, c)$

Table 1: Variable Table (Heylant System)

Variable (a)	Gas	Variable (b)	Variable (c)
h_0	$R\$$	T_0	P_1
h_1	$R\$$	T_1	P_1
h_2	$R\$$	T_2	P_2
s_0	$R\$$	T_0	P_1
s_1	$R\$$	T_1	P_1
s_2	$R\$$	h_2	P_2
T_e	$R\$$	s_2	P_1
h_e	$R\$$	T_1	P_1
s_f	$R\$$	x_f	P_1
T_f	$R\$$	x_0	P_1
h_f	$R\$$	x_f	P_1
T_g	$R\$$	x_1	P_1
s_g	$R\$$	x_1	P_1
T_3	$R\$$	h_3	P_2
s_3	$R\$$	T_3	P_2
h_3	$R\$$	T_3	P_2
$cp(hf)_{HX1}$	$R\$$	T_2	P_2
$cp(cf)_{HX1}$	$R\$$	T_7	P_1
C_{min}	-	C_{hot_HX1}	C_{cold_HX1}
$cp(hf)_{HX2}$	$R\$$	T_3	P_2
$cp(cf)_{HX2}$	$R\$$	$T_f - 1$	P_1
C_{min}	-	C_{hot_HX2}	C_{cold_HX2}
h_7	$R\$$	T_7	P_1
s_7	$R\$$	T_7	P_1
h_8	$R\$$	T_8	P_1
s_8	$R\$$	T_8	P_1
s_5	$R\$$	h_5	T_f
s_4	$R\$$	h_4	T_4
h_4	$R\$$	T_4	P_2
s_{g1}	$R\$$	h_g	P_1
s_5	$R\$$	x_5	P_1
h_6	$R\$$	x_6	P_1
s_6	$R\$$	T_6	P_1
h_6	$R\$$	T_6	P_1

4. Results and Discussions

In this study, Haylent system for liquefaction of various gases such as oxygen, nitrogen, argon, methane, fluorine and air are studied. Fig.2 shows the variations between COP of the system and the cycle pressure ratio. It has been seen that COP is decreasing with an increase in cycle pressure ratio and methane has the highest value of COP, which is decreasing from 1.662 to 1.244 between pressure ratio 40 to 220, followed by fluorine, oxygen, air, nitrogen and argon has the least value of COP, i.e., varies from 0.8802 to 1.247 for the cycle pressure ratio of 40 to 220. On the other hand, fig-2 shows the variations in second law efficiency with respect to cycle pressure ratio. It has been demonstrated that methane has the highest value of second law efficiency, which is increasing from 5.792% to 21.23% for the cycle pressure ratio of 40 to 220, followed by argon, oxygen, air, nitrogen and fluorine has the minimum value of second law efficiency i.e., changes from 2.889% to 9.342% for the cycle pressure ratio of 40 to 220. Furthermore, fig.-3 shows the variations in mass liquefaction rate of various gases as described above with respect to cycle pressure ratio. It has been observed that methane has the highest liquefaction rate, which is varying from 0.02952kg/s to 0.1446kg/s for the cycle pressure ratio of 40 to 220, followed by argon, oxygen, air, nitrogen and fluorine, it has the minimum value of mass flow rate i.e., varies from 0.01222kg/s to 0.05655kg/s for the selected range of cycle pressure ratio of 40 to 220.

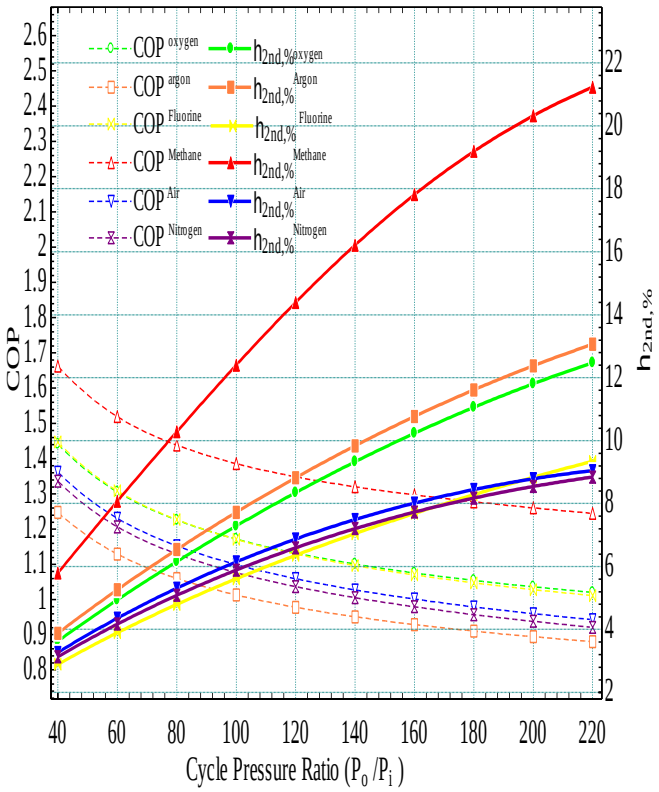


Figure 2: Variations in COP and second law efficiency with cycle pressure ratio

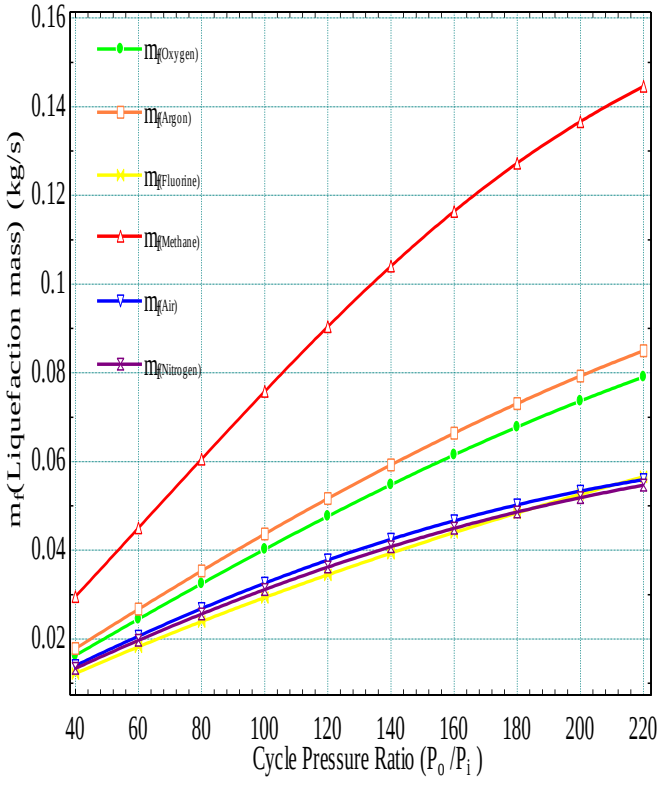


Figure 3: Variation in liquefaction mass flow with cycle pressure

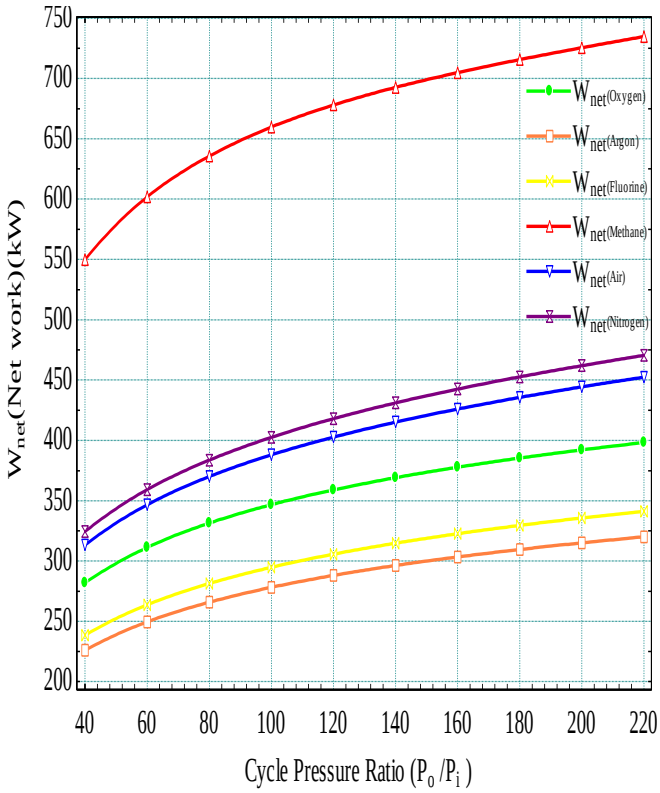


Figure 4: Variation in net work done with cycle pressure ratio

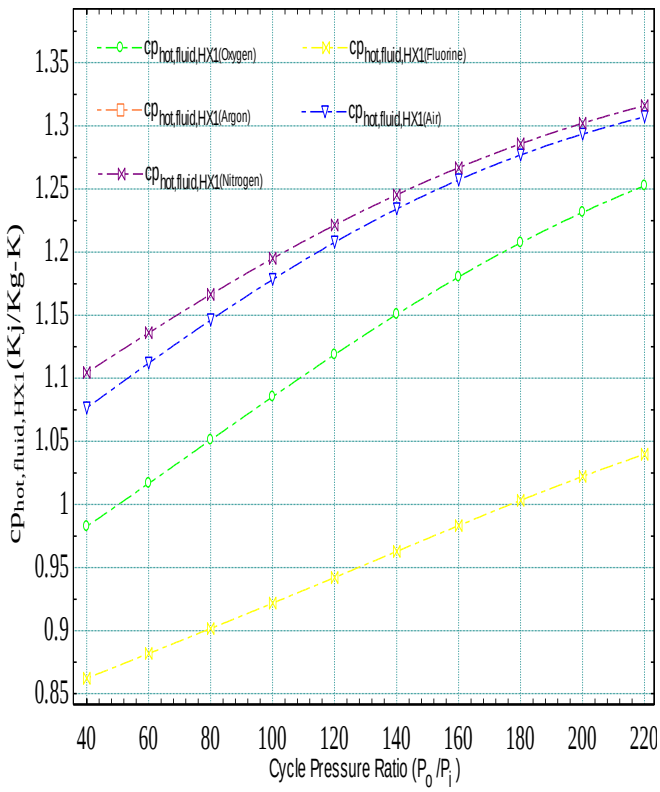


Figure 5: Variation in specific heat of hot fluid in HX1 with cycle pressure ratio

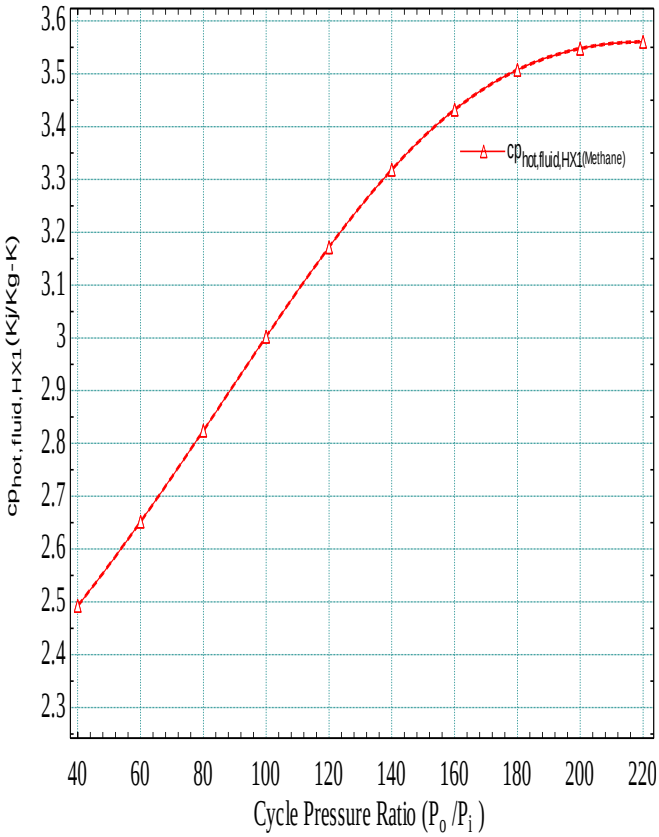


Figure 6: Variation in specific heat of hot fluid in HX1 with cycle pressure ratio

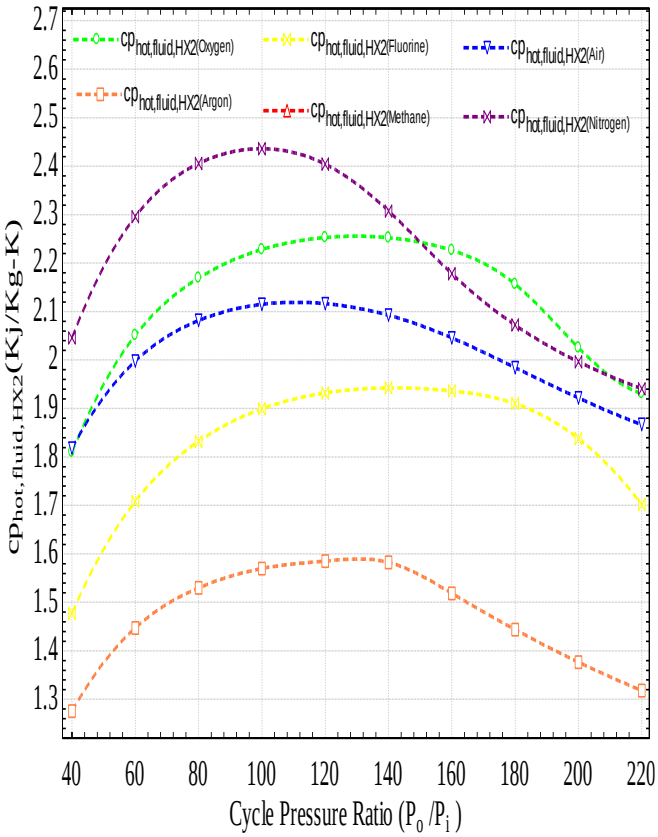


Figure 7: Variation in specific heat of hot fluid in HX2 with cycle pressure ratio

Fig.4 illustrates the variations in net work done with respect to cycle pressure ratio. It has been analyzed that methane has the highest value of net work done, which is increasing from 549.9kW to 734.8kW and argon has the least value of net workdone i.e., increasing from 226kW to 367.2kW for the selected range of cycle pressure ratio of 40 to 220.Fig.6 shows the variation in specific heat of hot fluid in HX1 with respect to cycle pressure ratio of 40 to 220. Fig.6 illustrates that methane has the highest value of specific heat for hot fluid, which is increasing from 2.493kJ/kg-K to 3.561kJ/kg-K. On the contrary side, fluorine has the least value of specific heat for hot fluid, which is enhanced from 0.8623kJ/kg-K to 1.04kJ/kg-K. Fig.7demonstrates the variations in specific heat of hot fluid in HX2 with respect to cycle pressure ratio of 40 to 220. It has been clearly understood from the fig.7 that nitrogen has the highest value of specific heat of hot fluid in HX2 among the other considered gases, which varies from 2.045 kJ/kg-K to 1.9411.04kJ/kg-K, and maximum value of specific heat of hot fluid is found to be 2.404 at cycle pressure ratio of 100, which is followed by oxygen, air, fluorine and argon, respectively.

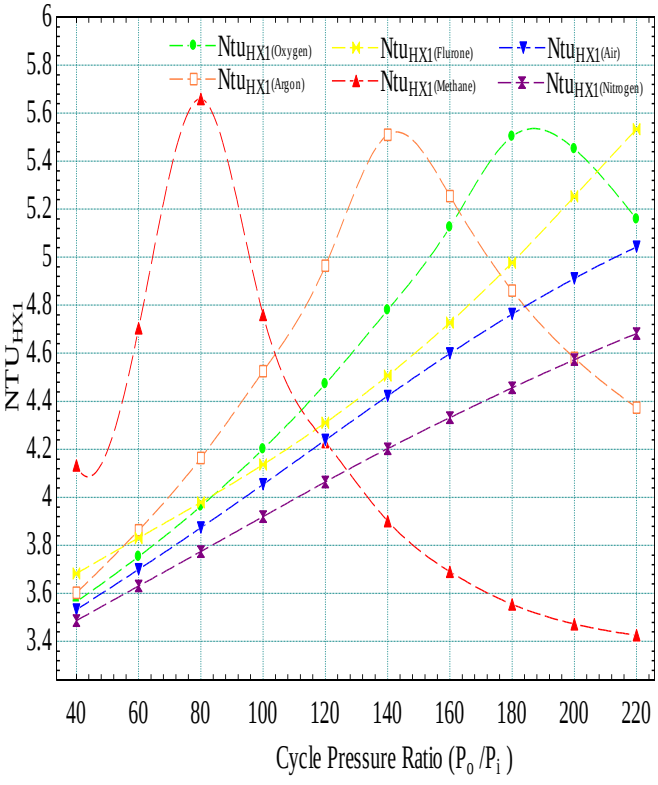


Figure 8: Variation in NTU in HX1 with cycle pressure ratio

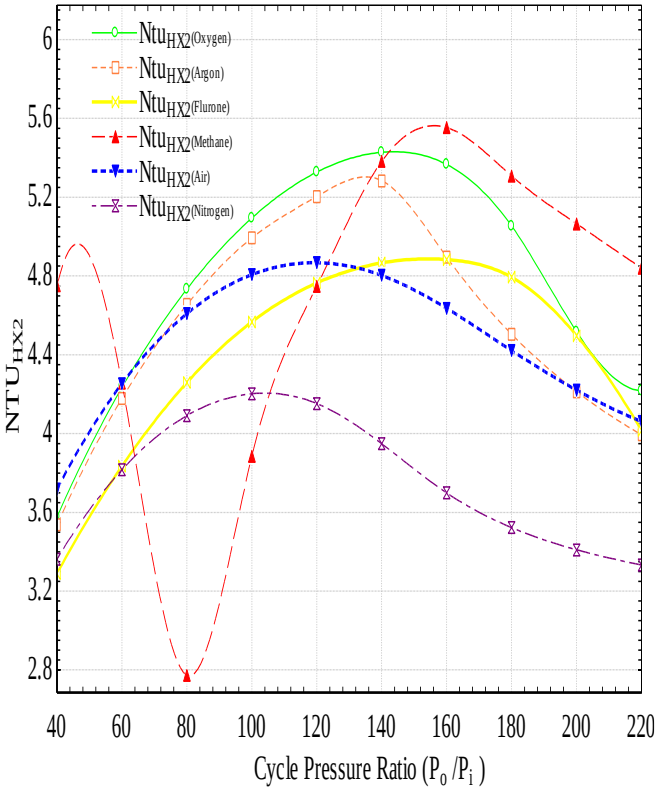


Figure 9: Variation in NTU in HX2 with cycle pressure ratio

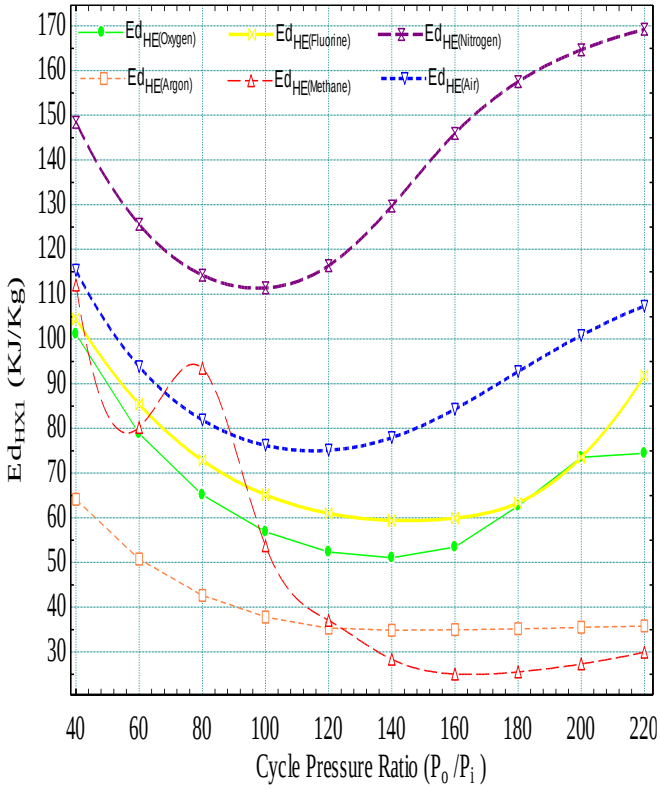


Figure 11: Variation in exergy destruction in HX1 with cycle pressure ratio

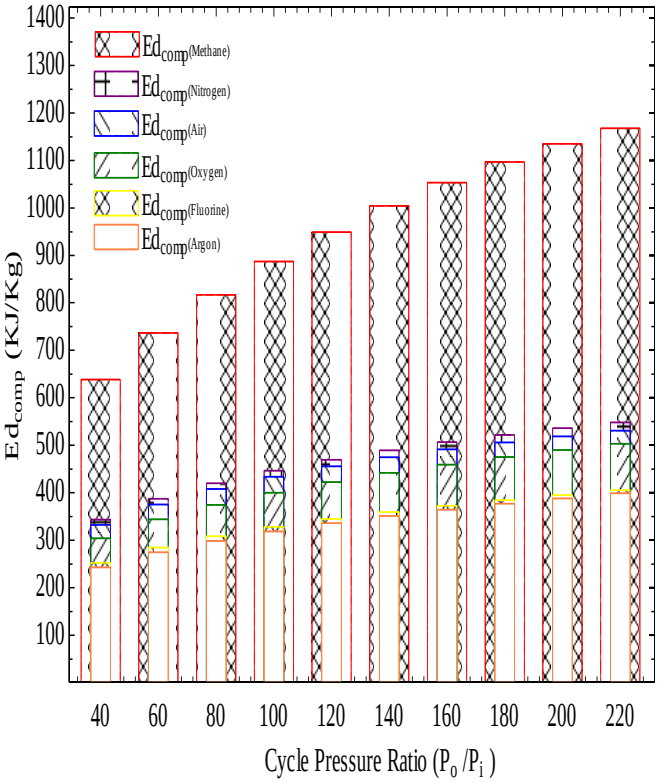


Figure 10: Variation of exergy destruction in compressor with cycle pressure ratio

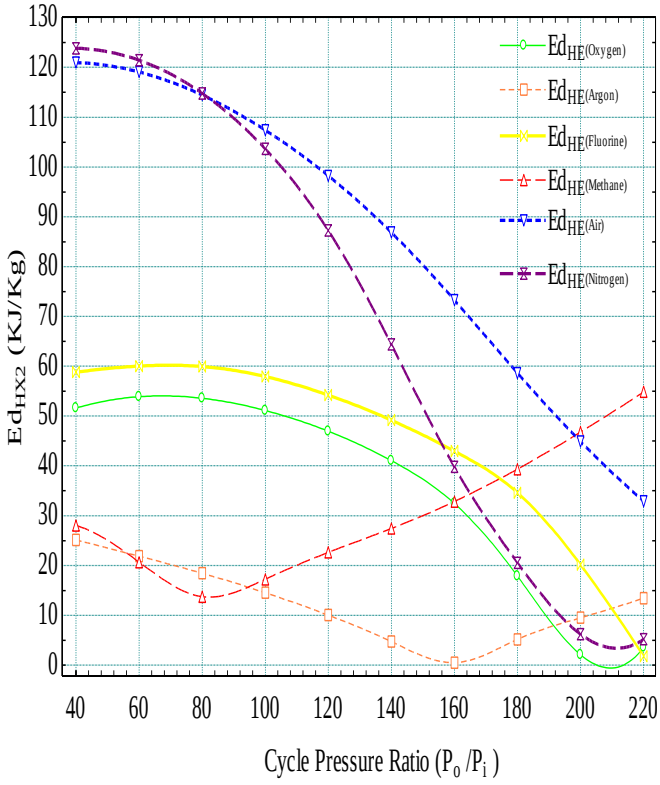


Figure 12: Variation in exergy destruction in HX2 with cycle pressure ratio

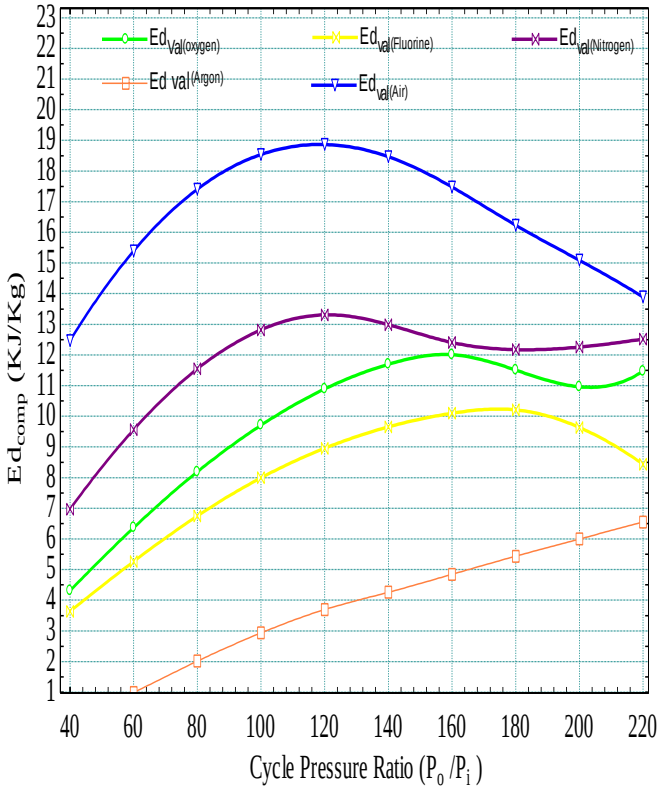


Figure 13: Variation in exergy destruction in compressor with cycle pressure ratio

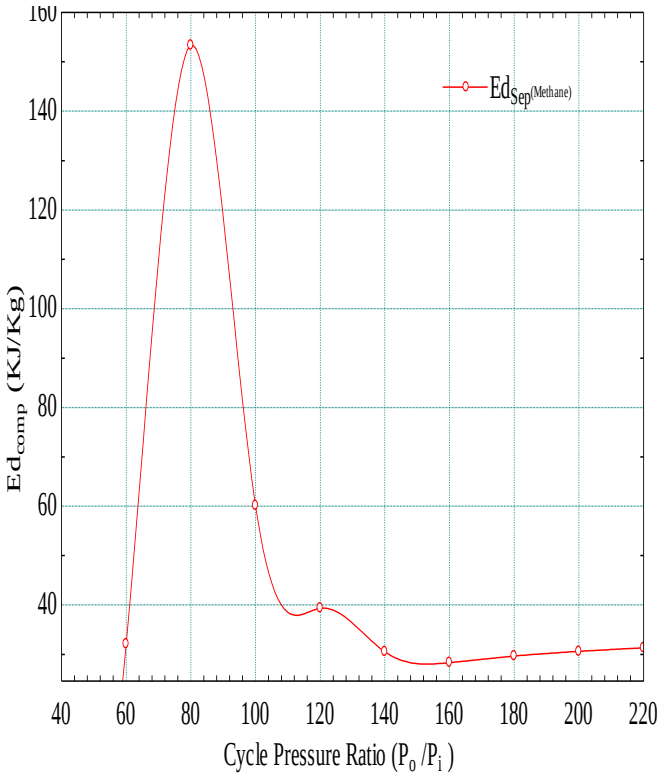


Figure 14: Variation in exergy destruction in compressor with cycle pressure ratio

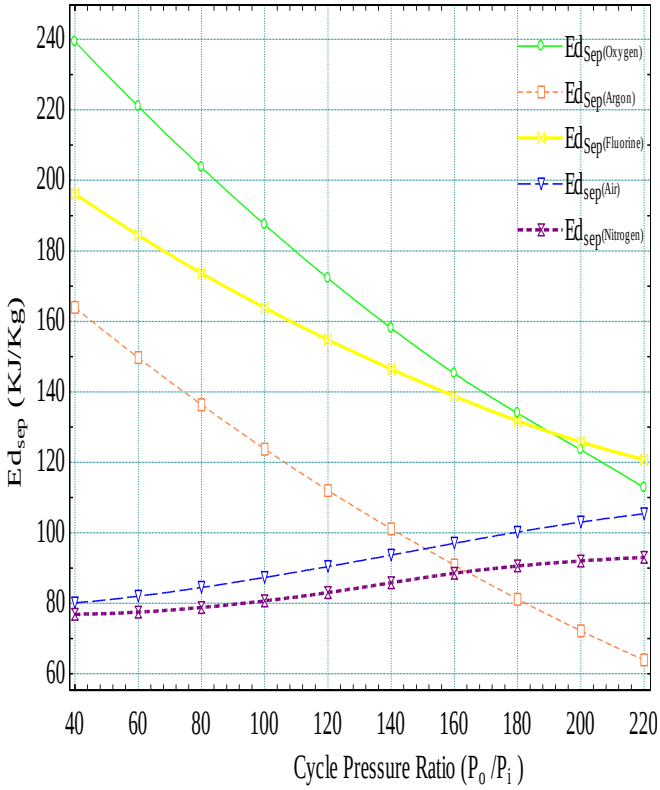


Figure 15: Variation in exergy destruction in separator with cycle pressure ratio

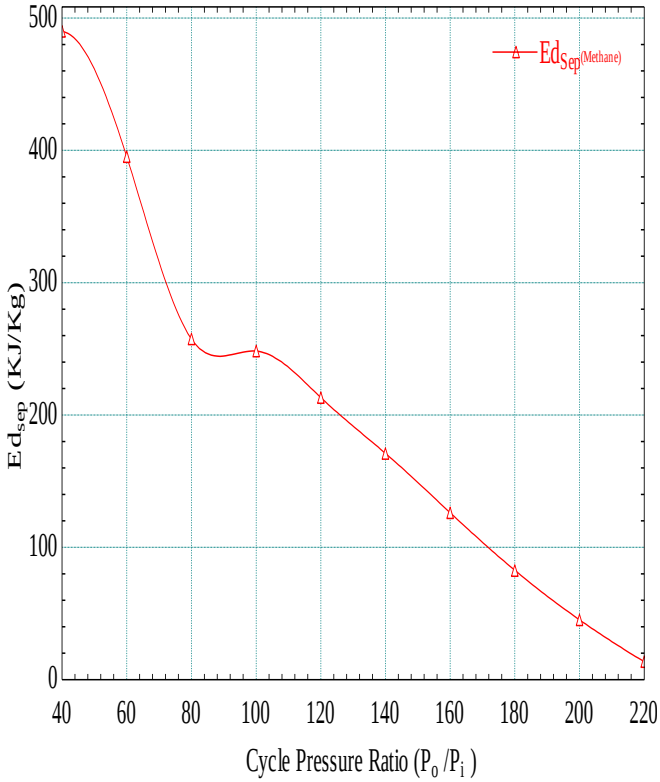


Figure 16: Variation in exergy destruction in separator with cycle pressure ratio

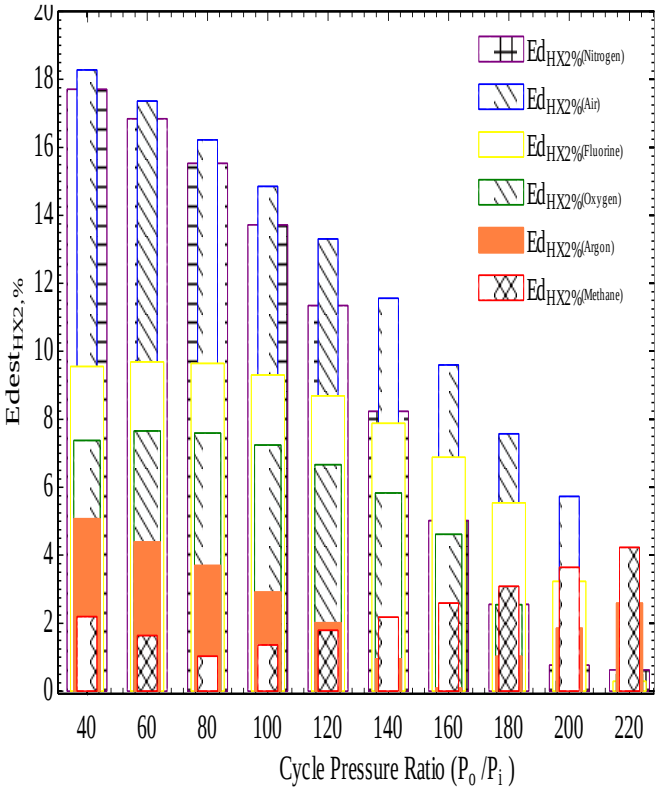


Figure 17: Variation in percentage exergy destruction in HX2 with cycle pressure ratio

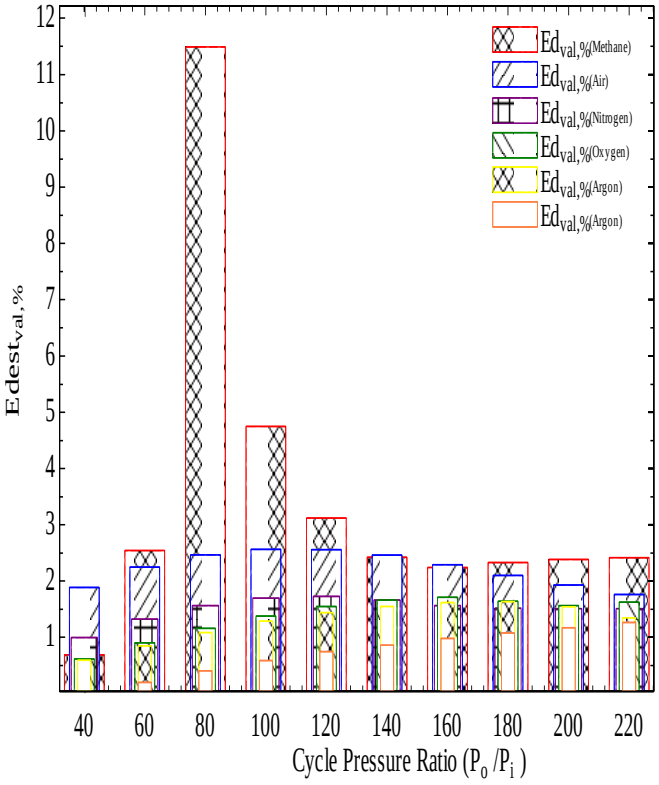


Figure 18: Variation in percentage exergy destruction in valve with cycle pressure ratio

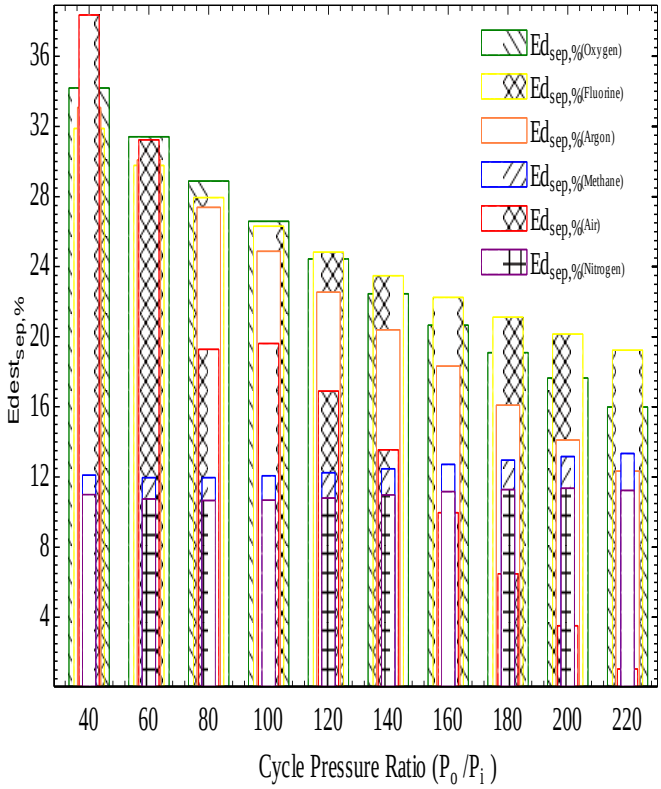


Figure 19: Variation in percentage exergy destruction with cycle pressure ratio

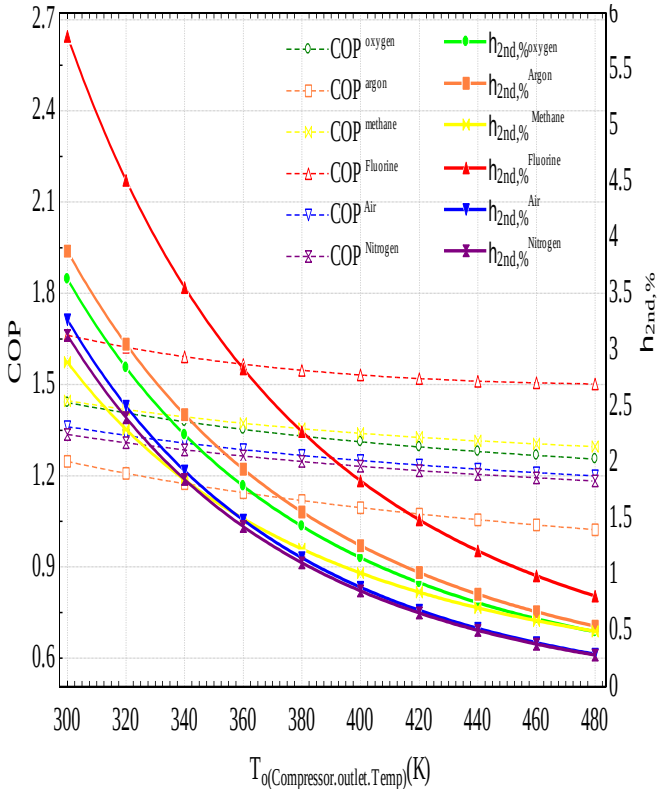


Figure 20: Variations in COP and second law efficiency with the compressor outlet temperature

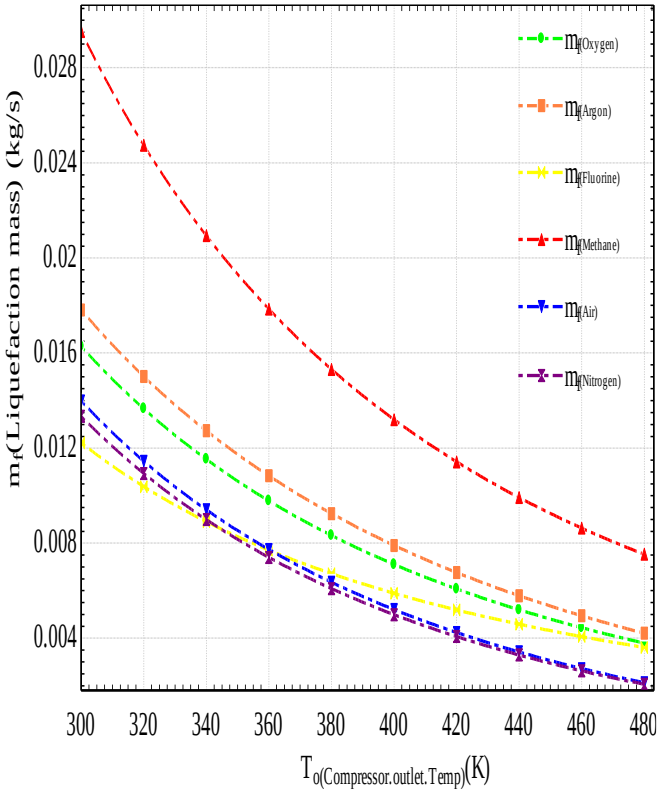


Figure 21: Variation in liquefaction mass flow with the compressor outlet temperature

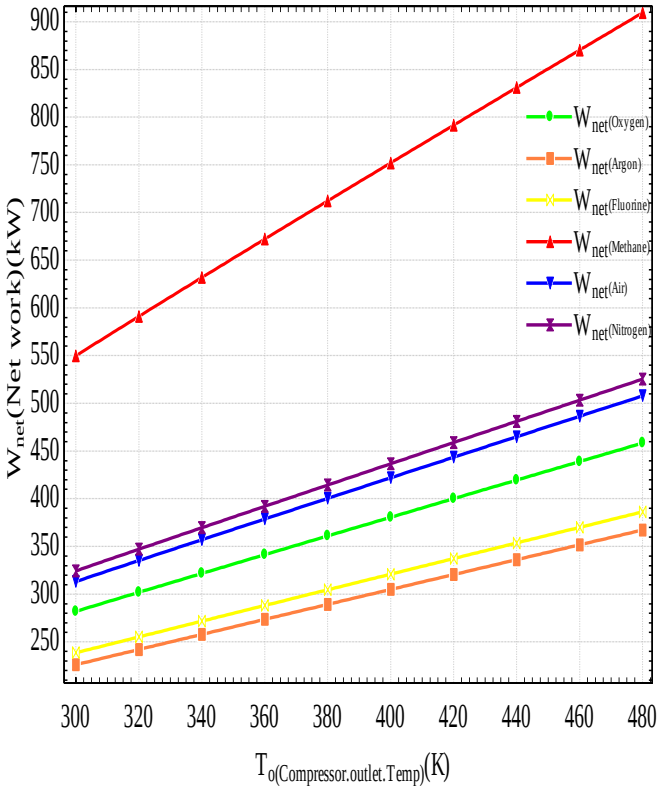


Figure 22: Variation in net work done with the compressor outlet temperature

Fig.8 shows the variations in NTU of HX1 with the cycle pressure ratio of 40 to 220. It has been seen that maximum incremental variations in NTU are found to be in methane i.e., 5.66 at cycle pressure of 80 and then its value suddenly decreases, which is followed by argon, oxygen, fluorine, air, and nitrogen shows the continuous increasing behaviour, i.e., varies from 3.487 to 4.682. On the other hand, fig.9 shows the variations in NTU of HX2 with the cycle pressure ratio of 40 to 220. It has been seen that methane shows decrement in NTU value initially then suddenly increase and goes up to the maximum point i.e. 5.553 at around 160. While all other gases shows almost the same type of behaviour i.e., increase first and then decrease. Oxygen shows the better results for NTU in HX2 i.e. changes from 3.577 to 4.217 followed by argon, air, fluorine, and nitrogen shows the least value i.e., varies from 3.362 to 3.333.Fig.10 illustrates the exergy destruction rate of compressor with respect to cycle pressure ratio of 40 to 220. It has been clearly understood from the graphs that exergy destruction rate is continuously increasing, and methane has the highest value of exergy destruction rate among the other gases and it is increasing from 638.3kJ/kg to 1168kJ/kg. Alternatively, argon has the least value of exergy destruction rate of compressor i.e. increases from 242.4kJ/kg to 371.5kJ/kg.

Fig.11 demonstrates the exergy destruction rate of HX1 with respect to cycle pressure ratio of 40 to 220. It has been found that nitrogen shows the highest exergy destruction rate in HX1, i.e., 148.4kJ/kg to 169.2kJ/kg. On the other side, fig.12 illustrates that nitrogen and air both show the highest rate of exergy destruction in HX2 among the other gases, i.e., 123.8kJ/kg and 120.9kJ/kg, respectively. Fig.13 and fig.14 shows the exergy destruction rate of valve with respect to cycle pressure ratio of 40 to 220. Methane shows the highest value of exergy destruction among the other gases, and it attains maximum value i.e. 153.4kJ/kg at cycle pressure ratio of 80 as shown in fig.14. While argon having the least value of exergy destruction rate, i.e., increases from 0.0399kJ/kg to 6.552kJ/kg as shown in Fig.13.

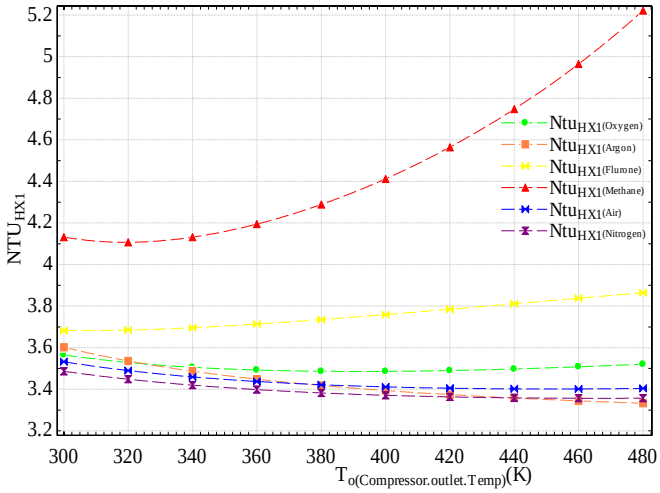


Figure 23: Variation in NTU in HX1 with compressor outlet temperature

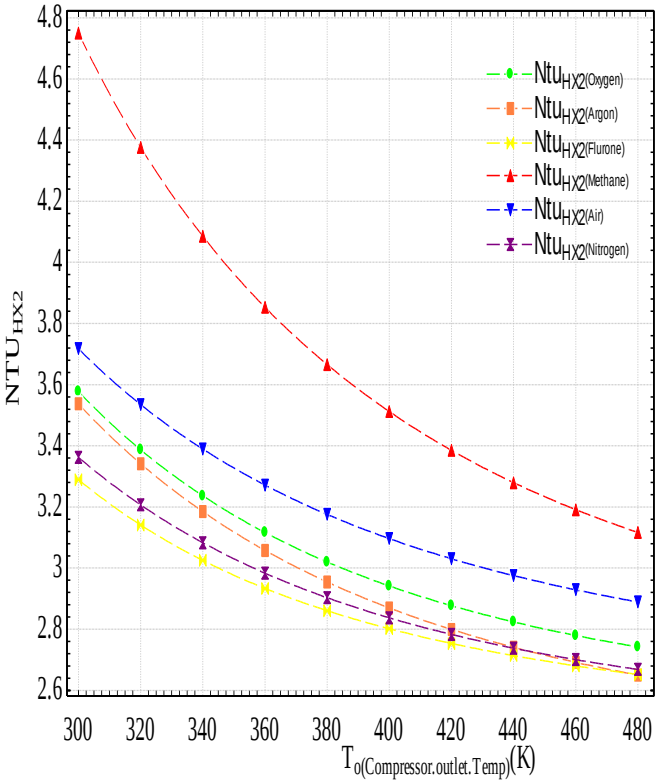


Figure 24: Variation in NTU in HX2 with compressor outlet temperature

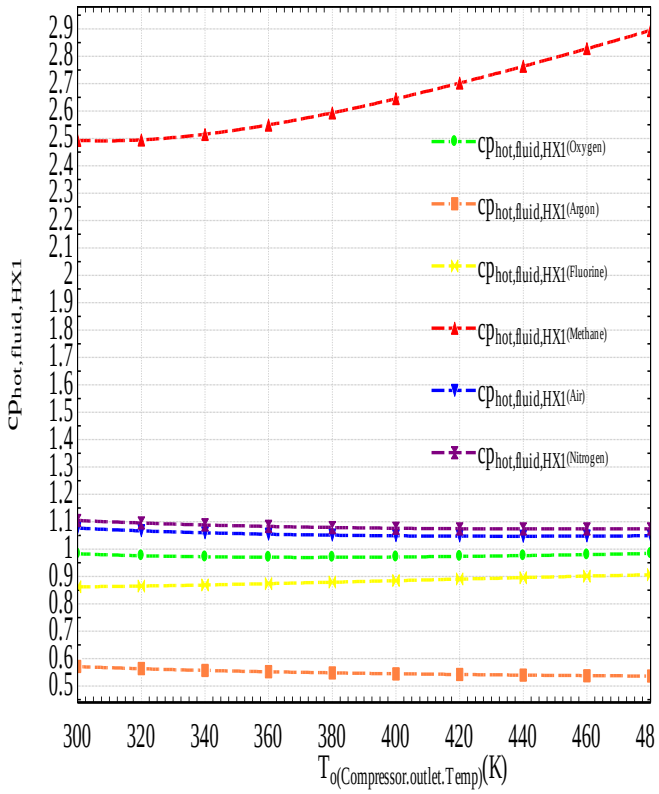


Figure 25: Variation in specific heat of hot fluid in HX1 with the compressor outlet temperature

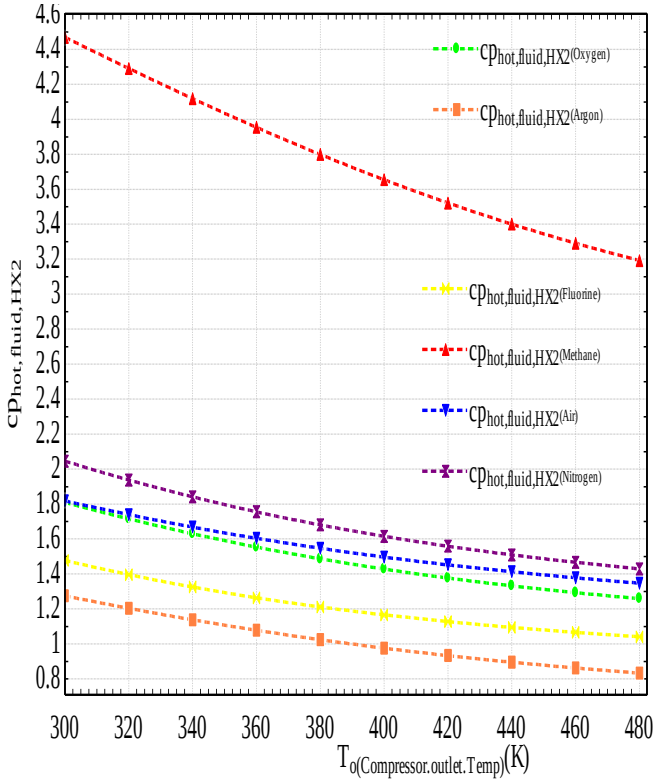


Figure 26: Variation in specific heat of hot fluid in HX2 with the compressor outlet temperature

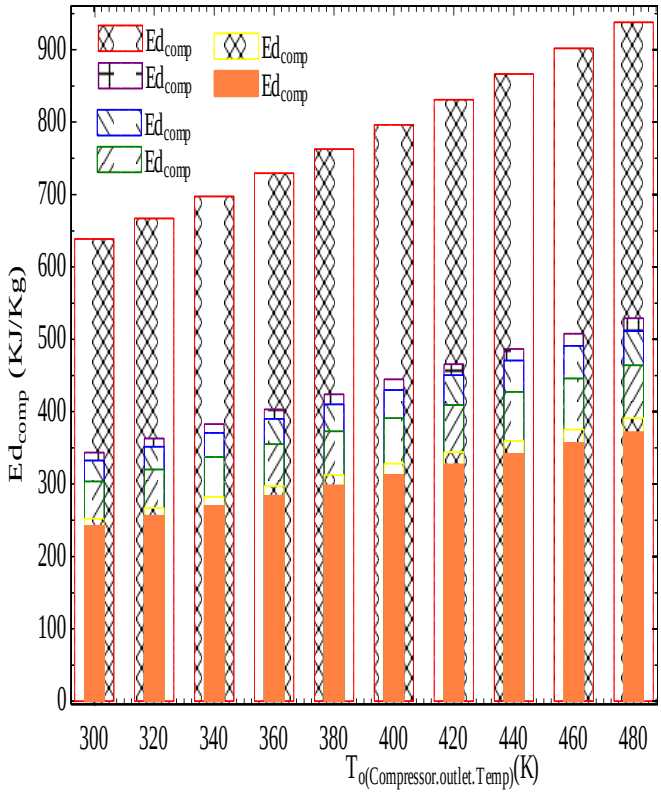


Figure 27: Variation in exergy destruction in compressor with the compressor outlet temperature

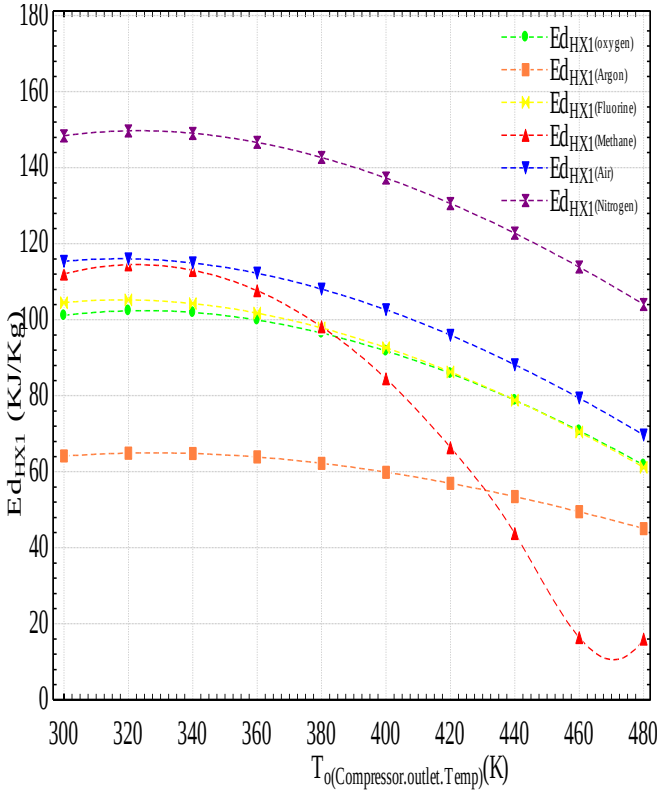


Figure 28: Variation in exergy destruction in HX1 with the compressor outlet temperature

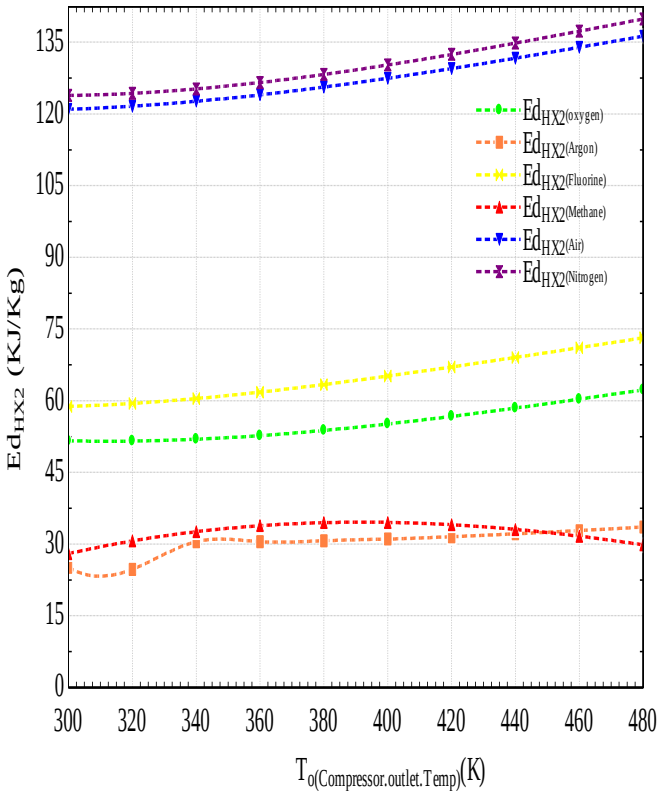


Figure 29: Variation in exergy destruction in HX2 with the compressor outlet temperature

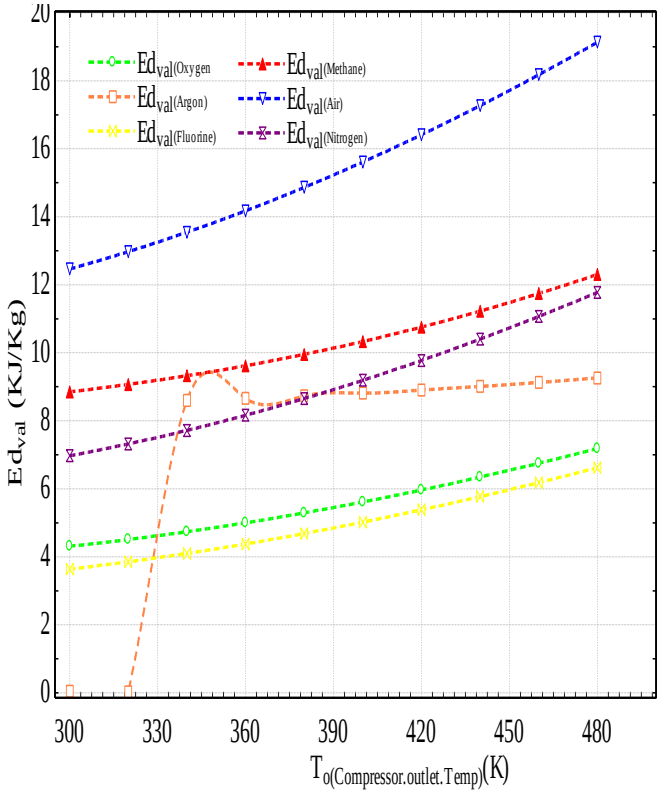


Figure 30: Variation in exergy destruction in VALVE with the compressor outlet temperature

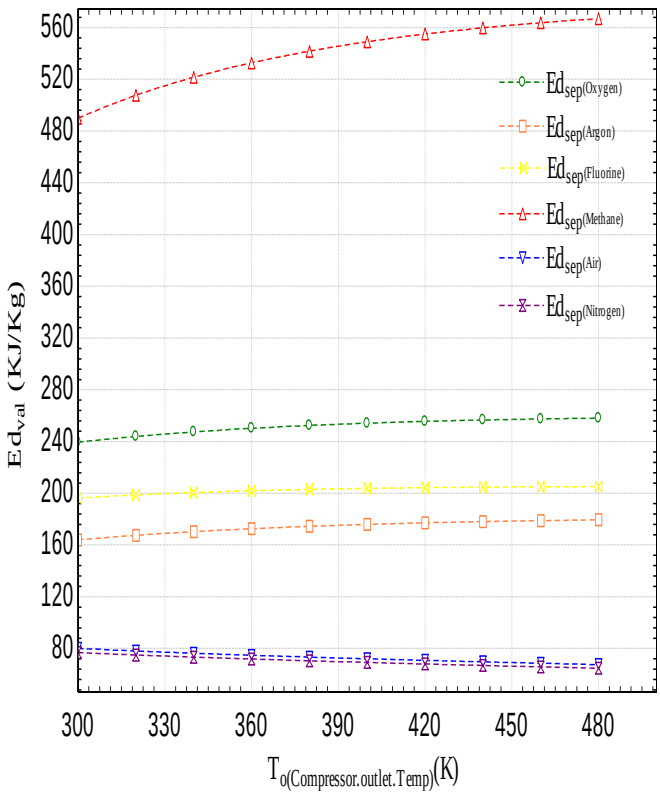


Figure 31: Variation in exergy destruction in valve with the compressor outlet temperature

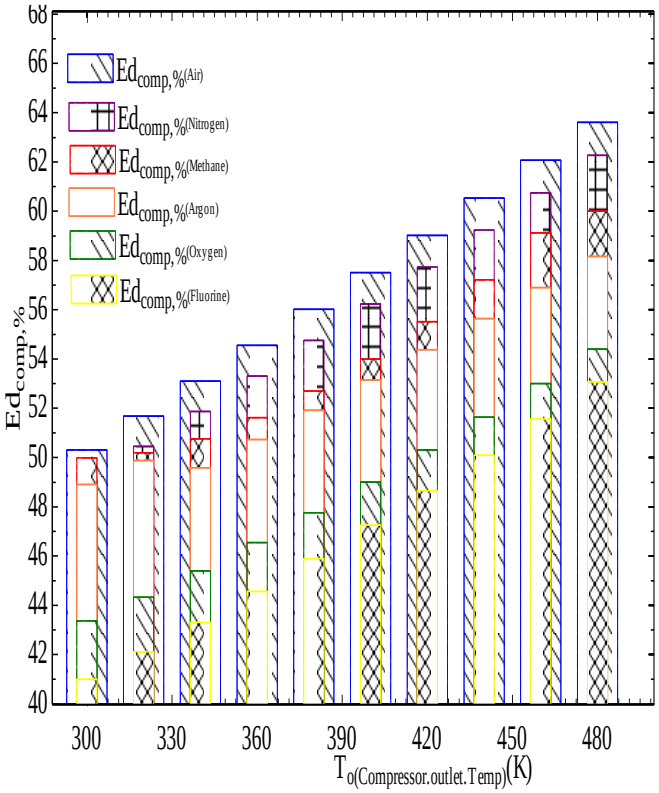


Figure 32: Variation in percentage exergy destruction in ompressor with the compressor outlet temperature

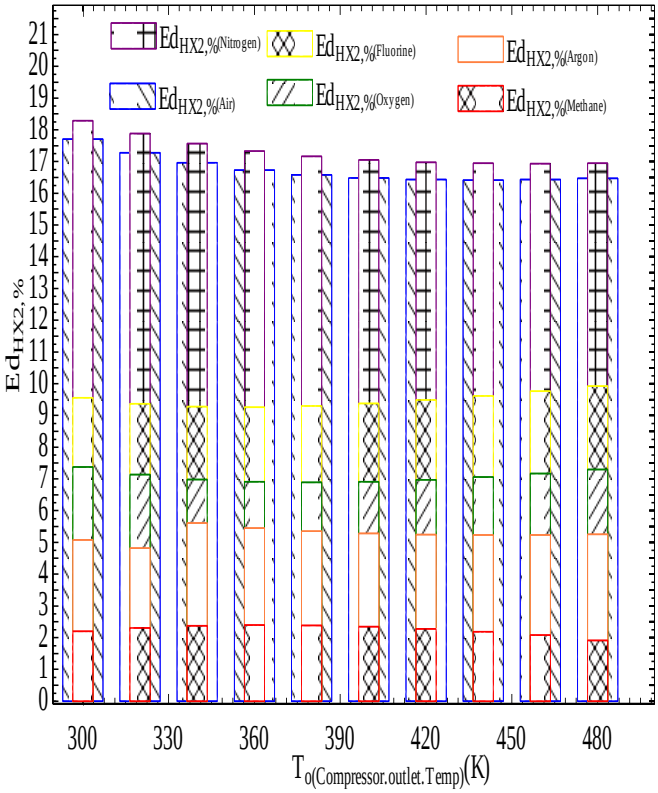


Figure 34: Variation in percentage exergy destruction in HX2 with the compressor outlet temperature

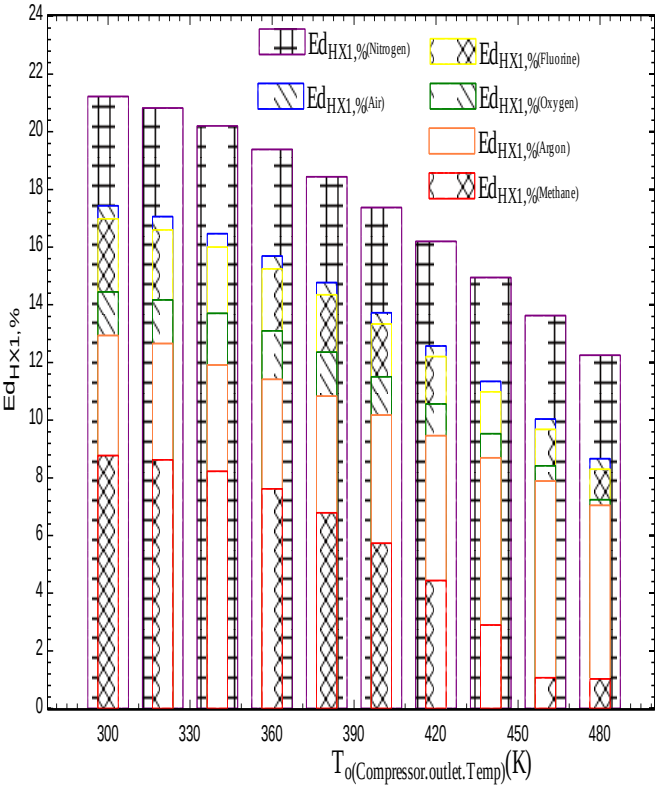


Figure 33: Variation in percentage exergy destruction in HX1 with the compressor outlet temperature

Fig.13 and fig.15 shows the exergy destruction rate of separator with the cycle pressure ratio of 40 to 220. It has been seen that methane has the highest rate of exergy destruction in separator, which decreases from 163.9kJ/kg to 63.86kJ/kg followed by oxygen, fluorine and argon. While air and nitrogen having the slightly increasing trend of exergy destruction rate with the lowest value in separator among other gases.

Fig.16 illustrates the percentage exergy destruction in compressor with cycle pressure ratio of 40 to 220. It has been observed that methane has the highest percentage exergy destruction rate and nitrogen having the least value of exergy destruction rate, which is around 49.98% to 90% and 49.09% to 66.19%, respectively. On the other hand, fig.17 demonstrates the percentage exergy destruction in HX1 with the cycle pressure ratio as described above. Nitrogen having the highest and methane has the lowest percentage of exergy destruction rate, i.e., around 21.22% to 20.44% and 8.772% to 2.307%, respectively. Furthermore, the variations in percentage exergy destruction in the HX2 with cycle pressure ratio of 40 to 220 as shown in Fig.18. It has been noticed that air has the highest percentage of exergy destruction, which is changing from 18.28% to 4.163%. While methane and argon have the minimum percentage of exergy destruction rate, i.e., varies from 2.193% to 4.228% and 5.074% to 2.588%. Fig.19 shows that methane has the highest variations in percentage of exergy destruction rate in valve, which is found to be 11.49% at cycle pressure ratio of 80. Moreover, fig.20 illustrates that fluorine and oxygen have comparatively highest percentage of

exergy destruction rate in separator among the other gases, which varies from 31.88% to 19.23% and 34.2% to 15.98%, respectively. Also, fig.21 shows the variations in the COP and second law efficiency with respect to compressor outlet temperature of 300K to 480K. It has been noticed that fluorine shows the highest value of COP and second law efficiency i.e., 1.447 to 1.296 and 2.889% to 0.4946%, respectively. Fig.22 shows the variations in the liquefaction mass flow rate with respect to compressor outlet temperature of 300K to 480K. It has been observed that methane has the highest value of liquefaction mass flow rate among the other gases i.e., 0.02952kg to 0.00753kg. Fig.23 demonstrates the variations in net work done with respect to compressor outlet temperature of 300K to 480K. It has been seen that methane shows the highest value of net work done among the other gases, which is increasing from 549.9kW to 909.4kW. Alternatively, argon having the minimum value of net workdone, i.e., increasing from 226kW to 367.2kW. Fig.24 shows the variations in NTU of HX1 with the compressor oulet temperature. The trend of this graph is first slightly decreasing and then increasing suddenly. It has been seen that methane has the highest NTU in HX1 among the other gases, i.e., 5.222 at 480K. On the other hand, Fig.25 illustrates the variations in NTU of HX2 with the compressor outlet temperature. It has been analyzed that methane has the maximum NTU in HX2, i.e., 4.75 at 300K and, graph is continuously decreasing. Fig.26 demonstrates the variations in specific heat of the hot fluid in HX1 and it has been observed that methane has the highest value of specific heat among the other gases, which is increases from 2.493kJ/kg-K to 2.895kJ/kg-K. While all other gases show slightly decreasing trend of specific heat of hot fluid in HX1. Alternatively, Fig.26 shows the variations in specific heat of hot fluid in HX2 with compressor outlet temperature. Again methane has the highest value of specific heat of hot fluid among other gases, i.e., 4.468 kJ/kg-K at 300K, and it is decreasing continuously. Fig.26 indicates the variations in exergy destruction rate variations with the compressor outlet temperature. It has been analyzed that methane has the highest rate of exergy destruction rate among the others i.e. 937.7kW at 480K. Fig. 33 shows the variations in exergy destruction rate in HX1 with the compressor outlet temperature and it has been observed that nitrogen has the highest rate of exergy destruction rate i.e. 148.4kW at 300K. Fig.27 shows the variations in exergy destruction rate in HX2 with the compressor outlet temperature and it has been observed that nitrogen has the highest rate of exergy destruction rate i.e., 139.9kW at 480K. Fig.28 shows the variations in exergy destruction rate in valve with the compressor outlet temperature and it has been observed that air has the again highest rate of exergy destruction rate i.e., 19.13kW at 300K. Fig.29 shows the variations in exergy destruction rate in separator with the compressor outlet temperature and it has been observed that methane has the highest rate of exergy destruction rate i.e., 566.8kW at 480K. In addition, Fig.30 shows the variations in percentage exergy destruction rate in compressor with the compressor outlet temperature and it has been observed that air has the highest rate of exergy destruction rate i.e., 63.61% at 300K.

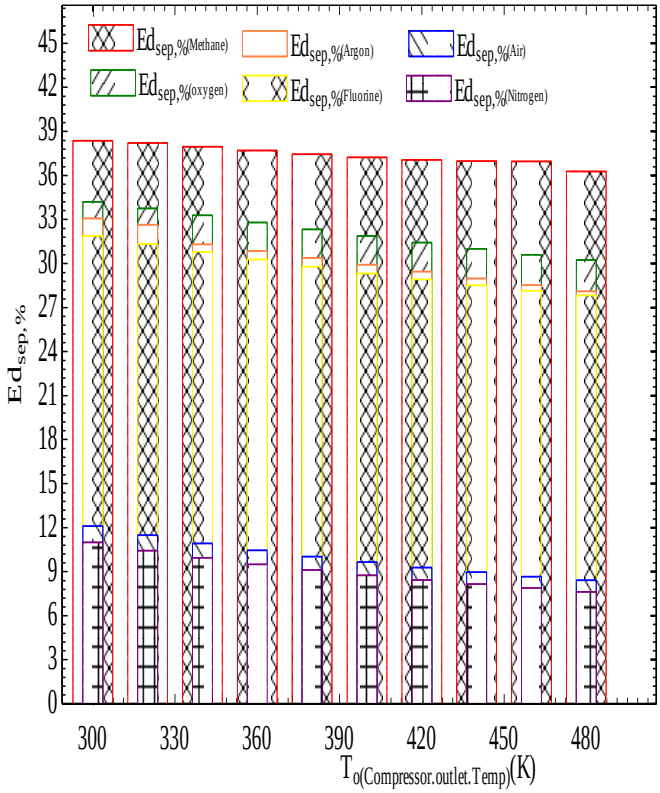


Figure 35: Variation in in exergy destruction in separator with the compressor outlet temperature

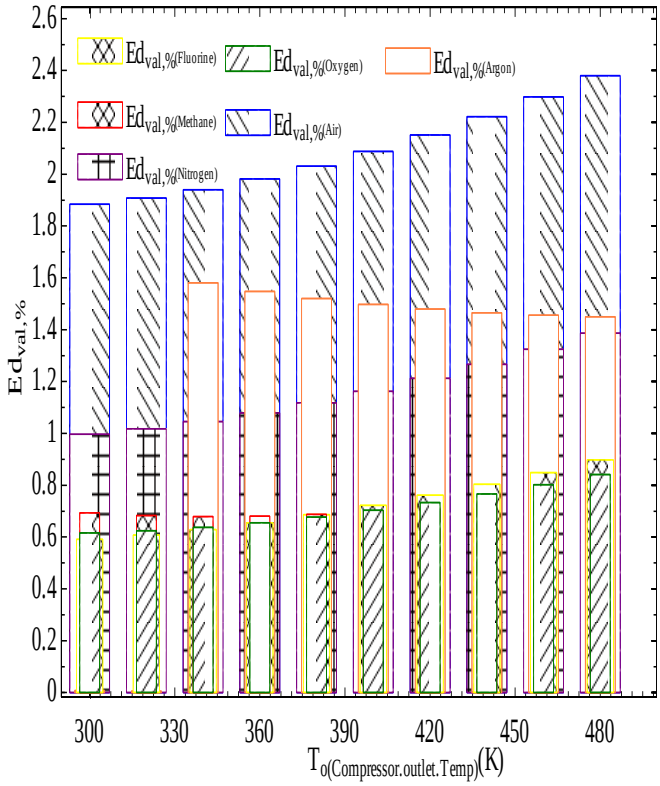


Figure 36: Variation in in exergy destruction in valve with the compressor outlet temperature

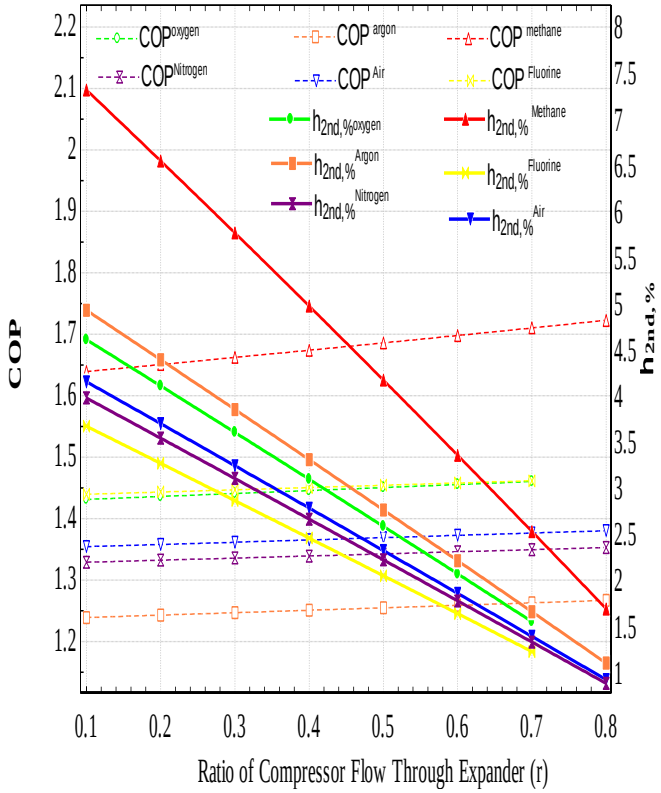


Figure 37: Variation in COP and second law efficiency with the ratio of compressor flow through expander

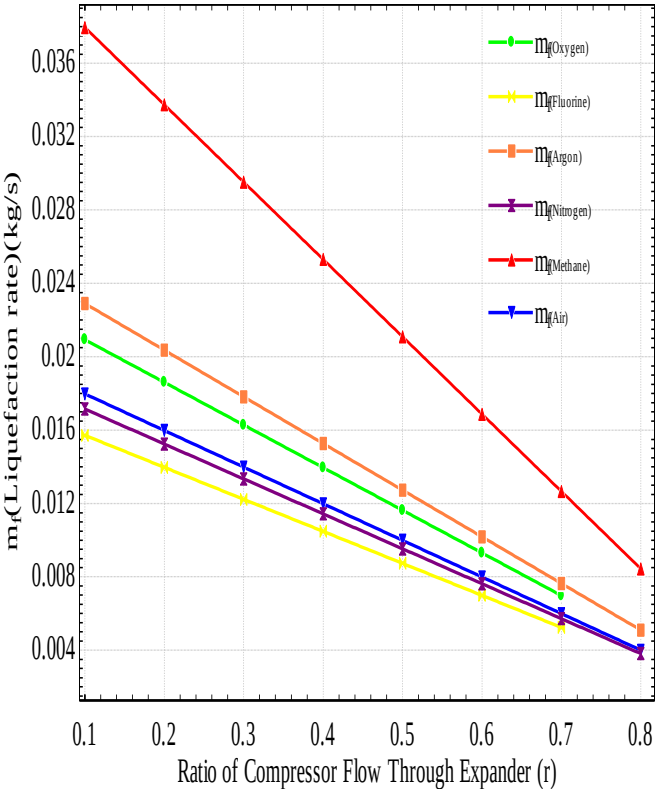


Figure 38: Variation in liquefaction mass flow with the ratio of compressor flow through expander

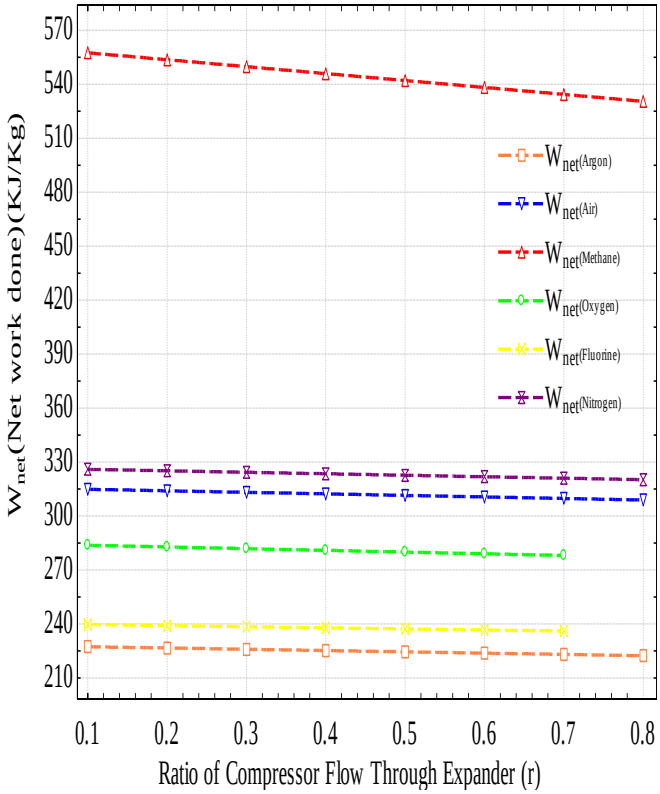


Figure 39: Variation in net work done with the ratio of compressor flow through expander

Fig.30 shows the variations in percentage exergy destruction rate in HX1 with the compressor outlet temperature and it has been observed that nitrogen has the again highest rate of exergy destruction rate i.e., 21.22% at 300K. Fig.31 illustrates the variations in percentage exergy destruction rate in HX2 with the compressor outlet temperature and it has been observed that nitrogen has the highest rate of exergy destruction rate i.e., 17.71% at 300K. Fig.32 illustrates the variations in percentage exergy destruction rate in separator with the compressor outlet temperature and it has been observed that methane has the highest rate of exergy destruction rate i.e., 38.36% at 300K. Fig.33 indicates the variations in percentage exergy destruction rate in valve with the compressor outlet temperature and it has been observed that air has the highest rate of exergy destruction rate i.e., 19.13% at 480K. Fig.34 illustrates variations in COP and second law efficiency with respect to ratio of compressor flow through expander. It has been seen that methane has the highest COP and second law efficiency among other gases i.e., 1.723 at 0.8 and 7.344% at 0.1, respectively. Fig.35 shows the variations in mass liquefaction rate with respect to ratio of compressor flow ratio and it has been analyzed that methane has the highest mass liquefaction rate i.e. 0.03795 at 0.1 and it is decreasing continuously, i.e. 0.008433 at 0.8 followed by other considered gases. Last but not the least, fig. 39 shows the variations in net work done with respect to the ratio of compressor flow ratio. It has been observed that methane has the highest net work done among other gases, which is exactly 557.6kW at 0.1 compressor flow ratio and argon shows the least value of net

work done i.e. 227.4kW at the same compressor flow ratio of 0.1.

5. Conclusions

Exergy analysis of Haylent system and its component with different gasses help in determine the best thermodynamic performance parameters for each given gas liquefaction process. Various performance parameters have been studied with increasing pressure ratio. Following points are concluded from the present investigation

(1) COP and Second law efficiency of system is degrading at high pressure for all gasses.
(2) The optimum performance pressure ratio range for system is140-160 bar.
(3) Among all six gases methane gas liquefaction process required more attention.
(4) Gas of the liquefaction is very important factor in determine the most exergy destructions causing component of Haylent system.

References

[1] R. Agrawal, D.W. Woodward, Efficient cryogenic nitrogen generators: An exergy analysis, Gas Separation & Purification, Volume 5, Issue 3, September 1991, Pages 139-150
[2] Yasuki Kansha, Akira Kishimoto, Tsuguhiko Nakagawa, Atsushi Tsutsumi, A novel cryogenic air separation process based on self-heat recuperation, Separation and Purification Technology, Volume 77, Issue 3, 4 March 2011, Pages 389-396
[3] Gadhiraju Venkatarathnam , "Simulation of cryogenic processes" , Cryogenic Mixed Refrigerant Processes ,International Cryogenics Monograph Series 2008, , Pages 51-63
[4] R.L. Cornelissen, G.G. Hirs, Exergy analysis of cryogenic air separation, Energy Conversion and Management, Volume 39, Issues 16–18, November–December 1998, Pages 1821-1826,.

Global Financial Crisis and Price Risk Management in Gold Futures Market- Evidences from Indian & US Markets

Narinder Pal Singh[1]
Archana Singh[2]

Abstract
Over the globe, gold is one of the most traded commodities. Due to its gobal demand, gold is traded in both spot and futures market. Price risk management is a fundamental but vital function of futures market. To effectively discharge this function, futures market has to be efficient. Thus, it is important to analyze efficiency of futures market. None of the studies in literature analyses price risk management role of gold futures in India and US with reference to global financial crisis of 2008-09. Thus, this study aims at investigating the gold futures role in managing price risk related to gold spot market before and after the crisis in Indian and US markets. The results of Johansen's cointegration test indicate that the gold spot and futures markets are cointegrated in both the sub-periods in both India and US. Granger causality test results signifies that gold futures play an important role in price discovery in both Indian and US markets, with some feedback from spot market at Multi Commodity Exchange (MCX), India . However, the price discovery role of gold futures markets has strengthened after the crisis in both the markets. Thus, we conclude that gold futures market performs price risk management function in the pre and the post–crisis periods at Multi Commodity Exchange (MCX), India and New York Merchantile Exchange (NYMEX) Comex, US.

Keywords: *Risk Management, Efficiency, Price Discovery, Gold Futures, Global Financial Crisis, Cointegration*

JEL Classification: *C22, G01, G14, Q02*

1. Introduction

Price risk management is a fundamental but vital function of futures market. To effectively discharge this function, futures market has to be efficient. Since the introduction of commodity futures trading , there have been questions on the very basic functions of commodity futures viz. Are commodity futures markets

[1]Narinder Pal Singh (Corresponding Author), Department of Management, Jagan Institute of Management Studies, Delhi, India, e-mail: narinderp.singh@jimsindia.org
[2] Archana Singh, Delhi School of Management, Delhi Technological University, Delhi 110042, India, e-mail: sarchana03@yahoo.co.in

performing price risk management function? Do these markets lead to price discovery? Are these markets informationally efficient? An efficient commodity futures market provides an estimate of future spot price of underlying commodity in the form futures price and hence helps in managing price risk associated with that commodity. There are numerous studies on commodity futures market efficiency in both developed and emerging economies. The findings of these studies are conflicting in nature. Many studies like Arora and Sandhar (2017), Malhotra and Sharma (2016), Singh and Singh (2015), Gupta and Ravi (2013), Ali and Gupta (2011), Singh (2010), Lokare (2007), Bose (2006), Gulen (2000), Oellermann, Brorsen and Farris (1989), Allen and Som (1987), Bigman, Goldfarb, and Schechtman (1983) and many others report evidences of efficient commodity markets. However, inefficiency evidence has been found in work of Inoue and Hamori (2012), Soni and Singla (2012), Easwaran and Ramasundaram (2008), Mananyi and Struthers (1997), Schroeder & Goodwin (1991) and many others while mixed results have been found in the studies of Goss (1981), Aulton, Ennew*, and* Rayner (1997), MacDonald and Taylor (1988a), Wang and Ke (2005), Singh (2007), Mckenzie and Holt (2002) etc. Commodity futures market can perform the function of price risk management provided the commodity futures markets are efficient. Thus it is imperative to analyze commodity market efficiency.

Over the globe, gold is one of most traded commodity and India is second largest gold jewellery market in the world. MCX is the leading commodity exchange for metals futures in India and NYMEX Comex gold futures ranks first in gold futures all over the world in 2014 FIA annual volume survey. Since USA was the epicenter of global turmoil of 2008, it looks interesting to study the gold futures market across the global financial crisis of 2008. However, there are a few studies on gold futures market efficiency. Also, *none of the studies in literature analyses price risk management role of gold futures in India and USA with reference to global financial crisis of 2008-09*. Thus, , this study aims at investigating the gold futures role in managing price risk with reference to global financial crisis of 2008-09. The remaining paper contains four sections. Section 2 presents some literature review, Section 3 defines the data and the research methodology, Section 4 presents the results and discussion, and Section 5 provides a conclusion and research implication.

2. Literature Review

Mckenzie and Holt (2002) using modern time series methodology suggest that futures markets of select commodities are efficient and unbiased in long run. Using GQARCH-M-EC, they however find corn and cattle futures markets to be inefficient and biased in short-run. Similar mixed results were reported by Wang and Ke (2005). They conclude that soybean futures market are weakly efficient

while the wheat futures market are inefficient due to over-speculation and government intervention. Meanwhile, the results of He and Holt (2004) indicate that the lumber, OSB and NBSK weekly spot and futures prices series are neither cointegrated nor unbiased i.e. markets are inefficient. On the contrary, Xin et al. (2006) report that Chinese copper and aluminium futures markets are efficient. In India, similar findings are indicated in the results of Lokare (2007). He finds that spot and future prices of the sample commodities (except sugar and nickel) are cointegrated. They report that most of the commodities show improved operational efficiency. Singh (2007) explore arbitrage opportunities across MCX, NCDEX and NBOT exchanges and find evidences of cointegration between the soya oil futures prices on these exchanges. His results also suggest that CBOT has relatively high hedging efficiency than these three domestic national exchanges. Sahoo and Kumar (2009) report that the five sample commodity futures markets in India are efficient and there is no evidence of their inflationary effect.

Singh (2010) find that guar gum and guar seed spot and futures markets were cointegrated and unbiased. Similar results are reported by Kaur and Rao (2010) in their study on the weak form efficiency of guar seed, refined soya oil, chana and pepper futures markets. The results of autocorrelation show that all select commodities except refined soya oil futures markets are efficient. The results of run test indicate that futures markets for all the select commodities are efficient. Pavabutr and Chaihetphon (2010) conclude that standard gold futures market performs price discovery function at MCX. They also find that mini gold contracts aid up to 30% in price discovery process probably due to efficient information flow in the market. Also, Ali and Gupta (2011) conclude that futures market is efficient for all select commodities except rice and wheat. They also report that for 6 out of 12 select commodities (Sugar, Castor Seed, Wheat, Soybean, Guar Seed and Chickpea), futures prices granger cause spot prices and for other 3 (Cashew, Rice and Red Lentil) spot prices granger cause futures price. However, the relationship is bi-directional for rest of the select commodities. Similarly, Sehgal et al. (2012) find that markets were efficient for all ten but one commodity (turmeric). However, their results indicate two-way causality for all select commodities except turmeric.

Inoue and Hamori (2012) in their study on MCX-comdex report that the commodity futures market is inefficient for the entire sample period but not for the sub-period July 2009 to March 2011. However, Soni (2013) investigate and conclude that guar gum futures market is inefficient. The possible reason for market inefficiency has been attributed to over-speculation/market manipulation. Arora and Kumar (2013) report that copper and aluminium futures markets perform price discovery function and there exists a bidirectional causality betewen futures and spot markets. Also, futures markets are more efficient than spot

markets for both the metals. However, Mahalik et al. (2014) in their study on agri, metals, energy and aggregate commodity indices conclude that these futures markets except metals perform price discovery function. Further they report that there is volatility transmission from futures to spot market in MCX energy and MCX comdex, but reverse spillover in case of MCX agri. Broll et al. (2015) show that the firm's optimal futures position depends on the nature and sign of expectation dependence. Malhotra and Sharma (2016) report long run equilibrium between the spot and futures guar market. They infer that the gaur seed futures market performs price discovery function while spot market causes increased volatility in futures market. Arora and Sandhar (2017) investigate hedging efficiency of crude oil futures traded at MCX, India. Their results indicate that crude oil futures market at MCX efficiently performs hedging function.

From literature, we can see that there a few studies on gold futures market's role to predict future spot price of gold. Also, none of the studies in literature analyses price risk management role of gold futures in India and US with reference to global financial crisis of 2008-09. Knowing the demand, the use and importance of gold in India, and the relevance of global financial crisis in US and Indian markets, there is a great scope for this type of study. Thus, we are motivated to study price risk management in gold futures market at MCX, India and NYMEX Comex, US across the global financial crisis of 2008-09.

3. Data and Research Methodology

This study uses secondary data on daily closing prices of gold in spot and futures markets. The sample period is from 6th June 2005 to 31 March 2017. The data has been divided into two sub-periods. The pre-crisis period encompasses of 971 (or 850) observations of MCX gold (or NYMEX Comex gold) spread over 6th June 2005 to 13th September 2008, and post-crisis period encompasses of 2354 (or 2226) observations of MCX gold (or NYMEX Comex gold) spread over 15th September 2008 to 31st March, 2017. For Indian market, the data is collected from the website of MCX, India. The spot market of gold is Mumbai. For US market, NYMEX (Comex) gold futures data is extracted from Bloomberg and gold spot prices data from World Gold Council. Natural log (ln) series have been used here. The following methods have been used in this study. Only those data points have been taken for this study for which data is available in both spot and futures markets.

3.1 Unit Root Tests:

Augmented Dickey Fuller (ADF) and Phillip Perron (PP) tests are the most widely used stationarity tests (Chowdhury, 1991; Lai and Lai, 1991; Mckenzie and Holt, 1998; Wang and Ke 2002; Yang et al., 2005; Ali and Gupta, 2011; Bohl and

Stephan, 2013; Arora and Kumar, 2013; Ahmad and Sehgal, 2015; Gupta and Varma, 2016). Here, Akaike Information Criterion (AIC) has been used to determine the number of lags. The null hypothesis assumes that the series is non-stationary. It is important to first test the stationarity of given series before applying cointegration. The two series are expected to be non-stationary on levels and stationary on first differencing.

3.2 Johansen's Cointegration Approach

If a linear combination of two non-stationary variables is I(0) i.e. stationary then the variables are cointegrated. In other words, the variables have long-run relationship. For *Johansen's cointegration* test, a VAR model with k lags containing the given two variables is represented as follows:

$$\Delta Y_t = \mu + \Pi Y_{t-1} + \sum_{i=1}^{k-1} \Gamma_i \Delta Y_{t-1} + \varepsilon_t \qquad \ldots . \quad (1)$$

Johansen test uses two test statistics to test cointegration. These are λ_{trace} is trace statistics and λ_{max} is max eigen value statistics. We assume that the data has linear deterministic trend. The given series are expected to bear a long-run relationship. This will be analyzed in empirical section of this paper.

3.3. Granger Causality Test

Granger causality test can be represented as a bi-variate of k[th] order VAR as given below:

$$Y_t = \alpha_0 + \sum_{i=1}^{k} \alpha_i Y_{t-i} + \sum_{j=1}^{k} \beta_j X_{t-j} + \epsilon_t \qquad (2)$$

$$X_t = \gamma_0 + \sum_{i=1}^{k} \gamma_i X_{t-i} + \sum_{j=1}^{k} \delta_j Y_{t-j} + \epsilon'_t \qquad (3)$$

Where X_t and Y_t are gold and gold spot price series variables, a_0 and γ_0 are constant drift terms, and ϵ_t and ϵ'_t are error terms. If *y (or x)* Granger causes *x (or y)* then the lags of *y (or x)* should be significant in the equation of *x (or y)*. In this case, it would be said that there is one-way causality running from *y (or x)* to *x (or y)*.

4. Results and Discussion

4.1 Unit Root Test

Here, we have used ADF and PP unit root tests to analyse the stationarity properties of the given series. The results for log series and their log returns for two sub-periods for Indian and US markets have been shown in Table 1. It is evident from the results that the log series of both spot and futures prices are non-stationary in levels at 5% significance level. However, the returns series (i.e. first difference of price series) are found to be stationary. The results are similar for both pre-crisis and post-crisis periods. In other words, we can say that for both Indian and US markets the log spot and futures price series are integrated series of first order in the two sub-periods, i.e. *I(1)* in both pre-crisis and post-crisis periods. Thus, we may proceed to test cointegration relationship between the given log price series.

4.2 Johansen Cointegration Test

Johansen's Co-integration test is the most extensively used cointegration technique in the literature (Mckenzie & Holt, 2002; Wang &Ke, 2005, Ali & Gupta, 2011; Arora and Kumar, 2013). To analytically examine cointegration, we run Johansen's cointegration test. We have used AIC criterion to determine optimal lag length (k). Here, k=6 for Indian market in both the pre-crisis and the post-crisis periods while k=6 in the pre-crisis and k=1 in the post-crisis periods for US market. The results shown in Table 2 indicate that LSP (logged spot price) and LFP (logged futures price) series are cointegrated in the pre-crisis period with one cointegrating relation at 5% level of significance in both Indian and US markets. For Indian market in the post-crisis period, the null hypothesis of 'no cointegrating relation (r=0)' is rejected The null hypothesis of 'at most one cointegrating relation (r≤1)' is also rejected at 5% but cannot be rejected at 1% level of significance. However for US market, the null hypothesis of r=0 is rejected while the null hypothesis of r≤1 is not rejected at 5% level of significance in the post-crisis period. Thus, we can say that the two series are cointegrated in both the sub-periods in both the markets, i.e., spot and futures markets of gold bear long run equilibrium at MCX, India and NYMEX, USA. This is one of the important basic conditions for futures market to perform price discovery and risk management. Similar results are obtained by Lokare (2007), Sahoo and Kumar (2009), and Pavabutr and Chaihetphon (2010).

4.3. Granger Causality Test

Table 3 shows the results of Granger causality test for Indian and US markets. From Table 3, the null hypothesis of 'no causality' from log return of gold spot prices (*RSP*) to log return of gold futures prices (*RFP*) in Indian market is rejected at 5% level of significance. It means RSP Granger causes

Table 1

ADF and PP Test Results on Levels for Pre and Post Crisis Periods

		ADF		PP	
Variable	**Model Form**	**Test Statistics**	***p*-value**	**Test Statistics**	***p*-value**
Pre-Crisis					
$\ln(SP_t)$	Intercept	-1.788411	0.3865	-1.788237	0.3866
	Trend and Intercept	-2.036947	0.5798	-2.096194	0.5468
$\ln(FP_t)$	Intercept	-1.734562	0.4135	-1.734310	0.4136
	Trend and Intercept	-1.932137	0.6367	-2.019167	0.5896
Return on $\ln(SP_t)$	Intercept	-30.69714	0.0000	-30.69706	0.0000
	Trend and Intercept	-30.70988	0.0000	-30.70988	0.0000
Return on $\ln(FP_t)$	Intercept	-31.25086	0.0000	-31.27545	0.0000
	Trend and Intercept	-31.26614	0.0000	-31.28283	0.0000
Post-Crisis					
$\ln(SP_t)$	Intercept	-2.710493	0.0723	-2.674897	0.0786
	Trend and Intercept	-1.929694	0.6385	-1.971086	0.6162
$\ln(FP_t)$	Intercept	-2.616662	0.0897	-2.634754	0.0861
	Trend and Intercept	-2.059869	0.5674	-2.035622	0.5809
Return on $\ln(SP_t)$	Intercept	-48.98858	0.0001	-49.01328	0.0001
	Trend and Intercept	-49.05469	0.0000	-49.07045	0.0000
Return on $\ln(FP_t)$	Intercept	-51.16039	0.0001	-51.10335	0.0001
	Trend and Intercept	-51.21841	0.0000	-51.16765	0.0000

Critical values for Intercept and Trend & Intercept forms are -2.863 and -3.412 respectively.
Source: Authors' Computation

Table 2

Johansen Test Results for Pre-crisis and Post-crisis periods

Period	**Hypothesised No of CE(s)**	**Indian Market**		**US Market**	
		λ_{trace} Stats (Prob.)	**λ_{max} Stats (Prob.)**	**λ_{trace} Stats (Prob.)**	**λ_{max} Stats (Prob.)**
Pre-Crisis	r=0 (None)	43.5841 (0.0000)	0.0410 (0.0000)	161.0231 (0.0001)	158.2413 (0.0001)
	r≤1 (at most 1)	3.2708 (0.0705*)	0.00338 (0.0705*)	2.7818 (0.0953*)	2.7818 (0.0953*)

Post-Crisis	r=0 (None)	74.5360 (0.0000)	70.0527 (0.0000)	216.9532 (0.0000)	115.1778 (0.0000)
	r≤1 (at most 1)	4.4833 (0.0342#)	4.4833 (0.0342#)	7.7537 (0.2725*)	7.7537 (0.2725*)

Note: The critical values are 15.4947 & 3.8414 for trace statistics and 14.26460 & 3.8414 for Max statistics at 5% level of significance. The probablity values have been shown in parentheses. # and * represents insignificant results at 1% and 5% level of significance respectively.
Source: Authors' Computation

RFP. Also, the null hypothesis of 'no causality' from log return of gold futures prices (*RFP*) to log return of gold spot prices (*RSP*) is rejected at 5% level of significance. It means there is bidirectional causality between spot and futures gold market in Indian market. Similar results are reported by Lakshmi et al. (2015). It signifies that gold futures play an important role in price discovery with some feedback from spot market in both the sub-periods. However, the price discovery role of gold futures markets has strengthened after the crisis.
Similarly in US market, a two way causality is observed between spot and futures gold market in the pre-crisis period. However, the results strongly indicate one-way causality from RFP to RSP in the post-crisis period. This leads to conclusion that the NYMEX comex gold futures market dominates the gold spot market in price discovery function in the post–crisis period. Thus, we infer that NYMEX comex gold futures market act as the centre of price discovery in gold in US.

Table 3

Granger Causality Test Results for Pre-crisis and Post-crisis periods

Null Hypothesis	**Indian Market**		**US Market**	
	F-Statistic & Probability			
	Pre-Crisis	**Post-Crisis**	**Pre-Crisis**	**Post-Crisis**
RSP does not Granger Cause RFP	192.187 (0.0000*)	4.04555 (0.0005*)	2.7936 (0.0164)	1.19398 (0.2746)
RFP does not Granger Cause RSP	2.32004 (0.0314*)	196.399 (0.0000*)	82.8274 (0.0000)	794.282 (0.0000*)

*Note: * represents significant results at 5% level of significance.*
Source: Authors' Computation

5. Conclusion and Research Implication

India is among the top two largest importers of gold and MCX is the leading commodity exchange for metals futures in India. NYMEX Comex gold futures ranks first in gold futures all over the world. Since USA was the epicenter of global turmoil of 2008, it looks interesting to study the gold futures market across

the global financial crisis of 2008. Thus, this study investigates the gold futures role in managing price risk in India and USA with reference to global financial crisis of 2008-09. The results of Johansen's Cointegration test are the same for Indian and US gold markets. The results indicate that the gold spot and futures markets are cointegrated in both the pre-crisis and the post-crisis periods. However, the results of Granger causality test differ for the two markets across the crisis. In the pre-crisis period, both Indian and US markets a bidirectional causality between spot and futures gold markets. In the post-crisis period, Indian market continues to show bi-directional causality while US market exhibit one-way causality from gold futures to gold spot market. It signifies that gold futures play an important role in price discovery in both Indian and US markets, with some feedback from spot market at Multi Commodity Exchange (MCX), India. However, the price discovery role of gold futures markets has strengthened after the crisis in both the markets but to a greater extend in US market. Thus, we infer that gold futures perform price risk management function in pre-crisis as well as post-crisis period at MCX, India and NYMEX Comex, US. The market participants like companies in gold industry, importers/exporters and jewelers can take position in gold futures market (long or short gold futures) to hedge their spot market position and hence manage price risk associated with trading in gold. In future, research can be extended to other commodities and high frequency data can be used to have more robust results.

References

Ali, J., & Gupta, K. B. (2011), "Efficiency in agricultural commodity futures markets in India: Evidence from cointegration and causality Tests." Agricultural Finance Review, 71(2):162-178.

Broll, U., Welzel, P., & Wong, K. P. (2015), "Futures hedging with basis risk and expectation dependence." International Review of Economics, 62(3):213–221.

Arora, S., & Kumar, N. (2013). Role of futures market in price discovery. Decision, 40(3), 165–179.

Arora, H. K., & Sandhar, S. K. (2017). Role of Commodity Market in Hedging Price Risk with Special Reference to Crude Oil Futures. Finance India, XXXI(1):233-244.

Bose, S. (2008). Commodity Futures Market in India: A Study of Trends in the Notional Multi-Commodity Indices. ICRA Bulletin-Money and Finance, May 2008:125-158.

Broll, U., Welzel, P., & Wong, K. P. (2015). Futures hedging with basis risk and expectation dependence. International Review of Economics, 62(3):213–221.

Easwarana, R. S., & Ramasundaramb, P. (2008). Whether Commodity Futures Market in Agriculture is Efficient in Price Discovery? — An Econometric Analysis. Agricultural Economics Research Review, 21:337-344.

He, D., & Holt, M. (2004, August). Efficiency of forest commodity futures markets. In Meetings of the American Agricultural Economics Association–Selected Paper.

Inoue, T., & Hamori, S. (2012). Market Efficiency of Commodity Futures in India. IDE Discussion Paper No. 370, Oct 2012, 1-18.

Lokare, S. M. (2007). Commodity Derivatives and Price Risk Management: An Empirical Anecdote from India. Reserve Bank of India Occasional Papers, 28(2):27-77.

Malhotra, M., & Sharma, D. K. (2016). Efficiency and Volatility Spillover in Guar Seed Futures Market in India: An Empirical Study. Finance India, Vol. XXX, No. 3:847-870.

Mananyi, A., & Struthers, J. J. (1997). Cocoa Market Efficiency: A Cointegration Approach. Journal of Economic Studies, 24(3):141-151.

Mckenzie, A. M. and Holt. M.T. (2002). Market Efficiency in Agricultural Futures Markets. Selected Paper presented at American Agricultural Economics Association Annual Meeting, Salt Lake City.

Pavabutr, P., & Chaihetphon, P. (2010). Price discovery in the Indian gold futures market. Journal of Economics and Finance, 34(4):455-467.

Sahoo. P. and Kumar. R. (2009). Efficiency and futures trading-price nexus in Indian commodity futures markets. Global Business Review, 10 (2):187-201.

Schroeder, T. C., & Goodwin, B. K. (1991). Price Discovery and Cointegration for Live Hogs. The Journal of Futures Markets (1986-1998); 11(6):685-696.

Singh, A. and Singh, N. P., (2015). "Testing Seasonality and Efficiency in Chana Futures Market", Apeejay Business Review, 14(2)

Singh, N. P. (2010). Efficiency of Agro Commodity Futures Market. Prabandhan: Indian Journal of Management, 3(2):47-53.

Soni, T. (2013). Testing Efficiency of Guar seed Futures: Empirical Evidence from India. The Romanian Economic Journal, XVI (47):211-228.

Wang, H. H., and Ke. B. (2005). Efficiency tests of agricultural commodity futures markets in China. The Australian Journal of Agricultural and Resource Economics, 49(2):125-141.

Honeycomb photonic crystal as a zero index metamaterial

Nishant Shankhwar[1*], **Yogita Kalra**[1], **Ravindra Kumar Sinha**[1,2]

[1]*TIFAC-Centre of Relevance and Excellence in Fiber Optics and Optical Communication, Department of Applied Physics, Delhi Technological University, Bawana Road, Delhi-110042, India*

[2]*CSIR-Central Scientific Instruments Organisation (CSIO), Chandigarh-160030, India.*

[*]*nishant.shankwhar@gmail.com*

Abstract: In this article zero index behaviour of honeycomb photonic crystal has been demonstrated. The zero index behaviour arises due to the dirac-like dispersion induced by degeneracy of modes at the dirac point

OCIS codes: 160.5298 (Photonic crystals) , 160.3918 (Metamaterials).

1. Introduction

Dielectric metamaterials are becoming increasingly popular as they do not come with intrinsic and inevitable ohmic losses as in metal-dielectric composites [1]. For all the interesting applications ranging from negative refractive index to electromagnetic cloaking, purely dielectric metamaterials are being explored. One such application is effectively zero refractive index. In 2011, Huang et al. [2] demonstrated the zero index beahaviour of dilectric rods in air type photonic crystal. The authors proposed that for a particular set design parameters, dispersion becomes linear near the center of the Brillouin zone and a triple degenrate Dirac point is observed. The Dirac like dispersion is main reason for the effective zero index. In this work, honeycomb type photonic crystal [3] has been analysed and it has turned out to be promising design of zero refractive index metamaterial.

2. Design

The proposed honeycomb structure is made up of a Silicon rods, of radius $r = 0.15a$, placed in air having center to center distance $a = 0.77\lambda$, where $\lambda = 1550$ nm is the wavelength of operation. Figure 1 shows the honeycomb lattice and its photonic band structure. One can notice the triple degenrate dirac point formed upon intersection of bands 5, 6 and 7.

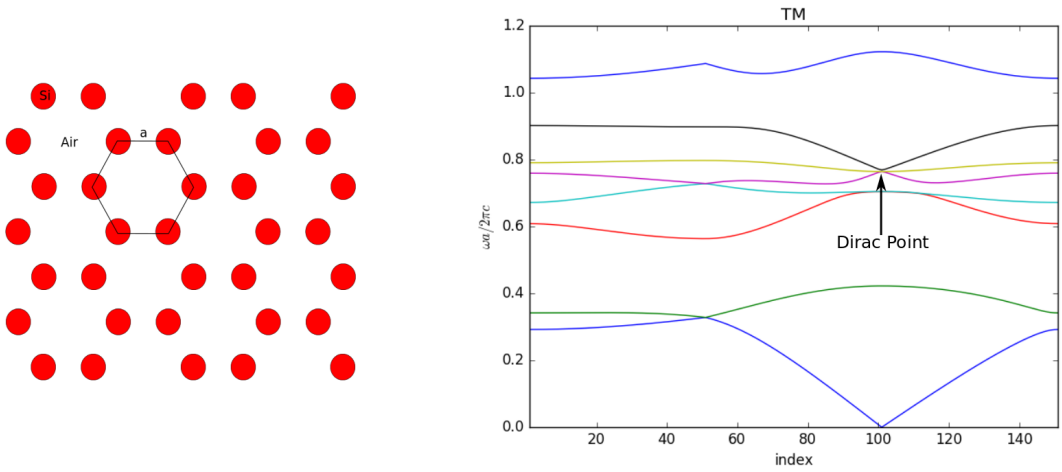


Fig. 1. (Left) Design of the honeycomb photonic crystal exhibiting zero index behaviour. (Right) Photonic band structure of the proposed design in which Dirac point is shown.

3. Results

Full wave analysis of the structure has been performed using finite element method based commercial software package COMSOL Multiphysics®. Phase and magnitude of the transmission coefficent , i.e. the S_{21} paramter, has been shown in figure 2. One can notice that phase of the transmission coefficient is zero at 1560 nm which is clear indication of effectively zero refractive index, as the wave doesn't undergo any change in phase upon going through the metamaterial.

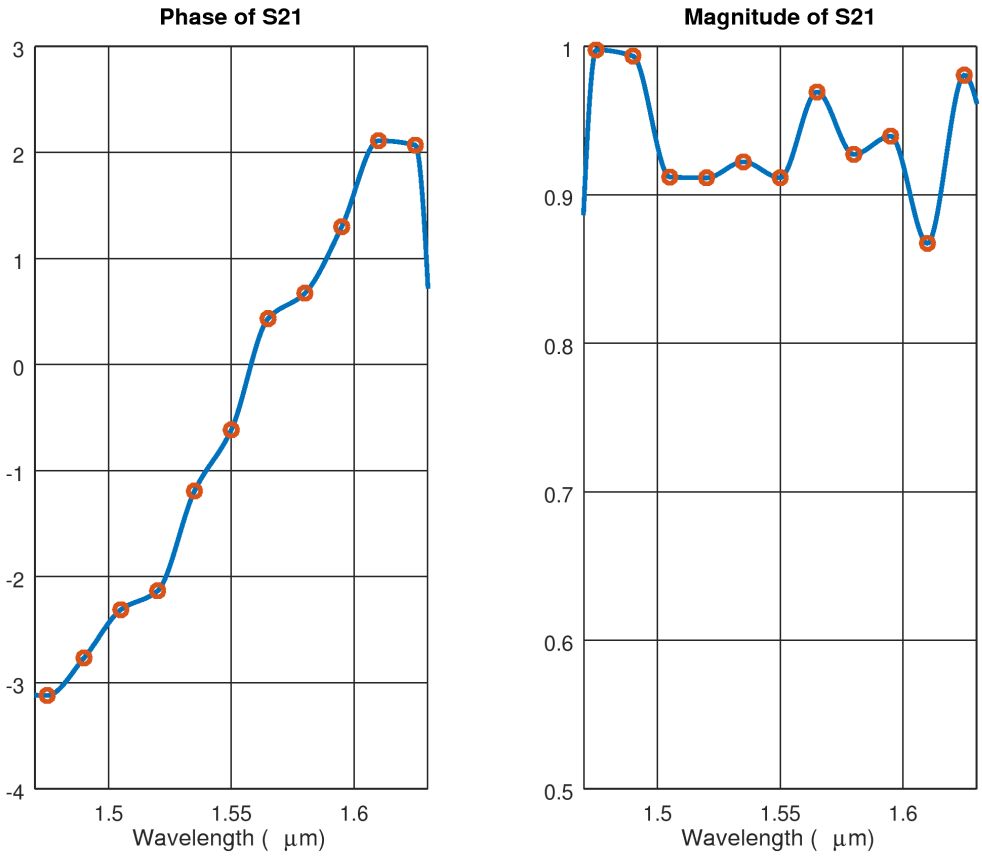


Fig. 2. (Left) Variation of the phase of the transmission coeffcient w.r.t. wavelength . (Right) Variation of the magnitude of the transmission coefficeint w.r.t. wavelength.

4. Conclusion

Zero index properties of honeycomb type metamaterial have been succesfully demonstrated.

References

1. Q. Zhao, J. Zhou, F. Zhang, and D. Lippens, "Mie resonance-based dielectric metamaterials," Materials Today **12**, 60–69 (2009).
2. X. Huang, Y. Lai, Z. H. Hang, H. Zheng, and C. Chan, "Dirac cones induced by accidental degeneracy in photonic crystals and zero-refractive-index materials," Nature materials **10**, 582 (2011).
3. S. G. Johnson, A. Mekis, S. Fan, and J. D. Joannopoulos, "Molding the flow of light," Computing in Science & Engineering **3**, 38–47 (2001).

games

MDPI

Article

Matrix Games with Interval-Valued 2-Tuple Linguistic Information

Anjali Singh and Anjana Gupta *

Department of Applied Mathematics, Delhi Technological University, Bawana Road, Rohini, Delhi 110042, India; anjilko1510@gmail.com

* Correspondence: anjanagupta@dce.ac.in; Tel.:+91-9810751432

Received: 11 July 2018; Accepted: 29 August 2018; Published: 2 September 2018



Abstract: In this paper, a two-player constant-sum interval-valued 2-tuple linguistic matrix game is construed. The value of a linguistic matrix game is proven as a non-decreasing function of the linguistic values in the payoffs, and, hence, a pair of auxiliary linguistic linear programming (LLP) problems is formulated to obtain the linguistic lower bound and the linguistic upper bound of the interval-valued linguistic value of such class of games. The duality theorem of LLP is also adopted to establish the equality of values of the interval linguistic matrix game for players I and II. A flowchart to summarize the proposed algorithm is also given. The methodology is then illustrated via a hypothetical example to demonstrate the applicability of the proposed theory in the real world. The designed algorithm demonstrates acceptable results in the two-player constant-sum game problems with interval-valued 2-tuple linguistic payoffs.

Keywords: 2-tuple linguistic model; interval-valued 2-tuple linguistic model; linguistic linear programming problem; interval-valued linguistic matrix game

1. Introduction

Classical non-cooperative game theory, introduced by Von Neumann and Morgenstern [1], speculates that each player is exposed to the precisely known information of the game. The precise knowledge allows the players to provide exact evaluations of their utility functions in terms of their strategies. The presumption of exact payoffs emerges as a stringent ideology in the era of real problems with uncertainty and ambiguity. The elements of vagueness and imprecision have been integrated into games using various frameworks—to mention but a few, stochastic and fuzzy. Numerous researchers have contributed remarkable theories and outlooks to enrich the literature of fuzzy game [2–4] and stochastic game [5,6] theories. However, in this uncertain world, the determination of membership functions of a fuzzy value or probability distributions in case of a stochastic game is not always feasible for players. In some uncertain scenarios, the payoffs may vary within a certain range resulting in matrix-games with interval-valued payoffs [7–11]. Collins and Hu [7,8,12] have significantly contributed to developing different perspectives and techniques in order to solve interval-valued matrix-game problems. Li et al. [13] developed auxiliary interval programming models to obtain a pair of bi-objective linear programming models to solve interval-valued matrix games. Li [14] proved the value of the interval-valued matrix-game to be a non-decreasing function of the interval payoffs of the matrix. He formulated a pair of auxiliary linear programming models to derive the upper bound and lower bound of the value of the interval-valued matrix-game. Annexing a new viewpoint to the game theory under uncertainty, Arfi [15,16] developed a linguistic fuzzy logic based game theoretic approach involving the idea of linguistic fuzzy domination and linguistic Nash equilibrium. To enhance the purview of ambiguity and vagueness in game theory, Singh et al. [17] presented a non-cooperative two-player constant-sum matrix game problem in the 2-tuple linguistic framework.

The 2-tuple linguistic model is first formalized by Herrera and Martinez [18]. Their competence to express any counting of information in the universe of discourse brings the edge over the other existing linguistic model. The veracious and interpretable 2-tuple linguistic model is widely used in decision sciences [18–20]. However, intermittently, the granularity of vagueness and ambiguity to assess some criteria cannot be catered entirely by the subjectivity of linguistic terms in the predefined linguistic term set. Indeed, the argument to enlarge the term set can always be suggested for enunciating better information; it results in increased cumbersome calculations for aggregating large sets of variables [21]. Zhang [21] presented an extended version of the linguistic model involving interval-valued 2-tuple linguistic variables. The model comprises of two 2-tuple linguistic variables in an interval from the predefined linguistic term set, to express the assessments of decision-makers. Various practitioners have adopted the interval-valued 2-tuple linguistic model to solve different real-world problems including but not limited to material selection [22] and supplier selection problems [23].

In this contribution, we have extended the matrix games to the interval-valued 2-tuple linguistic framework. Firstly, a two-player constant-sum interval-valued 2-tuple linguistic matrix game is defined, henceforth called an interval linguistic matrix game. Since the logic claims that the value of an interval linguistic matrix game must be an interval-valued 2-tuple linguistic information, we have verified the value of a linguistic matrix game as a non-decreasing function of the interval-valued payoffs in the matrix, as suggested by Li [14]. A pair of auxiliary linguistic linear programming (LLP) problems is then constructed to acquire the linguistic upper bound and linguistic lower bound of the interval-valued linguistic value of the game. The duality principle of LLP is also adopted to prove the equality of interval-valued linguistic lower value and interval-valued linguistic upper value of the game for players I and II, respectively. The designed methodology has a wide variety of applications in the domains where the two-players have the knowledge of their payoffs in terms of interval-valued 2-tuple linguistic variables.

The remainder of this paper is organized as follows. Section 2 presents the rudiments of 2-tuple linguistic model and two-player constant-sum 2-tuple linguistic matrix game. In Section 3, the fundamental structure of a two-player constant-sum interval-valued 2-tuple linguistic matrix game is discussed. Section 4 presents the LLP formulation for solving such a game with a flowchart in Figure 1 to summarize the method. Section 5 illustrates the hypothetical examples to demonstrate the methodology with result analysis. Section 6 concludes the paper.

2. Preliminaries

In this section, the 2-tuple linguistic variable with its extension to interval-valued 2-tuple linguistic variables are reviewed. In addition, the fundamentals of a two-player constant-sum 2-tuple linguistic matrix game are described.

2.1. 2-Tuple Linguistic Model

The following definitions are taken from the work of Herrera and Martinez [18].

The conventional linguistic model is comprised of ℓ_i, where ℓ_i depicts the linguistic term from a predefined linguistic terms set $LT = \{\ell_i : i = 0, 1, \ldots, g\}$ with cardinality $g + 1$. Usually, the index g of the granularity of vagueness in information is assumed an even positive integer. The value in $\{0, 1, \ldots, g\}$ represents the index of the closest linguistic label in LT.

The set LT is totally ordered with the following characteristics:

1. $\ell_i \geq \ell_j$ if $i \geq j$ (the set LT is ordered);
2. $\max(\ell_i, \ell_j) = \ell_i$ if $\ell_i \geq \ell_j$ and $\min(\ell_i, \ell_j) = \ell_i$ if $\ell_i \leq \ell_j$;
3. $neg(\ell_i) = \ell_j$, $j = g - i$.

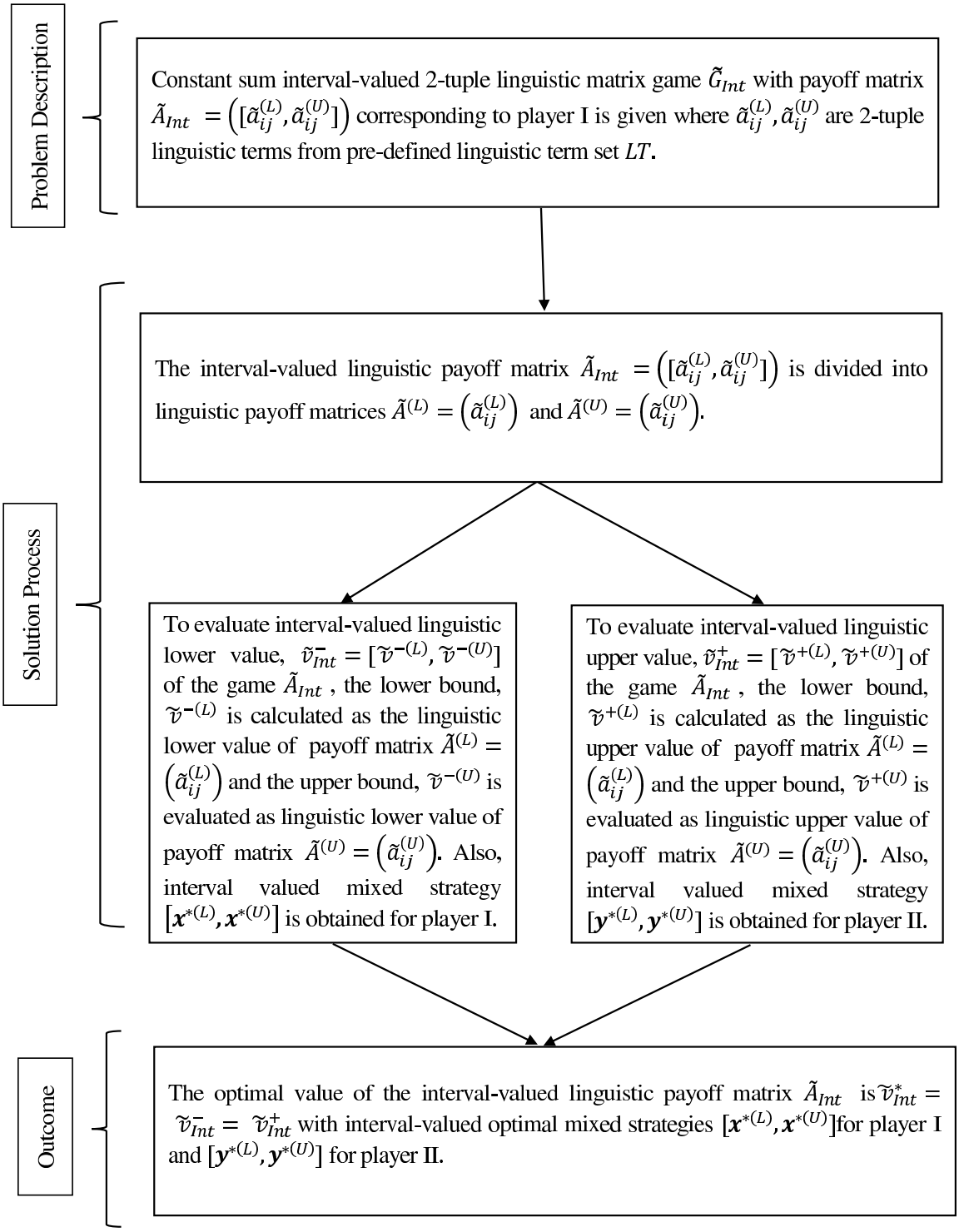


Figure 1. Proposed methodology

Definition 1. *Let $\beta \in [0, g]$ be the result of an aggregation of the indices of a set of labels assessed in LT. Suppose $i = round(\beta)$, where $round(\cdot)$ is the usual rounding operation, and $\alpha = \beta - i$, $\alpha \in [-0.5, 0.5)$. Then, α is called the symbolic translation.*

A 2-tuple linguistic variable is represented by (ℓ_i, α), where ℓ_i is a linguistic term and α is the symbolic translation.

Herrera and Martinez [18] proposed a 2-tuple linguistic model (ℓ_i, α_i) such that $\ell_i \in LT$ and $\alpha_i \in [-0.5, 0.5)$. They further defined the lexicographic ordering in the 2-tuple linguistic variables.

Definition 2. *Let (ℓ_i, α_i) and (ℓ_j, α_j) be two 2-tuple linguistic variables.*

1. *If $i < j$, then $(\ell_i, \alpha_i) < (\ell_j, \alpha_j)$.*
2. *If $i = j$, i.e., ℓ_i and ℓ_j are the same linguistics, then*
   - *(a) if $\alpha_i = \alpha_j$, then $(\ell_i, \alpha_i) = (\ell_j, \alpha_j)$, that is, (ℓ_i, α_i) and (ℓ_j, α_j) represent the same information;*
   - *(b) if $\alpha_i > \alpha_j$, then $(\ell_i, \alpha_i) > (\ell_j, \alpha_j)$;*
   - *(c) if $\alpha_i < \alpha_j$, then $(\ell_i, \alpha_i) < (\ell_j, \alpha_j)$.*

Definition 3. *Let $\beta \in [0, g]$ be the value representing the result of a symbolic aggregation. An equivalent 2-tuple linguistic variable can be obtained using the function $\Delta : [0, g] \to LT \times [-0.5, 0.5)$, defined by*

$$\Delta(\beta) = (\ell_i, \alpha_i) \text{ where } i = round(\beta) \text{ and } \alpha_i = \beta - i\,.$$

The function Δ is a bijection, and its inverse is given by

$$\Delta^{-1} : LT \times [-0.5, 0.5) \to [0, g] \text{ as } \Delta^{-1}(\ell_i, \alpha_i) = i + \alpha_i = \beta\,.$$

The literature describing diverse operators on the set of 2-tuple linguistic variables is vast and rich. Here, we cite the weighted average operator from [24] as it is used in the following:

Definition 4. *Let $\{(\ell_{r_i}, \alpha_{r_i}),\ r_i \in \{0, 1, \ldots, g\},\ i = 1, \ldots, q\}$ be a set of 2-tuple linguistic variables and $w = (w_1, \ldots, w_q)^T$ be the weight vector satisfying $0 \le w_i \le 1,\ i = 1, \ldots, q,\ \sum_{i=1}^{q} w_i = 1$. Then, the weighted average operator is defined as*

$$\begin{aligned} LWA[(\ell_{r_i}, \alpha_{r_i}) : i = 1, \ldots, q] &= (\ell_{r_1}, \alpha_{r_1})w_1 \oplus (\ell_{r_2}, \alpha_{r_2})w_2 \oplus \ldots \oplus (\ell_{r_q}, \alpha_{r_q})w_q \\ &= \Delta\Big(\sum_{i=1}^{q} w_i \Delta^{-1}(\ell_{r_i}, \alpha_{r_i})\Big). \end{aligned}$$

Consequently,

$$\Delta^{-1}\Big(\bigoplus_{i=1}^{q}(\ell_{r_i}, \alpha_{r_i})w_i\Big) = \sum_{i=1}^{q} w_i \Delta^{-1}(\ell_{r_i}, \alpha_{r_i}). \tag{1}$$

Here, $\oplus$ depicts the weighted addition of 2-tuple linguistic variables. Since, the usual addition of two 2-tuple linguistic variables is not well-defined, the weighted addition operator, $\oplus$, is used in place of usual addition.

The negation operator for a 2-tuple linguistic variable $\widetilde{v} = (l_i, \alpha_i)$ is taken to be

$$neg\,(\widetilde{v}) = \Delta(g - \Delta^{-1}(\widetilde{v})).$$

Note that when $\widetilde{v}$ is a linguistic variable only (that is, $\widetilde{v} = (\ell_i, 0)$), then $neg(\widetilde{v}) = \ell_{g-i}$, which is the same as the standard negation $neg(\ell_i)$ of the linguistic variable.

To illustrate the above definitions, consider the predefined linguistic term set

$$LT = \{\ell_0 : \text{Very Bad}, \ell_1 : \text{Bad}, \ell_2 : \text{Medium}, \ell_3 : \text{Good}, \ell_4 : \text{Very Good}\}.$$

Let $S = \{(\ell_1, -0.4), (\ell_3, 0.432), (\ell_1, 0.236), (\ell_4, -0.259)\}$ be a set of 2-tuple linguistic variables.

If $\beta = 3.432$ be the symbolic transformation, then the corresponding 2-tuple linguistic variable can be evaluated as, $i = \text{round}(\beta) = 3$ and $\alpha = \beta - i = 0.432$ i.e., $(\ell_3, 0.432)$, whereas, a 2-tuple

linguistic variable $(\ell_4, -0.259)$ can be transformed into its numeric value using Δ^{-1} operator as $\Delta^{-1}(\ell_4, -0.259) = 3.741$. Using the lexicographic ordering of the 2-tuple linguistic variables, the elements of the set S are ordered as $(\ell_1, -0.4) < (\ell_1, 0.236) < (\ell_3, 0.432) < (\ell_4, -0.259)$. For weight vector $w = (0.2, 0.1, 0.3, 0.4)^T$, the weighted average of S is

$$\begin{aligned}&(\ell_1, -0.4)0.2 \oplus (\ell_3, 0.432)0.1 \oplus (\ell_1, 0.236)0.3 \oplus (\ell_4, -0.259)0.4\\ &= \Delta[0.2 * 0.4 + 0.1 * 3.432 + 0.3 * 1.432 + 0.4 * 1.259] = \Delta[2.3304] = (\ell_2, 0.3304).\end{aligned}$$

To extend the degree of uncertainty, an interval-valued 2-tuple linguistic variable [21] can be defined as follows.

Definition 5. *Let $LT = \{\ell_0, \ldots, \ell_g\}$ be a predefined linguistic term set. Then, an interval-valued 2-tuple linguistic variable is defined as $[(\ell_i^{(L)}, \alpha^{(L)}), (\ell_i^{(U)}, \alpha^{(U)})]$ where $\ell_i^{(L)}, \ell_i^{(U)} \in LT$ with $\ell_i^{(L)} \leq \ell_i^{(U)}$ and $\alpha^{(L)}, \alpha^{(U)}$ are the symbolic translations.*

Remark 1. *Here, we consider that the symbolic translations $\alpha^{(L)}, \alpha^{(U)}$ take values in the interval $[-0.5, 0.5)$ in view of a definition given by Herrera and Martinez [18]. However, the interval-valued 2-tuple linguistic model defined by Zhang [21] is widely adopted in practice as it does not engage the granularity of the linguistic term set. As we do not require the computations involving interval-valued linguistics, here we are not discussing its operations. One can see [21] for comprehensive knowledge of computation with interval-valued 2-tuple linguistic variables.*

Now, we review the basics of two-player constant-sum 2-tuple linguistic matrix game from [17].

2.2. Constant-Sum Linguistic Matrix Game

Definition 6. *A two-player constant-sum linguistic game $\widetilde{G}$ is expressed as a quadruplet $(S^n, S^m, LT, \widetilde{A})$, where*

1. *S^n is a set of n strategies for player I defined as,*

$$S^n = \left\{(x_1, \ldots, x_n) \ : \ x_i \geq 0, \ i = 1 \ldots, n, \ \textstyle\sum_{i=1}^n x_i = 1\right\};$$

2. *S^m is a set of m strategies for player II given as,*

$$S^m = \left\{(y_1, \ldots, y_m) \ : \ y_j \geq 0, \ j = 1, \ldots, m, \ \textstyle\sum_{j=1}^m y_j = 1\right\};$$

3. *$LT = \{\ell_0, \ell_1, \ldots, \ell_g\}$ is a predefined linguistic term set with cardinality $g + 1$ for both the players, and*
4. *$\widetilde{A} = [\widetilde{a}_{ij}]_{n \times m}$ is the linguistic payoff matrix for player I where $\widetilde{a}_{ij} \in LT, i = 1, \ldots, n, j = 1, \ldots, m$, while $neg(\widetilde{A}) = [neg(\widetilde{a}_{ij})]_{n \times m}$ represents the payoff matrix for player II. Here, $\widetilde{a}_{ij}$, $i = 1, \ldots, n$, $j = 1, \ldots, m$ can depict a linguistic variable or a 2-tuple linguistic variable. The linguistic payoff determines how beneficial and favourable it is for a player to play a given strategy.*

Using the lexicographic ordering of 2-tuple linguistic variables, the value of the linguistic matrix game $\widetilde{G}$ is defined as follows.

Definition 7. *A linguistic matrix game $\widetilde{G}$ with linguistic payoff matrix $\widetilde{A} = [\widetilde{a}_{ij}]_{n \times m}$ is characterized by its lower and upper values defined, respectively, as*

$$\widetilde{v}^- = \max_{i=1,\ldots,n} \min_{j=1,\ldots,m} \widetilde{a}_{ij}, \qquad \widetilde{v}^+ = \min_{j=1,\ldots,m} \max_{i=1,\ldots,n} \widetilde{a}_{ij}.$$

The lower value $\widetilde{v}^-$ describes the minimum linguistic benefit that player I is assured to receive, whereas the upper value $\widetilde{v}^+$ is player II's linguistic loss-ceiling. The value $\widetilde{v}$ of game $\widetilde{G}$ is defined when $\widetilde{v}^- = \widetilde{v}^+ = \widetilde{v}$.

The strategies i^* and j^* with the payoff $\widetilde{a}_{i^*j^*}$, such that $\widetilde{a}_{i^*j^*} = \widetilde{v}^- = \widetilde{v}^+$, are optimal pure strategies for player I and player II, respectively. In this case, the strategy pair (i^*, j^*) is termed as the saddle point of game $\widetilde{G}$.

Since the existence of saddle point in each linguistic game $\widetilde{G}$ is hardly possible, it is essential to define the linguistic expected payoff of players as follows.

Definition 8. *Given a pair of mixed strategies $\mathbf{x} = (x_1, \ldots, x_n) \in S^n$ and $\mathbf{y} = (y_1, \ldots, y_m) \in S^m$ for player I and player II, respectively, the linguistic expected payoff of player I is defined by*

$$\widetilde{E}_{\widetilde{A}}(\mathbf{x}, \mathbf{y}) = \bigoplus_{i=1}^{n} \left(x_i \left(\bigoplus_{j=1}^{m} \tilde{a}_{ij} y_j\right)\right). \tag{2}$$

The linguistic expected payoff of player II is $neg(\widetilde{E}_{\widetilde{A}}(\mathbf{x}, \mathbf{y}))$.

It is noteworthy that the lower value and upper value of the linguistic game $\widetilde{G}$ given in Definition 7 are described in light of pure strategies. The structures of the two values change to some degree in the case of mixed strategies.

Suppose player I chooses any strategy $\mathbf{x} \in S^n$. Then, player I's linguistic expected gain-floor is defined as follows:

$$\widetilde{v}^-(\mathbf{x}) = \min_{\mathbf{y} \in S^m} \widetilde{E}_{\widetilde{A}}(\mathbf{x}, \mathbf{y}) = \min_{\mathbf{y} \in S^m} \left\{ \bigoplus_{i=1}^{n} \left(x_i \left(\bigoplus_{j=1}^{m} \tilde{a}_{ij} y_j\right)\right) \right\}. \tag{3}$$

Here, $\widetilde{E}_{\widetilde{A}}(\mathbf{x}, \mathbf{y})$ can be considered as the weighted average of player I's payoffs if the player I chooses mixed strategy $\mathbf{x} \in S^n$ against pure strategy of player II. Hence, the minimum is achieved by some pure strategy of player II:

$$\widetilde{v}^-(\mathbf{x}) = \min_{1 \le j \le m} \widetilde{E}_{\widetilde{A}}(\mathbf{x}, \mathbf{e_j}) = \min_{1 \le j \le m} \left\{ \bigoplus_{i=1}^{n} x_i \tilde{a}_{ij} \right\}, \tag{4}$$

where $e_j \in S^m$ is the unit vector with 1 at the jth position. Thus, player I should select $\mathbf{x}^* \in S^n$ in the interest of maximising $\widetilde{v}^-(\mathbf{x})$ to attain lower value of the game $\widetilde{G}$ as follows:

$$\widetilde{v}^- = \widetilde{v}^-(\mathbf{x}^*) = \max_{\mathbf{x} \in S^n} \widetilde{v}^-(\mathbf{x}) = \max_{\mathbf{x} \in S^n} \min_{1 \le j \le m} \widetilde{E}_{\widetilde{A}}(\mathbf{x}, \mathbf{e_j}). \tag{5}$$

The strategy $\mathbf{x}^* \in S^n$ is called optimal strategy for player I and $\widetilde{v}^- = \widetilde{v}^-(\mathbf{x}^*)$ is called the lower value of the game $\widetilde{G}$.

The computation of optimal strategy $\mathbf{x}^* \in S^n$ to achieve $\widetilde{v}^-(\mathbf{x}^*)$ is equivalent to solving the following linguistic linear programming (LLP) problem:

$$\begin{aligned} &\max \quad \widetilde{v}^- && \text{(M1)} \\ &\text{subject to} \\ &\widetilde{a}_{11}x_1 \oplus \widetilde{a}_{21}x_2 \oplus \ldots \oplus \widetilde{a}_{n1}x_n \ge \widetilde{v}^- \\ &\widetilde{a}_{12}x_1 \oplus \widetilde{a}_{22}x_2 \oplus \ldots \oplus \widetilde{a}_{n2}x_n \ge \widetilde{v}^- \\ &\vdots \\ &\widetilde{a}_{1m}x_1 \oplus \widetilde{a}_{2m}x_2 \oplus \ldots \oplus \widetilde{a}_{nm}x_n \ge \widetilde{v}^- \\ &x_1 + x_2 + \ldots + x_n = 1 \\ &x_1,\ x_2, \ldots, x_n \ge 0. \end{aligned}$$

Furthermore, correspondingly, the upper value of the game $\widetilde{G}$ can be defined in view of minimizing player II's linguistic expected loss-ceiling. Suppose that player II plays strategy $\mathbf{y} \in S^m$, then his/her linguistic expected loss-ceiling is given as

$$\widetilde{v}^{+}(\mathbf{y}) = \max_{1\le i\le n} \widetilde{E}_{\widetilde{A}}(\mathbf{e_i}, \mathbf{y}) = \max_{1\le i\le n} \left\{ \bigoplus_{j=1}^{m} \tilde{a}_{ij} y_j \right\}, \tag{6}$$

where $e_i \in S^n$ is the unit vector with 1 at ith position. Hence, player II should select strategy $\mathbf{y}^* \in S^m$ such that the minimum of $\widetilde{v}^{+}(\mathbf{y})$ is obtained. Hence,

$$\widetilde{v}^{+} = \widetilde{v}^{+}(\mathbf{y}^*) = \min_{\mathbf{y}\in S^m} \widetilde{v}^{+}(\mathbf{y}) = \min_{\mathbf{y}\in S^m} \max_{1\le i\le n} \widetilde{E}_{\widetilde{A}}(\mathbf{e_i}, \mathbf{y}). \tag{7}$$

Here, $\widetilde{v}^{+}$ is the upper value of the game $\widetilde{G}$ with optimal strategy $\mathbf{y}^* \in S^m$ of player II.

The equivalent LLP problem to evaluate player II's optimal strategy $\mathbf{y}^* \in S^m$ to obtain the upper value of the game is as follows:

$$\begin{aligned} &\min\ \widetilde{v}^{+} \qquad\qquad\qquad\

Here, we present an example to illustrate the structure of an interval linguistic matrix game for the better understanding of readers.

Example 1. *Consider the two contending insurance schemes proposed by two companies in the insurance market. The companies are planning to launch the schemes in the coming few months. The available options for the commencement are one month, two months and three months from now. The payoffs reflect how much market share a company can anticipate in view of the month of introducing the respective schemes. Since the estimation of the payoffs as 2-tuple linguistic variables is not always possible, the payoffs of the companies appear in the form of linguistic intervals from a predefined linguistic term set LT = {Very Low: VL, Low: L, Average: Avg, High: H, Very High: VH}. Let the payoff matrix of company I be as follows:*

$\widetilde{A}_{Int} =$

I/II	*1*	*2*	*3*
1	*[L, Avg]*	*[L, VH]*	*VH*
2	*[VL, L]*	*[VL, H]*	*[L, VH]*
3	*VL*	*[Avg, VH]*	*[H, VH].*

For instance, if company I and company II launch the corresponding insurance schemes in the second and third months, respectively, then company I is expected to receive Low to Very High (i.e., $[\widetilde{a}_{23}^{(L)}, \widetilde{a}_{23}^{(U)}]$*) market share. The payoff of company I, in case companies I and II decide to introduce their schemes in the first and third months, respectively, is anticipated to be Very High as it can be easily expressed as linguistic interval* $[VH, VH]$*. Furthermore, the payoff matrix corresponding to company II is expressed as follows:*

$neg(\widetilde{A}_{Int}) =$

I/II	*1*	*2*	*3*
1	*[Avg, H]*	*[VL, H]*	*VL*
2	*[H, VH]*	*[L, VH]*	*[VL, H]*
3	*VH*	*[VL, Avg]*	*[VL, L].*

The matrix $neg(\widetilde{A}_{Int})$ *suggests that on selecting second and third months by companies I and II, respectively, to launch their schemes, company II will receive Very Low to High market share. In particular, if company I gets High* $(H \in [L, VH])$ *market share on the given selection of months by the two companies, company II will receive* $neg(H) = L \in [VL, H]$ *market shares as it is a constant-sum interval linguistic matrix game. The interval payoffs provide a range of expected benefits to the players.*

4. Linguistic Linear Programming Approach to Solve Two-Player Constant-Sum Interval-Valued 2-Tuple Linguistic Matrix Game

This section proposes the LLP formulation of a constant-sum interval-valued linguistic matrix game $\widetilde{G}_{Int}$. Suppose the predefined linguistic term set with granularity g be $LT = \{\ell_0, \ell_1, \ldots, \ell_g\}$. Here, g is considered as a positive even integer. Consider the interval-valued linguistic payoff matrix of player I as follows:

$$\widetilde{A}_{Int} = \begin{pmatrix} [\tilde{a}_{11}^{(L)}, \tilde{a}_{11}^{(U)}] & [\tilde{a}_{12}^{(L)}, \tilde{a}_{12}^{(U)}] & \ldots & [\tilde{a}_{1m}^{(L)}, \tilde{a}_{1m}^{(U)}] \\ [\tilde{a}_{21}^{(L)}, \tilde{a}_{21}^{(U)}] & [\tilde{a}_{22}^{(L)} \tilde{a}_{22}^{(U)}] & \ldots & [\tilde{a}_{2m}^{(L)} \tilde{a}_{2m}^{(U)}] \\ \vdots & \ddots & \vdots & \\ [\tilde{a}_{n1}^{(L)} \tilde{a}_{n1}^{(U)}] & [\tilde{a}_{n2}^{(L)} \tilde{a}_{n2}^{(U)}] & \ldots & [\tilde{a}_{nm}^{(L)} \tilde{a}_{nm}^{(U)}] \end{pmatrix}.$$

For any given linguistic payoffs $\widetilde{a}_{ij} \in [\widetilde{a}_{ij}^{(L)}, \widetilde{a}_{ij}^{(U)}]$, $i = 1, \ldots, n$, $j = 1, \ldots, m$, a linguistic payoff matrix, $\widetilde{A}$, is given as

$$\widetilde{A} = \begin{bmatrix} \tilde{a}_{11} & \tilde{a}_{12} & \ldots & \tilde{a}_{1m} \\ \tilde{a}_{21} & \tilde{a}_{22} & \ldots & \tilde{a}_{2m} \\ \vdots & \ddots & \vdots & \\ \tilde{a}_{n1} & \tilde{a}_{n2} & \ldots & \tilde{a}_{nm} \end{bmatrix}.$$

It is evident from Equations (4) and (5) that the lower value of the linguistic game with payoff matrix $\widetilde{A}$ is function of the values $\widetilde{a}_{ij},\ i=1,\ldots,n,\ j=1,\ldots,m$. Hence, the value $\widetilde{v}^{-}$ can also be written as $\widetilde{v}^{-}=\widetilde{v}^{-}(\widetilde{A})=\widetilde{v}^{-}(\widetilde{a}_{ij},\ i=1,\ldots,n,\ j=1,\ldots,m)$ where $\widetilde{a}_{ij}\in[\widetilde{a}_{ij}^{(L)},\widetilde{a}_{ij}^{(U)}]$. Additionally, the optimal strategy $\mathbf{x}^{*}\in S^{n}$ of player I can also be considered as a function of the $\widetilde{a}_{ij}$ values, i.e., $\mathbf{x}^{*}=\mathbf{x}^{*}(\widetilde{A})=\mathbf{x}^{*}(\widetilde{a}_{ij},\ i=1,\ldots,n,\ j=1,\ldots,m)$.

Analogous to the above discussion, the upper value of the game $\widetilde{v}^{+}$ and the optimal strategy $\mathbf{y}^{*}\in S^{m}$ of player II for the payoff matrix $\widetilde{A}$ can also be considered as functions of linguistic values $\widetilde{a}_{ij},\ i=1,\ldots,n,\ j=1,\ldots,m$, expressed as $\widetilde{v}^{+}=\widetilde{v}^{+}(\widetilde{A})=\widetilde{v}^{+}(\widetilde{a}_{ij},\ i=1,\ldots,n,\ j=1,\ldots,m)$ and $\mathbf{y}^{*}=\mathbf{y}^{*}(\widetilde{A})=\mathbf{y}^{*}(\widetilde{a}_{ij},\ i=1,\ldots,n,\ j=1,\ldots,m)$.

Furthermore, consider the payoff matrices $\widetilde{A}=\left[\widetilde{a}_{ij}\right]_{n\times m}$ and $\widetilde{A}'=\left[\widetilde{a}'_{ij}\right]_{n\times m}$ such that $\widetilde{a}_{ij},\widetilde{a}'_{ij}\in[\tilde{a}_{ij}^{(L)},\tilde{a}_{ij}^{(U)}]$ with $\widetilde{a}_{ij}\leq\widetilde{a}'_{ij};\ i=1,\ldots,n,\ j=1,\ldots,m$, then $\widetilde{v}^{-}(\widetilde{A})\leq\widetilde{v}^{-}(\widetilde{A}')$, $\widetilde{v}^{+}(\widetilde{A})\leq\widetilde{v}^{+}(\widetilde{A}')$ and $\widetilde{v}(\widetilde{A})\leq\widetilde{v}(\widetilde{A}')$ i.e., the lower value, the upper value and hence the linguistic value of the game is a non-decreasing function of the values $\tilde{a}_{ij};\ i=1,\ldots,n,\ j=1,\ldots,m,$. The validation of the inequalities can be easily performed in the light of Equations (5) and (7).

In view of the above discussion, it can be concluded that the lower value, upper value and value of the interval game $\widetilde{G}_{Int}$ results in being closed intervals of linguistic variables and can be defined as follows.

Definition 10. *Given a two-player constant-sum interval-valued linguistic matrix game* $\widetilde{G}_{Int}=(S^{n},S^{m},LT,\widetilde{A}_{Int})$, *the interval-valued linguistic lower value,* $\widetilde{v}_{Int}^{-}$, *and the interval-valued linguistic upper value,* $\widetilde{v}_{Int}^{+}$ *of the game* $\widetilde{G}_{Int}$ *depicts the ranges of the gain-floor of player I and loss-ceiling of player II, respectively. The values are computed as follows:*

$$\widetilde{v}_{Int}^{-}=[\widetilde{v}^{-(L)},\widetilde{v}^{-(U)}]=[\widetilde{v}^{-}(\widetilde{A}^{(L)}),\widetilde{v}^{-}(\widetilde{A}^{(U)})],$$
$$\widetilde{v}_{Int}^{+}=[\widetilde{v}^{+(L)},\widetilde{v}^{+(U)}]=[\widetilde{v}^{+}(\widetilde{A}^{(L)}),\widetilde{v}^{+}(\widetilde{A}^{(U)})],$$

where $\widetilde{A}^{(L)}=[(\tilde{a}_{ij}^{(L)})]_{n\times m}$ *and* $\widetilde{A}^{(U)}=[(\tilde{a}_{ij}^{(U)})]_{n\times m}$.

The value $\widetilde{v}_{Int}$ *of the interval game* $\widetilde{G}_{Int}$ *is defined when* $\widetilde{v}_{Int}^{-}=\widetilde{v}_{Int}^{+}=\widetilde{v}_{Int}$.

Here, the optimal pure strategies for the interval-valued linguistic payoff matrix $\widetilde{A}_{Int}$ is challenging to deduce, whereas the optimal pure strategy for $\widetilde{A}^{(L)}$ and $\widetilde{A}^{(U)}$ could be easily computed.

Now, we elucidate the above discussion via an example.

Example 2. *Consider the illustration given in Example 1. The interval-valued linguistic payoff matrix of company I is as follows:*

$\widetilde{A}_{Int}=$

I/II	*1*	*2*	*3*
1	*[L, Avg]*	*[L, VH]*	*VH*
2	*[VL, L]*	*[VL, H]*	*[L, VH]*
3	*VL*	*[Avg, VH]*	*[H, VH].*

The corresponding matrices of lower terms and upper terms i.e., $\widetilde{A}^{(L)}$ *and* $\widetilde{A}^{(U)}$ *are given below:*

$$\widetilde{A}^{(L)}=\begin{bmatrix} L & L & VH \\ VL & VL & L \\ VL & Avg & H \end{bmatrix} \text{ and } \widetilde{A}^{(U)}=\begin{bmatrix} Avg & VH & VH \\ L & H & VH \\ VL & VH & VH \end{bmatrix}.$$

Using Definition 7, $\widetilde{v}^{-}(\widetilde{A}^{(L)})=L,\ \ \widetilde{v}^{+}(\widetilde{A}^{(L)})=L$, *hence* $\widetilde{v}(\widetilde{A}^{(L)})=L$.

In addition, $\widetilde{v}^{-}(\widetilde{A}^{(U)})=Avg,\ \ \widetilde{v}^{+}(\widetilde{A}^{(U)})=Avg$, *that concludes,* $\widetilde{v}(\widetilde{A}^{(U)})=Avg$.

Hence, $\widetilde{v}_{Int}^{-}=\widetilde{v}_{Int}^{+}=\widetilde{v}_{Int}=[L,Avg]$ *i.e., company I will receive atleast Low (L) to Average (Avg) market shares, whereas company II's benefit ranges between Average (Avg) and High (H), evaluated using neg*$[L,Avg]$. *It is also noteworthy that (1,1) is the saddle point for both the matrices* $\widetilde{A}^{(L)}$ *and* $\widetilde{A}^{(U)}$.

Here, it is important to mention that it is not always necessary that both matrices $\widetilde{A}^{(L)}$ and $\widetilde{A}^{(U)}$ have a saddle point at the same positions or even possess value of the linguistic games using pure strategy. Suppose the entry $[\tilde{a}_{21}^{(L)}, \tilde{a}_{21}^{(U)}]$ in the payoff matrix $\widetilde{A}_{Int}$ presented in the above example is changed to $[VL, H]$. Then, $\widetilde{A}^{(L)}$ has the same lower value and upper value with saddle point (1,1) as mentioned in the above example, but the value of the game of the payoff matrix $\widetilde{A}^{(U)}$ changes to H achieved at point (2,1), whereas the replacement of the entry $[\tilde{a}_{21}^{(L)}, \tilde{a}_{21}^{(U)}]$ with $[VL, VH]$ results in the same linguistic value of the game with payoff matrix $\widetilde{A}^{(L)}$ while the values for $\widetilde{A}^{(U)}$ change. Here, $\widetilde{v}^{-(U)} = \widetilde{v}^{-}(\widetilde{A}^{(U)}) = H, \quad \widetilde{v}^{+}(\widetilde{A}^{(U)}) = VH$. It suggests that $\widetilde{A}^{(U)}$ does not possess the linguistic value of the game using pure strategies.

The absence of pure optimal strategies for the matrices $\widetilde{A}^{(L)}$ and $\widetilde{A}^{(U)}$ incapacitate to define the value of the interval-valued linguistic game $\widetilde{G}_{Int}$. It necessitates obtaining the mixed strategies and the upper and lower values of $\widetilde{A}^{(L)}$ and $\widetilde{A}^{(U)}$ using a linguistic linear programming approach.

4.1. Evaluation of Interval-Valued Linguistic Lower Value $\widetilde{v}_{Int}^{-}$ of the Game $\widetilde{A}_{Int}$

In view of model (M1), the lower bound $\widetilde{v}^{-(L)}$ of the interval-valued linguistic lower value $\widetilde{v}_{Int}^{-}$ can be evaluated using the following model:

$$
\begin{aligned}
&\max \quad \widetilde{v}^{-(L)} \qquad \text{(M3)}\\
&\text{subject to}\\
&\tilde{a}_{11}^{(L)} x_1^{(L)} \oplus \tilde{a}_{21}^{(L)} x_2^{(L)} \oplus \ldots \oplus \tilde{a}_{n1}^{(L)} x_n^{(L)} \geq \widetilde{v}^{-(L)}\\
&\tilde{a}_{12}^{(L)} x_1^{(L)} \oplus \tilde{a}_{22}^{(L)} x_2^{(L)} \oplus \ldots \oplus \tilde{a}_{n2}^{(L)} x_n^{(L)} \geq \widetilde{v}^{-(L)}\\
&\vdots\\
&\tilde{a}_{1m}^{(L)} x_1^{(L)} \oplus \tilde{a}_{2m}^{(L)} x_2^{(L)} \oplus \ldots \oplus \tilde{a}_{nm}^{(L)} x_n^{(L)} \geq \widetilde{v}^{-(L)}\\
&x_1^{(L)} + x_2^{(L)} + \ldots + x_n^{(L)} = 1\\
&x_1^{(L)}, x_2^{(L)}, \ldots, x_n^{(L)} \geq 0.
\end{aligned}
$$

The model corresponds to the lower bound of each linguistic interval of the payoff matrix $\widetilde{A}_{Int}$ with mixed strategy set $\mathbf{x}^{(\mathbf{L})} = (x_1^{(L)}, \ldots, x_n^{(L)})$.

The model (M3) can be converted to a conventional linear programming problem with numerical coefficient using Δ^{-1} in view of [17].

Here, we assume that $\Delta^{-1}\left(\widetilde{v}^{-(L)}\right) = v^{(L)} > 0$. Consider $\Delta^{-1}(\tilde{a}_{ij}^{(L)}) = a_{ij}^{(L)}$, $i = 1, \ldots, n$, $j = 1, \ldots, m$, $X_i^{(L)} = \dfrac{x_i^{(L)}}{v^{(L)}}$, $i = 1, \ldots n$, and $V^{(L)} = \dfrac{1}{v^{(L)}}$.

Hence, model (M3) can be converted into the following LPP model:

$$
\begin{aligned}
&\min \; V^{(L)} = \quad X_1^{(L)} + X_2^{(L)} + \ldots + X_n^{(L)} \qquad \text{(M4)}\\
&\text{subject to}\\
&a_{11}^{(L)} X_1^{(L)} + a_{21}^{(L)} X_2^{(L)} + \ldots + a_{n1}^{(L)} X_n^{(L)} \geq 1\\
&a_{12}^{(L)} X_1^{(L)} + a_{22}^{(L)} X_2^{(L)} + \ldots + a_{n2}^{(L)} X_n^{(L)} \geq 1\\
&\vdots\\
&a_{1m}^{(L)} X_1^{(L)} + a_{2m}^{(L)} X_2^{(L)} + \ldots + a_{nm}^{(L)} X_n^{(L)} \geq 1\\
&X_1^{(L)}, X_2^{(L)}, \ldots, X_n^{(L)} \geq 0.
\end{aligned}
$$

Similarly, the upper bound $\widetilde{v}^{-(U)}$ of interval-valued linguistic lower value $\widetilde{v}^{-}_{Int}$ and corresponding optimal mixed strategy $\mathbf{x}^{(U)} \in S^n$ can be evaluated using the following LLP model:

$$\begin{aligned} &\max \quad \widetilde{v}^{-(U)} \\ &\text{subject to} \\ &\tilde{a}^{(U)}_{11} x^{(U)}_1 \oplus \widetilde{a}^{(U)}_{21} x^{(U)}_2 \oplus \ldots \oplus \widetilde{a}^{(U)}_{n1} x^{(U)}_n \geq \widetilde{v}^{-(U)} \\ &\widetilde{a}^{(U)}_{12} x^{(U)}_1 \oplus \widetilde{a}^{(U)}_{22} x^{(U)}_2 \oplus \ldots \oplus \widetilde{a}^{(U)}_{n2} x^{(U)}_n \geq \widetilde{v}^{-(U)} \\ &\vdots \\ &\widetilde{a}^{(U)}_{1m} x^{(U)}_1 \oplus \widetilde{a}^{(U)}_{2m} x^{(U)}_2 \oplus \ldots \oplus \widetilde{a}^{(U)}_{nm} x^{(U)}_n \geq \widetilde{v}^{-(U)} \\ &x^{(U)}_1 + x^{(U)}_2 + \ldots + x^{(U)}_n = 1 \\ &x^{(U)}_1, x^{(U)}_2, \ldots, x^{(U)}_n \geq 0. \end{aligned} \tag{M5}$$

Without loss of generality, we assume that $\Delta^{-1}\left(\widetilde{v}^{-(U)}\right) = v^{(U)} > 0$. We set $\Delta^{-1}(\widetilde{a}^{(U)}_{ij}) = a^{(U)}_{ij}$, $i = 1, \ldots, n$, $j = 1, \ldots, m$, $X^{(U)}_i = \dfrac{x^{(U)}_i}{v^{(U)}}$, $i = 1, \ldots n$, and $V^{(U)} = \dfrac{1}{v^{(U)}}$.

The transformed LPP for upper bound $\widetilde{v}^{-(U)}$ of interval lower bound $\widetilde{v}^{-}_{int}$ is as follows:

$$\begin{aligned} &\min \ V^{(U)} = \quad X^{(U)}_1 + X^{(U)}_2 + \ldots + X^{(U)}_n \\ &\text{subject to} \\ &a^{(U)}_{11} X^{(U)}_1 + a^{(U)}_{21} X^{(U)}_2 + \ldots + a^{(U)}_{n1} X^{(U)}_n \geq 1 \\ &a^{(U)}_{12} X^{(U)}_1 + a^{(U)}_{22} X^{(U)}_2 + \ldots + a^{(U)}_{n2} X^{(U)}_n \geq 1 \\ &\vdots \\ &a^{(U)}_{1m} X^{(U)}_1 + a^{(U)}_{2m} X^{(U)}_2 + \ldots + a^{(U)}_{nm} X^{(U)}_n \geq 1 \\ &X^{(U)}_1, X^{(U)}_2, \ldots, X^{(U)}_n \geq 0. \end{aligned} \tag{M6}$$

Hence, $\widetilde{v}^{-}_{int}$ can be obtained by solving models (M4) and (M6).

4.2. Evaluation of Interval-Valued Linguistic Upper Value $\widetilde{v}^{+}_{Int}$ of the Game $\widetilde{A}_{Int}$

The above discussion can be adhered to obtain the interval-valued linguistic upper value, $\widetilde{v}^{+}_{Int}$, and the corresponding optimal strategies.

The corresponding LLP models for $\widetilde{v}^{+(L)}$ and $\widetilde{v}^{+(U)}$ are as follows:

$$\begin{aligned} &\min \quad \widetilde{v}^{+(L)} \\ &\text{subject to} \\ &\tilde{a}^{(L)}_{11} y^{(L)}_1 \oplus \widetilde{a}^{(L)}_{12} y^{(L)}_2 \oplus \ldots \oplus \widetilde{a}^{(L)}_{1m} y^{(L)}_m \leq \widetilde{v}^{+(L)} \\ &\widetilde{a}^{(L)}_{21} y^{(L)}_1 \oplus \widetilde{a}^{(L)}_{22} y^{(L)}_2 \oplus \ldots \oplus \widetilde{a}^{(L)}_{2m} y^{(L)}_m \leq \widetilde{v}^{+(L)} \\ &\vdots \\ &\widetilde{a}^{(L)}_{n1} y^{(L)}_1 \oplus \widetilde{a}^{(L)}_{n2} y^{(L)}_2 \oplus \ldots \oplus \widetilde{a}^{(L)}_{nm} y^{(L)}_m \leq \widetilde{v}^{+(L)} \\ &y^{(L)}_1 + y^{(L)}_2 + \ldots + y^{(L)}_m = 1 \\ &y^{(L)}_1, y^{(L)}_2, \ldots, y^{(L)}_m \geq 0 \end{aligned} \tag{M7}$$

and

$$\begin{aligned}
&\min \quad \widetilde{v}^{+(U)} && \text{(M8)}\\
&\text{subject to}\\
&\tilde{a}_{11}^{(U)} y_1^{(U)} \oplus \widetilde{a}_{12}^{(U)} y_2^{(U)} \oplus \ldots \oplus \widetilde{a}_{1m}^{(U)} y_m^{(U)} \leq \widetilde{v}^{+(U)}\\
&\widetilde{a}_{21}^{(U)} y_1^{(U)} \oplus \widetilde{a}_{22}^{(U)} y_2^{(U)} \oplus \ldots \oplus \widetilde{a}_{2m}^{(U)} y_m^{(U)} \leq \widetilde{v}^{+(U)}\\
&\vdots\\
&\widetilde{a}_{n1}^{(U)} y_1^{(U)} \oplus \widetilde{a}_{n2}^{(U)} y_2^{(U)} \oplus \ldots \oplus \widetilde{a}_{nm}^{(U)} y_m^{(U)} \leq \widetilde{v}^{+(U)}\\
&y_1^{(U)} + y_2^{(U)} + \ldots + y_m^{(U)} = 1\\
&y_1^{(U)}, y_2^{(U)}, \ldots, y_m^{(U)} \geq 0.
\end{aligned}$$

Here, $\mathbf{y}^{(L)} = (y_1^{(L)}, \ldots, y_m^{(L)})$ and $\mathbf{y}^{(U)} = (y_1^{(U)}, \ldots, y_m^{(U)})$ are mixed strategies corresponding to the lower bound and upper bound, respectively, of interval-valued linguistic upper value $\widetilde{v}_{Int}^{+}$ of the game. Furthermore, since $\Delta^{-1}\left(\widetilde{v}^{-(L)}\right) = v^{(L)} > 0$ and $\Delta^{-1}\left(\widetilde{v}^{-(U)}\right) = v^{(U)} > 0$, if $v^{(L)}$ and $v^{(U)}$ are value of game with payoff matrices $\widetilde{A}^{(L)}$ and $\widetilde{A}^{(U)}$, respectively, then $v^{(L)} = \Delta^{-1}\left(\widetilde{v}^{+(L)}\right)$ with $v^{(U)} = \Delta^{-1}\left(\widetilde{v}^{+(U)}\right)$. Additionally, we assume that $Y_i^{(U)} = \dfrac{y_i^{(U)}}{v^{(U)}}$, $Y_i^{(L)} = \dfrac{y_i^{(L)}}{v^{(L)}}$ $i = 1, \ldots n$, and, as earlier, $\Delta^{-1}(\widetilde{a}_{ij}^{(L)}) = a_{ij}^{(L)}$, $\Delta^{-1}(\widetilde{a}_{ij}^{(U)}) = a_{ij}^{(U)}$, $i = 1, \ldots, n$, $j = 1, \ldots, m$.

The transformed LPP models corresponding to models (M7) and (M8) are as follows:

$$\begin{aligned}
&\max\ V^{(L)} = \quad Y_1^{(L)} + Y_2^{(L)} + \ldots + Y_m^{(L)} && \text{(M9)}\\
&\text{subject to}\\
&a_{11}^{(L)} Y_1^{(L)} + a_{12}^{(L)} Y_2^{(L)} + \ldots + a_{1m}^{(L)} Y_m^{(L)} \leq 1\\
&a_{21}^{(L)} Y_1^{(L)} + a_{22}^{(L)} Y_2^{(L)} + \ldots + a_{2m}^{(L)} Y_m^{(L)} \leq 1\\
&\vdots\\
&a_{n1}^{(L)} Y_1^{(L)} + a_{n2}^{(L)} Y_2^{(L)} + \ldots + a_{nm}^{(L)} Y_m^{(L)} \leq 1\\
&Y_1^{(L)}, Y_2^{(L)}, \ldots, Y_m^{(L)} \geq 0
\end{aligned}$$

and

$$\begin{aligned}
&\max\ V^{(U)} = \quad Y_1^{(U)} + Y_2^{(U)} + \ldots + Y_m^{(U)} && \text{(M10)}\\
&\text{subject to}\\
&a_{11}^{(U)} Y_1^{(U)} + a_{12}^{(U)} Y_2^{(U)} + \ldots + a_{1m}^{(U)} Y_m^{(U)} \leq 1\\
&a_{21}^{(U)} Y_1^{(U)} + a_{22}^{(U)} Y_2^{(U)} + \ldots + a_{2m}^{(U)} Y_m^{(U)} \leq 1\\
&\vdots\\
&a_{n1}^{(U)} Y_1^{(U)} + a_{n2}^{(U)} Y_2^{(U)} + \ldots + a_{nm}^{(U)} Y_m^{(U)} \leq 1\\
&Y_1^{(U)}, Y_2^{(U)}, \ldots, Y_m^{(U)} \geq 0.
\end{aligned}$$

Using the above models, $\mathbf{y}^{*(L)}$ and $\mathbf{y}^{*(U)}$ can be calculated along with $\widetilde{v}_{Int}^{+} = [\widetilde{v}^{+(L)}, \widetilde{v}^{+(U)}]$.

The models (M4), (M6), (M9) and (M10) provide the corresponding interval-valued optimal mixed strategies $[\mathbf{x}^{*(L)}, \mathbf{x}^{*(U)}]$ and $[\mathbf{y}^{*(L)}, \mathbf{y}^{*(U)}]$ along with the interval-valued linguistic value of the game $\widetilde{v}^{*}_{Int}$.

Remark 4. *Models (M4) and (M9) form a primal-dual pair of linear programs in numerical framework. Models (M6) and (M10) are another pair of primal-dual linear programs in the classical setup.*

Remark 5. *The duality theorem of LLP also proves that $\widetilde{v}^{-(L)} = \widetilde{v}^{+(L)}$ and $\widetilde{v}^{-(U)} = \widetilde{v}^{+(U)}$, which results in equality of interval-valued linguistic lower value and interval-valued linguistic upper value of the game.*

Remark 6. *It is noteworthy that the optimal linguistic value $\widetilde{v}^{*}$ of the linguistic game $\widetilde{A}$ always lies in the interval-valued linguistic value $\widetilde{v}^{*}_{Int}$ of interval linguistic game $\widetilde{A}_{Int}$, but the optimal mixed strategy may not lie in the interval-valued mixed strategy of player I and player II.*

The above algorithm to solve the interval-valued 2-tuple linguistic matrix game can be summarized using the following flowchart.

5. Illustrations and Result Analysis

The game theory has a wide variety of applications in finances, management, and decision sciences. It is also engaged in the real world competing and strategic interactions among players. The interval-valued 2-tuple linguistic game theory facilitates the situations where the range of the payoffs needs to be assessed through subjective thinking of the human mind. For example, the proposed algorithm can be adopted to estimate the market share if two competing companies need to launch their products with different advertising strategies as discussed in Example 1. Now, we present some hypothetical examples to illustrate the validity of the proposed methodology. Herein the examples considered are hypothetical and data is populated synthetically. However, it is not hard to implement these thoughts on real data.

Example 3. *Consider the constant-sum interval-valued linguistic matrix game with interval payoffs from the predefined linguistic term set $LT = \{\ell_0 : Very\ Poor\ (VP),\ \ell_1 : Poor\ (P),\ \ell_2 : Moderately\ Poor\ (MP),\ \ell_3 : Fair\ (F),\ \ell_4 : Moderately\ Good\ (MG),\ \ell_5 : Good\ (G),\ \ell_6 : Very\ Good\ (VG)\}$ with payoff matrix,*

$$\widetilde{A}_{Int} = \begin{pmatrix} [(G, 0.1818), VG] & [(MP, 0.1818), (MG, 0.2545)] \\ [VP, (P, 0.0909)] & [(G, 0.4545), VG] \end{pmatrix}.$$

Here,

$$\widetilde{A}^{(L)} = \begin{bmatrix} (G, 0.1818) & (MP, 0.1818) \\ VP & (G, 0.4545) \end{bmatrix} \text{ and } \widetilde{A}^{(U)} = \begin{bmatrix} VG & (MG, 0.2545) \\ (P, 0.0909) & VG \end{bmatrix}.$$

Suppose the mixed strategies for player I be $\mathbf{x}^{(L)} = (x_1^{(L)}, x_2^{(L)})$, $x_i^{(L)} \geq 0$, $i = 1, 2$, $\sum_{i=1}^{2} x_i^{(L)} = 1$, and $\mathbf{x}^{(U)} = (x_1^{(U)}, x_2^{(U)})$, $x_i^{(U)} \geq 0$, $i = 1, 2$, $\sum_{i=1}^{2} x_i^{(U)} = 1$ for $\widetilde{A}^{(L)}$ and $\widetilde{A}^{(U)}$, respectively. In addition, the mixed strategies for player II for linguistic payoff matrix $\widetilde{A}^{(L)}$ and $\widetilde{A}^{(U)}$ are defined as $\mathbf{y}^{(L)} = (y_1^{(L)}, y_2^{(L)})$, $y_j^{(L)} \geq 0$, $j = 1, 2$, $\sum_{j=1}^{2} y_j^{(L)} = 1$, and $\mathbf{y}^{(U)} = (y_1^{(U)}, y_2^{(U)})$, $y_j^{(U)} \geq 0$, $j = 1, 2$, $\sum_{j=1}^{2} y_j^{(U)} = 1$.

In view of the approach proposed in the paper, construct model (M3) to obtain the lower bound of the interval-valued linguistic lower value $\widetilde{v}^{-}_{Int}$ of the game with payoff matrix $\widetilde{A}_{Int}$. The formulated LLP problem is as follows:

$$\begin{aligned}
&\max \quad \widetilde{v}^{-(L)}\\
&\textit{subject to}\\
&(\ell_5, 0.1818)x_1^{(L)} \oplus (\ell_0, 0)x_2^{(L)} \geq \widetilde{v}^{-(L)},\\
&(\ell_2, 0.1818)x_1^{(L)} \oplus (\ell_5, 0.4545)x_2^{(L)} \geq \widetilde{v}^{-(L)},\\
&x_1^{(L)} + x_2^{(L)} = 1,\\
&x_1^{(L)},\, x_2^{(L)} \geq 0.
\end{aligned}$$

The above formulation can be converted into a linear programming problem in view of model (M4):

$$\begin{aligned}
&\min V^{(L)} = \quad X_1^{(L)} + X_2^{(L)},\\
&\textit{subject to}\\
&5.1818X_1^{(L)} + 0X_2^{(L)} \geq 1,\\
&2.1818X_1^{(L)} + 5.4545X_2^{(L)} + \geq 1,\\
&X_1^{(L)}, X_2^{(L)} \geq 0.
\end{aligned}$$

Similarly, the corresponding model for evaluating upper bound of gain-floor of player I can be constructed using model (M6):

$$\begin{aligned}
&\min V^{(U)} = \quad X_1^{(U)} + X_2^{(U)},\\
&\textit{subject to}\\
&6X_1^{(U)} + 1.0909X_2^{(U)} \geq 1,\\
&4.2545X_1^{(U)} + 6X_2^{(U)} \geq 1,\\
&X_1^{(U)}, X_2^{(U)} \geq 0.
\end{aligned}$$

The optimal solutions of the above problems are $(X_1^{(L)^*} = 0.193,\ X_2^{(L)^*} = 0.1061)$*, with optimal value* $V^{(L)^*} = 0.2991$ *and* $(X_1^{(U)^*} = 0.1565,\ X_2^{(U)^*} = 0.0557)$ *with optimal value* $V^{(U)^*} = 0.2123$*.*

Hence, for player I, the interval-valued linguistic gain-floor is $\widetilde{v}_{Int}^{-^*} = [(\ell_3, 0.3434), (\ell_5, -0.2897)]$ *with optimal mixed strategies* $([0.6453, 0.7372], [0.2624, 0.3547])$*. The interval-valued optimal mixed strategies suggest that the probability for choosing the strategies lie in the evaluated intervals such that the sum is 1.*

Likewise, the interval-valued loss ceiling of player II can be obtained using the LLP models (M7) and (M8). The corresponding transformed LPP models are as follows:

$$\begin{aligned}
&\max V^{(L)} = \quad Y_1^{(L)} + Y_2^{(L)},\\
&\textit{subject to}\\
&5.1818Y_1^{(L)} + 2.1818Y_2^{(L)} \leq 1,\\
&0Y_1^{(L)} + 5.4545Y_2^{(L)} \leq 1,\\
&Y_1^{(L)}, Y_2^{(L)} \geq 0,
\end{aligned}$$

and

$$\begin{aligned}
&\max V^{(U)} = \quad Y_1^{(U)} + Y_2^{(U)},\\
&\textit{subject to}\\
&6Y_1^{(U)} + 4.2545Y_2^{(U)} \leq 1,\\
&1.0909Y_1^{(U)} + 6Y_2^{(U)} \leq 1,\\
&Y_1^{(U)}, Y_2^{(U)} \geq 0.
\end{aligned}$$

The optimal solutions are $(Y_1^{(L)^*} = 0.1158,\ Y_2^{(L)^*} = 0.1833)$ *and* $(Y_1^{(U)^*} = 0.0557,\ Y_2^{(U)^*} = 0.1565)$ *with the optimal values as* $V^{(L)^*} = 0.2991$ *and* $V^{(U)^*} = 0.2122$*, respectively.*

It results in optimal strategy as $([0.2624, 0.3872], [0.6128, 0.7372])$ *with loss-ceiling as* $\widetilde{v}_{Int}^{+^*} = [(\ell_3, 0.3434), (\ell_5, -0.2897)]$.

Hence, interval-valued linguistic value of the game $\widetilde{G}_{Int}$ *is* $\widetilde{v}_{Int}^{*} = [(\ell_3, 0.3434), (\ell_5, -0.2897)]$.

Now, we present another example to demonstrate the applicability of the methodology to the problems with more than two strategies.

Example 4. *Consider the constant-sum interval-valued linguistic matrix game with interval payoffs from the predefined linguistic term set* $LT = \{\ell_0 : \textit{Very Poor}\ (VP),\ \ell_1 : \textit{Poor}\ (P),\ \ell_2 : \textit{Moderately Poor}\ (MP),\ \ell_3 : \textit{Fair}\ (F),\ \ell_4 : \textit{Moderately Good}\ (MG),\ \ell_5 : \textit{Good}\ (G),\ \ell_6 : \textit{Very Good}\ (VG)\}$ *with payoff matrix,*

$$\widetilde{A}_{Int} = \begin{pmatrix} [F, G] & [(MG, -0.5), G] & [MP, MG] & [MP, MG] & [MG, G] \\ [F, (G, -0.3)] & [MP, F] & [G, VG] & [F, G] & VP \\ [F, MG] & [(G, 0.2), VG] & [F, G] & [F, G] & [MP, (G, -0.2)] \end{pmatrix}.$$

Here,

$$\widetilde{A}^{(L)} = \begin{bmatrix} F & (MG, -0.5) & MP & MP & MG \\ F & MP & G & F & VP \\ F & (G, 0.2) & F & F & MP \end{bmatrix} \textit{ and } \widetilde{A}^{(U)} = \begin{bmatrix} G & G & MG & MG & G \\ (G, -0.3) & F & VG & G & VP \\ MG & VG & G & G & (G, -0.2) \end{bmatrix}.$$

Suppose the mixed strategies for player I be $\mathbf{x}^{(L)} = (x_1^{(L)}, x_2^{(L)}, x_3^{(L)}),\ x_i^{(L)} \geq 0,\ i = 1, \ldots, 3,\ \sum_{i=1}^{3} x_i^{(L)} = 1$, *and* $\mathbf{x}^{(U)} = (x_1^{(U)}, x_2^{(U)}, x_3^{(U)}),\ x_i^{(U)} \geq 0,\ i = 1, \ldots, 3,\ \sum_{i=1}^{3} x_i^{(U)} = 1$ *for* $\widetilde{A}^{(L)}$ *and* $\widetilde{A}^{(U)}$*, respectively. In addition, the mixed strategies for player II for linguistic payoff matrix* $\widetilde{A}^{(L)}$ *and* $\widetilde{A}^{(U)}$ *are defined as* $\mathbf{y}^{(L)} = (y_1^{(L)}, y_2^{(L)}, y_3^{(L)}, y_4^{(L)}, y_5^{(L)}),\ y_j^{(L)} \geq 0,\ j = 1, \ldots, 5,\ \sum_{j=1}^{5} y_j^{(L)} = 1$, *and* $\mathbf{y}^{(U)} = (y_1^{(U)}, y_2^{(U)}, y_3^{(U)}, y_4^{(U)}, y_5^{(U)}),\ y_j^{(U)} \geq 0,\ j = 1, \ldots, 5,\ \sum_{j=1}^{5} y_j^{(U)} = 1$.

In view of the approach proposed in the paper, construct model (M3) to obtain the lower bound of the interval-valued linguistic lower value $\widetilde{v}_{Int}^{-}$ *of the game with payoff matrix* $\widetilde{A}_{Int}$*. The formulated LLP problem is as follows:*

$$
\begin{aligned}
&\max \quad \widetilde{v}^{-(L)} \\
&\textit{subject to} \\
&(\ell_3, 0)x_1^{(L)} \oplus (\ell_3, 0)x_2^{(L)} \oplus (\ell_3, 0)x_3^{(L)} \geq \widetilde{v}^{-(L)}, \\
&(\ell_4, -0.5)x_1^{(L)} \oplus (\ell_2, 0)x_2^{(L)} \oplus (\ell_5, 0.2)x_3^{(L)} \geq \widetilde{v}^{-(L)}, \\
&(\ell_2, 0)x_1^{(L)} \oplus (\ell_5, 0)x_2^{(L)} \oplus (\ell_3, 0)x_3^{(L)} \geq \widetilde{v}^{-(L)}, \\
&(\ell_2, 0)x_1^{(L)} \oplus (\ell_3, 0)x_2^{(L)} \oplus (\ell_3, 0)x_3^{(L)} \geq \widetilde{v}^{-(L)}, \\
&(\ell_4, 0)x_1^{(L)} \oplus (\ell_0, 0)x_2^{(L)} \oplus (\ell_2, 0)x_3^{(L)} \geq \widetilde{v}^{-(L)}, \\
&x_1^{(L)} + x_2^{(L)} + \ldots + x_n^{(L)} = 1, \\
&x_1^{(L)}, x_2^{(L)}, \ldots, x_n^{(L)} \geq 0.
\end{aligned}
$$

The above formulation can be converted into a linear programming problem in view of model (M4)

$$
\begin{aligned}
&\min V^{(L)} = \quad X_1^{(L)} + X_2^{(L)} + X_3^{(L)}, \\
&\textit{subject to} \\
&3X_1^{(L)} + 3X_2^{(L)} + 3X_3^{(L)} \geq 1, \\
&3.5X_1^{(L)} + 2X_2^{(L)} + 5.2X_3^{(L)} \geq 1, \\
&2X_1^{(L)} + 5X_2^{(L)} + 3X_3^{(L)} \geq 1, \\
&2X_1^{(L)} + 3X_2^{(L)} + 3X_3^{(L)} \geq 1, \\
&4X_1^{(L)} + 0X_2^{(L)} + 2X_3^{(L)} \geq 1, \\
&X_1^{(L)}, X_2^{(L)}, X_3^{(L)} \geq 0.
\end{aligned}
$$

Similarly, the corresponding model for evaluating upper bound of gain-floor of player I can be constructed using model (M6):

$$
\begin{aligned}
&\min V^{(U)} = \quad X_1^{(U)} + X_2^{(U)} + X_3^{(U)}, \\
&\textit{subject to} \\
&5X_1^{(U)} + 4.7X_2^{(U)} + 4X_3^{(U)} \geq 1, \\
&5X_1^{(U)} + 3X_2^{(U)} + 6X_3^{(U)} \geq 1, \\
&4X_1^{(U)} + 6X_2^{(U)} + 5X_3^{(U)} \geq 1, \\
&4X_1^{(U)} + 5X_2^{(U)} + 5X_3^{(U)} \geq 1, \\
&5X_1^{(U)} + 0X_2^{(U)} + 4.8X_3^{(U)} \geq 1, \\
&X_1^{(U)}, X_2^{(U)}, X_3^{(U)} \geq 0.
\end{aligned}
$$

The optimal solutions of the above problems are $(X_1^{(L)^*} = 0.125, X_2^{(L)^*} = 0, X_3^{(L)^*} = 0.25)$ *with optimal value* $V^{(L)^*} = 0.375$ *and* $(X_1^{(U)^*} = 0.105, X_2^{(U)^*} = 0.017, X_3^{(U)^*} = 0.099)$ *with optimal value* $V^{(U)^*} = 0.221$.

Hence, for player I, the interval-valued linguistic gain-floor is $\widetilde{v}_{Int}^{-^*} = [(\ell_3, -0.3334), (\ell_5, -0.4752)]$ *with optimal mixed strategies* $([0.3334, 0.4751], [0, 0.0769], [0.448, 0.6667])$.

Likewise, the interval-valued loss ceiling of player II can be obtained using the LLP models (M7) and (M8). The corresponding transformed LPP models are as follows:

$$\begin{aligned}
\max V^{(L)} = \quad & Y_1^{(L)} + Y_2^{(L)} + Y_3^{(L)} + Y_4^{(L)} + Y_5^{(L)}, \\
& \textit{subject to} \\
& 3Y_1^{(L)} + 3.5Y_2^{(L)} + 2Y_3^{(L)} + 2Y_4^{(L)} + 4Y_5^{(L)} \leq 1, \\
& 3Y_1^{(L)} + 2Y_2^{(L)} + 5Y_3^{(L)} + 3Y_4^{(L)} + 0Y_5^{(L)} \leq 1, \\
& 3Y_1^{(L)} + 5.2Y_2^{(L)} + 3Y_3^{(L)} + 3Y_4^{(L)} + 2Y_5^{(L)} \leq 1, \\
& Y_1^{(L)}, Y_2^{(L)}, Y_3^{(L)}, Y_4^{(L)}, Y_5^{(L)} \geq 0,
\end{aligned}$$

and

$$\begin{aligned}
\max V^{(U)} = \quad & Y_1^{(U)} + Y_2^{(U)} + Y_3^{(U)} + Y_4^{(U)} + Y_5^{(U)}, \\
& \textit{subject to} \\
& 5Y_1^{(U)} + 5Y_2^{(U)} + 4Y_3^{(U)} + 4Y_4^{(U)} + 5Y_5^{(U)} \leq 1, \\
& 4.7Y_1^{(U)} + 3Y_2^{(U)} + 6Y_3^{(U)} + 5Y_4^{(U)} + 0Y_5^{(U)} \leq 1, \\
& 4Y_1^{(U)} + 6Y_2^{(U)} + 5Y_3^{(U)} + 5Y_4^{(U)} + 4.8Y_5^{(U)} \leq 1, \\
& Y_1^{(U)}, Y_2^{(U)}, Y_3^{(U)}, Y_4^{(U)}, Y_5^{(U)} \geq 0.
\end{aligned}$$

The optimal solutions are $(Y_1^{(L)^*} = 0, Y_2^{(L)^*} = 0, Y_3^{(L)^*} = 0, Y_4^{(L)^*} = 0.25, Y_5^{(L)^*} = 0.125)$ *and* $(Y_1^{(U)^*} = 0.1016, Y_2^{(U)^*} = 0, Y_3^{(U)^*} = 0, Y_4^{(U)^*} = 0.1045, Y_5^{(U)^*} = 0.0148)$ *with the optimal values as* $V^{(L)^*} = 0.375$ *and* $V^{(U)^*} = 0.221$, *respectively.*

It results in optimal strategy as $([0, 0.4597], 0, 0, [0.4728, 0.6667], [0.067, 0.3334])$ *with loss-ceiling as* $\widetilde{v}_{Int}^{+^*} = [(\ell_3, -0.3334), (\ell_5, -0.4752)]$. *For the strategies for which the optimal value is 0, it depicts that the player will never choose those strategies to maximize his/her payoff.*

Hence, interval-valued linguistic value of the game $\widetilde{G}_{Int}$ *is* $\widetilde{v}_{Int}^{*} = [(\ell_3, -0.3334), (\ell_5, -0.4752)]$.

Note 1: *It is noteworthy that in Example 2 of [17], the considered linguistic payoff matrix* $\widetilde{A}$ *is a particular matrix of* $\widetilde{A}_{Int}$ *i.e., each* $\tilde{a}_{ij} \in [\tilde{a}_{ij}^{(L)}, \tilde{a}_{ij}^{(U)}]$; $i = 1, 2, 3$, $j = 1, \ldots, 5$. *In addition, the linguistic value of the game,* $\widetilde{v}^* = (\ell_4, -0.3343) \in [(\ell_3, -0.3334), (\ell_5, -0.4752)]$, *but the optimal mixed strategy for both players corresponding to some strategies do not belong in the acquired intervals.*

6. Conclusions

In this paper, a two-player constant-sum interval-valued 2-tuple linguistic matrix game is defined and analyzed to acquire the mixed strategies and value of the game for players I and II. The interval linguistic matrix game is split into two linguistic matrix games to evaluate the value of the game in interval form. The linguistic linear programming is then adopted to solve each linguistic matrix game. A flowchart to summarize the algorithm is also given. In the suggested approach, the value of the game maintains the form of interval-valued linguistic variables, but the mixed strategies for each player are not in interval form. The methodology shows promising results in the game problems where the payoffs to the given strategies of two-players are not numerical or linguistic variables but interval-valued linguistic information. In this approach, we obtain two linguistic matrices from the given interval-valued linguistic payoff matrix. We envision that the interval linear programming can be adopted as the alternative approach to solve such class of game that results in the interval-valued linguistic value of the game as well as the mixed strategies also appearing as an interval. In addition, the bimatrix games with interval-valued linguistic payoff matrix can be explored in the future to enhance the applicability of game theory in this uncertain world.

Author Contributions: A.S. is a research scholar in the Department of Applied Mathematics, Delhi Technological University under the supervision of A.G. A.S. has designed the algorithm and prepared the manuscript in the present form with the guidance of A.G.

Funding: This research received no external funding.

Acknowledgments: The authors are thankful to the esteemed referees for their valuable suggestions for improving the paper. The authors thank the editor for being supportive and considerate.

Conflicts of Interest: The authors declare no conflicts of interest.

References

1. Neumann, J.V.; Morgenstern, O. *Theory of Games and Economic Behavior*; Princeton University Press: New York, NY, USA, 1994.
2. Campos, L. Fuzzy linear programming to solve fuzzy matrix games. *Fuzzy Sets Syst.* **1989**, *32*, 275–289. [CrossRef]
3. Bector, C.R.; Chandra, S. *Fuzzy Mathematical Programming and Fuzzy Matrix Games*; Springer: Berlin, Germany, 2005.
4. Nishizaki, I.; Sakawa, M. *Fuzzy and Multiobjective Games for Conflict Resolution*; Physica-Verlag: Heidelberg, Germany, 2001.
5. Avsar, Z.M.; Gursoy, M.B. A note on two-person zero-sum communicating stochastic games. *Oper. Res. Lett.* **2006**, *34*, 412–420. [CrossRef]
6. Kurano, M.; Yasuda, M.; Nakagami, J.I.; Yoshida, Y. An Interval Matrix Game and Its Extensions to Fuzzy and Stochastic Games. Available online: http://www.math.s.chiba-u.ac.jp/~yasuda/accept/SIG2.pdf (accessed on 5 June 2018).
7. Collins, W.D.; Hu, C.-Y. Fuzzily determined interval matrix games. In Proceedings of the Biscse 2005, Berkeley, CA, USA, 2–5 November 2005. Available online: http://www-bisc.cs.berkeley.edu/BISCSE2005/Abstracts-Proceeding/Friday/FM3/Chenyi-Hu.pdf (accessed on 9 June 2018).
8. Collins, W.D.; Hu, C.-Y. Studying interval-valued matrix games with fuzzy logic. *Soft Comput.* **2008**, *12*, 147–155. [CrossRef]
9. Hladik, M. Interval valued bimatrix games. *Kybernetika* **2010**, *46*, 435–446.
10. Liu, S.-T.; Kao, C. Matrix games with interval data. *Comput. Ind. Eng.* **2010**, *56*, 1697–1700. [CrossRef]
11. Shashikhin, V.N. Antagonistic game with interval payoff functions. *Cybern. Syst. Anal.* **2004**, *40*, 556–564. [CrossRef]
12. Collins, W.D.; Hu, C.-Y. Interval matrix games. In *Knowledge Processing with Interval and Soft Computing*; Hu, C.-Y., Ed.; Springer: London, UK, 2008; Chapter 7, pp. 1–19.
13. Li, D.-F.; Nan, J.-X.; Zhang, M.-J. Interval programming models for matrix games with interval payoffs. *Optim. Methods Softw.* **2010**, *27*, 1–16. [CrossRef]
14. Li, D.-F. Linear programming approach to solve interval-valued matrix games. *Omega* **2011**, *39*, 655–666. [CrossRef]
15. Arfi, B. Linguistic fuzzy-logic game theory. *J. Confl. Resolut.* **2006**, *50*, 28–57. [CrossRef]
16. Arfi, B. Linguistic fuzzy-logic social game of cooperation. *Ration. Soc.* **2006**, *18*, 471–537. [CrossRef]
17. Singh, A.; Gupta, A.; Mehra, A. Matrix Games with 2-tuple Linguistic Information. *Ann. Oper. Res.* **2018**. [CrossRef]
18. Herrera, F.; Martinez, L. A 2-tuple fuzzy linguistic representation model for computing with words. *IEEE Trans. Fuzzy Syst.* **2000**, *8*, 746–752.
19. Balezentis, A.; Balezentis, T. A novel method for group multi-attribute decision making with two-tuple linguistic computing: Supplier evaluation under uncertainty. *Econ. Comput. Econ. Cybern. Stud. Res.* **2011**, *4*, 5–30.
20. Wei, G.W. A method for multiple attribute group decision making based on the ET-WG and ET-OWG operators with 2-tuple linguistic information. *Exp. Syst. Appl.* **2010**, *37*, 7895–7900. [CrossRef]
21. Zhang, H. The multiattribute group decision making method based on aggregation operators with interval-valued 2-tuple linguistic information. *Math. Comput. Model.* **2012**, *56*, 27–35. [CrossRef]
22. Liu, H.-C.; Liu, L.; Wuc, J. Material selection using an interval 2-tuple linguistic VIKOR method considering subjective and objective weights. *Mater. Des.* **2013**, *52*, 158–167. [CrossRef]

23. You, X.-Y.; You, J.-X.; Liu, H.-C.; Zhen, L. Group multi-criteria supplier selection using an extended VIKOR method with interval 2-tuple linguistic information. *Exp. Syst. Appl.* **2015**, *42*, 1906–1916. [CrossRef]
24. Singh, A.; Gupta, A.; Mehra, A. An AHP-Promethee II method for 2-tuple linguistic multicriteria group decision making. In Proceedings of the 2015 4th International Conference on Reliability, Infocom Technologies and Optimization (ICRITO) (Trends and Future Directions), Noida, India, 2–4 September 2015; doi:10.1109/ICRITO.2015.7359374. [CrossRef]



© 2018 by the authors. Licensee MDPI, Basel, Switzerland. This article is an open access article distributed under the terms and conditions of the Creative Commons Attribution (CC BY) license (http://creativecommons.org/licenses/by/4.0/).

International Journal of Research in Engineering and Innovation (IJREI)
journal home page: http://www.ijrei.com
ISSN (Online): 2456-6934

Methods for improving thermal performances of vapour compression refrigeration systems using ecofriendly refrigerant in the expander

R.S. Mishra

Department of Mechanical & Production Engineering, Delhi Technological University Delhi, India

Abstract

The performance of refrigerator is evaluated in term of COP which is the ratio of refrigeration effect to the net work input given to the system. The COP of vapour compression refrigeration system can be improved either by increasing refrigeration effect or by reducing work input given to the system. In this paper, the thermodynamic performance of a vapour compression system that uses an expander was investigated. In the analysis, an expander flow model was used. Eighteen ecofriendly refrigerants (such as R134a , R245fa, R236fa, R227ea, R152a, R125, R123, R717, R1234yf, R1234ze, R600, R290, R600a, R507a, R404a, R410a, R-32, R407c etc.),were selected as the refrigerants. According to the obtained results, for any operating condenser/evaporator temperature there are different optimum values coefficient of performance (COP). As the condenser temperature increases, the first law efficiency in terms of coefficient of performance (COP) and exergetic efficiency decreases and exergy destruction ratio based on exergy output is increased. Similarly evaporator temperature increases, the first law efficiency in terms of coefficient of performance (COP) and exergetic efficiency increases and exergy destruction ratio based on exergy output is decreased. The numerical computation for finding First law and second law efficiencies and exergy destruction ratio were carried out for two systems. The 22.34%. Improvement in COP was observed in system -2 while replacing throttle valve by expander as compared to system-1 containing throttle valve. The thermal performances of both systems using HFO refrigerants were compared for replacing R134a in near future and it was found that HFO-1234ze gives similar thermodynamic performances and R1234yf is slightly lower 6-8% than using R134a without any change in system configuration. Worst thermodynamic performances were found using R125 as ecofriendly refrigerant and best performance was observed using R245fa. Although Thermal performance of R123 is found to be best slightly higher than R245fa but it containing chlorine.
© 2018 ijrei.com. All rights reserved
Keywords: Thermodynamic performance analysis, Improvements in Efficiencies, VCRS

1. Introduction

Vapor compression refrigeration system is based on vapor compression cycle. Vapor compression refrigeration system is widely used method for air-conditioning of buildings and automobiles. It is also used in domestic and commercial refrigerators, large-scale warehouses for chilled or frozen storage of foods and meats, refrigerated trucks and railroad cars, and a host of other commercial and industrial services. Oil refineries, petrochemical and chemical processing plants, and natural gas processing plants are among the many types of industrial plants that often utilize large vapor-compression refrigeration systems. The Vapor Compression Refrigeration system involves four components: compressor, condenser, expansion valve/throttle valve and evaporator. It is a compression process, whose aim is to raise the refrigerant pressure, as it flows from an evaporator.as shown in Fig-1.

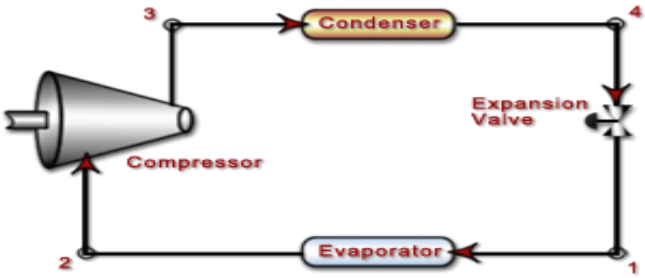


Figure 1: Vapour compression refrigeration system [1]

Corresponding author: R. S. Mishra
Email Address: hod.mechanical.rsm@dtu.ac.in

The systems under vapor compression technology consume huge amount of electricity, this problem can be solved by improving performance of system.

2. Literature review

2.1 Performance improvement of vapour compression refrigeration systems

The improvement of thermal performance of vapour compression refrigeration system is too important for achieving higher refrigerating effect. Therefore there is need of multi evaporator vapour compression refrigeration system or one can get reduced power consumption by using expander between condenser and evaporator and also connecting with compressor shaft for same refrigerating effect. Many efforts have to be done to improve thermal performance of vapour compression refrigeration system. The use of nano particles can also improve the first law and second law performance significantly. The best thermodynamic performance is found using R123 and worst performance is observed using R125.

Due to flammable nature of R290, R600, R600a and R152a.the R134a was used for replacing R11, R12, and R22, R502 .It is well recognized that throttling process in VCRS is an irreversible expansion process. Expansion process is one of the main factors responsible for exergy loss in cycle performance because of entering the portion of the refrigerant flashing to vapour in evaporator which will not only reduce the cooling capacity but also increase the size of evaporator. This problem can be eliminated by adopting multi-stage expansion where the flash vapours is removed after each stage of expansion as a consequence there will be increase in cooling capacity and reduce the size of the evaporator or insert expander and remove throttle valve to the vapour compression refrigeration systems, which utilizes the work expended in direct expansion of a refrigerant to power a turbine which drives a compressor of a refrigeration system in compressing gaseous vapours from evaporator pressure to condenser pressure. Refrigeration effect can also be increased using nano particles mixed with R718 in the secondary evaporator circuit and R134a in the primary evaporator circuit.

In the vapour compression refrigeration system, the evaporator overall heat transfer coefficient is also increases which enhanced refrigeration effect due to nano particles mixed with R718 in the secondary evaporator circuit and R134a in the primary evaporator circuit.

2.2 Use of ecofriendly refrigerants

Vapour compression refrigeration system based applications make use of refrigerants which are responsible for greenhouse gases, global warming and ozone layer depletion. Montreal protocol was signed on the issue of substances that are responsible for depleting Ozone layer and discovered how much consumption and production of ozone depletion substances took place during certain time period for both developed and developing countries. Another protocol named as Kyoto aimed to control emission of greenhouse gases in 1997. The relationship between ozone depletion potential and global warming potential is the major concern in the field of GRT (green refrigeration technology) so Kyoto proposed new refrigerants having lower value of ODP and GWP. Internationally a program being pursued to phase out refrigerants having high chlorine content for the sake of global environmental problems. Due to presence of high chlorine content high global warming potential and ozone depletion potential after 90.s CFC and HCFC refrigerants have been restricted. Thus, HFC refrigerants are used nowadays, showing much lower global warming potential value, but still high with respect to non-fluorine refrigerants. Lots of research work has been done for replacing old refrigerants with new refrigerants

Mishra et al. [1-3] performed numerical analysis of vapour compression refrigeration system using R134a, R143a, R152a, R404A, R410A, R502 and R507A, and discussed the effect of evaporator temperature, degree of sub cooling at condenser outlet, superheating of evaporator outlet, vapour liquid heat exchanger effectiveness and degree of condenser temperature on COP and exergetic efficiency. They reported that evaporator and condenser temperature have significant effect on both COP and exergetic efficiency and also found that R134a has the better performance while R404a has poor performance in all respect.

Xiaohui et al [4] presented the performance study of vapour compression system where the expander work recovered during the expansion process was also employed for sub cooling of the system and found higher COP of the system while using R12, R32, R22, R134a refrigerants. Victor et al [5] presented a performance study on automobile air-conditioning based on vapor compression refrigeration cycle with R134a as refrigerant by incorporating an expander and predicted reasonable gains in cycle performance. Mishra R.S. et al. [6] also compared the performance between R134a and R290/R600a mixture in their thermodynamic analysis highest irreversibility is obtained in compressor and found that R290/R600a hydrocarbon mixture showed higher COP and exergetic efficiency than R134a. Mishra et al. [7] developed numerical model for comparison of thermodynamic performance parameters of two systems. System-1 consists of & system-2). Thermodynamic analysis in terms of energy and exergy analysis of multiple evaporators and compressors with individual expansion valves (system-1) and multiple evaporators and compressors with multiple expansion valves (system-2) have been carried out and following conclusions was drawn from present investigation. For same degree of sub cooling, fixed evaporators and condenser temperatures system-2 is the best system with comparisons of system-1. R600, R600a and R152A show better performances than other refrigerants for both systems (system-1 & system-2) but due to inflammable property of R600 and R600a, R134a is preferred for both systems. First law efficiency and second law efficiency of system-2 is 3%- 6% higher than System-1. Mishra et al. [8] performed thermal modeling of Vapor

Compression Refrigeration System using R134a in primary circuit and Al_2O_3 Water based nano-fluids in secondary circuit. The performances of vapour compression have been studies in details and conclusions were made that the optimum temperature of evaporator is found to be -50C. Similarly exergy destruction ratio is also decreases up to 273K and then increases. The optimum evaporator temperature to be found to be 273K for optimum EDR condenser temperature with performance parameters. Also found that as condenser temperature increases, the first law efficiency of vapour compression refrigeration system is decreases. Also second law efficiency is also decreases. Similarly exergy destruction ratio is also decreases. Use of nano particle suspended in the water used as refrigerant in the secondary circuit in the evaporator greatly affecting its first law performance. As evaporator temperature is increases, the first law efficiency and second law efficiency increases. The increasing condenser temperature the First law and second law performance decreases. Mishra et al.[9] investigates Thermodynamic analysis in terms of consists of multiple evaporators and compressors with individual expansion valves while system-2 consists of multiple evaporators and compressors with multiple expansion valves (system-2) and found that R134a, R407c, show better thermal performances than other eco-friendly refrigerants in vapour compression refrigeration system. Due to flammable property of R290 and R600a, HFC-134a, R407c and R410a and R404a are preferred for vapour compression refrigeration systems. It is also found that the first law efficiency in terms of COP and second law efficiency in terms of exergetic efficiency of Vapour compression using R407c is lower around 3% to 6% than using R134a. Mishra et al. [10] performed first law and second law analysis of vapour compression refrigeration systems using multiple evaporators and single compressor and single expansion valve with eco-friendly refrigerants in the system and R718 (water used in secondary circuit with and without nano particles mixed with water used as refrigerant)and found that the First law efficiency in terms of COP and Second law efficiency (Exergetic efficiency) of vapour compression refrigeration systems using R718 mixed with nano particles gives better thermodynamic performance is than without nano particles used in the secondary circuit of water cooled evaporator for above mentioned ecofriendly refrigerants and also found that the vapour compression refrigeration systems using R152a refrigerant is higher but is has flammable nature similar to hydrocarbons and then safety measures to be taken while using R152a or hydrocarbons (R290, R600 and R600a). The thermodynamic performances can also improve by using TiO2 in the secondary evaporator circuit as compared to Al_2O_3 in the secondary circuit he found efficiency for R507a and R134a are nearly matching the same values are better than that for R125.For practical applications R-407c, R134a and R404a, R125 can be used instead of R-152a which was not applicable for commercial applications due to flammable nature and R717 is also toxic nature. Efficiency improved by using TiO2 is better than using Al_2O_3 with R718 refrigerant in the secondary evaporator circuit. Mishra et al. [11], investigated energy and exergy analysis of vapour compression refrigeration systems using R134a eco-friendly refrigerant in primary circuit and three nano particles mixed with R718 in the secondary evaporator is presented and found that copper oxide gives performance improvements in the range 11.23% to 18% without nano particles and better performance was found using copper oxide nano material in efficiency .The COP improvement is 18.35% and second law efficiency improvement is 18.31% observed using Al_2O_3 nano materials mixed with R718 in secondary circuit as compared to without nano refrigerants. Similarly 17.72% and 17.685% second law efficiency. Mishra et al [12] Analyzed, first law and second law analysis of vapour compression refrigeration system with and without nano particles using eco-friendly refrigerants (R134a, R1234yf, and R1234ze) and found that without Al_2O_3 nano particles mixed in R718 in the secondary evaporator circuit and eco-friendly refrigerants in the primary circuit (i.e. R134a and R1234ze) are matching the same values, both are better than that for R123yf which has low GWP (i.e. GWP =4) is showing 2–6% higher value of first law efficiency i.e. (COP) and second law efficiency i.e. (Exergetic efficiency) in comparison to R123yf.It was found that energetic and exergetic efficiency greatly affected by changes in evaporator and condenser temperature. R1234ze is the best among considered refrigerant since it has 218 times lower GWP values than R134a and R1234ze is eco-friendly has both ODP and GWP are lowest. The R1234yf and R1234ze can replace R-134a after 2030 due to low global warming potential.

Mishra et al[13] Performed first law and second law analysis of vapour compression refrigeration systems using multiple evaporators and single compressor and single expansion valve with thirteen ecofriendly refrigerants have been presented and found that First law efficiency (COP) and Second law efficiency (Exergetic efficiency) of vapour compression refrigeration systems using R717 refrigerant is higher but is has toxic nature can be used by using safety measure for industrial applications also efficiency for R152a and R600 are nearly matching the same values are better than that for R125 at 313K condenser temperature and showing higher value of COP and exergetic efficiency in comparison to R125.For practical applications R-134a is recommended because it is easily available in the market has second law efficiency slightly lesser than R-152a which was not applicable for commercial applications. The worst component from the viewpoint of irreversibility is expansion valve followed by condenser, compressor and evaporators, respectively. The most efficient component found to be sub-cooler. The R-152a has least efficiency defects for 313K condenser temperature. The Performance evaluation of vapour compression refrigeration system when calculated nucleate heat transfer coefficient enhancement factor based on Al_2O_3 nanoparticle mixed in the ecofriendly refrigerant and implement into the program results is to be found as 23% using R134a and 18% when using R407c in the primary circuit. Performance evaluation of vapour compression refrigeration system when

calculated nano-refrigerent property implement into the program based on Al_2O_3 nanoparticle mixed in the R134a ecofriendly refrigerant is 13% and Al_2O_3 nanoparticle mixed in the R407c is 9%. Performance evaluation of vapour compression refrigeration system when nanoparticle into refrigerant oil nanoparticle based on Al_2O_3 nanoparticle mixed in the ecofriendly R134a refrigerant is 11% The performance of vapour compression refrigeration systems using Al_2O_3 particles direct mixed in the R134a gives better first law performance than R407c and improvement in the first law performance is 28% using R134a and Al_2O_3 nano particles mixed with compressor oil and then used is 18.8% and 8% as heat transfer enhancement factor and implement into the refrigerant property and lowest improvement 2.64% when Al_2O_3 directly mixed with R407c, mixed with compressor oil and then used as refrigerant the primary circuit. Mishra et al [14] The computation modeling of vapor compression refrigeration systems was carried out for first and second law analysis in terms of energetic analysis i.e. COP (First law analysis) and exegetic analysis in terms of exergetic efficiency, exergy destruction ratio (EDR) and percentage exergetic destruction in each components (second law analysis). In this analysis we assumed negligible pressure losses and heat losses. The comparative performance of 4.75 KW window air conditioner is evaluated for condenser temperature varying between 300K to 327K with increment of 3 and evaporator temperature is varying from 274K to 278 K with increment of 1. The energy and exergy change in vapour compression refrigeration cycle have been calculated for various ecofriendly refrigerants such as R-1234yf, R-1234ze, R404a, R-290 (propane), R600 (butane), R-600a (isobutene) for environmental temperature of 298K. The variation of fist law efficiency in terms of cop and second law efficiency in terms of exergetic. As condenser temperature increases the first law efficiency decreases while second law efficiency decreases. Similarly with increasing evaporator temperature, the first law efficiency increases while second law efficiency decreases. Mishra et al [15] analyzed that first law and second law analysis of vapor compression refrigeration systems using multiple evaporators and single compressor and single expansion valve with eco-friendly refrigerants in the system and R718 (water used in secondary circuit with and without nano particles mixed with water used as refrigerant) have been presented. He found that R718 mixed with nano particles gives better performance is than without nano particles used in the secondary circuit of water cooled evaporator for above mentioned eco-friendly refrigerants he also found that R152a refrigerant is higher but is has flammable nature similar to hydrocarbons then safety measures to be taken while using R152a or hydrocarbons (R290, R600 and R600a) efficiency improved by using TiO2 in the secondary evaporator circuit as compared to Al_2O_3 in the secondary circuit .

Alison et al [16] did an economic analysis based on thermodynamic performance by using expander in the refrigeration systems of a medium refrigerating load for ambient temperature of 35 °C, evaporating temperature of 7.2 °C and the condensing temperature of 54.4 °C was considered. Bjorn [17] presented a study by compared properties of hydrocarbons, namely propane, propene and isobutene with R134a, R22 and ammonia and predicted the higher performance of hydrocarbons over R134a and R22 in vapour compassion refrigeration system

Based on the literature it was observed that researchers have gone through detailed first law analysis in terms of coefficient of performance and second law analysis in term of exergetic efficiency of simple vapour compression refrigeration system with throttle valve. This paper mainly deals with use of expander for replacing throttle valve so that net work done by vapour compression system is reduced which is a resultant of both compressor and expander work . We know that compressor is producing negative work and expander produced positive work. Therefore resultant work done by VCRS is reduced for same refrigerating capacity hence the first and second law efficiency [18]

Currently used third generation hydrofluorocarbon (HFC) refrigerants are known to be nonozone depleting agents, but are also characterized by their substantial global warming potential (GWP) values as shown in Fig.2 [19]

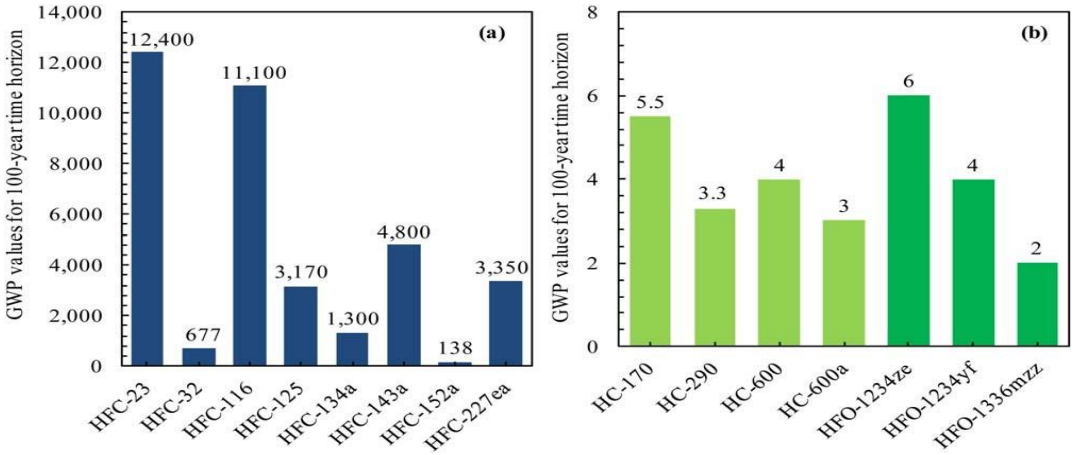


Figure 2: Hundred-year time horizon GWPs relative to CO2 of (a) HFC and (b) HC and HFO refrigerants [19]

Consequently, the year 2016 marked the launch of a global environmental deal to phase out the production and consumption of HFCs by years 2036 to 2047, starting in 2019. Most of the current effective (F-Gas in the European Union) and proposed (CARB and EC in North America) regulations target 150 GWP for refrigeration and 750 GWP for air conditioning applications, thus creating an immediate demand for developing new fourth generation refrigerants with low GWPs. In response to this need, the National Institute of Standards and Technology (NIST) recommended a list of new classes of refrigerants that would possess low values of GWPs based on estimates done using data on the chemical structure, the radiative efficiency, and the atmospheric lifetime of these molecules. Hydro-fluoro-olefins (HFOs) were included in the NIST list as one of the best candidates found so far, with GWP values comparable to those of hydrocarbon (HC)-based refrigerants. Furthermore, cycle performance tests carried out for HFOs shown in Fig.2 proved their suitability to act as a replacement for HFCs used in mobile air-conditioners, vending machines, and chillers. As a result, a major shift in the automobile industry is planned to start in the year 2017 to replace 1,1,1,2-tetrafluoroethane (HFC-134a) as a working fluid by 2,3,3,3-tetrafluoropropene (HFO-1234yf), a newly introduced fourth generation refrigerant. According to a roadmap report9 published in 2014 by the U.S. Department of Energy, the highest priority for research and development in refrigerants should focus on exploring and modeling the theoretical properties of low GWP azeotropic blends. Understanding the phase behavior and accurately predicting the thermo physical properties of these systems is essential for designing and evaluating refrigeration cycle performances and determining the optimal compositions. In addition, interfacial and transport properties of refrigerants play an important role in characterizing the two-phase heat transfer and fluid flow. Raabe and coworkers [20] have carried out a systematic study of thermo physical properties of selected HFOs and their mixtures by molecular simulations. The study includes vapor–liquid equilibrium (VLE) and thermo-physical properties of pure HFO refrigerants and their mixtures with carbon dioxide and HFCs. In terms of molecular theory, Lai and coworkers [21] applied the BACKBONE equation of state to predict the thermo-physical properties of pure HFO refrigerants. Moreover, Raabe [22] applied the perturbed chain form of the statistical associating fluid theory (PC-SAFT) to study the phase behavior of HFO-containing binary mixtures. However, multipolar interactions were not explicitly modeled within the SAFT framework.

To improve the coefficient of performance, its requires that the compressor work should decrease and refrigeration effect should increase. This paper mainly deals with replacing throttle valve by expander so that compressor work will reduced due to available net work done by the system which is compressor work minus expander work for same cooling capacity enhances first and second law efficiencies and increased exergy destruction ratio.

3. Results and Discussions

The performance of Vapour compression can be obtained by varying evaporator and condensing temperatures over the required range as shown in Table-1(a) to Table-13(c) respectively. Table-1(a-c) show the thermodynamic performances with various ecofriendly refrigerants for a given 50oC of condenser temperature and 0oC of evaporator temperature. The compressor and expander efficiency is taken to be 80% and it was observed that system-2 replace throttle valve has first law efficiency in terms of coefficient is higher (around 20% to 24%) than system-1 using throttle valve because of the effective net work done is reduced for same refrigeration effect hence increased and highest COP was found using R123 refrigerant. But R123 has chlorine content and second highest COP was observed by using R245fa and third highest COP was using hydrocarbon-R600. Although all three hydro-carbon have excellent first law performance (COP) but lower COP was observed between using hydrocarbons are by using hydrocarbon-R290. The first law efficiency (COP) of R134a is slightly less than hydrocarbon and but higher than R125, R407c, R410a and R404a, R-507a. Similar trends were observed for finding second law efficiency (in terms of exergetic efficiency) as shown in Table-1(b) respectively. The second law efficiency of system-2 using expander is higher than system -1 using throttle valve. The R245fa is second highest exergetic efficiency as shown in Table-1(b). Similarly EDR (exergy destruction ratio (i.e. which is a ratio of total exergy losses in the system to the exergy of product)) of the system is increased as exergetic efficiency is reduced as shown in table-1(c). Therefore, exergy destruction ratio using R123 refrigerant is reduced.

Table-1(a): Variation of first law efficiency (in terms of coefficient of performance) COP with different ecofriendly refrigerants of vapour compressor refrigeration system using (system-1: throttle valve) and System-2.expander

S.No	Refrigerant	System-1	System-2
1	R134a	3.246	3..928
2	R1234ze	3.215	3.931
3	R1234yf	3.027	3.806
4	R600a	3.291	3.953
5	R600	3.447	4.017
6	R290	3.166	3.89
7	R227ea	2.833	3.723
8	R236fa	3.168	3.897
9	R245fa	3.459	4.032
10	R407c	2.698	3.559
11	R410a	2.952	3.711
12	R404a	2.695	3.658
13	R152a	3.451	3.996
14	R717	3.546	3.847
15	R125	2.444	3.518
16	R123	3.575	4.082
17	R32	3.141	3.715
18	R507a	2.723	3.670

Table-1(b): Variation of second law efficiency (in terms of exergetic efficiency) COP with different ecofriendly refrigerants of vapour compressor refrigeration system using (System-1: throttle valve) and System-2.expander

S.No	Refrigerant	System-1	System-2
1	R134a	0.2973	0.3597
2	R1234ze	0.2944	0.360
3	R1234yf	0.2772	0.3485
4	R600a	0.3014	03620
5	R600	0.3157	03679
6	R290	0.2899	0.3563
7	R227ea	0.2594	0.3409
8	R236fa	0.2901	0.3569
9	R245fa	0.3168	0.3692
10	R407c	0.2470	0.3259
11	R410a	0.2703	0.3398
12	R404a	0.2468	0.3350
13	R152a	0.3160	0.3660
14	R717	0.3245	0.3523
15	R125	0.2238	0.3222
16	R123	0.3275	0.3738
17	R32	0.2877	0.3402
18	R507a	0.2493	0.3360

Table-1(c): Variation of exergy destruction ratio (EDR) based on system exergy output with different eco-friendly refrigerants of vapour compressor refrigeration system using (System-1: throttle valve) and System-2.expander

S.No	Refrigerant	System-1	System-2
1	R134a	2.364	1.78
2	R1234ze	2.396	1.778
3	R1234yf	2.608	1.869
4	R600a	2.318	1.763
5	R600	2.168	1.718
6	R290	2.45	1.807
7	R227ea	2.855	1.933
8	R236fa	2.447	1.802
9	R245fa	2.157	1.709
10	R407c	3.048	2.068
11	R410a	2.699	1.943
12	R404a	3.051	1.985
13	R152a	2.164	1.732
14	R717	2.080	1.838
15	R125	3.467	2.104
16	R123	2.059	1.675
17	R32	2.476	1.939
18	R507a	3.011	1.976

3.1 Performance evaluation of both systems using ecofriendly R245fa refrigerant

The thermodynamic performances using R245fa is given in tables-2 respectively. It is seen that COP increases as evaporator temperature increases and exergy destruction ratio is decreases. It is seen that sytem-2 using expander gives better first law performance than system-1 using throttle valve. Table-2(a) to Table-3(c) show the effects of evaporator and condensing temperatures with variation of thermodynamic performances of vapour compression refrigeration systems using R245fa refrigerant. Similarly first law efficiency (COP) and second law efficiency (exergetic efficiency) decreases as condenser temperature increases and exergy destruction ratio is increases. It is seen that sytem-2 using expander gives better first law performance than system-1 using throttle valve as shown in Tables-3 respectively

Table-2(a): Variation of first law efficiency (in terms of coefficient of performance) COP with variation of evaporator temperature using R245fa in the vapour compressor refrigeration system using (system-1: throttle valve) and System-2.expander

S.No	Evaporator Temperature (^{0}C)	System-1	System-2
1	20	6.803	7.442
2	15	5.605	6.223
3	10	4.708	5.309
4	5	4.013	4.599
5	0	3.459	4.032
6	-5	3.008	3.568
7	-10	2.634	3.182
8	-15	2.319	2.856
9	-20	2.051	2.577

Table-2(b): Variation of second law efficiency (in terms of exergetic efficiency with variation of evaporator temperature using R245fa in the vapour compressor refrigeration system using (System-1: throttle valve) and System-2.expander

S.No	Evaporator Temperature (^{0}C)	System-1	System-2
1	20	0.1161	0.1270
2	15	0.1946	0.2161
3	10	0.2496	0.2814
4	5	0.2887	0.3309
5	0	0.3168	0.3692
6	-5	0.3367	0.3994
7	-10	0.3505	0.4234
8	-15	0.3596	0.4427
9	-20	0.3648	0.4583

Table-2(c): Variation of exergy destruction ratio (EDR) based on system exergy output with variation of evaporator temperature using R245fa in the vapour compressor refrigeration system using (system-1: throttle valve) and System-2.expander

S.No	Evaporator Temperature (^{0}C)	System-1	System-2
1	20	7.613	6.875
2	15	4.138	3.628
3	10	3.007	2.553
4	5	2.464	2.022
5	0	2.157	1.709
6	-5	1.970	1.504
7	-10	1.853	1.362
8	-15	1.781	1.259
9	-20	1.742	1.182

Table-2(a) shows the variation of first law efficiency (COP) as defined “refrigeration effect to the net (i.e. effective) work done” by the vapor compression refrigeration system with variation of evaporator temperature. As shown in the table for

a given condenser temperature as evaporator temperature the specific refrigeration effect increases marginally. It can be seen that for a given evaporator temperature, the refrigeration effect decreases as condenser temperature increases. It can also be observed that the volumetric refrigeration effect increases rapidly with evaporator temperature due to the increase in specific refrigeration effect and decrease in specific volume of refrigerant vapour at the inlet to the compressor. Volumetric refrigeration effect increases marginally as condenser temperature decreases it shows that the specific work of compression decreases rapidly as the evaporator temperature increases and condenser temperature and pressure decreases. For a given condenser temperature, the work of compression increases initially, reaches a peak, then starts decreasing. This is due to the fact that as evaporator temperature increases the specific work of compression decreases and the specific volume at the inlet to the compressor also decreases. As a result, an optimum evaporator temperature and pressure exists at which the work of compression reaches a maximum. Physically, the work of compression is analogous to mean effective pressure of the compressor, as multiplying this with the volumetric flow rate gives the power input to the compressor. For a given power input, a high work of compression implies smaller volumetric flow rates and hence a smaller compressor shows the effect of evaporator and condenser temperatures on COP of the VCRS cycle. As expected, for a given condenser temperature the COP increases rapidly with evaporator temperature. For a given evaporator temperature, the COP decreases as condenser temperature increases. However, the effect of condenser temperature becomes marginal at low evaporator temperatures. The above results show that at very low evaporator temperatures, the COP becomes very low and also the size of the compressor becomes large (due to small refrigeration effect). It can also be shown that the compressor discharge temperatures also increase as the evaporator temperature decreases.

Table-3(a): Variation of first law efficiency (in terms of coefficient of performance) COP with variation of condenser temperature using R245fa in the vapour compressor refrigeration system (System-1: throttle valve) and System-2.expander

S.No	Condenser Temperature (^{0}C)	System-1	System-2
1	30	6.478	7.005
2	35	5.411	5.949
3	40	4.605	5.154
4	45	3.971	4.532
5	50	3.459	4.032
6	55	3.034	3.619
7	60	2.675	3.273

Table-3(b): Variation of second law efficiency (in terms of exergetic efficiency with variation of evaporator temperature using R245fa in the vapour compressor refrigeration system using (system-1: throttle valve) and System-2.expander

S.No	Condenser Temperature (^{0}C)	System-1	System-2
1	30	0.5932	0.6415
2	35	0.4955	0.5448
3	40	0.4217	0.4720
4	45	0.3637	0.415
5	50	0.3168	0.3692
6	55	0.2779	0.3314
7	60	0.2450	0.2997

Table-3(c): Variation of exergy destruction ratio (EDR) based on system exergy output with variation of evaporator temperature using R245fa in the vapour compressor refrigeration system (system-1: throttle valve) and System-2.expander

S.No	Condenser temperature (^{0}C)	System-1	System-2
1	30	0.6858	0.5589
2	35	1.018	0.8356
3	40	1.377	1.119
4	45	1.75	1.409
5	50	2.157	1.709
6	55	2.599	2.017
7	60	3.082	2.337

Table-4(a): Variation of first law efficiency (in terms of coefficient of performance) COP with variation of evaporator temperature using R236fa in the vapour compressor refrigeration system using system-1(throttle valve) and System-2using expander

S.No	Evaporator Temperature (^{0}C)	System-1	System-2
1	20	6.459	7.296
2	15	5.278	6.081
3	10	4.395	5.170
4	5	3.712	4.462
5	0	3.168	3.897
6	-5	2.726	3.435
7	-10	2.361	3.052
8	-15	2.054	2.728
9	-20	1.793	2.451

Table-4(b): Variation of second law efficiency (in terms of exergetic efficiency with variation of evaporator temperature using R236fa in the vapour compressor refrigeration system using (System-1: throttle valve) and System-2.expander

S.No	Evaporator Temperature (^{0}C)	System-1	System-2
1	20	0.1102	0.1245
2	15	0.1833	0.2111
3	10	0.2330	0.2740
4	5	0.2671	0.3210
5	0	0.2901	0.3569
6	-5	0.3052	0.3846
7	-10	0.3142	0.4061
8	-15	0.3184	0.4229
9	-20	0.3190	0.4360

Table-4(c): Variation of exergy destruction ratio (EDR) based on system exergy output with variation of evaporator temperature using RR236fa in the vapour compressor refrigeration system using (system-1: throttle valve) and System-2.expander

S.No	Evaporator Temperature (^{0}C)	System-1	System-2
1	20	8.072	7.032
2	15	4.457	3.736
3	10	3.292	2.649
4	5	2.744	2.115
5	0	2.447	1.802
6	-5	2.277	1.60
7	-10	2.183	1.462
8	-15	2.14	1.365
9	-20	2.135	1.294

3.2 Performance evaluation of both systems using ecofriendly R236fa refrigerant

The thermodynamic performances using R236fa is given in tables-4(a) to 5(c) respectively. It is seen that first law efficiency (COP) and second law efficiency (exergetic efficiency) increases as evaporator temperature increases and exergy destruction ratio is decreases. It is seen that sytem-2 using expander gives better first law performance than system-1 using throttle valve. Similarly first law efficiency (COP) and second law efficiency (exergetic efficiency) decreases as condenser temperature increases and exergy destruction ratio is increases. It is seen that sytem-2 using expander gives better first law performance than system-1 using throttle valve as shown in Tables-5 respectively

Table-5(a): Variation of first law efficiency (in terms of coefficient of performance) COP with variation of condenser temperature using R236fa in the vapour compressor refrigeration system using (system-1: throttle valve) and System-2.expander

S.No	Condenser Temperature (^{0}C)	System-1	System-2
1	30	6.21	6.88
2	35	5.141	5.825
3	40	4.33	5.028
4	45	3.689	4.403
5	50	3.168	3.897
6	55	2.733	3.478
7	60	2.362	3.122

Table-5(b): Variation of second law efficiency (in terms of exergetic efficiency with variation of evaporator temperature using R236fa in the vapour compressor refrigeration system using (system-1: throttle valve) and System-2.expander

S.No	Condenser Temperature (^{0}C)	System-1	System-20.630
1	30	0.687	0.630
2	35	0.708	0.5334
3	40	0.3965	0.4604
4	45	0.3379	0.4032
5	50	0.2901	0.3569
6	55	0.2503	0.3185
7	60	0.2163	0.2859

Table-5(c): Variation of exergy destruction ratio (EDR) based on system exergy output with variation of evaporator temperature using R236fa in the vapour compressor refrigeration system (system-1: throttle valve) and System-2.expander

S.No	Condenser temperature (^{0}C)	System-1	System-2
1	30	0.7585	0.5872
2	35	1.124	0.8748
3	40	1.522	1.172
4	45	1.96	1.480
5	50	2.447	1.802
6	55	2.995	2.14
7	60	3.622	2.497

3.3 Performance evaluation of both systems using ecofriendly R227ea refrigerant

The thermodynamic performances using R227a is given in tables-6(a) to 7(c) respectively. It is seen that first law efficiency (COP) and second law efficiency (exergetic efficiency) increases as evaporator temperature increases and exergy destruction ratio is decreases. It is seen that sytem-2 using expander gives better first law performance than system-1 using throttle valve as shown in Tables-6 respectively. Similarly first law efficiency (COP) and second law efficiency (exergetic efficiency) decreases as condenser temperature increases and exergy destruction ratio is increases. It is seen that sytem-2 using expander gives better first law performance than system-1 using throttle valve as shown in Tables-7 respectively. It was observed that the thermodynamic performances using R245fa is higher than R236fa and R227ea and exergy d destruction is more while using R227ea in the vapour compression refrigeration systems.

Table-6(a): Variation of first law efficiency (in terms of coefficient of performance) COP with variation of evaporator temperature using R227ea in the vapour compressor refrigeration system using (system-1: expander) and System-2 throttle valve.

S.No	*Evaporator Temperature* (^{0}C)	*System-1*	*System-2*
1	20	6.009	7.07
2	15	4.868	5.874
3	10	4.016	4.977
4	5	3.357	4.28
5	0	2.833	3.723
6	-5	2.408	3.268
7	-10	2.056	2.889
8	-15	1.763	2.570
9	-20	1.514	2.298

Table-6(b): Variation of second law efficiency (in terms of exergetic efficiency with variation of evaporator temperature using R227ea in the vapour compressor refrigeration system using (system-1: throttle valve) and System-2.expander

S.No	Evaporator Temperature (^{0}C)	System-1	System-2
1	20	0.1025	0.1206
2	15	0.1690	0.2040
3	10	0.2128	0.2638
4	5	0.2415	0.3079
5	0	0.2594	0.3409
6	-5	0.2695	0.3658
7	-10	0.2737	0.3845
8	-15	0.2733	0.3985
9	-20	0.2692	0.4087

Table-6(c): Variation of exergy destruction ratio (EDR) based on system exergy output with variation of evaporator temperature using R227eain the vapour compressor refrigeration system using (system-1: throttle valve) and System-2.expander

S.No	Evaporator Temperature (^{0}C)	System-1	System-2
1	20	8.752	7.289
2	15	4.917	3.903
3	10	3.698	2.791
4	5	3.141	2.248
5	0	2.855	1.933
6	-5	2.711	1.734
7	-10	2.654	1.601
8	-15	2.659	1.510
9	-20	2.714	1.447

Table-7(a): Variation of first law efficiency (in terms of coefficient of performance) COP with variation of condenser temperature using R227ea in the vapour compressor refrigeration system using (system-1: throttle valve) and System-2.expander

S.No	Condenser Temperature (^{0}C)	System-1	System-2
1	30	5.928	6.748
2	35	4.850	5.686
3	40	4.026	4.879
4	45	3.371	4.243
5	50	2.833	3.723
6	55	2.378	3.217
7	60	1.985	2.912

Table-7(b): Variation of second law efficiency (in terms of exergetic efficiency with variation of evaporator temperature using R227ea in the vapour compressor refrigeration system using (system-1: throttle valve) and System-2.expander

S.No	Condenser Temperature (^{0}C)	System-1	System-2
1	30	0.5429	0.6179
2	35	0.4441	0.5207
3	40	0.3687	0.4468
4	45	0.3087	0.3885
5	50	0.2594	0.3409
6	55	0.2178	0.3010
7	60	0.1818	0.2666

Table-7(c): Variation of exergy destruction ratio (EDR) based on system exergy output with variation of evaporator temperature using R227ea in the vapour compressor refrigeration system (System-1: throttle valve) and System-2.expander

S.No	Condenser temperature (^{0}C)	System-1	System-2
1	30	0.8421	0.6183
2	35	1.252	0.92.6
3	40	1.712	1.238
4	45	2.239	1.574
5	50	2.855	1.933
6	55	3.592	2.322
7	60	4.501	2.750

3.4 Performance evaluation of both systems using ecofriendly R-134a refrigerant

The thermodynamic performances using R134a is given in tables-8(a) to 9(c) respectively. It is seen from tables-8 that first law efficiency (COP) and second law efficiency (exergetic efficiency) increases as evaporator temperature increases and exergy destruction ratio is decreases. It is seen that sytem-2 using expander gives better first law performance than system-1 using throttle valve as shown in Tables-8 respectively. Similarly first law efficiency (COP) and second law efficiency (exergetic efficiency) decreases as condenser temperature increases and exergy destruction ratio is increases. It is seen that sytem-2 using expander gives better first law performance than system-1 using throttle valve as shown in Tables-9 respectively.

It was observed that the thermodynamic performances in terms of COP and exergetic efficiency using R245fa is higher than R134a and R134a has more exergy destruction ratio while using R 245fa has lower EDR in the vapour compression refrigeration systems.

Table-8(a): Variation of first law efficiency (in terms of coefficient of performance) COP with variation of evaporator temperature using R134a in the vapour compressor refrigeration system using (system-1: throttle valve) and System-2.expander

S.No	Evaporator Temperature (^{0}C)	System-1	System-2
1	20	6.429	7.278
2	15	5.286	6.08
3	10	4.43	5.182
4	5	3.732	4.485
5	0	3.246	3.928
6	-5	2.819	3.473
7	-10	2.464	3.473
8	-15	2.167	2.775
9	-20	1.914	2.502

Table-8(b): Variation of second law efficiency (in terms of exergetic efficiency with variation of evaporator temperature using R134a in the vapour compressor refrigeration system (system-1: throttle valve) and System-2.expander

S.No	Evaporator Temperature (^{0}C)	System-1	System-2
1	20	0.1097	0.1242
2	15	0.1836	0.2111
3	10	0.2350	0.2747
4	5	0.2714	0.3226
5	0	0.2973	0.3597
6	-5	0.3155	0.3887
7	-10	0.3280	0.4118
8	-15	0.3359	0.4303
9	-20	0.3404	0.4451

Table-8(c): Variation of exergy destruction ratio (EDR) based on system exergy output with variation of evaporator temperature using R134a in the vapour compressor refrigeration system using (System-1: throttle valve) and System-2.expander

S.No	Evaporator Temperature (^{0}C)	System-1	System-2
1	20	8.115	7.051
2	15	4.448	3.737
3	10	3.256	2.641
4	5	2.685	2.10
5	0	2.364	1.78
6	-5	2.169	1.572
7	-10	2.049	1.428
8	-15	1.977	1.324
9	-20	1.938	1.247

Table-9(a): Variation of first law efficiency (in terms of coefficient of performance) COP with variation of condenser temperature using R134a in the vapour compressor refrigeration system using (System-1: throttle valve) and System-2.expander

S.No	Condenser Temperature (^{0}C)	System-1	System-2
1	30	6.26	6.895
2	35	5.20	5.844
3	40	4.396	5.051
4	45	3.762	4.43
5	50	3.246	3.928
6	55	2.816	3.511
7	60	2.448	3.159

Table-9(b): Variation of second law efficiency (in terms of exergetic efficiency with variation of evaporator temperature using R134a in the vapour compressor refrigeration system using (system-1: throttle valve) and System-2.expander

S.No	Condenser Temperature (^{0}C)	System-1	System-2
1	30	0.5732	0.6314
2	35	0.4762	0.5352
3	40	0.4026	0.4626
4	45	0.3445	0.4057
5	50	0.2973	0.3597
6	55	0.2578	0.3215
7	60	0.224	0.2893

Table-9(c): Variation of exergy destruction ratio (EDR) based on system exergy output with variation of evaporator temperature using R134a in the vapour compressor refrigeration system (System-1: throttle valve) and System-2.expander

S.No	Condenser temperature (^{0}C)	System-1 With throttle Valve	System-2 with expander
1	30	0.7445	0.5838
2	35	1.10	0.8685
3	40	1.484	1.162
4	45	1.902	1.465
5	50	2.364	1.780
6	55	2.878	*2.11*
7	60	3.461	2.457

3.5 Performance evaluation of both systems using ecofriendly R-1234yf refrigerant

The thermodynamic performances using R1234yf is given in tables-10(a) to 11(c) respectively. It is seen from tables-10 that first law efficiency (COP) and second law efficiency (exergetic efficiency) increases as evaporator temperature increases and exergy destruction ratio is decreases. It is seen that sytem-2 using expander gives better first law performance than system-1 using throttle valve as shown in Tables-10 respectively. Similarly first law efficiency (COP) and second law efficiency (exergetic efficiency) decreases as condenser temperature increases and exergy destruction ratio is increases. It is seen that sytem-2 using expander gives better first law performance than system-1 using throttle valve as shown in Tables-11 respectively. It was observed that the thermodynamic performances in terms of COP and exergetic efficiency using R134a is higher than R1234yf and R134a has less exergy destruction ratio (EDR) while using R 1234yf has higher EDR in the vapour compression refrigeration systems.

Table-10(a): Variation of first law efficiency (in terms of coefficient of performance) COP with variation of evaporator temperature using R-1234yf in the vapour compressor refrigeration system using (system-1: throttle valve) and System-2.expander

S.No	Evaporator Temperature (^{0}C)	System-1	System-2
1	20	6.179	7.129
2	15	5.047	5.94
3	10	4.201	5.049
4	5	3.547	4.358
5	0	3.027	3.806
6	-5	2.604	3.355
7	-10	2.255	2.981
8	-15	1.962	2.665
9	-20	1.714	2.396

Table-10(b): Variation of second law efficiency (in terms of exergetic efficiency with variation of evaporator temperature using R134a in the vapour compressor refrigeration system (system-1: throttle valve) and System-2.expander

S.No	Evaporator Temperature (^{0}C)	System-1	System-2
1	20	0.1055	0.1217
2	15	0.1752	0.2062
3	10	0.2227	0.2676
4	5	0.2552	0.3135
5	0	0.2772	0.3485
6	-5	0.2915	0.3756
7	-10	0.3001	0.3967
8	-15	0.3042	0.4132
9	-20	0.3049	0.4261

Table-10(c): Variation of exergy destruction ratio (EDR) based on system exergy output with variation of evaporator temperature using R134a in the vapour compressor refrigeration system using (System-1: throttle valve) and System-2.expander

S.No	Evaporator Temperature (^{0}C)	System-1	System-2
1	20	8.483	7.22
2	15	4.707	3.849
3	10	3.491	2.736
4	5	2.919	2.19
5	0	2.608	1.869
6	-5	2.43	1.663
7	-10	2.332	1.521
8	-15	2287	1.42
9	-20	2.28	1.347

Table-11(a): Variation of first law efficiency (in terms of coefficient of performance) COP with variation of condenser temperature using R-1234yf in the vapour compressor refrigeration system using (system-1: throttle valve) and System-2.expander

S.No	Condenser Temperature (^{0}C)	System-1	System-2
1	30	6.099	6.79
2	35	5.0260	5.738
3	40	4.208	4.942
4	45	3.559	4.315
5	50	3.027	3.806
6	55	2.579	3.380
7	60	2.192	3.017

Table-11(b): Variation of second law efficiency (in terms of exergetic efficiency with variation of evaporator temperature using R-1234yf in the vapour compressor refrigeration system using (System-1: throttle valve) and System-2.expander

S.No	Condenser Temperature (^{0}C)	System-1	System-2
1	30	0.5585	0.6218
2	35	0.4602	0.5255
3	40	0.3853	0.4526
4	45	0.3259	0.3952
5	50	0.2772	0.3485
6	55	0.2362	0.3096
7	60	0.2008	0.2762

Table-11(c): Variation of exergy destruction ratio (EDR) based on system exergy output with variation of evaporator temperature using R-1234yf in the vapour compressor refrigeration system (system-1: throttle valve) and System-2.expander

S.No	Condenser temperature (^{0}C)	System-1 With throttle Valve	System-2 with expander
1	30	0.7906	0.6082
2	35	1.173	0.9030
3	40	1.595	1.210
4	45	2.068	1.531
5	50	2.608	1.869
6	55	3.234	2.230
7	60	3.981	2.620

Table-12(a): Variation of first law efficiency (in terms of coefficient of performance) COP with variation of evaporator temperature using R1234ze in the vapour compressor refrigeration system using (system-1: throttle valve) and System-2.expander

S.No	Evaporator Temperature (^{0}C)	System-1	System-2
1	20	6.446	7.308
2	15	5.287	6.10
3	10	4.421	5.196
4	5	3.75	4.493
5	0	3.215	3.931
6	-5	2.78	3.472
7	-10	2.42	3.09
8	-15	2.117	2.768
9	-20	1.86	2.493

Table-12(b): Variation of second law efficiency (in terms of exergetic efficiency with variation of evaporator temperature using R1234ze in the vapour compressor refrigeration system (System-1: throttle valve) and System-2.expander

S.No	Evaporator Temperature (^{0}C)	System-1	System-2
1	20	0.110	0.1247
2	15	0.1836	0.2118
3	10	0.2343	0.2754
4	5	0.2697	0.3232
5	0	0.2944	0.360
6	-5	0.3112	0.3887
7	-10	0.3221	0.4113
8	-15	0.3283	0.4292
9	-20	0.3308	0.4434

Table-12(c): Variation of exergy destruction ratio (EDR) based on system exergy output with variation of evaporator temperature using R1234ze in the vapour compressor refrigeration system using (system-1: throttle valve) and System-2.expander

S.No	Evaporator Temperature (^{0}C)	System-1	System-2
1	20	8.091	7.019
2	15	4.447	3.721
3	10	3.268	2.631
4	5	2.707	2.094
5	0	2.396	1.778

6	-5	2.213	1.573
7	-10	2.105	1.431
8	-15	2.046	1.330
9	-20	2.023	1.255

3.6 Performance evaluation of both systems using ecofriendly R-1234ze refrigerant

The thermodynamic performances using R1234ze is given in tables-12(a) to 13(c) respectively. It is seen from tables-12 that first law efficiency (COP) and second law efficiency (exergetic efficiency) increases as evaporator temperature increases and exergy destruction ratio is decreases. It is seen that sytem-2 using expander gives better first law performance than system-1 using throttle valve as shown in Tables-12 respectively. Similarly first law efficiency (COP) and second law efficiency (exergetic efficiency) decreases as condenser temperature increases and exergy destruction ratio is increases. It is seen that sytem-2 using expander gives better first law performance than system-1 using throttle valve as shown in Tables-13 respectively. It was observed that the thermodynamic performances in terms of COP and exergetic efficiency using R134a is slightly higher than R1234ze and R134a has slightly less exergy destruction ratio while using R 1234ze has higher EDR in the vapour compression refrigeration systems.

Table-13(a): Variation of first law efficiency (in terms of coefficient of performance) COP with variation of condenser temperature using R1234ze in the vapour compressor refrigeration system using (system-1: throttle valve) and System-2.expander

S.No	Condenser Temperature (^{0}C)	System-1	System-2
1	30	6.264	6.928
2	35	5.192	5.868
3	40	4.379	5.067
4	45	3.737	4.439
5	50	3.215	3.931
6	55	2.779	3.51
7	60	2.407	3.154

Table-13(b): Variation of second law efficiency (in terms of exergetic efficiency with variation of evaporator temperature using R1234ze in the vapour compressor refrigeration system using (system-1: throttle valve) and System-2.expander

S.No	Condenser Temperature (^{0}C)	System-1	System-2
1	30	0.5736	0.6345
2	35	0.4755	0.5373
3	40	0.4010	0.4640
4	45	0.3422	0.4065
5	50	0.2944	0.360
6	55	0.2545	0.3214
7	60	0.2205	0.2888

Table-13(c): Variation of exergy destruction ratio (EDR) based on system exergy output with variation of evaporator temperature using R1234ze in the vapour compressor refrigeration system (System-1: throttle valve) and System-2.expander

S.No	Condenser temperature (^{0}C)	System-1 With throttle Valve	System-2 with expander
1	30	0.7434	0.5761
2	35	1.103	0.8611
3	40	1.494	1.155
4	45	1.922	1.460
5	50	2.396	1.778
6	55	2.929	2.111
7	60	3.536	2.463

4. Conclusion

Following conclusions were drawn from thermodynamic analysis of vapour compression refrigeration system using (system-1: throttle valve and system-2: expander).

(i) The first law efficiency of vapour compression refrigeration system using expander is higher than other VCRS (system-1) using throttle valve.
(ii) The exergy destruction ratio (EDR) of VCRS is decrease in condenser temperature/ pressure and hence second law efficiency is increased.
(iii) Increase in temperature of evaporator/ pressure, the first law efficiency of vapour compression refrigeration system and second law efficiency of vapour compression refrigeration system is increased while the work input and Exergy destruction ratio is will decrease.
(iv) Decrease in temperature of condenser/ pressure, the first law efficiency of vapour compression refrigeration system and second law efficiency of vapour compression refrigeration system is decreased while the work input and exergy destruction ratio is will increase.
(v) Using expander in system-2 replaced throttle valve has higher first law efficiency in terms of coefficient is higher and second law efficiency in terms of exergetic efficiency (around 20% to 24%) than system-1 using throttle valve. Using R123 refrigerant in the vapour compression refrigeration system has highest COP.
(vi) R123 refrigerant has chlorine content. Therefore HFO refrigerants gives better thermodynamic performances can replace R134a abnd other HFC refrigerants, R152a and hydrocarbons have flammable nature, therefore R1234ze and R1234yf can replace R134a in near future.

References

[1] Mishra et.al, Methods for improving thermal performances of vapour compression Refrigeration system using eleven ecofriendly refrigerants", ISTE conference on "Technological Universities and Institutions in New Knowledge Age: Future Perspectives and Action plan, ISTE, 149, 9, Delhi Technological University, 2013.
[2] Mishra, Irriversibility Analysis of Multi-Evaporators Vapour Compression Refrigeration Systems Using New and Refrigerants: R134a, R290, R600, R600a, R1234yf,R502, R404a and R152a and R12,

[3] R502" International Journal of Advance Research & Innovations International Journal of Advance Research & Innovations, 1, 2013, 180-193.
[4] Mishra, Thermodynamic performance evaluation of multiple evaporators , single compressor ,single expansion valve and liquid vapour heat exchanger in vapour compression refrigeration systems using thirteen ecofriendly refrigerants for reducing global warming and ozone depletion, International Journal of Advance Research & Innovations, 1, 2014, 163-171.
[5] Xiaohui She, Yonggao Yin, Xiao song Zhang (2014) "A proposed subcooling method for vapor compression refrigeration cycle based on expansion power recovery", International Journal of Refrigeration, Vol 43; pp: 50-61.
[6] Victor A. Gonzalves, Jose A. R. Parise (2008) "A Study on the Reduction of Throttling Losses in Automotive Air Conditioning Systems Through Expansion Work Recovery", International Refrigeration and Air Conditioning Conference, Paper 882; pp: 1-8.
[7] Mishra, Thermodynamic performance evaluation of multiple evaporators , single compressor ,single expansion valve and liquid vapour heat exchanger in vapour compression refrigeration systems using thirteen ecofriendly refrigerants for reducing global warming and ozone depletion, International Research Journal of Sustainable Science & Engineering (Monthly Peer Review Journal , 2(3), 2014, 1-10.
[8] Mishra, Method for Improving Thermal Performances of Vapour Compression Refrigeration Systems Using Energy and Exergy Analysis for Reducing Global Warming and Ozone Depletioning Using Ecofriendly Refrigerants. Nature & Environment Vol. 19 (2), 2014: 219-231.
[9] Mishra, Performance evaluation of Vapour Compression Refrigeration system using eco friendly refrigerants in primary circuit and nanofluid (Water-nano particles based) in secondary circuit, International Journal of Advance Research and Innovation Volume 2, Issue 2 (2014) 350-362 ISSN 2347- 3258.
[10] Mishra, Appropriate Vapour Compression Refrigeration Technologies for Sustainable Development, International Journal of Advance Research and Innovation, Volume 2, Issue 3 (2014) 551-556 ISSN 2347 – 3258.
[11] Mishra, Methods for Improving Thermodynamic Performance of Vapour Compression Refrigeration Systems using Thirteen Ecofriendly Refrigerants in Primary Circuit and Tio2 Nano Particles Mixed with R718 used in Secondary Evaporator Circuit for Reducing Global Warming and Ozone Depletion, International Journal of Advance Research and Innovation, Volume 2, Issue 4 (2014) 732-735 ISSN 2347 – 3258.
[12] Mishra, Methods for Improving Thermodynamic Performance of Vapour Compression Refrigeration Systems Using R134a Ecofriendly Refrigerant in Primary Circuit and Three Nano Particles Mixed with R718 used in Secondary Evaporator Circuit for Reducing Global Warming and Ozone Depletion, International Journal of Advance Research and Innovation, Volume 2, Issue 4 (2014) 784-789 ISSN 2347 – 3258.
[13] Mishra, Irreversibility Reduction in Vapour Compression Refrigeration Systems Using Al_2O_3 Nano Material Mixed in R718 as Secondary Fluid, International Journal of Advance Research and Innovation, Volume 3, Issue 2 (2015) 321-327 ISSN 2347 – 3258.
[14] Mishra, Energy-Exergy Performance Comparison of Vapour Compression Refrigeration Systems using Three Nano Materials Mixed in R718 in the Secondry Fluid and Ecofriendly Refrigerants in the Primary Circuit and Direct Mixing of nano Materials in the Refrigerants, International Journal of Advance Research and Innovation, Volume 3, Issue 3 (2015) 471-477 ISSN 2347 – 3258.
[15] Mishra, Vapour Compression Refrigeration Technology for Sustainable Development, International Journal of Advance Research and Innovation, Volume 3, Issue 4 (2015) 647-652 ISSN 2347 – 3258.
[16] Mishra, Methods for Improving Thermodynamic Energy and Exergy Performance of Vapor Compression Refrigeration Systems Using Thirteen Eco-friendly Refrigerants in Primary Circuit and TiO2 Nano Particles Mixed with R718 Used in Secondary Evaporator Circuit for Reducing Global Warming and Ozone Depletion, International Journal of Advance Research and Innovation, Volume 4, Issue 1 (2016) 91-95 ISSN 2347 –3258.
[17] Alison Subiantoro, Kim Tiow Ooi (2013), " Economic analysis of the application of expanders in medium scale air-conditioners with conventional refrigerants, R1234yf and CO2", International Journal of Refrigeration, Vol 36, No. 5; pp: 1472-1482.
[18] Bjorn Palm (2007), "Hydrocarbons as refrigerants in small heat pump and refrigeration systems-A review", International Journal of Refrigeration, 31; pp: 552-563.
[19] Mishra R.S.{2018] Thermodynamic performance of vapour compression refrigeration systems using HFO refrigerants for replacing HFC refrigerants. International journal of research in Engineering and innovation , Vol-2, issue, 5, 492-497, 2018.
[20] Wael A. Fouad , et.al. [2018] Next Generation of Low Global Warming Potential Refrigerants: Thermodynamic Properties Molecular Modeling, AIChE journal, Vol-64 , No-1, DOI 10.1002/aic.15859 Published online July 24, 2017 in Wiley Online Library (wileyonlinelibrary.com).

International Journal of Research in Engineering and Innovation (IJREI)
journal home page: http://www.ijrei.com
ISSN (Online): 2456-6934

Modeling of variable speed compressor vapour compression refrigeration system using ecofriendly refrigerants and nano refrigerants and water cooled condenser-evaporator with experimental validation

Radhey Shyam Mishra

Department of Mechanical Engineering, Production & Industrial engineering and Automobiles Engineering
Delhi Technological University, Delhi 110042
E Mail-rsmishradtu@gmail.com, rsmishra@dce.ac.in , rsmishra@dtu.ac.in

Abstract

Lots of researches have been done and going on based on the performance evaluation of various metallic/ nonmetallic nanoparticle suspended into the conventional fluid to enhance the heat transfer property of base fluid. Also some theoretical analysis of suspension of nanoparticle Al_2O_3 in conventional refrigerant. On the other hand the performance of vapour compression cycle based chiller facility using nano refrigerant yet to be analyzed with different type, concentration and diameter of nanoparticle. Such as TiO_2, CuO nanoparticle suspension into conventional refrigerant with different concentration and diameter have been analyzed by several investigators and also effect of variation of concentration and nanoparticle diameter on the first and second law performance of vapour compression refrigeration system is presented. The effect of changing input parameter of VCRS using nano refrigerant also affecting significantly the evaporative heat transfer coefficient and very little condor heat transfer coefficient. The idea of Suspension nanoparticle into conventional refrigerant and theoretical analysis of VCRS using nano-refrigerant is proposed after going through extensive literature review presented in this paper.
© 2017 ijrei.com. All rights reserved
Keywords: VCRS, First & Second Law Performance, Nano Materials, Energy-Exergy Analysis

1. Introduction

Theoretical and experimental investigation of refrigeration systems based on first law and second law analysis using refrigerants.is carried out. Chopra, [1] investigated the exergy analysis of vapour compression refrigeration system with R134a R407Cand R410A. In their study they have calculated the effect of varying evaporator temperature of the C.O.P. of VCS for different types of ecofriendly refrigerant and also the effect of varying evaporator temperature on the exergetic efficiency of VCS. Chopra [2] developed a computational model for computing a coefficient of performance (COP), energy destruction, exergetic efficiency and energy defects for R502, R404A, and R507A of detailed energy analysis on actual vapor compression refrigeration cycle. It has been done for evaporator and condenser temperature in the range of 50^0C to 0^0C and 40^0C to 55^0 C respectively. He found that R507A is better substitute to R502 than R404A. The efficiency defects in condenser are highest and lowest in liquid vapour heat exchanger for the refrigerants considered. Choi, S. U. S, [3] investigated thermal properties and rheological behavior of water based Al_2O_3 nano fluid as a heat transfer fluid and found that Thermal conductivity and convective heat transfer of nano fluid increases as mass concentration of nano fluid increases. Jwo et.al, [4] presented the Effect of different nano particle shapes on shell and tube heat exchanger using different baffle angles and operated with nano fluid, in his study he has analyze the effect of nanoparticle volume fraction on overall heat transfer coefficient and entropy generation & heat transfer rate and found that as well as we increase the volume fraction of nano particle the overall heat transfer coefficient generation & heat transfer rate increases and

Corresponding Author: Radhey Shyam. Mishra
Email rsmishra@dtu.ac.in

entropy generation decreases. Simulation result has been plotted for the same. Lee K, Hwang [5] in his experimental measured on heat transfer coefficient using Al_2O_3 /water nano fluid in an air finned heat exchanger concluded the overall heat transfer coefficient of Fe_2O_3/water nano fluids in compact air cooled heat exchanger using LMTD technique under laminar flow regime. Joaquin Navarro, Francisco, Angel, [6] carried out thermal modelling analysis of vapour compression refrigeration system and found that the influence of an internal heat exchanger on the performance of a vapour compression system using R1234yf as replacement for R134a and compare the energy performance of vapour compression system using ecofriendly refrigerants,R134a and R1234yf, and found that the presence of an internal heat exchanger results, reductions in cooling capacity and COP between 6 and 13% , when R134a is replaced by the R1234yf. Although the presence of an Internal heat exchanger reductions between 2 and 6%. Murshed S. M. S., K. C. Leong, and C. Yang [7] in this study Comparison of convective heat transfer coefficient and friction factor of TiO_2 nano fluid flow in tube with twisted tape inserts' determined the heat transfer coefficient and friction factor of TiO_2/water nano fluid up to 3.0% volume concentration at an average temperature of 30°C and a significant enhancement of 23.2 % in heat transfer coefficient is observed at 1.0% concentration for flow in tube. An increase in the nanofluid concentration to 3.0% decreased heat transfer coefficient to value lower than water for flow in tube and with tape inserts. A thermal system with tape inserts of twist ration 15 and 1.0% TiO_2 concentration gives maximum advantage ratio, if pressure drop is considered along with enhancement in heat transfer coefficient. Hao Peng et.al [8] in his study on Heat transfer and flow characteristics of Al_2O_3 water nanofluid in a double tube heat exchanger and evaluated that the viscosity, relative viscosity of nano fluid at different mass fraction and sizes of nano particles and found that viscosity, Nusselt no. increases as mass fraction and size of nano particles. And observed that the, for a given refrigerating mass faction of nanoparticles, viscosity, Nusselt no. Reynolds No. increase of base fluid. Henderson et al. [9] evaluated the performance parameters of a vapour compression refrigeration system with different lubricants including nano lubricants and concluded that (i) R134a refrigerant and mineral oil mixture with nano particles worked normally (ii) Freezing capacity of the refrigeration system is higher (iii) The power consumption of the compressor reduces by 25% when the nano lubricant (iv) The coefficient of performance of the refrigeration system also increases by 33% with nano refrigerant (v) the energy enhancement factor in the evaporator is 1.53. Juan Carlos et al [10] investigated the use of nano fluids as secondary coolants in vapor compression refrigeration systems using different nanoparticles (Cu, Al_2O_3, CuO and TiO_2) for different volume fraction and particle diameters. Simulation results have shown that, for a given refrigerating capacity, evaporator area and refrigerant-side pressure drop are reduced when: (i) the volume fraction of nanoparticles increase; (ii) the diameter of nanoparticles decrease. Also, nano fluid side pressure drop and, consequently, pumping power, increase with nanoparticle volume fraction and decrease with nanoparticle size. Henderson et al. [9] Measured enhanced thermal conductivity of Cu-water Nano fluid using secondary circuit of evaporator and observed that the rate of heat transfer is increases with increasing flow rate and also its concentration. By nanoparticle dispersed into de-ionized base fluid a better enhancement is achieved. Xuan Y [10]. Investigated the nanoparticle collision and deposition in the surface investigated the base fluid should possess high prandle number, and get enhanced heat transfer rate by minimize particle-particle and particle-wall collision. Viscous dissipation effect is important of narrow channel, because Nusselt number high for high aspect ratio channel. Wang RX, Xie HB [11] studied experimentally the heat transfer coefficient and friction factor of a nano fluid consisting of water and 0.2 vol. % TiO_2 flowing a double pipe heat exchanger. They investigated the effects of the flow Reynolds number and the temperature of the nano fluid and the temperature and flow rate of the heating fluid on the heat transfer coefficient and flow characteristics. Their results showed that the convective heat transfer coefficient of nano fluid is slightly higher than that of the base liquid by about 6 -11%. The heat transfer coefficient of the nano fluid increased with an increase in the mass flow rate of the hot water and nano fluid.

Lee K, Hwang YJ, [12] Studied about the relation between thermal resistance-size of nanoparticle and found that the thermal resistance is directly proportional to the size of the nanoparticle. The maximum reduction of thermal resistance by using 10 nm sized particles, because particle size is increasing the wall temperature also increases. Due to sized particle suitable for enhanced heat transfer rate. Thermal resistance is decreases with increasing heat and concentration of Nano particle.

Murshed S. M. [13] numerically studied heat transfer characteristics of double-tube helical heat exchangers using nano fluids under laminar flow conditions. CuO and TiO_2 nano particles with diameters of 24 nm dispersed in water with volume concentrations of 0.5–3 vol. % were used as the working fluid. The overall heat transfer coefficient ratio was higher at higher nanoparticle concentrations. In other words, the overall heat transfer coefficient ratio was higher when the probability of collision between nanoparticles and the wall of the heat exchanger were increased under higher concentration, confirming that nano fluids. Wen, D., and Y. Ding (2004) [13] investigated convective heat transfer co efficient of diamond based Nano fluid by using heat tube apparatus and showed the heat transfer coefficient is increases with increasing concentration and Reynolds number of Nano fluid. I.M. Mahbubul, A. Saadah [14] investigated heat transfer enhancement and flow characteristic of Al_2O_3-Water Nano fluid using micro channel heat sink. The dimension of test section is 5x5 mm and 50W heat is

applied and found heat transfer is enhanced at high Reynolds number and high concentration of Nano fluid, because at high Reynolds number wall temperature is decreases and pressure drop is increased. Y. He, [15] investigated the thermal performance of air-water heat exchanger using TiO_2Nano fluid. And found that the heat transfer coefficient is increases with increasing Reynolds number at constant volume of friction up to 0.6%. D.P. Kulkarni [16] investigated heat transfer and fluid dynamic performance of nano fluids of silicon dioxide (SiO2) nanoparticles suspended in a 60:40 (% by weight) ethylene glycol and water (EG/water) mixture and observed increase in heat transfer coefficient due to nano fluids for various volume concentrations and loss in pressure was observed with increasing nanoparticle volume concentration. S.Z. Heris, et.al. [17] investigated the flow and heat transfer characteristic of spiral pipe heat exchanger using different type of Nano fluid with different concentration as Al_2O_3 water, TiO_2-water, CuO-water Nano fluid with 1%, 1% and 3% concentration respectively. And observed that the heat transfer enhanced 28% at 0.8% concentration of Nano fluid, due to, increased shear stress of Nano fluid. Bobbo S. et.al, [18] Investigated the friction factor and heat transfer rate of CuO Water and Al_2O_3 water and observed that the increase of Nusselt number with increasing the Reynolds number and concentration decreases the friction factor of Nano fluid. As compared the CuO-water and better enhancement as Al_2O_3 water Nano fluids by using CuO-water Nano fluid. Mishra [19-20] observed the overall heat transfer coefficient of nano fluids increases significantly with prandle number. For both nano fluids the overall heat transfer coefficient increases with nanoparticle concentration compared to the base fluid. The experimental results for the Nusselt number of Al_2O_3/water and TiO_2/water nano fluids and Results show that at 0.5 vol. % of Al_2O_3. Nano particles and at 0.3 vol. % of TiO_2 nanoparticles. Considerable enhancement in convective heat transfer coefficient of the nano fluids as compared to the base fluid, ranging from 2% to 50%. Moreover, the results indicated that with increasing nanoparticles concentration and nano fluid temperature, the convective heat transfer coefficient of nano fluid increases. The Nano fluid shows greater heat transfer coefficient compare with water and increase the inlet liquid temperature decreases the overall heat transfer coefficient. The increasing mass flow rate of brine increases Re and overall heat transfer coefficient.

2. Result and Discussion

The main heading should be A computational program has been developed to solve nonlinear equation of vapour compression refrigeration cycle by considering same performance parameter of the VCRS model (i.e. variation of mass flow rate of brine from 0.006 kg/sec to 0.010 kg/sec for fixing 0.008 condenser water flow rate , mass flow rate of water in condenser from 0.006 to 0.010kg/sec by fixing 0.008 kg/sec of brine mass flow rate at pressure of 2 bars , with 0.000010 m nano particle size mixed in the brine water, the theoretical analysis has been done using EES software for nano fluid (nanoparticle mixed with R718) flowing in secondary circuit and eco friendly refrigerant in primary circuit of VCRS and results are given below.

Table 1 shows the enhancement in C.O.P using different R-404a ecofriendly refrigerant of VCRS and maximum COP is found 14.8% using Cuo nano particles 10.7% using TiO2 and 11.5% using Al_2O_3 for 5% of Volume Fraction (ϕ). Although by varying Volume Fraction (ϕ) the first law performance is increased from 3.8% to 11.5% using Al_2O_3 and 2.6% to 10.5% and 5.2% to 14.8% using Cuo nano materials as compared without nano particles mixed in the brine water flowing in the secondary circuit of evaporator

Table 1: Enhancement in C.O.P using different nano refrigerant of Vapour compression Refrigeration System [21]

Refrigerant		R404a	
Nano particle	Volume Fraction (ϕ)	C.O.P.	% Enhancement
	0	2.379	-
Al_2O_3.	0.01	2.47	3.8%
	0.02	2.524	6.1%
	0.03	2.536	6.6%
	0.04	2.558	7.5%
	0.05	2.653	11.5%
TiO_2	0.01	2.44	2.6%
	0.02	2.498	5.0%
	0.03	2.548	7.1%
	0.04	2.594	9.0%
	0.05	2.634	10.7%
CuO	0.01	2.502	5.2%
	0.02	2.572	8.1%
	0.03	2.63	10.6%
	0.04	2.683	12.8%
	0.05	2.73	14.8%

Table 2 shows the enhancement in C.O.P using different R-407c ecofriendly refrigerant of VCRS and maximum COP is found 14.8% using CuO nano particles 10.7% using TiO_2 and 11.5% using Al_2O_3 for 5% of Volume Fraction (ϕ). Although by varying Volume Fraction (ϕ) the first law performance is increased from 2.9% to 9.4% using TiO_2 and 3.2% to 9.9% Al_2O_3 and 4.4% to 12.1% using Cuo nano materials as compared without nano particles mixed in the brine water flowing in these condary circuit of evaporator.

Table: 2 Enhancement in second law using different nano refrigerant of Vapour compression Refrigeration System [21]

Refrigerant		R407C	
Nano particle	Volume Fraction (ϕ)	C.O.P.	% Enhancement
	0	2.556	-
Al_2O_3	0.01	2.637	3.2%
	0.02	2.702	5.7%
	0.03	2.755	7.8%
	0.04	2.787	9.0%
	0.05	2.808	9.9%
TiO_2	0.01	2.629	2.9%
	0.02	2.685	5.0%
	0.03	2.733	6.9%
	0.04	2.765	8.2%
	0.05	2.795	9.4%
CuO	0.01	2.669	4.4%
	0.02	2.748	7.5%
	0.03	2.806	9.8%
	0.04	2.842	11.2%
	0.05	2.864	12.1%

Table 3 shows experimentally the enhancement in C.O.P using different R-404a ecofriendly refrigerant of VCRS and maximum COP is found 3.817 using CuO and 3.691 using TiO_2 and 3.748 using Al_2O_3. Similarly as volume fraction (ϕ) is increased the first law performance is increased maximum using R134a and minimum as using ecofriendly refrigerant R404a. The % improvement is found in Table-4 from 21.3% in case of Volume Fraction (ϕ) is 1% to 35.4% using R-134a and CuO as nano material and 16.6% to 30.9 % using TiO_2 and 22.8% to 32.9% using Al_2O_3.

Table: 3 Enhancement in C.O.P using different nano refrigerant of Vapour Compression Refrigeration System [22]

Refrigerant		R134a	R404A	R407c
Nano particle	Volume Fraction (ϕ)	C.O.P.	C.O.P.	C.O.P.
	0	2.82	2.379	2.556
CuO	0.01	3.421	2.47	2.637
	0.02	3.604	2.524	2.702
	0.03	3.701	2.536	2.755
	0.04	3.717	2.558	2.787
	0.05	3.817	2.653	2.808
TiO_2	0.01	3.287	2.44	2.629
	0.02	3.488	2.498	2.685
	0.03	3.603	2.548	2.733
	0.04	3.666	2.594	2.765
	0.05	3.691	2.634	2.795
Al_2O_3	0.01	3.464	2.502	2.669
	0.02	3.616	2.572	2.748
	0.03	3.681	2.63	2.806
	0.04	3.725	2.683	2.842
	0.05	3.748	2.73	2.864

Table-4, showing the enhancement in first law efficiency in terms of COP using different ecofriendly refrigerants of Vapour Compression Refrigeration System and maximum COP is found 14.8% using ecofriendly R404a refrigerant and Cuo nano particles, 10.7% using TiO_2 and 11.5% using Al_2O_3 for 5% of Volume Fraction (ϕ). Although by varying Volume Fraction (ϕ) the first law performance is increased from 3.2% to 9.9% using ecofriendly R407c refrigerant and Cuo nano particles and from 2.9% to 9.4% using R407c and TiO_2 as nano particles and 3.2% to 9.9% Al_2O_3 as compared to without nano particles mixed in the brine water flowing in these condary circuit of evaporator

Table: 4 Show % enhancement in C.O.P using different nanorefrigerant of Vapour Compression Refrigeration System [23]

Refrigerant		R134a	R404A	R407c
Nano particle	Volume Fraction (ϕ)	% Enhance ment	% Enhance ment	% Enhance ment
	0	-	-	-
CuO	0.01	21.3%	3.8%	3.2%
	0.02	27.8%	6.1%	5.7%
	0.03	31.2%	6.6%	7.8%
	0.04	31.8%	7.5%	9.0%
	0.05	35.4%	11.5%	9.9%
TiO_2	0.01	16.6%	2.6%	2.9%
	0.02	23.7%	5.0%	5.0%
	0.03	27.8%	7.1%	6.9%
	0.04	30.0%	9.0%	8.2%
	0.05	30.9%	10.7%	9.4%
Al_2O_3	0.01	22.8%	5.2%	4.4%
	0.02	28.2%	8.1%	7.5%
	0.03	30.5%	10.6%	9.8%
	0.04	32.1%	12.8%	11.2%
	0.05	32.9%	14.8%	12.1%

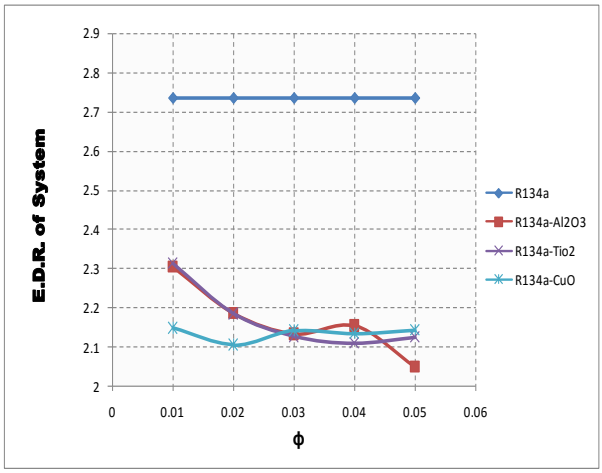


Figure: 1 Variation of Exergy destruction ratio with volume fraction (ϕ) of Vapour Compression Refrigeration System with R134a using different nano particles [24]

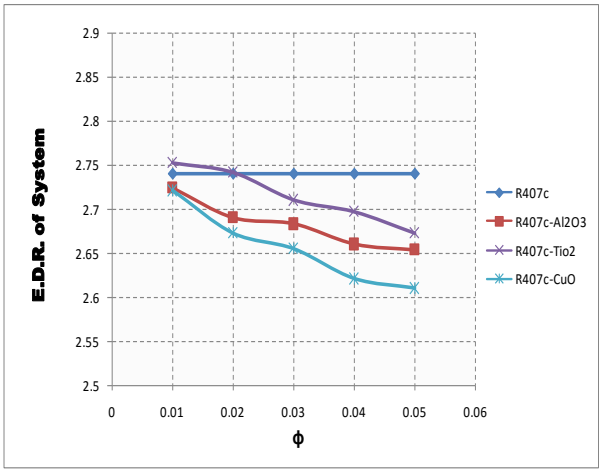


Figure: 2 Variation of Exergy Destruction ratio with volume fraction (ϕ) of Vapour Compression Refrigeration System with R407c using different nano particles [24]

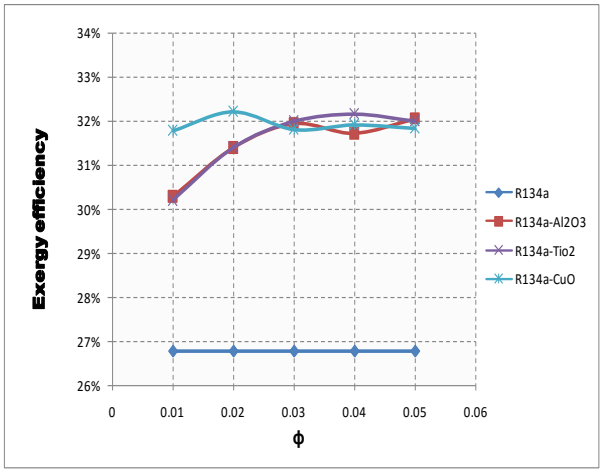


Figure: 4 Variation of Exergy Efficiency with volume fraction (ϕ) of Vapour Compression Refrigeration System with R134a using different nano particles [25]

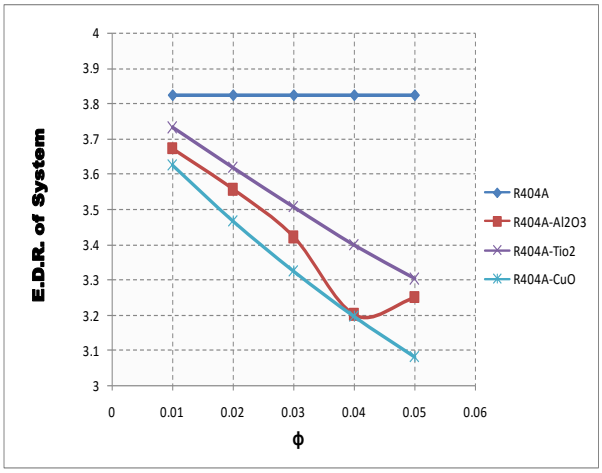


Figure: 3 Variation of Exergy destruction ratio with volume fraction (ϕ) of VCRS with R404A using different nano particles [24]

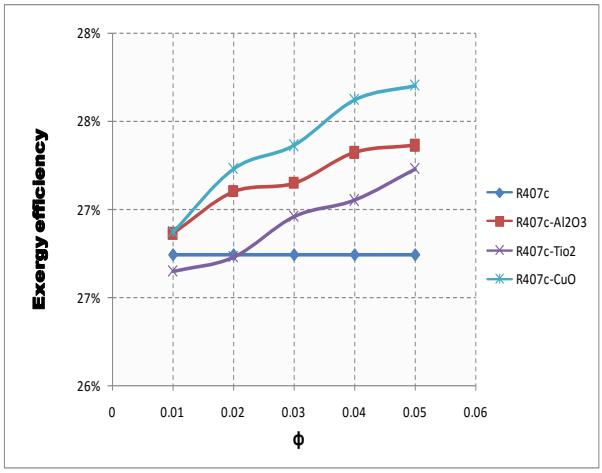


Figure: 5 Variation of Exergy Efficiency with volume fraction (ϕ) of Vapour Compression Refrigeration System with R407c using different nano particles [25]

Fig 1-3 shows that the Exergy .Destruction Ratio (EDR) of VCRS (i.e. which is a ratio of exergy losses in the system to the exergy of output is decreasing as volume fraction ratio is increasing) and will reduce by using nano fluid (nanoparticle based nano refrigerant) and thus improving second law efficiency

The Effect of nanoparticle volume fraction (ϕ) on the second law efficient using R134a as ecofriendly refrigerants in primary circuit of evaporator and with three type of nano materials of 0.000010(m) diameter is shown in Fig-4. As volume fraction Ratio is increasing from 0.01 to 0.05, the exergetic efficiency is increased.

Similarly The Effect of nanoparticle volume fraction (ϕ) on the second law efficiency using R407c and R404a as ecofriendly refrigerants in primary circuit of evaporator and with three type of nano materials of 0.000010(m) diameter is shown in Fig-5-6 respectively. As volume fraction Ratio is increasing from 0.01 to 0.05, the exergetic efficiency is also increasing sharply. The similar trend is also observed in case of using nano materials.

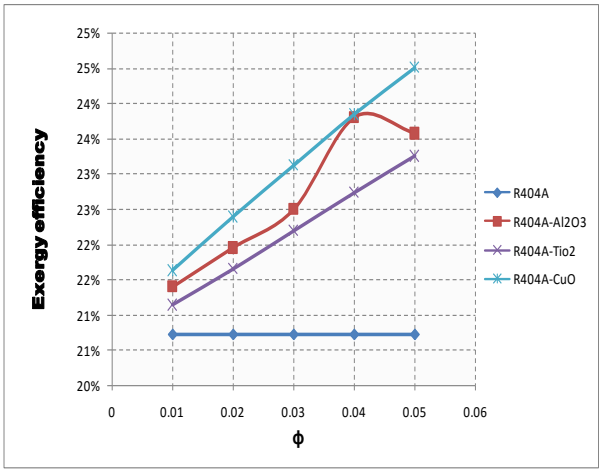


Figure: 6 Variation of Exergy Efficiency with volume fraction (ϕ) of Vapour Compression Refrigeration System with R404A using different nano particles [25]

It was observed that the 2nd Law efficiency will increase by using nano refrigerant. The 2nd law efficiency of vapour compression refrigeration system using nano refrigerant R134a/CuO is much higher than the other nano refrigerant having value approx 32%. A computational program has been developed to solve nonlinear equation of vapour compression refrigeration cycle Considering same geometric parameter of the VCRS model theoretical analysis has been done using EES software for nano fluid (nanoparticle mixed with R718) flowing in secondary circuit and eco friendly refrigerant in primary circuit of VCRS and Theoretical result of eight different ecofriendly refrigerants and using Al_2O_3 at 5 vol % nano fluid in secondary circuit as obtained from model is shown in Table-5.

Table 5 Enhancement in C.O.P in Vapour Compression Refrigeration System using Al_2O_3at 5 vol % nano fluid in Secondary circuit [26]

For Al_2O_3at volume fraction of 5 vol %		
Refrigerant	First law efficiency C.O.P.	% Improvement in first law efficiency (C.O.P.)
R134a	3.406	17.98%
R404A	3.0635	16.00%
R407c	3.110488	17.20%
R-152a	3.4102	18.00%
R-600	3.3402	17.20%
R-600a	3.466	19.90%
R-125	3.033016	14.80%
R-290	3.54312	19.70%

3. Conclusions

The research work presented in this thesis work following conclusion have been drawn.

1. Use of nanoparticles enhances thermal performance of vapour compression refrigeration system from 8 to 35 % using nano refrigerant in primary circuit.
2. Use of nanoparticles enhances the thermal performance of vapour compression refrigeration system from 7 to 19 % using nano fluid in secondary circuit.
3. Maximum enhancement in performance was observed using R134a/ Al_2O_3 nano refrigerant in primary circuit and water in secondary circuit of VCRS.
4. Lowest enhancement in performance was observed using R404Aa/TiO_2 nano refrigerant in primary circuit and water in secondary circuit of VCRS.

References

[1] Kapil Chopra .V.Sahni and R.S Mishra (2013)*Energetic and Exergetic Based Comparison Multiple Evaporators with Compound Compression and Flash Intercooler with Individual or Multiple Throttle Valves International Journal of Advance Research & Innovations (IJARI-Vol-1) ISSN No: 2347-3258, pp-73-81.

[2] Kapil Chopra .V.Sahni .R.S Mishra*(2014) "Thermodynamic Analysis of Multiple evaporators vapour compression Refrigeration Systems with R-410a, R290, R1234yf, R502, R404a, R152a and R134a " International Journal of Air conditioning and Refrigeration (Ms. No: IJACR-D-13-00043R1) , Paper Vol-22 No-1, 145-158.

[3] Choi, S. U. S. (1995). Enhancing thermal conductivity of fluids with nanoparticles, in *Developments and Applications of Non-Newtonian Flows* FED–31/MD-66:99–105.

[4] Jwo et.al, 2009. Effect of nano lubricant on the performance of Hydrocarbon refrigerant system. J. Vac. Sci. Techno. B, Vol.27, No. 3, pp. 1473-1477.

[5] K.S. Hwang, S.P. Jang, S. U. S. Choi, (2009) Flow and convective heat transfer characteristics of water-based Al_2O_3 nanofluids in fully developed laminar flow regime, Int. J. Heat Mass Transf. 52 193-199.

[6] Joaquin Navarro, Francisco, Angel, (2013). Experimental analysis of internal heat exchanger influence on vapour compression system performance working with R1234yf as drop in replacement of R134a. Applied thermal Engineering, 59, 153-161.

[7] Murshed S. M. S., K. C. Leong, and C. Yang (2005). Enhanced thermal conductivity of TiO_2-water based nanofluids, *Int. J. Therm. Sci.*, 44: 367–373.

[8] Hao Peng et.al., (2010). Nucleate pool boiling heat transfer characteristics of refrigerant/oil mixture with diamond nano parti cles. International Journal of Refrigeration, Vol.33, pp. 347-358.

[9] Henderson et al. (2010) Experimental analysis on the flow boiling heat transfer of R134a based nanofluids in a horizontal tube. IJHMT , Vol. 53, pp. 944-951.

[10] Xuan, Y., and Q. Li (2003). Investigation on convective heat transfer and flow features of nanofluids, *J. Heat Transfer*, 125: 151–155.

[11] Wang RX, et.al. [2003.] A refrigerating system using HFC134a and mineral lubricant appended with N- TiO_2(R) as working Fluids. In: Proceedings of the 4th international symposium on HAVC, Tsinghua University.

[12] Lee K, Hwang YJ, [2009]Performance evaluation of nano-lubricants of fullerene nanoparticles in refrigeration mineral oil. Curr Appl Phys;9:128–131.

[13] Wien, D., and Y. Ding (2004). Experimental investigation into convective heat transfer of nanofluids at the entrance region under laminar flow conditions, *Int. J. Heat Mass Transfer*, 47: 5181–5188.

[14] I.M. Mahbubul , A.Saadah (2015) Thermal performance analysis of Al_2O_3 R134a nanorefrigerant , international journal of heat and mass transfer 85 1034-1040.

[15] Y. He, (2007) Heat transfer and flow behavior of aqueous suspensions of TiO_2 nanoparticles (nanofluids) flowing upward through a vertical pipe, Int. J. Heat Mass Transf. 50 2272-2281.

[16] D.P. Kulkarni, (2008) Convective heat transfer and fluid dynamic characteristics of SiO_2-ethylene glycol/water nanofluid, Heat Transf. Eng. 29 (12) 1027-1035.

[17] S.Z. Heris, S.G. Etemad, M.N. Esfahany(2006), Experimental investigation of Al_2O_3 nanofluids laminar flow convective heat transfer, Int. Commun. Heat Mass Transf. 33 529535.

[18] Bobbo S. et.al, (2010). Influence of nanoparticles dispersion in POE oils on lubricity and R134a solubility. International Journal of Refrigeration, Vol.33, pp. 1180-1186.

[19] Lee K, Hwang YJ, Cheong S, Kwon L, Kim S, Lee J. Performance evaluation of nano-lubricants of fullerene nanoparticles in refrigeration mineral oil. Curr Appl Phys 2009;9:128–131.

[20] R.S. Mishra (2015) Irreversibility Reduction in Vapour Compression Refrigeration Systems Using Al_2O_3 Nano Material Mixed in R718 as Secondary Fluid s" International journal of Advance Research and Innovation Vol-3, Issue 2 (June-2015), pp. 321-327.

[21] R. S. Mishra (2015) "Performance Evaluation of Ecofriendly Refrigerants in the Low Temperature Circuit in Terms of First Law and Second Law Efficiency of Three Stages Cascade Vapour Compression Refrigeration of Biomedical Applications" International journal of Advance Research and Innovation Vol-3, Issue 2 (June-2015), pp. 332-339.

[22] R.S.Mishra (2015) Methods for Improving Thermodynamic Performance of Vapour Compression Refrigeration Systems Using Nano Mixed Ecofriendly Refrigerants in Primary Circuit and Comparsion with Nano Particles Mixed Wih R718 Used in Secondary Evaporator Circuit and Ecofriendly Refrigerants in Primary Circuit for Reducing Global Warming and Ozone Depletion, International journal of Advance Research and Innovation Vol-3, Issue 2 (June-2015), pp. 433-439.

[23] R. S. Mishra(2015) Modeling of Natural Convection Non Reversible Single Pass Pressurized and Non Pressurized Solar Hot Water Systems for Domestic Applications" International journal of Advance Research and Innovation , ISSN. No:2347 – 3258, Vol-3, Issue 3 (Sept-2015), pp. 451- 458.

[24] R. S. Mishra(2015) " Energy-Exergy Performance Comparison of Vapour Compression Refrigeration Systems using Three Nano Materials Mixed in R718 in the Secondry Fluid and Ecofriendly Refrigerants in the Primary Circuit and Direct Mixing of nano Materials in the Refrigerants" International journal of Advance Research and Innovation Vol-3, Issue 3 (Sept-2015), pp. 471-477.

[25] R. S. Mishra(2015) "Vapour Compression Refrigeration Technology for Sustainable Development" International journal of Advance Research and Innovation Vol-3, Issue 4 (Dec-2015)

[26] R. S. Mishra (2015) Thermodynamic performance comparison using HFO-1234yf and hfo-1234ze in the high temperature cascade refrigeration systems and ecofriendly refrigerants in low temperature applications, International journal of Advance Research and Innovation Vol-3, Issue 4 (Dec-2015).

[27] R. S. Mishra(2015) Energy-exergy performance comparison of vapour compression refrigeration systems using three nano materials mixed in r718 as secondry fluid and r-1234yf and r-1234ze ecofriendly refrigerants in the primary circuit International journal of Advance Research and Innovation Vol-3, Issue 2 (June-2015), pp. 321-327

[28] R.S. Mishra (2013) "Irriversibility Analysis of Multi-Evaporators Vapour Compression Refrigeration Systems Using New and Refrigerants: R134a, R290, R600, R600a, R1234yf,R502, R404a and R152a and R12, R502" International Journal of Advance Research & Innovations International Journal of Advance Research & Innovations (IJARI-Vol-1) , ISSN No: 2347-3258 , PP-180-193.

Near Field Enhancement in a Hollow Flower Shaped Nanoantenna

Parul Goyal[1], Nishant Shankhwar[1], Yogita Kalra[1]*

[1]*TIFAC-Centre of Relevance and Excellence in Fiber Optics and Optical Communication, Department of Applied Physics, Delhi Technological University, Delhi-110042, India*

**E-mail-dryogitakalra@gmail.com*

Abstract: In this paper, a metallic hollow flower shaped nanoantenna has been designed to obtain a near field enhancement in the feed gap of nanoantenna in the visible vision. The modeling of the nanoantenna has been done using COMSOL Multiphysics software.

OCIS codes: (260.5740) Resonance; (290.0290) Scattering

1. Introduction

Optical nanoantenna is a device which converts the free propagating optical radiation into localized energy and hence it has the ability to enhance the interaction of light with nanoscale matter [1-2]. Metallic nanoparticles have the ability to control and manipulate the optical fields for enhancing the performance of light sensing, photo detection, heat transfer, spectroscopy, microscopy, solar energy harvesting and light emission [3-9] by virtue of their surface plasmon resonances [10].

In this paper, a metallic hollow flower shaped nanoantenna, made using gold, has been designed in the visible region. As the main aim behind designing of this nanoantenna is to obtain the field enhancement in the feed gap of nanoantenna, the feed point is used at the centre of nanoantenna where the entire incident field is localized and thus gives a large electric field enhancement at the feed gap of the nanoantenna. The hollow structure is used to reduce the absorption losses in metal. The designed nanoantenna has a resonant wavelength of 500 nm.

2. Design of the flower shaped nanoantenna

The flower shaped nanoantenna consists of four antenna arms of equal length of 180 nm and a feed gap of 10 nm between any pair of nanoantennas as shown in Figure 1(a) and 1(b). The nanoantenna is modeled through finite element method (FEM) using COMSOL Multiphysics software. A perfectly matched layer is used to reduce the spurious reflections.

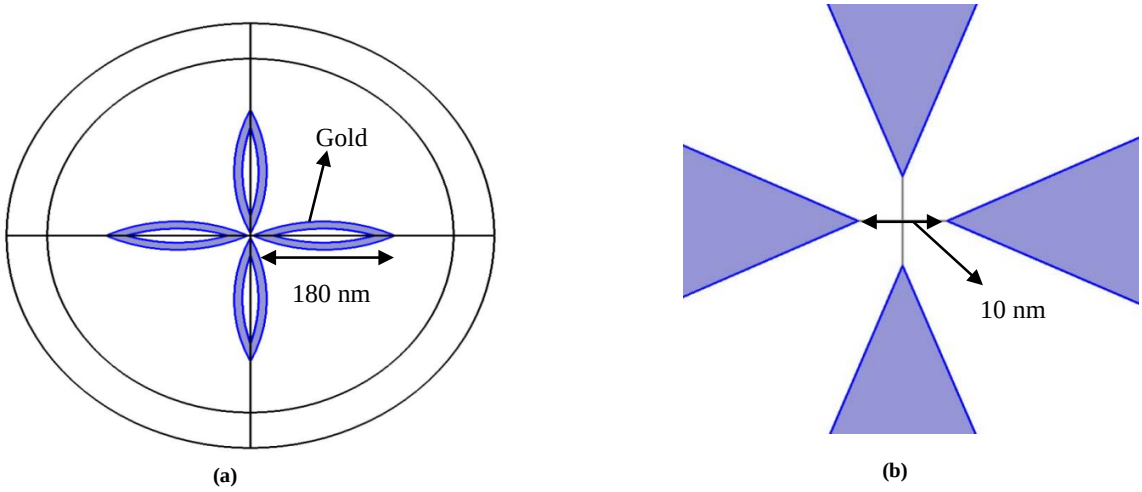


Figure 1 (a) Design of hollow flower shaped nanoantenna; **(b)** Zoomed-in design in which centre feed gap is clearly visible

3. Results and Discussion

An input power is made incident on the nanoantenna and the scattering cross-section and the field enhancement in the feed gap of nanoantenna have been analyzed as shown in Figure 2 and 3 respectively. From Figure 2, it is clear that resonant wavelength is 500 nm at which scattering cross-section is maximum. An electric field enhancement of 70 times is obtained in the feed gap of nanoantenna at the resonant wavelength as shown in figure 3.

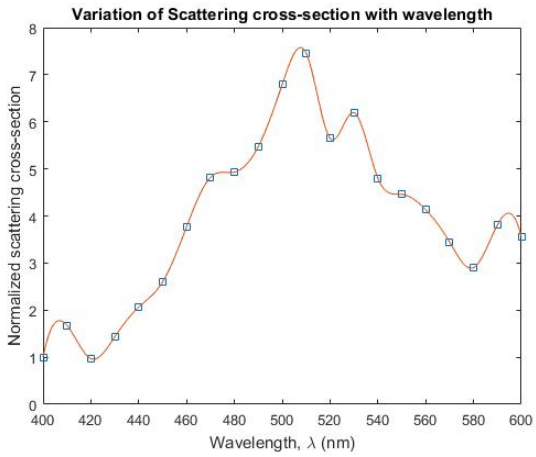


Figure 2: Variation of normalized scattering cross-section with wavelength.

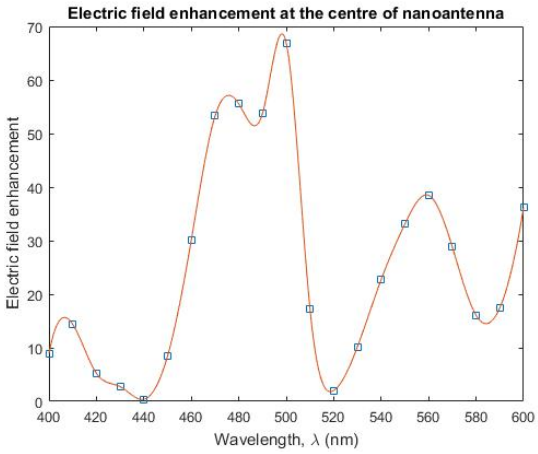


Figure 3: Variation of electric field enhancement at the centre of nanoantenna with wavelength.

4. Conclusion

A hollow flower shaped nanoantenna has been successfully designed. The variation of scattering cross-section and field enhancement at the centre of the nanoantenna with wavelength has been analyzed at the resonant wavelength of 500 nm. The designed nanoantenna has promising applications in solar energy harvesting as its resonant wavelength is 500 nm at which solar radiation is maximum.

5. References

[1] A.E. Krasnok *et al.*, "Optical nanoantennas," *Physics-Uspekhi*, vol. 56, no. 6, pp. 539–564, Jun. 2013.

[2] Bharadwaj, P., Deutsch, B., and Novotny, L., \Optical antennas," Advances in Optics and Photonics 1(3), 438{483 (2009).

[3] Novotny, L. & Stranick, S.J. Near-field optical microscopy and spectroscopy with pointed probes. Ann. Rev. Phys. Chem 57, 303-331 (2006).

[4] Tang, L. *et al.* Nanometre-scale germanium photodetector enhanced by a near-infrared dipole antenna. *Nature Photon.* **2,** 226–229 (2008).J. T. Mok and B. J. Eggleton, "Expect more delays," Nature, **433**,811–812 (2005).

[5] Cao, L., Park, J.S., Fan, P., Clemens, B. & Brongersma, M. L. Resonant Germanium nanoantenna photodetectors. Nano Lett. 10, 1229–1233 (2010).

[6] Pillai, S., Catchpole, K., Trupke, T. & Green, M. Surface plasmon enhanced silicon solar cells. J. Appl. Phys. 101, 093105 (2007).

[7] Anker, J. N. *et al.* Biosensing with plasmonic nanosensors. *Nature Mater.* **7,** 442–453 (2008).

[8] DeWilde, Y. *et al.* Thermal radiation scanning tunnelling microscopy. *Nature* **444,** 740 (2006).

[9] Ahmed M A Sabaawi. Nanoantennas for solar energy harvesting. PhD thesis, Newcastle University, 2015

[10] A.W. Powell, M. B. Wincott, A. A. R. Watt, H. E. Assender, and J. M. Smith, "Controlling the optical scattering of plasmonic nanoparticles using a thin dielectric layer," J. Appl. Phys. 113, 184311 (2013).

This article has been accepted for inclusion in a future issue of this journal. Content is final as presented, with the exception of pagination.

Numerical Investigation of Short-Channel Effects in Negative Capacitance MFIS and MFMIS Transistors: Subthreshold Behavior

Girish Pahwa, *Student Member, IEEE*, Amit Agarwal, and Yogesh Singh Chauhan, *Senior Member, IEEE*

***Abstract*— We present a detailed TCAD analysis of the impact of length scaling and the associated short-channel effects in the subthreshold regime of the two classes of double-gate negative capacitance transistors (NCFETs): metal–ferroelectric–metal–insulator–semiconductor (MFMIS) and metal–ferroelectric–insulator–semiconductor (MFIS). Our TCAD formulation takes into account both the out-of-plane and in-plane components of ferroelectric polarization. Contrary to the conventional FETs, both the configurations of NCFETs exhibit increase in the threshold voltage (V_t), reduction in subthreshold swing (SS), and drain-induced barrier lowering with scaling due to inner and outer fringing electric field effects. The existence of the internal metal layer causes these effects to be significantly higher in the MFMIS structure than the MFIS, where the fringing field impact remains confined to the channel edges only. The above-mentioned unconventional short-channel effects increase with the inclusion of spacer regions of high permittivity in both the MFMIS and MFIS devices. We also analyze the impact of source/drain doping on fringing field coupling to the ferroelectric and find that a higher doping of these regions improves the subthreshold characteristics of NCFETs, in contrast to conventional FETs.**

***Index Terms*— Ferroelectric, metal–ferroelectric–insulator–semiconductor (MFIS), metal–ferroelectric–metal–insulator–semiconductor (MFMIS), negative capacitance, negative capacitance transistor (NCFET), short-channel effects, TCAD.**

I. Introduction

THE conventional CMOS technology scaling persistent for the last several decades is now being expected to discontinue. The Boltzmann limit of 60-mV/decade subthreshold swing at room temperature hinders the reduction of the supply voltage with scaling, which can cause the chip power densities to reach undesirably high values [1]. Therefore, many alternate steep-slope devices are being explored to enable ultralow voltage operation. Among these, negative capacitance transistor (NCFET) has emerged as a very promising candidate that can offer a potential solution to the above-mentioned issues and is being widely researched upon. NCFET involves an additional layer of a ferroelectric material in the gate-stack of a conventional FET, which acts as a negative capacitor and, thus, provides a voltage amplification for the channel surface potential [2]. Mainly, two classes of NCFET structures have been demonstrated in the experimental studies: one with a floating metal layer between the ferroelectric and internal gate oxide [metal–ferroelectric–metal–insulator–semiconductor (MFMIS)] [3]–[7] and the other without this metal layer [metal–ferroelectric–insulator–semiconductor (MFIS)] [8]–[10], as shown in Fig. 1. The presence of floating metal gate in MFMIS masks the nonuniformity in potential along the source-to-drain direction resulting from the application of drain bias. This, in turn, results in an almost uniform polarization (out-of-plane, along y-axis) in the ferroelectric material. On the other hand, both the potential at the ferroelectric–oxide interface and polarization vary in the longitudinal direction in MFIS structure. In addition, electric field from the drain also induces a nonnegligible in-plane polarization (along x-axis).

Previous TCAD works have primarily focused only on MFMIS structure [11]–[16]. Recently, Dong and Guo [17] and Saha *et al.* [18] performed numerical simulations for

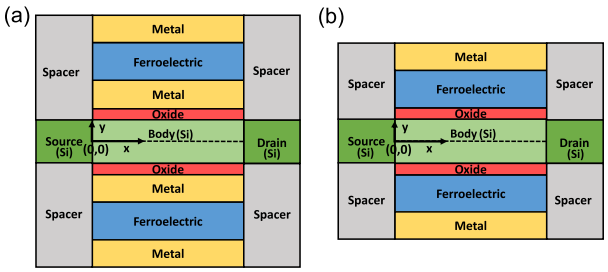


Fig. 1. Two classes of DG NCFET structures. (a) MFMIS. (b) MFIS. In the MFMIS, the floating metal gate between ferroelectric and oxide maintains a uniform potential at their interface. In the MFIS, however, potential distribution at the interface remains nonuniform.

Manuscript received February 16, 2018; revised June 24, 2018 and August 20, 2018; accepted September 11, 2018. This work was supported by the Department of Science and Technology, Government of India and Berkeley Device Modeling Center. The review of this paper was arranged by Editor A. Schenk. *(Corresponding author: Girish Pahwa.)*

G. Pahwa and Y. S. Chauhan are with the Nanolab, Department of Electrical Engineering, IIT Kanpur, Kanpur 208016, India (e-mail: girish@iitk.ac.in; chauhan@iitk.ac.in).

A. Agarwal is with the Department of Physics, IIT Kanpur, Kanpur 208016, India.

Color versions of one or more of the figures in this paper are available online at http://ieeexplore.ieee.org.

Digital Object Identifier 10.1109/TED.2018.2870519

0018-9383 © 2018 IEEE. Personal use is permitted, but republication/redistribution requires IEEE permission.
See http://www.ieee.org/publications_standards/publications/rights/index.html for more information.

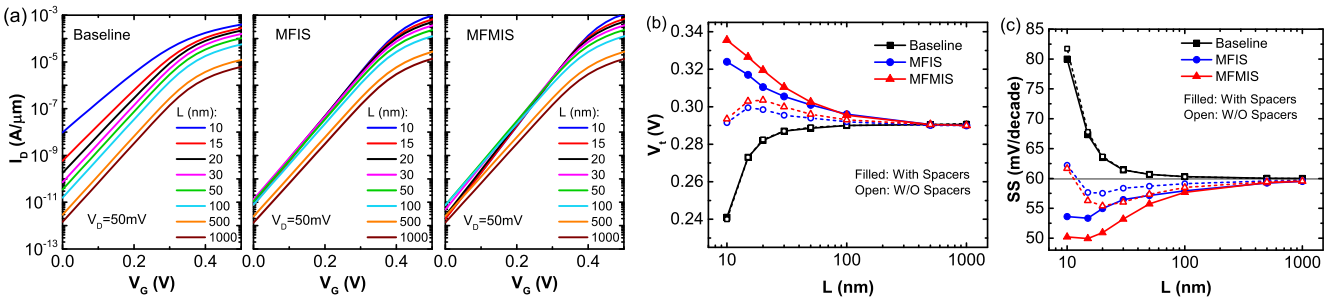


Fig. 2. Impact of length scaling on subthreshold characteristics at low $V_D = 50$ mV. (a) I_D–V_G characteristics of baseline, MFMIS, and MFIS FETs. Comparison of (b) threshold voltage and (c) subthreshold swing of these devices with and without spacers. Both the NCFETs exhibit higher V_t and lower SS as compared to the baseline FET due to source and drain electric field coupling to the ferroelectric. These effects are more significant in NCFETs with spacers.

MFIS FET but did not include the impact of channel length scaling. Moreover, the latter employs the Landau model only in the out-of-plane polarization component, which is not suitable for large ferroelectric thicknesses. Ota *et al.* [19] reported on TCAD simulation of both the NCFETs; however, scaling behavior and short-channel effects were discussed only for MFMIS NCFET. In our earlier works, we analyzed and compared the performance of the two NCFETs with long channels, using analytical modeling [20] or segmentation approach [21]. Since the variation of interface potential in MFIS NCFET becomes even larger with length scaling, it is important to recognize the resulting differences in its characteristics compared to MFMIS, which has not been thoroughly discussed in the literature. In this paper, we investigate the impact of channel length scaling in the subthreshold regime of device operation of both MFMIS and MFIS double-gate (DG) NCFETs. In addition, we also explore the impact of source/drain (S/D) doping in short-channel NCFET devices.

II. Numerical Simulation Methodology

We use COMSOL Multiphysics to perform all the numerical simulations presented in this paper [22]. 2-D electrostatics is used to simulate both the silicon and ferroelectric regions in the n-type DGNCFET structures shown in Fig. 1. For the silicon part, the Fermi–Dirac statistics is used for electrons with a drift-diffusion formulation for electrical transport. The high field velocity saturation of electrons in the channel is modeled using Caughey–Thomas mobility [23], assuming a low-field mobility of 300 cm^2/Vs for electrons in our undoped ultrathin silicon body (=5 nm) structure [24]–[26]. Note that the low-field mobility value may depend on several factors, such as silicon body thickness, applied stress via source–drain regions, channel orientation and doping, effective oxide thickness, and quality of the gate-stack. Different mobility values have been reported in the literature [27]–[30]. This, however, does not affect analysis and conclusions of this paper. To achieve accurate and reliable carrier transport in short-channel devices, the carrier saturation velocity is also assumed to have a length dependence of the form: $v_{\text{sat}} = a + b/L^c$ [31], where L is the gate length, and a, b, and c are empirical parameters, whose values have been obtained in [31] by fitting against the Monte Carlo simulations. All the Caughey–Thomas model parameters are taken from [31]. Unless otherwise stated, the following parameters are used for the baseline DG field effect transistor (DGFET) structure: channel width (W) = 1 μm, interfacial oxide (SiO_2) thickness = 0.6 nm, S/D lengths = 5 nm, gate metal work function (ϕ_m) = 4.45 eV, S/D doping = 10^{20} cm^{-3} with abrupt profiles at junctions, and spacer material relative permittivity $\varepsilon_{\text{spr}}/\varepsilon_0$ = 3.9. The short S/D lengths have been chosen to reduce the impact of series resistances. The thicknesses of the external and internal gate (in case of MFMIS) metals are taken to be 10 and 5 nm, respectively.

For the ferroelectric region, 2-D Landau–Devonshire equation [13], [32] is used, taking into account both the out-of-plane and in-plane polarizations as

$$\text{out of plane,} \quad E_y = \alpha P_y + \beta {P_y}^3 \tag{1}$$

$$\text{in plane,} \quad E_x = \alpha P_x + \beta {P_x}^3 \tag{2}$$

where E and P denote electric field and polarization, respectively, and α and β are ferroelectric material-dependent constants. $\alpha = -2.06 \times 10^9$ m/F and $\beta = 1.4 \times 10^{11}$ $\text{m}^5/(\text{Coul}^2\ \text{F})$ for a Gd-doped HfO_2 are used in all the simulations [33] with a ferroelectric thickness (t_{fe}) of 7 nm (unless otherwise stated). In (1) and (2), we have neglected coupling among ferroelectric dipoles, which is a reasonable assumption for Gd:HfO_2 material [33]. Different boundary conditions are applied to implement the MFIS and MFMIS configurations. In the MFIS structure, continuity of normal components of displacement vectors is used at the oxide/spacer-ferroelectric boundaries. For the MFMIS structure, the internal metal gate acts as a floating terminal, whose boundary conditions are stated in Fig. 3(c).

III. Impact of Scaling in Off Regime

In this section, we discuss the impact of channel length scaling on subthreshold characteristics of the two different NCFETs and baseline FETs for low and high values of drain bias.

A. Short-Channel Behavior at Low Drain Bias

Fig. 2(a) shows I_D–V_G characteristics of baseline, MFIS, and MFMIS FETs for different channel lengths at V_D = 50 mV. Both the NCFETs exhibit excellent immunity against

This article has been accepted for inclusion in a future issue of this journal. Content is final as presented, with the exception of pagination.

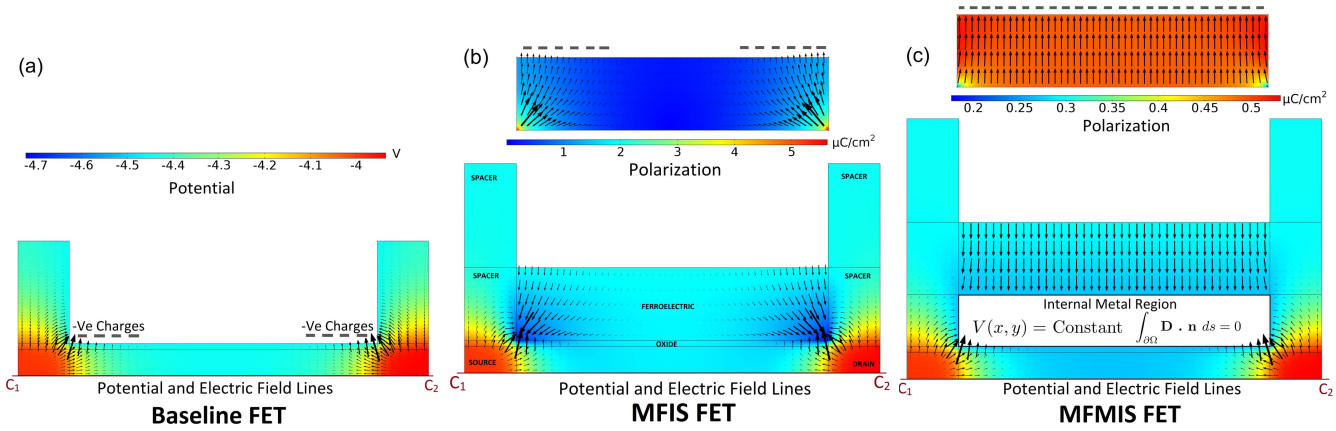


Fig. 3. Potential, electric field lines, and polarization (for NCFETs) distributions in (a) baseline FET, (b) MFIS NCFET, and (c) MFMIS NCFET for $L = 30$ nm at $V_G = 0$ and $V_D = 50$ mV. Potential in this figure is referenced to source-side Fermi level. The external metal gate is not explicitly shown in figures. In NCFETs, the fringing electric field lines emanating from source and drain couple to the ferroelectric and induce an electric polarization and an oppositely oriented electric field. The latter quantities have an approximately uniform distribution inside the ferroelectric in case of MFMIS due to the presence of equipotential internal metal gate. Note that for clarity of figures, different scales of electric field and polarization vector arrows have been used for the three different FETs. Similarly, different scales of these quantities have been used for ferroelectric and semiconductor regions even in the same MFIS or MFMIS NCFET.

short-channel effects for small lengths and offer much lower OFF currents than their baseline counterparts. Fig. 2(b) and (c) depicts the threshold voltage (V_t) and subthreshold swing (SS) as functions of channel length (L) for the two cases of with and without spacers regions. V_t is calculated using constant current method as $V_t = V_G$ for a fixed $I_D = 100$ nA$(2W/L)$. As shown in Fig. 2(b) and (c), NCFETs exhibit a completely opposite behavior to the baseline FET with scaling, except for very small lengths. In general, for NCFETs, V_t increases, while SS decreases with L. In addition, the MFMIS NCFET shows higher V_t and lower SS values compared with the MFIS NCFET. However, for very large lengths, all of the devices converge to the same values. In the following, we explain these trends of V_t and SS in detail.

1) Threshold Voltage Behavior: Before discussing the NCFETs, it is worthwhile to first inspect the behavior of the baseline FET in the OFF-state, i.e., at $V_G = V_S = 0$. We examine 2-D surface plots of potential with electric field lines for baseline FET in a short-channel scenario ($L = 30$ nm) in Fig. 3(a) (only half structure is shown). The effective potential at the gate terminal with respect to the source-side potential is negative for the chosen value of ϕ_m in this paper. As the channel is undoped, the fringing electric field lines from the source and drain dopant ions terminate on the gate metal via both the Si body and outer spacer regions and induce negative charges in the sides. The fringing fields are of a great significance to NCFETs. Fig. 3(b) shows the case of MFIS NCFET. The fringing electric field now directly couples to the ferroelectric and induce bound charge dipoles or a nonzero polarization density in the corners, which, in turn, also produce negative charges on the gate metal. Since the ferroelectric has a negative dielectric permittivity in negative capacitance (NC) region, the electric field lines reverse their direction inside it (usually called depolarizing field). The crowding of electric field lines near the corners of the ferroelectric causes the potential of these regions to become lower than that of the gate terminal, which, in turn,

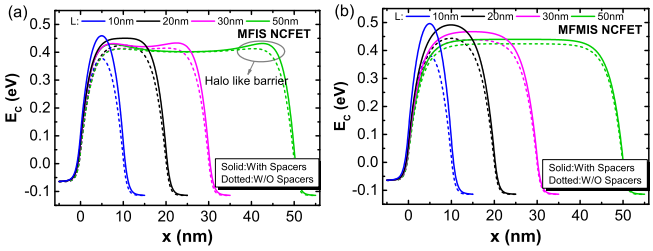


Fig. 4. Conduction band edge energy (E_c) profiles along the center line (C_1C_2) for (a) MFIS and (b) MFMIS FETs for different channel lengths. The reversed depolarizing electric field increases E_c level in NCFETs opposed to the conventional FETs. In MFIS, the ferroelectric impact is significant only in the corners and leads to the formation of halo-like energy barriers, which ultimately coalesce for very small lengths. While in MFMIS, this impact spreads over the full channel length owing to the presence of internal metal. $E_c = -qV - \chi_{si}$, where χ_{si} represents electron affinity of silicon.

increases the energy barrier for the charge carriers near source and drain, as depicted in Fig. 4(a) for the conduction band edge (E_c) along the center cutline C_1C_2 in the x-direction. E_c along the center line has been shown (instead of the oxide–semiconductor interface) since the leakage current along this path is maximum for a DG structure [34]. These energy barriers resemble well-known halo doping-generated barriers [35] and result in an increase in V_t and a reduction in the OFF-state current compared to the baseline FET, as shown in Fig. 2(a). This effect is more pronounced with the spacer regions included since both the inner and outer fringing fields contribute to raise the energy barrier. Moreover, with channel length scaling, the fringing field coupling to the ferroelectric becomes stronger, which increases its polarization and electric field (or the voltage drop across it). This results in further increase in the energy barrier height [see Fig. 4(a)] contrary to a barrier lowering observed with scaling in the conventional FETs and, thus, explains the V_t behavior observed for the MFIS NCFET in Fig. 2(a). However, at very small channel lengths, the fringing electric field starts to affect the entire

ferroelectric region. Therefore, the two side barriers seen in the longer channels coalesce into a single barrier in very short-channel MFIS NCFETs ($L \leq 20$ nm). On further shrinking the channel length, the conventional short-channel effects also become substantial and even result in a reduction in the barrier height in case of the MFIS device without spacers and, accordingly, in V_t, as shown in Figs. 2(a) and 4(a), respectively.

The MFMIS NCFET also exhibits trends similar to those of MFIS with a larger threshold voltage, as shown in Fig. 2(b). The difference arises due to the presence of the internal metal gate, which equalizes the potential everywhere at ferroelectric–oxide interface. Consequently, the fringing field induces an almost uniform vertical polarization and electric field (in the opposite direction), as shown in Fig. 3(c). Due to uniformly distributed electric field, the energy barrier of the entire channel region rises in the MFMIS NCFET, unlike the MFIS NCFET, where it occurs only in the channel sides, as shown in Fig. 4(b). This effectively increases the channel resistance of MFMIS [35], which accounts for its larger V_t than MFIS. With scaling, the energy barrier height increases except for very small lengths ($L < 15$ nm) of MFMIS devices without spacers for which it reduces again for the reasons similar to the case of MFIS structure without spacers. In fact, both of these structures have approximately equal V_t values for these lengths, as evident from their energy barrier profiles in Fig. 4(a) and (b) for $L = 10$ nm. This just follows from the fact that the ferroelectric impact is now over the full channel region even in MFIS structure. However, with spacers, the additional outer fringing field has a much stronger impact on MFMIS compared to MFIS due to the existence of an internal metal layer in the former; thus, the difference between the V_t values of the two continues to exist up to $L = 10$ nm, which is evident in Figs. 2(b) and 4(a) and (b).

2) Subthreshold Swing Behavior: To understand the SS behavior of NCFETs with scaling shown in Fig. 2(c), let us have a look at the SS expression and the factors affecting it. For simplicity, we will first consider the case of MFMIS NCFET for which ferroelectric and baseline FET can be separated. SS can be expressed as

$$\mathrm{SS} = \frac{\partial V_G}{\partial \log_{10} I_D} = \frac{\partial \psi_c}{\partial \log_{10} I_D} \frac{m}{A_{\mathrm{fe}}} \tag{3}$$

where ψ_c is the minimum potential along the center line [C_1C_2 in Fig. 3(c)], $m = \partial V_{\mathrm{int}}/\partial \psi_c$ is the body factor, and $A_{\mathrm{fe}} = \partial V_{\mathrm{int}}/\partial V_G$ is the voltage gain due to NC effect of the ferroelectric, where V_{int} denotes the potential at the internal metal gate. It is noteworthy that the ferroelectric can still provide a differential voltage gain (i.e., $A_{\mathrm{fe}} > 1$) even if the absolute value of V_{int} becomes lower than the applied V_G, as discussed earlier. The first term in (3) remains approximately a constant ≈60 mV/decade (the Boltzmann limit) with scaling. The other factor, whose inverse can be termed as an effective gain, $A_{\mathrm{eff}} = m^{-1}A_{\mathrm{fe}}$, governs the amount of SS lowering in the NCFET compared to the baseline FET. A_{fe} further depends on the ferroelectric and baseline FET

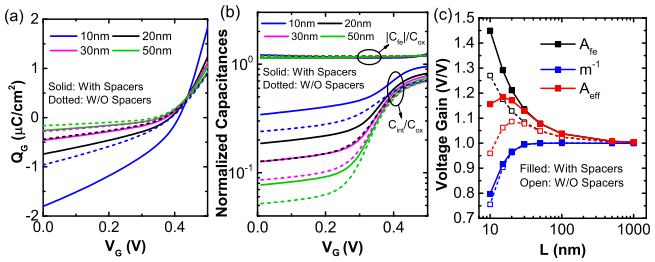


Fig. 5. (a) Gate charge (Q_G) and (b) ferroelectric (C_{fe}) and internal gate (C_{int}) capacitances normalized to oxide capacitance for MFMIS NCFET as functions of gate voltage for different channel lengths. (c) Governing factors of subthreshold swing (ferroelectric gain, A_{fe}, and body factor, m) and effective gain, $A_{\mathrm{eff}} = m^{-1}A_{\mathrm{fe}}$, as functions of channel length. A_{eff} increases with length scaling due to A_{fe} except for very small lengths, where the effect of m becomes significant.

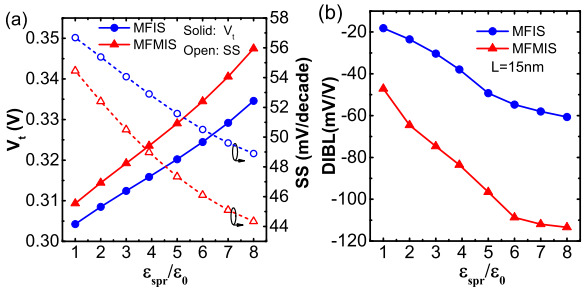


Fig. 6. Impact of spacer region permittivity on (a) threshold voltage (V_t) and subthreshold swing (SS) and (b) DIBL of MFIS and MFMIS configurations. Increasing the spacer permittivity enhances the outer fringing electric field, which leads to a rise in V_t and reduction in SS and DIBL.

capacitances, C_{fe} and C_{int}, (both per unit gate area) as [36]

$$A_{\mathrm{fe}} = \frac{1}{1 - (C_{\mathrm{int}}/|C_{\mathrm{fe}}|)}. \tag{4}$$

As evident in (4), a close matching of C_{fe} and C_{int} will result in a higher gain. Fig. 5(a) and (b) show gate charge density, Q_G, and C_{fe} and C_{int}, respectively, for different channel lengths. As explained earlier, decreasing L increases the ferroelectric polarization or, in the other words, negative charge on the gate terminal due to enhanced coupling of fringing field. Consequently, C_{int} increases with a reduction in L in the sub-V_t region even though $|C_{\mathrm{fe}}|$ remains almost a constant. Thus, A_{fe} increases with scaling of L, as shown in Fig. 5(c). On the other hand, the other factor m^{-1} in A_{eff} degrades with scaling due to conventional short-channel effects (coupling of S/D electric field to channel), as shown in Fig. 5(c). Except for a very small L (= 10 nm), A_{fe} dominates over m^{-1}, resulting in an increase in A_{eff}, which explains the SS behavior shown in Fig. 2(c). Even for $L = 10$ nm, A_{eff} is greater than 1, which effectively suppresses the SS below the Boltzmann limit. Similar behavior is observed in case MFIS NCFET too, however, with a less improvement in SS compared with the MFMIS NCFET. This can be attributed to only a sidewise impact of the ferroelectric in MFIS compared with MFMIS in which the ferroelectric impact extends uniformly over the internal gate, as explained earlier.

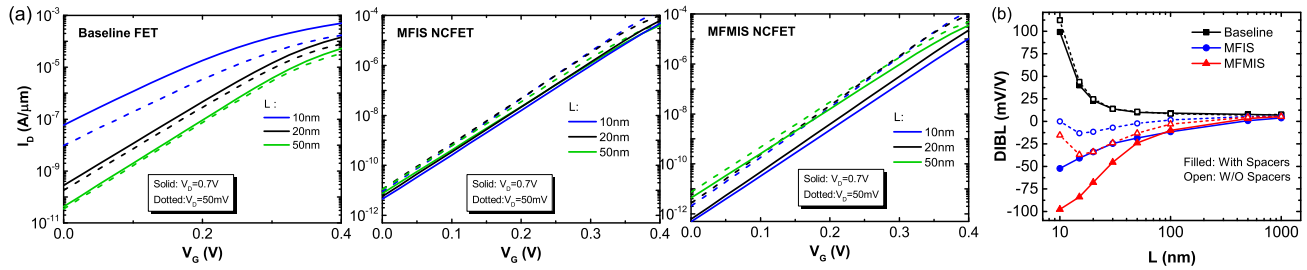


Fig. 7. Impact of V_D on subthreshold characteristics. (a) I_D–V_G of baseline, MFIS, and MFMIS FETs for low $V_D = 50$ mV and high $V_D = 0.7$ V for different channel lengths. (b) DIBL as a function of channel length for baseline, MFIS, and MFMIS FETs with and without spacers.

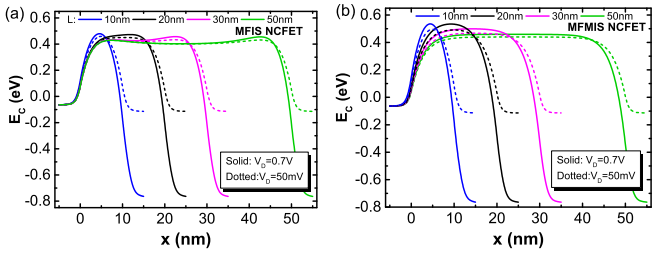


Fig. 8. Conduction band edge (E_C) profiles along the center line (C_1C_2) for (a) MFIS NCFET and (b) MFMIS NCFET for low $V_D = 50$ mV and high $V_D = 0.7$ V at $V_G = 0$. Both the NCFETs exhibit a rise in E_C with increase in V_D, which is implied by enhanced drain-to-ferroelectric coupling.

Furthermore, the SS improvement in Fig. 2(c) with spacers is significantly larger than without spacers, which is a direct consequence of the additional outer fringing field coupling through spacer regions. Fig. 6(a) shows the impact of spacer permittivity on V_t and SS. The increase in outer fringing field with ε_{spr} causes V_t to increase and SS to decrease for both the MFIS and MFMIS devices. These results are consistent with a previous study on MFMIS with spacers [16]. Note that the difference between MFIS and MFMIS devices also widens as ε_{spr} increases since the outer fringing affects the MFMIS structure to a greater extent, as explained earlier.

B. Impact of Drain Bias: Negative DIBL

Fig. 7(a) shows the impact of drain voltage, V_D, on the sub-V_t characteristics of the baseline, MFIS, and MFMIS FETs for different channel lengths. Unlike the conventional baseline FET, the NCFETs exhibit V_t increase with V_D. This opposite V_t shift in NCFETs is caused by an energy barrier rising with V_D [37] in contrast to a drain-induced barrier lowering (DIBL) in the conventional FETs, as shown in Fig. 8. In NCFETs, increasing V_D strengthens the drain-side fringing electric field, which increases the potential drop across the ferroelectric due to NC effect, for the same applied gate voltage. This effectively increases the energy barrier height in the channel. Note that the barrier rising in the OFF-state mainly comes from the fringing field coupling to the ferroelectric (in MFIS)/internal metal gate (in MFMIS), and only feebly through drain-to-channel coupling as the charge density in the channel is very small. The drain-to-channel coupling becomes important only in the ON-state and leads to a negative differential resistance in the I_D–V_D characteristics [12]. DIBL as a function of channel length, L, is shown in Fig. 7(b). As evident, DIBL for NCFETs is negative, which further decreases with a scaling of L due to increased impact of the fringing field. Since the fringing effects are more pronounced in the MFMIS structure than MFIS, it shows a more negative DIBL [see Fig. 8(a) and (b)]. Furthermore, the DIBL is smaller in the NCFETs with spacers, as expected. For NCFETs without spacers in Fig. 7(b), an increase in the DIBL can be observed for very small lengths, which is caused by counteracting conventional short-channel effects at these lengths. However, the NCFETs with spacers continue to show DIBL reduction with scaling even for these small lengths. DIBL in short-channel devices can be reduced further by increasing the permittivity of spacers for both the MFIS and MFMIS structures, as shown in Fig. 6(b) for $L = 15$ nm.

IV. Impact of Source/Drain Doping

We have already seen that the fringing electric field can significantly affect the OFF-state characteristics of NCFETs. As the fringing field originate from ionized S/D dopant ions, its strength also depends on the doping of these regions. A recent work [38] showed that a high S/D doping actually exacerbate the short-channel effects in the conventional DGFETs of very small lengths, which we have also shown for the baseline DGFET of $L = 15$ nm in Fig. 9(a). It also shows the impact of S/D doping on MFMIS NCFET (with spacers), which exhibits completely opposite trends. Fig. 9(b)–(d) show that contrary to the baseline FET, V_t increases, and SS and DIBL decrease with S/D doping for both the MFMIS and MFIS FETs. These behaviors are explained with the help of conduction band energy diagrams in Fig. 9(e). With the higher degenerate doping levels, the amount of space charge in S/D regions also increases, which in turn increases the strength of fringing field. This high fringing field pulls up the energy barrier height ($E_{c\max} - E_{fS}$) in MFMIS NCFET via coupling to the internal metal gate (or directly to the ferroelectric in the MFIS structure) contrary to the conventional baseline FET, which clearly explains the opposite trends of V_t. Similarly, SS and DIBL improvement in NCFETs with S/D doping can also be attributed to the increased fringing field (see Section III).

This article has been accepted for inclusion in a future issue of this journal. Content is final as presented, with the exception of pagination.

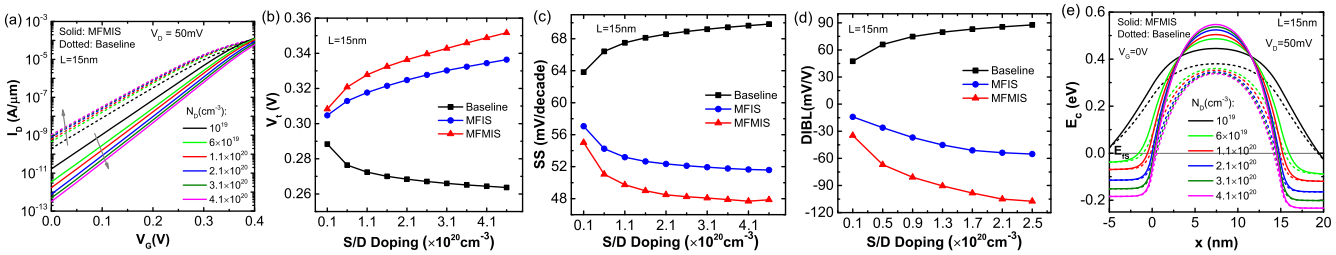


Fig. 9. Impact of S/D doping (N_D) on subthreshold characteristics. (a) I_D–V_G characteristics of MFMIS and baseline FETs. (b) V_t, (c) SS, and (d) DIBL of MFMIS, MFIS, and baseline FETs. (e) Conduction band edge profiles of MFMIS and baseline FETs. The NCFETs exhibit trends opposite to baseline FET with respect to the increase in N_D.

V. Conclusion

We have presented a detailed numerical analysis of short-channel effects in MFMIS and MFIS configurations of NCFETs. We explored the physical origins of unconventional effects, namely, V_t increase, SS reduction, and enhanced negative DIBL with scaling of channel length in different NCFETs. These effects essentially occur due to a S/D fringing field coupling to the ferroelectric in the OFF regime. All of these effects are found to be more pronounced in MFMIS structure compared to the MFIS structure. The existence of equipotential internal metal gate in the former spreads the impact of ferroelectric over the entire channel region, as compared to a localized ferroelectric influence to the channel sides only in the latter. The inclusion of spacer regions of high permittivity in both types of NCFETs also enhances these effects due to additional outer fringing field. Furthermore, we have demonstrated that contrary to the conventional FETs, increase in S/D region doping density improves the subthreshold characteristics of NCFETs.

References

[1] W. Haensch *et al.*, "Silicon CMOS devices beyond scaling," *IBM J. Res. Develop.*, vol. 50, nos. 4–5, pp. 339–361, Jul. 2006, doi: 10.1147/rd.504.0339.

[2] S. Salahuddin and S. Datta, "Use of negative capacitance to provide voltage amplification for low power nanoscale devices," *Nano Lett.*, vol. 8, no. 2, pp. 405–410, 2007, doi: 10.1021/nl071804g.

[3] A. Rusu, G. A. Salvatore, D. Jiménez, and A. M. Ionescu, "Metal-ferroelectric-meta-oxide-semiconductor field effect transistor with sub-60mV/decade subthreshold swing and internal voltage amplification," in *IEDM Tech. Dig.*, Dec. 2010, pp. 16.3.1–16.3.4, doi: 10.1109/IEDM.2010.5703374.

[4] J. Jo, W. Y. Choi, J.-D. Park, J. W. Shim, H.-Y. Yu, and C. Shin, "Negative capacitance in organic/ferroelectric capacitor to implement steep switching MOS devices," *Nano Lett.*, vol. 15, no. 7, pp. 4553–4556, 2015, doi: 10.1021/acs.nanolett.5b01130.

[5] K.-S. Li *et al.*, "Sub-60mV-swing negative-capacitance FinFET without hysteresis," in *IEDM Tech. Dig.*, Dec. 2015, pp. 22.6.1–22.6.4, doi: 10.1109/IEDM.2015.7409760.

[6] A. I. Khan *et al.*, "Negative capacitance in short-channel FinFETs externally connected to an epitaxial ferroelectric capacitor," *IEEE Electron Device Lett.*, vol. 37, no. 1, pp. 111–114, Jan. 2016, doi: 10.1109/LED.2015.2501319.

[7] J. Zhou *et al.*, "Ferroelectric $HfZrO_x$ Ge and GeSn PMOSFETs with sub-60 mV/decade subthreshold swing, negligible hysteresis, and improved I_{DS}," in *IEDM Tech. Dig.*, Dec. 2016, pp. 12.2.1–12.2.4, doi: 10.1109/IEDM.2016.7838401.

[8] M. H. Lee *et al.*, "Prospects for ferroelectric HfZrOx FETs with experimentally CET = 0.98nm, SS_{for} = 42mV/dec, SS_{rev} = 28mV/dec, switch-off <0.2V, and hysteresis-free strategies," in *IEDM Tech. Dig.*, Dec. 2015, pp. 22.5.1–22.5.4, doi: 10.1109/IEDM.2015.7409759.

[9] M. H. Lee *et al.*, "Physical thickness 1.x nm ferroelectric HfZrOx negative capacitance FETs," in *IEDM Tech. Dig.*, Dec. 2016, pp. 12.1.1–12.1.4, doi: 10.1109/IEDM.2016.7838400.

[10] Z. Krivokapic *et al.*, "14nm ferroelectric FinFET technology with steep subthreshold slope for ultra low power applications," in *IEDM Tech. Dig.*, Dec. 2017, pp. 15.1.1–15.1.4, doi: 10.1109/IEDM.2017.8268393.

[11] A. I. Khan, C. W. Yeun, C. Hu, and S. Salahuddin, "Ferroelectric negative capacitance MOSFET: Capacitance tuning & antiferroelectric operation," in *IEDM Tech. Dig.*, Dec. 2011, pp. 11.3.1–11.3.4, doi: 10.1109/IEDM.2011.6131532.

[12] G. Pahwa *et al.*, "Analysis and compact modeling of negative capacitance transistor with high on-current and negative output differential resistance—Part II: Model validation," *IEEE Trans. Electron Devices*, vol. 63, no. 12, pp. 4986–4992, Dec. 2016, doi: 10.1109/TED.2016.2614436.

[13] P. Lenarczyk and M. Luisier, "Physical modeling of ferroelectric field-effect transistors in the negative capacitance regime," in *Proc. Int. Conf. Simulation Semiconductor Process. Devices (SISPAD)*, Sep. 2016, pp. 311–314, doi: 10.1109/SISPAD.2016.7605209.

[14] H. Ota *et al.*, "Perspective of negative capacitance FinFETs investigated by transient TCAD simulation," in *IEDM Tech. Dig.*, Dec. 2017, pp. 15.2.1–15.2.4, doi: 10.1109/IEDM.2017.8268394.

[15] W.-X. You, C.-P. Tsai, and P. Su, "Short-channel effects in 2D negative-capacitance field-effect transistors," *IEEE Trans. Electron Devices*, vol. 65, no. 4, pp. 1604–1610, Apr. 2018, doi: 10.1109/TED.2018.2805716.

[16] J. Hattori *et al.*, "Fringing field effects in negative capacitance field-effect transistors with a ferroelectric gate insulator," *Jpn. J. Appl. Phys.*, vol. 57, no. 4S, p. 04FD07, 2018, doi: 10.7567/JJAP.57.04FD07.

[17] Z. Dong and J. Guo, "A simple model of negative capacitance FET with electrostatic short channel effects," *IEEE Trans. Electron Devices*, vol. 64, no. 7, pp. 2927–2934, Jul. 2017, doi: 10.1109/TED.2017.2706182.

[18] A. K. Saha, P. Sharma, I. Dabo, S. Datta, and S. K. Gupta, "Ferroelectric transistor model based on self-consistent solution of 2D Poisson's, non-equilibrium Green's function and multi-domain Landau Khalatnikov equations," in *IEDM Tech. Dig.*, Dec. 2017, pp. 13.5.1–13.5.4, doi: 10.1109/IEDM.2017.8268385.

[19] H. Ota, T. Ikegami, J. Hattori, K. Fukuda, S. Migita, and A. Toriumi, "Fully coupled 3-D device simulation of negative capacitance FinFETs for sub 10 nm integration," in *IEDM Tech. Dig.*, Dec. 2016, pp. 12.4.1–12.4.4, doi: 10.1109/IEDM.2016.7838403.

[20] G. Pahwa, T. Dutta, A. Agarwal, and Y. S. Chauhan, "Compact model for ferroelectric negative capacitance transistor with MFIS structure," *IEEE Trans. Electron Devices*, vol. 64, no. 3, pp. 1366–1374, Mar. 2017, doi: 10.1109/TED.2017.2654066.

[21] G. Pahwa, T. Dutta, A. Agarwal, and Y. S. Chauhan, "Physical insights on negative capacitance transistors in nonhysteresis and hysteresis regimes: MFMIS versus MFIS structures," *IEEE Trans. Electron Devices*, vol. 65, no. 3, pp. 867–873, Mar. 2018, doi: 10.1109/TED.2018.2794499.

[22] *COMSOL Multiphysics v. 5.3.1.180*. Accessed: Feb. 15, 2018. [Online]. Available: https://www.comsol.com

[23] R. E. Thomas, "Carrier mobilities in silicon empirically related to doping and field," *Proc. IEEE*, vol. 55, no. 12, pp. 2192–2193, Dec. 1967, doi: 10.1109/PROC.1967.6123.

[24] J. D. Bude, "MOSFET modeling into the ballistic regime," in *Proc. IEEE Int. Conf. Simulation Semiconductor Process. Devices*, Sep. 2000, pp. 23–26, doi: 10.1109/SISPAD.2000.871197.

This article has been accepted for inclusion in a future issue of this journal. Content is final as presented, with the exception of pagination.

[25] S. Choi, W. Sun, and H. Shin, "Analysis of stress-induced mobility enhancement on (100)-oriented single- and double-gate n-MOSFETs using silicon-thickness-dependent deformation potential," *Semicond. Sci. Technol.*, vol. 30, no. 4, p. 045009, Mar. 2015, doi: 10.1088/0268-1242/30/4/045009.

[26] N. Xu *et al.*, "Carrier-mobility enhancement via strain engineering in future thin-body MOSFETs," *IEEE Electron Device Lett.*, vol. 33, no. 3, pp. 318–320, Mar. 2012, doi: 10.1109/led.2011.2179113.

[27] K. Uchida, J. Koga, and S.-I. Takagi, "Experimental study on carrier transport mechanisms in double- and single-gate ultrathin-body MOSFETs—Coulomb scattering, volume inversion, and δ T_{SOI}-induced scattering," in *IEDM Tech. Dig.*, Dec. 2003, pp. 33.5.1–33.5.4, doi: 10.1109/IEDM.2003.1269402.

[28] D. Esseni, M. Mastrapasqua, G. K. Celler, C. Fiegna, L. Selmi, and E. Sangiorgi, "An experimental study of mobility enhancement in ultra-thin SOI transistors operated in double-gate mode," *IEEE Trans. Electron Devices*, vol. 50, no. 3, pp. 802–808, Mar. 2003, doi: 10.1109/ted.2002.807444.

[29] C.-H. Lin *et al.*, "Channel doping impact on FinFETs for 22nm and beyond," in *Proc. Symp. VLSI Technol. (VLSIT)*, Jun. 2012, pp. 15–16, doi: 10.1109/vlsit.2012.6242438.

[30] L.-Å. Ragnarsson, T. Chiarella, M. Togo, T. Schram, P. Absil, and T. Hoffmann, "Ultrathin EOT high-κ/metal gate devices for future technologies: Challenges, achievements and perspectives," *Microelectron. Eng.*, vol. 88, no. 7, pp. 1317–1322, Jul. 2011, doi: 10.1016/j.mee.2011.03.121.

[31] R. Granzner *et al.*, "Simulation of nanoscale MOSFETs using modified drift-diffusion and hydrodynamic models and comparison with Monte Carlo results," *Microelectron. Eng.*, vol. 83, no. 2, pp. 241–246, 2006, doi: 10.1016/j.mee.2005.08.003.

[32] A. F. Devonshire, "XCVI. Theory of barium titanate," *London, Edinburgh, Dublin Philos. Mag. J. Sci.*, vol. 40, no. 309, pp. 1040–1063, 1949, doi: 10.1080/14786444908561372.

[33] M. Hoffmann *et al.*, "Direct observation of negative capacitance in polycrystalline ferroelectric HfO_2," *Adv. Funct. Mater.*, vol. 26, no. 47, pp. 8643–8649, 2016, doi: 10.1002/adfm.201602869.

[34] M. V. Dunga, C.-H. Lin, A. M. Niknejad, and C. Hu, "BSIM-CMG: A compact model for multi-gate transistors," in *FinFETs and Other Multi-Gate Transistors*, J.-P. Colinge, Ed. New York, NY, USA: Springer, 2008, ch. 3, pp. 113–153, doi: 10.1007/978-0-387-71752-4_3.

[35] A. S. Roy, S. P. Mudanai, and M. Stettler, "Mechanism of long-channel drain-induced barrier lowering in halo MOSFETs," *IEEE Trans. Electron Devices*, vol. 58, no. 4, pp. 979–984, Apr. 2011, doi: 10.1109/TED.2011.2109387.

[36] G. Pahwa *et al.*, "Analysis and compact modeling of negative capacitance transistor with high ON-current and negative output differential resistance—Part I: Model description," *IEEE Trans. Electron Devices*, vol. 63, no. 12, pp. 4981–4985, Dec. 2016, doi: 10.1109/TED.2016.2614432.

[37] G. Pahwa, T. Dutta, A. Agarwal, and Y. S. Chauhan, "Designing energy efficient and hysteresis free negative capacitance FinFET with negative DIBL and 3.5X I_{ON} using compact modeling approach," in *Proc. IEEE Eur. Solid-State Circuits Conf. (ESSCIRC)*, Sep. 2016, pp. 49–54, doi: 10.1109/ESSCIRC.2016.7598240.

[38] H. H. Lin and Y. Taur, "Effect of source–drain doping on subthreshold characteristics of short-channel DG MOSFETs," *IEEE Trans. Electron Devices*, vol. 64, no. 12, pp. 4856–4860, Dec. 2017, doi: 10.1109/TED.2017.2766920.



Girish Pahwa (S'16) received the B.Tech. degree in electronics and communication engineering from Delhi Technological University, New Delhi, India, in 2014. He is currently pursuing the Ph.D. degree with IIT Kanpur, Kanpur, India.

His current research interests include physics and modeling of negative capacitance transistors.



Amit Agarwal received the M.Sc. and Ph.D. degrees in theoretical physics from the Indian Institute of Science, Bengaluru, India, in 2005 and 2009, respectively.

In 2012, he joined IIT Kanpur, Kanpur, India, as an Assistant Professor. His current research interests include theoretical condensed matter theory, particularly low-dimensional systems, and nanoscale device modeling.



Yogesh Singh Chauhan (SM'12) is currently an Associate Professor with IIT Kanpur, Kanpur, India. He has published over 200 papers in international journals and conferences.

Dr. Chauhan is a member of the IEEE-Electron Device Society Compact Modeling Committee. He is the Founding Chairperson of the IEEE Electron Devices Society U.P. Chapter. He is the Editor of the IEEE Transactions on Electron Devices and the Distinguished Lecturer of the IEEE Electron Devices Society.

This article has been accepted for publication in a future issue of this journal, but has not been fully edited. Content may change prior to final publication. Citation information: DOI 10.1109/TCSVT.2018.2870256, IEEE Transactions on Circuits and Systems for Video Technology

On the Minimum Perceptual Temporal Video Sampling Rate and its Application to Adaptive Frame Skipping

Christoph Bachhuber, Amit Bhardwaj, *Member, IEEE*, Rastin Pries, and Eckehard Steinbach, *Fellow, IEEE*

***Abstract*—Media technology, in particular video recording and playback, keeps improving to provide users with high-quality real and virtual visual content. In recent years, increasing the temporal sampling rate of videos and the refresh rate of displays has become one focus of technical innovation. This raises the question, how high the sampling and refresh rates should be? To answer this question, we determine the minimum temporal sampling rate at which a video should be presented to make temporal sampling imperceptible to viewers.**

Through a psychophysical study, we find that this minimum sampling rate depends on both the speed of the objects in the image plane, and the exposure time of the recording camera. We propose a model to compute the required minimum sampling rate based on these two parameters. In addition, state-of-the-art video codecs employ motion vectors from which the local object movement speed can be inferred. Therefore, we present a procedure to compute the minimum sampling rate given an encoded video and camera exposure time.

Since the object motion speed in a video may vary, the corresponding minimum frame rate is also varying. This is why the results of this paper are particularly applicable when used together with adaptive frame rate computer generated graphics or novel video communication solutions that drop insignificant frames. In our experiments, we show that videos played back at the minimum adaptive frame rate achieve an average bit rate reduction of 26% compared to constant frame rate playback, while perceptually no difference can be observed.

***Index Terms*—Video Sampling Frequency, Adaptive Sampling, Perception Limits.**

I. Introduction

Industry and science strive towards making the technology underlying visual media consumption and interaction imperceptible to the user. To make this happen, latencies need to be reduced, and spatial and temporal resolution need to be increased. Latencies are particularly relevant in interactive media consumption such as vision-based remote control, video conferencing, cloud gaming, or content consumption using a head-mounted display (HMD). State-of-the-art systems offer significant potential for improvement in this aspect [1]. There are novel systems that reduce latency by recording video sequences at high frame rate, and dropping insignificant frames (adapting the temporal sampling rate) even before encoding [2]. This frame dropping process decouples the display frame rate from the recording frame rate, and consequently from exposure time. One important parameter for driving the frame dropping process is the required minimum display frame rate[1]. In this paper we study the impact of the camera exposure time and the object motion velocity in the image plane on the required minimum display rate. We have not found any studies examining their combined effect on the minimum display rate.

More specifically, we answer the question of the required minimal displaying frame rate for a given constant camera exposure time (and constant camera frame rate) and object motion velocity. To this end, the paper analyses temporal sampling in video recording and display as well as how camera exposure time and scene motion affect the frame rate required to give the user the impression of continuous motion. These insights allow us to improve video compression efficiency by skipping perceptually insignificant video frames from a camera that is recording at a constant frame rate. Effectively, the algorithm adapts the video frame rate to scene motion and camera exposure time. The proposed adaptive frame skipping is designed to have no influence on what the video consumer perceives compared to a video played back at the original constant camera frame rate.

A. Related Work

Researchers in the field of psychophysics have thoroughly investigated how the human visual system creates the impression of an object in motion. However, the community has not yet agreed on the actual neural processes. This section summarizes research related to human motion perception relevant for this paper.

Johannson [3] discusses a major difference between the human eye and camera systems: the human eye does not have a shutter, and accordingly has unlimited exposure time. Nevertheless, humans perceive their moving environment not blurry, but perfectly clear. The author states that neural algorithms which process the continuous exposure data from the photoreceptors on the eye's retina are responsible for this impression.

Derrington et al. [4] provide a review of the state-of-the-art in motion perception research. The authors find evidence only

C. Bachhuber, A. Bhardwaj and E. Steinbach are with the Department of Electrical and Computer Engineering, Technical University of Munich, Germany, e-mail: {christoph.bachhuber, amit.bhardwaj, eckehard.steinbach}@tum.de.

R. Pries is with the Nokia Bell Labs Munich, e-mail: rastin.pries@nokia-bell-labs.com

Please direct correspondence to E. Steinbach.

This work was supported in part through a Humboldt Fellowship for Postdoctoral Research from the Alexander von Humboldt Foundation.

[1] At the minimum frame rate, the user should perceive perfectly continuous (fluid/smooth) motion, and effects from temporal sampling (jitter/jerkiness) should be imperceptible.

1051-8215 (c) 2018 IEEE. Personal use is permitted, but republication/redistribution requires IEEE permission. See http://www.ieee.org/publications_standards/publications/rights/index.html for more information.

This article has been accepted for publication in a future issue of this journal, but has not been fully edited. Content may change prior to final publication. Citation information: DOI 10.1109/TCSVT.2018.2870256, IEEE Transactions on Circuits and Systems for Video Technology

to support the assumption of a first-order motion detector on the retina, and propose that there is no evidence for processing steps that are more complex. First order motion detection means determining motion based on the spatiotemporal correlation of brightness or color changes. They review three candidate models for this detection. The paper does not contain a discussion of perception limits.

The results of Derrington et al. [4] are in contrast to the findings of Ledgeway and Smith [5], who found evidence to support that there are different pathways for processing first-order and second-order motion. Second-order motion is based on spatiotemporal variations such as depth, contrast and relative motion which do not yield a systematic motion in the Fourier domain. It is thus also named "texture-based" motion perception. Examples of such signals are given by Chubb and Sperling [6].

Seiffert and Cavanagh [7] conducted experiments to separately analyze first-order as well as second-order motion. They found that for first-order motion detection, the velocity of an object, and not the spatial displacement determines a lower bound for the perception of motion. Second-order motion perception is performed by tracking object features over time, and its lower thresholds, in contrast to first-order perception, are not affected by the speed of the object to be detected, but by a minimal position change.

Adelson and Bergen [8] suggest energy models for modeling motion perception. The authors conceptualize two dimensional motion as three dimensional patterns in the *x-y-t* space. Therefore, motion perception is analogous to identifying an orientation in the *x-y-t* space. They apply quadrature pair filters to extract spatiotemporal energy which is then further processed to determine perceived motion.

The paper by Watson et al. [9] is the most relevant reference for this work, it is hence discussed in greater detail. First, Watson et al. [9] define the *Window of Visibility* (WoV), depicted as gray rectangle in Fig. 1. The window shows the perception thresholds in one spatial frequency domain (ω [cycles/degree]) and the temporal frequency domain (f [Hz]). Visual information within the window is more or less visible to the user, everything outside is not. Thus, the WoV can be seen as a low-pass filter. The shape of the window indicates that the perception thresholds of temporal and spatial frequency are independent [9]. For simplicity, the WoV covers only one spatial dimension, but can be extended in a straightforward manner to two spatial dimensions. Imagine a second spatial dimension perpendicular to the paper plane. In the plane spanned by the two spatial dimensions, the shape of the WoV is a disk because (as we show in Section III-D) only motion magnitude, not motion direction is relevant for the perception limit. Together with the rectangular WoVs in both spatiotemporal planes, the disk in the spatial plane yields the *Cylinder of Visibility* in the three dimensional (two spatial dimensions, one temporal dimension) space.

In [9], the human temporal flicker frequency threshold f_{thr} was found to be $f_{\mathrm{thr},1} = 30\,\mathrm{Hz}$ and $f_{thr,2} = 33\,\mathrm{Hz}$ for two observers. Stationary temporal contrast fluctuations with a frequency higher than f_{thr} can not be seen. Analogously, ω_{thr} represents the human spatial sensitivity threshold, where the cycles per degree refer to the point of view of the human. In their experiments, Watson et al. [9] find that the thresholds are at $\omega_{thr,1} = 6$ [cycles/degree] and $\omega_{thr,2} = 13$ [cycles/degree] for two observers. The authors presume that the low contrast of the display causes these rather low threshold values. Experiments with more test subjects should lead to more generally valid numbers, the preceding values are only examples.

One-dimensional motion of a point with constant velocity v [degree/second] yields a straight line with slope $-1/v$ in the spatiotemporal frequency domain [9], see the diagonal line passing through the origin in Fig. 1a. This model assumes the point to exhibit infinitely high spatial frequencies. Time discretization or temporal sampling of the spatiotemporal process leads to periodic replication of the original signal (see additional lines in Fig. 1a), where the replication period in frequency domain is the sampling frequency f_s. In Fig. 1a, we can see that the periodic replications intersect with the WoV, so they pass through the pass-band of the low-pass filter. These aliasing artifacts are what humans perceive as jitter. Therefore, if the frequency spectra of the replications lie outside the WoV, humans will not be able to distinguish the time-sampled representation of the moving object from the continuous representation. The authors in [9] derived a minimum temporal sampling frequency, named critical sampling frequency f_c, which alleviates aliasing to a level below human perception thresholds. In the following we briefly review the findings from [9].

There will be imperceptible aliasing if the replicated spectra just touch the corners of the WoV, as illustrated in Fig. 1b. To satisfy this, the temporal sampling frequency $f_{s,1}$ has to be equal to or greater than the critical sampling frequency

$$f_{s,1} \geq f_c = f_{\mathrm{thr}} + v \cdot \omega_{\mathrm{thr}}, \tag{1}$$

as can be derived from Fig. 1b. As a result of the point symmetry of the WoV and the spectrum of the moving object, this condition also satisfies the first periodic replication at $-f_s$. If the maximum spatial frequency ω_0 of the object is lower than the spatial perception threshold ω_{thr} (see Fig. 1b), the condition for the sampling frequency $f_{s,2}$ accordingly changes to

$$f_{s,2} \geq f_c = f_{\mathrm{thr}} + v \cdot \omega_0. \tag{2}$$

Merging conditions (1) and (2) yields the general condition

$$f_s \geq f_c = f_{\mathrm{thr}} + v \cdot \min(\omega_{\mathrm{thr}}, \omega_0) \tag{3}$$

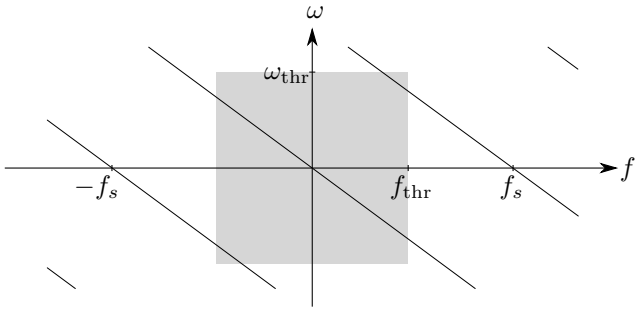
as the lower bound for the temporal sampling frequency. The consequential next step is to limit the temporal frequency to, e.g., f_0. This is done in [9], but does not give further insight in our context.

B. Building on Watson's Work

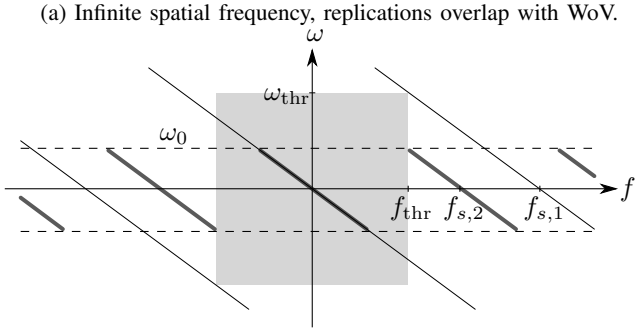
Eq. (3) leaves us with two key takeaways: first, objects with high speed v, yielding a flatter line in Fig. 1, require higher temporal sampling frequencies f_s to attenuate aliasing artifacts, making jitter imperceptible. Second, at a given speed v and all spatial frequencies below the perception threshold ω_{thr}, objects with high maximum spatial frequencies (sharp edges)

1051-8215 (c) 2018 IEEE. Personal use is permitted, but republication/redistribution requires IEEE permission. See http://www.ieee.org/publications_standards/publications/rights/index.html for more information.

This article has been accepted for publication in a future issue of this journal, but has not been fully edited. Content may change prior to final publication. Citation information: DOI 10.1109/TCSVT.2018.2870256, IEEE Transactions on Circuits and Systems for Video Technology



(a) Infinite spatial frequency, replications overlap with WoV.



(b) No periodic replications overlap with the WoV. Either because $f_{s,i}$ is chosen large enough (thin lines), or due to the limited spatial frequency ω_0 of the signal (thick lines).

Fig. 1: Window of visibility [9] depicted as gray rectangle. The diagonal line (slope $-1/v$) passing through the origin represents a point moving at constant velocity v. Due to temporal sampling, the diagonal line is replicated at integer multiples of the sampling frequency f_s.

require higher temporal sampling frequencies than objects with lower maximum spatial frequencies (blurry/smooth edges).

Watson et al. [9] did not investigate the influence of the exposure time of a camera. However, camera exposure time influences the maximum spatial frequency, as described in the following. For a better understanding, let us first outline how a (video) camera records an image. In the classical camera model, a shutter prevents light from falling onto the photosensitive material at all times except for the exposure time, also called light integration period. During this time, typically a fraction of a second, the shutter is open and photons keep falling onto the photosensitive material. In modern CMOS/CCD implementations, the photosensitive material is replaced by light sensors that record images in two-dimensional, usually rectangular pixel arrays. Each pixel can electronically be set to integrate light (shutter open, exposure), or to ignore incoming photons (shutter closed). This replaces the mechanical shutter.

If during the exposure time, the rate at which photons fall onto a pixel is constant, the output from this pixel will perfectly represent what can actually be seen from the pixel's perspective. If the rate of photons changes during exposure, for example if the camera or object is moving, the pixel's output will represent the *average* light intensity recorded during the exposure period. This is why quickly moving objects can appear blurred in photos and videos, exhibiting a limited

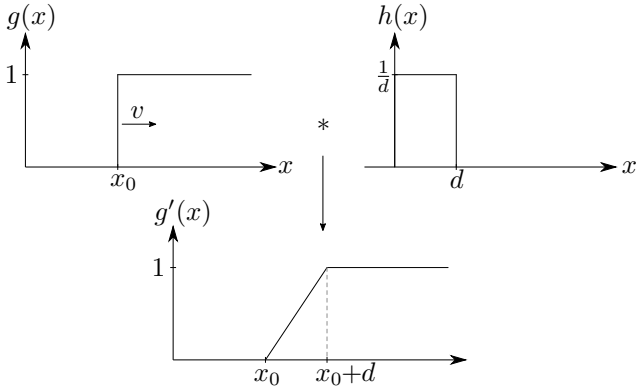


Fig. 2: The input signal $g(x)$ moves right with velocity v. Convolution with camera filter $h(x)$ creates the blurred output signal $g'(x)$. Camera filter $h(x)$ actually is a temporal filter, but in this example represented by its spatial equivalent for simplicity. Filter width d equals exposure time t_{exp} multiplied by speed v, see Eq. (6).

maximum spatial frequency.

The work by Watson et al. [9] provides the theoretical basis for this paper, but it does not answer how limits such as the maximum occurring spatial frequency ω_0 can be computed with given equipment parameters, or if they exist at all. In real-world applications, imperfect filters, spatial discretization and noise occur. In particular, an object moving through the field of view of a camera with finite exposure time will become blurred, its spatial patterns low-pass filtered. However, as we show in the following, blurring caused by exposure time integration will not have an upper bound in terms of spatial frequency, if the original signal's spatial frequency was not limited.

To illustrate this, imagine the one-dimensional spatial signal $g(x) = u(x - x_0)$ depicted in the top left graph in Fig. 2. The following explanations extend naturally to more spatial dimensions. Function $u(\cdot)$ denotes the Heaviside step function or unit step function, which is equal to zero for negative arguments, and equal to one for nonnegative arguments. For simplicity, the image signal is normalized to range $[0, 1]$ (where 0 and 1 correspond to black and white, respectively). Thus, the signal represents a perfectly sharp black-to-white edge. Its Fourier transform [10]

$$U(\omega) = \mathcal{F}\{u(x)\} = \pi\delta(\omega) + \frac{1}{j\omega} \tag{4}$$

contains the Dirac function $\delta(\cdot)$, which equals one if its argument equals zero, and equals zero otherwise. The Fourier transform of $u(\cdot)$ has a magnitude $|U(\omega)| \sim \frac{1}{\omega}$ when ignoring the $\delta(\cdot)$ function. Ignoring the Dirac function is reasonable because $\delta(\cdot)$ represents the frequency coefficient for $\omega = 0$, which is not relevant to the maximum frequency we are looking for.

The spatial signal $g(x)$ is a shifted version of $u(x)$, which corresponds to a multiplication of $U(\omega)$ with the complex exponential $e^{-j\omega x_0}$ [10]. This process does not change the magnitude of the original frequency spectrum of $u(x)$:

1051-8215 (c) 2018 IEEE. Personal use is permitted, but republication/redistribution requires IEEE permission. See http://www.ieee.org/publications_standards/publications/rights/index.html for more information.

This article has been accepted for publication in a future issue of this journal, but has not been fully edited. Content may change prior to final publication. Citation information: DOI 10.1109/TCSVT.2018.2870256, IEEE Transactions on Circuits and Systems for Video Technology

$$\begin{aligned} |G(\omega)| &= |\mathcal{F}\{g(x)\}| = |\mathcal{F}\{u(x)\}| \cdot |e^{-j\omega x_0}| \\ &= |\mathcal{F}\{u(x)\}| = |U(\omega)| \sim \frac{1}{\omega}, \end{aligned} \tag{5}$$

so it is still proportional to the reciprocal of ω. Signal $g(x)$ moves to the right at velocity v, as indicated in the top left graph in Fig. 2. This process is recorded by a camera with exposure time t_{exp}. Consequently, during the exposure time, $g(x)$ moves

$$d = v \cdot t_{\text{exp}} \tag{6}$$

to the right. The resulting, blurred signal $g'(x)$ is depicted in the bottom graph of Fig. 2. Note that at each location x, the signal is integrated over time. At locations $x < x_0$, input $g(x)$ will equal to zero at all times during exposure, and at locations $x > x_0 + d$, the input will equal one at all times during exposure. In these locations, $g(x) = g'(x)$ holds. At $x = x_0$, the signal on the (one-dimensional) camera sensor is for all times during exposure equal to zero, except for an infinitesimally small time at the very beginning. Thus, the resulting value in the blurred image in this location equals zero. At $x = x_0 + 0.1 \cdot d$, the signal is equal to one for ten percent of the exposure time, zero for the remaining 90 percent. Therefore, the resulting image value equals 0.1. The linear ascend spans the entire exposure time area, yielding the ramp that can be seen in Fig. 2. This linear dependency holds for every camera exposure process of an object moving at constant velocity.

The previous insight allows us to formalize how temporal integration during camera exposure affects the spatial frequency of an input signal $g(x)$ moving at constant velocity v. To simplify the following proof, we replace temporal integration of $g(x)$ during exposure time by the convolution $g(x) * h(x)$. The convolution needs to yield the same $g'(x)$ as temporal integration. To this end, we design the dimensions of $h(x)$ relative to movement speed v and exposure time t_{exp} using Eq. (6):

$$h(x) = \frac{1}{d}\left(u(x) - u(x-d)\right) \tag{7}$$

The convolution $g(x) * h(x)$ will always lead to the same $g'(x)$ as temporal integration with exposure time t_{exp} of a signal $g(x)$ moving at constant velocity v. Filter $h(x)$ is shown in the top right graph in Fig. 2. The magnitude of its Fourier transform

$$|H(\omega)| = |\mathcal{F}\{h(x)\}| = \frac{1}{d}|\mathcal{F}\{u(x)\}| \cdot |1 - e^{-j\omega d}| \tag{8}$$

equals the magnitude of $U(\omega)$ multiplied with the inverse of d and the magnitude of $1 - e^{-j\omega d}$. Let us derive

$$\begin{aligned} c(\omega, d) &= |1 - e^{-j\omega d}| && (9)\\ &= |1 - \cos(\omega d) + j \cdot \sin(\omega d)| && (10)\\ &= \sqrt{(1 - \cos(\omega d))^2 + (\sin(\omega d))^2} && (11)\\ &= \sqrt{1 - 2\cos(\omega d) + (\cos(\omega d))^2 + (\sin(\omega d))^2} && (12)\\ &= \sqrt{2 - 2\cos(\omega d)} \in [0, 2]. && (13) \end{aligned}$$

It is important to notice that $c(\omega, d)$ is a periodic function in the domain $c(\omega, d) \in [0, 2]$. $c(\omega, d)$ will therefore not play a significant role for the following proportionality considerations. Consequently, the magnitude from Eq. (8)

$$|H(\omega)| = \frac{c(\omega, d)}{d}|U(\omega)| \sim \frac{c(\omega, d)}{\omega d} \tag{14}$$

approximates $\frac{1}{d}|U(\omega)|$ and, more importantly, is approximately proportional to the reciprocal of the product ωd because $c(\omega, d) \in [0, 2]$. Thus, the filter width d, which is a function of t_{exp} and v, see Eq. (6), defines how quickly the frequency coefficients of $|H(\omega)|$ will converge to zero. Finally, we retrieve the magnitude spectrum of the output signal $g'(x)$:

$$\begin{aligned} |\mathcal{F}\{g'(x)\}| &= |\mathcal{F}\{g(x) * h(x)\}| && (15)\\ &= |\mathcal{F}\{g(x)\}| \cdot |\mathcal{F}\{h(x)\}| && (16)\\ &= |G(\omega)| \cdot |H(\omega)| && (17)\\ &= |U(\omega)|^2 \, \frac{c(\omega, d)}{d} \quad \left(\sim \frac{c(\omega, d)}{\omega^2 d}\right) && (18)\\ &= \left|\pi\delta(\omega) + \frac{1}{j\omega}\right|^2 \frac{\sqrt{2 - 2\cos(\omega d)}}{d} && (19)\\ &= \frac{1}{\omega^2}\frac{\sqrt{2 - 2\cos(\omega t_{\text{exp}} v)}}{t_{\text{exp}} v} \quad \forall \omega \in \mathbb{R} \setminus \{0\} && (20) \end{aligned}$$

The above calculation uses the convolution theorem [10] to transform line (15) to line (16), and Eq. (5) and (14) to convert line (17) to line (18). In line (18), we observe that the magnitude spectrum of output signal $g'(x)$ decreases faster than the input signal at higher frequencies ω because of its approximate proportionality to the reciprocal of $\omega^2 d = \omega^2 t_{\text{exp}} v$, which gives it the blurred appearance. Still, the magnitude spectrum does not generally vanish at an upper limit ω_0. This is why result (3) cannot be used directly on real signals and further investigations in the remaining sections of this paper need to be done.

We express the spectrum magnitude of output $g'(x)$ as a function of exposure time t_{exp} and speed v in Eq. (20) to give a better intuition of how these two variables influence the spatial frequency components. As we know from Eq. (13), the numerator in Eq. (20) can take values in [0, 2]. Therefore, the spectrum magnitude of $g'(x)$ is approximately proportional to, among others, $1/t_{\text{exp}}$. Thus, e.g. a longer exposure time t_{exp} will lead to faster decay of frequency components of the magnitude spectrum of $g'(x)$, allowing a smaller critical sampling frequency f_c.

The discussion in the previous paragraphs assumed infinitely high spatial resolution. In real systems, intensity signals are spatially sampled by the pixel matrix in the camera sensor. This leads to a staircase function instead of a ramp function for $g'(x)$ in Fig. 2. The staircase signal would be composed of unit step functions, yielding a spectrum magnitude that is vanishing slower than in Eq. (18), hence causing a larger critical sampling frequency f_c. However, at normal viewing conditions, state-of-the-art displays have pixel densities of usually 35 to 150 pixels per degree (an overview is provided in Tab. II). This is close to and often greater than the angular

1051-8215 (c) 2018 IEEE. Personal use is permitted, but republication/redistribution requires IEEE permission. See http://www.ieee.org/publications_standards/publications/rights/index.html for more information.

This article has been accepted for publication in a future issue of this journal, but has not been fully edited. Content may change prior to final publication. Citation information: DOI 10.1109/TCSVT.2018.2870256, IEEE Transactions on Circuits and Systems for Video Technology

resolution of the human eye, approximately 0.02 degrees with optimal eyesight [11], corresponding to 50 pixels per degree. Hence, the spatial discretization effect is negligible.

Our derivations in this section serve three purposes: first, they show that there is no upper bound on the spatial spectrum of an output image created with a conventional camera. Second, they introduce the reader to how the camera exposure process filters an input scene containing motion. Third, they provide the two central variables of interest in our experiments: camera exposure time t_{exp} and object velocity v. They define the width d (Eq. (6)) of the camera filter $h(x)$, the steepness of the ramp of the output image and how quickly the spatial frequency components of the output image will converge to zero. Furthermore, the steepness of the spatiotemporal spectrum is a function of v, see Fig. 1. Higher velocity v decreases the steepness of the spectrum, leading to a higher f_c, see Eq. (3). On the other hand, a higher speed v increases the filter width d (Eq. (6)), which causes high-frequency components to decay more quickly (Eq. (18)), accordingly reducing f_c. In Section III-A, we will investigate which of these two opposing effects of v prevails.

Overall, these insights lead us to four hypotheses which we are going to verify through experiments in Section III:

1) Higher speed v changes f_c
2) Longer exposure time t_{exp} decreases f_c
3) Higher speed v increases the influence of t_{exp} on f_c
4) Longer exposure time changes the influence of v on f_c

C. Contributions

As argued in Section I-B, hard cut-off thresholds usually do not exist in real signals, making additional tests on top of Watson's work in [9] necessary. We proceed in Section II with the description of our experiment including presented sequences, their creation and presentation, as well as the experimental procedure. Results from these experiments are presented in Section III, and discussed in Section IV. We have found that both, the speed of a moving object and the exposure time of the camera recording the object, have a statistically significant influence on the critical sampling frequency f_c. We create a model to determine f_c for a given object speed and camera exposure time and propose a formula to compute the object speed from an encoded video sequence and the display dimensions. These models are applied to actual video sequences in Section V and show a clear bit rate reduction compared to constant sampling frequency playback. Finally, Section VI concludes the paper, giving an outlook to future research.

II. Experimental Setup

We conducted a series of experiments to find the previously mentioned threshold for perceiving jitter in time-sampled motion sequences. This section describes the presented sequences, sequence creation, sequence playback, the participants and how participants performed the experiment.

We separated sequence creation and sequence playback because real-time creation was not possible (see Section II-B).



Fig. 3: Sequence C (see Tab. I) at three time instances during playback (from top to bottom): first, the bar is starting at the left side of the monitor, second after moving half way to the right, and third when the bar is crossing the right display border to reappear at the left border. In this figure, each image is shown at 1/3 vertical height.

A. Sequences and Sequence Parameters

As it is common practice in psychometrics, we present an object moving in one dimension to the users [4], [8], [9]. Our sequences are shown on a special computer monitor, which is described in more detail in Section II-C. The shown sequences, for an example see Fig. 3, contain a vertical white bar that spans the entire display height, and one fifth of the display width. The white bar moves from left to right over black background at constant speed. This setting gives us maximum contrast and clearly perceivable intensity edges. When general video content is presented to users, lower contrasts might be present, which would require lower frame rates. Therefore, our results will serve as an upper bound for the critical sampling frequency f_c.

The bar starts at the left side of the monitor, and when it moves out of the display on the right side, it moves into the display again on the left side. We compute the moving bar with a simulation rate of 20 kHz. This allows us to simulate the relevant exposure times for the camera and the resulting motion blur. The simulation of exposure time is described in Section II-B. The blurring caused by exposure time can be seen at the edges of the white bar in Fig. 3.

For each set of sequences, we set a constant speed v for the bar, and a constant exposure time t_{exp} for the camera. Each set contains sequences with frame rates f_{seq} ranging from 10 Hz to 90 Hz in steps of 2 Hz. For referencing, we label the sets in Tab. I. In this table, the speed and exposure time increase from bottom to top, and from left to right, respectively. Hence, the camera filter width d (as defined in Eq. (6)) decreases from top right to bottom left and consequently, the intensity of motion blur decreases from the top right to the bottom left. Only two subjects (authors of this paper) have conducted tests on all sets. The nine sets A to I have been used in experiments for all ten test subjects. This sub-sampling has been performed to reduce the duration of the experiment for the test subjects. For a detailed discussion of test length and difficulty, see Section III-C. For all test subjects, we chose the highest speed to

1051-8215 (c) 2018 IEEE. Personal use is permitted, but republication/redistribution requires IEEE permission. See http://www.ieee.org/publications_standards/publications/rights/index.html for more information.

This article has been accepted for publication in a future issue of this journal, but has not been fully edited. Content may change prior to final publication. Citation information: DOI 10.1109/TCSVT.2018.2870256, IEEE Transactions on Circuits and Systems for Video Technology

v \ t_{exp}	5 ms	10 ms	15 ms	20 ms	25 ms
72.5 deg/s	J	K	L	M	N
48.3 deg/s	**A**	O	**B**	P	**C**
36.3 deg/s	Q	R	S	T	U
24.2 deg/s	**D**	V	**E**	W	**F**
18.1 deg/s	X	Y	Z	a	b
12.1 deg/s	c	d	e	f	g
6.0 deg/s	**G**	h	**H**	i	**I**

TABLE I: Labels for the used sequence sets with various speeds v [degree/second] and exposure times t_{exp} [milliseconds]. Two authors of this paper performed psychophysical tests on all sets, the remaining subjects only on sequence sets with bold letters and gray background.

be 48.3 deg/s (i.e., sequence sets A, B and C). We did not choose 72.5 deg/s as at such a high speed, the bar is passing the display width so quickly that it is extremely exhausting for test subjects to register the presence or absence of jitter.

We chose the parameter limits based on the following considerations: in conventional modern video applications, videos are recorded at frame (image) rates between 30 Hz and 60 Hz. This yields sampling periods between 33.3 ms and 16.7 ms, which serve as an upper bound for the exposure time because exposure of one image in a video may not take more time than the corresponding sampling period. We are in addition particularly interested in short exposure times of high frame rate videos with around 200 Hz of frame rate, as used in low delay video communication such as [2]. Therefore, we set the exposure range to [5.0, 25.0] ms to cover current and future applications.

The upper speed limit is decided by what participants were able to judge with reasonable effort. It is observed that higher speeds are difficult to follow given that the display covers only 46.4 degrees of the subject's field of view (FoV). The lower speed bound is dictated by the spatial resolution of the utilized computer display (details in Section II-C), which provides 1920 pixels in horizontal direction. In early experiments, we found that at speeds below 6.0 deg/s, spatial discretization effects turned out to be perceivable, which distorted the results of our experiments. In summary, the subjects and discrete spatial resolution of the display set the upper and lower speed bounds, respectively, and this yields a speed range of [6.0, 72.5] deg/s.

The first two subjects performed the experiment for 7x5 pairs of speed and exposure times, and the remaining subjects for 3x3 pairs. We observe that the sub-sampled pairs (speed, exposure) for all subjects are sufficient to capture all effects on the (speed, exposure) plane. It should be noted that the angular speed values in Tab. I are determined by the chosen bar speed and the angle covered by the display in the FoV of the subjects (i.e., 46.4 degrees). During creation of the sequences, we defined the bar speed relative to the pixels on the display and chose values (e.g. 0.025, 0.1 or 0.2 pixels per simulation step) to minimize spatial discretization effects at the expense of obtaining aesthetically less appealing angle speed values.

B. Sequence Creation

A Python script creates the sequences using OpenCV [12], encodes the resulting video in h.264 [13] and writes it to a file for later presentation to the users. The script simulates the movement of the vertical bar at speed v in discrete-time steps at $f_{\text{sim}} = 20\,\text{kHz}$. This means that the script creates an image showing the bar at its current position 20,000 times per second in simulation time, and then applies the camera exposure time filter to create the output video sequence with a given frame rate, object speed, and exposure time. The simulation frequency was chosen considering that it provides a sufficiently small simulation complexity (all sequence sets could be created in approximately three days) and imperceptibly small time discretization effects. At $f_{\text{sim}} = 20\,\text{kHz}$, the temporal offset of capturing an event at an exact simulation time is at most $25\,\mu$s, which proved to be small enough for not being perceived by the test subjects. At lower simulation frequencies, time discretization effects become visible in some sequences.

The discretization effect can influence the resulting sequence in two perceivable ways: first, if temporal or spatial sampling frequencies are lower than human perceptual thresholds, test subjects will directly perceive temporal or spatial sampling. Second, imagine a bar that moves to the right 1.01 pixels per simulation step. After spatial discretization, its position will be incremented by one pixel, except for every 100th step, at which the position is incremented by two pixels. In this case, test subjects will be exposed to flicker with a frequency which is 100 times smaller than the simulation frequency. The analogous insight holds for the discretization of time.

In the temporal domain, this discretization effect is attenuated below the human perceptual threshold by choosing a large enough simulation frequency of 20 kHz. However in spatial domain, we are limited by the resolution of our display panel. This proved to be insufficient, which is the reason why we added linear interpolation at the edges of the bar: imagine that the left edge of the bar should be drawn at pixel position 2.4 (between pixels 2 and 3). Without interpolation, pixel 1 would be black (value 0), and pixels 2 and 3 would be white (value 255). With linear interpolation, pixels 1 and 3 retain their value, but the value of pixel 2 equals to $(1-0.4)\cdot 255 = 153$, where the term $(1-0.4)$ generalizes to "One minus distance to the closest integer pixel position". The use of linear interpolation reduced spatial discretization below human perception thresholds. In general, the degree of interpolation of pixel values has to equal the degree of the equation for object location with respect to time. A linear acceleration for example would require quadratic interpolation. Other movements could be interpolated using approximation through splines. As in our experiment, the white bar is moving at constant velocity (linear motion through space), linear interpolation is sufficient.

Finally, the script needs to simulate motion blur caused by the exposure time of the camera and the movement of the bar. This is done in a rather simple way: the script always keeps the bar images from the past $k = f_{\text{sim}} \cdot t_{\text{exp}}$ simulation steps. In order to create an output image of the camera, the script

1051-8215 (c) 2018 IEEE. Personal use is permitted, but republication/redistribution requires IEEE permission. See http://www.ieee.org/publications_standards/publications/rights/index.html for more information.

This article has been accepted for publication in a future issue of this journal, but has not been fully edited. Content may change prior to final publication. Citation information: DOI 10.1109/TCSVT.2018.2870256, IEEE Transactions on Circuits and Systems for Video Technology

computes the mean image of the past k images, which equals convolving the input image with the camera filter $h(x)$, see Fig. 2.

C. Sequence Playback

This section discusses the sequence player, the display, and the physical experimental setup. The player should be able to play the high-resolution sequences from the Python script (Section II-B) with precise frame timing. No available video player could meet this requirement, so we created our own player. It uses libav[2] for decoding, and SDL[3] for displaying. The decoder can decode any frame from any sequence within 1.5 ms, which is much smaller than the minimum frame period (i.e., 11.1 ms) we have in our sequences.

In the following, we assume that we want to display a video at a frame rate f_s with frame period $t_s = 1/f_s$. For frame timing, we used the *wait_until*() function of the chrono library. Just before showing a frame/image on the screen, we record the current time in time stamp $t_0 = t$. Next, we update the screen content and perform all computationally intensive and time varying tasks such as file reading, decoding, color space conversion and copying to the GPU. Then we wait until t_0+t_s, set the new time stamp to the current time $t_0 = t$ and update the screen content with the newly decoded image. This process is repeated until there is no frame left in the video file.

Because of processing overhead from setting the time stamp, the actual frame rate of the player was, depending on the frame rate, up to 1 Hz lower than the target frame rate f_s. This has been fixed by reducing t_s (increasing the frame rate) in the player according to a regression based on previous playback timing data. With that, the average playback frame rate did not deviate more than 0.05 Hz from the target frame rate. In addition, we evaluated the playback frame periods, and found them to closely match t_s, with a maximum absolute deviation of 30 μs per frame period.

We used an Acer XB270H as display. It has a 27-inch TN-panel, with a resolution of 1920 horizontal times 1080 vertical pixels. It supports Nvidia G-Sync, which refreshes the image whenever a new frame is available in the frame buffer (i.e., in contrast to conventional monitors) up to a maximum refresh rate of 144 Hz. With our sequences, we do not exceed 144 Hz, so this display allows us to show videos with the exact frame rate defined by our video player. Conventional monitors have fixed refresh rates, leading to delayed presentation of some video frames.

We evaluated both the player and the display time precision by encoding a video sequence that showed black and white frames interchangeably. While playing back this sequence, we put a photoresistor on the display surface and sampled its resistance with 8 kHz to observe the brightness change of the monitor with a high time resolution. This experiment proved that the setup is working as expected, frame period variations were smaller than 1/8 kHz = 125 μs.

The width of the display panel is $w = 60$ cm, test subjects are seated with an eye-to-panel distance of approximately $d = 70$ cm in front of the monitor. Therefore, the display spans 46.4 degrees of the horizontal field of view of the test subjects. Lighting in the room is dominated by artificial light to eliminate the influence of daylight or weather conditions.

[2]https://www.libav.org/, last visited 03.09.2018
[3]https://www.libsdl.org/, last visited 03.09.2018

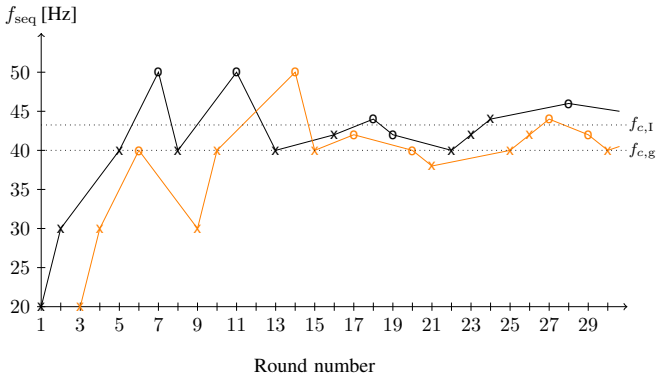


Fig. 4: Example of an adaptive interleaved staircase test with two sequence sets. In each round, set I (black line, absolute frame rate threshold $f_{c,\text{I}}$) or set g (orange line, absolute frame rate threshold $f_{c,\text{g}}$) is chosen randomly. Within each set, the answer to a sequence (x: could perceive stutter, o: could not perceive stutter) increases (x) or decreases (o) frame rate f_{seq} of the next sequence from that set by the current step size. Step size is 10 Hz in the beginning, and reduced to 2 Hz after four reversals in that set.

D. Participants

In addition to the two authors, seven male and one female subject were recruited to participate in the experiment. The age of all participants at experiment time ranged from 23 to 30 years, with a mean of 27.6 years. All participants have either normal or corrected-to-normal eyesight.

E. Experimental Procedure

In preliminary experiments, we used the method of constant stimuli [14] to retrieve a prior estimate of the absolute frame rate threshold, equal to the critical sampling frequency f_c from Section I-A, at which humans can distinguish time-discrete presentation of a video sequence from the continuous presentation of the same scene 50 % of the time. In the method of constant stimuli, test subjects are randomly presented a stimulus (video sequence) from a range of stimulus parameter values, in our case from a frame rate range. Stimuli from the range have to be sampled with equal spacing, and each stimulus must have equal probability for presentation to avoid errors of habituation and expectation. Hence, this method frequently presents stimuli which are rather distant from threshold f_c and accordingly easy to classify (redundant).

To avoid this issue, we used a modified variant of the simple up-down or staircase method [15], [16]. In the up-down method, the next sequence is chosen based on the answer for the previous sequence: if jerkiness was perceived (answer **x** in Fig. 4), the frame rate of the next sequence will be increased by for example 2 Hz, if no jerkiness was perceived (answer **o** in Fig. 4), frame rate will be lowered by the same step size of

1051-8215 (c) 2018 IEEE. Personal use is permitted, but republication/redistribution requires IEEE permission. See http://www.ieee.org/publications_standards/publications/rights/index.html for more information.

This article has been accepted for publication in a future issue of this journal, but has not been fully edited. Content may change prior to final publication. Citation information: DOI 10.1109/TCSVT.2018.2870256, IEEE Transactions on Circuits and Systems for Video Technology

2 Hz, see the black line at test round number 13 and greater in Fig. 4. This procedure ensures that frame rates close to threshold f_c will be frequently sampled, avoiding redundant stimuli. However, test participants will be able to predict frame rate, which leads to errors of expectation.

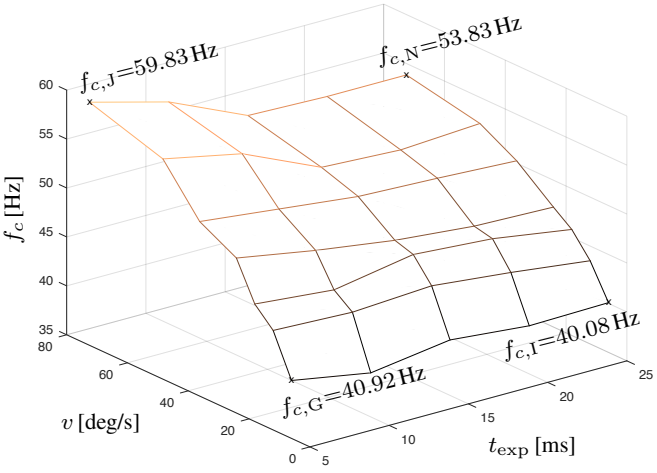
This is why we used the interleaved staircase method [16]. Here the test subject is presented, e.g., sequence sets I and g (see Tab. I for parameters, and Fig. 4 for an example). For each sequence set individually, the simple staircase method is used. In addition, the sequence sets are randomly interleaved, meaning that the next sequence to be presented is randomly chosen from the sequence sets I and g. After choosing the set of the next sequence, the sequence frame rate f_{seq} is determined according to the simple staircase based on the previous answer for the chosen set. This strongly impedes predicting frame rate, in particular if the number of sets is large enough and if the set parameters speed and exposure are sufficiently similar. In our experiments, we used at least three sequence sets for interleaving, making it impossible for test subjects to predict frame rates.

Further potential in increasing the efficiency of our experiment lies in its beginning: we start at a low [16] frame rate $f_{\text{seq}} = 20\,\text{Hz}$, which all test subjects classified as jerky for all sequence sets. The following considerations apply to one set: during the test, participants first have to converge to the absolute frame rate threshold f_c before being able to give the most relevant answers.

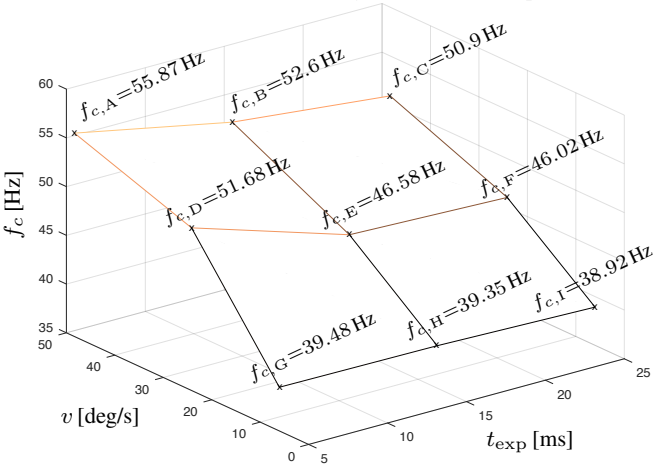
To speed up convergence, a step size larger than, e.g., 2 Hz could be used, which would decrease the precision of the result. Therefore, we use an adaptive step size in two experiment phases [17], [18], as shown in Fig. 4: in the first phase, we prefer to quickly converge to f_c, and thus choose a large step size of 10 Hz. This phase terminates when the test subject's answers have caused four reversals. A reversal takes place when the chosen frame rates f_{seq} pass through an extremum, meaning that frame rate was first decreased and then increased, or vice versa. After four reversals, the second phase, in which we use a smaller step size of 2 Hz, starts. The experiment finishes when twelve reversals have taken place during the second phase in each of the sequence sets.

We gave an oral introduction to all test subjects. In addition, they received an introductory sheet, which described the experiment, the user interface and encouraged behavior for result consistency, such as keeping a constant distance to the monitor (not leaning towards or away from it) and taking breaks if needed. The sheet states that "sequences are randomly chosen without any correlation", concealing the underlying adaptive interleaved staircase method. Distinguishing monocular from binocular vision is not necessary for motion perception [3], so we did not take any precautions in this respect.

The 35 sequence sets of the two author subjects from Tab. I were divided into eight interleaved experiment blocks with four sequence sets each, and one experiment block with three sequence sets. The nine sequences of the remaining eight test subjects, highlighted in Tab. I, were divided into one experiment block with the four sequence sets A to D, and one experiment block with the five sequence sets E to I.



(a) Plot for the two author test subjects on all 35 sequence sets.



(b) Plot for all test subjects on nine sequence sets.

Fig. 5: Surface plots of the average absolute frame rate thresholds (critical sampling frequencies) f_c. Corner points of the tetragons that constitute the bent planes correspond to the tested sequence sets and their absolute frame rate threshold f_c. The horizontal layout of the sample points in the velocity/exposure plane is based on Tab. I. Box plots corresponding to Fig. 5b are depicted in Fig. 6.

III. Results

The participants' answers were used to compute an absolute frame rate threshold f_c for each sequence set, which equals the mean of the last twelve reversals [18] on that set. These results are presented in the following.

A. Average Behavior of the Author Test Subjects

First, we conducted the experiment on all 35 sequence sets with the two author test subjects. The resulting f_c for all sets are depicted in Fig. 5a. In the horizontal layout of the graph in Fig. 5a, the array of sequence sets from Tab. I can be recognized.

We do not give a more precise plot or more values of f_c because this experiment is motivational and its exact values do not generalize, since it was conducted on only

1051-8215 (c) 2018 IEEE. Personal use is permitted, but republication/redistribution requires IEEE permission. See http://www.ieee.org/publications_standards/publications/rights/index.html for more information.

This article has been accepted for publication in a future issue of this journal, but has not been fully edited. Content may change prior to final publication. Citation information: DOI 10.1109/TCSVT.2018.2870256, IEEE Transactions on Circuits and Systems for Video Technology

two users. Still, the experiment shows that test sequence set sub-sampling is feasible. Revisiting the four hypotheses from Section I-B, we observe the following: first, we can see that higher speed v increases the absolute frame rate threshold f_c (hypothesis 1). Compare, for example, $f_{\mathrm{c,J}} = 59.83\,\mathrm{Hz}$, which shows the moving bar at an angular speed of 72.5 deg/s and $f_{\mathrm{c,G}} = 40.92\,\mathrm{Hz}$, which has an angle speed of 6.0 deg/s (see Tab. I). Hence, from the two opposing effects of speed v on f_c presented in Section I-B, the effect changing the steepness of the spatiotemporal spectrum (Fig. 1 and Eq. (3)) has more influence than the filter width d (Eq. (6) and Eq. (18)).

The second hypothesis, stating that higher exposure will decrease f_c, holds only for large enough speeds. There is a 6 Hz difference between $f_{\mathrm{c,J}}$ and $f_{\mathrm{c,N}}$, but only a 0.84 Hz difference between $f_{\mathrm{c,G}}$ and $f_{\mathrm{c,I}}$. The decrease in influence is understandable because the width of the camera filter $h(x)$ is equal to the product of speed and exposure time. Also, this insight confirms the third hypothesis, stating that at reduced speed the influence of exposure time will diminish.

Finally, the difference between $f_{\mathrm{c,J}}$ and $f_{\mathrm{c,G}}$ is larger than the difference between $f_{\mathrm{c,N}}$ and $f_{\mathrm{c,I}}$, confirming the fourth hypothesis: longer exposure time (causing increased motion blur) decreases the influence of speed.

All previous insights also hold for all test subjects, as we show in Section III-B.

B. Average Behavior of All Test Subjects

The graph in Fig. 5b illustrates the results for the average absolute frame rate threshold f_c. It can be seen that the conclusions from Section III-A generalize to all test subjects. The tendencies of frame rate thresholds of individual participants match the tendencies in Fig. 5b well; corresponding box plots are given in Fig. 6. We also see a grouping effect: sequence set D was presented in an interleaved experiment together with sets A, B, and C. This results in a comparably high $f_{\mathrm{c,D}} = 51.68\,\mathrm{Hz}$, in contrast to $f_{\mathrm{c,E}} = 46.58\,\mathrm{Hz}$ from sequence set E, which was interleaved with sets F to I.

Section IV-A gives a statistical analysis of the results.

C. Test Length and Difficulty

The ten test subjects spent overall 6 hours and 40 minutes performing the experiments for sets A to I, giving 2734 answers. Experiment time per participant was between 25 and 61 minutes, with an average of 44 minutes. For each sequence, participants spent on average 8.8 seconds from starting to watch the sequence until submitting an answer (fastest participant: on average 5.8 seconds, slowest participant: on average 15.6 seconds).

Users took on average two seconds more per sequence on the first experiment block with sets A to D than on the second block with sequence sets E to I. This is understandable since they started with the first block and had to get used to the experiment. Otherwise, we found no statistically significant difference in the average time users spent on classifying one set, or the average number of answers given for a set. Given no statistically significant difference, we can say that for none of the chosen sequence set parameters, test subjects had difficulties to complete the experiment.

D. Directional Independence

Existing literature does not observe a dependency between the direction of motion and the corresponding absolute frame rate threshold f_c. Cox and Derrington [19] presented eight motion directions to participants and found only minor and inconsistent differences for the temporal frequency threshold for a motion signal to be perceivable in contrast to no motion. The authors in [7] use a rotating disk for presenting motion in their experiments and do not report any direction influence.

To confirm these results, we rotated our screen 90 degrees, such that the bar was moving from top to bottom, and performed the tests from Section II-E on one participant. As expected, the differences to the thresholds f_c from the horizontal experiment were small and inconsistent. Thus, motion direction does not change the absolute frame rate perception threshold f_c. We use this result for simplifying the computation of required video frame rates in Section V-B.

IV. Discussion

In this paper, a constant sampling frequency (CSF) system denotes a system which samples signals with a constant period of time between two successive samples. Therefore, sampling with constant frequency is, in this manuscript, also temporally uniform sampling. In contrast to that, adaptive sampling frequency (ASF) systems do not have a fixed sampling period. The period between two successive samples is adapted to the sampled data.

To make notation more consistent, we consider sampling rates or frequencies for cameras as well as for displays. The notation is clear for cameras, which sample the incoming light. On the other hand, the data update process in displays is typically called image refresh, and thus refresh rate or refresh frequency describe the display update process. Actually, in display refresh, the display samples the contents of the frame buffer of the graphics processing unit that the display is attached to. This is why it is correct to call the display refresh process a sampling process and accordingly call the refresh rate of a display a sampling frequency.

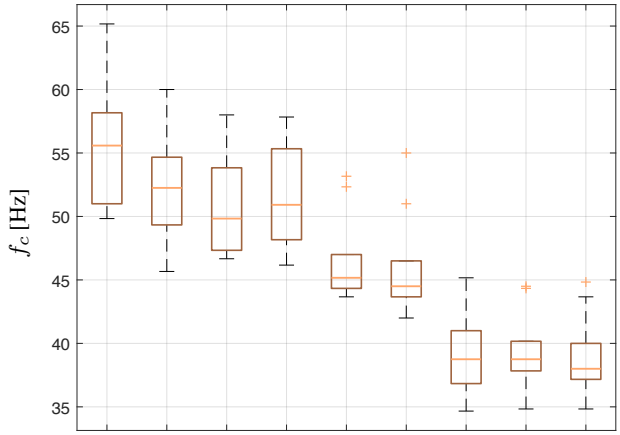
In summary, we refer in this paper to CSF and ASF cameras as well as CSF and ASF displays.

A. Statistical Significance of Tendencies

We analyze the statistical significance of the results from Section III. For a better understanding, box plots of the absolute frame rate thresholds f_c are depicted in Fig. 6. In Fig. 5b we see that increasing speed seems to increase the absolute frame rate threshold f_c for each of the exposure times 5 ms, 15 ms, and 25 ms. Applying Fisher's one-way analysis of variance (ANOVA) test [20] to the results from sets A, D, and G ($t_{\mathrm{exp}} = 5\,\mathrm{ms}$) reveals significant differences ($F(2, 27) = 37.24, p < 0.001$) of the thresholds. We find similar results ($F(2, 27) = 32.83, p < 0.001$) for sets B, E, and H ($t_{\mathrm{exp}} = 15\,\mathrm{ms}$) and for sets C, F and I ($t_{\mathrm{exp}} = 25\,\mathrm{ms}$), in which the ANOVA values ($F(2, 27) = 26.65, p < 0.001$) are once more statistically significant. The post-hoc Tukey test further revealed that the mean threshold of one set is

1051-8215 (c) 2018 IEEE. Personal use is permitted, but republication/redistribution requires IEEE permission. See http://www.ieee.org/publications_standards/publications/rights/index.html for more information.

This article has been accepted for publication in a future issue of this journal, but has not been fully edited. Content may change prior to final publication. Citation information: DOI 10.1109/TCSVT.2018.2870256, IEEE Transactions on Circuits and Systems for Video Technology



v [deg/s]	48	48	48	24	24	24	6	6	6
t_{exp} [ms]	5	15	25	5	15	25	5	15	25
Set	A	B	C	D	E	F	G	H	I

Fig. 6: Box plots of all participant thresholds for each of the nine sequence sets A to I. The boxes contain 50% of the data, the horizontal lines in them represent the median. Whiskers are at most 1.5 times the box height (interquartile range) and end at the lowest or highest found threshold value. Pluses denote outliers.

statistically significantly different ($p < 0.01$) from the other two set means for each exposure time.

As can be seen in Fig. 6, the influence of exposure time on threshold f_c is smaller than the effect of speed. Observing the box plots from sets A, B, and C, we also see that the variance of thresholds between sequence sets is small compared to the variance of thresholds within sets. Nevertheless, for the majority of test subjects, we saw a strong and consistent correlation between the individual test subject thresholds and exposure time t_{exp}. Therefore, the subjective differences between test subjects would conceal the existing dependency of threshold f_c on exposure time t_{exp} in a classical ANOVA test. This is why we apply a repeated measures ANOVA (RANOVA) test [20] to check statistical significance of the effect of exposure time t_{exp} on f_c. The RANOVA test computes the statistical significance of difference among data sets while ignoring variations between test subjects.

Applying RANOVA to sets A, B, and C yields significant differences ($F(2, 18) = 29.69, p < 0.001$) for thresholds f_c for varying exposure times at speed $v = 48$ deg/s. In addition, the post-hoc Tukey test reports significant pairwise differences for all set mean thresholds. The difference is significant at the 0.01 level in set pairs (A,B) and (A,C) and significant at the 0.05 level in set pair (B,C). For sets D, E, and F, RANOVA ($F(2, 18) = 17.05, p < 0.01$) again yields significant differences, but the post-hoc Tukey test finds a significant difference only on the pairs (D,E) and (D,F) at the 0.01 level. This result has to be read with caution, since the threshold result $f_{\text{c,D}}$ is higher than what we expected because of the grouping effect discussed in Section III-B. Finally, for $v = 6$ deg/s on sets G, H, and I, RANOVA ($F(2, 18) = 3.19, p = 0.065$) reveals that statistical significance at the 0.05 level is just missed. To back up this result, the post-hoc Tukey test finds no statistically significant differences in all three set pairs.

In summary, the tests confirm hypothesis 3: exposure time significantly affects f_c at high speeds v, while the influence vanishes at lower speeds.

B. Conclusions on the Absolute Frame Rate Threshold

In the previous sections, we found that both speed and exposure time have a significant influence on the absolute frame rate threshold, rendering Fig. 5b a valid model for predicting f_c. To be able to apply these insights to general scenarios, we fit a linear function to the data from Fig. 5b:

$$f_c(t_{\text{exp}}, v) = 40.44 - 153.2 \cdot t_{\text{exp}} + 0.3230 \cdot v, \qquad (21)$$

where t_{exp} is given in milliseconds and v in degree per second. We chose a linear model as with higher degrees for the polynomial we can achieve a closer fit of the model to the values present in Fig. 5b, but the higher degree polynomial does not extrapolate well to values of v and t_{exp} outside the region investigated in our experiment (overfitting). The linear model is based on the mean f_c, and hence critical sampling frequencies computed by it will make temporal sampling imperceptible to 50% of users. To satisfy a greater fraction of users, we can add a frequency offset f_o to Eq. (21), as done in Algorithm 1.

C. Mapping the Absolute Frame Rate Threshold to Constant Sampling Frequency Devices

Nowadays, in the vast majority of used displays, the constant sampling frequency (CSF) is not synchronized to the image source, in contrast to the specific display used in our experiment from Section II. In addition, practically all cameras in use (except dynamic vision sensors [21]) have constant sampling frequencies. Hence, we show how to map the frame rate threshold $f_c \in \mathrm{R}^+$ to its quantized version $\hat{f}_c$, dictated by the sampling frequencies of the involved CSF devices. The effective sampling frequency f_s of images visible at the display is equal to the minimum of the involved sampling frequencies. Assume for example a 50 Hz camera and a 60 Hz display, or the other way around: the effective displaying rate will in both cases be 50 Hz, as the device with higher sampling frequency will sample at least once during the sampling period of the lower sampling frequency device. The example shows that it does not matter whether the camera or the display is sampling at a lower frequency. For the following thought experiment, we assume the display to have the lower, constant sampling frequency.

A constant sampling frequency display can show videos with the original sampling rate f_s and integer fractions ($f_s/2$, $f_s/3$ etc.) of f_s by skipping one or more new images. Fig. 7 shows the possible reduced display sampling frequencies for $f_s \in [30, 350]$ Hz. As target displaying frequencies for this thought experiment, we take the range of $f_c \in [40, 60]$ Hz from Fig. 5 plus/minus a plausible safety margin of 20 Hz. Therefore, we target displaying frequencies in the range from 20 Hz to 80 Hz. We are in this example not interested in

1051-8215 (c) 2018 IEEE. Personal use is permitted, but republication/redistribution requires IEEE permission. See http://www.ieee.org/publications_standards/publications/rights/index.html for more information.

This article has been accepted for publication in a future issue of this journal, but has not been fully edited. Content may change prior to final publication. Citation information: DOI 10.1109/TCSVT.2018.2870256, IEEE Transactions on Circuits and Systems for Video Technology

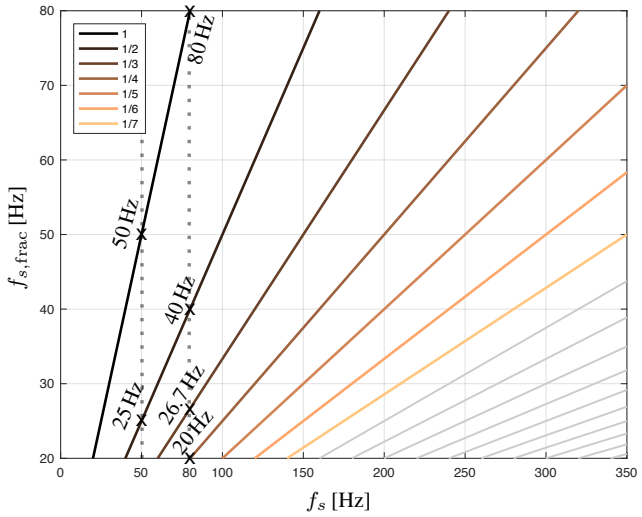


Fig. 7: Possible display sampling frequencies $f_{s,\mathrm{frac}}$ for given original sampling frequency f_s. Available display sampling frequencies are highlighted for $f_s = 50\,\mathrm{Hz}$ and for $f_s = 80\,\mathrm{Hz}$. For clarity, we show the legend only for the first seven integer fractions of each f_s. Greater fractions are depicted by gray lines.

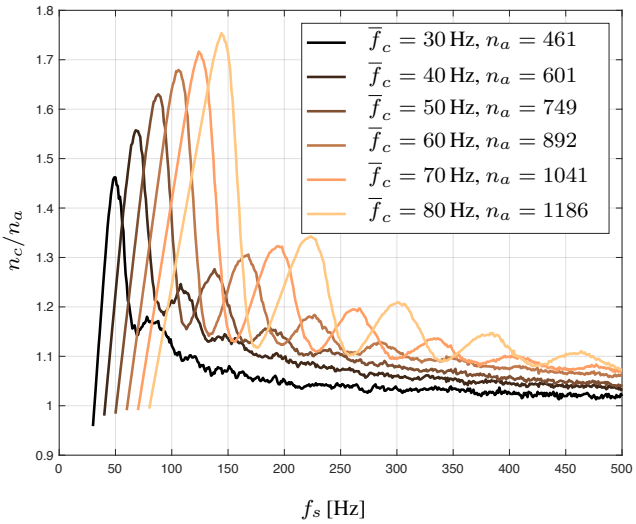


Fig. 8: Ratio of required frames n_c for playback on CSF displays compared to the number of frames required for playback on ASF displays n_a. Note that for $f_s < \overline{f}_c + 15$, users will be able to perceive stutter because in this model, the maximum occurring f_c is in that case greater than f_s.

displaying higher frequencies than 80 Hz, as users will probably not perceive the increase in frame rate over 80 Hz, and we are also not interested displaying a video below 20 Hz, as humans will certainly perceive temporal sampling at that frequency. It can be seen in Fig. 7 that for low $f_s = 50\,\mathrm{Hz}$ we can only choose between two target frequencies (50 Hz and 25 Hz) in the relevant range between 20 Hz and 80 Hz, while for increased sampling frequencies there are more displaying frame rates available (e.g. for $f_s = 80\,\mathrm{Hz}$, these are 80 Hz, 40 Hz, 26.7 Hz, and 20 Hz). In Section IV-D, we analyze how this frame rate quantization deteriorates the frame rate reduction that can be achieved by using the adaptive sampling rate proposed in this paper.

Since the goal is that the user is unable to perceive the sampling process, we want to display the video with the absolute frame rate threshold f_c or a higher frequency. As an example, let us assume that we have a display with 120 Hz, and the video content characteristics demand that it is shown at $f_c = 50\,\mathrm{Hz}$. With the given display, we can display 120 Hz, 60 Hz, 40 Hz and so on. Thus, we choose to display it with the frame rate just above f_c, which is in this case $\hat{f}_c = 60\,\mathrm{Hz}$. The analog thought experiment can be done for a CSF camera. We have implemented this temporal quantization in Section V-C. Fig. 9 shows the trace of the desired f_c for a video sequence and the actually displayed quantized frame rate $\hat{f}_c$.

D. Reduction of the Number of Frames in Constant Sampling Frequency Devices

As can be seen in Fig. 9, CSF systems require the video sequence to be displayed at a higher frequency $\hat{f}_c$ than requested by Eq. (21). In this section, we analyze the number and ratio of additional frames needed to show the video when a constant sampling rate device is involved.

We do so by simulating traces of f_c. The traces are created using an autoregressive model that reflects the trace characteristics seen in Fig. 9 and Section V-C. The mean absolute frame rate thresholds $\overline{f}_c$ range from 30 Hz to 80 Hz in steps of 10 Hz. The traces cover the 30 Hz interval $[\overline{f}_c - 15, \overline{f}_c + 15]$ Hz. For each of these traces, we compute the number of displayed frames n_a required to show the corresponding video when only ASF devices are involved.

In addition, we compute the number of displayed frames n_c required to show the video if CSF processes (camera or display) with sampling frequencies $f_s \in [30, 500]\,\mathrm{Hz}$ are involved. The ratio n_c/n_a depicted in Fig. 8 expresses the amount of additionally shown frames of a CSF device compared to an ASF device. Most importantly, the overhead n_c/n_a decreases with increasing sampling rate f_s. This is expected, as with higher f_s, we have more levels for the quantization of f_c. The worst case investigated here is for the trace with $\overline{f}_c = 80\,\mathrm{Hz}$ at $f_s = 144\,\mathrm{Hz}$. In this case, the amount of additionally played frames is 75% (factor $n_c/n_a = 1.75$ in Fig. 8). For commonplace 240 Hz devices, the ratio of additionally played frames never exceeds 20%. In Section V-C, we use a CSF camera with $f_s = 339\,\mathrm{Hz}$ and an ASF display. The mean display frame rates range from $\overline{f}_c = 46\,\mathrm{Hz}$ to $\overline{f}_c = 76\,\mathrm{Hz}$. Thus, the bit rate saving results presented in Tab. III are approximately between 5% and 12% worse than what would ideally be possible.

V. Applications in Video Compression

The insights from Section IV can be applied to video compression. To do so, we need to know pixel densities of various display classes, so an overview is given in this section. Subsequently, we present the procedure of extracting the adaptive playback frame rate from a coded video sequence. Finally, we provide experimental results of the proposed technique.

1051-8215 (c) 2018 IEEE. Personal use is permitted, but republication/redistribution requires IEEE permission. See http://www.ieee.org/publications_standards/publications/rights/index.html for more information.

This article has been accepted for publication in a future issue of this journal, but has not been fully edited. Content may change prior to final publication. Citation information: DOI 10.1109/TCSVT.2018.2870256, IEEE Transactions on Circuits and Systems for Video Technology

A. Display Classes

Various display classes have different pixel densities ρ. In our overview, we only cover horizontal size and angle, since the vertical size as well as angle directly follow for a given aspect ratio. Hence, knowing the size in one dimension allows us to map motion given as pixel offset to motion in centimeters per second on the screen. Typical display dimensions, distance of the user to the display, user's FoV covered by the display, the number of pixels in a display row, and the pixel density ρ from user perspective are given in Tab. II. In this table, we see that even within one display class pixel density can vary widely. The values in the last column of Tab. II can be used in Eq. (23) to map the on-screen speed to an angular velocity v from a spectator's perspective.

B. Extracting f_c from Coded Video Sequences

From motion vectors of a coded video sequence (in our example the h.264 [13] video codec), we can obtain the absolute frame rate threshold f_c for each video frame. The procedure is summarized in Algorithm 1.

Algorithm 1 Frame rate determination for frame i

1: Extract motion vectors $mv_{k,l,i}$
2: Scale motion vectors based on distance to reference frame
3: Apply 3D median filter (22) to the motion vectors
4: Compute maximum motion vector magnitude m_i
5: Calculate speed v_i using Eq. (23)
6: Compute frame rate threshold $f_{c,i}$ using Eq. (21)
7: Add desired frequency offset f_o to $f_{c,i}$
8: Quantize $f_{c,i}$ to an integer fraction of f_s

The h.264 codec identifies a matching block in the reference frame for each block in the current frame. The matching block is later used for prediction. Ideally, the matching block corresponds to the same image content, which has been offset as a result of motion apparent in the video. This is why the vectors indicating the spatial relation between the two blocks are called motion vectors. Occasionally, block similarity is not caused by motion, but just by similarity of image content in different locations. In that case, motion vectors do not represent the true motion. Hence, we need to filter the set of motion vectors.

Given the motion vectors $mv_{k,l,i}$ at block locations k, l (vertical, horizontal) of frame i, we first scale the motion vectors according to the temporal distance to their reference frame. If the reference frame is temporally adjacent, no scaling is done, if the reference is two frames away, the motion vector is divided by two, and so on. Afterwards, we apply the three-dimensional, spatiotemporal median filter (22) to suppress motion vectors that do not represent an actual motion. The filter

$$mvp_{k,l,i} = \underset{\substack{m,n\in[-2,2],\\ j\in[-6,0]}}{\text{median}} (mv_{k+m,l+n,i+j}) \tag{22}$$

takes the current motion vector and its spatially as well as temporally neighboring samples as in Eq. (22) as input. These filter dimensions have yielded good results in empirical tests. The filter only uses past and current motion vector samples to ensure causality.

The 3D median filter is applied to each spatial dimension of the motion vector separately. In the next step, we compute the motion vector magnitude. We are not interested in the direction, as discussed in Section III-D. Finally, for each frame i, we compute the maximum motion vector magnitude m_i from all motion vector magnitudes in the frame. This is done for the reason that the maximum motion apparent in the video is going to define the absolute frequency threshold for jitter perceptibility for the person viewing the video. Next, we compute the angular speed v from the user's perspective.

The maximum motion vector magnitude m_i within a frame divided by the temporal sampling frequency f_s of the video gives us the maximum occurring speed on the display. Together with display pixel density ρ (Tab. II) we can map speed m_i relative to the display panel to an angular speed v_i from the user's perspective:

$$v_i(m_i, \rho, f_s) = \frac{m_i \cdot f_s}{\rho} \ \ [\mathrm{deg/s}] \tag{23}$$

The resulting speed from Eq. (23) can be inserted into Eq. (21) to compute the current critical sampling frequency $f_{c,i}$ for video frame i. In the final steps, the frequency offset f_o is added to $f_{c,i}$, and the result is quantized to an integer fraction of f_s, as described in Section IV-C.

We have verified the correctness of the algorithm by watching the video and extracting the maximum object offset for a number of frames per hand. Comparing the manually extracted results to the values obtained with the algorithm presented in this section showed that steps 1-4 of Algorithm 1 are working precisely.

An alternative to using the results from video encoder motion analysis is applying a real-time optical flow algorithm [23], [24] to extract motion vectors for each frame. This might be necessary if e.g. video coding parameters restrict the motion vector length.

C. Experimental Results

We cannot apply the proposed methods to widely used test sequences such as the "Foreman" sequence because most of them have been recorded at 30 Hz, which is below f_c for almost all content. Consequently, we created our own sequences: At an exposure time of 2.5 ms, we recorded videos at $f_s = 339$ Hz and a resolution of 960×270 pixels using a XIMEA MQ022CG-CM camera. The raw image sequences were encoded using the x264 encoder [25], an implementation of the h.264 coding standard [13]. To ensure applicability in low delay video communication scenarios [2], we used the tunings *zerolatency* and *fastdecode* as well as preset *ultrafast* in the encoder.

We recorded sequences in which single or multiple objects are moving in front of a static background and sequences in which the camera is panning at varying speed and direction over three dimensional scenes, yielding various on-screen speeds. In Fig. 9, we can see the resulting f_c (orange) for a part of one sequence. Despite using the ASF display from Section

1051-8215 (c) 2018 IEEE. Personal use is permitted, but republication/redistribution requires IEEE permission. See http://www.ieee.org/publications_standards/publications/rights/index.html for more information.

This article has been accepted for publication in a future issue of this journal, but has not been fully edited. Content may change prior to final publication. Citation information: DOI 10.1109/TCSVT.2018.2870256, IEEE Transactions on Circuits and Systems for Video Technology

Class	Width [m]	User Dist. [m]	Covered FoV [deg]	Hor. Pix.	Pix. Density ρ [1/deg]
TV set	0.8 - 1.3	2 - 5	9 - 36	1280 - 4096	35 - 455
Smartphone	0.06	0.3 [22]	11	720 - 1440	65 - 130
Laptop	0.24 - 0.38	0.5	27 - 42	1440 - 4096	71 - 151
Computer	0.44 - 0.66	0.6 - 0.8	31 - 58	1440 - 4096	25 - 132
Head-Mounted Display	0.09	0.07	110	1080 - 1600	10 - 15

TABLE II: Typical display characteristics for representative display classes. In Head-Mounted Displays, a lens between display and eye widens the covered FoV.

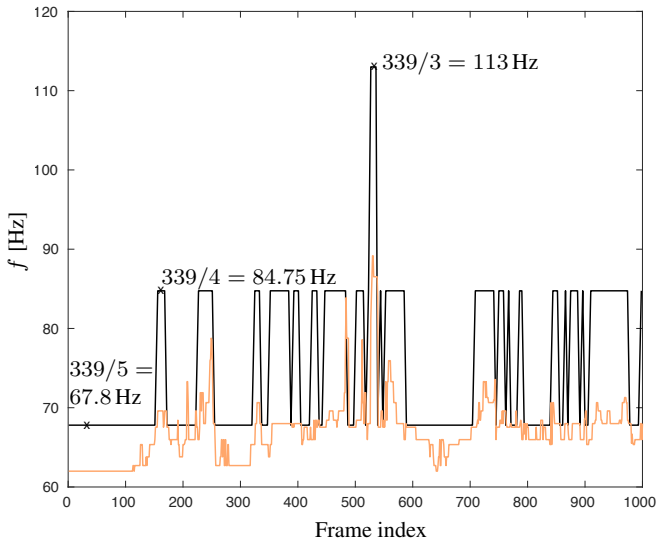


Fig. 9: f_c (orange), and its quantization $\hat{f}_c$ (black) for a video sequence with a constant sampling rate of $f_s = 339\,\text{Hz}$. We can see the three levels $339/3 = 113\,\text{Hz}$, $339/4 = 84.75\,\text{Hz}$, and $339/5 = 67.8\,\text{Hz}$ for $\hat{f}_c$.

II-C, we need to quantize f_c as a CSF camera is involved in the video processing chain. The quantization to integer fractions of $f_s = 339\,\text{Hz}$ is shown by the black line in Fig. 9.

A note on how adding f_o nonlinearly affects the maximum playback frequency $f_{\max}$: in Fig. 9 ($f_o = 0\,\text{Hz}$), the highest non-quantized f_c is approximately 90 Hz. The frequency quantization rule forces the playback frame rate to the next higher available frequency, therefore $f_{\max} = 339/3 = 113\,\text{Hz}$. In the example in Fig. 9, if we add a frequency offset f_o of e.g. 20 Hz, the maximum playback frequency $f_{\max}$ will not change because $f_c + f_o = 90 + 20\,\text{Hz} < 113\,\text{Hz}$. If, for example, we add a frequency offset of $f_o = 30\,\text{Hz}$ (now, $f_c + f_o = 90 + 30 = 120\,\text{Hz} > 113\,\text{Hz}$), the algorithm would quantize to the next higher available frequency, therefore $f_{\max} = 339/2 = 169.5\,\text{Hz}$. In conclusion: depending on its value, f_o might have no effect on $f_{\max}$, or it might push $f_{\max}$ to another available frequency quantization level.

We verified the model in Eq. (21) and Algorithm 1 by letting users view the sequences played back at $\hat{f}_c$. As predicted in Section IV-B, we noted that different users require different frequency offsets f_o to be added to the result of model (21) in order not to notice any jitter. The most sensitive participant required $f_o = 20\,\text{Hz}$ to be added to Eq. (21). After this addition and video playback with the corresponding frequency, users did not notice any temporal sampling.

The bit rate of a video played back with ASF can be compared to the required bit rate of a video played back with CSF. The constant sampling and display frequency f_s has to correspond to the highest frequency $f_{\max}$ in the ASF sequence for humans never to be able to perceive temporal sampling. In the following, we investigate three video sequences recorded with parameters presented in the beginning of this section:

- **MessyRoom**: The camera pans over an untidy room with many details. Camera motion is random, and the camera almost never rests.
- **Whiteboard**: The camera pans over a whiteboard with written text on it, and towards the end of the video, an arm is moving through the camera's field of view.
- **Catwalk**: The camera is in a fixed position, and a person walks multiple times through the camera's field of view. The person swings his arms actively, so various objects are moving at different speeds and directions at once.

Tab. III shows the frequency and average bit rate results for these sequences. All videos are encoded at the same default image quality settings to achieve the same (except negligible numerical variations) picture quality for all encoded videos. We investigate ASF Algorithm 1 for frequency offsets $f_o = 0\,\text{Hz}$ and $f_o = 20\,\text{Hz}$. In the corresponding columns, the entries show the average video bit rate r in megabits per second (Mbps), mean playback frequency $\overline{f}_c$, and maximum playback frequency $f_{\max}$.

For CSF playback, Tab. III shows the average bit rates r at sampling frequencies f_s corresponding to the maximum playback frequencies in the previous columns. We compare the maximum frequency because in both the ASF and the CSF playback, humans may not be able to perceive temporal sampling. Hence, in the CSF case, the sequence has to be played back at $f_s = f_{\max}$. This is why we present CSF bit rates only at the frequencies occurring in the ASF cases. Finally, the last two columns summarize the bit rate savings

$$\Delta r = \frac{r_{\text{CSF}} - r_{\text{ASF}}}{r_{\text{CSF}}} \tag{24}$$

of ASF over CSF video processing.

We can see that the reduction of average bit rate ranges from 15.4% to 39.1%. The exact amount of rate savings depends mainly on the variance of motion speed v. If variance of speed v is large, we can expect a greater reduction: ASF would exhibit the greatest bit rate savings if there is high speed apparent for a short period of time (leading to a high $f_{\max}$,

1051-8215 (c) 2018 IEEE. Personal use is permitted, but republication/redistribution requires IEEE permission. See http://www.ieee.org/publications_standards/publications/rights/index.html for more information.

This article has been accepted for publication in a future issue of this journal, but has not been fully edited. Content may change prior to final publication. Citation information: DOI 10.1109/TCSVT.2018.2870256, IEEE Transactions on Circuits and Systems for Video Technology

Sampling	ASF, $f_o = 0\,\mathrm{Hz}$			ASF, $f_o = 20\,\mathrm{Hz}$			CSF: $r(f_s)$			$\Delta r(f_o)$	
Metric	r	$\overline{f}_c$	$f_{\max}$	r	$\overline{f}_c$	$f_{\max}$	$r(67.8)$	$r(84.75)$	$r(113)$	$\Delta r(0)$	$\Delta r(20)$
MessyRoom	**4.75**	50.45	84.75	**6.98**	75.88	113	-	**7.80**	**10.44**	39.1%	33.1%
Whiteboard	**4.54**	49.95	84.75	**6.58**	71.46	113	-	**7.86**	**10.24**	16.3%	35.7%
Catwalk	**2.64**	46.36	67.8	**3.73**	69.08	84.75	**3.12**	**4.47**	-	15.4%	16.6%

TABLE III: Bit rate savings of adaptive sampling frequency (ASF) over constant sampling frequency (CSF). Average bit rate r is given in megabits per second, frequencies in Hz. The bit rate savings in the rightmost two columns are the relative difference between the CSF bit rate and the ASF bit rate with the corresponding highest frequency $f_{\max}$ computed using Eq. (24).

defining f_s for CSF), and most of the time there is little to no motion (leading to a low $\overline{f}_c$). On the other hand, with constant speed v, there would be no difference between ASF and CSF. From these examples it becomes clear that ASF does never increase bit rate r compared to CSF if the video is played back at a frequency such that temporal sampling is imperceptible to humans.

VI. Conclusions

Our psychophysical study showed that the critical temporal video sampling rate depends on both object speed and camera exposure time. Based on the retrieved data, we built a model to compute this sampling rate as a function of speed as well as exposure time. In experiments, we have seen that playback at an adaptive sampling frequency defined by this model on average yields a 26% bit rate saving compared to constant sampling frequency playback.

This work will be used to refine the frame skipping algorithm in [2] and make temporal sampling imperceptible to viewers. However, the results of this paper are not constrained to that usage scenario, they can be applied to any video application with variable frame rate. For example, the frame rate of a video can be well below the perception threshold, but at a level that provides a user experience equal to a given, fixed frame rate video playback. This will reduce video bit rate, while not changing the perceived video quality.

Computer-generated graphics (CG) can also profit from our results: using a speed-dependent frame rate can reduce energy consumption in low-motion scenes and increase user satisfaction in motion-rich scenes. Furthermore, CG applications can model exposure time as in [26] to reduce the required frame rate.

References

[1] Christoph Bachhuber and Eckehard Steinbach, "Are today's video communication solutions ready for the tactile internet?," in *Wireless Communications and Networking Conference Workshops (WCNCW)*. IEEE, 2017, pp. 1–6.

[2] Christoph Bachhuber, Eckehard Steinbach, Martin Freundl, and Martin Reisslein, "On the minimization of glass-to-glass and glass-to-algorithm delay in video communication," *IEEE Transactions on Multimedia*, vol. 20, no. 1, pp. 238–252, 2018.

[3] Gunnar Johansson, "Visual motion perception," *Scientific American*, vol. 232, no. 6, pp. 76–89, 1975.

[4] Andrew M Derrington, Harriet A Allen, and Louise S Delicato, "Visual mechanisms of motion analysis and motion perception," *Annual Review of Psychology*, vol. 55, pp. 181–205, 2004.

[5] Timothy Ledgeway and Andrew T Smith, "Evidence for separate motion-detecting mechanisms for first-and second-order motion in human vision," *Vision Research*, vol. 34, no. 20, pp. 2727–2740, 1994.

[6] Charles Chubb and George Sperling, "Drift-balanced random stimuli: a general basis for studying non-fourier motion perception," *Journal of the Optical Society of America A*, vol. 5, no. 11, pp. 1986–2007, 1988.

[7] Adriane E Seiffert and Patrick Cavanagh, "Position displacement, not velocity, is the cue to motion detection of second-order stimuli," *Vision research*, vol. 38, no. 22, pp. 3569–3582, 1998.

[8] Edward H Adelson and James R Bergen, "Spatiotemporal energy models for the perception of motion," *Journal of the Optical Society of America A*, vol. 2, no. 2, pp. 284–299, 1985.

[9] Andrew B Watson, Albert J Ahumada, and Joyce E Farrell, "Window of visibility: a psychophysical theory of fidelity in time-sampled visual motion displays," *Journal of the Optical Society of America A*, vol. 3, no. 3, pp. 300–307, 1986.

[10] Ronald Newbold Bracewell, *The Fourier transform and its applications*, vol. 31999, McGraw-Hill New York, 1986.

[11] Myron Yanoff, Ben S Fine, and J Donald M Gass, *Ocular pathology*, Mosby-Wolfe London, 1996.

[12] Gary Bradski, "The OpenCV Library," *Dr. Dobb's Journal of Software Tools*, 2000.

[13] Thomas Wiegand, Gary J Sullivan, Gisle Bjontegaard, and Ajay Luthra, "Overview of the h.264/AVC video coding standard," *IEEE Transactions on Circuits and Systems for Video Technology*, vol. 13, no. 7, pp. 560–576, 2003.

[14] Donald Laming and Janet Laming, "F. Hegelmaier: On memory for the length of a line," *Psychological Research*, vol. 54, no. 4, pp. 233–239, 1992.

[15] Harry Levitt, "Transformed up-down methods in psychoacoustics," *The Journal of the Acoustical Society of America*, vol. 49, no. 2B, pp. 467–477, 1971.

[16] Tom N Cornsweet, "The staircase-method in psychophysics," *The American Journal of Psychology*, vol. 75, no. 3, pp. 485–491, 1962.

[17] Marjorie R Leek, "Adaptive procedures in psychophysical research," *Attention, Perception, & Psychophysics*, vol. 63, no. 8, pp. 1279–1292, 2001.

[18] Federico Barbagli, Ken Salisbury, Cristy Ho, Charles Spence, and Hong Z Tan, "Haptic discrimination of force direction and the influence of visual information," *ACM Transactions on Applied Perception (TAP)*, vol. 3, no. 2, pp. 125–135, 2006.

[19] Michael J Cox and Andrew M Derrington, "The analysis of motion of two-dimensional patterns: do fourier components provide the first stage?," *Vision Research*, vol. 34, no. 1, pp. 59–72, 1994.

[20] Ralitza Gueorguieva and John H Krystal, "Move over anova: progress in analyzing repeated-measures data and its reflection in papers," *Archives of General Psychiatry*, vol. 61, no. 3, pp. 310–317, 2004.

[21] Patrick Lichtsteiner, Christoph Posch, and Tobi Delbruck, "A 128x128 120 db 15us latency asynchronous temporal contrast vision sensor," *IEEE Journal of Solid-State Circuits*, vol. 43, no. 2, pp. 566–576, 2008.

[22] Yuliya Bababekova, Mark Rosenfield, Jennifer E Hue, and Rae R Huang, "Font size and viewing distance of handheld smart phones," *Optometry and Vision Science*, vol. 88, no. 7, pp. 795–797, 2011.

[23] Ted Camus, *Real-time optical flow*, Society of Manufacturing Engineers, 1994.

[24] Javier Díaz, Eduardo Ros, Francisco Pelayo, Eva M Ortigosa, and Sonia Mota, "Fpga-based real-time optical-flow system," *IEEE Transactions on Circuits and Systems for Video Technology*, vol. 16, no. 2, pp. 274–279, 2006.

[25] Loren Merritt and Rahul Vanam, "x264: A high performance h. 264/avc encoder," *https://www.videolan.org/developers/x264.html*, 2006.

[26] Michael Potmesil and Indranil Chakravarty, "Modeling motion blur in computer-generated images," *ACM SIGGRAPH Computer Graphics*, vol. 17, no. 3, pp. 389–399, 1983.

1051-8215 (c) 2018 IEEE. Personal use is permitted, but republication/redistribution requires IEEE permission. See http://www.ieee.org/publications_standards/publications/rights/index.html for more information.

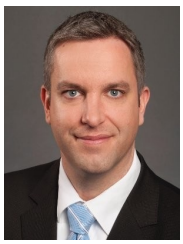
This article has been accepted for publication in a future issue of this journal, but has not been fully edited. Content may change prior to final publication. Citation information: DOI 10.1109/TCSVT.2018.2870256, IEEE Transactions on Circuits and Systems for Video Technology



Christoph Bachhuber received the B.Sc. degree in electrical engineering and information technology from Technical University of Munich (TUM), Germany, in 2012 and the corresponding M.Sc. degree in 2014. He joined the Chair of Media Technology at TUM in 2014, where he is a member of the Research and Teaching Staff and is working towards his Ph.D. degree. His research interests include delay in video communication, vision-based control, augmented reality, and video coding.



Amit Bhardwaj received his B.Tech. degree in Electronics and Communication Engineering (ECE) in 2009 from YMCAIE Faridabad, Haryana, India, and his M.Eng. degree in ECE in 2011 from the Delhi College of Engineering, Delhi, India. In July 2011, he joined the department of Electrical Engineering (EE) at the Indian Institute of Technology (IIT) Bombay, Mumbai, India to pursue his Ph.D. degree, and completed the degree in June 2016. From June 2016 to January 2017, he was a research associate in the EE department at the IIT Bombay, Mumbai. From February 2017 to December 2017, he was an Alexander von Humboldt post-doctoral fellow at the Chair of Media Technology, Technical University of Munich, Germany. Since February 2018, he is a post-doctoral researcher at the Haptics and Virtual Reality (HVR) lab, Pohang University of Science and Technology (POSTECH), South Korea. He is a co-author of the book *Kinesthetic Perception - A Machine Learning Approach* published by Springer. His current research interests are in the area of data-driven haptic modeling and rendering, haptic perception, haptic data communication, signal processing, and applications of machine learning.



Rastin Pries studied Computer Science at the University of Wuerzburg (Germany). From 2004 to 2012 he was a member of the research staff of the Chair of Communication Networks at the University of Wuerzburg, where he received his doctoral degree in 2010. From 2012 to 2015 he was a technical consultant at VDI/VDE-IT for publicly funded research projects. In 2015 he joined NOKIA Bell Labs in Munich, Germany. His current research interests are the applicability of network slicing, NFV and data plane programmability concepts to 5G mobile networks as well as networked and interactive multimedia systems using edge clouds.



Eckehard Steinbach (M96-SM08-F15) studied Electrical Engineering at the University of Karlsruhe (Germany), the University of Essex (Great Britain), and ESIEE in Paris. From 1994 to 2000 he was a member of the research staff of the Image Communication Group at the University of Erlangen-Nuremberg (Germany), where he received the Engineering Doctorate in 1999. From February 2000 to December 2001 he was a Postdoctoral Fellow with the Information Systems Laboratory of Stanford University. In February 2002 he joined the Department of Electrical Engineering and Information Technology of Technical University of Munich, Germany, where he is currently a Full Professor for Media Technology. His current research interests are in the area of audio-visual-haptic information processing and communication as well as networked and interactive multimedia systems.

1051-8215 (c) 2018 IEEE. Personal use is permitted, but republication/redistribution requires IEEE permission. See http://www.ieee.org/publications_standards/publications/rights/index.html for more information.

International Journal of Research in Engineering and Innovation (IJREI)
journal home page: http://www.ijrei.com
ISSN (Online): 2456-6934



Performance parametric analysis of retrofitted Gas turbine cycle using STIG and Evaporative cooling techniques

R.S. Mishra, Shyam Agarwal

Department of Mechanical & Production Engineering, Delhi Technological University Delhi, India

Abstract

The present paper represents the parametric analysis of retrofitted gas turbine cycle on the basis of energy and exergy principles of thermodynamics. The retrofitting techniques i.e. inlet air evaporative cooling (EVC) and steam injection to gas turbine (STIG) have been considered incorporation to the basis gas turbine cycle to investigate the performance of cycle. An Engineering Equation Solver (EES) software program has been developed to explore the effect of ambient temperature and relative humidity of air on various performance parameters i.e. power output, heat rate, thermal efficiency, generation efficiency, first law efficiency, exergetic efficiency and exergy destruction rate. It has been observed that the power output, thermal efficiency, generation efficiency, first law efficiency and exergetic efficiency get enhanced; however, heat rate declines with increase in ambient temperature. The association of combined EVC and STIG technologies to the basic gas registers 45% increment in power output, 4.5% increment in thermal efficiency and 26% enhancement in exergetic efficiency during summer days at 50^0C ambient temperature and 80% relative humidity of ambient air. The combustion chamber is the most sensitive system component in exergy destruction. © 2018 ijrei.com. All rights reserved
Keywords: Gas turbine, Retrofitting, EVC, STIG, Exergy

1. Introduction

The thermodynamic processes of a simple cycle gas turbine can be approximately modeled as a Brayton cycle, in which the back work ratio is usually very high, and the exhaust temperature is often 500 ^{0}C. A high exhaust temperature implies that there is plenty of useful energy has waste to the environment. The recovery of this otherwise waste energy can be used to improve either the power generation capacity or efficiency. Simple gas turbine power generation systems are widely used in Indian industries due to quick startup and shutdown capabilities. These units are mostly used to fulfill the peak load demand but unfortunately suffer from very low overall efficiency and reduction in power output during the summer season, when electricity demand is the highest. To investigate the anticipated power shortage, retrofitting projects have been seriously gaining momentum to covert these existing simple gas turbine systems into relatively advanced cycle units resulting in both improved efficiency and power output.

Various research and development work is going on around the world to reduce the compressor work and simultaneously reduce the heat supplied. The compressor work can be reduced by cooling the inlet air to the compressor. It can be achieved by an efficient and economical spray cooling technique. In which, the ambient air has been cooled by adding spray of water at wet bulb temperature up to its saturation limit in an isolated chamber (spray chamber). The adiabatic mixing of air and water exchange heat and the sensible heat of air has been transferred to the water and the water has become evaporated. In this manner, the addition of water vapour has been taken places to the air and the temperature of the resulting air has been reduced and mass flow rate gets improved by means of fog cooling unit or (EVC) evaporative cooling system. The performance of gas turbines can be enhanced by doing minor modifications in gas turbines without major destruction to its original integrity. One of the most interesting aspect of gas turbine is that waste heat of flue gases can be used in generating steam at high pressure. Higher pressure steam can be used for injection in combustion chamber as STIG (steam injected gas turbine) at different injection ratio from 0 to 0.2. These attractive features can improve the power generation capacity and efficiency of the power generation system to a considerable extent. Again, steam injection can reduce NO_x

Corresponding author: R. S. Mishra
Email Address: hod.mechanical.rsm@dtu.ac.in

and SO_2 emissions. These enhancements are nowadays in application in some parts of the world and expected to widen throughout the world because gas turbine is thermo economically advantageous. Performance improvement through retrofitting is the main motivation of this work. Bhargava & Homji [1] have studied parametric analysis of existing gas turbines with inlet evaporative and overspray fogging. This study shows the effects of inlet fogging on a large number of commercially available gas turbines. Chaker et al. [2] have developed the formulation for fog droplet sizing analysis and discussed various nozzle types, measurement and testing. This study describes the different available measurement techniques, design aspects of nozzles, with experimental and provides recommendations for a standardized nozzle testing method for gas turbine inlet air fogging. Sinha & Bansode [3] have studied the effect of fog cooling system for inlet air cooling. They concluded that performance parameters indicative of inlet fogging effects have a definite correlation with the climate condition (humidity and temperature) and showed improvement in turbine power and heat rate. Moran et al. [4] has developed design and economic methodology for the gas turbine cogeneration system. Wang & Chiou [5] suggested that application of IAC and STIG technique can boost the output and generation efficiency. They concluded that implementing both STIG and IAC features cause more than a 70% boost in power and 20.4 % improvement in heat rate. Kumar et al. [6] have been developed design methodology for parametric study and thermodynamic performance evaluation of a gas turbine cogeneration system (CGTS). Pelster et al. [7] studied the combined cycle with advanced options viz. compressor air inter-cooling, water injection and reheating. They studied environmental and economic analysis simultaneously. They have optimized the system for economic and other better operations. Korakianitis et al. [8] investigated parametric performance of combined-cogeneration power plants with various power and efficiency enhancements. The performance of combined-cogeneration power plants is dominated by the gas turbine performance. The performance of these plants is optimized by A. maximizing turbine rotor inlet temperature in the gas turbine. B. Optimizing the gas turbine pressure ratio for gas-turbine performance. C. Optimizing steam turbine boiler pressure and D. Maximizing steam injection in the gas turbine. Hawaj & Mutairi [9] studied a cogeneration system comprising a combined cycle power plant (CCPP) with an absorption chiller used for space cooling. They have also studied the relative advantage of using CCPP with absorption cooling over thermally equivalent mechanical vapor compression (MVC).They found that a cogeneration CCPP with absorption cooling yields significantly less power penalty than a CCPP with a MVC cooling. Facchini [10] has performed the detailed study of reheat gas turbine/combined cycle and close loop steam gas cooled gas turbine. The detailed exergy balance is used in this study to compare the performance of plant sections and to understand the margin for potential improvement. Nishida et al. [11] have analyzed the performance characteristics of two configurations of regenerative steam-injection gas turbine (RSTIG) systems. They concluded that the thermal efficiencies of the RSTIG systems are higher than those of regenerative, water injected and STIG systems. Many researchers [12-21] have investigated the performance of simple and combined gas turbine cycle. Retrofitted techniques have also explored and it is observed that the retrofitted technologies like inlet air evaporative cooling (EVC) and steam injection to gas turbine improves the performance of the cycle [21].

From the above gathered literature review from different established data sources like Research Gate, Science Direct and Google Scholar etc. It has been concluded that opportunities are available to analyze different retrofitted techniques for gas turbine cycles viz. spray cooling technique, combined evaporative cooling and STIG etc. In this communication, a simple cycle gas turbine unit is considered as base unit and this unit has been retrofitted with fog cooling or EVC (evaporative cooling), STIG (steam injected gas turbine) and combined cycle (fog cooling and STIG both). The performance improvement has been thermodynamically analysed and discussed for above mentioned retrofitted techniques followed by performance studies.

2. Thermodynamic model for parametric analysis

2.1 Description of system

Fig.1 shows the schematic diagram of simple gas turbine integrated to evaporative cooling system (fog cooling system) and STIG system. It consists of an evaporative cooling system (fog cooling system), a compressor, a combustion chamber unit, a simple gas industrial turbine and a HRSG unit. HRSG unit consists of an economizer, an evaporator and a super-heater. Evaporative cooling system consists of nozzles and an isolated chamber (duct) in which adiabatic heat transfer takes place. Pressurized liquid water is sprayed into the duct through nozzles at corresponding wet-bulb temperature. Fog cooling is an evaporative cooling method of cooling the intake air by demineralised water. Water is converted into fog droplets by means of special atomizing nozzles operating at approximately 138bar. The evaporation of small size (5-20 microns) droplets in the intake duct cools the air and consequently increases the mass flow rate. This technique allows close to 100% evaporative effectiveness in terms of attaining saturation conditions and wet-bulb temperature at the gas turbine inlet. The evaporative cooling process works essentially with conversion of sensible heat in latent heat. The surrounding ambient air is cooled by evaporation of water from the wet surface of the panel to the air. The addition of water vapour to the air increases its latent heat and relative humidity. If the process is adiabatic, this increases the latent heat compensated by a reduction of the sensible heat and consequent reduction of the dry bulb temperature of air as shown in Fig. 1.

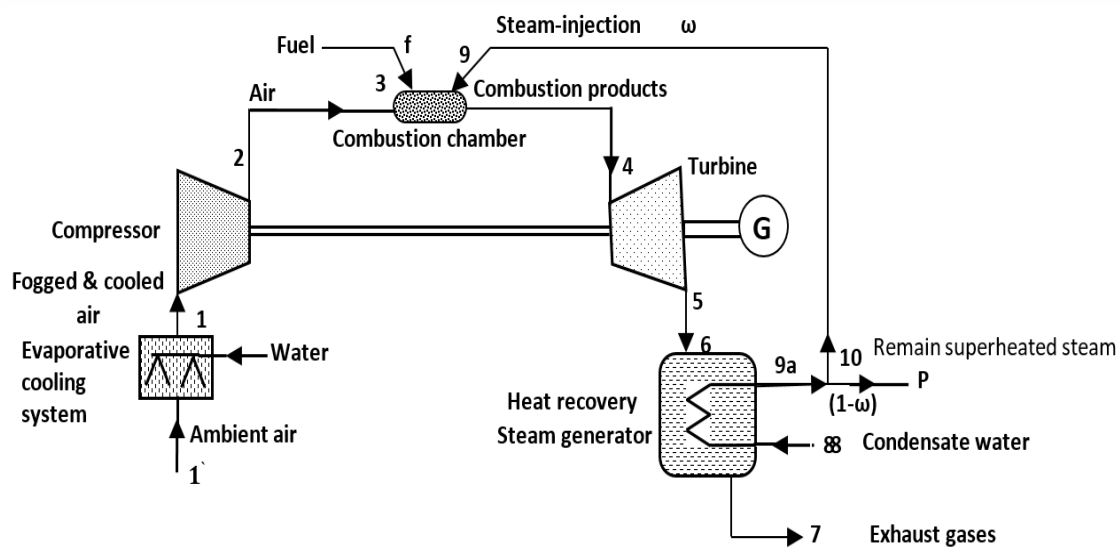


Figure 1: Schematic diagram of Simple gas turbine cycle retrofitted to EVC and STIG

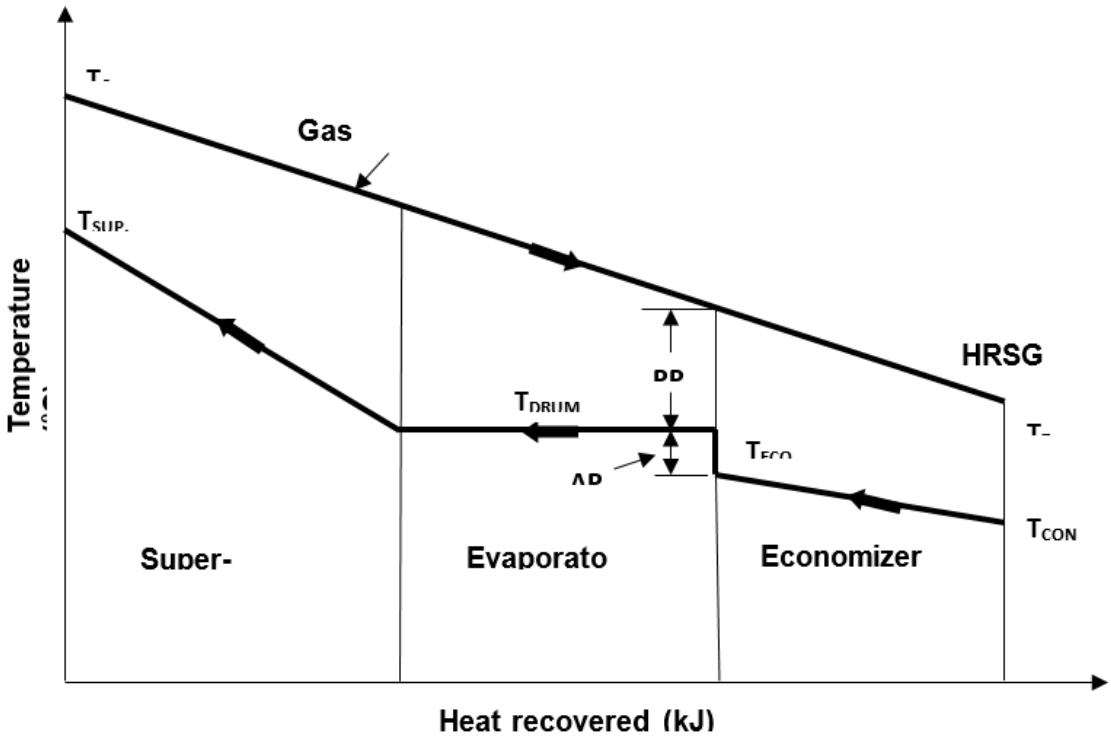


Figure 2: Temperature- heat energy diagram of HRSG

The amount of fog is to be monitored base on dry and wet bulb ambient conditions to achieve the required cooling. A typical fog cooling system consists of a high pressure pump skid connected for feeding to an array of manifolds located at a suitable place across the compressor inlet duct. The manifolds have a requisite number of fog nozzles[6] which inject very fine droplets of water into the inlet air. The discharge through each nozzle is around 3ml/s and produces 3 billion droplets per second. The fine fog evaporates very fast, thus dropping inlet air temperature. The simple cycle gas turbine system integrated to both IAC and STIG feature has been shown in Fig. 1. A heat recovery steam generator (HRSG) has been installed at the downstream exit of the turbine (state point 5) in order to recover the heat from the exhaust gases as shown in Fig.1 and 2. The fraction of superheated steam generated from the HRSG is used for STIG (state point 9) and the remaining steam is used

for process application. HRSG consists of an economizer, evaporator and super-heater. The waste heat received from the exhaust of turbine at the inlet of HRSG at state point 6 converts the condensate water passing through economizer, evaporator and superheat into superheated steam at state 9a as shown in Fig.2. A fraction (ω) of superheated steam is fed to the combustion chamber at state9. The remain superheated steam (1-ω) is available to use in other process applications.

2.2 Mathematical modeling

The current analysis presents the parametric investigations of simple gas turbine cycle which has been retrofitted to evaporative cooling (EVC) and steam injection gas turbine (STIG). The retrofitted techniques improve the performance of the cycle. A computer code has been developed in Engineering Equation Solver (EES) [16] software for the computation of performance parameters. Steady state governing equations based on first and second law of thermodynamics have been formulated for control volume systems. Mass and energy conservation principles have been considered and the following assumptions have been assumed to develop complex thermodynamic model. [4, 20]

- The temperature of combustion chamber is assumed to be constant.
- 100% relative humidity to the ambient air in the evaporative cooling system.
- The ambient air is at dry bulb temperature and having 60% of R.H. (except where the variation has been done).
- The composition of dry and ambient air assumed in terms of molar fraction of 1 mole of air is: (N_2 = 0.78981, O_2 = 0.20989, CO_2 = 0.00031 and H_2O = 0) & (N_2=0.7748, O_2=0.2059, CO_2=0.00030 and H_2O=0.0190).
- The fuel (natural gas) is taken as methane modeled as an ideal gas. The fuel is provided to the combustion chamber at the required pressure.
- The combustion in the combustion chamber is complete and N_2 is assumed as inert gas.
- The pressure of water injected from the nozzle into the evaporative cooling chamber has been assumed 138 bar.

A set of governing equations for a particular component (k) is expressed as:

Mass rate balance

$$\sum_i \dot{m}_{i,k} = \sum_e \dot{m}_{e,k} \quad (1)$$

Energy balance

$$\dot{Q}_{cv,k} - \dot{W}_{cv,k} = \sum_e \dot{m}_{e,k}\, h_{e,k} + \sum_i \dot{m}_{i,k}\, h_{i,k} \quad (2)$$

Exergy balance

$$\dot{E}_{D,k} = \sum \dot{E}_{q,k} - \dot{W}_{cv,k} + \sum_i \dot{E}_{i,k} - \sum_e \dot{E}_{e,k} \quad (3)$$

2.3 Evaporative cooling system

$$\dot{m}_w(h_{v1} - h_{w1}) = \dot{m}_a(h_{a1`} - h_{a1}) + \omega_{1`}\dot{m}_a(h_{v1`} - h_{v1}) \quad (4)$$

where $\dot{m}_w$ is the mass flow rate of cooling water and $h_{w1`}$ is its enthalpy, $\dot{m}_a$ is the mass flow rate of dry air ($h_{a1`} - h_{a1}$) is the enthalpy change of dry air, $\omega_{1`}$ is the humidity ratio (specific humidity ) of inlet-air in kg of water per kg of dry air, and ($h_{v1`} - h_{v1}$) is the enthalpy change of water vapour after cooling.

The humidity ratio ($\omega_{1`}$) can be specified directly or calculated from:

$$\omega_{1`} = \frac{0.622 P_{v1`}}{P_{1`} - P_{v1`}} \quad (5)$$

Where $P_{v1`}$the partial pressure of water is vapour and $P_{1`}$ is the total atmospheric pressure. From conservation of mass, the amount of water sprayed is equal to the mass of water vapour at point 1minus the water vapour originally in the air at point1'.

$$\dot{m}_w = (\omega_1 - \omega_{1`})\dot{m}_a \quad (6)$$

where ω_1 is the humidity ratio of air after cooling, which can also be specified directly or found from the Eq.(3.56) if $P_{v1`}$ is replaced by $P_{v1}$. The partial pressure of water vapour at point 1` and 1 can be found from the respective relative humidity (ϕ), which is given by equation (7)

$$P_{v1} = \phi_1 P_{sat1} \quad (7)$$

Where $P_{sat1`}$ and $P_{sat1}$ are the saturation pressures of water at the corresponding temperatures ($T_{1`}$ *or* T_1). Neglecting pressure losses in the process and P_1 is equal to $P_{1`}$.

2.4 Heat Recovery Steam Generator

The superheated steam generated $\dot{m}_{S,SUP}$for each kg/s of exhaust gases can be determined by applying the mass and energy conservation principles across superheater and economizer as:

$$\dot{m}_{S,SUP}\left(h_{S,SUP} - h_{COND}\right) = \dot{m}_P(h_6 - h_7) \quad (8)$$

Where $h_{S,SUP}$the enthalpy of superheated steam is generated in HRSG, h_{COND} is enthalpy of condensate water at inlet to HRSG, $\dot{m}_P$ is mass flow rate of flue gases, h_6 and h_7 are enthalpy of flue gases at inlet and exit of HRSG respectively.

2.5 Exergy destruction in HRSG

$$\dot{E}_{D,HRSG} = \dot{E}_6 - \dot{E}_7 + \dot{E}_8\text{-}\dot{E}_9 \quad (9)$$

2.6 Compressor

In a compressor, a gas is caused to flow in the direction of increasing pressure and/or elevation by means of a mechanical or electrical power input which is given by:

$$\dot{W}_C = \dot{m}_a(h_2 - h_1) \quad (10)$$

Where h_2 and h_1 are specific enthalpies at state point 2 and 1 respectively.

$$\eta_C = \frac{(h_{2s}-h_1)}{(h_2-h_1)} \quad (11)$$

Where h_{2s} is the isentropic specific enthalpy at state point 2.

2.7 Exergy destruction in compressor

$$\dot{E}_{D,C} = W_C + \dot{E}_1 - \dot{E}_2 \quad (12)$$

Where $\dot{E}_1$ and $\dot{E}_2$ are exergy at state point 1 and 2.

2.8 Combustion chamber

$$\frac{n_f}{n_a} = \lambda \quad (13)$$

$$\frac{n_P}{n_a} = 1 + \lambda \quad (14)$$

Where the subscripts f, p and a denote fuel, combustion products & air respectively and λ is the fuel-air ratio.
For complete combustion of natural gas (methane) with steam injection (Fig. 1) in the combustion chamber, chemical equation takes the following form:

$$\bar{\lambda}\, CH_4 + \left[X_{1,N_2}N_2 + X_{1,O_2}O_2 + X_{1,CO_2}CO_2 + X_{1,H_2O}H_2O\right] + \omega \rightarrow \left[1 + \bar{\lambda} + \omega\right]\left[X_{2,N_2}N_2 + X_{2,O_2}O_2 + X_{2,CO_2}CO_2 + X_{2,H_2O}H_2O\right] \quad (15)$$

Where ω is the steam injection ratio defined as the ratio of mass of steam injected to the mass of inlet air.

$$\omega = \frac{\dot{m}_s}{\dot{m}_a} \quad (16)$$

$$\omega = \left(\frac{\dot{m}_s}{\dot{m}_f}\right) \times \left(\frac{\dot{m}_f}{\dot{m}_a}\right) \quad (17)$$

$$\omega = \omega`(1 + \lambda) \quad (18)$$

$$\omega` = \frac{\dot{m}_s}{\dot{m}_g} \quad (19)$$

$$\omega`` = \frac{\omega_s}{\omega_f} \quad (20)$$

Where ω'is the ratio of mass of steam injected to the mass of combustion gases formed. $\dot{m}_s$ and $\dot{m}_f$ are the mass rate of steam injected and mass rate of combustion gases formed respectively. λ is the fuel-air ratio.

2.9 Exergy destruction in combustion chamber

$$\dot{E}_{D,CC} = \dot{E}_3 + \dot{E}_f - \dot{E}_4 \quad (21)$$

The isentropic efficiency of turbine is given by eq. (22)

$$\eta_T = \frac{h_4-h_5}{h_4-h_{5s}} \quad (22)$$

Where η_T is isentropic efficiency of turbine, h_4 and h_5 are enthalpies of flue gas at state 4 and 5. h_{5s} is the isentropic enthalpy at turbine exit.

2.10 Exergy destruction in turbine

$$\dot{E}_{D,T} = \dot{E}_6 + \dot{E}_4 - \dot{E}_5 \quad (23)$$

2.11 Exergy destruction of stack-losses

$$\dot{E}_{D,Stack-losses} = \dot{E}_7 \quad (24)$$

Thermal Efficiency (η_{Th}): Thermal efficiency of a thermal system is defined as the ratio of net work output $(\dot{W}_{net})$ to the total heat input of the fuel$(\dot{Q}_f)$.

$$\eta_{Th} = \frac{\dot{W}_{net}}{\dot{Q}_f} \quad (25)$$

2.12 First–Law Efficiency (η_I)

The ratio of all the useful energy extracted from the system (electricity and process heat) to the energy of fuel input is known as first-law efficiency. First-law efficiency is also known as fuel utilization efficiency or utilization factor or energetic efficiency.

$$\eta_I = \frac{\dot{W}_{El}+\dot{Q}_{Pro}}{\dot{Q}_f} \quad (26)$$

Where $\dot{W}_{El}$ and $\dot{Q}_{Pro}$ are electric work done and process heat rate respectively.

2.12.1 Heat-Rate (HR)

Heat rate is defined as the ratio of heat rate produced by the fuel to the electrical power out of the thermal system.

$$HR = \frac{\dot{Q}_f}{W_{el}} \quad (27)$$

2.13 Second–Law Efficiency (η_{II})

Since exergy is more valuable than energy according to the second law of thermodynamics, it is useful to consider both output and input in terms of exergy. The amount of exergy supplied in the product to the amount of exergy associated with the fuel is a more accurate measure of thermodynamic performance of a system, which is called second-law efficiency. It is also called exergetic efficiency (effectiveness or rational efficiency).

$$\eta_{II} = \frac{\dot{W}_{El}+\dot{E}_{Pro}}{\dot{E}_f} \quad (28)$$

Where $\dot{E}_{Pro}$the exergy is content of process heat and $\dot{E}_f$ is the exergy content of fuel int.

2.14 Effectiveness (Exergetic efficiency) of component (ε)

Exergetic efficiency of component is defined as the ratio of exergy rate recovered from the component $(\dot{E}_R)$ to the exergy rate supplied to the component$(\dot{E}_S)$. Exergetic efficiency gives true measure of useful energy which cannot be obtained from energy criteria.

$$\varepsilon = \frac{\dot{E}_R}{\dot{E}_S} = \frac{\dot{E}_R}{\dot{E}_R+\dot{E}_D} = 1 - \frac{\dot{E}_D}{\dot{E}_R+\dot{E}_D} \quad (29)$$

2.15 Exergy-Destruction Rate$(\dot{E}_{D,R})$

The component exergy destruction rate can be compared to the total exergy destruction rate within the system.

$$\dot{E}_{D,R} = \frac{\dot{E}_D}{\dot{E}_{D,Total}} \quad (30)$$

2.16 Exergy-Destruction Rate(MW)per MW of Power Output

It is defined as the ratio of exergy destruction rate of component $(\dot{E}_{D,k})$ to the net power output $(\dot{W}_{net})$ of the system cycle.

$$\dot{E}_{D,R/MWP} = \frac{\dot{E}_{D,k}}{\dot{W}_{net}} \quad (31)$$

3. Results and discussions

The present work analyzed a retrofitted simple gas turbine cycle incorporated to evaporative inlet air cooling (EVC) and steam injection to gas turbine (STIG) techniques energetically and energetically. A computer program has been developed in Engineering Equation Solver (EES) [16] software to compute the performance parameters (Power output, Thermal efficiency, First law efficiency, exergetic efficiency, exergy destruction rate). The effect of ambient temperature has been observed on various performance parameters.

Table 1: Input parameters of retrofitted simple gas turbine cycle Moran et al.[4]and Agarwal et al.[20]

S.N	Input parameters	Numerical values
1.	Ambient air temperature, pressure and relative humidity at state point 1`	25^0C, 1.013bar & 60%
2.	Spray water temperature and pressure at state point1`	25^0C, 138bar
3.	Inlet air temperature, pressure and relative humidity (T_1, P_1 & ϕ_1) to compressor at state point 1	25^0C, 1.013bar & 100%
4.	Pressure ratio of compressor (r_P)	10:1
5.	Isentropic efficiency of compressor (η_C)	0.86
6.	Isentropic efficiency of turbine (η_T)	0.86
7.	Mass flow rate of air ($\dot{m}_a$)	81.4 kg/s
8.	Lower heating value of fuel	802361 kJ/kmol
9.	Turbine inlet temperature (TIT) (T_4)	1247^0C
10.	Injection temperature and pressure of fuel (T_f, P_f)	25^0C, 12bar
11.	Exhaust temperature and pressure of combustion products after HRSG (T_7, P_7)	130^0C, 1.013 bar
12.	Temperature and pressure of condensate water at inlet of HRSG (T_8, P_8)	25^0C, 20 bar
13.	Steam generation pressure (P_{9a})	20 bar
14.	Pressure drop in combustion chamber and HRSG on gas side	5%
15.	Amount of steam injected (ω), (% of the mass flow rate of the air)	10%
16.	Temperature of superheated steam STIG (T_9)	480^0C
17.	Approach and pinch point	2^0C, 20^0C

3.1 Model Validation

The results of current analysis have been compared to Moran et al. [4] and Agarwal et al. [20] as shown in Table2. The variation in the results is within ±1%. The variation is due to the consideration of pressure drop in combustion chamber and HRSG.

3.2 Parametric Analysis

3.2.1 Effect of ambient temperature on percentage power output difference with respect to simple cycle.

Fig. 3 shows that the variation of percentage power output difference with ambient temperature for wide range of relative humidity for evaporative cooling cycle (EVC) as compared to simple cycle.

As the temperature of ambient air increases, the power output of simple cycle decreases due to decrease in density of air for a specified relative humidity. For a constant volume machine, decrease in density of air reduces the mass flow rate of air

Table 2: Comparison of operational parameters ($\dot{m}$, P, T)(a:Simple

cycle, b:Simple+EVC, c:Simple+STIG, d:simple+EVC+STIG)[4, 20]

State points	Mass flow rate ($\dot{m}$) kg/s			
	a	b	c	d
1`	---	81.4, 1.14		81.4, 1.14
1	81.4	82.54	81.4	82.54
2	81.4	82.54	81.4	82.54
4	83.36	84.56	91.79	92.98
5	83.36	84.56	91.79	92.98
7			91.79	92.98
8			21.23	21.51
9			8.14	8.14
P			13.09	13.37
f	1.96	2.01	2.247	2.297
	Temperature (T) K			
1`	---	298.15, 292.6		298.15, 292.6
1	298.15	292.62	298.15	292.62
2	604.95	594.75	604.95	594.75
4	1520	1520	1520	1520
5	985.6	985.95	1006.15	1006.15
7			403.15	403.15
8			298.15	298.15
9			753.15	753.15
P			753.15	753.15
f	298.15	298.15	298.15	298.15
	Pressure (P) bar			
1`	---	1.013, 138		1.013,138
1	1.013	1.013	1.013	1.013
2	10.13	10.13	10.13	10.13
4	9.62	9.62	9.624	9.624
5	1.013	1.013	1.066	1.066
7			1.013	1.013
8			20	20
9			20	20
P			20	20
f	12	12	12	12

It is interesting to observe that the difference in power output for with or without evaporative cooling at given R.H. increases with increasing temperature due to increase in intake mass flow rate of air (mass flow rate of ambient air + mass flow rate of fog water) and at lower temperature. The percentage difference in power output is lower for high R.H. line while higher for a low R.H. line because the higher amount of water vapour added to the air at low R.H. during evaporative cooling (fog cooling) to get saturated air which increases the overall mass flow rate of air. At high temperature the saturation capacity of air increases (i.e. at high temperature and R.H., amount of water vapour required to obtain 100% saturation is more than at low temperature) due to which there is significant increase in mass flow rate and hence power output increases rapidly and the effect can be observed in the Fig. 3 such that the 80% R.H. line coincide with 60% R.H. line at 50^0C.

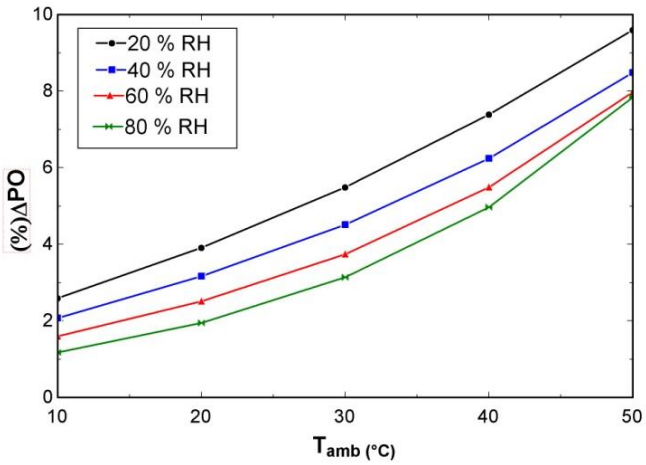


Figure 3: Effect of ambient temperature on % difference in power output (Simple cycle+EVC)

Fig. 4 shows a significant increase in power output for STIG (steam injected gas turbine) due to increase in mass flow rate of intake air to the turbine (mass flow rate of air from compressor + mass flow rate of STIG). It reflects that the variation in percentage power output difference with temperature and relative humidity for STIG cycle with respect to simple cycle.

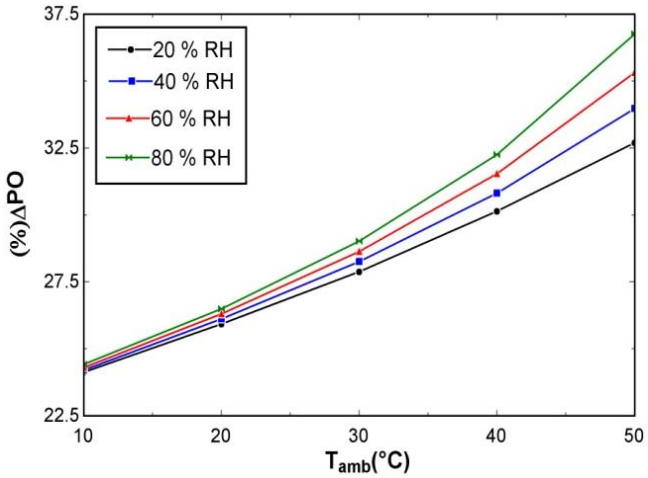


Figure 4: Effect of ambient temperature on % difference in power output (Simple cycle+STIG)

At constant ambient temperature the percentage power output

difference is higher for high R.H. value and lower for low R.H. value because for high R.H. value, the intake mass flow rate of air to compressor (mass flow rate of dry air + mass flow rate of water vapour contents) increases. As the temperature of ambient air increases the density of air decreases, so the intake mass flow rate of air to compressor decreases with the same rate for simple cycle as well as for STIG cycle. Though the ambient temperature increases the power output for both the cycles decreases for a constant R.H. condition yet the percentage power output difference increases. The reason is that at higher temperature the power output of simple cycle falls rapidly while the power output of STIG cycle fall gradually (as the STIG steams has higher latent heat).
Combined effect of evaporating cooing and STIG has been shown in Fig. 5. As the mass flow rate of air increases during evaporating cooling (mass flow rate of air from compressor + mass flow rate of STIG) and for STIG (mass flow rate of air from compressor + mass flow rate of STIG) , the increase in power output is higher than that of EVC and STIG cycle.

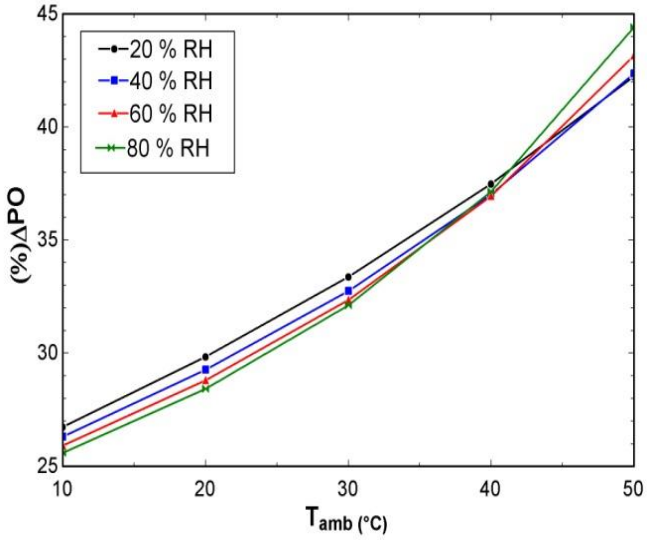


Figure 5: Effect of ambient temperature on % difference in power output (Simple cycle+EVC+STIG)

Fig.5 shows the variation in percentage power output difference with temperature and R.H. At a constant temperature, the percentage difference in power output is higher for low R.H. value than that of high R.H. value due to high mass flow rate of intake air to compressor (mass flow rate of dry air + mass flow rate of water vapour). At low R.H ambient conditions air reuqires higher amount of water vapour to get saturated. The increase in ambient temperature lowers the mass flow rate of air but the difference in power output is higher due to rapid fall in power out of simple cycle. At high temperature and high R.H. value the the amount of water vapour added to air is higher to get saturated air. Thus the percentage difference in power output jumps suddenly for 50^0C and 80% R.H. It can be observed form the psychometric chart that the humidity ratio is higher for high D.B.T. and high R.H. value. As the R.H. lines gets diversed and more steep for high R.H. value, the moisture contents are higher for higher D.B.T. and R.H.

3.2.2 Effect of ambient temperature on percentage heat-rate difference with respect to simple cycle

Fig. 6 shows the variation of percentage heat rate difference with ambient temperature for wide range of relative humidity for evaporative cooling cycle as compared to simple cycle. For a constant R.H. value as the temperature of ambient air increases the mass flow rate of air intake air to compressor decreases due to reducing density results reducing electrical work output and mass of fuel consumed and hence heat rate falls rapidly. It has been observed that the heat rate falls rapidly for low R.H. as compared to higher R.H. for a constant temperature due to high air fuel ratio which increases heat flow rate for high R.H. values and the difference between two heat rates for EVC cycle and simple cycle reduces.

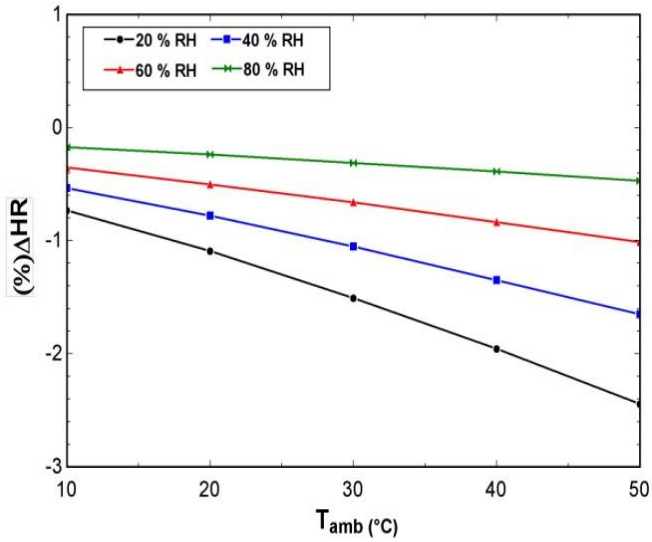


Figure 6: Effect of ambient temperature on % difference in heat rate (Simple cycle+EVC)

The gap between high R.H. is less at high temperature and high R.H. because at high temperature and R.H. the larger amount of water vapours are required to get saturated air.
The variation of percentage heat rate difference with ambient temperature for wide range of relative humidity has been shown in Fig. 7. As the ambient temperature increases the density of air decreases and the mass flow rate of combustion products decreases and mass of STIG remains constant so, the total mass of combustion products decreases and heat rate decreases with increasing temperature for a constant R.H. value.

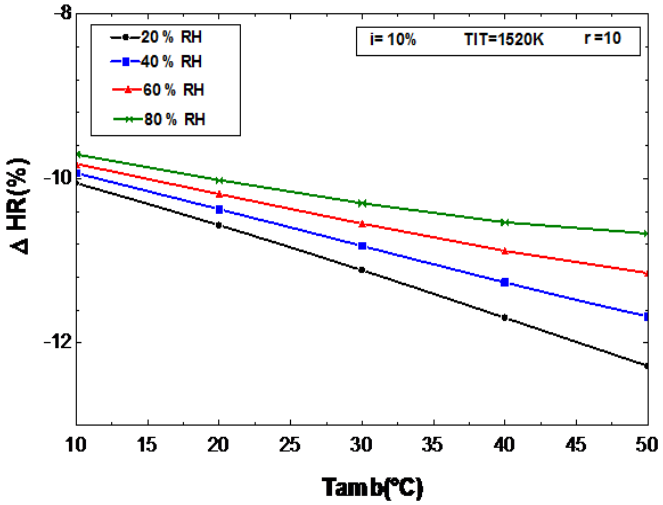


Figure 7: Effect of ambient temperature on % difference in heat rate (Simple cycle+STIG)

On the other hand, the mass flow rate of intake air to compressor decreases rapidly with increasing temperature for a constant R.H. value and hence the difference of heat rate between simple cycle and STIG cycle increases. At a constant temperature, the decrease in heat rate is higher for high R.H. and lower for low R.H. because the mass flow rate of air increases with increasing R.H.

Fig. 8 shows the variation percentage heat rate difference with ambient temperature along wide range of R.H. for combined evaporative and STIG cycle.

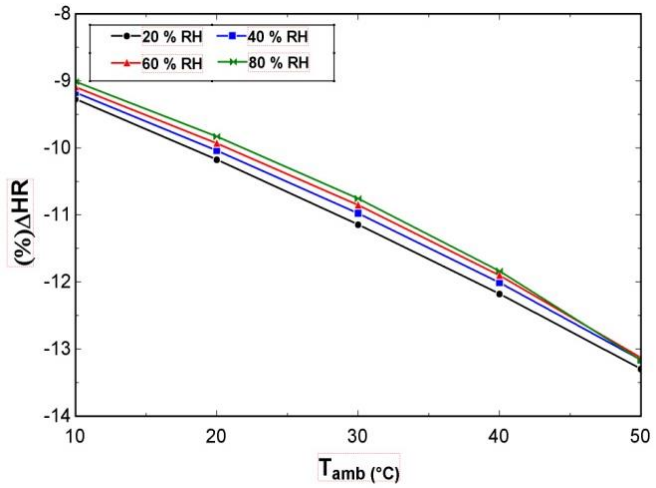


Figure 8: Effect of ambient temperature on % difference in heat rate (Simple cycle+EVC+STIG)

As the temperature of ambient air increases at constant R.H. value the mass flow rate of combustion product (mass of air+mass of fuel+mass of STIG) reduces rapidly as compared to mass of fuel consumed so that the power output decreases and hence the heat rate increases. The heat rate difference between simple cycle and combined cycle decreases with increase in ambient temperature as the heat-rate increases rapidly for simple cycle. It is an interesting fact that the heat rate falls rapidly for low R.H. as compared to higher R.H. for a constant temperature due to high air fuel ratio (les mass of fuel consumed) which increases heat flow rate for high R.H. values and the difference between two heat rates for combined cycle and simple cycle reduces. At high temperature (50^0C) and R.H. (80%), the heat rate falls rapidly as the amoun of water vapour added to the air increases (as the R.H. lines gets diverged and more steep for high R.H. value at the psychometric chart, the moisture contents are higher for higher D.B.T. and R.H.) and hence high R.H. line coincides with low R.H. lines at high temperature (50^0C) and R.H. (80%).

3.2.3 *Effect of ambient temperature on thermal efficiency difference with respect of simple cycle (comparison of retrofitted cycles)*

Fig. 9 predicts variation in thermal efficiency (%) difference with temperature along wide range of R.H. for EVC cycle. As the mass flow rate of air decreases with increasing temperature for a constant R.H. value due to rapid decrease in density of air as compared to mass flow rate of fuel consumed and hence the thermal efficiency decreases rapidly for simple cycle. On the other hand, the thermal efficiency of EVC cycle decreases slowly as compared to simple cycle. Hence the difference becomes wider for a particular R.H. with increasing temperature. For constant temperature and low R.H.(20%), the moisture contents added to the air during evaporative cooling are higher to get saturated therefore the difference in thermal efficiency is higher for lower R.H.

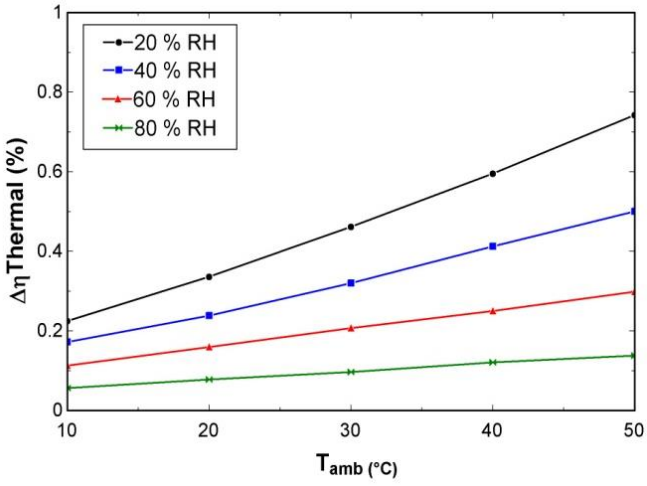


Figure 9: Effect of ambient temperature on % difference in thermal efficiency (Simple cycle+EVC)

The gap among lower R.H. lines is more than that of high R.H. line due to higher moisture contents added to air at high ambient temperature (50^0C) and R.H. (80%) (as the humidity ratio increases rapidly for high D.B.T. and R.H. at

psychometric chart). The variation in thermal efficiency (%) difference with temperature along wide range of R.H. for STIG cycle has been shown in Fig. 10.

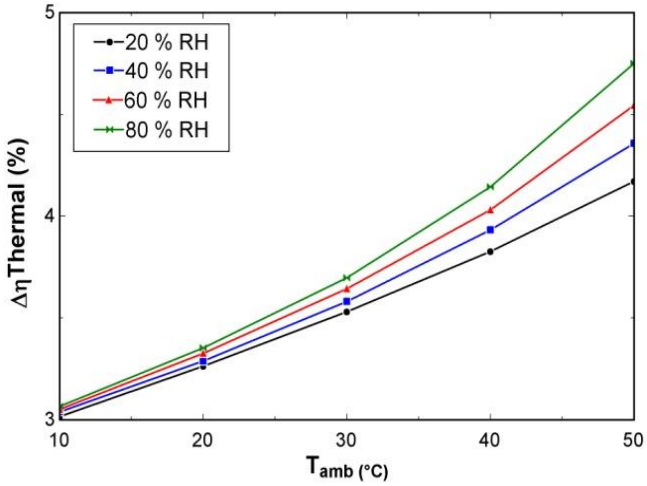


Figure 10: Effect of ambient temperature on % difference in thermal efficiency (Simple cycle+STIG)

As the temperature of air increases for a constant R.H., the density of air decreases, the mass flow rate of air and mass flow rate of fuel consumed decreases as well as the mass of STIG decreases hence mass of combustion products decreases rapidly for simple cycle as compared to STIG cycle by which difference in thermal efficiency (%) increases. The difference in thermal efficiency (%) is higher for high value as compared to low R.H. value at a constant temperature. At high R.H., the mass of water vapour contents are higher which increases mass flow rate of air and ultimately thermal efficiency.
Fig. 11 shows the variation in thermal efficiency (%) with temperature along wide range of R.H. for combined cycle.

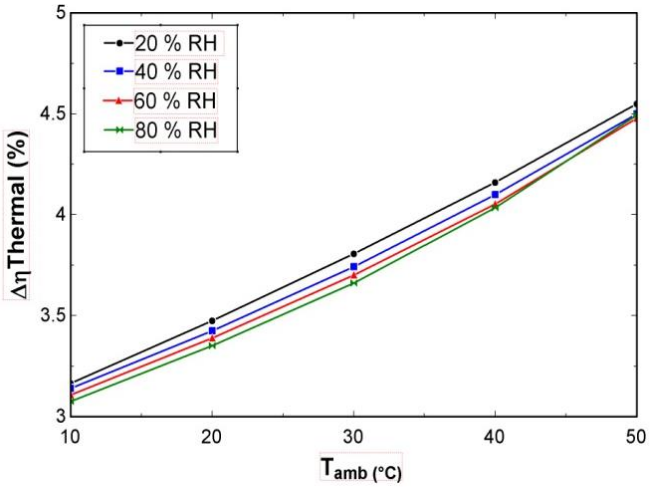


Figure 11: Effect of ambient temperature on % difference in thermal efficiency (Simple cycle+STIG)

As the mass flow rate of combined cycle enhances by two ways (a) using evaporative cooling, the amount of water vapour added (b) the amount of STIG added to the air, and the mass flow rate of fuel consumed also decreases with increasing temperature at constant R.H. value as the air fuel ratio increase. Hence the mass flow rate of combustion products has become higher than that of an individual cycle and difference in thermal efficiency increases. As ambient air at low R.H. value requires high amount of water vapour to get saturated therefore the difference in thermal efficiency (%) is higher for low R.H. value as compared to low R.H. value at constant ambient temperature. At high temperature the gap among high R.H. lines becomes wider due to higher moisture contents added to air at high ambient temperature (50^0C) and R.H. (80%) (as the humidity ratio increases rapidly for high D.B.T. and R.H. at psychometric chart).

3.2.4 Effect of ambient temperature on first-law efficiency (comparison of simple and retrofitted cycles)

Fig. 12 shows the variation of first law efficiency (%) with temperature for various cycles.

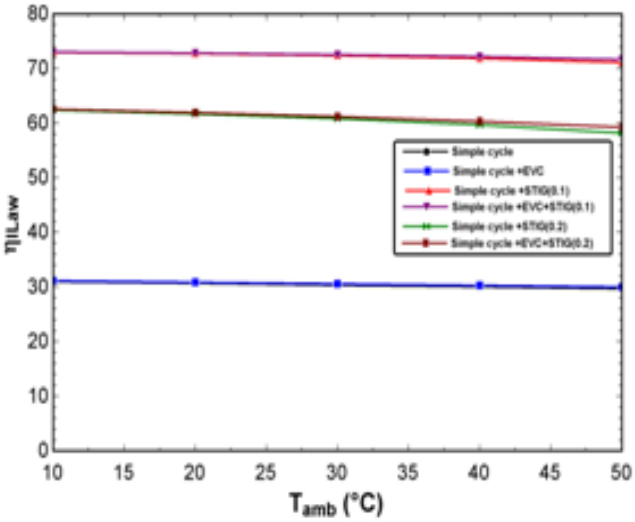


Figure 12: Effect of ambient temperature on first law efficiency for retrofitted cycles

As the temperature of ambient air increases for a constant R.H. value, the mass flow rate of intake air decreases by which power output and process heat available in exhaust gases also decreases. As the air-fuel ratio increases, the mass flow rate of fuel consumed decreases result the first law efficiency remains constant for a specified cycle. As the water vapours contents increases during evaporative cooling, the mass flow rate of intake to compressor increases results power output and process heat increases minutely for EVC cycle. Hence, first law efficiency for EVC cycle coincides with simple cycle. As the amount of STIG added to the air is more significant for

STIG cycle, the mass flow rate of combustion products increases results increase in power output and process heat and the increase in air fuel ratio reduces the mass flow rate of fuel consumed results higher first law efficiency for STIG cycle as shown in fig. 13. The amount of STIG (0.2) cycle imparts large amount of STIG to the air which increases large amount of mass flow rate of air as compared to STIG (0.1) cycle results higher first law efficiency for STIG (0.2) cycle. Combined cycle for STIG (0.1) coincides with STIG (0.1) cycle and combined cycle (0.2) coincides with STIG (0.2) cycle as the effect of evaporative cooling is no much significant.

3.2.5 *Effect of ambient temperature on power output and generation efficiency (comparison of simple and retrofitted cycles)*

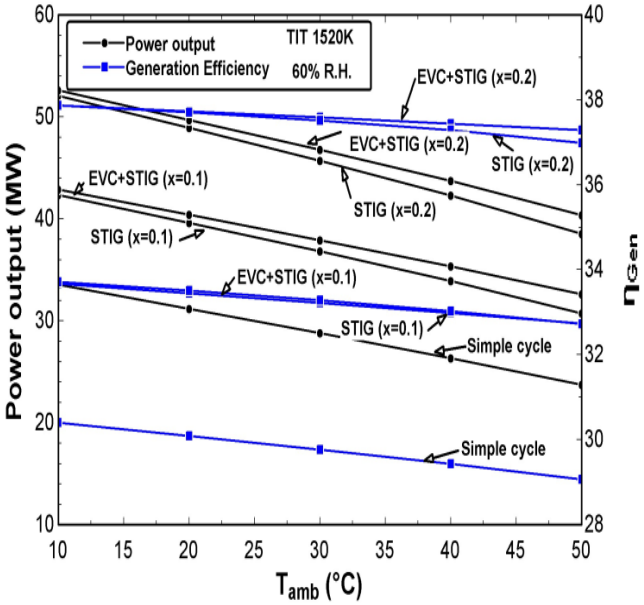


Figure 13: Variation in power output, generation efficiency with ambient temperature for retrofitted cycles

Fig. 13 shows the variation of power output and generation efficiency with ambient temperature at constant R.H. condition (60%) for different cycles. As the ambient temperature increases, the density of air decreases for constant volume machine (compressor and turbine) results mass flow rate of intake air decrease by which mass flow rate of STIG also decreases. Hence the power output decreases for different cycles. The increase in air fuel ratio reduces the mass flow rate of fuel consumed by which generation efficiency reduces gradually for different cycles.

Fig. 14 shows the variation of power output and generation efficiency with relative humidity at constant temperature.

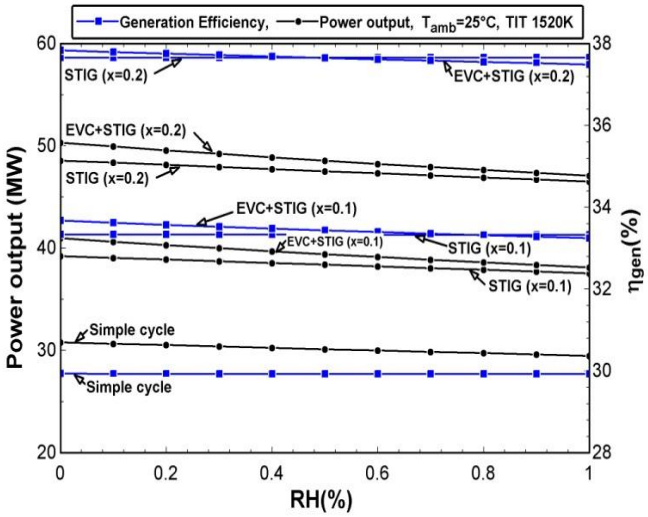


Figure 14: Variation in power output, generation efficiency with relative humidity for retrofitted cycles

. At low temperature, the density of air is higher and the addition of water vapour reduces the average density of air by which power output decreases with increasing R.H. for different cycles while the generation efficiency remains constant due to slight increase in air fuel ratio.

3.2.6 *Effect of ambient temperature on second-law efficiency difference with respect to simple cycle (comparison of retrofitted cycles)*

Fig. 15 shows the variation in second law efficiency (%) difference with temperature along wide range of R.H. for EVC cycle.

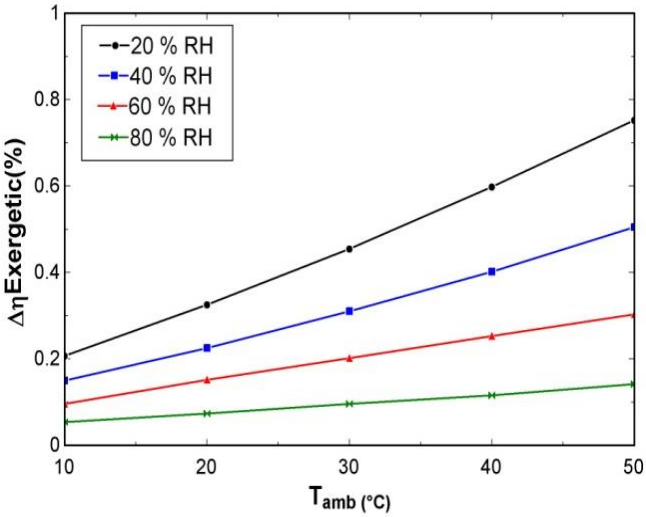


Figure 15: Variation in % difference in exergetic efficiency with ambient temperature (Simple cycle+EVC)

As the temperature of ambient temperature of air increases for a constant R.H. value, the mass flow rate decreases due to decrease density of air by which power output decreases and the exergy of fuel decreases rapidly for simple cycle as compared to EVC cycle. Therefore the difference in exergetic efficiency (%) for simple cycle and EVC cycle increases. For a constant ambient temperature the exertetic efficiency is higher for lower R.H.(20%) condition as compared high R.H.(80%) due to the moisture contents added to the air for low R.H. during evaporative cooling are higher to get saturated air.

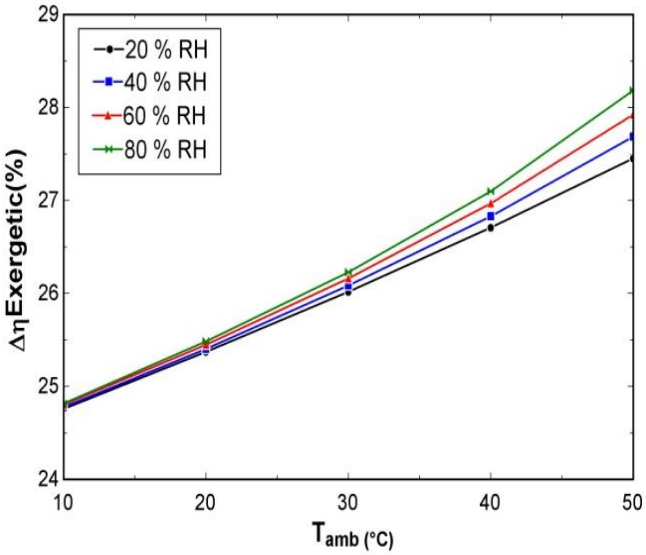


Figure 16: Variation in % difference in exergetic efficiency with ambient temperature (Simple cycle+STIG)

Fig. 16 shows the variation in second law efficiency (%) difference with temperature along wide range of R.H. for STIG cycle. As the temperature of ambient air increases for constant R.H. value, the decreasing mass flow rate reduces power output and mass flow rate of STIG and the mass flow rate of fuel also decreases by which exergy of fuel and exergy of STIG decreases and the exergy of intake ambient air first decreases and then increases hence the second law efficiency increases for STIG cycle and the second law efficiency of simple cycle decreases rapidly results the increase in difference between heat rate for STIG cycle and simple cycle. The second law efficiency is higher for high R.H. as compared to low R.H. for a constant temperature as the the moisture contents are higher for high R.H.

Fig. 17 shows the variation in second law efficiency (%) difference with temperature along with wide range of R.H. for combined cycle.

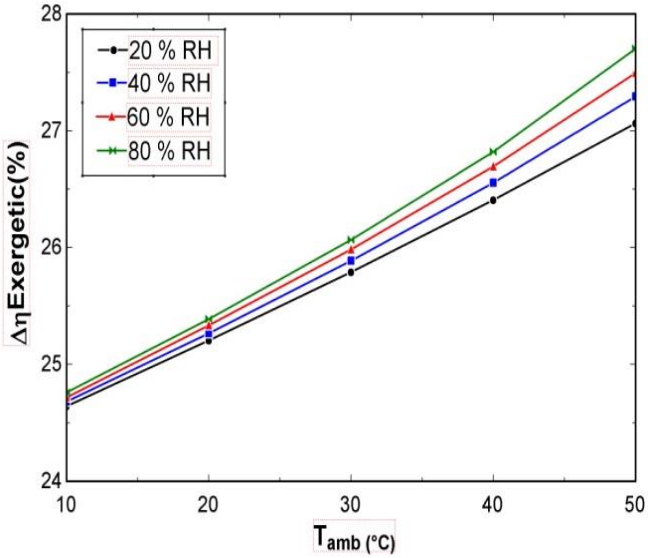


Figure 17: Variation in % difference in exergetic efficiency with ambient temperature (Simple cycle+EVC+STIG)

As the temperature of ambient air increases for a constant R.H., the power output decreases and the mass flow rate of fuel consumed decreases hence the second law efficiency first increases and then decreases for combined cycle while the second law efficiency decreases rapidly for simple cycle and hence the difference in second law efficiency (%) for simple cycle and combined cycle increases. The second law efficiency is higher for high R.H.(80%) condition as compared to low R.H.(20%) for a constant temperature due to decrease in power output is less and the exergy of intake air and fuel reduces sharply.

3.2.7 Comparison of simple and retrofitted cycles for exergy-destruction rate of system components

Fig. 18 shows the exergy destruction rate (MW) for different system components of simple and retrofitted cycles. As the mass flow rate of air increases due to addition of water vapours during evaporative cooling the rate of exergy destruction of compressor increases for EVC cycle and combined cycles. The exergy destruction rate of combustion chamber, gas turbine and HRSG also increases for retrofitted cycles as compared to simple cycle. As the mass flow rate of air also increases due STIG amount, the exergy destruction rate (MW) for combustion chamber, gas turbine and HRSG increases while the compressor remains unaffected.

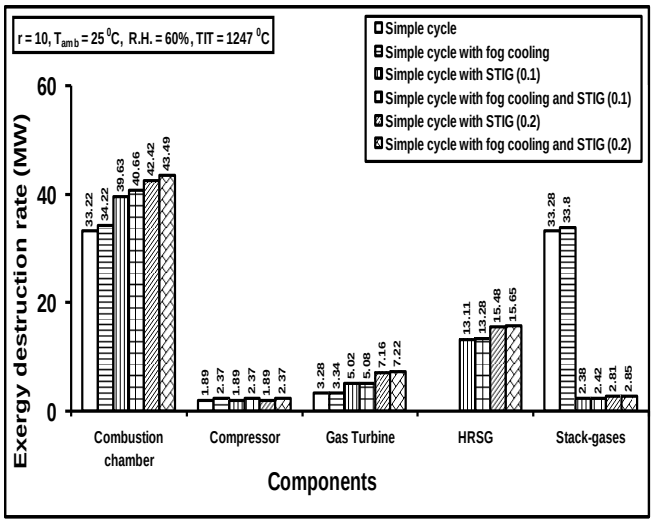


Figure 18: Exergy destruction rate (MW) of system components for simple and retrofitted cycles

Combustion chamber is the most sensitive component for exergy destruction because the mixing of air and high temperature STIG increases the average temperature of the air by which exergy destruction rate increases and highest for Combined cycle with STIG (0.2). It has been noted that the exergy of stack-gases has been fully utilized by STIG (0.1) cycle as the large amount of STIG increases the exergy destruction rate of stack-gases. Therefore STIG cycle can be optimized between STIG (0.1) and STIG (0.2).

Fig 19 shows the ratio of exergy destruction rate (MW) to the power output (MW) for different system components of simple and retrofitted cycles. Evaporative cooling and STIG both increases the mass flow rate of air due to which power output increases (maximum for combined cycle with STIG (0.2)).

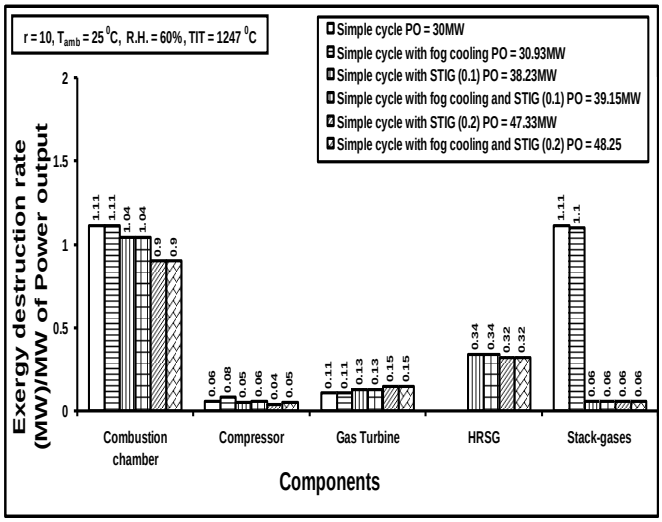


Figure 19: Exergy destruction rate (MW) per MW of output of system components for retrofitted cycles

Hence the exergy destruction rate (MW) per MW of power output decreases for combustion-chamber, HRSG. Evaporative cooling reduces the ratio of exergy destruction and power output for gas-turbine because the average temperature of combustion products reduces slightly and hence exergy destruction rate of gas-turbine increases gradually as compared to power output for same increment of mass flow rate. Although evaporative cooling reduces the inlet air temperature to compressor yet the increases mass flow rate enhance the exergy destruction in to the compressor.

Table 3: Comparison of performance parameters of simple and retrofitted cycles.

S.N	Performance Parameters	Simple cycle	Simple cycle+EVC	Simple cycle +STIG	Simple cycle+EVC+STIG
1.	First law efficiency (%)	30.54	30.72	72.57	72.69
2.	Second law efficiency (%)	29.51	29.70	55.3	55.2
3.	Power generation efficiency (%)	29.93	30.11	33.33	33.4
4.	Thermal efficiency (%)	30.54	30.72	34.01	34.08
5.	Heat rate (kW/kWh)	12029	11958	10800	10780
6.	Air fuel ratio	23.20	22.96	20.28	20.13
7.	Specific fuel consumption(kg/kWh)	0.2357	0.2343	0.2116	0.2112
8.	Net Power output (MW)	30	30.93	38.23	39.15
9.	Electric work done (MW)	29.4	30.31	37.46	38.36
10.	Total exergy destruction per MW of output$\sum \dot{E}_D/MW$	2.39	2.38	1.623	1.629
11.	System running cost	Very high	High	Low	Least
12.	Implementation cost	Not required	Very low	Low	Low
13.	Environmental-pollution	Very high	High	Very low	Very low

4. Conclusions

The present work analysed retrofitted gas turbine cycle energetically and exergetically. An EES program has been formulated to compute the result of analysis. A detailed parametric analysis has been presented for the relative comparison of retrofitted cycles such as EVC, STIG and combined cycle. The comparison of various performance parameters, environmental factors and cost factors predicts and concludes that the combined effect of evaporative cooling and

STIG technology enhances the overall performance of the power generation system along with cost reducing and low environmental pollution view. As the implementation of combined technology does not require complex machine operations, construction and asset, the simple cycle gas turbines in India can be retrofitted with combined technology to obtain an energy and cost optimum system. The major concluding points are mentioned below:

- Simple cycle gas turbine has been retrofitted with a) Fog cooling (or evaporative cooling) b) STIG c) Fog cooling (or evaporative cooling) and STIG both (combined cycle), which has been included in various power generation plants in India as well as abroad. The utility of retrofitted cycles has become more significant especially in summer season whenever the density of air gets reduced by which the power output of plant falls. The power output and thermal efficiency of a simple cycle gas turbine can be triggered using combined (evaporating cooling and STIG) retrofitting technology. The NOx or SO_2 emission can also be reduced and controlled using above technologies which proceeds towards environment friendly power generation systems. Whenever the high temperature exhaust gases have been left in to the environment (i.e. open circuit simple cycle gas turbine, Industrial turbines for electricity production and Air-craft engines), cause thermal pollution and reduce oxygen capacity of air. As the energy of exhaust gases have been utilized at their full extent, the retrofitted technologies reduce running cost of the power generation system and leads towards a cost effective and environment-friendly system. Results of parametric study of retrofitting system have been registered at designed conditions.
- Evaporative cooling enhances the power output 3.1% and thermal efficiency 0.18% while decreases heat rate by 0.6% which proves that the EVC cycle is more efficient than that of simple cycle. However some additional maintenance cost is required to implement evaporative cooling system. The EVC has been registered its superiority over simple cycle especially for high ambient temperature and low R.H. the percentage increase in power output reaches up to 10%.
- STIG cycle improves the net power output by 27.4% and thermal efficiency by 3.5% while reduces heat rate by 10.2%. In this way the importance of STIG cycle is more than that of EVC cycle. The improvement in power output is about 9 times and in thermal efficiency is about 20 times than that of EVC cycle. Therefore the STIG cycle registers more significant results than that of EVC cycle as well as it is more environment-friendly, however some implementing cost (initial cost) is higher. The utility of STIG cycle is more significant in summer seasons (when ambient temperature and R.H. is high), the increment in power output reaches up to 36% which makes the STIG cycle superior than that of other cycles.
- Combined cycles improves the net power output by 30.5% and thermal efficiency by 3.54% while reduces heat rate by 10.4%. Therefore the combined cycle registers highest superiority among all cycles. The combined cycle is more environment friendly and cost effective however the implementing cost is little higher. The increment in power output has been registered up to 45 % during summer season at high ambient temperature (50 ^{0}C) and high R.H. (80%). The thermal efficiency also enhances up to 4.5% and second law efficiency about 26%. Therefore, the implementation of combined technology is a justified decision to obtain a energy and cost efficient power generation plant.

In the light of above points, it is observed that the retrofitted techniques improve the performance of the simple gas turbine cycle which have been incorporated with it. The retrofitted techniques are economical, simple and eco-friendly which may fulfill the peak load demand of electricity as well as save fuel consumption.

References

[1] Bhargava, R. and Meher-Homji, C. B., "Parametric analysis of existing gas turbines with inlet evaporative and overspray fogging", Journal of engineering for gas turbines and power, vol.127 issue 145 2005, pp.145-154.

[2] Chaker, M. Meher-Homji, C.B. Mee, I.I.I.T., "Inlet fogging of gas turbine engines-PartII: fog droplet sizing analysis, nozzle types, measurement, and testing", Journal of engineering for gas turbines and power vol.126 2004, pp. 559-571.

[3] Sinha, R. Bansode, S., "A thermodynamic analysis for gas turbine power optimization by fog cooling system" 20th national and 9th International ISHMT-ASME heat and mass transfer conference 2010.

[4] Moran, M.J., "Thermal System design and optimization 1996, pp. 156-158, 187-193, 517-21.

[5] Wang, F.J. Chiou, J.S. Wu, P.C., "Economic feasibility of waste heat to power conversion", Applied Energy, vol.84 2007, pp. 442-454.

[6] Kumar, A Kachhwaha, S.S. Mishra, R.S., "Thermodynamics analysis of a regenerative gas turbine cogeneration plant", Journal of Scientific & Industrial Research, vol. 69 2010, pp. 225-231.

[7] Pelster, S. Favrat, D. Von Spakovsky, M.R., "The thermo economic analysis and enivironomic modelling and optimization of the synthesis and operation of combined cycle with advanced options", Engineering for gas turbine and Power, Transaction of the ASME, vol. 123 2001, pp. 717-26.

[8] Korakianitis, T. Grantstrom, J.P. Wassingbo, P., "Parametric Performance of Combined-Cogeneration Power Plants with Various Power and Efficiency Enhancements", Engineering for gas turbine and Power, Transaction of the ASME, vol. 128 2005, pp. 65-72.

[9] Al-Hawaj, O.M. AL-Mutairi, H., "A combined power cycle with absorption air cooling", Energy, vol. 32 2007, pp. 971-982.

[10] Facchini, B. Daniele, F. Giampoalo, M., "Exergy analysis of combined cycles using latest generation gas turbines", Engineering for gas turbine and Power, Transaction of the ASME, vol. 122 2000, pp. 233-37.

[11] Nishida, K. Takagi, T. Kinoshita, S., "Regenerative stem-injection gas-turbine systems", Applied Energy, vol. 81 2005, pp. 231-246.

[12] Yadav J.P., "Exergy analysis of novel gas/steam combined cycle gas turbines configuration", ETME journal-MC, 2005.

[13] Bellorio M.B. Primenta J.M.D., "Theoretical analysis of air conditioning by evaporative cooling influence on gas turbine cycles performance", 18 International Congress of Mechanical Engineering, 2005, Ouro Preto, MG.

[14] Kumar R. N., Krishna K. R., "second law analysis of gas turbine power plant with alternative regeneration", ISHMT.Heat and mass transfer conference, 2006 Pp1813-18.

[15] Arora, A., "Energy and exergy analyses of compression, absorption, and combined cycle cooling systems", PhD thesis, Centre for Energy Studies: IIT Delhi 2009.
[16] Klein, S. A., Alvarado, F.: Engineering Equation Solver, F Chart Software, Middleton, WI. Version 9. 224-3D, 2012.
[17] Kalla, S. K., Arora, B. B., Usmani, J. A., "Alternative refrigerants for HCFC- A review", J. Thermal Engg., vol. 4 issue 3 2018, pp. 1998-2017.
[18] Srinivas T., Gupta A.V.S.S.K.S., Reddy B.V., "Sensitivity analysis of STIG based combined cycle with dual pressure HRSG", International Journal of Thermal Science, 2007, India.
[19] Bouam A., Aissani S., Kadi R., "Combustion chamber steam injection for gas turbine performance improvement during high ambient temperature operation", Journal of engineering for gas turbines and power, vol. 130 issue 0417 2008, pp. 1-10.
[20] Agarwal, S., Kachhwaha, S. S., Mishra, R. S., "Performance improvement of a simple gas turbine cycle through integration of inlet air evaporative cooling and steam injection", J. Sci. & Ind. Research, vol. 70 July 2011, pp. 544-553.
[21] Arora, B. B., Rai, J. N., "Optimization of thermal efficiency of combined cycle power generation", National seminar on energy & environment, Dec. 2001, Anand Engineering College, Agra.

Nomenclature

Abbreviations

AP	Approach point (^{0}C)
Cond.	Condenser
dbt	Dry bulb temperature (^{0}C)
$\dot{E}$	Exergy rate (kW)
$\dot{E}_D$	Exergy destruction rate (kW)
EVC	Evaporative cooling of inlet air
HRSG	Heat recovery steam generator
HR	Heat rate
$\dot{m}$	Mass flow rate
PP	Pinch point (^{0}C)
STIG	Steam injection to gas turbine
TIT	Turbine inlet temperature
U	Internal energy
wbt	Wet bulb temperature (^{0}C)

Rectangular Core Dispersion Engineered Photonic Crystal Fiber for Supercontinuum Generation

Pooja Chauhan[1], Ajeet Kumar[1]*, Yogita Kalra[2], and Than Singh Saini[3]
[1]*Advanced Photonics Simulation Research Laboratory, Department of Applied Physics, Delhi Technological University, Delhi-110 042, INDIA*
[2]*TIFAC-Centre of Relevance and Excellence in Fiber Optics and Optical Communication, Department of Applied Physics, Delhi Technological University, Delhi-110 042, INDIA.*
[3]*Optical Functional Materials Laboratory, Toyota Technological Institute, Nagoya, JAPAN*
**e-mail address: ajeetdph@gmail.com*

Abstract: Design of a rectangular core photonic crystal fiber in $Ge_{20}Sb_{15}Se_{64}$ chalcogenide glass is presented for mid-IR. Our simulation results include the study of dispersion, nonlinearity and fundamental effective mode area.

OCIS codes: (190.0190) Nonlinear optics; (190.4370) Nonlinear optics, fibers

Photonic crystal fiber (PCF) is proven a new developing class of fibers for the mid-infrared applications such as nonlinear microscopy, communication, optical coherence tomography (OCT), optical metrology, cosmology, frequency comb generation [1, 2]. When an input femtosecond laser pulse gets interact with the nonlinear medium due to linear and nonlinear processes (group velocity dispersion, self-phase modulation, cross-phase modulation, self-steepening, etc.), the input pulse becomes broader and produce a bandwidth called the process of supercontinuum generation [1]. Chalcogenides glasses are always favorable as compared to silica, tellurite and fluoride glasses due to their high transparency window up till 25 µm and high nonlinearity in the mid-infrared region [2].

In our study we have taken a highly nonlinear chalocgenide glass named $Ge_{20}Sb_{15}Se_{64}$ with its nonlinear refractive index as 6.98 m^2/W [3]. This chalcogenide glass is non-toxic and is highly durable for thermal and mechanical processes [3]. We have theoretically and numerically proposed a rectangular solid core photonic crystal fiber for mid-infrared application sources (supercontinuum generation). The proposed design is made up of the air-holes arrangement in rectangular periodic lattice with $Ge_{20}Sb_{15}Se_{64}$ chalcogenide glass as cladding material as shown in Fig. 1. The diameter of smaller air-hole and bigger air-hole are denoted by d_1 and d_2 respectively and the center-to center distance (pitch) between the air-holes is represented as Λ and taken as 1µm. 'COMSOL Multiphysics' software based on finite element method has been practiced during simulation of the fundamental mode characteristics in proposed PCF structure.

The process of optimization of geometrical parameters (diameter of air-holes, arrangement of air-holes, and pitch) of a photonic crystal fiber is the basic key step in order to reduce the effect of dispersion at pump wavelength and to increase the nonlinearity with low effective mode area of the fundamental propagating mode. Initially, we have studied the effect of increased values of diameter of smaller and bigger air-holes (d_1 and d_2) on dispersion characteristic curve as shown in Fig. 2 (a), (b). With increase of diameter d_1, the zero dispersion wavelengths (ZDWs) shifted slightly towards the smaller wavelength side. But as we increased the diameter d_2, a very less noticeable change is observed in shifting of ZDWs. For the optimized parameters i.e., d_1=0.6 µm, d_2=1.20 µm and pitch Λ=1 µm, the dispersion is found to be zero at 1510 µm. At pump wavelength of 1700 nm, the dispersion value is obtained as +22 ps/nm/Km in the anomalous region. The normal dispersion region is restricted up till wavelength 1510 nm and the anomalous region is initiated beyond ZDW of 1510 µm.

The nonlinear factors such as nonlinearity and effective mode area are the important parameter in order to control the bandwidth of the supercontinuum generation in the mid-infrared region. The nature of nonlinear coefficient is found to be decreasing with increase of wavelength as framed in Fig. 2 (c). Fig. 2 (d) is showing the nature of effective mode area of the fundamental mode with wavelength. The effective mode area always kept low for enhancing the nonlinearity of the proposed PCF design. The value of nonlinear refractive index is found to be very high as 38,220 $W^{-1}Km^{-1}$ and effective mode area is very low as 0.67 μm^2 at pump wavelength of 1700 nm.

The proposed design of a rectangular solid core photonic crystal fiber in $Ge_{20}Sb_{15}Se_{64}$ chalcogenide glass is probable to have a broad bandwidth of supercontinuum generation in the mid-infrared region. The fabrication of such photonic crystal fibers is possible with stack and draw technique [4].



Fig. 1 (a) Cross-sectional view of proposed PCF design; **(b)** Electric field distribution of fundamental mode at pump wavelength of 1700 µm in transverse symmetry using a COMSOL Multiphysics Software.

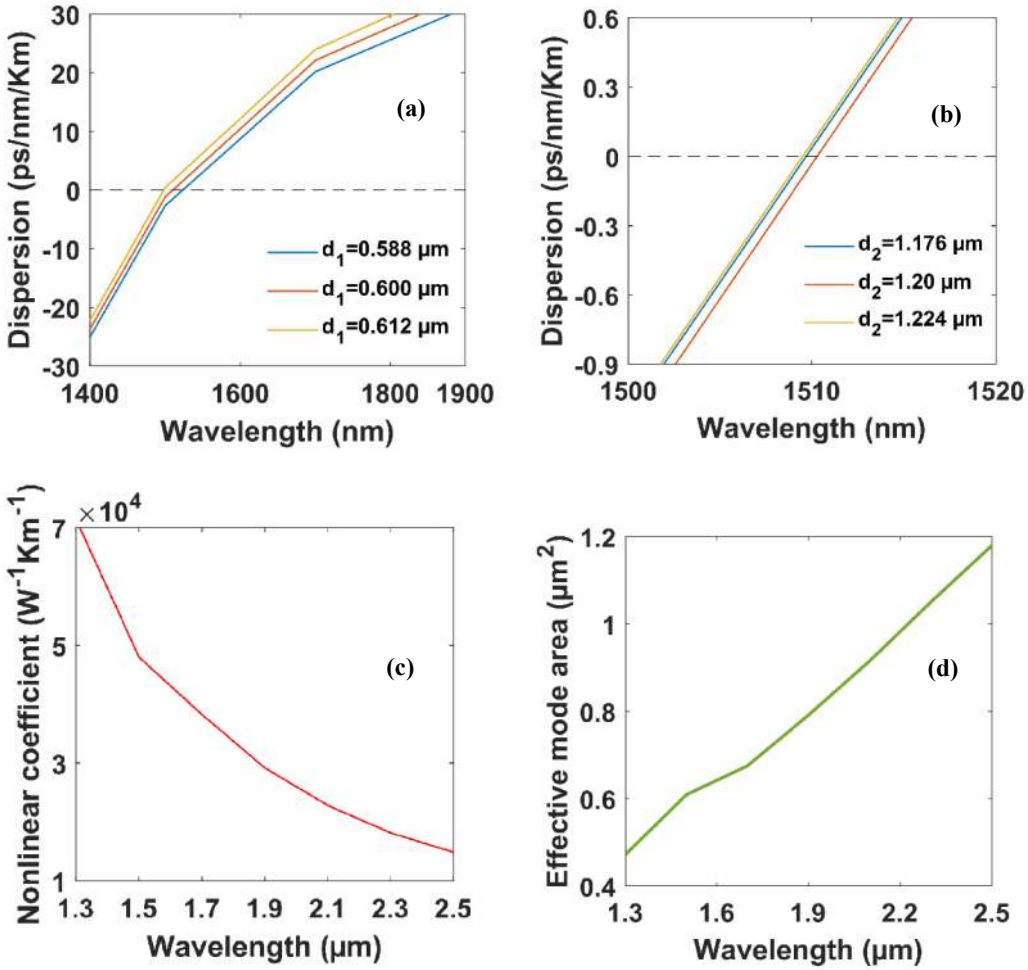


Fig. 2 Dispersion study with **(a)** variation in diameter d_1; **(b)** variation in diameter d_2; **(c)** variation of nonlinear coefficient for geometrical parameters d_1=0.600 µm, d_2=1.20 µm and Λ=1 µm; **(d)** effective mode area of different fundamental mode.

4. References

[1] G. P. Agarwal, *Nonlinear Fiber Optics,* 5th ed. (Elsevier Academic Press, 2013).
[2] P. Russell, "Photonic Crystal Fibers," Science 299, pp. 358-362 (2003).
[3] Zhanqiang Hui, Youkun Zhang, Min Yang, Feng Zhao, Meizhi Zhang, Zhanyun Wang, and Abdel-Hamid Soliman, "Midinfrared high birefringence $Ge_{20}Sb_{15}Se_{64}$ –based photonic crystal fiber with large nonlinearity using dual-rhombic air hole", J. Nanophoton, 12(1), 016018 (2018).
[4] M. Liao, C. Chaudhari, G. Qin, X. Yan, C. Kito, T. Suzuki, Y. Ohishi, M. Matsumoto, and T. Misumi, "Fabrication and characterization of a chalcogenide-tellurite composite microstructure fiber with high nonlinearity," Opt. Express 17, pp. 21608–21614 (2009).

14.139.251.107 {ts '2018-09-16 01:18:32'}

PAPER • **OPEN ACCESS**

Selection of Traceable Technology in Food Supply Chain

To cite this article: Mr Shahbaz Khan *et al* 2018 *IOP Conf. Ser.: Mater. Sci. Eng.* **404** 012010

View the article online for updates and enhancements.



IOP ebooks™

Bringing you innovative digital publishing with leading voices to create your essential collection of books in STEM research.

Start exploring the collection - download the first chapter of every title for free.

This content was downloaded from IP address 14.139.251.107 on 04/10/2018 at 06:39

Selection of Traceable Technology in Food Supply Chain

Mr Shahbaz Khan[1], Mr Mohd Imran Khan[1*], Dr Abid Haleem[2], Mr Mohd Shuaib[3]
[1]Research Scholar, Department of Mechanical Engineering Faculty of Engineering and Technology, Jamia Millia Islamia, New Delhi-110025, India
[2]Professor of Mechanical Engineering, Faculty of Engineering and Technology, Jamia Millia Islamia, New Delhi-110025, India,
[3] Assistant Professor, Mechanical Engineering, Delhi Technological University, Delhi

imrankhan@st.jmi.ac.in

Abstract Traceability is an essential tool to provide the product information throughout the Food Supply Chain (FSC), this help protecting the consumer welfare and in developing global competencies. Several technologies are available to implement the traceability system in FSC; these are barcoding, QR code, edible label, DNA- barcoding and paper-based systems. In this paper, we have tried to identify the significant factors towards the selection of the traceable technology within FSC through the literature review and supported by the expert opinion. These factor and sub-factors are prioritised using Analytic Hierarchy Process (AHP). The findings of this work suggest that product-related factors have the highest weight, and needs attention while selecting the traceable technology in FSC. This work may assist the practitioners in the selection of traceable technology for their FSC in an efficient manner.
Keywords: Analytic Hierarchy Process (AHP); Factors; Food supply chain (FSC); Traceability; Traceable technology

1. Introduction

Consumer concerns have increased towards the food safety, hygiene, and environment which has made the role of traceability important. Traceability is implemented not only to assure the consumer expectation but also to provide the effective management of product flow, increase the speed throughout the FSC [1]. Traceability systems are considered as the prerequisite for the food industry to explore the global market [2] as well as protecting the public health.

Olsen and Borit [3] define the traceability in a generic way as “The ability to access any or all information relating to that which is under consideration, throughout its entire lifecycle, using recorded identifications". In the context of food "all information" refer to the information related to ingredient origin, processing, logistics and retailing of the food products. The recoded information is stored and carried with the help of the “traceability information carriers” such as a barcode, RFID, edible label, DNA barcode and other advanced technologies. The term "tracing" and "tracking" is widely used in the literature of traceability. Tracing is a backward process where the origin is identified by history or records in the supply chain, and tracking is the forward process where consumers and supply chain partners are identified by location in the supply chain [4]. The traceability is the combination of the "tracing" and "tracking" of the product information in a backward and forward direction in the supply chain.

The implementation of traceability in the FSC gets strengthened with the adoption of technologies having the ability to track the product related information. Effective monitoring is the focus of the food industries which want low cost and easily applicable traceability technology. Thus, the selection of these traceable technologies is based on the several factors to provide product-related information to consumers. In this paper, the selection criteria of traceable technology are identified and ranked through the Multi-Criteria Decision Making (MCDM) techniques.

1.1 Need for the Study

The selection of the traceable technology is a difficult and complex task because of the several factors are involved. In the context of the food industry, it becomes more complicated because of the huge variation in the perception of the food consumers. Thus, in such situation, the selection of the traceable

Content from this work may be used under the terms of the Creative Commons Attribution 3.0 licence. Any further distribution of this work must maintain attribution to the author(s) and the title of the work, journal citation and DOI.
Published under licence by IOP Publishing Ltd

technology for the food product is quite important for practitioners. Through this paper, we have tried to identify the factors and subfactors which are important in the selection of traceability technology is identified and prioritise to assist the practitioners.

1.2 Objective of the Research

The notable objectives of this research are:

- To identify the factors and sub-factors for the selection of traceable technology FSC
- To prioritise the factors and sub-factors for the selection of traceable technology in FSC
- To provide the managerial implications

1.3 Factors related to the selection of traceable technology in FSC

The factors which influence the selection of traceable technology are categorised and grouped namely: "product-related factor", "process related factor", "social factor" and "other factor". These factors are further divided into sub-factors and shown in figure 1.

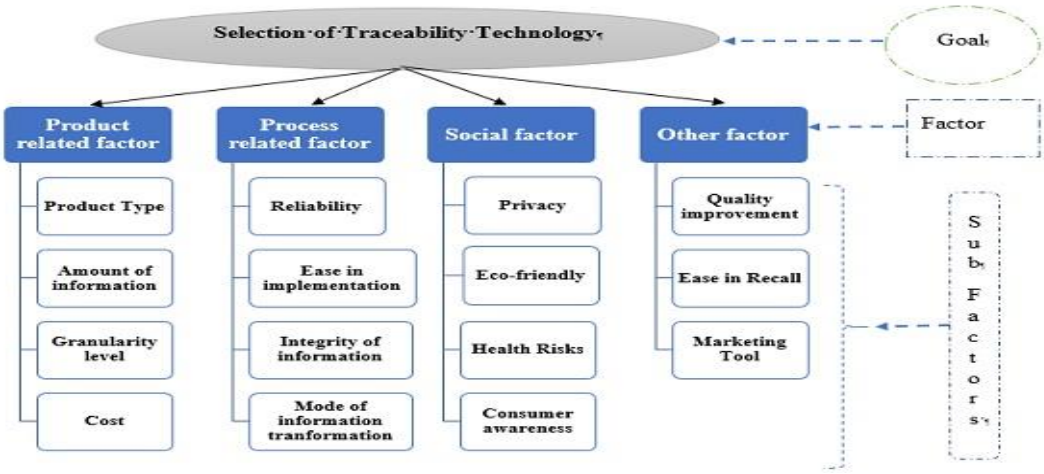


Figure 1: AHP hierarchical framework for the selection of traceable technology

2. Methodology

To accomplish the research objective, we have identified to use a suitable multi-criteria decision-making (MCDM) technique. Previous studies suggest that for prioritising the criteria/factors or factors some MCDM tools such as AHP [5], TOPSIS [6] and DEMATEL [7]. AHP seems to be a proper MCDM technique to provide the relative measurement or priorities by relative importance in this study. A group of five experts from academician and professionals gave their opinion through the AHP decision matrix. A brief about the AHP and process adopted are given below:

2.1Analytical Heretical Process (AHP)

AHP is a technique from the MCDM family and is extensively used in different applications such as supply chain, supplier selection, technology selection [8,9]. MCDM is used to rank or select a set of alternatives under usually independent, incommensurate or conflicting attributes [10]. In brief, the steps followed are given below:

Step 1: MCDM is structured as a hierarchy and decomposed into a hierarchy of interrelated decision elements. The hierarchical structure is used to arrange criteria/factors and sub-criteria/sub-factors.

Step 2: Here the pairwise comparisons between criteria and sub-criteria undertook using a nine-point ratio scale by experts (please see Table 1).

Table 1: Scales in pairwise comparisons

Definition	Equally important	Moderately important	Strongly important	Extremely important	Extremely more important	Intermediate values
Value	1	3	5	7	9	2,4,6,8

Step 3: The criteria are compared pair-wise according to their influence and based on the specified criteria in the higher level [11]. The weights are calculated from equation (1) as given below:

$$AW=\lambda_{max}W \qquad (1)$$

In Equation 1; A is the priority matrix; W is weight, and λ_{max} is the maximum Eigenvalue of Matrix A

Step 4: The matrix A is checked for the consistency ratio (CR), this to be less than 0.10.

The consistency ratio is the ratio of consistency index (CI) and the random index number (RI). The CR and CI are defined as follows:

$$CI = \frac{\lambda max-1}{n-1} \qquad (2) \quad CR=\frac{CI}{RI} \qquad (3)$$

For the different count of criteria, it has a different value as is shown in Table 2.

Table 2: Random Index (RI)

N	1	2	3	4	5	6	7	8	9
RI	0	0	0.58	.90	1.12	1.24	1.32	1.41	1.45

If CR is less than 0.10, the result can be acceptable, and matrix A is sufficient consistent. Otherwise, one has to return to step 1 and repeat the steps.

3. Results

In evaluating the relative importance of the factors to select the traceable technology AHP is used, here, a group of five experts from food manufacturing company and academician is formed. Experts inputs were collected and used in finalising the factors and sub-factors (Please see figure 1). After finalising the factors and sub-factors, expert's opinion is again used through Saaty scale to perform the pairwise comparison of factors and sub-factors. The pairwise comparison matrix for factors has been framed, and their relative weights are summarised in Table 3.

Table 3: Pair-wise comparison matrix for factors

	Product-related factor	Process-related factor	Social factor	Other factor	Weights	Rank
Product-related factor	1	2	2	4	0.435	1
Process-related factor	0.5	1	2	3	0.286	2
Social factor	0.5	0.5	1	2	0.182	3
Other factor	0.25	0.33.	0.50	1	0.097	4
Consistency Ratio (CR)=0.017						

The “product-related factor” having weight 0.435 is the most important factors for the selection of traceable technology for the FSC, followed by “process related factor” (0.286); “social factor” (0.182), and “other factor” (0.097). The pairwise comparison is performed for the subfactors and relative weights are calculated. These relative weights of sub-factors along with the global weight are shown in Table 4.

It is observed that the consistency ratio of pairwise comparison matrix of each factor and sub-factors is less than 0.1 in all the cases. Hence these matrices are highly consistent and acceptable. Table 4 also shows the relative rank and global rank of the sub-factors for the selection of traceable technology.

Table 4: Global Ranking of the factor and sub-factors to select the traceable technology in FSC

Factors	**Relative weight**	**Sub Factors**	**Relative weight**	**Relative rank**	**Global weight**	**Global rank**
Product-related factor	0.435	Product Type	0.274	2	0.11919	**3**
		Amount of information	0.086	4	0.03741	**10**
		Granularity level	0.178	3	0.07743	**5**
		Cost	0.462	1	0.20097	**1**
Process-related factor	0.286	Reliability	0.073	4	0.020878	**13**
		Ease in implementation	0.498	1	0.142428	**2**
		Integrity of information	0.172	3	0.049192	**9**
		Mode of information	0.258	2	0.073788	**6**
Social factor	0.182	Privacy	0.467	1	0.084994	**4**
		Eco-friendly	0.160	3	0.02912	**11**
		Health Risks	0.277	2	0.050414	**8**

		Consumer awareness	0.095	4	0.01729	**14**
Other factor	0.097	Quality improvement	0.297	2	0.028809	**12**
		Ease of Recall	0.54	1	0.05238	**7**
		Marketing Tool	0.163	3	0.015811	**15**

4. Discussion

Based on Table 4, the order of relative importance of the factors for selection of traceable technology for FSC as: 'Product-related factors' > 'Process related factors' > 'Social factors' > 'Other factors'. The order of relative importance of sub-factors is given in Table 4.

The 'product-related factors' are the most important factors for the selection of traceable technology in the FSC. This factor has four sub-factors namely: "product type", "amount of information", "granularity level" and "cost". The major sub-factors for the selection of traceable technology is the cost of the product having the highest weight. The second highest weight is the "product type" and the second major consideration for traceability technology selection. The product type refers to the perishability level, freshness, physical state of the product and their size. These aspects affect the selection of the traceable technology. Next important factors are the "Granularity level" after the "product type". The "granularity level" is defined as the *"...reflects the levels and size of the Identifiable unit, that are handled by the particular system*" [12]. The fine granularity level requires high cost and detailed information than the coarse granularity level. The last important sub-factors are "amount of information". The traceable information carrier limitations such as QR code having the capacity to contain more information than the barcode. Thus, these factors play an important role in the selection of traceable technology for the FSC.

The second important factor is the "Process related factor" which are having the weight 0.286. This factor has four sub-factors. In the context of this factor, most important sub-factor is the "Ease in implementation". Before implementing any technology, the organisation assesses the implementation issue. Similar to other technology, 'ease in implementation' is an important factor in the traceable technology selection. Next important sub-factor is the "mode of information" which refer to the "how information is processed (paper-based or digital)?". After the mode of information, the next important sub-factor is the "integrity of the information". The information integrity is an aspect of the food integrity which is protected through the traceability. Reliability of the traceable technology is the lowest relative weight to select the traceable technology for FSC.

The social factor is the next most important factor for the selection of traceable technology in FSC. This factor also has four sub-factors. "Privacy" is a most important factor for the traceability technology selection for the food product. The consumer's concern about their privacy and some traceable technology traces the product up to their fridge, and so the consumer loses their privacy [13]. Second important sub-factor is the "Health risk of the consumers". Some traceability carriers such as a barcode on fruits and fruits edible label are placed on the surface of the food product which is harmful to the health of the consumers [14]. Next important sub-factor is the "Eco-friendly". The traceable technology should be an eco-friendly and having the less effect on the environment. The advanced traceable technology is eco-friendly such as an elidable label. Selection of traceable technology also depends on the consumer awareness about the traceability of food product because the industries do not want to engage their resources in an environment where demand is very low [15].

Finally, the fourth important factor is "Other factor" which have the three sub-factors namely: 'Quality improvement'; 'ease in recall' and 'marketing tool'. The suitable traceable technology is utilised for the effective recall system especially in case of the food crisis. So, this sub-factor is most important sub-factor in this context. Second important sub-factor is the "quality improvement". Traceability technology is used for the purpose to improve the quality of the food product by effective monitoring the food throughout the supply chain. The next important sub-factor is the "marketing tool". The food companies provide the information about the food product through the traceability, and these systems are used as a marking tool.

5. Implications

This study provides the understanding of the factors and sub-factors for the selection of traceable technology in FSC. The significant implication of this research suggests for facilitating the managers and professionals of food industries; to select a suitable traceable technology for their respective supply chain. The finding of this work provides a direction to the decision maker of the specific FSC such as fruit, vegetables, and dairy supply chain in selecting the traceable technology.

6. Conclusions

The factor and sub-factor for the selection of traceable technology in FSC are identified through the literature survey and are supplicated by the expert's opinion. These factors played a significant role in the selection of the traceable technology for FSC. After achieving the four main factors and fifteen sub-factors, AHP is used for prioritising these factors and their associated sub-factors as per their relative importance and global importance. Finally, the finding of this work is presented, and the implications are provided.

References

1. Leat, P., Marr, P., & Ritchie, C. (1998). Quality assurance and traceability—the Scottish agri-food industry's quest for competitive advantage. Supply Chain Management, 3,115–117.
2. Khan, S., Haleem, A., Khan, M., Abidi, M., & Al-Ahmari, A. (2018). Implementing Traceability Systems in Specific Supply Chain Management (SCM) through Critical Success Factors (CSFs).*Sustainability*,10(2), 204.
3. Olsen, P., & Borit, M. (2013). How to define traceability. Trends in Food Science & Technology
4. Van Dorp, K. J. (2002). Tracking and tracing: A structure for development and contemporary practices. Logistics Information Management, 15(1), 24-33.
5. Luthra S, Garg D, Haleem, A (2013) Identifying and ranking of strategies to implement green supply chain management in Indian manufacturing industry using Analytical Hierarchy Process. Journal of Industrial Engineering and Management 6(4):
6. Kumar S, Singh B, Qadri MA, Kumar YVS, Haleem A (2013) A framework for comparative evaluation of lean performance of firms using fuzzy TOPSIS. International Journal of Productivity and Quality Management 11(4): 371-392
7. Kumar S, Luthra S, Haleem A, Mangla S.K, Garg D. (2015) Identification and Evaluation of Critical Factors to Technology Transfer Using AHP Approach. International Strategic Management Review 3 (1): 24–42
8. Subramanian N, Ramanathan R (2012) A review of applications of Analytic Hierarchy Process in operations management. International Journal of Production Economics 138 (2): 215–241
9. Kumar S, Luthra S, Haleem A (2015) Benchmarking supply chains by analyzing technology transfer critical barriers using AHP approach. Benchmarking: An International Journal 22(4)
10. Hwang CL, Yoon K (1981) Multiple attribute decision making: Methods and applications. A state of the art survey. New York: Springer-Verlag
11. Chrysochou, P., Chryssochoidis, G., & Kehagia, O. (2009). Traceability information carriers. The technology backgrounds and consumers' perceptions of the technological solutions. *Appetite,53*(3), 322-331. doi:10.1016/j.appet.2009.07.011
12. Bollen, A.F., Riden, C.P. & Cox, N.R. (2007). Agricultural supply system traceability, part I: Role of packing procedures and effects of fruit mixing. Biosystems Engineering, 98(4): 391-400
13. von Locquenghien, K. (2006). On the potential social impact of RFID-containing everyday objects. Science, Technology and Innovation Studies, 2, 57–78.
14. Khan, M. I., Khan, U., & Haleem, A. (2014). Corporate Social Responsibility: Modelling of Critical Factors using an Integrated ISM and Fuzzy-Micmac approach. International Journal of Global Business and Competitiveness, 9(1).
15. Haleem, A., & Khan, M. I. (2017). Towards successful adoption of Halal Logistics and its' implications for the stakeholders. British Food Journal, 119 (7).
16. Khan, S., Asjad, M., and Ahmad, A. (2015), "Review of Modern Optimization Techniques", International Journal of Engineering Research and Technology, 4(4).

Journal of Materials Science: Materials in Electronics
https://doi.org/10.1007/s10854-018-0035-8

Significant improvement in morphological, dielectric, ferroelectric and piezoelectric characteristics of $Ba_{0.9}Sr_{0.1}Ti_{0.9}Zr_{0.1}O_3$–$BaNb_2O_6$ nanocomposites

Aditya Jain[1] · Amrish K. Panwar[1] · A. K. Jha[2]

Received: 30 March 2018 / Accepted: 7 September 2018
© Springer Science+Business Media, LLC, part of Springer Nature 2018

Abstract
Multifunctional composite with material composition $(1-x)Ba_{0.9}Sr_{0.1}Ti_{0.9}Zr_{0.1}O_3$–$xBaNb_2O_6$ ($x=0.0$, 0.05, 0.1, 0.2 and 0.3) has been successfully synthesized using mechano-chemical activation process. The co-existence of perovskite tetragonal phase of BSTZ and niobate orthorhombic phase of BNO was detected by X-ray diffraction measurement and confirmed by Rietveld analysis. All the BSTZ–BNO composites show a polygonal grain type morphology with clearly visible grain boundaries. BSTZ–BNO composites possessed a thermally stable dielectric constant within a broad range of temperature. The obtained results show a strong influence of BNO addition on the microstructural, dielectric, ferroelectric, piezoelectric and breakdown strength of bare BSTZ ceramic. For $x=0.10$, the composite exhibit optimum properties with high dielectric constant $\varepsilon_m=5842$, large remnant polarization $P_r=9.25$ μC/cm^2, improved piezoelectric constant $d_{33}=296$ pC/N and high breakdown strength $E_{bd}=304$ kV/cm. The high dielectric constant accompanied by very low dielectric loss and large piezoelectric constant make BSTZ–BNO a suitable material for ceramic capacitors and electromechanical device applications.

1 Introduction

Miniaturization of solid state electronic devices has been accomplished by multifunctionality and downscaling. Multifunctional ceramic composites have drawn much attention in recent owing to their promising applications in novel technological devices. Characteristically, they possess more than one order parameter which can be coupled to one another. $BaTiO_3$ based composite materials and investigation of their properties have attracted much recognition with advances of novel procedures for the development of perovskite and phosphor materials, expanding their usage in other areas, for example, light emitting devices, ceramic capacitors, microwave devices, field emission devices, etc. [1]. On the other hand, micro and nano-electronics research in the larger portion is driven by the need for smaller component devices exhibiting better performance. For capacitive components, those are considered as an integral part of many memory devices for example, read-only memory (ROM), random access memory (RAM) and USB flash drives, the dielectric constant of the materials restricts the degree of miniaturization—a limit that has been rigorously attempted to overcome in the last decade. Till now, improvement in dielectric constant value has been attained by using mainly barium zirconium titanate, barium strontium titanate, etc. [2, 3].

Among lead-free ferroelectric materials, (Ba,Sr)(Zr,Ti)O_3 have been paid much consideration for their possible application in dielectric tunable devices and dynamic random access memories. It has been observed that the diffuse phase transition in BSTZ is advantageous in attaining better piezoelectric properties and high electrocaloric constant [4]. In these materials, the ferroelectric and optical characteristics along with degree of coupling are mainly reliant on the microstructure, including the domain pattern as well as grain shape [5]. In the present study, $Ba_{0.9}Sr_{0.1}Ti_{0.9}Zr_{0.1}O_3$ (BSTZ) has been taken as the host matrix. BSTZ exhibit a perovskite structure (ABO_3), where barium and strontium occupy the A-site and titanium and zirconium occupy the B-site of the lattice. In BSTZ, various characteristics such as dielectric

Electronic supplementary material The online version of this article (https://doi.org/10.1007/s10854-018-0035-8) contains supplementary material, which is available to authorized users.

✉ Amrish K. Panwar
panwaramar@gmail.com

[1] Lithium Ion Battery Technology Lab, Delhi Technological University, New Delhi 110042, India

[2] Department of Applied Science, A.I.A.C.T.R., Geeta Colony, New Delhi 110031, India

Published online: 14 September 2018

constant, transition temperature, electrical resistance, etc. can be efficiently manipulated by combining it with individual compounds or dopants.

Niobate group materials have attracted much consideration by researchers owing to their promising piezoelectric, pyroelectric, electro-optic and nonlinear properties combined with their industrial as well as scientific applications in the area of photonics, microwave dielectric materials, holographic storage devices and frequency doublers [6]. Amongst all the intrinsic alkaline earth meta-niobate compounds such as, $CaNb_2O_6$, $SrNb_2O_6$ and $BaNb_2O_6$, the charge generation in $BaNb_2O_6$ was found to be higher which is attributed to smaller energy band gap as compared to other meta-niobates materials [7, 8]. Microwave dielectric properties and photocatalytic activities of barium niobates have been copiously explored in recent time [2, 9, 10]. Till now, numerous groups of materials have been studied to improve the ferroelectric ordering and electro-optical properties, but still, particular attention has been paid to lead-free composites due to their better electro-optical coupling and environmental friendliness [11, 12]. However, a detailed literature survey reveals that the investigation of ferroelectric and piezoelectric properties along with electrical breakdown strength of $Ba_{0.9}Sr_{0.1}Ti_{0.9}$ $Zr_{0.1}O_3$–$BaNb_2O_6$ (BSTZ–BNO) has not been reported so far.

It is a well-known fact that conventional high energy ball milling technique can be used for synthesizing crystalline micro and nano-composites. This technique has many benefits, for example, applicability to any class of materials, production simplicity and relatively inexpensive synthesis [13–15]. Mechanochemical activation technique has another benefit that it can initiate solid-state reactions at comparatively lesser temperature than those required in conventional techniques of material synthesis. In the present work, $(1-x)$ $Ba_{0.9}Sr_{0.1}Ti_{0.9}Zr_{0.1}O_3$–$(x)BaNb_2O_6$ has been prepared via conventional ball milling technique and their morphological, electrical and optical characteristics have been explored rigorously. The aim of the current investigation is to examine the orientation and mixed phase properties of BSTZ–BNO composites.

2 Experimental

Particulate composite with $Ba_{0.9}Sr_{0.1}Ti_{0.9}Zr_{0.1}O_3$ (BSTZ) as a host material and $BaNb_2O_6$ (BNO) as another part of the composite material were prepared by conventional ball milling technique. $Ba_{0.9}Sr_{0.1}Ti_{0.9}Zr_{0.1}O_3$ was synthesized by taking high-purity Sigma-Aldrich make analytical reagent grade chemicals barium carbonate (99.99%), strontium carbonate (99.9%), titanium dioxide (99.8%) and zirconium dioxide (99.0%) as the raw materials. All raw chemicals were mixed in the required ratio, which is followed by ball milling in an air environment at 475 rpm for 24 h. Ball milling of the samples was carried out using *Retsch make* planetary ball mill. A jar made of ZrO_2 having 50 ml capacity, 45 mm diameter along with 125 Zirconia balls of 5 mm diameter have been used as milling environment. Initially, the as-prepared BSTZ solid solution was calcined at 1025 °C for 5 h at a slow heating rate of 3 °C/min. The calcination was followed by sintering for 4 h at an optimized temperature of 1260 °C.

Extremely pure analytical reagent grade Barium carbonate (99.99%) and Niobium pentoxide (99.99%) in stoichiometric proportion were milled alongside Toluol to synthesize the $BaNb_2O_6$ solid solution for 24 h in the same environment as used for preparing BSTZ. The milled powder was calcinated at 625 °C for 1 h which is followed by high-temperature sintering at 1200 °C for 5 h. Subsequently, these composite solid solutions $(1-x)$ $Ba_{0.9}Sr_{0.1}Ti_{0.9}Zr_{0.1}O_3$–$(x)$ $BaNb_2O_6$ (where $x=0$, 5, 10, 20 and 30 wt%) were collected by thoroughly blending the constituent phases BSTZ and BNO in required proportion inside the ball milling for effective 8 h. The as obtained sintered composite solid solutions were finally blended with 3 wt% of water-soluble synthetic polymer 'polyvinyl alcohol' followed by pressing them into thin cylindrical pellets of 8 mm diameter and nearly thickness of 0.8 mm by applying a force of 75 kN using a pelletizer. The pellets were then heated in air environment at 600 °C. Henceforward, these composites are termed as BBN0, BBN5, BBN10, BBN20 and BBN30 having the weight ratio of $x=0$, 0.05, 0.10, 0.20 and 0.30, respectively.

Bruker D8 Advance X-ray diffractometer has been used to determine the crystallographic structure and phase of BBNx composites. Rietveld refinement of BSTZ–BNO composites was carried out using a computer program package *X'Pert Highscore Plus*. The surface morphology, microstructural features and grain size were examined using *Hitachi S-3700N* scanning electron microscope. Grain size distribution analysis of SEM images has been performed using *ImageJ* software. TEM, HRTEM and SAED study of the optimized sample has been performed using TEM (JEOL 3010) operating at 270 kV. For further electrical measurements, electrodes were designed by coating silver paste on both faces of pellet samples, which was followed by curing the pellets at 150 °C for 10 min. The obtained pellets were then used to measure dielectric characteristics by using an *Agilent 4284A* LCR meter operating at wide range of frequencies over a broad temperature range of 25–200 °C. The electric field versus polarization hysteresis characteristics of all the composite specimens were measured using E–P loop analyzer (*M/s Marine India, New Delhi*). Piezoelectric properties measurement of the samples was carried out using *PIEZOTEST* system UK. Measurement of dielectric breakdown strength (E_{bd}) were carried out on a sample coated with silver paste. This electroded sample is dipped in a bath

filled with silicon oil and placed on a baseplate of high conductivity copper.

3 Result and discussion

3.1 X-ray diffraction (XRD)

To comprehend the structural and phase modification with the addition of $BaNb_2O_6$ in $Ba_{0.9}Sr_{0.1}Ti_{0.9}Zr_{0.1}O_3$, Rietveld technique has been used for structural refinement. Figure 1a demonstrate the comparative XRD patterns of $(1-x)Ba_{0.9}Sr_{0.1}Ti_{0.9}Zr_{0.1}O_3$–$xBaNb_2O_6$ ($x=0$, 0.05, 0.1, 0.2 and 0.3). The intense and sharp XRD peaks indicate the crystalline nature of the bare and composite samples. The dotted rectangular boxes indicate that as BNO content increases, some extra peaks begin to appear in the XRD pattern. Figure 1b–f depicts the Rietveld-refined XRD patterns of $(1-x)$BSTZ–(x)BNO. Barium titanate (JCPDS database no. 000-005-0626) and barium niobate (JCPDS database no. 001-077-0589) were considered as the reference diffraction patterns. A clear and well-identifiable tetragonal phase with P4*mm* space group is detected for BBN0, although, as the BNO concentration is increased, the diffraction peaks of barium niobate start appearing. The BSTZ–BNO composites synthesized using the mechano-chemical activation

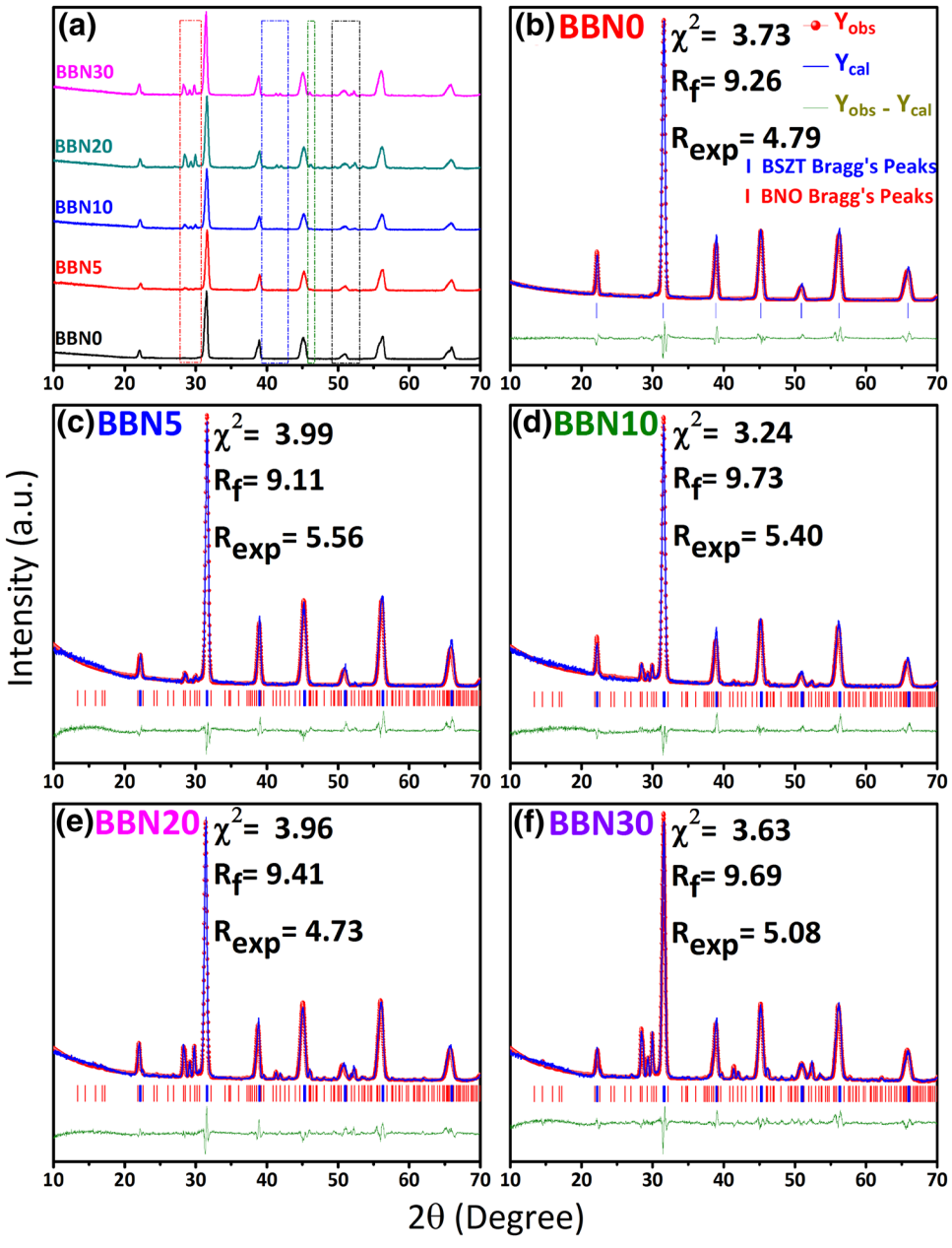


Fig. 1 Comparative and Rietveld refined XRD spectra of as-synthesized $(1-x)$BSTZ–xBNO composite ceramics: **a** combined XRD spectra of all the five samples **b** $x=0.0$, **c** $x=0.05$, **d** $x=0.10$, **e** $x=0.20$ and **f** $x=0.30$

technique exhibited a mixed tetragonal-orthorhombic structure and did not show any significant observable impurity. The calculated and observed *d* spacing values of all the diffraction peaks in bare and composite samples specify that there is no change in the parent crystal structure (tetragonal) as *x* is increased from 0.05 to 0.3. However, there is a slight change in tetragonality of the samples, which is attributed to change in lattice parameters *'a'* and *'c'* changes with an increase in BNO content.

Further, the results approve the successful synthesis of the di-phasic composite materials. Further, this also suggests that both (BSTZ and BNO) the parent phases have retained their basic identity in the composite materials and no unwanted reaction took place between the ferroelectric BSTZ and phosphor BNO phases during the final annealing of the materials. The host ferroelectric BSTZ phase of the composite exhibit a P4*mm* space group and crystallizes in a tetragonal structure whereas, BNO has an orthorhombic structure with $C222_1$ space group. It was observed that the intensity of diffraction peaks of the orthorhombic phase increases with increase in BNO content. The detailed structural parameters achieved after the Rietveld refinement analysis are shown in Table 1. By observing at the XRD pattern of composites, it can be concluded that at higher BNO content samples limited reaction took place amid the ferroelectric-phosphor phases of BSTZ and BNO, respectively. Figure 2a, b demonstrate the as obtained crystal structure of both the compounds i.e. BSTZ and BNO. The crystal structures were obtained with the help of VESTA software from the refined atomic positions found after the Rietveld analysis of BBN10 composite. The blue and light green colored stripes at Barium and Titanium site show the occupancy of strontium and zirconium ions, respectively. Further, the obtained atomic positions also confirm that in BBN10 sample, the BSTZ exists in tetragonal phase and BNO is present in orthorhombic phase.

3.2 Microstructural studies

SEM micrographs of five synthesized specimens are depicted in the Fig. 3a–e. All the samples exhibit dense grain structure with clearly distinguished grain boundaries. The grain size and homogeneity of these composites were significantly affected by BNO addition. However, the surface morphology was found to be relatively identical. BBN10 sample shows fairly homogeneously distributed grains compared to BBN20 and BBN30, both of which reveals rather more inhomogeneous grain distribution. The average grain size of these samples was found to be approximately 1.51, 1.44, 1.61, 1.76 and 1.81 μm for BBN0, BBN5, BBN10, BBN20

Table 1 Rietveld refined XRD parameters for bare BSTZ and BSTZ–BNO composite samples

Sample	Space group	Crystal structure	Lattice parameters (Å)	Cell volume (Å^3)	χ^2	R_{exp}	R_f	R_{Bragg}
BBN0	*P*4*mm*	Tetragonal	a = 4.0125 c = 4.0257	64.8154	3.73	4.79	9.26	3.03
BBN5								
BSTZ phase	*P*4*mm*	Tetragonal	a = 4.0051 c = 4.0291	64.6306	3.99	5.56	9.11	6.16
BNO phase	$C222_1$	Orthorhombic	a = 7.8712 b = 12.201 c = 10.268	987.727				4.16
BBN10								
BSTZ phase	*P*4*mm*	Tetragonal	a = 4.0047 c = 4.0278	64.5963	3.24	5.40	9.73	5.79
BNO phase	$C222_1$	Orthorhombic	a = 7.8615 b = 12.210 c = 10.277	986.600				3.83
BBN20								
BSTZ phase	*P*4*mm*	Tetragonal	a = 4.0038 c = 4.0251	64.5226	3.96	4.73	9.41	3.09
BNO phase	$C222_1$	Orthorhombic	a = 7.8608 b = 12.193 c = 10.272	984.670				3.92
BBN30								
BSTZ phase	*P*4*mm*	Tetragonal	a = 3.9966 c = 4.0168	64.1611	3.63	5.08	9.63	2.65
BNO phase	$C222_1$	Orthorhombic	a = 7.8400 b = 12.159 c = 10.248	977.627				4.01

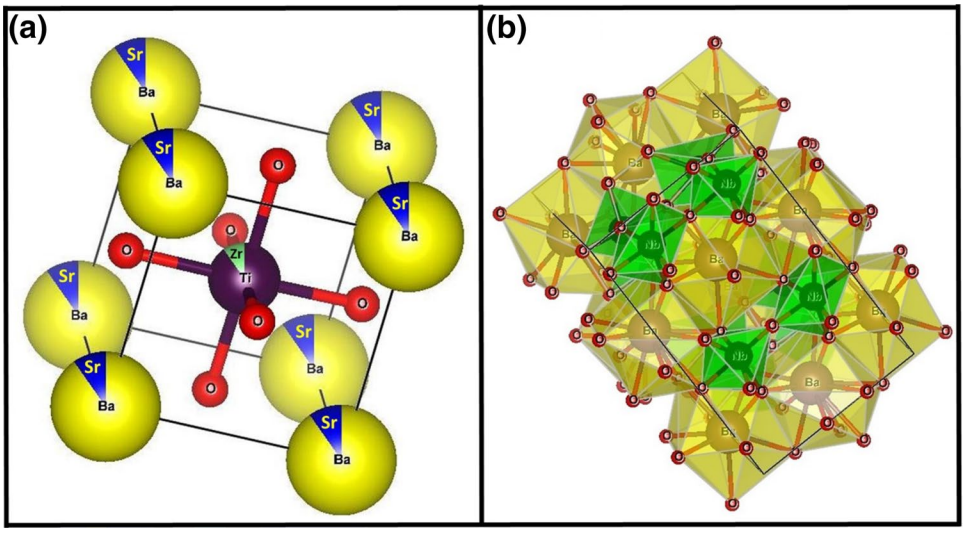


Fig. 2 Crystal structure of **a** BSTZ and **b** BNO; drawn from the atomic positions obtained after the Rietveld analysis of BBN10 sample

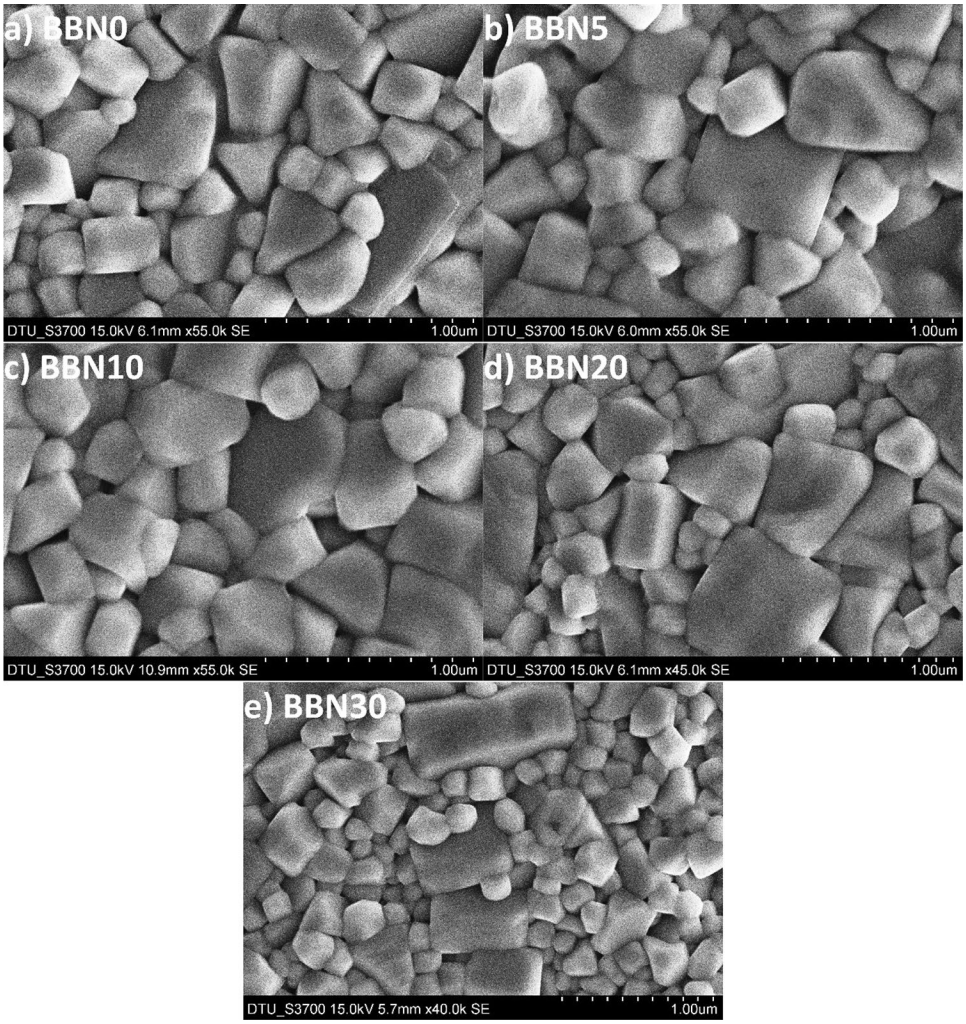


Fig. 3 SEM micrograph of high temperature sintered pellets of $(1-x)$BSTZ–xBNO composites: **a** $x=0.0$, **b** $x=0.05$, **c** $x=0.10$, **d** $x=0.20$ and **e** $x=0.30$

Table 2 Room temperature saturation polarization (P_s), remnant polarization ($2P_r$), coercive field ($2E_c$), breakdown strength (E_{bd}) and piezoelectric constant (d_{33}) for bare BSTZ and BSTZ–BNO composite samples

Sample	Relative density	$2P_s$ (μC/cm^2)	$2P_r$ (μC/cm^2)	$2E_c$ (kV/cm)	E_{bd} (kV/cm)	d_{33} (pC/N)
BBN0	5.697	17.0	5.5	4.8	235	269
BBN5	5.701	33.8	15.4	15.9	267	302
BBN10	5.719	36.7	18.5	18.8	304	296
BBN20	5.671	24.1	13.4	13.8	249	241
BBN30	5.673	20.2	8.62	9.1	223	176

and BBN30, respectively. Further, to clearly understand the grain growth and porosity inside the material, authors have carried out the density measurement of all the five samples and shown in Table 2. The piezoelectric properties of polycrystalline materials are affected by both intrinsic and extrinsic parameters [16, 17]. The grain size as extrinsic parameter strongly affect the piezoelectric properties of any material. In earlier reports, it has been reported that coarse-grained ceramics show improved piezoelectric response compared to finely-grained ceramics [18]. Moreover, the coarse grain ceramics facilitate better polarization and enhanced domain mobility, resulting in a higher degree of polarization in the material and hence superior electrical properties [19, 20]. Furthermore, it is eminent that the grain size as well as the morphology of the ceramics heavily rely on its calcination and sintering temperature along with the soaking time span at the peak temperature [21, 22]. These two aspects also change the microstructure of the final sintered sample and henceforth, they affect the electrical characteristics of the ceramic materials. In higher BNO content composites, the occurrence of two types of grains having a significant difference in grain size may be attributed to the fact that the particles of one phase may have a higher likelihood of growing as compared other at higher sintering temperature and consequently larger grains grows at the cost of smaller grains. Furthermore, in case of composites, it is rather strenuous to produce a homogeneous morphology along with uniform grain size owing to the significant difference in the optimum heating environments and the thermal expansion constant of two different compounds.

TEM and HRTEM imaging of BBN10 has been carried out since it demonstrates overall superior dielectric, ferroelectric and piezoelectric characteristics among all the synthesized specimens. The TEM technique offers valuable insight in identifying the particle morphology and intergrowth of a material. The average particle size of BBN10 solid solution obtained using TEM study is shown in Fig. 4a were found to be ~ 160 nm. These parallelly aligned lattice fringes in the HRTEM image of BBN10 shows that the sample is perfectly crystalline. The HRTEM images of BBN10 particle depicted in Fig. 4b, c demonstrate the lattice fringes corresponding to various planes having an inter-fringe distance of 1.35 Å, 1.69 Å and 1.57 Å, respectively. In Fig. 4c, a twinned region is marked with a triangle, that may be identified as an area where $Ba_{0.9}Sr_{0.1}Ti_{0.9}Zr_{0.1}O_3$ and $BaNb_2O_6$ particles have submerged into one another and subsequently leading to twinning of the lattice fringes. The Prallelly aligned lattice fringes in the HRTEM image of BBN10 having an inter-fringe distance of 1.35 Å and 1.69 Å can be allocated to BSTZ phase with corresponding (212) and (112) planes having conventional d spacing value of 1.34 Å and 1.66 Å, respectively. Also, the lattice fringes located inside the twinned interface with 1.57 Å inter-fringe distance can be allocated to BNO phase with analogous (442) plane with 1.575 Å as the conventional d spacing. Figure 4d depicts the selected area electron diffraction (SAED) pattern which is in good agreement with HRTEM results and approves the crystalline nature of BBN10 specimen. The bright and dark spots in SAED pattern can be allocated to various planes in the tetragonal and orthorhombic crystal. The SAED pattern was measured for the twinned region of the HRTEM image that demonstrates two sets of bright and dark spots confirming the diffusion of BSTZ and BNO compounds for observed area. Furthermore, both of the HRTEM image as well as SAED patterns investigated for the specimen having optimum properties i.e. BBN10, shows no noteworthy structural defects upon HRTEM investigation.

3.3 Dielectric studies

The temperature dependency of dielectric characteristics of BSTZ–BNO composite materials have been investigated and are shown in Fig. 5a–e. The inset of the dielectric curve shows the magnified view of variation in dielectric constant with temperature. The dielectric properties were studied at eight different frequencies. BNO addition in BSTZ lattice has resulted in a significant change in phase transition characteristics as compared to BNO free BSTZ sample. At lower frequency, BNO substituted samples show a sharp transition compared to the bare sample, however, at high frequency, the phase transition becomes progressively diffused (flattened and broad) type. The occurrence of a single broad peak in BBN0 and comparatively narrower peak in composite samples signifies the transition of ferroelectric to paraelectric phase or tetragonal to cubic phase. Further, the dielectric constant (ε_m) at phase transition temperature decreases with even a small rise in frequency and is observed to be minimum at 1 MHz. It is observed that permittivity maxima

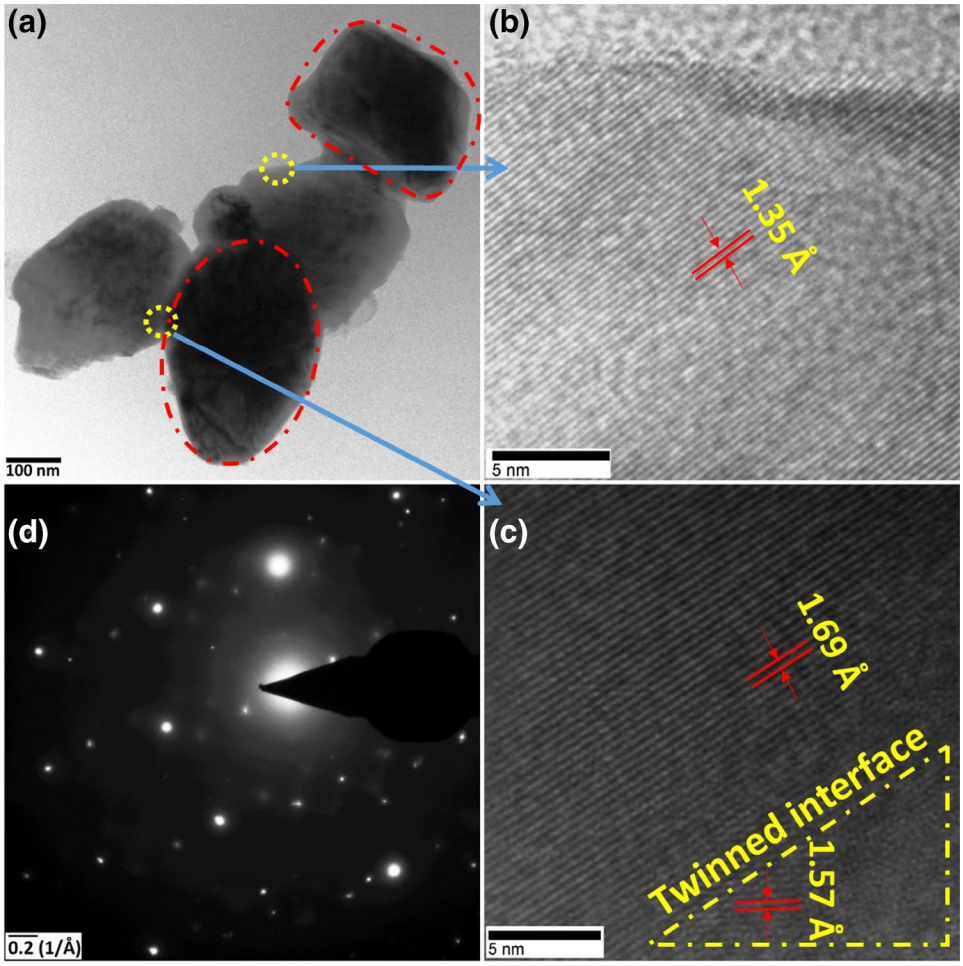


Fig. 4 TEM/HRTEM micrographs of BBN10: **a** TEM, **b, c** HRTEM, **d** SAED pattern

of BBN5 and BBN10 have been enhanced compared with that of BNO free BSTZ sample. The dielectric constant of the samples shows a gradual rise with an increase in BNO concentration becomes maximum for BBN10 composite and decreases on further increasing the BNO concentration. The dielectric constant at phase transition temperature for the samples BBN0, BBN5, BBN10, BBN20 and BBN30 at 20 Hz was found to be ~4361, 5105, 5842, 3570 and 2547, respectively. The high dielectric constant of BBN10 sample may be due to optimum grain size, grain homogeneity as well as higher density of the material among all the prepared samples. Larger grain size corresponds to less number of insulating grain boundaries layers. This decrease in number of grain boundaries leads to lesser trapping of space charge and thus lesser domain wall pinning resulting in overall high dielectric constant [23, 24]. One more possibility for the reduction in dielectric constant at higher BNO concentration might be due to inhibition of Nb^{5+} at Ti^{4+}/Zr^{4+} site of ABO_3 perovskite unit cell, resulting in weakening of bonding force between the oxygen atom and B-site ion. A clear ferroelectric to paraelectric phase transition peak can be seen for all the five samples, which clearly indicate that even at higher BNO concentration dielectric properties of the composites are still governed by BSTZ phase.

At high frequency, the dielectric properties of BSTZ–BNO composites become frequency independent. Moreover, considering only the high-frequency characteristics, the phase transition curve appears to be more diffusive compared to BNO free BSTZ sample. This indicates that the addition of BNO results in a gradual transformation from typical ferroelectric to relaxor type characteristics. Further, at lower frequencies, i.e. 20 Hz, 100 Hz and 1 kHz, more dielectric dispersion is observed. The reason for higher dispersion in composite samples is the occurrence of large number of defects produced by the inequivalent displacement of dopant atoms. The phenomena of coulombic interaction inside the material causes negatively charged defects to attract positively charged defects resulting in the development of associated defect pairs. Also, the movement of oxygen vacancies in the vicinity of oxygen octahedron or back and forth motion of holes result in reorientation of dipoles. Therefore, at lower frequency, the higher dielectric constant is attributed to the contribution of (i) interfacial, (ii) electronic, (iii) dipolar and (iv) ionic polarization. At

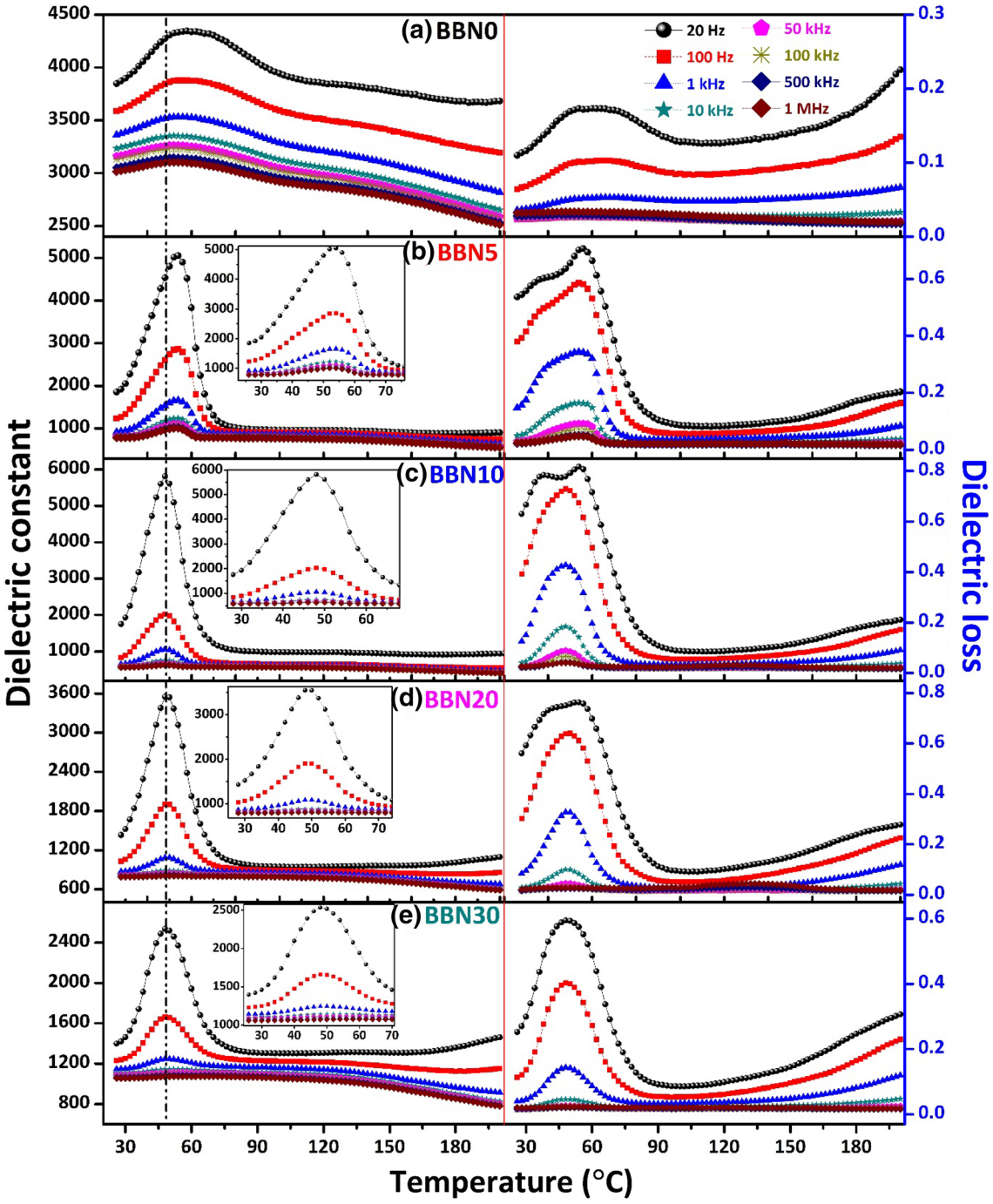


Fig. 5 Temperature dependences of dielectric constant and dielectric loss for $(1-x)$BSTZ–xBNO composites: **a** $x=0.0$, **b** $x=0.05$, **c** $x=0.10$, **d** $x=0.20$ and **e** $x=0.30$

higher frequencies, some of the polarizations do not contribute to the total polarization and only electronic and dipolar polarization are responsible for the net polarization inside the material [25]. Thus, the polarization inside the material decreases subsequently resulting in reduction in dielectric constant value at higher frequency. BBN5, BBN10 and BBN20 sample show a very good temperature stable dielectric constant at temperature higher than 75 °C. This characteristic of BSTZ–BNO composite samples can be used in high-temperature electronic switching applications. The phase transition temperature of $(1-x)$BSTZ–xBNO composites decreases gradually up to $x=0.10$. However, the Curie temperature remains nearly constant on further increasing the BCT content.

The correlation between temperature and dielectric loss is depicted in Fig. 5. Similar to dielectric constant, the dielectric loss curve also shows a dielectric loss maxima at the phase transition temperature. Above phase transition temperature, the dielectric loss decreases, becomes constant for a certain range of temperature and again increases on increasing the temperature. The dielectric loss of bare as well as composite samples is observed to be maximum at lower frequencies and decreases abruptly at higher frequencies. A gradual rise in dielectric loss of composite sample at higher temperature may be due to Debye-type relaxation of space charge at the interface between the electrodes and material, which is the typical nature of oxide-based perovskites having titanium as constituent element [26]. Moreover, ferroelectrics generally exhibit non-linear dielectric characteristics, which is due to reversible polarization in the presence of an applied electric field [27, 28]. Henceforth, their dielectric characteristics rely on both the frequency and magnitude of the applied bias voltage. In Fig. 5, it can be observed that both dielectric constant and dielectric loss were found to be dependent on the frequency of the applied ac signal. Further, at low frequency of operation, the dielectric loss curve of most of the samples is showing relaxation anomaly; this anomaly is attributed to increase in electrical conductivity at lower frequency [29]. This increase in electrical conductivity results in rapid increase and decrease in dielectric loss value around Curie temperature.

3.4 Ferroelectric studies

The Electric field versus polarization hysteresis loop of bare and composite ceramic samples at three different temperatures of 25, 75 and 125 °C is demonstrated in Fig. 6a–c. The P–E loops were recorded by applying an external electric field of up to 40 kV/cm. The inset of Fig. 6a–c show the variation of saturation polarization ($2P_s$) and remnant polarization ($2P_r$) with increasing BNO concentration. As shown in Fig. 6, all the synthesized samples exhibit ferroelectric hysteresis loops at all three temperatures. At ambient temperature, under the application of electric field, the remnant polarization and saturation polarization are found to be maximum for BBN10 specimen. Further BNO addition beyond $x = 0.10$ results in reduction of remnant and saturation polarization value. This shows that suitable BNO addition has an obvious influence in improving ferroelectric characteristics of BSTZ. The observed enhancement in the values of polarization is not intrinsic. This increased polarization demonstrated by BBN5 and BBN10 sample may be attributed to the space charge polarization effect [30] whose influence to ferroelectricity increases as BNO concentration increases in the composite. Moreover, the ferroelectric characteristics of ceramic materials are affected by their crystal phase, lattice defects like oxygen vacancies, microstructure and composition [31, 32]. Further, the structural transition occurring inside the material also controls the stability of the ferroelectric phase. It is evident that long-range polar orders of the dipoles inside the material results in superior ferroelectric properties [33]. In addition, a slight disruption in the polar ordering would affect the ferroelectricity of the material.

The observed increase in remnant polarization up to $x = 0.10$ may be due to both, reduction in leakage current and structural distortion induced by BNO addition [30, 34]. At elevated temperatures of 75 °C and 125 °C, the remnant polarization demonstrates almost identical characteristics. However, the loops were found to be slightly shifted around the origin. This abnormality can be elucidated by the existence of an internal electric field initiating from the off-centering and intrinsic movement of bound electrons inside the material. Furthermore, the area of the loop has also been increased for BBN10 sample, which may be attributed to low resistivity of the sample. The decrease in remnant polarization at higher temperatures may be ascribed to decrease in ferroelectric and increase in Para-electric phase of the materials. At room temperature, the increase in coercive field with BNO content may be attributed to dipole friction that arises owing to the domain orientation. The smaller grain size may have also contributed in enhancing the friction during domain orientation [35].

3.5 Breakdown strength measurement

Figure 7a shows the schematic diagram of breakdown measurement arrangement of a pellet. The electric breakdown strength of ceramics relies on many aspects such as grain size, porosity, etc. and extrinsic measurement constraints including electrode configuration, sample area and sample thickness [36, 37]. The external parameters for example frequency and the rate at which electric field is applied also influence the dielectric breakdown strength. Based on the above factors, it is possible that the improvement of E_{bd} in BBN10 sample is primarily due to increase in density, reduction in pore size of the material. The E_{bd} is found to be maximum for BBN10 sample, which may be ascribed to higher density among the five synthesized samples. Furthermore, as the BNO concentration rises beyond $x = 0.10$, the dielectric breakdown strength of the materials are observed to decrease. In ceramics as well as in ferroelectric composites, under an externally applied electric field, as the amount of weakly bonded ions with lower density and high porosity increases, the value of space displacement polarization also rises. Consequently, this enhancement in space displacement polarization forces the micro-pores and nano-pores inside the material to offer little resistance to electrical breakdown and deteriorate the dielectric breakdown strength [38]. Also, inner stress resulting from the non-uniform and

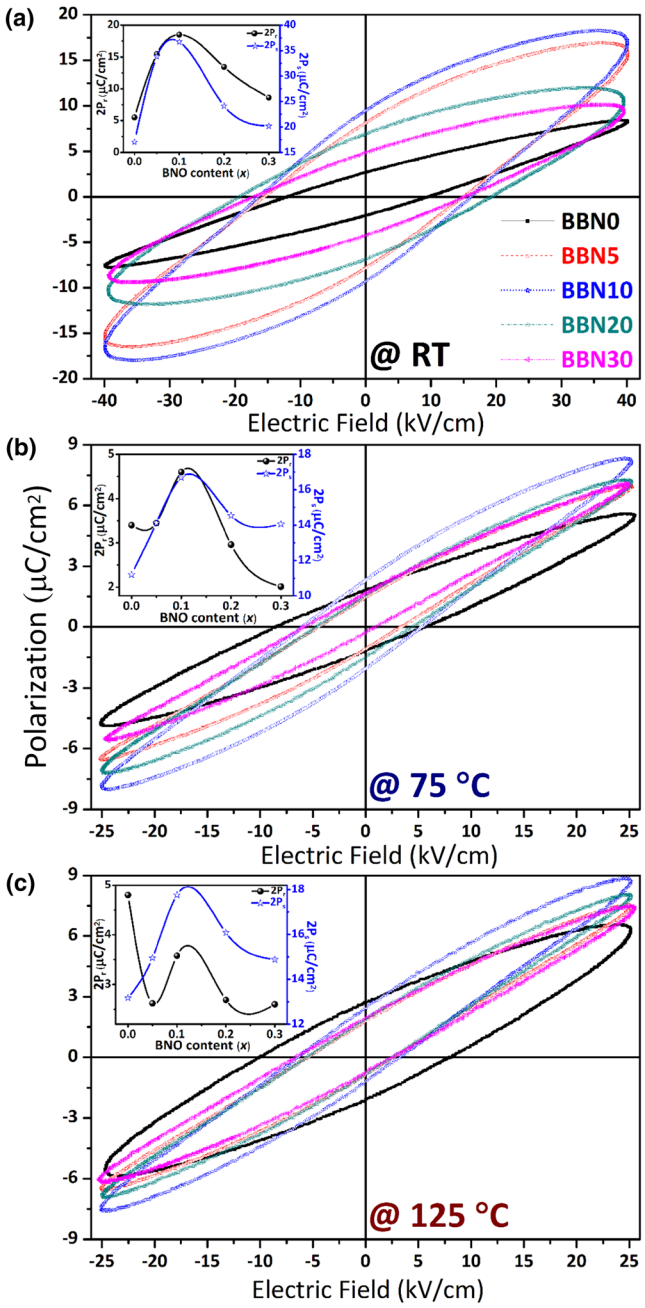


Fig. 6 Ferroelectric P–E hysteresis loops of $(1-x)$ BSTZ–xBNO at three different temperatures: **a** at room temperature, **b** at 75 °C and **c** at 125 °C; inset shows the variation in remnant polarization and saturation polarization with change in BNO content

inhomogeneous morphology can increase the ion mobility under the application of an electric field and hence reduces the E_{bd} value.

Thickness-dependent dielectric breakdown strength measurement of BBN10 specimen is depicted in the inset of Fig. 7b. As the thickness increases, there is reduction in breakdown strength. Thick dielectric pellets have the disadvantage that they possess a large number of internal and external defects such as micro-pores and micro-cracks. Figure 7c shows the schematic for breakdown of material in the presence of a micro-pore through a dendrite. Such imperfect areas are more liable to electrical breakdown, that results to a decrease in material thickness and a subsequent rise in voltage per unit thickness leading to avalanche breakdown [39]. In the present investigation, all the composites possess the same phase structure, nearly similar morphology and measurement environment. Therefore, it can be concluded that the significant enhancement in dielectric breakdown strength is mainly attributed to appropriate amount of BNO addition.

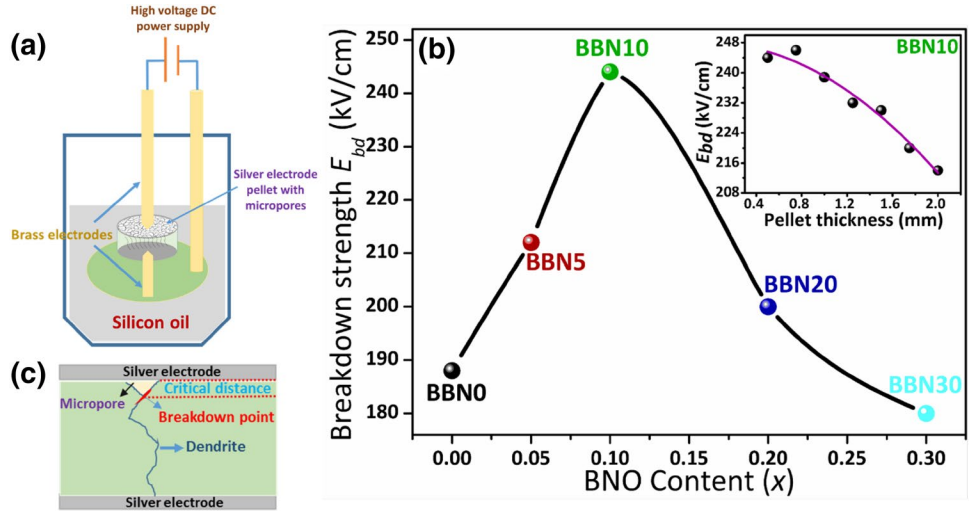


Fig. 7 **a** Schematic of dielectric breakdown strength measurement setup, **b** dielectric breakdown strength (E_{bd}) as a function of BNO content and **c** schematic showing the breakdown in any material in the presence of micropore through a dendrite

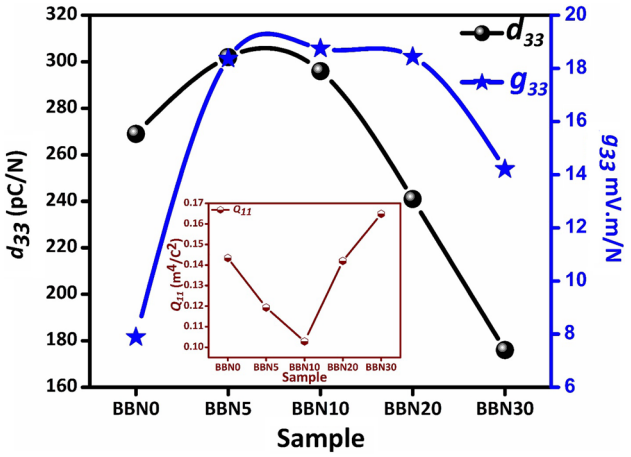


Fig. 8 Variation of piezoelectric charge coefficient (d_{33}), piezoelectric voltage constant (g_{33}) and electrostrictive constant (Q_{11}) (inset) for the $(1-x)$BSTZ–xBNO composites

3.6 Piezoelectric studies

In this study, piezoelectric response as a function of BNO content has been investigated. Figure 8 shows the variation in piezoelectric strain coefficient, piezoelectric voltage constant and electrostrictive coefficient (inset) with change in BNO content. Electrical poling conditions strongly affect the piezoelectric characteristics of any ceramic material. The domains are distributed randomly in an as-prepared material and therefore they need to be aligned in a certain direction on the application of an externally applied electric field. Typically, a high electric field is essential to attain homogeneously distributed domains, however at high electric field, the materials are prone to get damaged because of electrical breakdown. Therefore, an optimum electric field is vital to acquire superior piezoelectric properties. Moreover, poling temperature, as well as poling time, also influence the piezoelectric characteristics and therefore they are also required to be optimized. In this work, all the five cylindrical pellet specimens were poled electrically at $E \sim 18$ kV/mm for 75 min with poling temperature kept to be $T_P \sim 65$ °C, at which optimum piezoelectric characteristics were recorded. After 75 min of electrical poling, the piezoelectric charge coefficient, d_{33} did not show any significant increment and found to saturate. Further, poling a sample at an appropriate temperature results in accumulation of positive and negative charge carriers around the grain boundary interface leading to the emergence of an internal bias electric field which can increase the piezoelectric characteristics of the material. The addition of BNO results in a slight increase in piezoelectric constant for BBN5 specimen, however, it decreases with further increase in BNO concentration. It is to be worth noting that BBN10 sample still shows higher d_{33} value compared to BBN0 sample. The high value of BBN5 and BBN10 sample may be attributed to better crystallinity, high density and optimum combination of grain size and grain homogeneity in the material [19]. Another possibility for the slight increase in d_{33} value may be attributed to domain wall pinching effect with reduction in oxygen vacancy caused by BNO addition [40]. The piezoelectric voltage coefficient (g_{33}) of the five synthesized samples were measured by dividing the piezoelectric charge constant of the materials by their relative permittivity (ε). The piezoelectric constant of the material can be described by the thermodynamic theory of ferroelectricity as follows [41]:

$$d_{33} = 2\varepsilon_{33} P_r Q_{11} \quad (1)$$

where, ε_{33} represents the dielectric permittivity, P_r denotes remnant polarization and Q_{11} is the electrostrictive constant. Hence, from Eq. 1 it can be inferred that for any ceramic material with high dielectric constant and high remnant polarization may also exhibit large piezoelectric coefficient. Electrostrictive constant for the five compositions has been

evaluated using Eq. 1 and is shown in the inset of Fig. 8. An enhancement in piezoelectric properties demonstrates that BSTZ–BNO composites can prove to be a potential material for lead-free piezoelectric ceramic.

It is known that dielectric, ferroelectric and piezoelectric properties of the material are closely related to each other [42]. Further, it has also been reported that the electrical properties of the ferroelectrics are highly dependent on shape, morphology and relative density of the material [43]. Among the five synthesized materials, BBN10 has shown the optimum properties, which may solely be attributed to slightly higher relative density and comparatively homogeneous grain size of the material. So, in conclusion, the relative density of the material can be considered as the dominating mechanism among others in improving the electrical properties of the BBN10 composite. In addition, the reduction in oxygen vacancies, higher crystallinity and optimum solid solubility of BSZT and BNO may be considered as the other factors that are contributing in enhancing the electrical properties.

4 Conclusion

A new series of lead-free ceramic composite with enhanced microstructural and electrical properties were successfully synthesized. The BSTZ–BNO composites studied in this study requires lower sintering temperature for the phase formation. The co-existence of tetragonal and orthorhombic phase in the composite samples has been confirmed by Rietveld analysis. All the samples possess a polygonal grain type morphology with clearly distinguishing grain boundaries. In addition, the BSTZ–BNO composites have shown improved dielectric constant, better remnant polarization and high piezoelectric constant. These superior properties of BSTZ–BNO composites (especially BBN10) are mainly attributed to uniform grain distribution, high density of the materials and solid solubility of BNO in BSTZ up to a certain extent. At higher BNO content (BBN20 and BBN30), the dielectric constant, remnant polarization, piezoelectric constant and breakdown strength were found to decrease which indicate limited compatibility of tetragonal perovskite with orthorhombic niobate. The BSTZ–BNO composites are inexpensive and easy to fabricate. Further, the relatively homogeneous microstructure, superior electrical properties and high breakdown strength indicate that the mechano-chemical synthesis method represents a viable approach to produce such materials and can have potential application in field of ceramic capacitors.

References

1. R. Grigalaitis, M.V. Petrović, J. Bobić, A. Dzunuzovic, R. Sobiestianskas, A. Brilingas, B. Stojanović, J. Banys, Dielectric and magnetic properties of $BaTiO_3$–$NiFe_2O_4$ multiferroic composites. Ceram. Int. **40**, 6165–6170 (2014)
2. D.W. Kim, K.S. Hong, C.H. Kim, K. Char, Crystallographic orientation dependence of the dielectric constant in polymorphic $BaNb_2O_6$ thin films deposited by laser ablation. Appl. Phys. A **79**, 677–680 (2003)
3. N. Maikhuri, A.K. Panwar, A. Jha, Investigation of A-and B-site Fe substituted $BaTiO_3$ ceramics. J. Appl. Phys. **113**, 17D915 (2013)
4. J.P. Praveen, K. Kumar, A.R. James, T. Karthik, S. Asthana, D. Das, Large piezoelectric strain observed in sol–gel derived BZT–BCT ceramics. Curr. Appl. Phys. **14**, 396–402 (2014)
5. H. Zheng, F. Straub, Q. Zhan, P.L. Yang, W.K. Hsieh, F. Zavaliche, Y.H. Chu, U. Dahmen, R. Ramesh, Self-assembled growth of $BiFeO_3$–$CoFe_2O_4$ nanostructures. Adv. Mater. **18**, 2747–2752 (2006)
6. A.K. Vishwakarma, K. Jha, M. Jayasimhadri, A.S. Rao, K. Jang, B. Sivaiah, D. Haranath, Red light emitting $BaNb_2O_6$:Eu^{3+} phosphor for solid state lighting applications. J. Alloys Compd. **622**, 97–101 (2015)
7. I.-S. Cho, S.T. Bae, D.H. Kim, K.S. Hong, Effects of crystal and electronic structures of ANb_2O_6 (A=Ca, Sr, Ba) metaniobate compounds on their photocatalytic H_2 evolution from pure water. Int. J. Hydrog. Energy **35**, 12954–12960 (2010)
8. Y. Ebina, T. Higuchi, T. Hattori, T. Tsukamoto, Ferroelectric and structural properties of $Sr_{0.5}Ba_{0.5}Nb_2O_6$ thin films on $La_{0.05}Sr_{0.95}TiO_3$ substrate. Jpn. J. Appl. Phys. **45**, 7300 (2006)
9. D.W. Kim, H.B. Hong, K.S. Hong, C.K. Kim, D.J. Kim, The reversible phase transition and dielectric properties of $BaNb_2O_6$ polymorphs. Jpn. J. Appl. Phys., Part **41**, 6045–6048 (2002)
10. S.P. Gaikwad, V. Samuel, R. Pasricha, V. Ravi, Preparation of nanocrystalline ferroelectric $BaNb_2O_6$ by citrate gel method, Bull. Mater. Sci., 28 121–123 (2005)
11. M. Sahoo, Z. Yajun, J. Wang, R. Choudhary, Composition control of magnetoelectric relaxor behavior in multiferroic $BaZr_{0.4}Ti_{0.6}O_3$/$CoFe_2O_4$ composites. J. Alloys Compd. **657**, 12–20 (2016)
12. T. Takenaka, K. Maruyama, K. Sakata, $(Bi_{1/2}Na_{1/2})TiO_3$–$BaTiO_3$ system for lead-free piezoelectric ceramics. Jpn. J. Appl. Phys. **30**, 2236 (1991)
13. T. Badapanda, S. Sarangi, B. Behera, S. Parida, S. Saha, T. Sinha, R. Ranjan, P. Sahoo, Optical and dielectric study of strontium modified barium zirconium titanate ceramic prepared by high energy ball milling. J. Alloys Compd. **645**, 586–596 (2015)
14. C.C. Koch, Y. Cho, Nanocrystals by high energy ball milling. Nanostruct. Mater. **1**, 207–212 (1992)
15. L. Kong, W. Zhu, O. Tan, Preparation and characterization of $Pb(Zr_{0.52}Ti_{0.48})O_3$ ceramics from high-energy ball milling powders. Mater. Lett. **42**, 232–239 (2000)
16. Q.M. Zhang, H. Wang, N. Kim, L.E. Cross, Direct evaluation of domain-wall and intrinsic contributions to the dielectric and piezoelectric response and their temperature dependence on lead zirconate-titanate ceramics. J. Appl. Phys. **75**, 454–459 (1994)
17. G. Arlt, N.A. Pertsev, Force constant and effective mass of 90° domain walls in ferroelectric ceramics. J. Appl. Phys. **70**, 2283–2289 (1991)
18. D. Damjanovic, M. Demartin, H. Shulman, M. Testorf, N. Setter, Instabilities in the piezoelectric properties of ferroelectric ceramics. Sens. Actuators A: Phys. **53**, 353–360 (1996)
19. C.A. Randall, N. Kim, J.P. Kucera, W. Cao, T.R. Shrout, Intrinsic and extrinsic size effects in fine-grained

morphotropic-phase-boundary lead zirconate titanate ceramics. J. Am. Ceram. Soc. **81**, 677–688 (1998)
20. T.M. Kamel, G. de With, Grain size effect on the poling of soft $Pb(Zr,Ti)O_3$ ferroelectric ceramics. J. Eur. Ceram. Soc. **28**, 851–861 (2008)
21. A. Herabut, A. Safari, Processing and electromechanical properties of $(Bi_{0.5}Na_{0.5})_{(1-1.5x)}$ La_xTiO_3 ceramics. J. Am. Ceram. Soc. **80**, 2954–2958 (1997)
22. S. Sarraute, O.T. Sørensen, B.F. Sørensen, E.R. Hansen, Microstructure dependent thermophysical properties of Ni–Zn ferrite–$BaTiO_3$ functionally graded ceramics, J. Mater. Sci. **34**, 99–104 (1999)
23. A.K. Singh, T. Goel, R. Mendiratta, O. Thakur, C. Prakash, Dielectric properties of Mn-substituted Ni-Zn ferrites. J. Appl. Phys. **91**, 6626–6629 (2002)
24. A. Jain, A.K. Panwar, A.K. Jha, Influence of milling duration on microstructural, electrical, ferroelectric and piezoelectric properties of $Ba_{0.9}Sr_{0.1}Zr_{0.04}Ti_{0.96}O_3$ ceramic. Ceram. Int. **42**, 18771–18778 (2016)
25. N. Zhang, L. Li, J. Yu, High dielectric constant and good thermal stability from − 55 °C to 450 °C in $BaTiO_3$-based ceramics. Mater. Lett. **160**, 128–131 (2015)
26. X.Y. Ye, Y.M. Li, J.J. Bian, Dielectric and energy storage properties of Mn-doped $Ba_{0.3}Sr_{0.475}La_{0.12}Ce_{0.03}TiO_3$ dielectric ceramics. J. Eur. Ceram. Soc. **37**, 107–114 (2017)
27. L.H. Parker, A.F. Tasch, Ferroelectric materials for 64 Mb and 256 Mb DRAMS. IEEE Circuits Devices Mag. **6**, 17–26 (1990)
28. L. Testardi, W. Moulton, H. Mathias, H. Ng, C. Rey, Large static dielectric constant in the high-temperature phase of polycrystalline $YBa_2Cu_3O_x$. Phys. Rev. B: Condens. Matter **37**, 2324 (1988)
29. H.G. Bohn, T. Schober, Electrical conductivity of the high-temperature proton conductor $BaZr_{0.9}Y_{0.1}O_{2.95}$. J. Am. Ceram. Soc. **83**, 768–772 (2000)
30. R. Sharma, P. Pahuja, R.P. Tandon, Structural, dielectric, ferromagnetic, ferroelectric and ac conductivity studies of the $BaTiO_3$–$CoFe_{1.8}Zn_{0.2}O_4$ multiferroic particulate composites. Ceram. Int. **40**, 9027–9036 (2014)
31. S.K. Das, R.N. Mishra, B.K. Roul, Magnetic and ferroelectric properties of Ni doped $BaTiO_3$. Solid State Commun. **191**, 19–24 (2014)
32. W. Cai, C. Fu, J. Gao, H. Chen, Effects of grain size on domain structure and ferroelectric properties of barium zirconate titanate ceramics. J. Alloys Compd. **480**, 870–873 (2009)
33. M. Kuehn, H. Kliem, The method of local fields: a bridge between molecular modelling and dielectric theory. J. Electrostat. **67**, 203–208 (2009)
34. Y. Wang, C.-W. Nan, Effect of Tb doping on electric and magnetic behavior of $BiFeO_3$ thin films. J. Appl. Phys. **103**, 4103 (2008)
35. R. Muduli, R. Pattanayak, S. Raut, P. Sahu, S. V, S. Rath, P. Kumar, S. Panigrahi, R.K. Panda, Dielectric, ferroelectric and impedance spectroscopic studies in TiO_2-doped $AgNbO_3$ ceramic. J. Alloys Compd. **664**, 715–725 (2016)
36. A.L. Young, G.E. Hilmas, S.C. Zhang, R.W. Schwartz, Mechanical vs. electrical failure mechanisms in high voltage, high energy density multilayer ceramic capacitors. J. Mater. Sci. **42**, 5613–5619 (2007)
37. T. Tunkasiri, G. Rujijanagul, Dielectric strength of fine grained barium titanate ceramics. J. Mater. Sci. Lett. **15**, 1767–1769 (1996)
38. W. Lei, R. Ang, X.-C. Wang, W.-Z. Lu, Phase evolution and near-zero shrinkage in $BaAl_2Si_2O_8$ low-permittivity microwave dielectric ceramics. Mater. Res. Bull. **50**, 235–239 (2014)
39. W. Lei, Y.-Y. Yan, X.-H. Wang, W. Lu, Z.-B. Yang, W.-Z. Lu, Improving the breakdown strength of $(Mg_{0.9}Zn_{0.1})_2(Ti_{1-x}Mn_x)O_4$ ceramics with low dielectric loss. Ceram. Int. **41**, 521–525 (2015)
40. Y. Tian, S. Li, Y. Gong, D. Meng, J. Wang, Q. Jing, Effects of Er^{3+}–doping on dielectric and piezoelectric properties of $0.5Ba_{0.9}Ca_{0.1}TiO_3$–$0.5BaTi_{0.88}Zr_{0.12}O_3$–0.12%La–xEr lead–free ceramics. J. Alloys Compd. **692**, 797–804 (2017)
41. J.P. Praveen, T. Karthik, A. James, E. Chandrakala, S. Asthana, D. Das, Effect of poling process on piezoelectric properties of sol–gel derived BZT–BCT ceramics. J. Eur. Ceram. Soc. **35**, 1785–1798 (2015)
42. B. Jaffe, *Piezoelectric Ceramics*, (Elsevier, New York, 2012)
43. C. Duran, S. Trolier-McKinstry, G.L. Messing, Fabrication and electrical properties of textured $Sr_{0.53}Ba_{0.47}Nb_2O_6$ ceramics by templated grain growth. J. Am. Ceram. Soc. **83**, 2203–2213 (2000)

Slow Light Generation in Decagonal Liquid Core Photonic Crystal Fiber

Rahul Kumar[1], Pooja Chauhan[2], Ajeet Kumar[1]*

Advanced Photonics Simulation Research Lab., Department of Applied Physics Delhi Technological University, Delhi-110 042, India
ajeetdph@gmail.com

Abstract: Liquid Core Photonic Crystal Fiber has been designed using carbon-disulphide as core material and silica as cladding material. Confinement loss has been plotted and a time delay of 166.70ns is calculated for maximum power of 102 mW at 1.55µm.
OCIS codes: (060.4370) Nonlinear optics, fibers; (190.5890) Scattering, stimulated; (290.5900) Scattering, stimulated Brillouin.

Introduction:

When light propagation speed is reduced in a medium, the light is termed as Slow light [1]. Many techniques can be used such as stimulated Brillouin scattering [2], stimulated Raman scattering [3], coherent population oscillation [4] and electromagnetically induced transparency [5]. SBS is favored over other methods.

In this paper, a decagonal-shaped liquid core PCF has been designed as shown in Fig 1. The modelling has been done using COMSOL Multiphysics Software.

Design of PCF:

A decagonal liquid core photonic crystal fiber has been designed with pitch at 4 µm and diameter of air holes is varied from 1 µm to 1.8 µm as shown in Fig 1. Perfectly matched layer (PML) of thickness 2 µm is used. The electric field distribution of PCF is shown in Fig 2. The carbon-disulphide parameters used for simulation are [6]: fiber material loss, α = 0.3 dB/m; the Brillouin gain coefficient, g_B = 1.5 × 10-9 m⁄W; Brillouin gain bandwidth, $\Delta\nu_B$ = 23 MHz; Refractive index, n= 1.595.

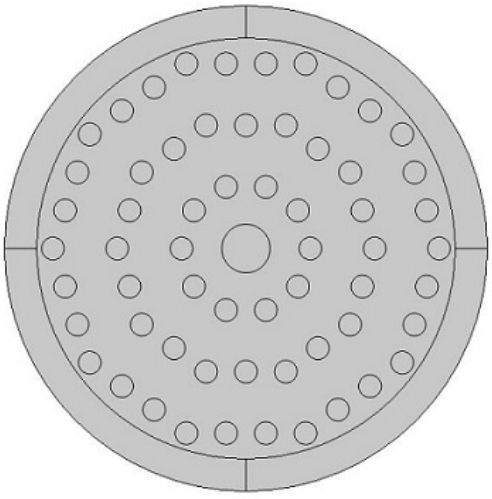


Fig 1: Cross-section of Decagonal Structure

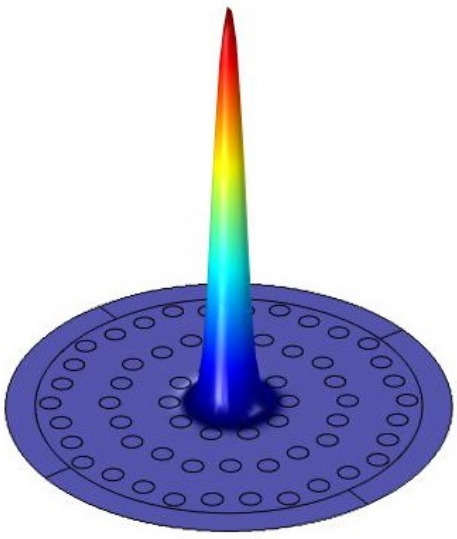


Fig 2: Electric field distribution at 1.55µm

Simulated results:

Fig 3 shows the confinement loss variation with d/Λ. The confinement loss has been calculated at d/Λ = 0.35 and is found to be 0.75 * 10^{-6} dB/m. Fig 4 shows the time delay variation with d/Λ. We have calculated time delay variation for input pump power from 2 mW to 102 mW and is found to be 166.70 ns. The different parameters of proposed PCF like maximum pump power, minimum pump power and effective mode area have been analysed.

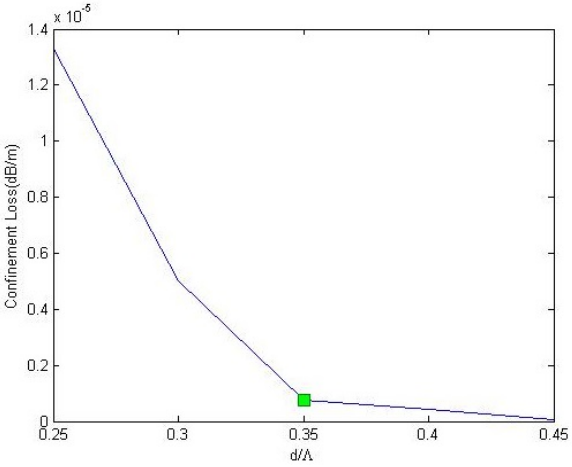


Fig 3: Variation of Confinement loss with d/Λ

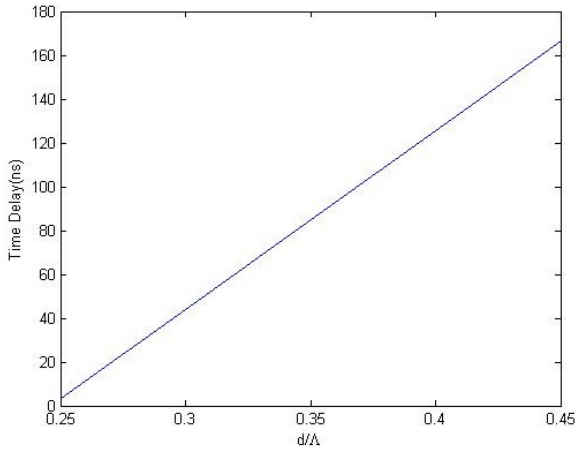


Fig 4: Variation of Time delay with d/Λ

Conclusion:

The proposed PCF has been successfully designed and analysed. Maximum time delay of 166.70 ns is obtained for 1m long liquid core fiber for the pump power of 102 mW. The simulated results show that proposed PCF has been successfully designed with tunable features.

References:

[1] Shuzhen Dang, Jing Shu, "Study and analysis on slow light in photonic crystal waveguide", Proc. SPIE 10256, Second International Conference on Photonics and Optical Engineering, 102565X (28 February 2017).

[2] Y. Okawachi, M. S. Bigelow, J. E. Sharping, Z. Zhu, A. Schweinsberg, D. J. Gauthier, R. W. Boyd, and A. L. Gaeta, "Tunable all-optical delays via Brillouin slow light in an optical fiber," Phys. Rev. Lett.94, 1–4 (2005).

[3] J. Sharping, Y. Okawachi, and A. Gaeta, "Wide bandwidth slow light using a Raman fiber amplifier," Opt. Express 13, 6092–6098 (2005).

[4] NS.-W. Chang, P. Kondratko, H. Su, and S. L. Chuang, "Slow light based on coherent population oscillation in quantum dots at room temperature," IEEE J. Quantum Electron. 43, 196–205 (2007).

[5] LJ. Zhang, G. Hernandez, and Y. Zhu, "Slow light with cavity electromagnetically induced transparency," Opt. Lett. 33, 46–48 (2008).

[6] KMonfared, Yashar & A. Ponomarenko, Sergey "Slow light generation via stimulated Brillouin scattering in liquid-filled photonic crystal fibers," Optik - International Journal for Light and Electron Optics. 127. 10.1016/j.ijleo.2016.04.017(2016).

14.139.251.107 {ts'2018-09-16 01:21:06'}

Structure, magnetism and electrical transport in epitaxial $La_{0.23}Pr_{0.41}Ca_{0.36}MnO_3$ thin films: Consequences of film thickness

Sandeep Singh, P. K. Tyagi, and H. K. Singh

Citation: AIP Advances **8**, 095002 (2018); doi: 10.1063/1.5026543
View online: https://doi.org/10.1063/1.5026543
View Table of Contents: http://aip.scitation.org/toc/adv/8/9
Published by the American Institute of Physics

Articles you may be interested in

Constitutive behaviour and life evaluation of solder joint under the multi-field loadings
AIP Advances **8**, 085001 (2018); 10.1063/1.5044446

Ferromagnetic resonance in coupled magnetic nanostructured arrays
AIP Advances **8**, 085002 (2018); 10.1063/1.5038093

Atomic-scale structure and chemistry of YIG/GGG
AIP Advances **8**, 085117 (2018); 10.1063/1.5018795

High performance top gate a-IGZO TFT utilizing siloxane hybrid material as a gate insulator
AIP Advances **8**, 095001 (2018); 10.1063/1.5027276

Synthesis of β-$FeSi_2$ nanowires by using silicon nanowire templates
AIP Advances **8**, 085324 (2018); 10.1063/1.5041024

A modified model for simulating the effect of temperature on ultrasonic attenuation in 7050 aluminum alloy
AIP Advances **8**, 085003 (2018); 10.1063/1.5045627



Structure, magnetism and electrical transport in epitaxial $La_{0.23}Pr_{0.41}Ca_{0.36}MnO_3$ thin films: Consequences of film thickness

Sandeep Singh,[1,2] P. K. Tyagi,[2,a] and H. K. Singh[1,b]
[1]*CSIR-National Physical Laboratory, Dr. K. S. Krishnan Marg, New Delhi 110012, India*
[2]*Department of Applied Physics, Delhi Technological University, Delhi 110042, India*

(Received 21 February 2018; accepted 7 May 2018; published online 4 September 2018)

A systematic study of the consequences of in-plane tensile strain on the correlation between structure/microstructure and magneto-electrical properties of $La_{0.23}Pr_{0.41}Ca_{0.36}MnO_3/SrTiO_3$ (001) thin films is performed. At lower film thickness ($d \leq 27$ nm) the dominant tensile strain supports layered morphology. At d=41 nm structural/microstructural crossover takes place and at $d \geq 41$ nm relaxation induced tilt and dilations of the lattice generate defects like dislocations, which in turn transforms the layer by layer growth into disordered brick type morphology. It appears that the relaxation even at higher thickness (~81 nm) is partial only and the strain may have a self-sustained nature. The domination of the tensile strain suppresses the ferromagnetic-metallic phase due to the possible electronic reconstruction which could give rise to a magnetically disordered insulator 'dead' layer and a sizeable non-magnetic insulator state at $d \leq 27$ nm. In this thickness regime the possible selective orbital stabilization could also contribute to carrier localization. At $d \geq 41$ nm the severity of the impact of the interfacial electronic reconstruction is reduced with concomitant relaxation of the tensile strain which favors carrier delocalization and yields well defined metallic-ferromagnetic phase transitions. The hysteretic nature of the phase transitions reflects the thermal cycle dependent nature of the metallic-ferromagnetic and insulating antiferromagnetic phases in this strongly phase separated material. © *2018 Author(s). All article content, except where otherwise noted, is licensed under a Creative Commons Attribution (CC BY) license (http://creativecommons.org/licenses/by/4.0/).* https://doi.org/10.1063/1.5026543

INTRODUCTION

The generic perovskite manganese oxides $RE_{1-x}AE_xMnO_3$ (RE being a trivalent rare earth ion and AE a divalent one, commonly an alkaline earth) are metallic and ferromagnetic over a certain range of x-values, which is dependent on the average size of the RE/AE site cations and hence the tolerance factor.[1–4] The major electronic properties of these compounds are controlled by the 3d orbitals and the simultaneous ferromagnetic and metallic behaviors are explained to a certain extent by the double-exchange (DE) mechanism proposed by Zener, wherein it was considered that the interatomic Hund rule exchange was strong and carriers do not change their spin orientation while hoping from one ion to next. The carriers can only hop if the spins of the two ions are parallel. It was also found through energy minimization that ferromagnetic interactions are favored when magnetic atoms are well separated and conduction electrons are present. This theory as applied to perovskite manganites which explains the strong correlation between ferromagnetism and conductivity.[1–6] The ferromagnetic transition temperature (T_C) in the DE mechanism, scales as[7]

$$T_C \sim J \sim t_{dp}^2 \sim S_{dp}^2$$

[a]Email pawankumartyagi@gmail.com
[b]hks65@nplindia.org (Dr. H. K. Singh)

 © Author(s) 2018

Where J is the effective exchange parameter between the adjacent Mn ions, t_{dp} is the Mn_d-O_{2p} transfer integral and S_{dp} is the overlap between the Mn_d and O_{2p}. In such materials the modification of the geometrical surroundings of the Mn e_g orbitals, e.g., $d_{3z^2-r^2}$ and the $d_{x^2-y^2}$ orbitals, offers an extrinsic degree of freedom for physical property tailoring. The manganese e_g shell is doubly degenerate in a regular octahedral surrounding and is only partly occupied. The Mn^{3+} ions are thus Jahn-Teller (JT)[8] active, and small distortions of the oxygen octahedra can shift the relative stability of the two e_g orbitals. A desirous choice between the $d_{3z^2-r^2}$ and the $d_{x^2-y^2}$ orbitals for occupancy could be possible if the Mn ions are subjected to suitable geometric constraints. If $d_{3z^2-r^2}$ is occupied, the DE will take place essentially along the out of plane direction, while the occupation of the $d_{x^2-y^2}$ orbitals strengthens the intralayer DE with concomitant weakening of the interlayer interaction.

In thin films the substrate induced strain modifies the octahedral geometry and therefore is potentially an important extrinsic degree of freedom (in addition the intrinsic ones like lattice, spin, charge degrees of freedom) and has been invoked to tune the physical properties of manganites.[9,10] Specifically, a tensile strain causes in-plane stretching of the MnO_6 octahedra in the in-plane direction, which in turn enhances the JT distortion and thus favors the antiferromagnetic (AFM) ordering and the charge ordered insulator (COI) states. An in-plane compression of the MnO_6 octahedra by the compressive strain weakens the JT distortion and favors the ferromagnetic (FM) – double exchange (DE).[8–12] The elastic energy released during relaxation of the strain is dissipated through the formation of defects. These defects which comprise mostly of dislocations and stacking faults disrupt the cooperative nature of the JT distortion network. Tensile strain induced in-plane stretching of the MnO_6 octahedra increases in the in-plane Mn-O bond length and therefore it makes occupation of the dx^2-y^2 orbital energetically favorable.[12] In-plane compression of the MnO_6 stabilizes the out-of-plane $d3z^2$-r^2 orbital. The above orbital selectivity caused by in-plane compressive and tensile strains has been seen in x-ray absorption[13] as well as in angle resolved photoemission[14] experiments. The volume conserving tensile strain causes higher occupancy of the in-plane dx^2-y^2 orbital, a larger out-of-plane hopping and smaller in-plane hopping compared to the unstrained values. Thus in-plane tensile strain stabilizes insulators that can have either FM or AFM spin textures.[12]

In low bandwidth manganites, which exhibit intrinsic tilting/twisting of the MnO_6 octahedra due to smaller average RE/AE site cationic size and have much stronger JT distortion, the role of strain could be more intricate and hence can have novel experimental implications. A prototypical low bandwidth compound which shows very prominent multiorder electronic coupling and therefore has been investigated extensively is $La_{1-x-y}Pr_yCa_xMnO_3$. In such compounds which exhibit nearly isoenergetic existence of multiple electronic phases (like FM and AFM/COI) even the subtle changes in the substrate induced strain (and hence also the variation in the film thickness) can also modify the electronic phase profile and associated phase transitions.[11,15–24] In addition to the phase transitions, the strain could also impact the non-equilibrium states like the magnetic liquid and the strain glass (SRG).[24] Although several studies have reported the impact of substrate induced strain in $La_{1-x-y}Pr_yCa_xMnO_3$ at different values of the composition x,[14,18–27] investigations embodying a wide range of film thickness sufficient to provide a high strain and strain relaxed states are lacking. Jeon et al.[19] have studied the impact of the film thickness in $La_{0.35}Pr_{0.35}Ca_{0.30}MnO_3$ in which the composition is far away from the one conducive to the delicate balance between AFM/COI and FMM. A more recent study by V. Agarwal et al.[24] demonstrated that in single crystalline $La_{1-x-y}Pr_yCa_xMnO_3$ (x∼0.42, y∼0.40) thin films on $LaAlO_3$ (001) substrates having thickness in the range 20–140 nm, the multiple magnetic phase transitions, insulator–metal transition (IMT), the supercooling characteristics of the dynamical magnetic liquid and the nature of the glassy state are all sensitive to the compressive strain and its relaxation.[24] The same work also shows that at lower film thickness there is significant depression in the magnetization, possibly due to the formation of a dead layer. However, the impact of in-plane tensile strain in the prototypical strongly phase separated manganite La1-x-yPryCaxMnO3 has not been studied in a systematic way. In the present study we have selected a composition in which the electronic phase balance is tilted slightly in favor of the FM metal (the bandwidth in the present study is between those investigated in references 19 and 24). Such a selection gives a possibility of the occurrence of FM-metallic behavior even at sufficiently small film thickness where the tensile strain is very large. It appears quite pertinent to mention here that at very small film thickness such

thin films generally show strong insulator behavior. In the present study we have investigated films having different thicknesses in the range 13 - 81 nm.

EXPERIMENTAL DETAILS

In the present case the nominal composition of the target is $La_{0.22}Pr_{0.40}Ca_{0.38}MnO_3$. During all the sputtering depositions the same experimental parameters were employed. The temperature of the (001) oriented STO substrates (three substrates at a time for comparison) of dimension LxWxt=5x3x0.5 mm^3 were maintained at ≈870 °C. The distance between the target and the substrate was fixed at ≈5 cm. The base pressure achieved was $3x10^{-5}$ torr and the dynamic pressure during sputtering was maintained at 200 ± 10 mtorr of Ar~80 % and O_2~20 %. To prepare films of different thickness the depositions were done for ~5, ~10, ~15 and 30 minutes. Post deposition *in-situ* annealing at ~900 °C and ~ 1 atmosphere O_2 for about 4 hrs was done to achieve the optimum oxygen stoichiometry. The magnetization measurements employ the same protocol as in Refs. 22–24. The self-field (in absence of external magnetic field) transport was measured by the standard four contact technique with the Keithley delta mode setup and the temperature of the 6-400 K closed cycle refrigerator was controlled by the lakeshore 332S cryogenic temperature controller at 2K/minute during cooling/warming.

RESULTS AND DISCUSSION

Chemical composition, thickness, and structure

The energy dispersive X-ray spectra recorded from several places on the films were used to evaluate the chemical composition of the film. The average chemical composition is found to be $La_{0.23}P_{0.41}Ca_{0.36}MnO_3$. We did not observe any noticeable spatial variation in the chemical composition of each of the films. The chemical composition of the films did not show any noticeable dependence on the film thickness. In fact films on all the three substrates grown together also have the same chemical composition. However, the slight difference in the chemical stoichiometry of the target and the thin films shows the inexact stoichiometry transfer in the RF magnetron sputtering process employed in the present growth process.

The film thickness is estimated from the XRR data of 10 minute RF sputtered films. The XRR data of the 10 minute sputter deposited thin film is plotted in Fig. 1. The film thickness (d) was calculated from the separation of the Keissig fringes (Fig. 1) employing the formula: $d=\lambda/2(1/\theta_{m+1} - 1//\theta_m)$; where λ (=1.5406 Å) is the wavelength of the Cu-Kα X-ray employed and θ_m is the angle of incidence of the m^{th} Keissig fringe. The thickness of the 10 minute sputtered film is found

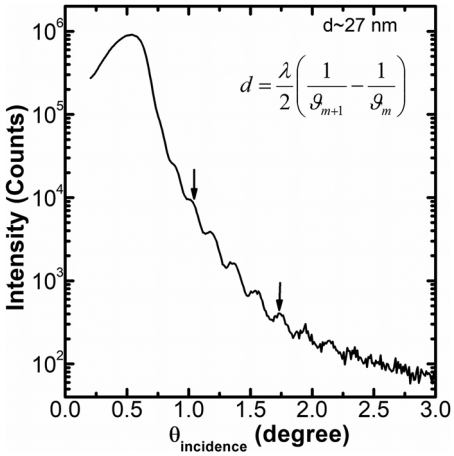


FIG. 1. X-ray reflectivity plot of 10 minute sputtered deposited $La_{0.23}P_{0.41}Ca_{0.36}MnO_3$ (LPCMO) thin film on (001)-STO substrate. The inset shows the expression used to calculate the thickness of the film.

to be d ≈27 nm. This yields an average growth rate of ≈ 2.7 nm per minute. From this data thickness of the 15 and 30 minute sputtered films is found to be ≈ 41 nm and 81 nm, respectively.

The bulk target used for sputtering has orthorhombic structure with lattice constants a=5.429 Å, b=7.667 Å and c=5.439 Å. The average in-plane lattice parameter, $a_B = 1/2(a/\sqrt{2} + c/2) = 3.836$ Å and the out-of-plane lattice constant is a_{CB}=3.846 Å. The (100)-STO has the cubic lattice constant a_{CS} = 3.905 Å. Hence the induced strain is tensile in nature. The strain is calculated using $\varepsilon=(a_S - a_B)^*100/a_S = 1.77$ %. The 2θ/ω scan of all the films are plotted in Fig. 2. All the films show almost identical diffraction patterns with the only visible difference being the shift of the materials peaks towards the substrate with increase in the film thickness. This indicates relaxation of the tensile strain at higher film thickness. The observed 2θ values are used to calculate the out-of-plane lattice constants (a_c) of all the films. The thinnest film (13 nm) has a_c=0.3791 ± 0.0002 nm, which is much smaller than the out-of-plane lattice constant of the target (a_{CB} = 0.3846 nm). This marks the presence of large in-plane tensile strain. Given the tensile nature of the in-plane strain, the MnO_6 octahedron stretches along the plane (a-b plane) of the substrate and compress along the normal 'c' direction. This behavior strengthens the JT distortion, and hence the AFM and CO insulator phases are favored. With an increase in the film thickness, the out-of-plane lattice constant shows an abrupt rise as the thickness increases from 27 nm to 41 nm (Fig. 3). Interestingly, except the point corresponding to d_{film} = 41 nm, all the points connect linearly. It is demonstrated that the compression along the 'c' direction (caused by an in-plane tensile strain) (i) makes the $d_{x^2-y^2}$ orbitals energetically favorable, (ii) a larger (smaller) out-of-plane (in-plane) hopping compared to the unstrained values, (iii) stabilizes the insulating state which may either have FM or AFM spin flavor.[12–14,25,26]

Since the subtle energetic difference between the coexisting FMM and AFMI/COI phases, sizeable tensile strain (as in the case of 13 nm and 27 nm thin films) could lead to a robust insulating state and hence can have dramatic effect on the magnetic and transport properties of the film. The elongation of the out-of-plane lattice constant with increase in the film thickness is due to the relaxation of the manganite lattice. As the thickness increases the clamping effect of the substrate which ideally remains fully effective only for the initial few layers of the film, eases up. The trend in the a_C - d_{film} dependence (Fig. 3) suggests a linear relaxation of the in-plane tensile strain up to 27 nm. The sudden decrease in a_c beyond 27 nm shows the presence of some curious relaxation process or morphological changes above this thickness. At 81 nm thickness the OP lattice constant is a_C=0.3816 ± 0.0002 nm, which is still appreciably smaller than that of the corresponding bulk. This confirms that the substantial strain present at higher thickness may become self-sustained and hence survive at higher film thicknesses.

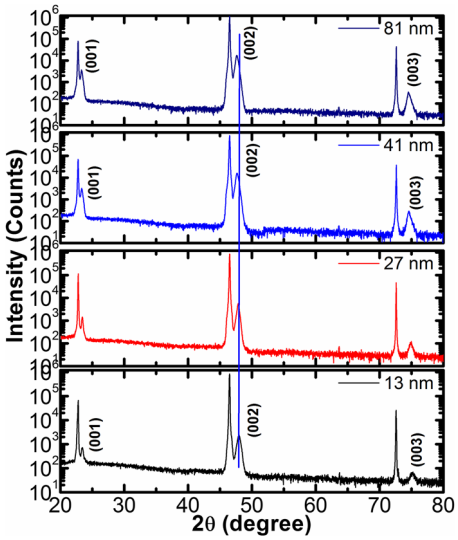


FIG. 2. 2θ/ω plot of 13 nm, 27 nm, 41 nm and 81 nm thin films on (001)-STO substrate. The film peaks are indexed. The higher intensity peaks belong to the substrate.

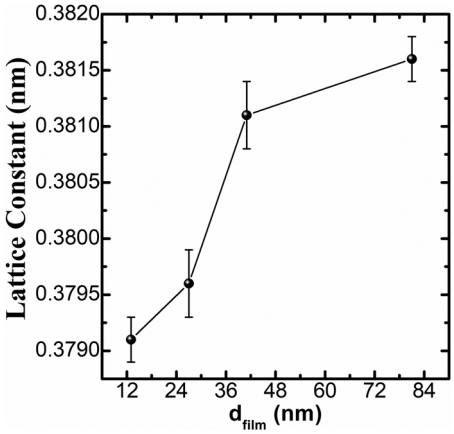


FIG. 3. Variation of the out-of-plane lattice constant as a function of the film thickness.

The rocking curves (RCs) of differently thick films (Fig. 4) shows that the crystalline nature and in-plane mosaic structure of the films are coupled to the film thickness. The full width at half maximum (FWHM, denoted hereafter by δω) of the RCs were obtained from the Lorentzian fit to the experimental data. The RC of thinnest film (~13 nm) has δω = 0.277° ± 0.002°. The FWHM then decreases to δω = 0.199° ± 0.001° when the thickness increases to 27 nm. As the film thickness is increase further, the RC again shows broadening and at d = 81 nm, it shows δω=0.269° ± 0.003°. The broadening of RC is influenced by several factors such as (a) strain due to the lattice mismatch between the substrate and the material, (b) a mosaic spread, and (c) variation in the tilt and dilations in crystal due to the presence of dislocations. Since the present measurements were carried out in the triple axis geometry, therefore the contributions of the mosaic spread and that of the strain can be separated.[27] The FWHM of the all the films was carried out at varying beam widths from 1/16° to 1/4°. The 13 nm film did not show any significant change in the FWHM as a function of the beam width. This suggests that in the 13 nm film the profile broadening is mainly to the strain, which in

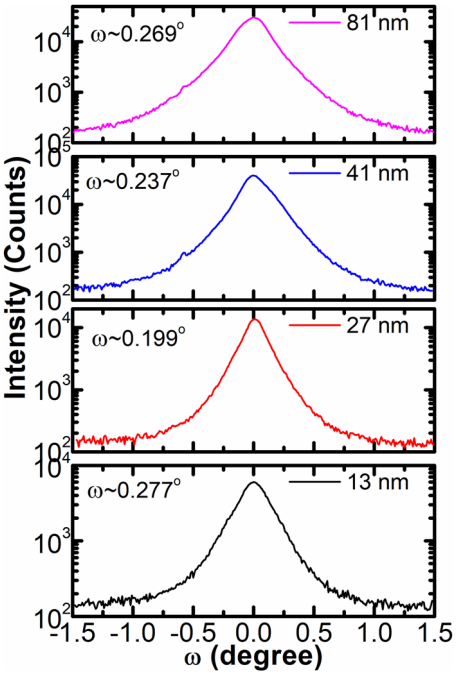


FIG. 4. Rocking curve (ω-scan) plot of the (002) diffraction peak of 13nm, 27nm, 41nm and 81nm thick film.

this case is due to the lattice mismatch. The FWHM of 27 nm film also follows the same trend as a function of the beam width. Hence as the strain is reduced the FWHM also decreases significantly. Strain further relaxes as the film thickness is increased and in view of this the FWHM of 41 and 81 nm thick films should decrease to further lower values. But the contrary happens and the FWHM increases as the film thickness is increased to 81 nm. This clearly shows that the contribution to the mosaic profile broadening in higher thickness films is due to the mosaic spread caused by the dislocation induced tilt and dilations of the lattice. Since the cooperativeness of the JT distortion, which favors the AFM ordering, is disrupted by the presence of lattice defects such as dislocations, the thicker films are expected to have higher FMM phase fraction.

The surface morphology of the films was probed by atomic force microscopy. The surface of the 13 nm film shows two distinct kinds of growth features, viz., the terrace like growth and above it small nano-sized platelets spread all over the surface. The presence of holes/vacancies in the under grown terraces suggests that the nano platelets could have come out of them due to lattice and thermal strain during the in-situ annealing. The average surface roughness in this case is 0.388 nm, which is just equal to an unit cell. This shows despite the presence of nano platelets the surface quality of the 13 nm thin film is very good and that bottom layers are epitaxially grown. Almost similar surface features are also observed in the case of 27 nm film except that the surface roughness increases slightly to ~0.42 nm. The surface of the 41 nm film shows weakening of the terrace like features with a simultaneous increase in the nano platelets surface density. As the strain relaxes rather abruptly at this film thickness, we believe that changes in the surface topography are also due to the elastic energy dissipated during strain relaxation. The surface roughness in the case increases appreciably to ~0.766 nm, which almost two unit cells. Thus at 41 nm the epitaxial nature appears to be under stress and is prone to reorganization at further higher film thickness. The surface of the 81 nm film is found to consist of uniformly distributed platelet like features. The surface roughness in this case is 0.946 nm, which is almost equal to three unit cells. This shows the transition from the epitaxial to disordered brick type single crystalline surface phase. Representative topographs of 13 and 81 nm thick films are shown in Fig. 5.

Self-field electrical transport

The self-field electrical transport of all the $La_{0.23}P_{0.41}Ca_{0.36}MnO_3$ films was analyzed through temperature dependent resistivity (ρ-T) (Fig. 6) scaling. The data was acquired at rate of 2K/minute in cooling as well as warming cycles. The 13 nm and 27 nm thin films showed behaviors characteristic of a good insulator so much so that the resistivity became immeasurable in the lower temperature range. Among these two the 27 nm film has a lower resistivity and the cooling and warming cycle ρ-T of both the films shows complete reversibility over the measured temperature range. We would like to mention that in our earlier study on $La_{0.18}P_{0.40}Ca_{0.42}MnO_3$ thin films we have found similar trend even in compressively strain thin films on $LaAlO_3$ substrates.[24] The ρ(T) of 41 nm film

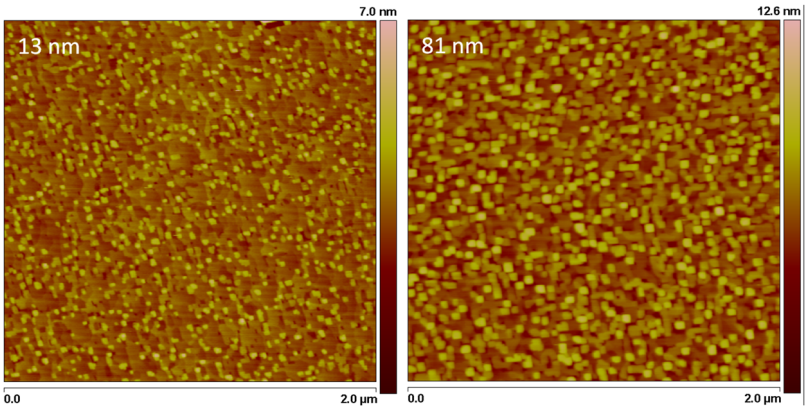


FIG. 5. Tapping mode representative atomic force microscope images of the LPCMO thin film (13 nm and 81 nm) on STO substrate.

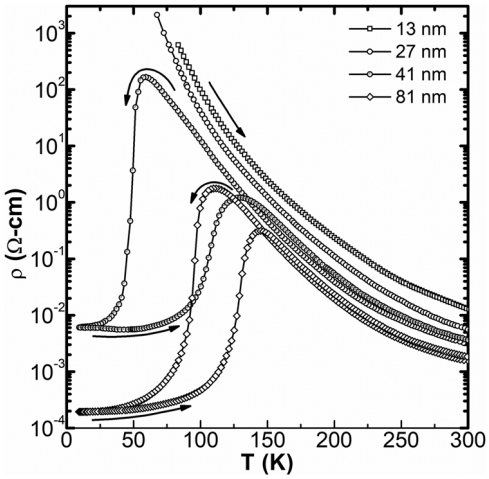


FIG. 6. Self-field resistivity of the LPCMO thin films of varying thickness measured as a function of temperature (ρ (T) curves).

increases from ~$3x10^{-3}$ Ohm-cm at room temperature to ~165 Ohm-cm at ~59 K and then sharp IMT is observed at T_{IM}^{C}=59.3 K. The resistivity drops by more than four orders of magnitude within a very short temperature span below T_{IM}^{C}. During the warming after the initial reversibility, the ρ-T curve shows a minimum at T_m=42.8 K and then increase showing an IMT at T_{IM}^{C}=131.8 K. At higher temperatures it follows temperature dependence of the cooling cycle ρ-T curve. The 81 nm film, after the initial insulating behaviour, which is much weaker as compared that observed in the thinner films, undergoes an IMT at T_{IM}^{C}=111.7 K. The drop in the ρ-T just below the IMT is less sharp (by three orders of magnitude within 15 K range). During the warming cycle a very weak resistivity minimum is seen at T_m=12 K and IMT appears at T_{IM}^{W}= 144.5 K. The above results clearly show that these in-situ annealing thin films do not show any IMT up to a thickness of d=27 nm. As the film thickness increases to 41 nm IMT appears and the cooling and warming cycle ρ-T shows colossal thermal hysteresis where the two IMTs differ by 72.5 K. As the thickness rises to 81 K, the IMTs scale up to higher temperatures with a concomitant narrowing of the thermal hysteresis.

To gain more insight into the nature of electrical transport, we analysed the ρ-T data in terms of the Emin-Holstein small polaron hopping model in the adiabatic limit generally given by[28,29]

$$\rho(T) = ATe^{E_a/k_bT} \quad \& \quad A = \frac{2k_b}{3ne^2a^2\nu}$$

Here, 'n' is the polaron concentration, 'a' is the site-to-site hopping distance, 'ν' is the attempt frequency, and k_b is the Boltzmann constant. The activation energy, E_a is the height of the potential barrier, and related to the overlap integral 't' through the relation $E_a=E_P/2-t$. In general, the overlap integral is so small that it could be neglected and then, $E_a=E_P/2$, or the polaron binding energy $E_P=2E_a$. In all the cases we have used the warming cycle data for fitting with the above equation. The data of the 13 and 27 nm thick films was well fitted from room temperature down to ~180 K (at this temperature the AFM transition generally takes place), while the fitting was good till ~160 K in case of the 41 and 81 nm thick films. From the fitting parameter (the slope $\frac{E_a}{k_b}$ of the $\ln\left(\frac{\rho}{T}\right) = \ln(A) + \left(\frac{E_a}{k_b}\right)\frac{1}{T}$) we calculated the E_a and its dependence on thickness is plotted in Fig. 7. The value of the activation energy is found to be 170.30±0.52 meV, 175.56±0.61 meV, 161.75±0.35 meV and 158.30±0.61 meV, respectively for 13, 27, 41 and 81 nm films (Fig. 7). These values show that a decrease in the carrier localization is one of the factors responsible for the appearance of IMT is films having thickness d ≥ 41 nm. These values are much larger than those reported in case of the large BW manganites like $La_{1-x}Sr_xMnO_3$.[29] However, these values are comparable to those observed in case of other low BW manganites like $Sm_{1-x}Sr_xMnO_3$[30] and close to the values reported for nearly similar $La_{1-x-y}Pr_yCa_xMnO_3$ thin films.[31]

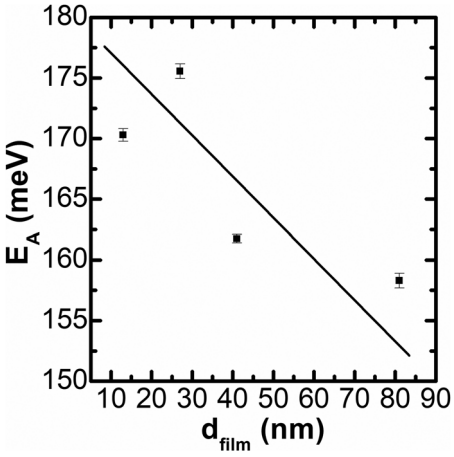


FIG. 7. Variation of the small polaron activation energy (E_A) as a function of the film thickness (d_{film}).

Here we would like to add that the low temperature electrical resistivity of manganites is generally described in terms of the two major scattering contributions, viz., (i) the electron–electron (e–e) scattering which yields a temperature dependence of the type $\rho_{ee} \propto T^2$ and (ii) the electron–phonon (e–ph) scattering having the form $\rho_{eph} \propto T^5$ [Ref. 32, related references therein]. In addition the contributions of the two magnon process ($\rho_{mag} \propto T^{4.5}$) and small polaron ($\rho_{spol} \propto \sinh^2(\hbar\omega_s/2k_BT)$) to the low temperature resistivity has also been demonstrated.[33,34] However, as shown by Agarwal et al.,[32] in the case of strongly phase separated manganites like $La_{1-x-y}Pr_yCa_xMnO_3$ thin films, the major contribution to the low temperature resistivity is from the e–e scattering. Depending on the degree of phase separation the additional contribution from e–ph scattering and disorder-enhanced strong Coulomb interaction between the carriers ($\rho_c \propto T^{0.5}$) is also present. In the present case, only the 41 nm and 81 nm thin films show IMT. The cooling cycle low temperature resistivity data of both the films is well described by the $\rho_{ee} \propto T^2$ and $\rho_{eph} \propto T^5$ contributions (data not plotted). The warming cycle data of the 41 nm film is fitted with the two major contributions $\rho_c \propto T^{0.5}$ and $\rho_{ee} \propto T^2$, while the resistivity of the 81 nm film contributions from the e–e and e–ph scatterings. A more detailed study of the low temperature resistivity in all the films (at different magnetic fields) could be a useful separate study.

Magnetic properties

Since the insulator-metal transition in manganites is simultaneous to the ferromagnetic transition, therefore in order to unravel the magnetic phase profile of the films we measured temperature and magnetic field dependent magnetization (M-T and M-H). The M-T was measured employing the zero filed cooled (ZFC), field cooled cooling (FCC), and field cooled warming (FCW) protocols. M-H was measured after zero-field cooling of the film to the desired temperature (10 K). The final magnetization data was obtained after the subtraction of the substrate contribution. The M-T data is plotted in Fig. 8 shows some interesting features. In case of the thinnest (13 nm) film the magnetization is very small and very noisy throughout the measured temperature range. Despite the small magnetic moment the FCC and FCW curves show FM transition like signature at $T_C \approx 140$ K and the ZFC shows a down turn at $T_P \approx 70$ K. The magnetization at 10 K is found to be ≈8 emu/cm^3. This is much smaller than that recently reported for a ∼20 nm thick compressively strained $La_{0.18}Pr_{0.40}Ca_{0.42}MnO_3$ thin film on $LaAlO_3$ substrate.[24] One of the factors, apart from the higher film thickness, that could cause difference in the magnetization of the two set of films could also be the difference in the nature of the substrate induced strain. The compressive nature of the strain in the $LaAlO_3$ thin films favors the FMM. The small and noisy magnetization could be understood in terms of the magnetic dead layer that forms at the various interfaces of the film. As the film thickness increases to 27 nm, the FCW magnetization substantially and 10 K it is ≈35 emu/cm^3. The increase in magnetization is accompanied by a much better defined FM transition. The temperature at which the M-T curve starts rising can be taken as the

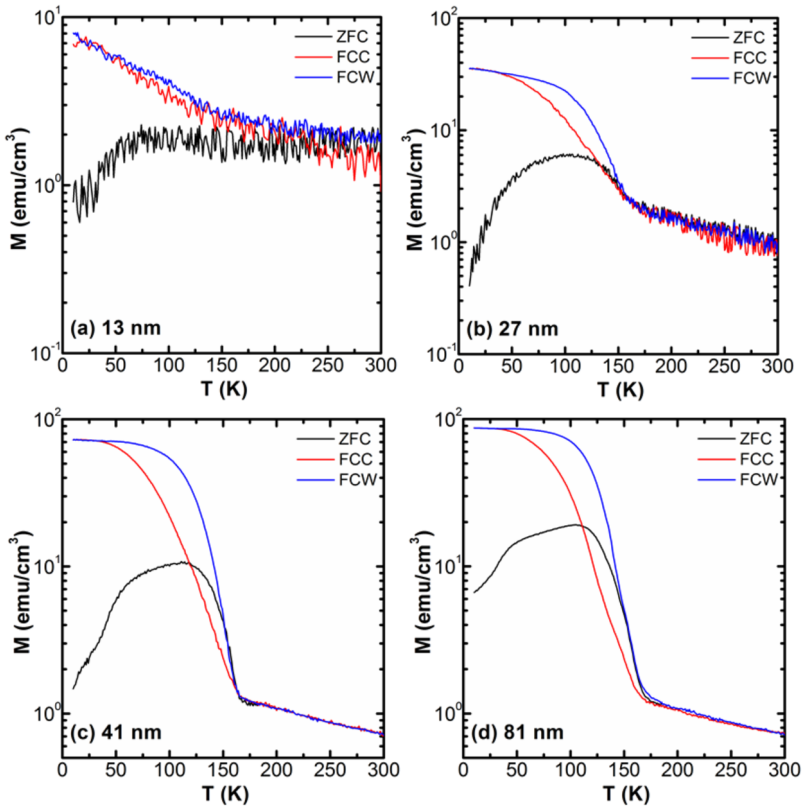


FIG. 8. ZFC, FCC, and FCW magnetization (M-T) of LPCMO thin films measured at H=100 Oe applied parallel to the film surface along the longer dimension.

FM transition temperature (T_C). For this film $T_C \approx 158$ K. The magnetization continues to increase with film thickness with a simultaneous sharpening of the FM transition. However, the T_C remains almost constant at ≈160 K for the thicker 41 nm and 81 nm films. The increase in the magnetic moment at higher film thickness is due to the (i) reduced impact of the interfacial electronic reconstruction that forms the dead layer, (ii) relaxation of the substrate induced tensile strain which favors carrier delocalization.

In addition to the increase in magnetization following features are observed in all the films having thickness d≥27 nm: (i) the FCC and FCW curves show hysteresis which widens with increase in the film thickness, (ii) the ZFC and FCW curves show huge divergence that begins just below the T_C. The diverging ZFC-FCW nature differs from that observed in case of canonical spin glass systems but is a common signature of the spin cluster glass.[35] This kind of cluster glass is common to large bandwidth manganite with low hole doping,[36] half doped medium bandwidth or low bandwidth manganites[37] or over a wide range of divalent doping (x) in low bandwidth manganites[30,38] and originates due to the coexistence of FMM and AFM/COI phases below the Neel temperature. The FCC-FCW hysteresis at $T<T_C$ is manifestation of the existence of a magnetic liquid phase consequent to the strong intrinsic electronic phase separation.[15–24]

The M-H loops measured at T=10 K are plotted in Fig. 9. The thinnest film (13 nm) does not show any saturation like behavior and possesses the lowest magnetic moment. In rest of the films saturation is observed as H approaches ~20 kOe. The remanence (M_r) also increases with increasing film thickness (inset of Fig. 9). This behavior confirms that at lower thickness the films have significant fraction of (i) AFM ordered phase, and (ii) magnetically disordered non-FM phase. The thinnest film shows very small coercivity. As the film thickness increases the coercivity (inset of Fig. 9) first increases for the 27 nm film and then decreases at higher film thicknesses. The increase in the coercivity of the 27 nm film could be due to the pinning of the FM domains by the non-FM

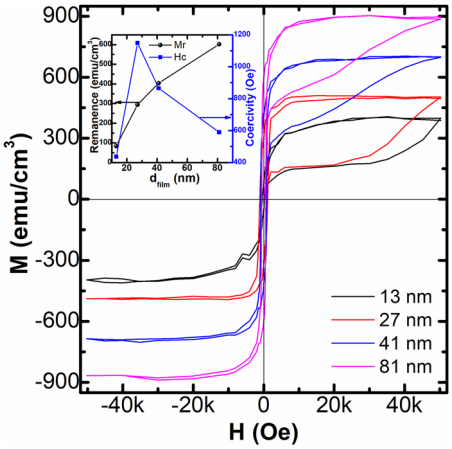


FIG. 9. Magnetization of LPCMO thin films (13 nm, 27 nm, 41nm and 81 nm) measured at 10 K as a function of magnetic field (H) applied parallel to the film surface along the longer dimension. Inset shows remanence and coercivity as function of the film thickness.

matter in the film. At higher film thickness the coercivity decreases is due to the conversion of the non-FM phases into FM ordered phase.

In general a decrease in the magnetic moment is ascribed to electronic phase separation and structural inhomogeneity driven electronic interfacial reconstruction. A magnetic dead layer is the reason of disordered spin structure at the substrate-film interface.[39,40] The existence of the dead layer is attributed to the decrease in the double exchange energy at the FM (film)/non-FM (Substrate) interface.[41] However, as emphasized by Bibes et al.[37] the dead layer approach alone is not sufficient to explain the scaling of FM/IM transitions with the film thickness. They have demonstrated that in fully tensile strained $La_{2/3}Ca_{1/3}MnO_3$ thin films on (001)-$SrTiO_3$ the T_C/T_{IM} decay rapidly at thickness d<50 nm with significant decrease (increase) in magnetization (resistivity). Employing the ^{55}Mn NMR they have established the (i) existence of a prominent non-FM insulator in ultrathin films (d≤5 nm) and (ii) occurrence of a inhomogeneous FM insulator in the range 5 nm<d<40 nm. Abad et al. have also studied $La_{2/3}Ca_{1/3}MnO_3/SrTiO_3$ thin films[42] and established the depression in the magnetic and transport properties as a consequence of the strain induced selective e_g orbital occupancy. The variation of magnetic and magnetotransport properties as a function of the film thickness is generally different in manganites having different bandwidth (BW), e.g., in large BW compounds like $La_{1-x}Sr_xMnO_3$ even ultrathin films show well defined paramagnetic (PM) – ferromagnetic (FM) and insulator –metal (IM) transitions [Refs. 29 and 34]. As the bandwidth is lowered by substitution of smaller cations at the RE/AE-site of the perovskite structure (as in case of the presently studied composition), the well-defined PM-FM and IM transitions shift to higher film thickness [Ref. 24]. Hence the dead layer is expected to be significantly thicker in lower BW thin films. However, the minimum/critical thickness at which these transitions appear is not rigorously determined in case of low BW compounds. In view of the presently obtained results and the data reported earlier, we believe that the minimum thickness at which the well-defined transitions appear and hence the thickness of the dead layer is strongly dependent on the (i) bandwidth of the compound (lower sensitivity at higher bandwidths), (ii) the nature of the strain (whether compressive or tensile), (iii) the oxygen stoichiometry. Hence in low bandwidth manganite thin films under tensile strain (like the present one) the dead layer thickness could be larger than in the low bandwidth manganite films. From the above discussion it follows that the existence of magnetic disordered insulator layer results in reduced magnetization and also has adverse effect on the magnetotransport properties. Since the $La_{1-x-y}Pr_yCa_xMnO_3$ has (i) much smaller bandwidth (due to the more dominant presence of Pr^{3+} in the lattice), (ii) higher cationic disorder than $La_{1-x}Ca_xMnO_3$ therefore it has stronger intrinsic tendency towards phase separation. Consequently, the role of interfacial electronic reconstruction as well as the dead layer effect could be more dramatic in $La_{1-x-y}Pr_yCa_xMnO_3$. Further, in this particular case of the $La_{0.23}P_{0.41}Ca_{0.36}MnO_3$/STO interface the strain that dominates the interface is tensile and

this can further accentuate the dead layer effect. The other possible lattice disorder that could yield a depressed magnetic moment could be the strain induced oxygen vacancies.[24] At lower film thickness the dead layer effect is expected to be more visible.

CONCLUSIONS

The impact of tensile strain induced modifications in the structure, microstructure, morphology and their cumulative consequences on the magneto-electrical properties of $La_{0.23}P_{0.41}Ca_{0.36}MnO_3$ thin films deposited on (001) oriented $SrTiO_3$ is studied. At lower thickness (~13 nm) the films bear strong tensile strain and its relaxation even at higher thickness (~81 nm) is partial only. This shows that that higher thickness the tensile strain may remain self-sustained. A sudden jump in the scaling of the out-of-plane lattice constant with films thickness suggests noticeable microstructural changes in films having d≥41 nm. Analysis of the rocking curve broadening shows at lower film thickness (~13 and 27 nm) the microstructure is dominated by the strain, which in this case is due to the lattice mismatch. At higher film thickness the mosaic broadening starts dominating due to the dislocation induced tilt and dilations of the lattice. The degradation of the layer by layer growth and increase in the surface roughness at higher film thickness as observed through the atomic force microscopic measurements also supports the above observations. The lower thickness films (d~13 and ~27 nm) show higher electrical resistivity and insulator like behavior throughout the measured temperature range. At d≥41 nm, an insulator metal transition bearing a strong thermal hysteresis, which narrows down with increase in film thickness is seen. The insulator region electrical conduction in all the films is well described by the Emin-Holstein small polaron hopping, wherein the lower thickness films possess higher activation energies. At lower film thickness a strong depression in the magnetic moment which is accompanied by a broad and diffuse FM transition is observed. The magnetization scaling with the film thickness shows the possible existence of a spin disordered insulator layer, the associated electronic reconstruction and a sizeable non-ferromagnetic insulator state at d≤27 nm. As thickness increases there is increase in magnetic moment which is attributed to reduced impact of the interfacial electric reconstruction that forms the dead layer and relaxation of the substrate induced tensile strain which favors carrier delocalization.

ACKNOWLEDGMENTS

Authors thankfully acknowledge Department of Science and Technology for providing the magnetic measurement facility (MPMS) facility at CSIR-NPL. The work has been financially supported by Council of Scientific and Industrial Research (CSIR) through the 12th five year plan project grant number PSC0110.

[1] J. M. D. Coey and M. Viret, Adv. Phys. **48**, 167 (1999).
[2] M. B. Salamon and M. Jaime, Rev. Mod. Phys. **73**, 583 (2001).
[3] E. Dagotto, T. Hotta, and A. Moreo, Phys. Rep. **344**, 1 (2001).
[4] Y. Tokura, Rep. Prog. Phys. **69**, 797 (2006).
[5] C. Zener, Phys. Rev. **81**, 440 (1951).
[6] C. Zener, Phys. Rev. **82**, 403 (1951).
[7] A. Sadoc, B. Mercey, C. Simon, D. Grebille, W. Prellier, and M.-B. Lepetit, Phys. Rev. Lett. **104**, 046804 (2010).
[8] J. B. Goodenough, Annu. Rev. Mater. Sci. **28**, 1–27 (1998).
[9] W. Prellier, Ph. Lecoeur, and B. Mercey, J. Phys. Condens. Matter **13**, R915 (2001).
[10] A.-M. Haghiri-Gosnet and J.-P. Renard, J. Phys. D: Appl. Phys. **36**, R127 (2003).
[11] D. Gillaspie, J. X. Ma, H.-Y. Zhai, T. Z. Ward, H. M. Christen, E. W. Plummer, and J. Shen, J. Appl. Phys. **99**, 08S901 (2006).
[12] A. Mukherjee, W. S. Cole, P. Woodward, M. Randeria, and N. Trivedi, Phys. Rev. Lett. **110**, 157201 (2013).
[13] C. Aruta, G. Ghiringhelli, A. Tebano, N. Boggio, N. Brookes, P. Medaglia, and G. Balestrino, Phys. Rev. B **73**, 235121 (2006).
[14] A. Tebano, A. Orsini, P. G. Medaglia, D. Di Castro, G. Balestrino, B. Freelon, A. Bostwick, Y. J. Chang, G. Gaines, E. Rotenberg, and N. L. Saini, Phys. Rev. B **82**, 214407 (2010).
[15] T. Dhakal, J. Tosado, and A. Biswas, Phys. Rev. B **75**, 092404 (2007).
[16] J. Q. He, V. V. Volkov, T. Asaka, S. Chaudhuri, R. C. Budhani, and Y. Zhu, Phys. Rev. B **82**, 224404 (2010).
[17] T. Z. Ward, S. Liang, K. Fuchigami, L. F. Yin, E. Dagotto, E. W. Plummer, and J. Shen, Phys. Rev. Lett. **100**, 247204 (2008).
[18] W. Wu, C. Israel, N. Hur, S. Park, S.-W. Cheong, and A. de Lozanne, Nat. Mater. **5**, 882 (2006).
[19] J. Jeon, H. S. Alagoz, R. Boos, J. Jung, and K. H. Chow, Appl. Phys. Lett. **104**, 122405 (2014).

[20] V. G. Sathe, A. Ahlawat, R. Rawat, and P. Chaddah, J. Phys.: Condens. Matter **22**, 176002 (2010).
[21] D. K. Mishra, V. G. Sathe, R. Rawat, and V. Ganesan, J. Phys.: Condens. Matter **25**, 175003 (2013).
[22] S. Singh, P. Kumar, P. K. Siwach, P. K. Tyagi, and H. K. Singh, Appl. Phys. Lett. **104**, 212403 (2014).
[23] V. Agarwal, P. K. Siwach, V. P. S. Awana, and H. K. Singh, Solid State Commun. **202**, 43 (2015).
[24] V. Agarwal, L. M. Kandpal, P. K. Siwach, V. P. S. Awana, and H. K. Singh, J. Mag. Magnet. Mater. **394**, 299 (2015).
[25] D. Okuyama, M. Nakamura, Y. Wakabayashi, H. Itoh, R. Kumai, H. Yamada, Y. Taguchi, T. Arima, M. Kawasaki, and Y. Tokura, Appl. Phys. Lett. **95**, 152502 (2009).
[26] Z. Q. Yang, Y. Q. Zhang, J. Aarts, M.-Y. Wu, and H. W. Zandbergen, Appl. Phys. Lett. **88**, 072507 (2006).
[27] D. K. Bowen and B. K. Tanner, *High Resolution X-ray diffractometry and topography*, Taylor & Francis, London (1998).
[28] D. Emin and T. Holstein, Ann. Phys. (Paris) **53**, 439 (1969).
[29] R. Prasad, H. K. Singh, M. P. Singh, W. Prellier, P. K. Siwach, and A. Kaur, J. Appl. Phys. **103**, 083906 (2008).
[30] M. K. Srivastava, P. K. Siwach, A. Kaur, and H. K. Singh, Appl. Phys. Lett. **97**, 182503 (2010).
[31] H. S. Alagoz, M. Khan, M. M. Saber, S. T. Mahmud, K. H. Chow, and J. Jung, Appl. Phys. Lett. **102**, 242406 (2013).
[32] V. Agarwal, G. Sharma, P. K. Siwach, K. K. Maurya, and H. K. Singh, Appl. Phys. A **119**, 899–908 (2015).
[33] G.-m. Zhao, H. Keller, and W. Prellier, J. Phys.: Condens. Matter **12**, L361 (2000).
[34] P. Graziosi, A. Gambardella, M. Prezioso, A. Riminucci, I. Bergenti, N. Homonnay, G. Schmidt, D. Pullini, and D. Busquets-Mataix, Phys. Rev. B **89**, 214411 (2014).
[35] J. A. Mydosh, *Spin Glasses: An Experimental Introduction*, 2nd ed., Taylor & Francis, London (1993).
[36] A. Dutta, N. Gayathri, and R. Ranganathan, Phys. Rev. B **68**, 054432 (2003).
[37] R. Prasad, M. P. Singh, P. K. Siwach, A. Kaur, P. Fournier, and H. K. Singh, Appl. Phys. A **99**, 823 (2010).
[38] V. Agarwal, R. Prasad, M. P. Singh, P. K. Siwach, A. Srivastava, P. Fournier, and H. K. Singh, Appl. Phys. Lett. **96**, 052512 (2010).
[39] J. Z. Sun, D. W. Abraham, R. A. Rao, and C. B. Eom, Appl. Phys. Lett. **74**, 3017 (1999).
[40] M. Bibes, L. Balcells, S. Valencia, J. Fontcuberta, M. Wojcik, E. Jedryka, and S. Nadolski, Phys. Rev. Lett. **87**, 067210 (2001).
[41] M. B. Lepetit, B. Mercey, and C. Simon, Phys. Rev. Lett. **108**, 087202 (2012).
[42] L. Abad, V. Laukhin, S. Valencia, A. Gaup, W. Gudat, L. Balcells, and B. Martínez, Adv. Fun. Mater. **17**, 3918 (2007).

International Journal of Research in Engineering and Innovation (IJREI)
journal home page: http://www.ijrei.com
ISSN (Online): 2456-6934

Thermal optimization of three stage vapour compression cascade refrigeration system using entropy generation principle for reducing global warming and ozone depletion using ecofriendly refrigerants

R.S. Mishra

Department, of Mechanical, Production, Industrial and Automobiles Engineering, Delhi Technological University Delhi-110042

Abstract

Lot of literature review is available on vapour compression cascade refrigeration system so far. But these investigator has not optimized the performance parameters at optimum condition and also not computed optimum second law performances based on optimum performance parameters. In this papers, optimum performance have been predicted for optimum conditions for two cascade refrigeration systems. It was observed that optimum Evaporator temperature in high temperature circuit using R1234ze ecofriendly refrigerant is ranging from 269K to 270K Optimum evaporator temperature in medium (intermediate temperature circuit using (R1234yf) is ranging from 229K to 230K. The optimum evaporator temperature in low temperature circuit is ranging from 183 to 186K using R134a and R404a ecofriendly refrigerants. The thermodynamic performances for these optimum performance parameters for two cascade refrigeration systems have been presented. © 2017 ijrei.com. All rights reserved

Keywords: Low temperature Refrigeration, Cascade system, Energy-Exergy analysis, Parameter optimizations

1. Introduction

Low-temperature refrigeration systems are typically required for low temperature range from –40°C to –100°C for applications chemical, food, pharmaceutical, and other industries. Cascade refrigeration cycles are commonly used in the liquefaction of natural gas, which consists basically of hydrocarbons of the paraffin series, of which methane has the lowest boiling point at atmospheric pressure. Refrigeration down to that temperature can be provided by a ternary cascade refrigeration cycle using propane, ethane and methane, whose boiling points at standard atmospheric pressure .The high-temperature circuit uses high boiling point refrigerants such as R-1234ze, R 717 and R152a and Intermediate circuit's ecofriendly refrigerants such as R-1234yf, etc. are used. Similarly for the low-temperature cascade circuit low boiling refrigerants R134a, 404a, R This paper mainly deals with thermodynamic optimization of three stages cascade vapour compression refrigeration systems using ecofriendly refrigerants used for low temperature applications. The effect of optimum thermal performance parameters (i.e. approaches, condenser temperature, and temperature variations in the evaporators) on the first law thermal performances in terms of the system COP, and also in terms of second law efficiency exergetic Efficiency of the cascade system and System exergy destruction ratio (SEDR) have been computed thermodynamically using entropy generation principle. The utility of R1234ze in the high temperature circuit and R1234yf in the medium (intermediate) temperature circuits and new ecofriendly refrigerants in the intermediates circuits and R134a or R404a in the low temperature cascade circuit between-80oC to -100oC) applications have been optimized.. It was observed that the best combination in terms of R1234ze-R1234yf -R134a gives better thermal performance than using R-1234ze-R1234yf-R404a. The optimum Evaporator temperature in High temperature circuit, and optimum Evaporator temperature in medium temperature circuit and Low temperature evaporator have been predicted and their thermal performance have been presented in this paper.

2. Literature Review

Mishra [1] work carried out critical issue in the field of green technologies is to develop the relationship between ODP and GWP and suggest new and alternative refrigerants which do

Corresponding author: R.S. Mishra
Email :rsmishra@dce.ac.in

not damage ozone layer and not to increase global warming. The Numerical computation have been carried out using energy - exergy Analysis of two and three stages cascade vapour refrigeration system of 10 ton capacity for seven eco-friendly refrigerants such as R-1234yf and R-1234ze in high temperature circuit, and R134a , R-404a, R-407C, R-502, propane(R-290), isobutene (R-600a), butane (R-600)) in lower temperature circuit in two stage and above refrigerants in intermediate circuit in three stage system. The performance parameters such as COP, EDR, exegetic efficiency, have been predicted. Lima et.al. [2] studied thermodynamic performance of a cascade refrigeration system using the refrigerant R22 as the working fluid in the high temperature circuit (HT) and the refrigerant R404a as the working fluid in the low temperature circuit (LT) and developed thermodynamic analysis to obtain the evaporation temperature in high temperature cycle , ,condensing temperature of the LT and effect of temperature overlapping (effect of approach) which provides the optimal value for first law efficiency in terms of coefficient of performance (COP) of the cycle and compared with experimental results obtained from a prototype which showed closed agreement and found that by increasing the intermediate temperature varied COP of the system. Messineo et.al.[3] presented thermodynamic analysis of a cascade refrigeration system working at TE=-35^{0}C and TC= 35^{0}C using six different refrigerants in the HTC,in which three were natural refrigerants (R717, R290 and R600), and three were synthetic refrigerants (R404A, R410A and R134a).along with carbon dioxide In the Low temperature circuit, and concluded that , the results obtained show that a cascade refrigeration system using natural refrigerants is an interesting alternative to systems as compared to the synthetic refrigerants for energetic, security and environmental reasons. Prasanna et.al [4] studied comparison of synthetic and natural refrigerants in cascade refrigeration system for low temperature application. Synthetic refrigerants have been used in all refrigeration systems and comparison of various refrigerant pairs such as R507-R23, R717-R23, R290-N2O, and R717- N_2O. The System performance was predicted with the variation in evaporator temperature, condensing temperature, isentropic efficiency of compressor, temperature overlap in cascade condenser. The computed Results shows that, COP of the system with R717-N_2O is higher than other pairs and it can also be used as alternative refrigerant for low temperature application in vapour compression cascade refrigeration system. M. Idrus Alhamid et.al [5] builds a prototype cascade refrigeration machine using the environmentally friendly hydrocarbon refrigerants (propane, ethane and CO and compared thermal performances in terms of COP with experimental COP. Nimai et.al [6] developed theoretical model of solar-assisted cascade refrigeration system in cold storage. The system consists of electricity-driven vapor compression refrigeration system and solar-driven vapour absorption refrigeration system. The vapour compression refrigeration system was connected in series with vapour absorption refrigeration system. The computed results shows higher COP as compared with the conventional vapour compression refrigeration system. Parmar et.al [7] studied thermodynamic analysis of eco-friendly/natural fluids used in cascade refrigeration systems. He used R744 is used in Low-temperature cycle whereas R134a, R290, R717 and R404a (R125 (44%)/R143a (52%)/R134a (4%)) are used in the High-temperature cycle. The effects of evaporator temperature, condenser temperature and temperature overlapping (in terms of temperature difference in cascade condenser and low temperature cycle condenser temperature) on the thermal performance parameters in terms of . COP and refrigerant mass flow ratio have been computed. Dopazo et.al [8] used statistical procedure to analyse the parameters of design and operation of a CO cascade cooling system and their effect on the system's COP and exergetic efficiency. The analysis was carried through his mathematical model the first law efficiency in terms of system's COP and its second law efficiency in terms of exergetic efficiency. Heobtained functional relationship between six design/operating parameters using statistical procedure and obtained parametric results. Rawat et.al [9] developed thermodynamic model for cascade refrigeration system using NH3 in high temperature circuit (HTC) and CO2 in low temperature circuit (LTC) at different operating conditions to find out the effect of various designs and operating parameters on the thermal performance of the cycle. These design and operating parameters include: condenser temperature; evaporator temperature; coupling temperature; compressor isentropic efficiency and temperature difference in cascade heat exchanger and observed that the use of internal heat exchanger has undesirable effect on the performance of the R744-R717 cascade system and also advisable that, internal heat exchanger should be never used for this pair of refrigerants in cascade system. However, degree of sub cooling always desirable feature in R744-R717 cascade system. Messineo [10] developed thermodynamic model of a cascade refrigeration system using as refrigerant carbon dioxide in low-temperature circuit and ammonia in high-temperature circuit. The operating parameters include condensing, evaporating, superheating and sub cooling temperatures in the ammonia (R717) high temperature circuit and in the carbon dioxide (R744) low-temperature circuit. The computed Results show that a carbon dioxide-ammonia cascade refrigeration system is an interesting alternative toR404A two-stage refrigeration system for low evaporating temperatures (–30°C to –50(°C) in commercial refrigeration for energy, security and environmental reasons. Winkler et.al [11] developed component-based simulation model for vapour compression cascade systems and predicted COP. Gami et.al [12] developed thermodynamic energy and exergy analysis for two cascade refrigeration systems using refrigerants pairs R134a R23and R290-R23 to optimize the operating parameters of the system. The computed results show that COP and exergetic efficiency decreases when degree of superheating increases in LT system and increases when degree of superheating increases in HT system and also be remain constant when degree of superheating increases in HT and LT system and

founds that COP and exergetic efficiency increases when degree of sub cooling increases in all two systems B. Agnew, et.al [13] conducted finite time analysis of a cascade refrigeration system using alternative refrigerants. Bansal P.K [14] used thermodynamic analysis of carbon dioxide–ammonia (R744–R717) cascade refrigeration system.

3. Modelling Three Stage Vapour Compression Cascade Refrigeration Systems using ecofriendly Refrigerants

The following assumptions have been taken for analyzing three stages cascade vapour compression system for low temperature applications. The cooling load in the low temperature evaporator is considered to be 70 [kW]. Temperature of condenser using R1234ze is to be 50^0C and temperature of high temperature circuit evaporator to be 0^0C, The temperature of low temperature evaporator to be -100^0C, temperature of secondary intermediate cascade evaporator using R1234yf is to be -50^0C, The effect of temperature overlapping (approach means temperature difference between cascade condenser and cascade evaporator is 10^0C in each stage is considered

4. Result and Discussion

Three stages cascade vapour compression refrigeration have been considered and following optimum values have been found were shown in Table-1-8 respectively.

T_Eva2=-43 (oC),T_eva3=-89^{0}C T_Cond=50^{0}C, Approach_1=Approach_2=10 and Q_Eva3=70"kW"
Compressor Efficiency-1= Compressor Efficiency-2= Compressor Efficiency-3=0.8

Table- 1: Optimum Performance of three stages Cascade Refrigeration Systems using ecofriendly R1234ze-R1234yf-R-134a refrigerants.

T_EVA_1 (oC)R134a	COP_Overall	EDR_Overall	ETA_Second	COP_HTC	COP_MTC	COP_LTC
-3	0.6029	1.68	0.3732	2.944	2.90	2.098
-4	0.6018	1.682	0.3729	2.861	2.979	2.098

T_Eva2=-43 (oC),T_eva3=-89^{0}C, T_Cond=50^{0}C Approach_1=Approach_2=10 and Q_Eva3=70"kW"

Table-2: Optimum Performance of three stages Cascade Refrigeration Systems using ecofriendly R1234ze-R1234yf-R-404a refrigerants.

T_EVA_1 (oC)R404a	COP_Overall	EDR_Overall	ETA_Second	COP_HTC	COP_MTC	COP_LTC
-3	0.5966	1.744	0.3644	2.944	2.51	2.333
-4	0.5964	1.745	0.3643	2.861	2.575	2.333
-5	0.5962	1.746	0.3641	2.78	2.643	2.333

.T_Eva2=-44 (oC),T_eva3=-89^{0}C, T_Cond=50^{0}C Approach_1=Approach_2=10 and Q_Eva3=70"kW"

Table-3: Optimum Performance of three stages Cascade Refrigeration Systems using ecofriendly R1234ze-R1234yf-R-407c refrigerants

T_EVA(oC)	COP_Overall	EDR_Overall	ETA_Second	COP_HTC	COP_MTC	COP_LTC
-3	0.6019	1.681	0.3729	2.944	2.815	2.147
-4	0.6015	1.683	0.3727	2.861	2.892	2.147

T_Eva2=-43 (oC),T_eva3=-89^{0}C, T_Cond=50^{0}C Approach_1=Approach_2=10 and Q_Eva3=70"kW"

Table-4: Optimum Performance of three stages Cascade Refrigeration Systems using ecofriendly R1234ze-R1234yf-R404a refrigerants.

T_EVA3 (oC)	COP_Overall	EDR_Overall	ETA_Second	COP_HTC	COP_MTC	COP_LTC
-88	0.6104	1.682	0.3729	2.861	2.892	2.21
-89	0.6015	1.683	0.3727	2.861	2.892	2.147
-90	0.5927	1.685	0.3725	2.861	2.892	2.086

T_Eva2=-43 (oC),T_eva1=-3^{0}C T_Cond=50^{0}C Approach_1=Approach_2=10 and Q_Eva3=70"kW

Table- 5: Optimum Performance of three stages Cascade Refrigeration Systems using ecofriendly R1234ze-R1234yf-R-134a refrigerants.

T_EVA3 (oC)	COP_Overall	EDR_Overall	ETA_Second	COP_HTC	COP_MTC	COP_LTC
-87	0.6053	1.744	0.3645	2.944	2.51	2.405
-88	0.5966	1.744	0.3644	2.944	2.51	2.333
-89	0.5879	1.745	0.3643	2.944	2.51	2.264

T_Eva1=-4 (oC),T_eva3=-89^{0}C T_Cond=50^{0}C Approach_1=Approach_2=10 and Q_Eva3=70"kW

Table- 6: Optimum Performance of three stages Cascade Refrigeration Systems using ecofriendly R1234ze-R1234yf-R-134a refrigerants.

T_EVA(oC) R134a	COP_Overall	EDR_Overall	ETA_Second	COP_HTC	COP_MTC	COP_LTC
-43	0.6018	1.682	0.3729	2.861	2.979	2.098
-44	0.6015	1.683	0.3727	2.861	2.892	2.147

T_Eva1=-4 (oC),T_eva3=-89^{0}C T_Cond=50^{0}C Approach_1=Approach_2=10 and Q_Eva3=70"kW

Table- 7: Optimum Performance of three stages Cascade Refrigeration Systems using ecofriendly R1234ze-R1234yf-R-134a refrigerants.

T_EVA (oC)R404a	COP_Overall	EDR_Overall	ETA_Second	COP_HTC	COP_MTC	COP_LTC
-47	0.5970	1.742	0.3647	2.944	2.582	2.2768
-48	0.5966	1.744	0.3644	2.944	2.51	2.333
-49	0.5960	1747	0.3640	2.944	2.441	2.392

T_Eva1=-4 (oC),T_eva3=-89^{0}C, T_Cond=50^{0}C Approach_1=Approach_2=10 and Q_Eva3=70"kW

Table- 8: Optimum Performance of three stages Cascade Refrigeration Systems using ecofriendly R1234ze-R1234yf-R-134a refrigerants.

T_EVA(oC) R134a	COP_Overall	EDR_Overall	ETA_Second	COP_HTC	COP_MTC	COP_LTC
-43	0.6023	1.68	0.3732	2.944	2.90	2.098
-44	0.6019	1.681	0.3729	2.944	2.815	2.147

Table-1 showing the optimum first law efficiency of the three stage cascade refrigeration system usingR1234ze in the high temperature circuit and R1234yf in the secondary cascade intermediate temperature circuit and R134a in a lower temperature circuit. It was observed that the use of R1234ze in higher temperature circuit gives better thermodynamic performance than using R1234yf in high temperature circuit up to temperature range of -30oC. However for low temperature applications. The best combination of three stage cascade is system is to be R1234ze-R1234yf-R134a as compared to R1234ze-R1234yf-R404a. Therefore R1234ze-R1234yf-R134a is most suitable for practical applications. Because of The other refrigerants such as R123 and hydrocarbons containing chlorine and R152a, R600a , R290and R600 are also flammable in nature can be considered by adopting safety measures while R717 in toxic in nature.

5. Conclusions

The following conclusions were drawn while optimizing performance parameters in the three stages cascade refrigeration systems.

(i) The use of R1234ze has replaced in high temperature circuit of three stages cascade refrigeration systemas compared to R717 which is toxic in nature.

(ii) There is significant performance improvements using R1234yf in the intermediate temperature circuit as compared with R407c.

(iii) The second law efficiency using R134a in the low temperature evaporator circuit gives better performance as compared with R404a in low temperature circuit.

References

[1] R. S. Mishra ,(2013) "Thermodynamic analysis of three stages cascade vapour Compression refrigeration system for biomedical applications", Journal of Multi-Disciplinary Engineering Technologies Volume 7 No.1.

[2] C. U. S. Lima, (2012) et. al. "Theoretical & experimental Evaluation ofaA cascade refrigeration system for low temperature applications Using R22/R404A", Thermal Engineering, Vol. 11 • No. 1-2 , page. 07-14

[3] Antonio Messineo,et.al (2012) "Performance Evaluation Of Cascade Refrigeration Systems Using Different Refrigerants", International Journal of Air-Conditioning and Refrigeration Vol. 20, No. 3 1250010.

[4] Prasanna Songire, et.al (2015) "Comparative Assessment of Alternative Refrigerants in Cascade Refrigeration System". ISSN (Print): 2319-3182, Volume -4, Issue-2.

[5] M.Idrus et.al. (2013) "Characteristics and Cop Cascade Refrigeration System Using hydrocarbon Refrigerant (Propane, Ethane And Co) At Low Temperature Circuit (Ltc) International Journal of Technology 2: 112-120 ISSN 2086-9614.

[6] Dr. Nimai Mukhopadhyay,et.al.(2013) Performance Analysis of Solar Assisted Cascade Refrigeration System of Cold Storage System, IJAREEIE Vol. 2, Issue 4,

[7] Gajendrasinh G. Parmar, Dr. R. G. Kapadia (2015) Thermodynamic Analysis of Cascade Refrigeration System using a Natural Refrigerants for Supermarket Application, ijirset Vol. 4, Special Issue 6.

[8] J. Alberto Dopazo, et.al (2008) "Theoretical analysis of a CO2-NH3 cascade refrigeration system for cooling applications at low-temperatures", Applied Thermal Engineering 10.1016/j.applthermaleng..07006.

[9] K.S. Rawat, (2015), "Parametric Study of R744-R717 Cascade Refrigeration System",IJREST, Vol. 2, Issue-7.

[10] Antonio Messineo,(2012) "R744-R717 Cascade Refrigeration System: Performance Evaluation compared with a HFC Two-

Stage System", Article in Energy Procedia , DOI:10.1016/j.egypro.2011.12.896

[11] Winkler, J. el.al [2008] "Simulation and Validation of a R404A/CO2 Cascade Refrigeration System", International Refrigeration and Air Conditioning Conference at Purdue.

[12] Heena M. Gami, Mohammad Azim, (2014) "Thermodynamic analysis of cascade refrigeration system using refrigerants pairs R134a-R23 and R290-R23", International Journal of Engineering Sciences & Research Technology 3(4): ISSN: 2277-9655.

[13] B. Agnew, et.a.,[2004], A finite time analysis of a cascade refrigeration system using alternative refrigerants, Applied Thermal Engineering, 24, , 2557–2565.

[14] P. K. Bansal [2008], Thermodynamic analysis of an R744–R717 cascade refrigeration system, international journal of refrigeration 31, 45-54.

International Journal of Research in Engineering and Innovation (IJREI)
journal home page: http://www.ijrei.com
ISSN (Online): 2456-6934

Thermodynamic (energy-exergy) analysis of hydrogen liquefaction system

R.S. Mishra, Devendra Kumar

Department of Mechanical, Production & Industrial and Automobiles Engineering, Delhi Technological University, Delhi

Abstract

Hydrogen system is a unique design system for liquefaction of hydrogen gas. It comprises as liquid nitrogen chamber which helps the system to attain critical temperature point of hydrogen. From the exergy analysis study of hydrogen system it observed that System output does not deteriorate during off design condition when operated in selected operated range of PR 20-52 bar. Exergetic efficiency of the low temperature heat exchanger (HXD) at the lowest temperature of a hydrogen liquefier improved by increasing the pressure ratio because the mass imbalance gets compensated by the specific heat imbalance. Initial feasible range of pressure ratio 20 to 87 bar, COP of the system decrease at very rapidly.
© 2017 ijrei.com. All rights reserved
Keywords: Hydrogen liquefaction System, Thermodynamic Analysis, Energy-Exergy Analysis

1. Introduction

Hydrogen system is a unique design system for liquefaction of hydrogen gas. It comprises as liquid nitrogen chamber which helps the system to attain critical temperature point of hydrogen. Hydrogen derived from renewable energies eventually will contribute to meet the energy demand of word and help in sustainable development of countries [1]. Hydrogen combustion produces water vapor that does not make any pollution. Hydrogen is in gas form occupies a large volume, having low density (0.0897 kg/m3) and high pressure, thus need to liquefy hydrogen for an easier transportation and safety . Production of liquefy hydrogen is a challenging task due to its very low cryo-temperature of liquefaction. The major components of liquefaction cycle are: compressor powered by external energy source, four heat exchanger including nitrogen fill chamber, Joule Thomson valve and separator, which are shown in the Fig.1 Various important properties of H2 are represented in Table 1.Saturated temperature and pressure at (STP) condition is denoted by T0 and P0, respectively. Exergy is consumed or destroyed due to entropy generation based upon related processes, exergy destruction in various components of the system are not same. Thermodynamic analysis is to be made to identify the exergy losses in the system.

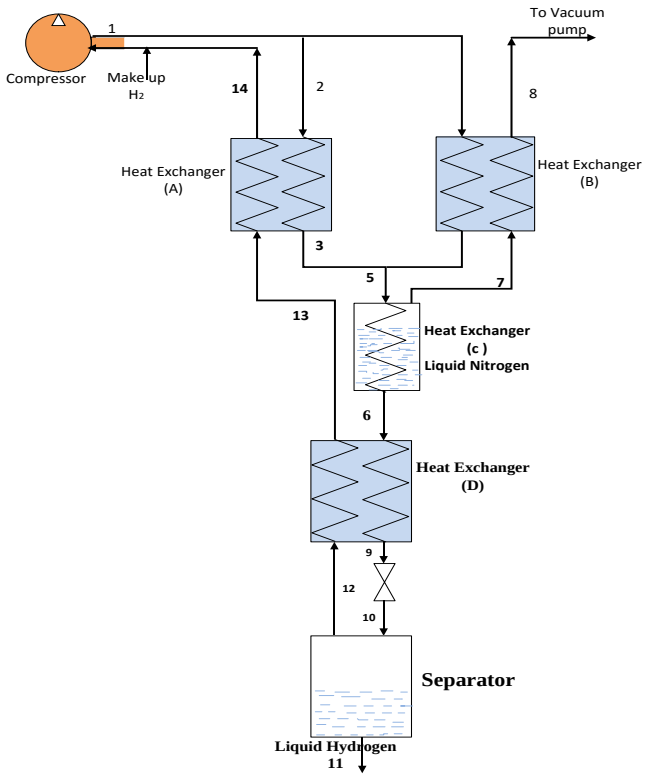


Figure 1: Block diagram of hydrogen liquefaction system

Corresponding author: R.S. Mishra
Email Id: rsmishradtu@gmail.com

2. Literature Review

Ibrahim Dincer et.al [1] carried out Exergy Analysis of Cryogenic and Liquefaction Systems and compared the numerical results with experimental measurements while M.T. Syed, [2] carried out the economic analysis of three hydrogen liquefaction systems, Akihiro Nakano, et.al.[3], analyzed Small-scale hydrogen liquefaction with a two-stage Gifford–McMahon cycle refrigerator. David O. et.al [4], also considered Large-scale hydrogen liquefier utilizing mixed-refrigerant pre-cooling", David O. Berstadet.al [5], carried out Comparison for large-scale hydrogen liquefaction processes. Gianluca Valenti and Ennio Macchi [6] proposed innovative, high-efficiency, large-scale hydrogen liquefier Neksa, [7] carried out Simulation on a proposed large-scale liquid hydrogen plant using a multi-component refrigerant refrigeration system. Gianluca Valenti [8], developed thermodynamic model of equilibrium-hydrogen on the simulation of its liquefaction

3. Thermodynamic (Energy-Exergy) Model hydrogen liquefaction system [1]

Following assumptions are made in the exergy analysis:

1. Steady state conditions are remained in all the components.
2. Pressure loses in the pipelines are neglected.
3. Heat gains and heat loses from the system or to the system are not considered.
4. Kinetic and potential energy and exergy losses are not considered.
5. With reference to cited literatures, it is assumed that mechanical efficiency of the compressor is 90% and the electrical efficiency of the motor is 90%.

Energy and exergy analyses need some mathematical formulations for the hydrogen liquefaction cycle. Mathematical formulation for exergy analysis in different components can be arranged in the following way:
The equations for exergy balance of Hydrogen Liquefaction systems are written as

3.1 Compressor analysis

$$Q = m_2 * (h_2 - h_1)$$

Specific exergy in any state is expressed as
$Ex_{state} = (h_{state} - h_0) - T_0 * (s_{state} - s_0)$
Where 'Q' is the rate of heat transfer across boundary, T2 and T0 is the temperature after the compression and reference state temperature. Exergy transfer accompanying the work interaction equals the electrical or mechanical work W (kW) itself. The exergy transfer accompanying mass crossing the boundaries at the inlet and outlet of the Compressor is expressed as

$$Ex_{comp} = \begin{pmatrix} m * ((h_2 - h_0) - (h_1 - h_0)) - \\ ((s_2 - s_0) - (s_1 - s_0)) \end{pmatrix}$$

Where 'm' represents the mass flow rate, (kg/s), 'Ex' represents the exergy per unit mass, 'h' and 's' correspond to the enthalpy and entropy of the fluid, h0 and s0 represent the enthalpy and entropy at the reference state (T0, P0) respectively. For this analysis, the atmospheric condition is taken as the reference state (T0 = 300K and P0 = 1.01325bar).

$$W_{comp} = \left(m_2 * ((h_2 - h_1)) - T_2 * (s_2 - s_1)\right)$$

$$COP = \frac{m_2 * (h_1 - h_{11})}{W_{comp}}$$

$$Ed_{comp} = \left(m_2 * T_1 * (s_1 - s_2) - \left(Q * \left(\frac{T_0}{T_1}\right)\right)\right)$$

Unlike energy, exergy would be destroyed due to irreversibility associated with the processes. The term 'Ed' of Eq. (1) accounts for the destruction of exergy and according to Gouy Stodola theorem it is expressed as

$$Ed = T_0 * \Delta S_{gen}$$

Where 'ΔS_{gen}' represent the rate of entropy generation during the process.

$$Ed_{comp_{\%}} = \left(\frac{Ed_{comp}}{Ed_{HLsys}}\right) * 100$$

$$Eta_{2nd_{\%}} = \left(\frac{m_f * ((h_{11} - h_1) - T_0 * (s_{11} - s_1))}{(h_2 - h_1) - T_1 * (s_2 - s_1)} * m_2\right) * 100$$

3.2 Heat Exchanger (HX) analysis

The function of heat exchanger is to exchange heat between two moving fluid streams without mixing; the hot fluid is releasing heat to the cold and the changes of kinetic and potential energy negligible.
The mass low rate of hot fluids and cold fluid should be constant. Energy balance equation can be expressed as follows:

$$Ex_{in_{HX}} - Ex_{out_{HX}} - Ed_{HX} = \Delta E_{x_{HX}} = 0 => \text{steady}$$

$$Ex_{HX} = m_i * \left((h_{in} - h_{out}) - \left(T_0 * (s_{in} - s_{out})\right)\right)$$

$$Ed_{HX} = \left(\left(Ex_{in_{HX}}\right) - \left(Ex_{out_{HX}}\right)\right)$$

$$m_{h_{HX}} * \left(h_{h,i} - h_{h,o}\right) = m_{c_{HX}} * \left(h_{c,o} - h_{c,i}\right) + q$$

Considering the heat transfer rate is the function of fluid mass flow rate and the inlet and outlet temperature different, the function can be written as:
q=f(m,T)
The heat transfer rates from the hot fluid to cold fluid are calculated by using following

$$q_{HX} = C_{h,HX} * \left(T_{h_i} - T_{h_o}\right)$$

The rate of heat received by the cold fluid can be calculated:

$$q_{HX} = Cc_{,HX} * \left(T_{c_o} - T_{c_i}\right)$$

In the heat exchanger, maximum heat exchange is occurred when the fluid temperature will be in a constant mass flow rate of the fluids.

$$T_{h_i} = T_{c_o};\ T_{h_o} = T_{c_i}$$

Maximum heat transfer rate capacity $q_{\max HX}$ can be calculated by using the following equation:

$$q_{max_{HX}} = C_{min_{HX}} * \left(T_{h_i} - T_{c_i}\right)$$

The expression of heat energy effectiveness (epsilon) of the heat exchanger considered in the present study are based on the

following definition.

$$\text{epsilon} = q_{HX}/q_{max_{HX}} = \left(\frac{\frac{\text{Atual heat}}{\text{actual energy transfer}}}{\frac{\text{Maximum heat possible}}{\text{Maximum energytransfer}}}\right)$$

$$Ntu_{HX} = (G_{HX})/C_{min_{HX}}$$

As the heat transfer is from the hot stream to cold stream in heat exchanger, the entropy of the hot stream decreases. This decrease in entropy is achieved by supplying exergy from the cold stream to the hot stream. In the case of heat exchangers employed in a refrigeration/ liquefaction system, the objective is to increase the exergy of the high pressure hot stream such that finally it is capable enough to absorb heat from the given external load. So the rational exergetic efficiency of the heat exchanger is defined as

$$\eta_{HX} = (m_h * (Ex_{h,out_{HX}} - Ex_{h,in_{HX}}))/(m_c * (Ex_{c,out_{HX}} - Ex_{c,in_{HX}}))$$

In the considered case the changes of kinetic and potential energy are neglected so change of exergy destruction of each stream can be written in the following form

$$Ex_{in_{HXD}} = m_2 * \left((h_6 - h_9) - \left(T_0 * (s_6 - s_9)\right)\right)$$

$$Ex_{out_{HXD}} = m_g * \left((h_{12} - h_{13}) - \left(T_0 * (s_{12} - s_{13})\right)\right)$$

$$Ed_{HXD} = \text{abs}\left(\left(Ex_{in_{HXD}}\right) - \left(Ex_{out_{HXD}}\right)\right)$$

$$Ed_{HXD}\% = \left(\frac{Ed_{HXD}}{Ed_{HLsys}}\right) * 100$$

$$T_6 = T_7 = -77°C(\text{Liq Nitrogen temp})$$

$$T_{h_i} = T_6;\ T_{c_o} = T_{13}$$

$$m_{h_{HXD}} = m_2,\ m_{c_{HXD}} = m_g$$

$$T_{h_o} = T_9;\ T_{c_i} = T_{12}$$

$$C_{h_{HXD}} = m_{h_{HX}} * cp_{fluid_{hot_{HXD}}}$$

$$C_{c_{HXD}} = m_{c_{HX}} * cp_{fluid_{cold_{HXD}}}$$

3.3 Heat Exchanger 'C' Analysis

$$m_2 * h_5 + m_{LN} * HF_N = m_{LNevop} * h_7 + m_2 * h_6 \quad (32)$$

$$m_{LN} = m_{LNevop}$$

$$T_5 * m_2 = m_a * T_3 + m_b * T_4$$

3.4 Expansion Valve Analysis

$$h_9 = h_{10};\ T_{10} = T_{12}$$

$$x_{10} = \frac{m_f}{m_f + m_g}$$

$$Ex_{in_{Val}} = m_2 * \left((h_9 - h_0) - T_0 * (s_9 - s_0)\right)$$

$$Ex_{out_{val}} = m_2 * \left((h_{10} - h_0) - T_0 * (s_{10} - s_0)\right)$$

$$Ed_{val} = \text{abs}\left(Ex_{in_{Val}} - Ex_{out_{val}}\right)$$

$$Ed_{val}\% = \left(\frac{Ed_{val}}{Ed_{HLsys}}\right) * 100$$

3.5 Separator Analysis

$$m_2 * h_{10} = m_f * h_{11} + m_g * h_{12}$$

$$x_{11} = 0;\ x_{12} = 1$$

$$Ed_{sep} = T_0 * \left(\left(m_g * s_{12} - m_2 * s_{10}\right) + \left(\frac{m_g * h_{12} - m_f * h_{11}}{T_0}\right)\right)$$

$$Ed_{sep}\% = \left(\frac{Ed_{sep}}{Ed_{HLsys}}\right) * 100$$

$$Ed_{HLsys} = Ed_{comp} + Ed_{HXC} + Ed_{HXA} + Ed_{HXD} + Ed_{val} + Ed_{sep} + Ed_{HXB}$$

4. Results and Discussions

Thermodynamic model for hydrogen liquefaction cycle has been developed using numerical computational technique. In the thermodynamic analysis of cycle, considered parameters like COP ,liquefaction rate ,compressor work and exergy destruction etc. with the cyclic pressure ratio, which have direct relationship with the performance of cycle have been varied. The effect of these parameters on the performance of the cycle is computed. In order to understand the individual effect of cycle parameters on the performance of the cycle, when varying a cycle parameter, other parameters are kept constant. The efficiency of the compressor (COMP) is kept constant at 85% and for all heat exchangers the effectiveness is kept at 0.85.The liquefaction temperature of liquid nitrogen (LN) is taken as 196 K(Liquefaction temperature of nitrogen). The above parameters have been chosen on the basis of the practical data available in open literature. An illustrative example is presented for the Hydrogen liquefaction cycle shown in fig.1 at 20 bar outlet pressure of compressor. Apart from above constant terms following other assumption are also considered while working on cycle like the compression is isothermal; expansion valve is isenthalpic and there is no heat leakage to the cycle. Furthermore the gas is taken is pure hydrogen at the inlet of compressor at 300 K and 1 bar. With all these assumption and constant parameters each of system component is studied and various performance parameters at every state is listed in Table-1&2. The properties of Hydrogen gas are obtained using computation software.

Table.1: various performance parameters

$COP = 1.064$	$m_{LNevop} = 0.4$ [Kg/s]	$m_b = 0.5$ [Kg/s]
$\eta_{2nd_{\%}} = 53.79$	$m_2 = 1$ [Kg/s]	$\varepsilon_{HXA} = 0.85$
$P_1 = 1$ [bar]	$m_a = 0.5$ [Kg/s]	$\varepsilon_{HXB} = 0.85$
$P_2 = 20$ [bar]	$m_b = 0.5$ [Kg/s]	$\varepsilon_{HXD} = 0.85$
$m_f = 0.166$[Kg/s]	$m_{HXD} = 1$[Kg/s]	$NTU_{HXA} = 3.886$
$m_g = 0.833$[Kg/s]	$HF_N = 25.35$ [kJ/kg	$NTU_{HXB} = 4.363$
$m_{LN} = 0.49$[Kg/s]	$W_c = 5770$ kj/kg	$NTU_{HXD} = 3.943$

Table 2: Various performance parameters

Temperature [K]	Enthalpy [kJ/kg]	Entropy [kJ/kg − K]	Specific Heat [kJ/kg − K]
$T_0 = 298$	$h_0 = 3929$	$s_0 = 53.42$	$cp_{c_{f_{HXA}}} = 10.55$
$T_1 = 300$	$h_1 = 3958$	$s_1 = 53.52$	$cp_{c_{f_{HXB}}} = 10.68$
$T_2 = 300$	$h_2 = 3966$	$s_2 = 41.14$	$cp_{c_{f_{HXD}}} = 11.71$
$T_3 = 103.2$	$h_3 = 1316$	$s_3 = 27.02$	-----
$T_4 = 132.3$	$h_4 = 1669$	$s_4 = 30.03$	----
$T_5 = 117.7$	$h_5 = 1490$	$s_5 = 28.6$	--------
$T_6 = 77$	$h_6 = 1007$	$s_6 = 23.57$	--------
$T_7 = 77$	$h_7 = 1007$	$s_7 = 36.4$	--------
$T_8 = 266.5$	$h_8 = 3488$	$s_8 = 51.83$	--------
$T_9 = 44.87$	$h_9 = 373.5$	$s_9 = 11.12$	--------
$T_{10} = 20.32$	$h_{10} = 373.5$	$s_{10} = 3.664$	--------
$T_{11} = 20.32$	$h_{11} = 0.4445$	$s_{11} = 0.02093$	--------
$T_{12} = 20.32$	$h_{12} = 448.4$	$s_{12} = 22.06$	--------
$T_{13} = 68.5$	$h_{13} = 962.9$	$s_{13} = 35.16$	--------
$T_{14} = 229.2$	$h_{14} = 2958$	$s_{14} = 49.72$	--------

The pressure ratio which is defined as the ratio of outlet pressure (P2) to inlet pressure (P1) at the compressor side put marked effect upon the performance and energy required in a liquefaction cycle. The inlet pressure (P1) is kept constant at 1.0133 bar where as for study, the cyclic pressure ratio is varied by changing the outlet pressure between the low pressures to high pressure range to analyze the behavior of hydrogen liquefaction system. Detroit of performance largely depend upon the pressure range in which they are designed to function whereas inlet pressure also depend upon the lower temperature required by the application and other operating condition so inlet pressure also have to be choose carefully. The Fig.2 depicts that when the cycle pressure ratio PR is in between 35 and 60, there is condition when system give maximum output with less compressor work input. There is a particular pressure ratio within this range for which the cycle output is at its maximum for the given configuration and operating conditions, this corresponds to PR = 55. Fig.2 shows that the work requirement for the cycle is increasing proportionally with the compressor pressure corresponding to its input pressure, whereas there is decrease in output of the system (liquefaction mass) with increase of pressure ratio. However, the actual energy input to the system is the exergy supplied to it (kW), and is expressed as:

$$Ex_{system} = m * (Ex_{system,in} - Ex_{system,out})$$

Where '$Ex_{system,in}$' and '$Ex_{system,out}$' are the flow exergies of the high pressure stream out of the after cooler and the low pressure stream input to the compressor respectively.

A part of the work input to the compressor is destroyed inside various components of the cycle. But as discussed above at right hand side of Fig.2. ,the maximum output at the approx. PR=55,at this PR the exergy destruction is more contributed by heat exchanger HXD, Separator and compressor while other components HXA,HXB and HXC is showing less destruction and minimum in JT valve of system. Exergy destruction in HXD, HXA, HXB and HXC decreases with increasing pressure ratio, this trend is reverse for the rest of the components of the system. The exergy destruction of each heat exchanger in the cycle with increasing cycle pressure ratio is shown in Fig.3 It shows that for all heat exchanger except HXD, the trend of decreasing the destruction with increasing pressure ratio is same in all, destruction is first increases up to PR=70 then start decreasing with increasing compressor pressure while in HXD this trend is from the initial stage, destruction start decreasing from initial point of increasing compressor pressure. It shows that appropriate care should be taken for HXD which also a JT-heat exchanger (Heat exchanger connected to Joule Thomson valve) and separator while designing the cycle. It also notice that all the heat exchangers in a liquefaction cycle are not equally balanced primarily due to reasons:

(1) As the liquid is drawn out of the system, the return stream flow is less than the high pressure forward stream.
(2) At temperatures below 20 K, there is considerable mismatch in their specific heats due to the pressure difference between the forward and return streams. For all the heat exchangers in the cycle, the specific heat capacity of the hot forward stream is plotted as a function of cycle pressure ratio (Fig.3).

For hydrogen at very low temperatures, the higher pressure stream has a lower specific heat than low pressure stream. In Fig.4 shows the heat exchanger HXD, which is working at the lowest temperature level, there is a large variation in specific heat (Cphf) with compression pressure ratio. The specific heat at high pressure side is maximum at PR=105 for HXD, and then there is significant drop in the Cp with increase in compressor pressure, other side the heat exchanger HXA and HXB having same inlet but still showing the different trend of variation in their respective specific heat, this variation is due to difference in the cold side inlet. Heat exchanger HXA have inlet of residual mass of which is not liquefy while HXB have vapors of LN which is form when hot Hydrogen is passes from LN chamber (HXC).

In optimization of system the first and second law analysis play a very important role carefully study relation between these two help in identifying the losses of the system which degrade the performance of system. Fig.5. show the effect of pressure ratio upon the COP and second law of system From the graph study it determined that there is high reduction in COP of system with increase of pressure ratio between 20- 87 bar but after that the reduction start stable and showing very less effect on COP with increases in pressure whereas right hand side second law show continuous decrease with high slop with increase of compressor pressure. At 262.5 bar the COP and Second law efficiency intersect each other. From the Fig. 5 it notice that; low compressor pressure in feasible range show high performance characteristics. NTU is very important term defining the number of transfer unit and very useful estimating the surface area of HX under design condition. In our Hydrogen liquefaction process we required three HX and one liquefy nitrogen chamber, NTU help us in estimating the size of all heat exchanger at various range of pressure ratio. Fig.6 show variation in dimensionless NTU at different pressure

ratio, from fig. 6 it depicted that the lowest temperature heat exchanger HXD show NTU decrement upto 70 bar then it became constant upto 105 bar but after this pressure range it increase at a very fast rate, which show gradually increase in size of heat exchanger while NTU trend of HXB is reverse of HXD and its value start decreasing after 105 bar. The variation in HXA NTU is very less. The mass vapour fraction ratio after J-T valve effect gives an idea how much mass can be liquefied. By using right technique the maximum output is can gathered e.g. three column separator is more efficient than two column separator. Fig.7 follow the same trend of liquefy mass as in above fig. 2 and show highest mass vapour fraction between 35 bar to 70 bar. The analysis is repeated at different pressure ratio and as a part of analysis, exergy destructions of each component is computed and various results of these studies are discussed in Fig 2 to 7.

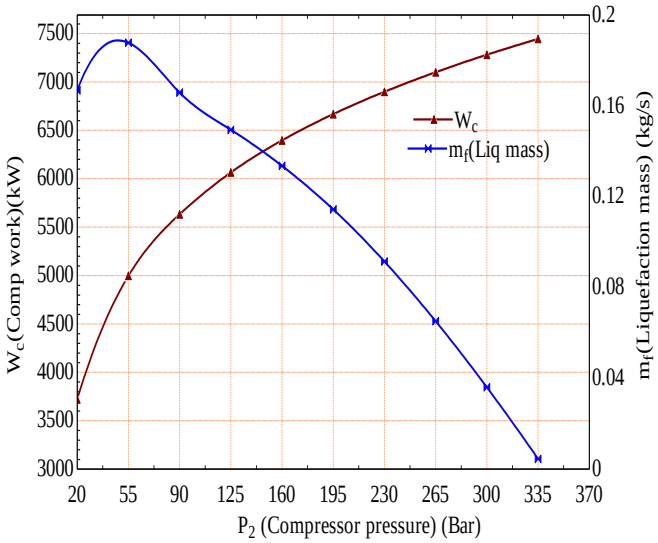


Figure 2: Work input (Compressor workW_c) and rate of liquefied mass m_f versus compressor pressure

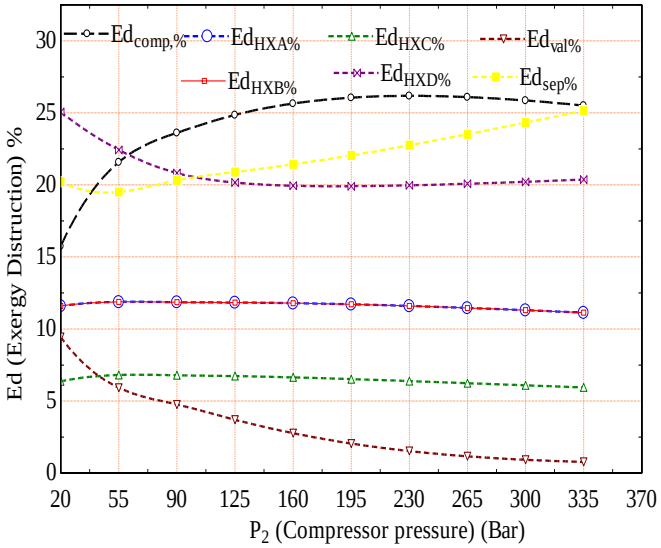


Figure 3: Variation in Ed (Exergy destruction) % versus compressor pressure

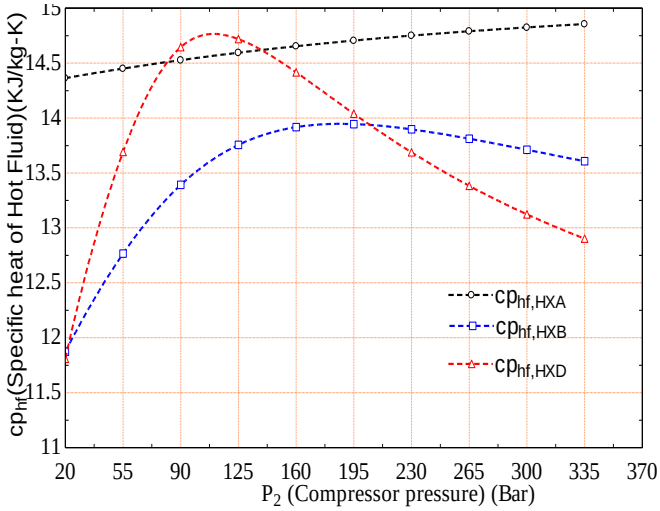


Figure 4: Variation in Cp_hf (specific heat of hot fluid) versus compressor pressure

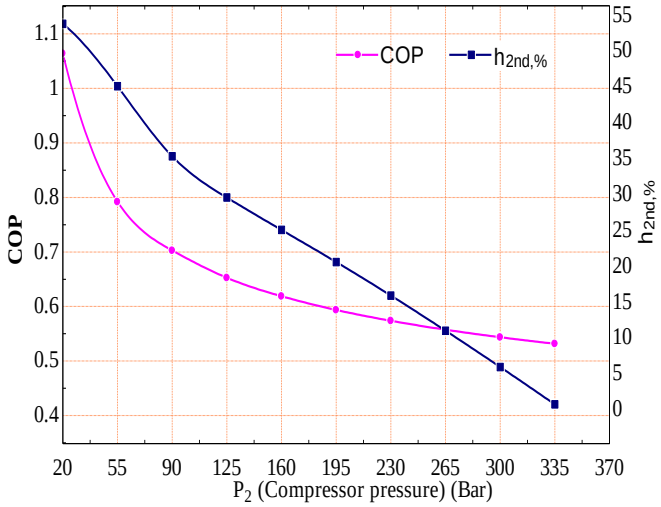


Figure 5: Variation in COP and Second law efficiency versus compressor pressure

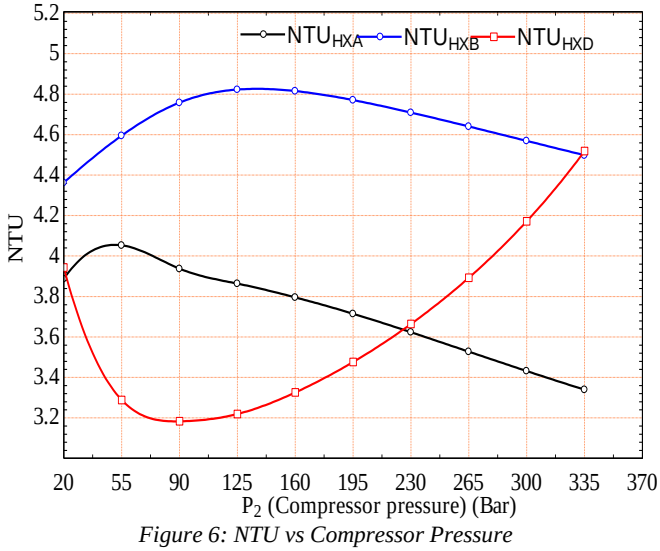


Figure 6: NTU vs Compressor Pressure

Using the above methodology, exergetic analysis of cycle design parameters on the performance of the hydrogen liquefaction cycle has been performed for obtaining optimum design guidelines. The observations and findings are described in the form of following graphic data mention below.

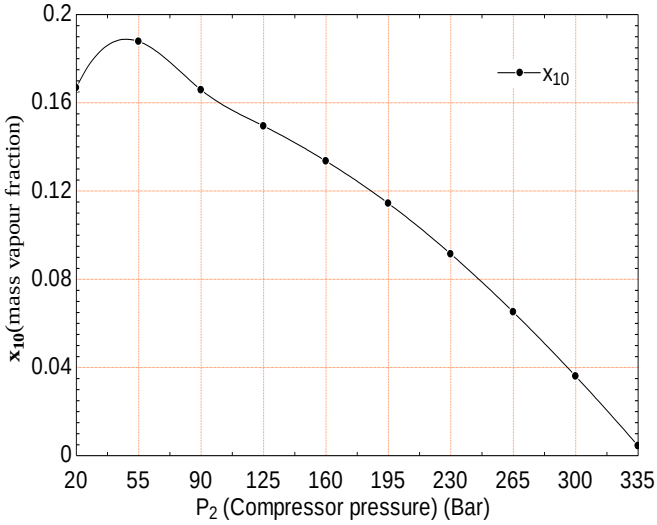


Figure 7: Mass Vapour fraction versus compressor pressure

5. Conclusion

- Second law efficiency in terms of Exergetic Efficiency of liquefaction in hydrogen system is 17.29 % and it start decreasing with further increases of compressor pressure
- COP of the liquefaction in hydrogen system is 0.8687 when input at ambient condition and compressor pressure is 15 bar and as like second like efficiency it also start decreasing with increases of compressor pressure.
- Liquefaction mass ratio and Total work done is increases with increase in compressor pressure in the hydrogen liquefaction system

References

[1] Ibrahim Dincer and Marc A. Rosen "Exergy Analysis of Cryogenic and Liquefaction Systems" Exergy (Second Edition) Energy, Environment and Sustainable Development, 2013, Pages 319–334.

[2] M.T. Syed, S.A. Sherif, T.N. Veziroğlu, J.W. Sheffield, An economic analysis of three hydrogen liquefaction systems, International Journal of Hydrogen Energy, Volume 23, Issue 7, July 1998, Pages 565-576

[3] Akihiro Nakano, Tetsuhiko Maeda, Hiroshi Ito,Masao Masuda, Yoshiaki Kawakami, Atsushi Kato, Manabu Tange,Toru Takahashiand Masahiro Matsuo, "Small-scale hydrogen liquefaction with a two-stage Gifford–McMahon cycle refrigerator" , International Journal of Hydrogen Energy, Volume 35, Issue 17, September 2010, Pages 9088–9094

[4] David O. Berstad, Jacob H. Stangand Petter Neksa, "Large-scale hydrogen liquefier utilising mixed-refrigerant pre-cooling", International Journal of Hydrogen Energy, Volume 35, Issue 10, May 2010, Pages 4512–4523

[5] David O. Berstad,Jacob H. Stangand Petter Neksa, "Comparison criteria for large-scale hydrogen liquefaction processes" International Journal of Hydrogen Energy, Volume 34, Issue 3, February 2009, Pages 1560–1568.

[6] Gianluca Valenti andEnnio Macchi, "Proposal of an innovative, high-efficiency, large-scale hydrogen liquefier" International Journal of Hydrogen Energy, Volume 33, Issue 12, June 2008, Pages 3116–3121.

[7] Songwut Krasae-in,Jacob H. Stangand Petter Neksa, "Simulation on a proposed large-scale liquid hydrogen plant using a multi-component refrigerant refrigeration system" International Journal of Hydrogen Energy, Volume 35, Issue 22, November 2010, Pages 12531–12544.

[8] Gianluca Valenti,Ennio Macchi and Samuele Brioschi, "The influence of the thermodynamic model of equilibrium-hydrogen on the simulation of its liquefaction" International Journal of Hydrogen Energy, Volume 37, Issue 14, July 2012, Pages 10779–10788.

.

International Journal of Research in Engineering and Innovation (IJREI)
journal home page: http://www.ijrei.com
ISSN (Online): 2456-6934



Thermodynamic (energy-exergy) analysis to improve its efficiencies of multiple stage vapour compression refrigeration systems

Radhey Shyam Mishra

Department of Mechanical, Production, Industrial & Automobiles Engineering, Delhi Technological University Delhi, India

Abstract

The performance of refrigerator is evaluated in term of COP which is the ratio of refrigeration effect to the net work input given to the system. The COP of vapour compression refrigeration system can be improved either by increasing refrigeration effect or by reducing work input given to the system. A higher COP, indices the better performance of refrigeration system. COP of the system can be increased either by decreasing the work of compression by using multi stage compound compression or increasing the refrigerating effect or both. It is possible to reduce the compressor work to considerable extent by compressing the refrigerant very close to the saturated line. This can be accomplished by compressing the refrigerant in the more stages with intermediate intercoolers. The refrigerating effect can be increased by maintaining the condition of the refrigerant very close to the liquid line. The expansion can be brought close to the liquid line by sub cooling the refrigerant and refrigerant and by removing the flashed vapour. By incorporating the flash chamber in the working cycle, the evaporator size is reduced as unwanted vapour formed is removed before the liquid refrigerant enters the evaporator. It is well known that throttling process in VCR is an irreversible expansion process. Expansion process is one of the main factors responsible for exergy loss in cycle performance because of entering the portion of the refrigerant flashing to vapour in evaporator which will not only reduce the cooling capacity but also increase the size of evaporator. This problem can be eliminated by adopting multi-stage expansion where the flash vapours is removed after each stage of expansion as a consequence there will be increase in cooling capacity and reduce the size of the evaporator. © 2018 ijrei.com. All rights reserved

Keywords: VCRS, Energy-Exergy-analysis, Thermodynamic Performances, Irreversibility analysis

1. Introduction

In the vapour compression refrigeration systems, the major operating cost is the energy input to the system in the form of mechanical work (i.e. compressor work). Thus any method of increasing coefficient of performance is advantageous so long as it does not involve too heavy an increase in other operating expenses, as well as initial plant cost and consequent maintenance. Since the coefficient of performance of a vapour compression refrigeration system is the ratio of refrigerating effect to the compressor work, therefore the coefficient of performance can be increased either by increasing the refrigerating effect or by decreasing the compressor work.

Several methods are available for improving first law efficiency in the terms of coefficient of performance (COP) of vapour compression refrigeration systems as given below. By introducing the flash chamber between the expansion valve and the evaporator. However the refrigerating effect and coefficient of performance and the power required are similar as that of a simple vapour saturation cycle when the flash chamber is not used. Thus the use of flash chamber has no effect on the thermodynamic cycle. The only effect resulting from the use of flash chamber is the reduction in the mass of refrigerant flowing through the evaporator and hence the reduction in the size of evaporator. By using the accumulator or pre cooler. When the accumulator is used in the vapour compression refrigeration system, the refrigerating effect, coefficient of performance, and power required to run the compressor is same as the simple saturation cycle. The accumulator or pre cooler is used only to protect the liquid refrigerant to flow into the compressor and thus dry compression is always used. By subcooling the liquid refrigerant by the vapour refrigerant. We know that subcooling the liquid refrigerant by the vapour refrigerant, the coefficient

Corresponding author: R.S. Mishra
Email Id: rsmishra@dtu.ac.in

of performance of cycle is reduced and by subcooling the liquid refrigerant leaving the condenser by liquid refrigerant from the expansion valve. In this process, the mass of refrigerant required in the heat exchanger is exactly equal as the mass of flash and that forms in the simple saturation cycle. Since the COP of this modified cycle and the power required to derive the compressor is same as that of simple saturation cycle. Therefore, this arrangement of subcooling the liquid refrigerant has no advantage because this method of subcooling of thermodynamically same as the simple saturation cycle. A liquid suction heat exchanger is used to sub-cool the liquid refrigerant from the condenser by exchanging heat with cold suction vapour. The subcooling would increase the refrigerating effect per kg of refrigerant. Also the suction vapour gets superheated, and it ensures that no liquid droplets should enter the compressor , thereby preventing any damage to the compressor valve. But at the same time, the compressor work would increase. However, there may be some improvement in COP of the cycle.

The performance of vapour compression refrigeration system, be improved by a little consideration in compression in refrigerant a reduction of compressor work very closed to saturated vapour line. This can be achieved by compressing the refrigerant in a more stages with intermediate intercooling. It is economically only where the pressure ratio is considerable as would be the case when very low evaporator are desired or when high condenser temperature may be required. Therefore compound compression is generally economical in the large refrigeration plants. The refrigerating effect can be increased by maintaining the condition of refrigerant in more liquid state at the entrance to the evaporator. This can be achieved by expanding the refrigerant very close to the saturated liquid line. It was observed that by subcooling the refrigerant and by removing the flashed vapour as they are during multi stage expansion, the expansion can be brought closed to the liquid line.

2. Improvements in Vapour Compression Refrigeration Systems

Refrigeration is a technology which absorbs heat at low temperature and provides temperature below the surrounding by rejecting heat to the surrounding at higher temperature. Simple vapour compression refrigeration system which consists of four major components compressor, expansion valve, condenser and evaporator in which total cooling load is carried at one temperature by single evaporator but in many applications like large hotels, food storage and food processing plants, food items are stored in different compartment and at different temperatures. Therefore there is need of multi evaporator vapour compression refrigeration system. The systems under vapour compression technology consume huge amount of electricity, this problem can be solved by improving performance of system. Performance of systems based on vapour compression refrigeration technology can be improved .The performance of refrigerator is evaluated in term of COP which is the ratio of refrigeration effect to the net work input given to the system. The COP of vapour compression refrigeration system can be improved either by increasing refrigeration effect or by reducing work input given to the system. It is well known that throttling process in VCR is an irreversible expansion process. Expansion process is one of the main factors responsible for exergy loss in cycle performance because of entering the portion of the refrigerant flashing to vapour in evaporator which will not only reduce the cooling capacity but also increase the size of evaporator. This problem can be eliminated by adopting multi-stage expansion where the flash vapours is removed after each stage of expansion as a consequence there will be increase in cooling capacity and reduce the size of the evaporator.

Kumar et al. [1] did energy and exergy analysis of vapour compression refrigeration system by the use of exergy-enthalpy diagram. They did first law analysis or energy analysis for calculating the coefficient of performance and exergy analysis for evaluation of various losses occurred in different components of vapour compression cycle using R11 and R12 as refrigerants.

Nikolaidis and Probert [2] studied analytically that change in evaporator and condenser temperatures of two stage vapour compression refrigeration plant using R22 add considerable effect on plant irreversibility. They suggested that there is need for optimizing the conditions imposed upon the condenser and evaporator.

Yumrutas et al [3] carried out exergy analysis based investigation of effect of condensing and evaporating temperature on vapour compression refrigeration cycle in terms of pressure losses, COP, second law efficiency and exergy losses. Variation in temperature of condenser as well as have negligible effect on exergy losses of compressor and expansion valve, also first law efficiency and exergy efficiency increase but total exergy losses of system decrease with increase in evaporator and condenser temperature.

Halimic et al. [4] compared performance of R401A, R290 and R134A with R12 by using in vapour compression refrigeration system, which is originally designed for R12.Due to similar performance of R134a in comparison with R12,R134A can be replaced in the same system without any medication in the system components. But in reference to greenhouse impact R290 presented best results. `

Xuan and Chen [5] presented in this manuscript about the replacement of R502 by mixture of HFC-161.Through experimental study it was found that mixture of HFC-161 gives same and higher performance than R404A at lower and higher evaporative temperature respectively on the vapour compression refrigeration system designed for R404A.

Cabello et al. [6] effect of condensing pressure, evaporating pressure and degree of superheating was experimentally investigated on single stage vapour compression refrigeration system using R22, R134a and R407C.It was observed that mass flow rate is greatly affected by change in suction conditions of compressor in results on refrigeration capacity because refrigeration capacity depended on mass flow rate

through evaporator. It was also found that for higher compression ratio R22 gives lower COP than R407C.

Spatz and Motta [7] focused on replacement of R12 with R410a through experimental investigation of medium temperature vapour compression refrigeration cycles. In terms of thermodynamic analysis, comparison of heat transfer and pressure drop characteristics, R410a gives best performance among R12, R404a and R290a.

Han et al. [8] under different working conditions experimental results revealed that there could be replacement of R407C in vapour compression refrigeration system having rotor compressor with mixture of R32/R125/R161 showing higher COP, less pressure ratio and slightly high discharge compressor temperature without any modification in the same system.

Cabello et al. [9] had studied about the effect of operating parameters on COP, work input and cooling capacity of single-stage vapour compression refrigeration system. There is great influence on energetic parameters due change in suction pressure, condensing and evaporating temperatures.

Mohanraj et al. [10] through experimental investigation of domestic refrigerator they arrived on conclusions that under different environmental temperatures COP of system using mixture of R290 and R600a in the ratio of 45.2: 54.8 by weight showing up to 3.6% greater than same system using R134a, also discharge temperature of compressor with mixture of R290 and R600a is lower in the range of 8.5-13.4K than same compressor with R134a.

Getu and Bansal [11] had optimized the design and operating parameters of like condensing temperature, subcooling temperature, evaporating temperature, superheating temperature and temperature difference in cascade heat exchanger R744-R717 cascade refrigeration system. A regression analysis was also done to obtain optimum thermodynamic parameters of same system.

Padilla et al. [12] exergy analysis of domestic vapour compression refrigeration system with R12 and R413A was done. They concluded that performance in terms of power consumption, irreversibility and exergy efficiency of R413A is better than R12, so R12 can be replaced with R413A in domestic vapour compression refrigeration system.

Stanciu et al. [13] did numerical and graphical investigation on one stage vapour compression refrigeration system for studied refrigerants (R22, R134a, R717, R507a, R404a) in terms of COP, compressor work, exergy efficiency and refrigeration effect. Effect of subcooling, superheating and compression ratio was also studied on the same system using considered refrigerants and present system optimization when working with specific refrigerant.

Ahamed et al. [14] emphasized on use of hydrocarbons and mixture of hydrocarbons and R134a in vapour compression refrigeration system. By studying of various research papers they found that compressor shows much higher exergy destruction as compared to rest of components of vapour compression refrigeration system and this exergy destruction can be minimized by using of nanofluid and nanolubricants in compressor.

Bolaji et al. [15] had done experimentally comparative analysis of R32, R152a and R134a refrigerants in vapour compression refrigerator. They reached to the conclusions that R32 shows lowest performance whereas R134a and R152a showing nearly same performance but best performance was obtained of system using R152a.

Ahamed et al. [16] had performed experimental investigation of domestic refrigerator with hydrocarbons (isobutene and butane) by energy and exergy analysis. They reached to the results that energy efficiency ratio of hydrocarbons comparable with R134a but exergy efficiency and sustainability index of hydrocarbons much higher than that of R134a at considered evaporator temperature. It was also found that compressors shows highest system defect (69%) among components of considered system.

Reddy et al. [17] performed numerical analysis of vapour compression refrigeration system using R134a, R143a, R152a, R404A, R410A, R502 and R507A and discussed the effect of evaporator temperature, degree of subcooling at condenser outlet, superheating of evaporator outlet, vapour liquid heat exchanger effectiveness and degree of condenser temperature on COP and exergetic efficiency. They reported that evaporator and condenser temperature have significant effect on both COP and exergetic efficiency and also found that R134a has the better performance while R407C has poor performance in all respect

Mastani Joybari et al. [18] performed experimental investigation on a domestic refrigerator originally manufactured to use of 145g of R134a.They concluded that exergetic defect occurred in compressor was highest as compare to other components and through their analysis it has been found that instead of 145g of R134a if 60g of R600a is used in the considered system gave same performance which ultimately result into economic advantages and reduce the risk of flammability of hydrocarbon refrigerants.

Anand and Tyagi [19] did detailed exergy analysis of 2TR window air conditioning test rig with R22 as working fluid and reached to the conclusions that irreversibility in system components will be highest when the system is 100% charged and lowest when 25% charged and irreversibility in compressor is highest among system components.

Selladurai and Saravanakumar[20]compared the performance between R134a and R290/R600a mixture on a domestic refrigerator which is originally designed to work with R134a and found that R290/R600a hydrocarbon mixture showed higher COP and exergetic efficiency than R134a. In their analysis highest irreversibility obtained in the compressor compare to condenser, expansion valve and evaporator.

Arora and Kaushik [21] developed numerical model of actual vapour compression refrigeration system with liquid vapour heat exchanger and did energy and exergy analysis on the same in the specific temperature range of evaporator and condenser. They concluded that R502 is the best refrigerant compare to R404A and R507A, compressor is the worst and liquid vapour heat exchanger is best component of the system.

Mishra [22] carried out detailed energy and exergy analysis of multi-evaporators at different temperatures with multiple compressors and multiple expansion valves in parallel and series with intercooler and flash chambers in the six type vapour compression refrigeration systems in terms of performance parameter for R410a, R290, R600, R600a, R1234yf, R502, R404a and R152a refrigerants and numerically computed thermal performances in terms of COP, exergy Destruction Ratio and exergetic efficiency for six systems and found that the first law and second law efficiency improved by 22% and found that the thermal performance in terms of first law efficiency (i.e. coefficient of performance) and Second law efficiency (i.e. exergetic efficiency) of six systems using R600 and R152a nearly matching same values under the accuracy of 5%. The worst component from the viewpoint of irreversibility is expansion valve followed by condenser, compressor and evaporators, respectively. The most efficient component is sub-cooler. The R-152a has least effciency defects for 313K condenser temperature. Similarly the increase in dead state temperature has a positive effect on energetic effciency and Exergy destruction ratio (EDR). The Exergy destruction ratio (EDR) decreases and exergetic efficiency increases with increase in dead state temperature. Both R-152a and R-600 show the identical trends for exergetic efficiency are nearly overlapping. The exergetic efficiency for R-600 is 0.40.5% higher than that of R-152a for the range of dead state temperature considered [22].

The above investigators did not go through:

The detailed irreversibility analysis or second law analysis of multiple evaporators systems with multi-stage expansion in vapour compression refrigeration systems and component's irreversibility and second law analysis of single and multi-stage vapour compression refrigeration systems.

Detailed theoretical analysis in terms of first law efficiency, second law efficiency, and exergy destruction of single and multiple stages vapour compression refrigeration systems using ecofriendly refrigerants using ecofriendly HFO refrigerants.

3. Results and Discussion

Table-1.1 to Table 8.2 show, the effect of different ecofriendly refrigerants of three stage vapour compression refrigeration

Table-1.1:Thermal performance of Three stage vapour compression refrigeration system using multiple Evaporators at different temperatures with single compressor and individual expansion valves and back pressure valves ($T_{_R1}$=263+5 (K),$T_{_R2}$=278+5 (K), $T_{_R3}$=283+5 (K), T_1=263K, , T_5=283K, T_5=278K,T_3=313K, $T_{_Ambient}$= 298KQ_{Eva2}=105kW, Q_{Eva1}=70kW,,Q_{Eva3}=35kW, $ETA_{_Comp1}$=0.8 , $ETA_{_Comp2}$=0.8, $ETA_{_Comp3}$=0.8)

Refrigerant	COP	EDR	$EFF_{_Second}$	$EDR_{_Rational}$	$Exergy_{_Fuel}$ kW	$Exergy_{_Product}$ kW	2nd Law Efficiency
R134a	3.582	1.84	0.2664	0.7336	39.8	10.41	0.3370
R1234yf	3.524	1.994	0.2536	0.7464	39.73	10.07	0.3227
R1234ze	3.616	2.02	0.2510	0.7490	38.72	9.717	0.3217
R227ea	3.448	2.246	0.2289	0.7711	40.6	9.293	0.2959
R236fa	3.606	2.335	0.2259	0.7741	38.82	8.768	0.2954
R245fa	3.742	2.102	0.2457	0.7543	37.45	9.201	0.3182

Table-1.2:Percentage Exergy Losses in the Components based on exergy of fuel of multiple Evaporators at different temperatures with single compressor and individual expansion valves and back pressure valves($T_{_R1}$=263+5 (K),$T_{_R2}$=278+5 (K), $T_{_R3}$=283+5 (K), T_1=263K, , T_5=283K, T_5=278K,T_3=313K, $T_{_Ambient}$= 298KQ_{Eva2}=105kW, Q_{Eva1}=70kW,,Q_{Eva3}=35kW, $ETA_{_Comp1}$=0.8 , $ETA_{_Comp2}$=0.8, $ETA_{_Comp3}$=0.8)

Refrigerant	% Exergy $Loss_{_Comp}$	% Exergy $Loss_{_Cond}$	% Exergy $Loss_{_Eva}$	% Exergy $Loss_{_Valve}$	% Exergy $Loss_{_Total}$	Rational Efficiency (%)
R134a	17.93	22.34	5.286	3.459	49.02	0.5009
R1234yf	18.49	22.03	5.169	3.609	49.3	0.5070
R1234ze	18.36	21.36	6.997	3.54	50.26	0.4974
R227ea	18.95	19.61	8.457	4.392	51.41	0.4859
R236fa	18.64	20.7	9.896	3.485	52.73	0.4727
R245fa	18.25	22.21	8.523	2.661	51.64	0.4836

Table-1.3 :Percentage Exergy Losses in the Components of multiple Evaporators at different temperatures with single compressor and individual expansion valves and back pressure valves($T_{_R1}$=263+5 (K),$T_{_R2}$=278+5 (K), $T_{_R3}$=283+5 (K), T_1=263K, , T_5=283K, T_5=278K,T_3=313K, $T_{_Ambient}$= 298KQ_{Eva2}=105kW, Q_{Eva1}=70kW,,Q_{Eva3}=35kW, $ETA_{_Comp1}$=0.8 , $ETA_{_Comp2}$=0.8, $ETA_{_Comp3}$=0.8)

Refrigerant	% Exergy Loss_Comp	% Exergy Loss_Cond	% Exergy Loss_Eva	% Exergy Loss_Valve	Second law Efficiency	Rational Efficiency (%)
R134a	36.58	45.58	10.78	7.056	0..5098	0.3370
R1234yf	37.5	44.69	10.58	7.32	0.507	0.3227
R1234ze	36.53	42.51	13.92	7.043	0.4974	0.3217
R227ea	36.86	38.15	16.45	8.544	0.4859	0.2959
R236fa	35.36	39.26	18.72	6.61	0.4727	0.2954
R245fa	35.34	43.0	16.5	5.154	0.4236	0.3182

System-2

Table-2.1: Thermal performance of Three stage vapour compression refrigeration system using multiple evaporators at different temperatures with compressor and individual expansion valves using $T_{_R1}$=263+5 (K),$T_{_R2}$=278+5 (K), $T_{_R3}$=283+5 (K) T_1=263K, T_5=283K, T_5=278K,T_3=313K,$T_{_Ambient}$= 298KQ_{Eva2}=105kW, Q_{Eva1}=70kW, Q_{Eva3}=35kW, $ETA_{_Comp1}$=0.8, $ETA_{_Comp2}$=0.8 $ETA_{_Comp3}$=0.8

Refrigerant	COP	EDR	EFF_Second	EDR_Rational	Exergy_Fuel kW	Exergy_Product kW	2nd Law Efficiency
R134a	4.033	1.13	0.3203	0.6797	52.07	16.68	0.5367
R1234yf	3.84	2.278	0.3051	0.6949	54.67	16.68	0.5112
R1234ze	4.009	2.14	0.3184	0.6816	52.38	16.68	0.5336
R227ea	3.657	2.443	0.2904	0.7096	51.43	16.68	0.4866
R236fa	3.956	2.183	0.3142	0.6858	53.03	16.68	0.5265
R245fa	4.233	1.973	0.336	0.664	49.61	16.68	0.5633

Table-2.2:Percentage Exergy Losses in the Components based on exergy of fuel of Three stage vapour compression refrigeration system using multiple evaporators at different temperatures with compressor and individual expansion valves $T_{_R1}$=263+5 (K),$T_{_R2}$=278+5 (K), $T_{_R3}$=283+5 (K) T_1=263K, T_5=283K, T_5=278K,T_3=313K, $T_{_Ambient}$= 298K, Q_{Eva2}=105kW,, Q_{Eva1}=70kW,, Q_{Eva3}=35kW, $ETA_{_Comp1}$= $ETA_{_Comp2}$= $ETA_{_Comp3}$=0.8

Refrigerant	% Exergy Loss_Comp	% Exergy Loss_Cond	% Exergy Loss_Eva	% Exergy Loss_Valve	% Exergy Loss_Total	Rational Efficiency (%)
R134a	19.47	24.41	8.0	15.98	67.87	0.3213
R1234yf	19.71	25.81	6.428	18.17	69.49	0.3051
R1234ze	20.06	24.06	7.604	16.73	64.14	0.3186
R227ea	19.78	22.78	7.077	21.32	70.96	0.2904
R236fa	19.78	23.75	7.881	17.16	68.58	0.3142
R245fa	19.71	24.93	8.394	13.32	66.34	0.336

Table 2.3: Percentage Exergy Losses in the Components of Three stage vapour compression refrigeration system using multiple evaporators at different temperatures with compressor and individual expansion valves

Refrigerant	% Exergy Loss_Comp	% Exergy Loss_Cond	% Exergy Loss_Eva	% Exergy Loss_Valve	EDR	EFF_Second
R134a	28.69	35.97	11.8	23.95	1.13	0.3203
R1234yf	28.37	36.23	9.25	26.15	2.278	0.3051
R1234ze	28.97	35.31	11.8	23.95	2.14	0.3184
R227ea	27.88	32.1	9.973	30.04	2.443	0.2904
R236fa	28.84	34.64	11.49	25.03	2.183	0.3142
R245fa	29.7	37.51	12.65	20.07	1.973	0.336

Table-3.1:Thermal performance of Three stage vapour compression refrigeration system using multiple evaporators at different temperatures with single compressor and multiple expansion valves and back pressure valves for T_1=263K, T_5=283K, T_5=278K,T_3=313K, $T_{Ambient}$= 298K Q_{Eva1}=105kW,, Q_{Eva2}=70kW,, Q_{Eva3}=35kW, ETA_{Comp}=0.8

Refrigerant	COP	EDR	EFF_{Second}	$EDR_{Rational}$	$Exergy_{Fuel}$ kW	$Exergy_{Product}$ kW
R134a	3.579	1.747	0.2997	0.7003	58.68	17.59
R1234yf	3.509	1.842	0.2859	0.7141	59.85	17.11
R1234ze	3.603	1.846	0.2882	0.7118	58.28	16.8
R227ea	3.419	2.088	0.2618	0.7382	61.41	16.08
R236fa	3.582	2.074	0.2667	0.7333	58.62	15.64
R245fa	3.727	1.871	0.2890	0.711	56.35	16.28

Table-3.2:Percentage Exergy Losses in the Components based on exergy of fuel of Three stage vapour compression refrigeration system using multiple evaporators at different temperatures with single compressor and multiple expansion valves and back pressure valves for T_1=263K, T_5=283K, T_5=278K,T_3=313K, $T_{Ambient}$= 298K, Q_{Eva1}=105kW,, Q_{Eva2}=70kW,, Q_{Eva3}=35kW, ETA_{Comp}=0.8

Refrigerant	% Exergy $Loss_{Comp}$	% Exergy $Loss_{Cond}$	% Exergy $Loss_{Eva}$	% Exergy $Loss_{Valve}$	% Exergy $Loss_{Total}$
R134a	18.06	21.96	8.462	3.825	52.36
R1234yf	18.62	21.71	8.317	4.015	52.67
R1234ze	18.51	20.99	9.74	3.968	53,208
R227ea	19.03	19.35	11.37	4.915	54.66
R236fa	18.83	20.35	12.23	3.916	55.33
R245fa	18.42	21.81	10.84	3.00	54.07

Table-3.3: Percentage Exergy Losses in the Components of Three stage vapour compression refrigeration system using multiple evaporators at different temperatures with single compressor and multiple expansion valves and back pressure valves

Refrigerant	% Exergy $Loss_{Comp}$	% Exergy $Loss_{Cond}$	% Exergy $Loss_{Eva}$	% Exergy $Loss_{Valve}$
R134a	34.49	41.94	16.16	7.402
R1234yf	35.36	41.22	15.79	7.624
R1234ze	34.79	39.45	18.3	7.457
R227ea	34.81	35.4	20.79	8.991
R236fa	34.04	36.78	22.11	7.078
R245fa	*34.07*	*40.33*	*20.04*	*5.554*

Table-4.1: Thermal performance of three stage vapour compression refrigeration system using multiple evaporators at different temperatures individual compressors and individual expansion valves

Refrigerant	COP	EDR	EFF_{Second}	$EDR_{Rational}$	$Exergy_{Fuel}$ kW	$Exergy_{Product}$ kW
R134a	4.399	2.264	0.3062	0.6938	47.74	14.62
R1234yf	4.204	2.418	0.2926	0.7074	49.96	14.62
R1234ze	4.379	2.281	0.3038	0.6962	47.95	14.62
R227ea	4.018	2.575	0.2797	0.7203	52.26	14.62
R236fa	4,329	2.319	0.3013	0.6083	48.51	14.62
R245fa	4.612	2,114	0.3210	0.6790	45.53	14.62

Table-4.2:Percentage Exergy Losses in the Components based on exergy of fuel of Three stage vapour compression refrigeration system using multiple evaporators at different temperatures individual compressors and individual expansion valves

Refrigerant	% Exergy $Loss_{Comp}$	% Exergy $Loss_{Cond}$	% Exergy $Loss_{Eva}$	% Exergy $Loss_{Valve}$
R134a	19.35	26.18	8.572	15.2
R1234yf	19.59	27.06	6.854	17.24
R1234ze	19.63	25.84	8.178	17.24
R227ea	19.66	24.55	7.622	20.20
R236fa	19.65	25.54	8.465	16.21
R245fa	19.59	26.74	8.996	12.54

Table-4.3: Percentage Exergy Losses in the Components of Three stage vapour compression refrigeration system using multiple evaporators at different temperatures individual compressors and individual expansion valves

Refrigerant	% Exergy Loss_Comp	% Exergy Loss_Cond	% Exergy Loss_Eva	% Exergy Loss_Valve
R134a	27.92	37.78	12.37	21.93
R1234yf	27.69	38.25	9.69	24.36
R1234ze	28.23	37.17	11.76	22.83
R227ea	27.29	34.08	10.58	28.05
R236fa	28.13	36.55	12.12	23.2
R245fa	28.87	39.4	13.26	18.48

Table-4.4: Percentage Exergy Losses in the Compressors of Three stage vapour compression refrigeration system using multiple evaporators at different temperatures individual compressors and individual expansion valves

Refrigerant	Power (kW) Required_Comp1	Power (kW) Required_Comp2	Power (kW) Required_Comp3	Total Power Required/ Exergy_Fuel kW	% Exergy Loss_comp
R134a	7.265	5.484	34.99	47.74	27.92
R1234yf	7.863	5.824	36.27	49.96	27.69
R1234ze	7.422	5.544	34.99	47.95	28.23
R227ea	8.571	6.182	37.51	52.26	27.29
R236fa	7.661	5.658	35.19	48.51	28.13
R245fa	5.213	6.905	33.41	45.53	28.87

Table-5.1:Thermal performance of Three stage vapour compression refrigeration system using multiple evaporators at different temperatures with individual compressors and multiple expansion valves

Refrigerant	COP	EDR	EFF_Second	Exergy_Fuel kW	Exergy_Product kW	2nd Law Efficiency
R134a	4.877	1.824	0.3674	42.81	15.82	0.5460
R1234yf	4.815	1.866	0.3627	43.71	15.82	0.539
R1234ze	4.908	1.816	0.3697	42.69	15.82	0.5403
R227ea	4.744	1.935	0.3574	44.77	15.82	0.5311
R236fa	4.895	1.837	0.3688	42.93	15.82	0.548
R245fa	5.023	1.749	0.3784	41.42	15.82	0.5623

Table-5.2:Percentage Exergy Losses in the Components based on exergy of fuel of Three stage vapour compression refrigeration system using multiple evaporators at different temperatures with individual compressors and multiple expansion valves

Refrigerant	% Exergy Loss_Comp	% Exergy Loss_Cond	% Exergy Loss_Eva	% Exergy Loss_Valve	% Exergy Loss_Total
R134a	18.59	26.57	15.47	6.386	67.01
R1234yf	18.97	27.36	14.46	6.892	67.68
R1234ze	19.0	26.04	15.51	6.599	67.15
R227ea	19.02	24.97	16.73	8.431	69.15
R236fa	19.04	25.76	16.33	6.624	67.75
R245fa	18.98	26.8	15.38	5.013	66.17

Table-5.3: Percentage Exergy Losses in the Components of three stage vapour compression refrigeration system using multiple evaporators at different temperatures with individual compressors and multiple expansion valves

Refrigerant	% Exergy Loss_Comp	% Exergy Loss_Cond	% Exergy Loss_Eva	% Exergy Loss_Valve
R134a	27.75	39.65	23.08	9.529
R1234yf	28.03	40.42	21.37	10.18
R1234ze	28.3	38.78	23.1	9.828
R227ea	27.51	36.11	24.2	12.19
R236fa	28.1	38.02	24.1	9.776
R245fa	28.68	40.5	23.24	9.577

Table-6.1: Thermal performance of three stage vapour compression refrigeration system using multiple evaporators at different temperatures individual compressors and multiple expansion valves

Refrigerant	COP	EDR	EFF_{Second}	$Exergy_{Fuel}$ kW	$Exergy_{Product}$ kW	2^{nd} Law Efficiency
R134a	4.905	1.867	0.3414	42.81	14.62	0.3626
R1234yf	4.804	1.915	0.3344	43.71	14.62	0.3598
R1234ze	4.919	1.858	0.3424	42.69	14.62	0.3639
R227ea	4.69	1.98	0.3265	44.77	14.62	0.3536
R236fa	4.892	1.878	0.3405	42.93	14.62	0.3601
R245fa	5.070	1.791	0.3529	41.42	14.62	

Table-6.2:Percentage Exergy Losses in the Components based on exergy of fuel of Three stage vapour compression refrigeration system using multiple evaporators at different temperatures individual compressors and multiple expansion valves

Refrigerant	% Exergy $Loss_{Comp}$	% Exergy $Loss_{Cond}$	% Exergy $Loss_{Eva}$	% Exergy $Loss_{Valve}$	% Exergy $Loss_{Total}$
R134a	18.57	26.73	8.881	9.559	63.86
R1234yf	18.97	27.31	7.834	9.914	64.02
R1234ze	18.99	26.10	9.186	9.33	63.61
R227ea	19.02	24.74	8.897	11.99	64.64
R236fa	19.04	25.75	9.56	9.533	63.93
R245fa	18.96	27.02	9.889	7.34	63.21

Table-6.3: Percentage Exergy Losses in the Components of Three stage vapour compression refrigeration system using multiple evaporators at different temperatures individual compressors and multiple expansion valves

Refrigerant	% Exergy $Loss_{Comp}$	% Exergy $Loss_{Cond}$	% Exergy $Loss_{Eva}$	% Exergy $Loss_{Valve}$
R134a	29.14	41.93	12.37	13.93
R1234yf	29.62	42.66	12.24	15.48
R1234ze	29.86	41.03	14.44	14.67
R227ea	29.43	38.27	13.74	18.54
R236fa	29.79	40.28	14.97	14.97
R245fa	30.0	42.74	15.64	11.61

Table-6.4: Percentage Exergy Losses in the Compressors of three stage vapour compression refrigeration system using multiple evaporators at different temperatures individual compressors and multiple expansion valves

Refrigerant	Power (kW) $Required_{Comp1}$	Power (kW) $Required_{Comp2}$	Power (kW) $Required_{Comp3}$	Total Power Required/ $Exergy_{Fuel}$ kW	% Exergy $Loss_{comp}$
R134a	19.6	18.2	5.0	42.81	29.14
R1234yf	20.19	18.47	5.052	49.96	29.62
R1234ze	19.62	18.1	4.966	47.95	29.86
R227ea	20.92	18.75	5.102	52.26	29.43
R236fa	19.84	18.13	4.96	48.51	29.79
R245fa	18.92	17.64	4.855	41.42	30.0

Table-7.1:Thermal performance of Three stage vapour compression refrigeration system using multiple evaporators at different temperatures with individual compressors and multiple expansion valves

Refrigerant	COP	EDR	EFF_{Second}	$EDR_{Rational}$	$Exergy_{Fuel}$ kW	$Exergy_{Product}$ kW	2^{nd} Law Efficiency
R134a	5.173	1.825	0.3601	0.6399	40.59	14.62	0.6968
R1234yf	5.127	1.848	0.3589	0.6411	40.96	14.62	0.6824
R1234ze	5.213	1.81	0.3628	0.6372	40.29	14.62	0.6937
R227ea	5.072	1.898	0.3530	0.6470	41.4	14.62	0.6750
R236fa	5.207	1.824	0.3624	0.6376	40.33	14.62	0.693
R245fa	5.318	1.758	0.3702	0.6298	39.49	14.62	0.7078

Table-7.2:Percentage Exergy Losses in the Components based on exergy of fuel of Three stage vapour compression refrigeration system using multiple evaporators at different temperatures with individual compressorsand multiple expansion valves

Refrigerant	% Exergy Loss_Comp	% Exergy Loss_Cond	% Exergy Loss_Eva	% Exergy Loss_Valve	% Exergy Loss_Total	Rational Efficiency (%)
R134a	18.59	27.88	14.02	5.219	65.7	0.3430
R1234yf	18.97	28.83	12.69	8.301	65.96	0.3404
R1234ze	19.0	27.39	13.95	5.337	65.67	0.3433
R227ea	19.02	26.4	14.83	6.765	67.01	0.3299
R236fa	19.04	27.13	14.68	5,273	66.12	0.3388
R245fa	18.97	28.11	14.04	3.698	65.09	0.3491

Table-7.3: Percentage Exergy Losses in the Components of three stage vapour compression refrigeration system using multiple evaporators at different temperatures with individual compressors and multiple expansion valves

Refrigerant	% Exergy Loss_Comp	% Exergy Loss_Cond	% Exergy Loss_Eva	% Exergy Loss_Valve	Rational Efficiency (%)
R134a	28,3	42.23	21.33	7.943	0.3430
R1234yf	28.76	43.7	19.24	8.30	0.3404
R1234ze	28.93	41.7	22.24	8.127	0.3433
R227ea	28.38	39.4	22.12	6.765	0.3299
R236fa	28.8	41.03	22.2	7.976	0.3388
R245fa	29.15	43.19	21.57	6.096	0.3491

Table-7.4: Percentage Exergy Losses in the Compressors of Three stage vapour compression refrigeration system using multiple evaporators at different temperatures with individual compressors and multiple expansion valves

Refrigerant	Power (kW) Required_Comp1	Power (kW) Required_Comp2	Power (kW) Required_Comp3	Total Power Required/ Exergy_Fuel kW	% Exergy Loss_comp
R134a	15.92	15.86	8.817	40.59	28.3
R1234yf	15.69	15.65	9.614	40.96	28.76
R1234ze	15.64	15.62	8.192	40.29	28.93
R227ea	15.51	15.49	10.4	41.4	28.38
R236fa	15.57	15.52	9.24	40.33	28.8
R245fa	15.68	15.61	8.192	39.49	29.15

Table-8.1:Thermal performance of three stage vapour compression refrigeration system using multiple evaporators at different temperatures with compound compression and multiple expansion valves and flash intercoolers (system-6)

Refrigerant	COP	EDR	EFF_Second	EDR_Rational	Exergy_Fuel kW	Exergy_Product kW	2nd Law Efficiency
R134a	4.465	1.82	0.3547	0.6453	47.03	16.68	0.5943
R1234yf	4.361	1.887	0.3464	0.6436	48.5	16.68	0.5804
R1234ze	4.473	1.815	0.3552	0.6548	46.95	16.68	0.5952
R227ea	4.248	1.964	0.3374	0.6426	49.44	16.68	0.5653
R236fa	4,443	1.834	0.3529	0.6471	47.27	16.68	0.5912
R245fa	4.620	1.725	0.3669	0.6331	45.46	16.68	0.6148

Table-8.2: Percentage Exergy Losses in the Components three stage vapour compression refrigeration system using multiple evaporators at different temperatures with compound compression and multiple expansion valves and flash intercoolers

Refrigerant	% Exergy Loss_Comp	% Exergy Loss_Cond	% Exergy Loss_Eva	% Exergy Loss_Valve	% Exergy Loss_Subcooler	% Exergy Loss_Total	Rational Efficiency (%)
R134a	19.41	24.41	8.121	10.47	1.994	64.53	35.47
R1234yf	19.71	25.20	6.456	11.66	2.36	65.36	34.64
R1234ze	19.74	24.08	7.696	10.96	2.0	64.48	35.52
R227ea	19.78	24.84	7.227	13.92	2.48	66.26	33.74
R236fa	19.78	24.79	8.030	8.03	1.87	64.71	35.29
R245fa	19.71	24.94	8.513	8.513	1.40	63.31	36.69

system using multiple evaporators at different temperatures with single compressor and individual expansion valves and back pressure valves and it was observed that first law performance in terms of coefficient of performance (COP) of HFO-1234ze is better than HFC -134a refrigerant but higher than another HFO-1234yf refrigerant. While COP of R236fa is slightly lower than R1234ze but higher than HFC-134a. However, the COP of R245fa is highest. Similarly second law efficiency of of Three stage vapour compression refrigeration system using multiple evaporators at different temperatures with single compressor and individual expansion valves and back pressure valves is highest by using HFC-134a which gives the exergy destruction ratio based on exergy of product is lowest in case of HFC-134a . However, the second law efficiency in terms of exergetic efficiency using HFO-1234yf refrigerant is slightly less than HFC 134a and higher than HFO-1234ze. The exergy destruction ratio (based on exergy of fuel which meant the total power required to run the system) is highest for R236fa because exergetic efficiency of system using R236fa is lowest. Similarly exergy of fuel in terms of the total power required to run the system is lowest by using HFC-134a. The power consumption using R227ea is higher and lower by using R245fa . The exergy of product is higher by using R134a and slight lower by using HFO-1234yf refrigerant. The percentage exergy losses using similar trens with minor variation nealy in the all components of vapour compression refrigeration systems. The exergy losses based on the total exergy destruction is computed Three stage vapour compression refrigeration system using multiple evaporators at different temperatures with single compressor and individual expansion valves and back pressure valves is shown in table-1(b) -1(c) respectively. It was found that percentage exergy losses in the compressor using ecofriendly R227ea refrigerant is more than while the using ecofriendly R245fa refrigerant. Similarly for low GWP and zero ODP HFO refrigerants using R 1234yf is 18.49% while using R1234ze is 18.36% as compared to HFC R134a is 17.93 %. The maximum exergy destruction is found in condenser is 22.34% by using HFC-134a refrigerant while by using R1234yf is 22.03% and slightly higher than HFO-1234yf. The percentage exergy losses in the various system are shown in Table-1(b)-1(c) respectively. Similar trend is found in Table-1(c) where % exergy destruction in the component based on total exergy destruction in all components of the system have been observed. Table- 9 shows the comparison between developed model and data [20] taken from reference for assuming 80% compressor efficiencies, . And it was found that thermal models developed gives similar results under the limits to validates our model as shown in Table-9

Table9: Comparison between developed model and data [22]

S.No.	Parameters	Ref [24].	(Developed Model)
1	COP	4.465	4.465
2	W_Comp	49.9 kW	47. 3kW

To improve thermal performance of vapour compression refrigeration systems (both single and multiple evaporator system) by improving:

First law efficiency

According to first law of thermodynamic energetic efficiency /COP is defined as the ratio of net refrigeration effect to the per unit power consumed. First law analysis restricted to calculate only coefficient of performance of the systems. Detailed theoretical analysis in terms of first law efficiency, second law efficiency, and exergy destruction of single and multiple stages vapour compression refrigeration systems using ecofriendly refrigerants.

Second law efficiency

The concept of exergy was given by second law of thermodynamics. Second law efficiency is the exergy of the heat abstracted in to the evaporators from the space to be cooled and exergy of fuel is actual compressor work input. Effect of subcooling on first law efficiency, second law efficiency and irreversibility of each component of both systems (single and multi-stage) vapour compression refrigeration systems.

4. Conclusion

The following conclusions were drawn

(i) The increase in COP decreases EDR and increases exergetic efficiency.
(ii) The subcooling increases refrigeration capacity.
(iii) The subcooling has no effect on compressor work.
(iv) COP and exergetic efficiency are almost same for considered eco-refrigerants as compared with R-12 refrigerant.
(v) Both COP and EDR will decrease with increase in condenser temperature.
(vi) EDR increase with increase in condenser temperature.

The exergetic (rational) efficiency increases with increase in condenser temperature for 273K temperature of all evaporators with 5K degree of subcooling.

References

[1] S.Kumar, M.Prevost, R.Bugarel- Exergy analysis of a vapour compression refrigeration system. Heat Recovery Systems & CHP.1989;9:151-157
[2] C. Nikolaidis, D. Probert-Exergy method analysis of a two-stage vapour-compression refrigeration-plants performance. Int J Applied Thermal Engineering.1998; 60:241-256.
[3] RecepYumrutas, Mehmet Kunduz, Mehmet Kanoglu-Exergy analysis of vapor compression refrigeration systems. Exergy, An International Journal.2002; 2:266-272.
[4] E. Halimic, D. Ross, B. Agnew, A. Anderson, I. Potts. A comparison of the operating performance of alternative refrigerants. Int J Applied Thermal Engineering.2003; 23:1441-1451

[5] Yongmei Xuan, Guangming Chen. Experimental study on HFC-161 mixture as an alternative refrigerant to R502. Int J Refrigeration. Article in Press.
[6] R. Cabello, J. Navarro-Esbrı, R. Llopis, E. Torrella. Analysis of the variation mechanism in the main energetic parameters in a single-stage vapour compression plant. Int J Applied Thermal Engineering.2007; 27:167-176.
[7] Mark W. Spatz, Samuel F. Yana Motta. An evaluation of options for replacing HCFC-22 in medium temperature refrigeration systems. Int J Refrigeration.2004; 27:475-483.
[8] X.H. Han, Q. Wang, Z.W. Zhu, G.M. Chen. Cycle performance study on R32/R125/R161 as an alternative refrigerant to R407C. Int J Applied Thermal Engineering.2007; 27:2559-2565.
[9] R.Cabello a, E.Torrella b, J.Navarro-Esbr. Experimental evaluation of a vapour compression plant performance using R134a, R407C and R22 as working fluids. Int J Applied Thermal Engineering.2004; 24:1905-1917.
[10] M. Mohanraj, S. Jayaraj, C. Muraleedharan, P. Chandrasekar.Experimental investigation of R290/R600a mixture as an alternative to R134a in a domestic refrigerator. Int J Thermal Sciences.2009; 48:1036-1042.
[11] H.M Getu, P.K Bansal. Thermodynamic analysis of an R744-R717 cascade refrigeration system. Int J Refrigeration.2008; 31:45-54.
[12] M. Padilla, R. Revellin, J. Bonjour. Exergy analysis of R413A as replacement of R12 in a domestic refrigeration system. Int J Energy Conversion and Management.2010; 51:2195-2201.
[13] Camelia Stanciu, Adina Gheorghian, Dorin Stanciu, Alexandru Dobrovicescu- Exergy analysis and refrigerant effect on the operation and performance lomits of a one stage vapour compression refrigeration system.Termotehnica.2011;1:36-42.
[14] J.U. Ahamed, R.Saidur, H.H.Masjuki. A review on exergy analysis of vapor compression refrigeration system. Int J Renewable and sustainable energy reviews.2011; 15:1593-1600.
[15] B.O. Bolaji, M.A. Akintunde, T.O. Falade. Comparative analysis of performance of three ozone-friends HFC refrigerants in a vapor compression refrigerator. Int J Sustainable Energy & Environment.2011; 2:61-64.
[16] J.U. Ahamed, R.Saidur, H.H.Masjuki. A review on exergy analysis of vapor compression refrigeration system. Int J Renewable and sustainable energy reviews.2011; 15:1593-1600.
[17] V. Siva Reddy, N.L Panwar, S.C Kaushik-Exergy analysis of a vapour compression refrigeration system with R134a,R143a,R152a,R404A,R407C,R410A,R502 and R507A.Clean Techn Environ Policy.2012;14:47-53.
[18] MahmoodMastaniJoybari,MohammadSadeghHatamipour, Amir Rahimi, FatemehGhadiriModarres- Exergy analysis and optimization of R600a as a replacement of R134a in a domestic refrigerator system. International Journal of refrigeration.2013; 36:1233-1242.
[19] S.Anand ,S.KTyagi-Exergy analysis and experimental study of a vapour compression refrigeration cycle.Int J Therm Anal Calorim.2012; 110:961-971.
[20] R.Saravanakumar, V.Selladurai-Exergy analysis of a domestic refrigerator using eco-friendly R290/R600a refrigerant mixture as an alternative to R134a.Int J Therm Anal Calorim.2013;
[21] AkhileshArora, S.C. Kaushik. Theoretical analysis of a vapour compression refrigeration system with R502, R404A and R507A. Int J Refrigeration.2008; 31:998-1005.
[22] R.S. Mishra Journal of Multi Disciplinary Engineering Technologies Volume 7 No.2 ,July-Dec., 2013.

International Journal of Research in Engineering and Innovation (IJREI)
journal home page: http://www.ijrei.com
ISSN (Online): 2456-6934

Thermodynamic analysis of modified rankine cycle used for power generation

R.S. Mishra, Manish Kumar

Department of Mechanical Engineering, Delhi Technological University, Bawana Road, Delhi, India

Abstract

In this study the modified Organic Rankine Cycle focuses the performance of Internal Heat Exchanger (IHE) in ORC (Organic Rankine Cycle) systems. Although previous studies hold multitudinous opinions, this study gives clear statements of IHE is both subcritical and supercritical ORC systems by setting a new model taking pressure drop in loops and pinch point into consideration. Commonly used working fluids R123 and R245fa are chosen for subcritical and R600 for supercritical cases. The temperature of the heat source applied is 200 ºC and the mass flow rate of it is 1kg/s. A modified method of calculating maximum heat exchange in the international heat exchanger (IHE). The results provides that IHE is beneficial to a subcritical case. © 2018 ijrei.com. All rights reserved
Keywords: Modified Rankine Cycle, Thermodynamic Analysis

1. Introduction

Energy security, economic development and environment protection are not well balanced today and the energy demand is still closely connected to the economic growth. At the same time, the increasing consumption of fossil fuels has led to more and more environment problems such as global warming, ozone depletion and atmospheric pollution. Fossil fuels still play the dominant role in energy resources worldwide, accounting for 77% of the increasing energy demand 2007-2030 (IEA, 2009). Furthermore, along with the fast Development of industry, energy shortages and blackouts have appeared more and more frequently all over the world. Due to all these reasons, utilizing low-grade waste heat for energy production has attracted more and more attention for its potential in reducing the fossil fuel consumption.

The most commonly investigated in low-grade heat source and waste heat utilizations today are Organic Rankine Cycles (ORCs) and Kalinga cycle (binary fluids and fluid mixtures). When utilizing low grade waste heat, the traditional steam Rankine cycle does not give satisfactory performance due to its low thermal efficiency and large volume flows; and thus so called Organic Rankine cycle (ORCs) have been proposed. These cycle use organic substances as working fluid system consist of at least five major comparison with the CO2 process later, a regenerator is also included in the current calculation. According to waste heat recovery report by U.S. DOE, industrial processes in the United States consumes approximately 35 quadrillion VTU (Quads) of energy per year (BCS Inc., 2008). This amount is about 30% of total energy consumed in the United States. This report categorizes the waste heat based on the temperature of the waste products. The three waste heat groups are: low, medium, high temperature. Table 1 also shows of waste heat and work potential of each waste heat group (BCS Inc., 2008). The waste heat and work potential is based on the reference temperature of

Table 1: Yearly National Unrecovered Heat

	Temperature		Waste Heat (trillion BTU per year)		Work Potential (trillion BTU per year) 770F [25ºC] Ref [2]
	0F	0C	770F [25ºC] Ref [2]	3000F[150ºC] Ref [2]	
Low	< 450	<230	903	37	287
Med	450-1200	230-650	466	130	216
High	>1200	>650	108	89	86
Total	-	-	1478	256	589

Corresponding author: R.S. Mishra
Email Id: hod.mechanical.rsm@dtu.ac.in

This data indicates that low temperature heat source results in 60% of total waste heat source. It is estimated that 290 trillion BTU per year or 33% of this low temperature heat can be recaptured into useful works. Low temperature heat source recovery presents the largest opportunity to recover among other discarded heat.

2. Organic Rankine Cycle

Organic Rankine Cycle cane generate power from natural and waste heat sources such as geothermal sources, biomass, solar radiation and waste heat coming from industrial processes and fuel consumption, solar radiation etc. Therefore, it is considered an important and promising method of renewable energy production process. The organic Rankine cycle uses an organic substance as a working fluid as is implied by the word "organic". In organic Rankine cycle power system, the working fluid selected should maximize the thermal efficiency considering the heat source and long term performance temperature range. The temperature range is from~100ºC to about ~ 350ºC.Rankine cycle gives the highest efficiency when low temperature heat is converted into electricity. The waste heat coming from combustion engines and processes in industries: hot exhaust gases coming from blast furnaces in steel industry and from the kilns in ceramic industry, exhaust gases coming from the engines and turbines, hot liquids that are used to cool kilns and furnaces etc. The organic rankine cycle uses organic fluid as working fluid instead of water. Organic Rankine Cycle is used for establishment of many commercial plants and test plants. The refrigerants that are used most commonly in ORC include R123, R600, R11, R114 etc. These days the interest is focused on new refrigerants like R1234yf, R1234ze etc. The net output, first and second law efficiency are the indicators of system performance besides the working fluid properties. As far as maximum pressure is concerned, the ORC can be subcritical or supercritical. The cycles can be employed with internal heat exchanger or without IHE. Certain discussions are continuing with some reports station that exergy efficiency and power output stays unchanged while some stating thermal efficiency rises but output is stationary. It is also stated that induction of IHE greatly reduces expansion ratio, evaporation pressure being below a certain limit. Rankine Cycle gives the best efficiency and power output with an organic fluid as a working fluid instead of water when waste heat at moderate inlet temperature is used as a heat source. This is attributed to the fact that the specific vaporization heat of water is much higher than organic fluids. Thus, the heat source fluid that is to be cooled is followed better by the organic working fluid. In the ORC process more electric power can be generated from a heat source as the exhaust gas is cooled to a lower temperature.

2.1 Working Fluids

The following working fluids in this study: R123, R600, HFO-1234yf, HFC-134a, HFC-245fa, iso-pentane. Many researchers investigated these working fluids and are representative working fluids that are used in ORC, Not only HFC-134a is used but also HFC-245fa and iso-pentane are used in ORC to recover low heat from the industrial plants.
Ethanol performs very well at medium temperature levels i.e. 200-300ºC hence, it is also recently being used as automotive ORC working fluid. The evaporation temperature of organic substances is relatively lower as compare to steam, this being the main reason and advantage of using them as working fluid in ORC. The low evaporation temperature makes it possible for them to vaporize or superheat by low or medium temperature heat sources. In addition to this, the expander life can be extended by using the organic substances which are categorized as dry or isentropic fluids. Under the saturated or superheated vapour conditions, the vapour that is expanded inside the expander tends to be dry. The major focus today is kept on the subcritical cycle, but some of the research on supercritical cycle employing heat exchanger has also been done. The goal of this study is to find the essential effects of internal heat exchanger on the subcritical as well as supercritical organic rankine cycle. The performance evaluation parameters consists of net power output, thermal efficiency and also the exergy efficiency.The study analyses the subcritical and supercritical model separately and for locating the pinch point and calculating hot stream outlet temperature, a nested iteration method is proposed. It is found in the conclusion that the system performance is promoted by internal heat exchanger in subcritical case whereas in supercritical cases the internal heat exchanger's effects are dependent on a certain evaporation pressure.

2.2 Saturated Cycle Model

It is the most basic cycle that can achieve a compact system design relative to acceptable thermal efficiency when recovering low temperature waste heat.
The T-S diagram of the cycle in the Fig 1.2. The working fluid in the evaporator at a constant pressure after isentropic pumping until it becomes saturated vapor which is then followed by isentropic expansion process.
Depending on the working fluid, the phase condition of working fluid during the expansion process goes two-phase mixture for wet fluids, goes to superheated state for dry fluids and becomes saturated vapour for isentropic fluid. After the expansion process, isobaric condensation takes place in the condenser, which return fluid to saturated liquid state.

2.3 Trilateral Cycle Model

It is a simple cycle as compare to conventional binary cycle, its performance is more competitive for low temperature heat sources, especially when a proper two phase expander is employed. Furthermore, it has a lower operational cost for equivalent sized components.
This cycle consists of two features, first being that the working fluid temperature profile tends to match the heat source temperature profile perfectly and the second one is that it operates at reasonable pressure. The schematic diagram is

shown in the Figure 1.3. The pumping pressure which is theoretically same as evaporation pressure lies below the critical pressure of working fluid, and the temperature at expander inlet is maintained at a target saturated temperature.
The cycle consists of isentropic state of working fluid followed by isobaric heating of the working fluid to the bubble point. Isentropic expansion of working fluid to a two phase mixture is then induces and finally an isobaric condensation occurs to return the two phase mixture back to a liquid state.
The primary difference between natural and conventional cycle is that the working fluid remains a liquid as it leaves the evaporator and the fluid expansion through expander occurs within the two-phase range.

2.4 Superheated Cycle Model

As compared to trilateral and saturated cycle, the superheated cycle allows more heat to enter the ORC system and changes the working fluid state to superheated state. In some cases, the superheated cycle results in higher thermal efficiency than that of saturated cycle.
After the isentropic pumping process, heating process takes place until the working fluid phase changes to superheated state, the temperature being higher than saturated vapour state, the pressure level being kept the same. As the higher expander inlet temperature results in higher power production therefore the temperature is kept higher than the critical temperature at the expander inlet. The working fluid then passes through the expander with isentropic expansion and then condenses to saturated liquid at constant pressure.

2.5 Subcritical Cycle Model

The subcritical cycle have almost operational condition as in superheated cycle, however, the pumping pressure is kept higher than the pressure used for the superheated cycle but slightly lower than the critical pressure.
The T-S diagram is shown in the Figure 1.5 which looks like the superheated cycle. The processes involve isentropic pumping followed by isobaric heating, isentropic expansion and finally isobaric condensation. The expander inlet temperature is kept higher than the critical temperature of working fluid after the expansion process in this cycle.

2.6 Supercritical Cycle Model

In the supercritical Cycle, the expander inlet conditions i.e. pressure and temperature are kept higher than the critical point of working fluid. The main advantage of the cycle is that the hot source temperature can be raised to a higher level that cannot be reached in other cycles.
Serrano et al. [1], did the theoretical investigation and has suggested the feasibility of introducing a waste heat recovery system in two stage turbocharged HDD engine. The WHR is attained by introducing a Rankine cycle, which uses an organic substance or directly water as working fluid depending on energetic performance considerations. They also suggested an alternative for improving the overall thermal efficiency of Diesel engine consists of recovering the energy lost by means of a waste heat recovery (WHR) system. These solutions are based on adapting one of the turbochargers by removing its turbine and trying to recover the energy by Rankine cycle. Finally, the turbine of the rankine cycle supplies the recovered energy directly to the compressor of this turbocharger.
J. et al. [3] suggested the method for customizing an organic rankine cycle to a complex heat source for efficient energy conversion, demonstrated on a Fischer Tropsch plant. Organic Rankine Cycle provide an alternative to traditional steam rankine cycle for the conversion of low grade heat source into power, where conventional steam power cycle is known to be inefficient. A large processing plant often has multiple low temperatures waste heat source available for conversion to electricity by a low temperature cycle, resulting in composite heat source with a complex temperature-enthalpy profile. Organic fluids are modeled using a pure substance database. The pinch analysis technique of forming composite curve is applied to analyze the effect of each building block on the temperature-enthalpy profile of the ORC heat requirement.
Wang et al. [4] did the performance analysis of double organic rankine cycle for discontinuous low temperature waste heat recovery. The optimal operation of several working fluids have been calculated by a procedure employing MATLAB and REPROP. The influence of outlet temperature of heat source on the net power output, thermal efficiency, power consumption, mass flow rate, expander outlet temperature, cycle irreversibility and exergy efficiency at a given pinch temperature difference has been employed to obtain a thermodynamic understanding of the ORC performance.
Larjola [5] suggested that electricity from industrial waste heat using high speed organic rankine cycle. In the conversion of low temperature heat into electricity the greatest efficiency is obtained in many cases by using an Organic Rankine Cycle. The ORC process may be feasible also in high temperature applications. This paper deals with an ORC design, in which a high speed oil free turbo generator feed pump is used.
Li et al. [6] did evaluation of external heat loss from a small scale expander used in organic rankine cycle. With the scaling down of the ORC, the engine shaft power is not only determined by the enthalpy drop in the expansion process but also the external heat loss from the expander. Theoretically and experimentally support in evaluating small scale expander heat loss is rare. They presented a quantitative study on the convection, radiation and conduction heat transfer from a kw-scale expander. A mathematical model is built and validated.
Quoilin et al. [7] did performance and design optimization of a low cost solar organic Rankine cycle for remote power generation. Recent interests in small scale solar thermal combined heat and power system has coincided with the demand growth for distributed electricity supplies in area poorly served by centralized power stations. One potential technical approach to meet this demand is parabolic trough solar thermal collector coupled with Organic Rankine Cycle heat engine. He also describes the design of solar organic rankine cycle being installed in Lesotho for rural electrification

purpose. The system consist of parabolic trough collectors, a storage tank, a small scale ORC engine scroll expanders. A model of each component is developed which allows sizing the different components of cycle and evaluates the performance of system. Heberle et al [8] did energy based fluid selection for a geothermal Organic Rankine Cycle for combined heat power generation. In this study the option of combined heat and power generation was considered for geothermal resources at a temperature level below 450k. Series and parallel circuits of an organic rankine cycle and additional heat generation was organized by second law analysis. The result shows that the second law efficiency of geothermal power plant can be significantly increased in comparison to power generation.

Liu et al. [9] did investigation of two stage Rankine cycle for electric power plant. A two stage Rankine cycle for power generation is presented in this paper. It is made of water steam Rankine Cycle and Organic Rankine bottoming Cycle. By using an organic fluid with density higher than water. The performance of two stage Rankine cycle operating with those different working fluids is evaluated. System efficiency can also be enhanced by introducing a regenerator for some of working fluids. Aleksandra &Borsukiewicz [10] suggested pumping work in rankine cycle and made calculation based result for the pumping work on ORC. Analysis has been carried out for 18 different organic fluids that can be used a working fluids in the subcritical ORC system. An attempt was made to find correlations between various thermo-physical properties of working fluids, specific work and power of cycle. Clemente et al. [11] proposed the energy efficiency analysis of organic rankine cycle with scroll expanders for co-generative applications. The model of scroll machine is applicable to calculate the performance of both a compressor and expander, as function of geometry of device and working fluid.

Garcia-Rodriguez et al. [12] proposed solar powered Rankine cycle for fresh water production. He also focused that on the analysis of distributed solar powered generation systems for driving a reverse osmosis desalination process. Results point out the desalination system coupled to solar powered organic rankine cycle exhibit lower specific consumption of solar energy than solar distillation. Sprousell and Depick [13] suggested the review of Rankine Cycle for internal combustion engine exhaust waste heat recovery. This paper review the history of internal combustion engine exhaust waste heat recovery focusing on organic rankine cycle since this thermodynamic cycle works well with medium grade energy of exhaust. Selection of cycle expander and working fluid are primary focus of the review. Results demonstrate a potential fuel economy improvement around 10%. Florian and Dieter [14] suggested exergy based fluid selection for a geothermal Organic Rankine Cycle for combined heat and power generation. Algieri and Morrne [15] suggested the comparative energetic analysis of high temperature subcritical and transcritical Organic Rankine cycle in a biomass application in the Sibari district. The present work aims to analyze the energetic performance of ORC's for small scale applications.

Hui-tao et al. [16] did the optimization of Low temperature exhaust gas waste heat fuelled organic Rankine cycle. Cycle parametric analysis was performed to examine the effects of thermodynamic parameters on the cycle. Kosmadakis et al. [17] suggested the parametric theoretical study of a two stage solar rankine cycle for RO distillation. The present work concerns the parametric study of an autonomous two stage solar ORC for Ro desalination. The main aim is to estimate the efficiency as well as to calculate annual mechanical energy available for desalination. J.P. Roy and Ashok Mishra [18] presented analysis of regenerative Organic RankineCycle (ORC), based on parametric optimization using R-123 and R-134a during superheating at a constant pressure of 2.50 MPa under realistic conditions. The aim was to select a better working fluid on the basis of obtained system efficiency, turbine work output, irreversibility rate and second law efficiency under applied fixed and variable heat source temperature conditions, R-123 has been found a better working fluid than R-134 for converting low grade heat to power. A computer program has been developed to parametrically optimize and compare the system and irreversibility ratio with increases in turbine inlet temperature (TIT) under different heat source temperature conditions to obtain the optimum operating conditions while using R-123 as the working fluid during superheating at various turbine inlet pressures for the utilization of the waste heat sources of temperatures above 150ºC. The calculated results reveal that an inlet pressure of 2.70 MPa gives the maximum system efficiency, turbine work output and second law efficiency with minimum irreversibility rate, irreversibility ratio and system mass flow rate up to a TIT in the range of 165ºC-250ºC. W.Li et al. [19] set some initial & boundary conditions, for a mathematical model. In the analysis , three types pure fluid and one mixture were selected as working fluids and their parametric changes were calculated under different evaporating temperatures. When organic Rankine cycle (ORC) is equipped with internal heat exchanger (IHE), its parameters varies while using different working fluids. Dai Y et al. [20] did parametric optimization and comparative study of Organic Rankine Cycle for low grade waste heat recovery in saturated cycle. Karellas et al. [21] had presented a subcritical cycle and stimulated it under the same operation conditions as superheated cycle, however, the pumping pressure is kept higher than the pressure used for superheated cycle but slightly lower than the critical pressure for working fluids. V. Lemort et al. [22] presented results of an experimental study carried out on a prototype of an open-drive oil-free scroll expander integrated into an ORC working with refrigerant HCFC-123. By exploiting the overall expander performance measurements, the eight parameters of a scroll expander semi-empirical model are then identified. The model is able to compute variables of first importance such as the mass flow rate, the delivered shaft power and the discharge temperature, and secondary variables such as the supply heating-up, the exhaust cooling-down, the ambient losses, the internal leakage and the mechanical losses. The maximum deviation between the predictions by the model and the measurements is 2% for the mass flow rate, 5% for the shaft power and 3K for the discharge temperature. The validated model of the expander is finally used to quantify the different

losses and to indicate how the design of the expander might be altered to achieve better performances. This analysis pointed out that the internal leakages and, to a lesser extent, the supply pressure drop and the mechanical losses are the main losses affecting the performance of the expander. A Schuster et al. [23] used of organic working fluids organic Rankine cycle (ORC) for decentralized combined heat and power production (CHP). In the cycle process allows the use of low temperature heat sources, offering an advantageous efficiency in small scale applications. This is the reason why the number of geothermal and biomass fired power plants based on this technology have been increased within the last years. The favorable characteristics of ORC make them suitable for being integrated in applications like solar desalination with reverse osmosis system, waste heat recovery from biogas digestion plants or micro-CHP systems. In this paper, the state of the art of ORC applications will be presented together with innovative systems which have been simulated in a process simulation environment using experimental data. The results of the simulations like efficiencies, water production rates or achievable electricity production cost have been validated with experimental results. F.Herbele& D. Bruggemann [24] studied the option of combined heat and power generation was considered for geothermal resources at a temperature level below 450 K. Series and parallel circuits of an Organic Rankine Cycle (ORC) and an additional heat generation were compared by second law analysis. Depending on operating parameters criteria for the choice of the working fluid were identified. The results show that due to a combined heat and power generation, the second law efficiency of a geothermal power plant can be significantly increased in comparison to a power generation, the second law efficiency of a geothermal power plant can be significantly increased in comparison to a power generation. The most efficient concept is a series circuit with an organic working fluid that shows high critical temperatures like iso-pentane. For parallel circuits and for power generation, fluids like R227ea with low critical temperatures are to be preferred. J.P. Roy, M.K. Mishra, A. Mishra [25] carried out parametric optimization and performance analysis of a waste heat recovery system based on Organic Rankine Cycle, using R-12, R-123 and R-134a as working fluids for power generation have been studied. The cycles are compared with heat source as waste heat of flue gas at 140ºC and 312 Kg/s/unit mass flow rate at the exhaust of ID fans for 4×210 MW, NTPC Ltd. Kahalgaon, India, optimized turbine inlet pressure for maximum work and efficiencies of the system along the saturated vapor line and isobaric superheating at different pressures has been carried out for the selected fluids. The results show that R-123 at corrected pressure evaluated among all the selected fluids. The Carnot efficiency for R-123 at corrected pressure evaluated under similar conditions is close to the actual efficiency. It can generate 19.09 MW with a mass flow rate of 341.16 Kg/s having a pinch point of 5ºC, First law efficiency of 25.30% and the second law efficiency of 64.40%. Hence selection of an Organic Rankine Cycle with R-123 as working fluid appears to be a choice system for utilizing low-grade heat sources for power generation.

J.Li, G.Pei, Y.Z.Li, J.Ji [26] presented a quantitative study on the convection, radiation and conduction heat transfer from a kW-scale expander. A mathematical model is built and validated. The results show that the external radiative or convective heat loss coefficient was about 3.2 or 7.0 W/m^2K when the ORC operated around 100ºC. Radiative and convective heat loss coefficients increased as the expander operation temperature increased. Conductive heat loss due to the connection between the expander and the support accounted for a large proportion of the heat loss. The fitting relationships between heat loss and mean temperature difference were established. It is suggested that low conductivity material be embodied in the support of expander. Mattress insulation for compact expander could be eliminated when the operation temperature is around 100ºC. S. Quoilin et al. [27] studied small-scale solar thermal combined heat and power(CHP) power systems has coincided with demand growth for distributed electricity supplies in areas poorly served by centralized power stations. One potential technical approach to meeting this demand is the parabolic trough solar thermal collector coupled with an organic Rankine cycle (ORC) heat engine. The design of a solar organic Rankine cycle being installed in Lesotho for rural electrification purpose. The system consists of parabolic trough collectors, a storage tank, and a small scale ORC engine using scroll expanders. A model of each component is developed taking into account the main physical and mechanical phenomena occurring in the cycle and based on experimental data for the main key components. The model allows sizing the different components of the cycle and evaluates the performance of the system. Different working fluids are compared, and two different expansion machine configurations are simulated (single and double stage). N.Yamada, M.N.A. Mohamad, T.T. Kien [28] HFO-1234yf is a new refrigerant with a nearly zero global warming potential (GWP) and ozone depletion potential (ODP); it exhibits thermodynamic properties similar to HFC-134a. The potential if HFO-1234yf as a working fluid for organic Rankine cycle (ORC) is elucidated through a first order simulation. A fundamental thermodynamic model of ORC with five types of cycles trilateral, saturated, superheated, sub-critical, and supercritical used to compare the thermal efficiency of HFO-124yf with that of other working fluids. HFO-1234yf was found to offer a thermal efficiency that was comparable to that of HFC-134a. This paper provides a useful clearly shows the best possible thermal efficiency among the five types of cycle for various expander inlet and condensation temperatures. The highest thermal efficiency range (8.8%-11.4%) was obtained when the supercritical ORC was used at an expander inlet temperature of 170ºC and condensation temperature range of 20-40ºC for the given pump and expander efficiency.

F.A. Al-Sulaiman, I. Dincer, F. Hamdullahpur [29] This part of the study presents the thermo economic optimization formulations of three new trigeneration systems using organic Rankine Cycle (ORC): SOFC-trigeneration, biomass-trigeneration, and solar-trigeneration systems. A thermo-

economic modeling is employed using the specific exergy costing (SPECO) method while the optimization performed using the Powell's method to minimize the product cost of trigeneration (combined cooling, heating, and power). The results help in understanding how to apply the thermodynamic modeling and thermoeconomic optimization to a trigeneration system.

F.A. Al-Sulaiman, I. Dincer, F. Hamadullahpur [30] studied, three new trigeneration systems are examined. These systems are SOFC-trigeneration, biomass-trigeneration, and solar-trigeneration systems. This study reveals that the maximum trigeneration-exergy efficiencies are about 38% for the SOFC-trigeneration system, 28% for the biomass-trigeneration system and 18% for the solar-trigeneration system. Moreover, the maximum cost per exergy unit for the SOFC-trigeneration system is approximately 38$/GJ, for the biomass-trigeneration system is 26$/GJ and for the solar-trigeneration system is 24 $/GJ. This study reveals that the solar trigeneration system offers the best thermo-economic performance among the three systems. This is because the solar-trigeneration system has the lowest cost per exergy unit. Furthermore, the solar trigeneration system has zero CO_2 emissions.

3. System Description

3.1 Subcritical ORC

In the Subcritical ORC configuration of ORC system which is compared of an evaporator, an expansion device, a condenser, a pump and a cooling cycle. The condenser and the evaporator are both described as three-stage models by Quoilin and Wei. The thermodynamic processes of the subcritical ORC system

When IHE is proposed, the liquid working fluid before entering the evaporator exchanges heat with the gas working fluid coming out of expander in the IHE. The liquid working fluid gets heated from T8 to T19 whereas the gas working fluid gets cooled.

As it is very well known that if we know any two parameters out of the four parameters Ti, Pi, hi, si of the state point than the other two parameters can be determined. And for doing all these thermodynamic calculations use of E E .S. This software is easy and flexible to use and has the advantage of ready to use optimization techniques and fluid properties. It makes use of the same equation of state as used in REFPROP-NIST. This is a versatile software and a very useful tool.

3.2 Supercritical ORC

In a supercritical organic Rankine cycle, the process that occurs in evaporator is a complex two phase process, simply implying that a three stage model cannot be used. However the other facilities are same with almost no differences among them with the only difference that an evaporator is replaced by a one stage model. Due to the complexity of two phase change, there occurs a difficulty in locating the position of pinch point. In a subcritical cycle, by default the pinch point is assumed between point 9 and point 13, which in most cases is tenable, and the added condition that the temperature difference between T11 and T1 is too large. However, in a supercritical cycle, trends of working fluid evaporation progress and constant pressure lines of the heat source are similar, hence it becomes difficult to identify the pinch point position qualitatively. Some previous studies did their simulation by assuming the outlet temperature of the heat source or by assuming the location of pinch point, or setting and defining effectiveness of internal heat exchanger at a constant value of €. It simplified the calculation while it would also lead to the consequence that the temperature difference of the pinch point would be less or more than the value which is already set, which is not in conformity with the real condition in heat exchanger. The given minimum heat transfer temperature difference ΔT_{pp} is used for calculating the effectiveness of Internal heat exchanger i.e. €, but the derivation of reversing process is not real. Here, an iteration method is suggested through which the pinch point position in the supercritical cycle can be located. Once ΔTe is set, the working fluid's evaporation zone is divided equally to N number of parts in the direction of entropy. The lowering of the outlet temperature of heat source is used to find the minimum gap between the working fluid evaporation isobar and the heat source isobar. When this equals ΔTpp, the outlet temperature can be determined and the position of pinch point is N. Fig. 3.5 demonstrates this method and Fig. 3.6 is the flow diagram which is written as per this method. The application of this approach includes the calculation of outlet temperature of heat source in supercritical systems, which strictly suggests that ΔTpp should be at the set value of 10ºC.

3.3 Global Model

The system safety, economic efficiency of ORC system and environmental protection is greatly influenced by the choice of working fluids. The widely used fluids includes the applicable fluids with good thermodynamics, safety and economic characteristics, environmental protection, such as fluids with low liquid specific heat, viscosity, toxicity, flammability, ozone depletion potential, global warming, and price.

Based upon above criterion, the working fluid R600 and R123 are chosen for subcritical and supercritical cases separately. The basic environmental and thermodynamic properties of the above mentioned fluids are shown in Table 2.

Table 2: Basic thermodynamic and environmental properties of R123 and R600

Working Fluid	Tcr (ºC)	Pcr (MPa)	Tfp (ºC)	Tbp (ºC)	Safety	ODP	GWP
R123	183.7	3.668	-107.2	27379	B1	0.012	120
R600	152	3.796	-138.3	-0.5208	A3	0	-20

The following assumptions are made in the analysis in order to simplify the computing and complicacy which are neither the key points not they affect the accuracy of results coming in the model suggested.

(i) The whole system is under equilibrium state.
(ii) The specific heat of the hot stream is replaced with one the one of hot air.
(iii) The heat losses and leakages through the pipeline and components are ignored.

Some unchanged parameters involved in the calculations are shown in Table 3

Table 3: Assumptions of Streams and Components

Parameter	Sign	Unit	Value
Environment temperature	T0	ºC	15
Low Grade Heat flow temperature	Th,in	ºC	200
Cooling water temperature	Tc,in	ºC	15
Condensation Temperature	Tcond	ºC	30
Low Grade Heat Mass Flow Rate	qv,h	Kg/s	1
Superheat Degree	Tsup	ºC	3
Degree of Subcooling	Tsub	ºC	1
Pinch Point	ΔTpp	ºC	10
Temperature difference at hot stream inlet of Evaporator	ΔTe	ºC	15
Acid Dew Point	Tad	ºC	110
Adiabatic efficiency of Expander	ηT,i	1	0.65
Mechanical Efficiency of Expander	ηT,m	1	0.9
Working fluid pump Adiabatic efficiency	ηis	1	0.8
Working fluid pump Mechanical efficiency	ηPm	1	0.9
Efficiency of cyclic pump	ϩcpump	1	0.8
Total circulation loop Flow resistance	dPif	kPa	600
Total resistance at condenser cooling water side	dPcf	kPa	300

4. Thermodynamic Modelling

In the thermodynamic modelling the following set of mathematical equations are used analysis for computing system thermal performances as given below.

4.1 Energy Analysis

The first law of thermodynamics is the basis for the energy analysis. The final results includes the net output and the thermal efficiency. As already mentioned in the assumptions, their value is dependent only on evaporation pressure i.e. Pevap = P1 = P8. Following are the set of equations for different components.

4.2 Subcritical ORC

Since all the used formulas in supercritical case are same as that of the subcritical case hence suggesting that the energy analysis in both the cases are almost same. At the critical point the specific heat of working fluid changes dramatically in case of supercritical cycle. These variation characteristics are shown in the temperature range that is considered in simulation which is assumed constant in case of subcritical cycle. Then there is required a modification in the cycle to take these variations into account. The following equation represents the heat between two streams in internal heat exchanger.

$$QIHE = \dot{m}h * (h19 - h8) = \dot{m}f * (h2 - h20)$$

The following situation occurs when minimum heat transfer temperature difference i.e. ΔTpp is taken into account which in turn depends on which of the two streams in internal heat exchanger has smaller heat capacity.

4.3 Exergy Analysis

The drawback of energy analysis is that the conversion of energy of evaporator and condenser could not be done. Exergy analysis is a energy conversion coefficient that focuses on quantity as well as quality of energy, and this parameter more profoundly tells the essence of losses and energy conversion as compared to energy analysis. The exergy destruction in each component can also be calculated by this analysis.
The exergy analysis can be done by calculating the specific flow exergy at exit and entry of sources and also at each state point in cycle. The following expression gives the quantity:
Where the subscript 0 represents the environmental conditions which are considered to be 15ºC and atmospheric pressure. Following are the equations for different components.

5. Result and Discussion

In this study, the simulation of subcritical and supercritical organic Rankine cycle system with or without internal heat exchanger using respectively R123 and R600 is done which illustrates the impacts of internal heat exchanger on ORC systems. The mass flow rate taken into account for analysis is 1 kg/s and the heat source temperature is taken as 200ºC. The temperature difference of 10ºC is set as the minimum heat transfer temperature difference of heat exchanger. When a supercritical system is modeled, a modified method for maximum heat exchanger in an internal heat exchanger is given, which is attributed by the fact that in the supercritical system when working conditions lies near critical point conditions of the working fluid, then the specific heat of the fluid should not be considered as constant, which is different from subcritical system temperature of heat source in subcritical system. Also, a new approach is suggested for calculating the location of pinch point and outlet temperature of heat source in subcritical system which specifies that the minimum temperature difference of evaporator for heat transfer should be equal to the set value of 10ºC. And, when acid dew point is considered, it is observed that the internal heat exchanger improves the net output and justifies the applicability of system.

6. Conclusion

The following conclusions were drawn from present investigation.

(i) The internal heat exchanger always increases the exergy efficiency, thermal efficiency, and the outlet temperature of heat source in subcritical ORC system. However, there is no change in the net output of the system which remains the same.

(ii) The supercritical ORC system consists of a Range C in which the thermal efficiency, outlet temperature of heat source and exergy efficiency improves by the application of internal heat exchanger, keeping the system net output to be the same. The system performance degrades when an internal heat exchanger is used outside of this range.

(iii) When acid dew point Tad is considered, the net output of system is increased indirectly in a subcritical system on the application of internal heat exchanger while in supercritical system, the evaporation pressure starts obeying the rule Th,out> Tad. It is found that the applicability of system is strengthened by the application of IHE.

(iv) Comprehensive analysis of different upcoming working fluids comparison is to be done in both subcritical and supercritical systems that are equipped with IHE.

(v) More economical indicators like UA values and heat exchanger area is to be investigated.

References

[1] Serrano J.R., Dolz V., Novella R., Garcia A., [2011]. HD Diesel engine equipped with a bottoming Rankine cycle as a waste heat recovery system. Applied Thermal Kevinj Engineering 36, page- 279-287.

[2] Wang X. D., Zhao L., Wang J.L., Zhang W.Z., Zhao X.Z., W.Wu. 2009, Performance evaluation of low temperature Solar Rankine Cycle System utilizing R245fa. Solar Energy 84(2010), 353-364.

[3] Di GenovaKevinj., Botros Barbara B, Brisson J.G., [2012] Method for customizing on Organic rankine cycle to a complex heat source for efficient energy conversion, demonstrated on Fischer Tropsch Plant. Applied Energy 102, page-746-754.

[4] Wang Dongxiang, Ling Xiang, PengHao, [2012]. Performance Analysis of double organic rankine cycle for discontinuous low temperature waste heat recovery. Applied thermal Engineering 48, page-63-71.

[5] Larjola J., [1994], Electricity from industrial waste heat using high speed organic rankine cycle. International journal of Production Economics 41, page-227-235.

[6] Li Jing., Pei Gang, Li Yumhuli, JiJie., [2012]. Evaluation of External heat loss from small scale expander used in organic rankine cycle. Applied Thermal Engineering 31, page-2694-2701.

[7] Quilin S., Orosz M.,Hemond H., Lemort V., [2012]. Performance and design optimization of Low cost solar organic rankine cycle for remote power generation. Solar Energy 85, page-955-966.

[8] Herberle Florian, Bruggemann Dieter, [2010]. Exergy based fluid selection for geothermal organic rankine cycle for combined heat and power generation. Applied Thermal Engineering 30 , page-820-880.

[9] Liu Bo., Riviere Philippe, Coquelet Christopher, Gicquel Renaud, David Frank, [2012]. Investigation of a two stage Rankine cycle for Electric power Plants. Applied energy 100 , page-285-294.

[10] Borsukiewiz- Gozdur Aleksandra, [2013]. Pumping work in organic Rankine cycle. Applied thermal engineering 51, page-781-786.

[11] Clemente Stefno, Michel Diego, Mauro Reini, TaccaoniRodolf, [2012]. Energy Efficiency analysis of organic rankine cycle with scroll expander. Appplied energy 97, page-792-801.

[12] Garcia Lourdes Rodriguez, Austin M.Delgado-Torres, [2007]. Solar powered Rankine cycle for fresh water production. Desalination 212, page-319-327.

[13] Sprousell Charles, Depicl Christopher, [2013]. Review of organic Rankine cycle for internal combustion engine Exhaust waste heat recovery. Applied Thermal Engineering 51, page-711-722.

[14] Herberle Florian, Bruggemann Dieter, [2010]. Exergy based fluid selection for Geothermal Organic Rankine cycle for combined heat and power generation. Applied Thermal Engineering 30 , page-1326-1332.

[15] Algieri Angelo, Morrone Pietropaolo, [2012]. Comparative energetic analysis of high temperature sub-critical and transcritical organic rankine cycle. Applied Thermal Engineering 36, page-236-244.

[16] Hui-tao Wang, Hu Wang, Zhu-ming Zhang, 2011. Optimization of low temperature exhaust gas waste heat fuelled organic rankine cycle. Journal of Iron and Steel Research, International , Vol-19, No.6 , page-30-36.

[17] Kosmadakis G, Manolakos D, Papadakis G, [2010]. Parametric Theoretical study of a two stage solar organic rankine cycle for RO desalination, Renewable Energy 35, page-989-996.

[18] PJ. Mago, K.K. Srinivasan, L.M. Chamra, C. Simayaji, [2008] An examination of exergy destruction in organic rankine cycles, Int. J.Energy Res 32, page-926-938.

[19] W. Li, X. Feng, L.J. Yu, J. Xu, [2011] Effects of evaporating temperature and internal heat exchanger on organic Rankine cycle, Appl. Therm. Eng. 31, page- 4014-4023.

[20] Y.P. Dai, J.f. Wang, L. Gao, [2009] Parametric optimization and comparative study of organic Rankine cycle (ORC) for low grade waste heat recovery, Energy Convers, Manag. 50 , page-576-582.

[21] Karellas S, Schuster A.,[2008] Supercritical fluid parameter in organic Rankine cycle Applications. International Journal of Thermodynamics,. 11(3) , page-101-8.

[22] V. Lemort, S. Quoilin, C. Cuevas, J. Lebrun, [2009]Testing and modeling a scroll expander integrated into an organic Rankine cycle, Appl. Therm. Engg. 29, page- 3094-3102.

[23] A. Schuster, S. Karellas, E. Kakaras, H. Spliethoff,[2009] Energetic and economic investigation of organic rankine cycle applications, Appl. Therm. Eng. 29, page-1809-1817.

[24] F. Heberle, D. Bruggemann, [2010]Exergy based fluid selection for a geothermal organic Rankine cycle for combined heat and power generation, Appl. Therm. Eng. 30, page-1326-1332.

[25] J.P. Roy, M.K. Mishra, A. Mishra, [2010] Parametric optimization and performance analysis of a waste heat recovery system using organic Rankine cycle, Energy 35 , page-5049-5062.

[26] J. Li, G. Pei, Y.Z. Li, J. Ji, [2011]Evaluation of external heat loss from a small-scale expander used in organic Rankine cycle, Appl. Therm. Eng. 31, page-2694-2701.

[27] S. Quoilin, R. Aumann, A. Grill, A. Schuster, V. Lemort, H. Spliethoff, [2011] Dynamic modeling and optimal control strategy of waste heat recovery organic Rankine cycle, Appl. Energy. 88, page-2183-2190.

[28] N. Yamada, M.N.A. Mohammad, T.T. Kien, [2012] Study on thermal efficiency of low to medium temperature organic Rankine cycles using HFO-1234yf, Renew. Energy 41, page-368-375.

[29] F.A. Al-Sulaiman, I. Dincer, F. Hamdullahpur, [2013] Thermo-economic optimization of three trigeneration systems using organic Rankine cycles: part 1 – formulations, Energy Convers. Manag. 69, page-199-208.

[30] F.A. Al-Sulaiman, I. Dincer, F. Hamdullahpur, [2013]Thermo-economic optimization of three trigeneration systems using organic Rankine cycles: part II – applications, Energy Convers. Manag. 69 , page-209-216.

International Journal of Research in Engineering and Innovation (IJREI)
journal home page: http://www.ijrei.com
ISSN (Online): 2456-6934



Thermodynamic analysis of solar integrated waste heat recovery systems for power generation industry using eco-friendly fluids

R.S. Mishra[1], Kaushalendra Kumar Dubey[2]

[1]*Department of Mechanical & Production Engineering, Delhi Technological University Delhi, India*
[2]*Department, Mechanical Engineering, Galgotia University, Greater Noida, India*

Abstract

This paper explores eco-friendly material R134a and activated carbon-methanol based organic Rankine model and solar integrated vapor adsorption cooling system for waste heat utilization of condenser unit of steam power plant. The results of proposed model analysis is to explain the environmental parameters of used material, effect of operating parameters and cooling-power output. The proposed analysis is concern with the condenser heat recovery of reheating-Rankine steam power plant by using eco-friendly material based ORC and vapor adsorption cooling system for simultaneously power and cooling generation. Two models have been analyzed in this paper, model-1 (Fig-1) integrated with solar ORC and model-2(fFg-2) equipped with double bed adsorption refrigeration system.Model-2 have two different adsorbed bed. Bed-1 is connected with condenser outlet of reheating-Rankine steam plant and AC-Methanol material pair is used and bed-2 integrated with solar parabolic collector for condenser water heating, that heated water circulating to bed-2 for generator purpose. The main objective of this analysis to estimate the multiple thermal effect (heating-power and cooling) from available un-covered heat of power plant by using different novel thermal system. The application of R134a and AC-Methanol type material helps to produce required cooling effect at low grade of thermal availability with environmental safety aspect.
© 2018 ijrei.com. All rights reserved
Keywords: Organic Rankine Cycle, Vapor Adsorption System, Waste Heat Recovery

1. Introduction

The uncovered heat from power plants and heavy industry is dumped into atmosphere and it causes of severe impact on atmosphere in terms of greenhouse effect. The US Dept. of Energy reported that the cement/ captive power plants have, nearly 35% heat is lost, and this corresponds to around 70 to 75 MW of thermal energy.

EPA estimated that the 65% of world CO_2 emission is recorded from greenhouse gas emission from fissile fuel burning during intensive industrial process. This un-used or waste heat have tremendous potential to generate heating-power and cooling generation for industrial process by using eco-friendly material based novel thermodynamic system like, organic Rankine system (ORC), kalina system for cooling-power generation, vapor absorption and adsorption refrigeration techniques. The employment of solar energy will enhance the system performance. All these systems work as waste heat recovery generator (WHRG). For a 6000 ton per day (tpd) capacity of cement plant can be reduced around 70,000 ton/annum of CO_2 by installation of WHRG.

The proposed analysis is concern with the condenser heat recovery of reheating-Rankine steam power plant by using eco-friendly material based ORC and vapor adsorption cooling system for simultaneously power and cooling generation. Two models have been analyzed in this paper, model-1 (Fig-1) and part description is given in Table-1(a) respectively.

Corresponding author: R. S. Mishra
Email Address: hod.mechanical.rsm@dtu.ac.in

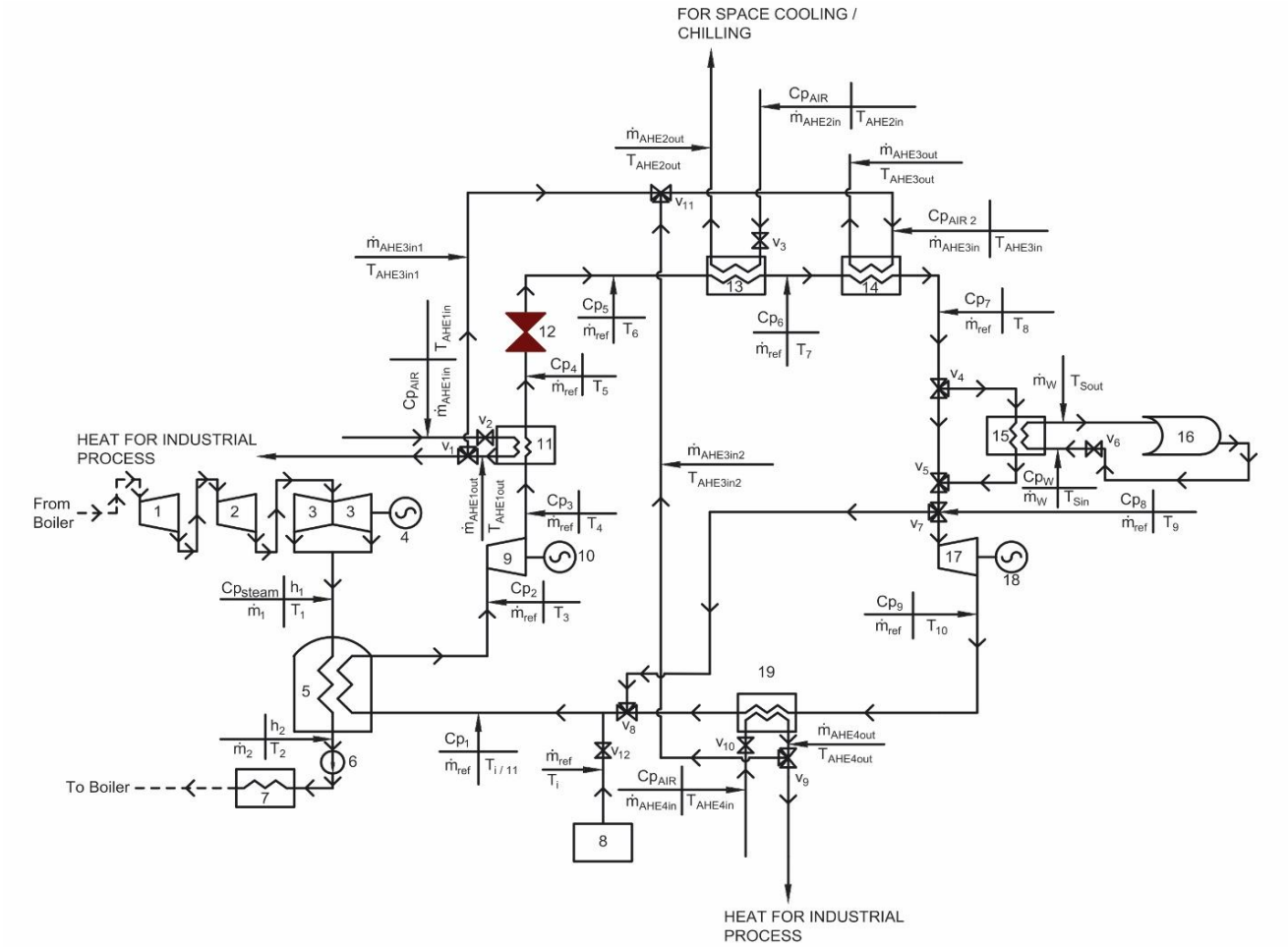


Figure 1: Schematic of R134a Based ORC heat recovery Unit

Table 1(a): Description of systems used in the schematic (Fig. - 1)

System number	System description	System number	System description	System number	System description
1	High pressure turbine	12	Throttle	V4	Three way flow control valve
2	Intermediate pressure turbine	13	Heat exchanger 2	V5	Three way flow control valve
3	Low pressure turbine	14	Heat exchanger 3	V6	Two way flow control valve
4	Power generator	15	Solar heat exchanger	V7	Three way flow control valve
5	Condenser	16	Solar heater	V8	Three way flow control valve
6	Circulation Extraction pump	17	Expander 2	V9	Three way flow control valve
7	Feedwater Heater	18	Power generator	V10	Two way flow control valve
8	Refrigerant tank	19	Heat exchanger 4	V11	Three way flow control valve
9	Expander 1	V1	Three way flow control valve	V12	Two way flow control valve
10	Power generator	V2	Two way flow control valve		
11	Heat exchanger 1	V3	Two way flow control valve		

Integrated with solar ORC and model-2(Fig-2) equipped with double bed adsorption refrigeration system. And part description is given in Table-1(b) respectively.

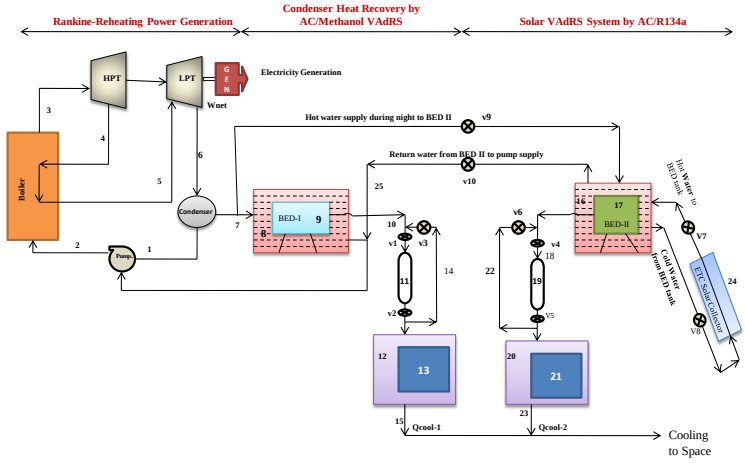


Figure 2: Solar Integrated Vapor Adsorption System for Condenser Heat Recovery

Table-1(b)-Parts Description of Model-2

S.N	Specification	S.N	Specification	S.N	Specification
1	Condensed steam feed to pump	15	Chilled air supply to space where cooling is required through cooling line.	v3	Valve 3 open for adsorption of vapor refrigerant into adsorbent bed after evaporation.(v1 & v2 remain closed when adsorption is happening)
2	Feed water supply to boiler for steam formation	16	Outer chamber of BED-2 for hot water collection, (need of hot water for adsorption of heat from adsorbate).	v4	Valve 4 open and allow to vaporized refrigerant into condenser for condensation
3	Steam from boiler supply to high pressure turbine (HPT)	17	Inner chamber of bed -2, where Activated carbon-R134a pair is filled, Its utilize condenser heat.	v5	Valve 5 allow Condensed refrigerant into evaporator and chiller unit.
4	Exhaust steam from HPT supply for reheating process	18	Vapor refrigerant (R134a) supply to condenser of VAdRS after desorption process.	v6	Valve 6 open for adsorption of vapor refrigerant into adsorbent bed after evaporation.(v1 & v2 remain closed when adsorption is happening)
5	Reheated steam supply to low pressure turbine (LPT) for more work output.	19	Refrigerant liquefy by using condenser	v7	Valve 7 open for hot water supply from ETC to BED-2 for desorption of refrigerant.(V9 & V10 are closed)
6	Exhaust steam from LPT supply to condenser unit for condensation process	20	Refrigerant liquefy by using condenser	v8	Valve 8 open for cold water return in to ETC after desorption. (V9 & V10 are closed)
7	Hot water proceed to BED-1 and only during night to BED-2 for adsorption cooling process.	21	Chiller get to be cooled during evaporation	v9	V9 works during night, whenETC does not work. It open for hot water supply from condenser exhaust to BED-2.
8	Outer chamber of BED-1 for hot water collection, (need of hot water for adsorption of heat from adsorbate).	22	Evaporated refrigerant adsorbed in adsorbent bed	v10	V 10 allow return cold water from BED-2 after adsorption and water mixed with water line for pumping into boiler.
9	Inner chamber of bed -1, where Activated carbon-Methanol pair is filled, Its utilize condenser heat.	23	Chilled air supply to space where cooling is required through cooling line.	CONDENSER	Condensation of exhaust steam and refrigerant vapor condensation process
10	Vapor refrigerant (Methanol) supply to condenser of VAdRS after desorption process.	24	ETC solar thermal water heater for hot water supply to BED-2.	HPT & LPT	High pressure turbine and low pressure turbine. LPT use for reheated steam expansion.

11	Refrigerant liquefy by using condenser	25	Return cold water from BED-2 and mixed with water line for pumping to boiler.	GEN	Generator for electricity generation.
12	Liquid refrigerant get evaporation by evaporator	v1	Valve 1 open and allow to vaporized refrigerant into condenser for condensation	BOILER	Steam formation thermal utilities
13	Chiller get to be cooled during evaporation	v2	Valve 2 allow Condensed refrigerant into evaporator and chiller unit.	14	Evaporated refrigerant adsorbed in adsorbent bed

Model-2 have two different adsorbed bed. Bed-1 is connected with condenser outlet of reheating-Rankine steam plant and AC-Methanol material pair is used and bed-2 integrated with solar parabolic collector for condenser water heating, that heated water circulating to bed-2 for generator purpose. The main objective of this analysis to estimate the multiple thermal effect (heating-power and cooling) from available un-covered heat of power plant by using different novel thermal system. The application of R134a and AC-Methanol type material helps to produce required cooling effect at low grade of thermal availability with environmental safety aspect.

2. Literature Review

The worldwide two major issues are being discussed in these days, CO2 concentration in atmosphere on one hand and energy crisis on other hand. All possible savings of reducing CO2 generation. Fossil fuels depletion, control in energy prices increments, achievable by adaptation of eco-friendly energy efficient material based technology. The un-arrested heat (waste heat) discharge from energy intensive industries like captive power plants, cement production, steel industry, Oil-refineries, etc have tremendous potential for multiple energy generation (heating-power & cooling) for further industrial process with dumped heat recovery [1-4]

The numerous researches have been developed and analyzed eco-friendly material based novel thermodynamic model in environmental concern. The selection of a suitable working material depends on its great influence in the design of the process, application, heat source and the temperature level. The used material must have optimum thermodynamic properties at the lowest possible temperatures and pressures, and also satisfy several criteria such as economical, nontoxic, nonflammable, environmentally-friendly. An extensive literature review of R134a was chosen as working fluid. This selection has been done on the basis that R134a: is a nontoxic and nonflammable fluid and its Ozone Depletion Potential (ODP) is zero. R134a has a high molecular mass (chemical formula: CF3CH2F, MM=102kg/kmol).It has a temperature and critical pressure of 101.1ºC and 40.6 bar, respectively, R134a based heat recovery ORC of condenser operates at a higher pressure than atmospheric, and therefore air in-leakages do not occur. [1,2-4]. Several researchers have investigated the application and performance of ORC with R134a as a working fluid, the efficiency of the ORC using benzene, ammonia, R134a, R113, R11 and R12 was analyzed [5-7]. An analysis of a regenerative ORC based on the parametric optimization, using R12, R123, R134a, and R717 as working fluids superheated at constant pressure was carried out and. results revealed that selection of a regenerative ORC during overheating using R123 as working fluid appears to be a good system for converting low-grade waste heat to power [8]. In a low-temperature solar organic Rankine cycle system was designed and built with R134a as working fluid that works between 35^{0}ºC and 75.8ºC for reverse osmosis desalination in Greece, the results showed a system efficiency of about 7% and 4%, respectively [8-10]. Other studies that have analyzed the use of R134a as working fluid in the ORC cycles for reverse osmosis desalination at an experimental level [11], and also as a theoretical manner showed a simulation to estimate the increase in the efficiency and the energy available for desalination of an upper ORC coupled with a lower ORC with R134a, obtaining an efficiency for the latter of 4.2%. Other cycles with R134a for applications for geothermal sources are reported also and R134a integrated with internal combustion engine for heat recovery as bottoming cycle [12-21].The overall screening of all heat recovery fluids R134a was found to be the most suitable in terms of most eco-friendly, non-toxic, high thermal performance for cooling and power generation with optimized system.

The other category of energy recovery material for green refrigeration technology as vapor adsorption refrigeration. Activated carbon is a form of carbon that has been processed to make it extremely porous, and it has a large surface area available for adsorption. Methanol and ammonia are the most common refrigerants paired with activated carbon. Activated carbon−methanol is one of the most promising working pairs in practical systems because of its large adsorption quantity and low adsorption heat (about 1800 to 2000 kJ/kg [22]. Low adsorption heat is beneficial to the system's performance because the majority of heat consumption in the desorption phase is the adsorption heat. Another advantage of activated carbon−methanol is low desorption temperature (about 100°C), which is within a suitable temperature range for using solar energy as a heat source[26].Activated carbon−ammonia has almost the same adsorption heat as the activated carbon−methanol working pair. The main difference is the much higher operating pressure (about 1600 kPa when the condensing temperature is 40°C of activated carbon−ammonia. The high operating pressure leads to rather small pipe diameters and relatively compact heat exchangers,

as compared to activated carbon− methanol. Another advantage of activated carbon−ammonia is the possibility of using heat sources at 200°C or above [23]. The drawbacks of this working pair are the toxicity and pungent smell of ammonia. Silica gel is a granular, highly porous form of silica made synthetically from sodium silicate. For the silica gel−water working pair, the adsorption heat is about 2500 kJ/kg and the desorption temperature could be as low as 50°C [22]. Such a low desorption temperature makes it suitable for solar energy use with availability of 80-100 0C. One of the drawbacks of the silica gel−water working pair is its low adsorption quantity (about 0.2 kg water/kg silica gel). Another drawback is the limitation of evaporating temperature due to the freezing point of water [22-23]. Zeolite is a type of alumina silicate crystal composed of alkali or alkali soil. The adsorption heat of zeolite−water is higher than that of silica gel−water, at about 3300 to 4200 kJ/kg. The desorption temperature of zeolite−water is higher than 200°C due to its stable performance at high temperatures. The drawbacks of zeolite−water are the same as for silica gel−water, low adsorption quantity and inability to produce evaporating temperatures below 0°C [22].

3. Thermodynamic Analysis of R134a Based Heat Recovery System

Fig-1 shows the Schematic of R134a Based ORC heat recovery Unit and description of systems used in the schematic is shown in Table-1(a), The steam from the outlet of low pressure turbine of the Rankine cycle enters the condenser at temperature T_1, having mass flow rate $\dot{m}_1$, enthalpy h_1 and temperature T_1. Condensed water leaves the condenser at temperature T_2 having mass flow rate $\dot{m}_2$ (= $\dot{m}_1$) and enthalpy h_2, the heat rejection by the steam in the condenser heat exchanger is calculated using heat balance equation.

$$Q_{COND} = \dot{m}_1 Cp_{steam} (T_1 - T_2) \quad (1)$$

Taking the latent heat rejected by the steam in the condenser heat exchanger as Q_{LH} and the condenser heat loss 15%, the total heat available to the refrigerant vapour is calculated from

$$Q_{Total} = \{Q_{COND} + (Q_{LH} * \dot{m}_1)\} - [\{Q_{COND} + (Q_{LH} * \dot{m}_1)\} * 0.15] \quad (2)$$

Superheated refrigerant (R 134a) vapour from the refrigerant storage is introduced into the system at a known temperature $T_i$for the startup cycle. In all operation cycle the refrigerant vapour enters the condenser heat exchanger at temperature T_{11}.the superheated refrigerant vapour is calculated using heat balance equation

$$Q_{Total} = \dot{m}_{ref} Cp_1 (T_1 - T_{i/11}) \quad (3)$$

The efficiency of expander 1 (η_{E1}), T_4 and the work done by expander 1 (W_{E1}) is calculated using the equations.

$$\eta_{E1} = W_{E1} / Q_{Total} \quad (4)$$

Where,

$$W_{E1} = \dot{m}_{ref} Cp_2 (T_3 - T_4) \quad (5)$$

Heat available in heat exchanger 1 (Q_{HE1}) for different values of mass flow rate, $\dot{m}_{AHE1in}$, are calculated using heat balance equation.

$$Q_{HE1} = \dot{m}_{ref} Cp_3 (T_4 - T_5) - [\{\dot{m}_{ref} Cp_3 (T_4 - T_5)\} * 0.15] \quad (6)$$

$$Q_{HE1} = \dot{m}_{AHE1in} Cp_{AIR} (T_{AHE1out} - T_{AHE1in}) \quad (7)$$

The heat available in heat exchanger 2 (Q_{HE2}) for different values of mass flow rate of air ($\dot{m}_{AHE2in}$) are calculated using heat balance equation

$$Q_{HE2} = \dot{m}_{ref} Cp_5 (T_7 - T_6) - [\{\dot{m}_{ref} Cp_5 (T_7 - T_6)\} * 0.15] \quad (8)$$

$$Q_{HE2} = \dot{m}_{AHE2in} Cp_{AIR} (T_{AHE2in} - T_{AHE2out}) \quad (9)$$

Where

$$\dot{m}_{AHE3in} = \dot{m}_{AHE3in1} + \dot{m}_{AHE3in2} \quad (10)$$

The values of T_7, $\dot{m}_{ref}$, Cp_6 and Cp_{AIR2} are known. T_{AHE3in} is calculated using the equation

$$\dot{m}_{AHE3in1} Cp_{AIR} (T_{AHE3in1} - T_{AHE3in}) = \dot{m}_{AHE3in2} Cp_{AIR} (T_{AHE3in} - T_{AHE3in2}) \quad (11)$$

Taking the heat exchanger heat loss as 15%, T_8, $T_{AHE3out}$ and heat available in heat exchanger 3 (Q_{HE3}) for different values of mass flow rate of air ($\dot{m}_{AHE3in}$) are calculated using the equation.

$$Q_{HE2} = \dot{m}_{AHE3in} Cp_{AIR2} (T_{AHE3in} - T_{AHE3out}) - [\{\dot{m}_{AHE3in} Cp_{AIR2} (T_{AHE3in} - T_{AHE3out}) * 0.15] \quad (12)$$

$$Q_{HE2} = \dot{m}_{ref} Cp_6 (T_8 - T_7) \quad (13)$$

$\dot{m}_{AHE3in1}$and $\dot{m}_{AHE3in2}$ are optimized from the data generated.

3.1 Solar thermal Generator Energy Equation

$$Q_{Solar} = \dot{m}_w Cp_w (T_{Sin} - TSout) - [\{\dot{m}_w Cp_w (T_{Sin} - T_{Sout})\} * 0.15] \quad (14)$$

$$Q_{Solar} = \dot{m}_{ref} Cp_7 (T_9 - T_8) \quad (15)$$

Superheated refrigerant vapour leaves the condenser heat exchanger and enters expander 2 at temperature T_9, having mass flow rate $\dot{m}_{ref}$ and specific heat capacity Cp_8. It leaves expander 2 at temperature T_{10}, having mass flow rate $\dot{m}_{ref}$ and

specific heat capacity Cp_9. Knowing the value of the specific heat capacity, $Cp_{8,}$ of the superheated refrigerant vapour at the inlet of expander 1 and taking different values for efficiency of expander 1(η_{E1}) T_{10} and the work done by expander 2 (W_{E2}) is calculated using the equations.

$$\eta_{E2} = W_{E2} / Q_{Solar} \quad (16)$$

$$\text{Where, } W_{E2} = \dot{m}_{ref}\, Cp_8\, (T_9 - T_{10}) \quad (17)$$

Superheated refrigerant vapour leaves expander 2 and enters heat exchanger 4 as the hot fluid at temperature T_{10} and having mass flow rate $\dot{m}_{ref}$ and specific heat capacity Cp_9. It leaves heat exchanger 4 at temperature T_{11}, having mass flow rate $\dot{m}_{ref}$ and specific heat capacity Cp_1.The value of Cp_1 will change in the transition from startup cycle to operation cycle. Air enters heat exchanger 2 as the cold fluid at temperature T_{AHE4in}, having mass flow rate $\dot{m}_{AHE4in}$ and specific heat capacity Cp_{air}. It leaves heat exchanger 4 at temperature $T_{AHE4out}$ and having mass flow rate $\dot{m}_{AHE4out}$ (= $\dot{m}_{AHE4in}$). The values of T_{10}, $\dot{m}_{ref}$, Cp_9 and Cp_{air} are known. T_{AHE4in} is taken as 288.15 K as per standard atmosphere data. Taking the heat exchanger heat loss as 15%, assuming that no makeup is required, T_{11}, $T_{AHE4out}$ and heat available in heat exchanger 4 (Q_{HE4}) for different values of mass flow rate of air ($\dot{m}_{AHE4in}$) are calculated using heat balance equation.

$$Q_{HE4} = \dot{m}_{ref}\, Cp_9\, (T_{11} - T_{10}) - [\{\dot{m}_{ref}\, Cp_9\, (T_{11} - T_{10})\} * 0.15] \quad (18)$$

$$Q_{HE4} = \dot{m}_{AHE4in}\, Cp_{air}\, (T_{AHE4out} - T_{AHE4in}) \quad (19)$$

3.2 Model-2-Activated Carbon based Solar Integrated Vapor Adsorption Cooling System for Condenser Waste Heat Recovery.

The proposed model which is shown in fig-2 of double bed vapor adsorption system is adopted for heat recovery of condenser of reheating-Rankine steam power cycle. In this system two eco-friendly materials-pair have been used Activated carbon (AC) methanol and activated carbon-R134a. 1st bed is equipped with AC-Methanol and 2nd bed is running with AC-R134a.The solar parabolic trough collector is integrated with 2nd bed for more heating at generator of 2nd bed. In the beginning of the desorption process in both bed, the desorbed is heated by the waste heat of Reheating Rankine condenser and solar collector to begin desorbing, and the condensation process occurs firstly in the evaporator because the evaporator temperature is lower than the condenser temperature at that time. Such process will continue until the evaporator temperature rises higher than the condenser temperature. Thereafter, the condenser will be in condensing mode, and the evaporator will be idle.Table-4 describe all parts of model-2.

4. Thermodynamics model of Double bed VADRS

The total energy input to the system is given by, The total heat input to the system is estimation of energy liberated during adsorption is called isostatic heating and heat due to desorption The equations for thermal analysis of model2 is adopted from Mahesh and Kausik model[32].

$$Q_{heat_total} = Q_{isosteric} + Q_{desorption} \quad (20)$$

Mahesh and Kaushik [32] is written as

$$Q_{heat_total} = \sum m_{ad} [(Cp_{ad} + Cp_r * X_{max})(T_g - T_{ad}) + (Cp_{ad} + \Delta X/2)(T_{des} - T_g) + \Delta X * H_D]_{BED\text{-}1\ \&\ BED\text{-}2} \quad (21)$$

After condensation of desorbed refrigerant, the liquid refrigerant in the evaporator will absorb the heat of vaporization from liquid to be cooled, this cause the refrigeration effect and it can be estimate as

$$Q_{Ref} = \sum [(m_{ad} * \Delta X * L_E)]_{BED\text{-}1\ \&\ BED\text{-}2} \quad (22)$$

The amount of energy used in cooling the evaporated adsorbate when passing through the condenser is given by

$$Q_{Cool} = \sum [(m_{ad} * \Delta X * Cp_r\, (T_C - T_E)]_{BED\text{-}1\ \&\ BED\text{-}2} \quad (23)$$

The useful cooling of vapor adsorption system can be estimated by

$$Q_{cool\ useful} = \sum m_{ad} [(L_E * \Delta X - Cp_r\, (T_C - T_E)]_{BED\text{-}1\ \&\ BED\text{-}2} \quad (24)$$

The compactness or size of system is important parameter, Specific cooling power (Useful cooling per unit mass) of adsorption system decide the compactness. Desorption and Adsorption time (second) play key role here for cooling effect of VAdRS and its SCP.

$$SCP_{VADRS} = Q_{cooluseful} / m_{ad} \quad (25)$$

The ratio of useful cooling and total heat input for adsorption and desorption account the refrigeration capacity of cooling machine.

$$COP_{VADRS} = Q_{cooluseful} / Q_{heat_total} \quad (26)$$

The refrigeration effect of solar vapor adsorption refrigeration system account by COP_{SOLAR}, The ratio of net cooling heat and heat gain by solar thermal system is express as

$$COP_{SOLAR} = Q_{cooluseful} / Q_G = Q_{cool\ useful} / (I * Ac) \quad (27)$$

5. Results and Discussions

The numerical computation were carried out for Energy Recovery using eco-friendly materials for ORC and Adsorption cycle and the energy recovery heat grades, and efficient materials have been shown in table 2-4 respectively. Similarly all parametric results are shown in Table 5 to 8 respectively.

Table-2 Energy recovery and its sources [26]

Heat Categories	Heat Sources	Temperature in 0C	Suggested recovery technology
High Grade (>650^{0}C)	Solid waste	650-1000	Air preheating
	Nickel refining furnace	1370-1650	Steam generation for heating
	Copper reverberatory furnace	760-815	Thermoelectric and thermal PV
	Glass melting furnace	1000-1550	Heat exchanger for preheating
	Hydrogen plant	650-1000	Thermal PV
Medium Grade (230-650^{0}C)	Steam boiler exhaust	230-480	Steam rankine cycle
	Gas turbine exhaust	370-540	Organic rankine cycle
	Drying and baking ovens	230-600	Thermal PV
	Catalytic crackers	425-650	Thermal PV
	Reciprocating engine exhaust	315-600	Thermoelectric
Low Grade (>230^{0}C)	Welding and injection molding	32-88	Kalina cycle
	Hot processed liquids and solids	32-233	Organic rankine cycle
	Drying,Baking and Curing ovens	93-230	Absorption and adsorption cooling
	Bearing	32-88	Piezoelectric

Table-3: Summary of Commercialized Working fluids [27-29]

S. N	Working Fluids	Physical Data				Safety Data	Environmental Data		
		Molecular Mass (Kg/K mol)	Normal Boiling Point Temp (Tbp) in ^{0}C	Critical Temp (Tcriti) in 0C	Critical Pressure (Pcriti) in MPa	ASHRAE Group	Atmospheric Life Time (ALT) in years	Ozone Depletion potential (ODP)	Global Warming Potential (GWP) of 100 years
1	RC118	200.03	-6.0	115.2	2.778	A1	3200	0	10225
2	R600a	58.12	-11.7	135	3.647	A3	0.017	0	˜˜20
3	R114	170.92	3.6	145.7	3.289	A1	300	1.00	10040
4	R600	58.12	-0.5	152	3.796	A3	0.018	0	˜˜20
5	R601	72.15	36.1	196.5	3.364	NA	0.01	0	˜˜20
6	R113	187.38	47.6	214.1	3.439	A1	85	1.000	6130
7	Cyclohexane`	84.16	80.7	280.5	4.075	A3	NA	NA	NA
8	R290	44.10	-42.1	96.68	4.247	A3	0.041	0	~20
9	R407C	86.20	-43.6	86.79	4.597	A1	NA	0	1800
10	R32	52.02	-51.7	78.11	5.784	A2	4.9	0	675
11	R500	99.30	-33.0	105.5	4.455	A1	NA	0.738	8100
12	R152a	66.05	-24.0	113.3	4.520	A2	1.40	0	124
13	R717 Amonia)	17.03	-33.3	132.3	11.333	B2	0.1	0	<1
14	Ethanol	46.07	78.4	240.8	6.148	NA	NA	NA	NA
15	Methanol	32.04	64.4	240.2	8.104	NA	NA	NA	NA
16	R718 (Water)	10.2	100	374	22.064	A1	NA	0	<1
17	R134a	102.03	-26.1	101	4.059	A1	14.0	0	1430
18	R12	120.91	-29.8	112	4.114	A1	100	1.000	10890
19	R123	152.93	27.8	183.7	3.668	B1	1.3	0.02	77
20	R141b	116.95	32.0	204.2	4.249	NA	9.3	0.120	725
21	R245fa	134.05	15.3	154.1	3.64	B1	8.8	0	820
22	R236fa	152.0	-1.5	124.0	3.20	-	209	0	6300
23	R227ea	170.0	-17.5	102.0	2.95	-	36.5	0	2900
24	R1234yf	114.02	-29.45	94.7	3.382	A1	NA	0	4

Table-4-Energy Recovery Materials for Adsorption Refrigeration Techniques of Heat Recovery [24]

Material	Heat Source	Performance Index(COP)	Application
AC-Methanol	20 MJ/m^2 per Day	0.12	Ice Making
	18 to 19.2 MJ/m^2 per Day	0.12 to 0.14	
	17 to 20 MJ/m^2 per Day	0.13 to 0.15	
	<120 degree C	0.18	
AC-NH3	105 degree C	0.10	
Silica Gel-Water	15.4 MJ/m^2 per Day	0.16	
AC-Blanked steel-Methanol	20 MJ/m^2 per Day	0.18	
AC+CaCl2-NH3	115 degree C	0.39	
Silica Gel-Water	55 degree C	0.36	Chilled Water
	65 degree C	0.28	
	75-90 MJ/m^2 per Day	0.35 to 0.60	
	80 to95 MJ/m^2 per Day	0.35 to 0.60	
	80 MJ/m^2 per Day	0.33to 0.50	
AC-NH3	232 degree C	0.42 to 1.19	Air Conditioning
	100^0 C	0.20	
Zeolite-Water	204^0 C	0.60 to 1.60	
	230^0 C	0.41	
	310^0C	0.38	
	230 to 300^0C	0.20 o 0.21	

Table 5: Parametric results of orc heat recovery system

Parametric Results	Cycle without solar	Cycle with solar
$\eta_{thermal}$	8-15%	12-27%
$\eta_{expander}$	10-25%	10-25%
Process Heat ($Q_{process\ heat}$)	900-1100 kW	1200-1500 kW
Cooling Effect ($Q_{Cooling}$)	14- 19.25 kW	35- 38.5 kW
Expander work ($W_{expander}$)	200-470 kW	260-650 kW
Solar Heating (Q_{Solar})	N/A	460 kW
Solar Collector Efficiency	N/A	20-25%
Water Temp through solar field	N/A	343.15-363.15 K

Table 6: Performance of Adsorption bed-1

COP_{TH}	Q_{COOL}(kJ)	Q_{HEAT}(kJ)	Q_{REF}(kJ)	SCP(kW/kg)	T_{GEN} (K)
0.488	854.6	33543	17222	23.32	328
0.4852	1688	58643	30139	40.53	333
0.4803	2687	84050	43056	57.51	338
0.4749	3850	109765	55973	74.25	343
0.4692	5179	135787	68890	90.76	348

Table 7: Performance of Adsorption bed-2

COP_{SOLAR}	COP_{TH}	I_G (W/m^2)	Q_{COOL}(kJ)	Q_{HEAT}(kJ)	Q_{REF}(kJ)	SCP(kW/kg)	T_{GEN}(K)
0.4811	0.507	750	1570	19858	11638	38.18	333
0.5529	0.482	775	1865	24804	13820	45.34	340.5
0.6202	0.4593	800	2159	30136	16002	52.49	348
0.6834	0.4387	825	2454	35855	18184	59.65	355.5
0.7429	0.4199	850	2748	41961	20366	66.81	363

Table 8: Parametric Results of combined double bed vapor adsorption System

Performance Parameter	Resultant Values	Performance Parameter	Resultant Values	Performance Parameter	Resultant Values
Turbine work output (W_{HPT}& W_{LPT})	294.7 & 1072 kJ/kg	Condenser heat exhaust (Q_{OUT})	2133 kJ/kg	COP of combined VAdRS ($COP_{COMBINEDVADRS}$)	0.46 to 0.51 (13-15% increment in overall COP)
Pump Work (W_{PUMP})	16.23 kJ/kg	Plant Efficiency (η_P)	0.388	Sp. Cooling Power ($SCP_{COMBINEDVADRS}$)	70-90 W/kg (10-16% increment in overall SCP)
Boiler Heat Generation (Q_{IN})	3484 kJ/kg	Net Work Output (W_{NET})	1350 kJ/kg	COP gain by Solar energy (COP_{SOLAR})	0.48-0.74 (most effective COP)

Fig -3 depicts the efficiency of scroll type expander is in the range of 14% to 25% of model-1. The expander in case of cycle without solar integration will do more work. In case of solar integration, more heat for industrial process will be obtained. By increasing the mass flow rate of air in HE-2 increases the heat obtained thereby reducing the cooling effect and heating the air more. In operation cycle with solar heater the change in heat obtained and the rise in air temperature for a small increase in mass flow rate of air is much more than that in the operation cycle without solar heater. Fig 4 shows the integrating solar heating with operation cycle increases the process heat obtained for industrial purpose. When solar heating is not implemented, the heat for process obtained from HE 1 will be more in both cycles than that obtained when solar heating is implemented. Moreover, the gain in the heat obtained from HE 1, for process, per unit increase of mass flow rate of air passing through the HE-1, in case of operation cycle, is greater when solar heating is not implemented than when solar heating is implemented. Fig 5 shows the expander work obtained and the thermal efficiency will be more in case of startup and operation cycle without solar heating. This is because in case of startup and operation cycle without solar heating, work output is being provided by only one expander and also heat obtained for industrial process is only from one heat exchanger as opposed to the case of startup and operation cycle with solar heating where the work output is being provided by two expanders and the heat obtained for industrial process is only from two heat exchanges with additional heat input to the cycle through the utilization of solar energy. The variation of COP with variation of source temperature of VADRS is shown in Fig-6 and it is found that COP o of both Beds are decreasing with increasing source temperature of VADRS. However the COP of bed A is higher than COP of Bed B. Similarly the variation of combined COP with variation of source temperature of VADRS is shown in Fig-7 respectively. It is found that combined COP is increasing order as source temperature of VADRS is increased.

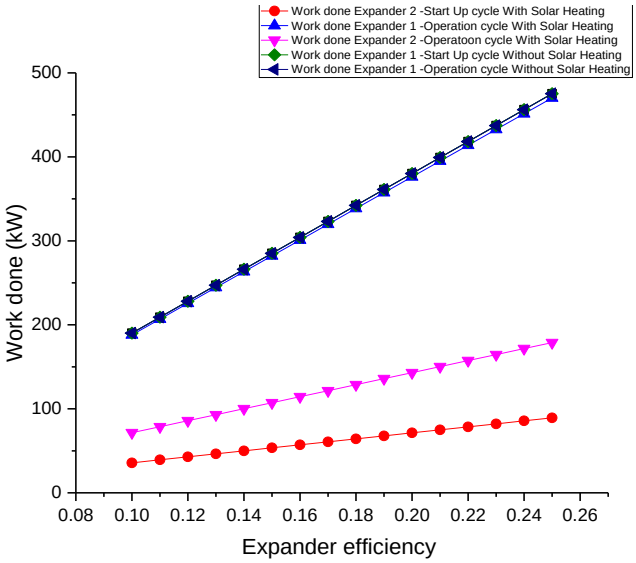


Figure 3: Effect of expander efficiency on work done by expander

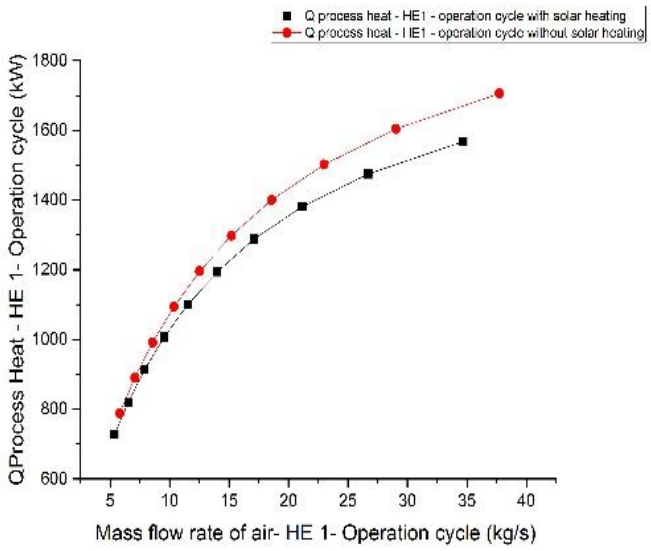


Figure 4: Effect of mass flow rate of air, flowing through HE 1, on Q process heat in operation cycle and startup cycle

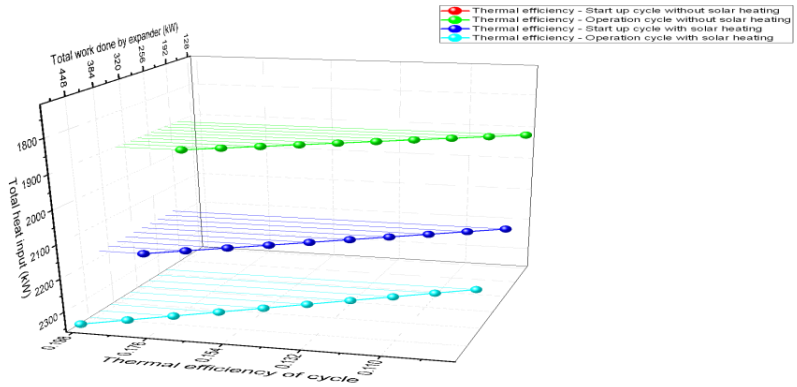


Figure 5: Total work done by expander v/s total heat input V/s thermal efficiency

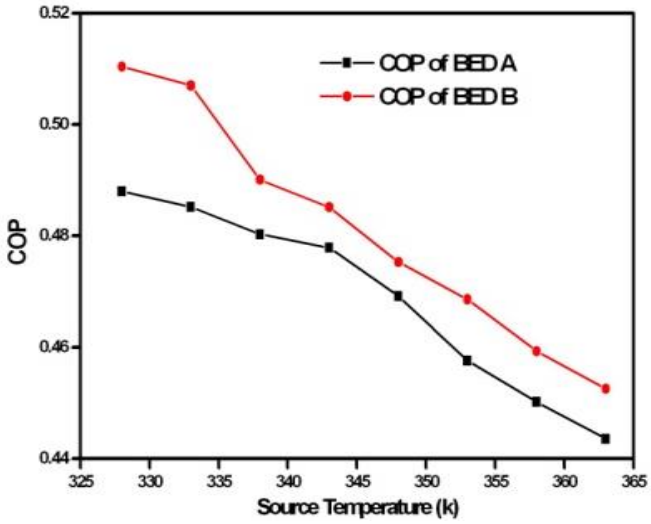


Figure 6: Variation of COP with variation of Source Temp of VADRS

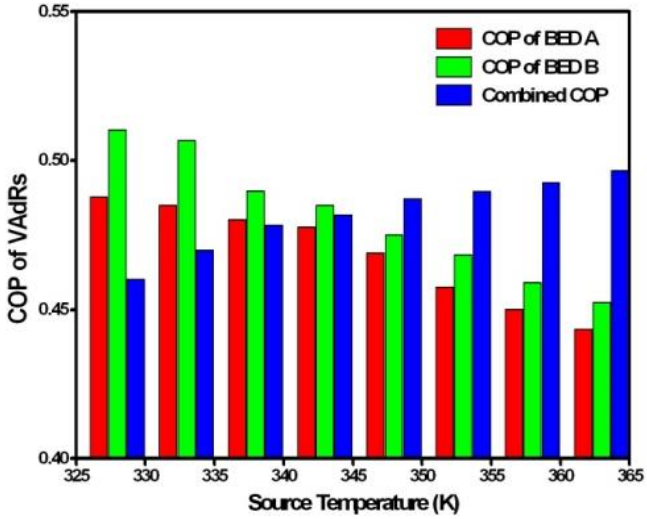


Figure 7: Variation of Combined COP Vs variation of Source Temp of VADRS

6. Conclusion

The selection of a suitable working material depends on its process, application, heat source and the temperature level. The used material must have optimum thermodynamic properties at the lowest possible temperatures and pressures, and also satisfy the several criteria such as being economical, nontoxic, nonflammable, environmentally-friendly.

All conventional refrigeration systems consume precious fuel or electricity to attain refrigeration. ORC and Adsorption systems are heat-operated units that need only heat in terms of un-covered heat from the energy intensive sectors, so they can utilize waste heat and generate multiple effects like heating, power and cooling.

The major conclusion are drawn from both model analysis are given below

1. Rankine Cycle with solar coupling provides more heat for process. This is nearly two times that of the heat provided for process by the cycle without solar coupling, but the total work achieved in case of solar heating is less than that achieved without solar heating.
2. More power from the expanders is achieved when solar heating is not implemented. This is due to the the heat generated by the solar heater is converted into process heat. Therefore, solar integration is recommended, for the purpose of obtaining more process heat, in summer and for the purpose of power generation in winter.
3. Solar integrated thermal circuit in combined power generation system enhance the cooling effect due to more heat addition through solar heating in R134a ORC system.R134a will attain superheating, and produce cooling effect.
4. The parametric table-5 concludes that the performance indicators (thermal efficiency, heating and cooling effect) of proposed system is increased by 30-40% using solar system.
5. Parametric results which is shown in table-8 of double bed vapor adsorption refrigeration system for heat recovery of Reheating-Rankine condenser, the overall COP and SCP enhanced by 10-16% shown in figure 7.
6. Solar connected vapor adsorption bed gives more COP individually as compare to condenser connected vapor adsorption bed. The specific cooling power (SCP) of solar vapor adsorption bed is increasing but increasing of evaporation temperature will decrease the SCP of solar vapor adsorption bed due to conversion of solar gain into heating (Qheat-solar) by double rate.
7. The present combination of adsorbent-adsorbate material is suitable for low grade heat recovery with solar thermal integration for continuous cooling effect generation and applicable for space cooling purpose. The used material R134a and methanol with activated carbon is most suitable pair under the category of eco-friendly material as per AHRAE guidelines of environmental safety protocol.
8. The different materials have reviewed in present analysis. The two parameters are very important for environmental aspect, like GWP and ODP values. Minimum value of GWP &OPD shows non-toxic and eco-friendly nature of material for power and cooling generation system.
9. The proposed material also applicable for low grade heat recovery purpose due to its low boiling and freezing temp thermal property.

References

[1] Vélez, F., Segovia, J., Martín, M.C., Antolín, G., Chejne, F. and Quijano, A., A technical, economical and market review of organic Rankine cycles for the conversion of low-grade heat for power generation. Renewable & Sustainable Energy Reviews, vol. 16, pp. 4175–4189, 2012. pp. 188–195, 2012.

[2] Saleh, B., Koglbauer, G., Wendland, M. and Fischer, J., Working fluids low temperature organic Rankine cycles. Energy, Vol. 32, pp. 1210– 1221, 2007.

[3] Quolin, S., Declaye, S., Tchange, B.F. and Lemort, V., Thermo-Economic optimization of waste heat recovery organic Rankine cycles. Applied Thermal Engineering, vol. 31, pp. 2885-2893, 2011.

[4] Tchange, B.F., Papadakis, G., Lambrinos, G. and Frangoudakis, A.,Fluid selection for a low-temperature solar organic Rankine cycle. AppliedThermal Engineering, vol. 29, pp. 2468–2476, 2009.

[5] Hung, T.C., Shal, T.Y. and Wang, S.K., A review of organic Rankine cycles (ORC`s) for the recovery of low-grade waste heat. Energy, vol. 22(7), pp. 661-667, 1997.

[6] Chen, H., Goswami, Y. and Stefanakos, E., A review of thermodynamic cycles and working fluids for the conversion of low-grade heat. Renewable& Sustainable Energy Reviews, vol. 14, pp.3059–3067, 2010.

[7] U.S. Environmental Protection Agency. Class I Ozone Depleting Substances. [Online]. [date of reference March 11th of 2013] Available at: www.epa.gov/ozone/science/ods/classone.html.

[8] Roy, J.P., Mishra, M.K. and Misra, A., Parametric optimization and performance analysis of a waste heat recovery system using organic Rankine cycle. Energy, vol. 35, pp. 5049-5062, 2010.

[9] Manolakos, D., Papadakis, G., Mohamed, E., Kyritsis, S. and Bouzianas, K., Design of an autonomous low-temperature solar Rankine cycle system for reverse osmosis desalination. Desalination, vol. 183, pp. 73–80, 2005.

[10] Manolakos, D., Papadakis, G., Kyritsis, S. and Bouzianas, K., Experimental evaluation of an autonomous low-temperature solar Rankine cycle system for reverse osmosis desalination. Desalination, vol. 203, pp. 366–374, 2007.

[11] Manolakos, D., Kosmadakis, G., Kyritsis, S. and Papadakis, G., On site experimental evaluation of a low-temperature solar organic Rankine cycle system for RO desalination. Solar Energy, vol. 83, pp. 646–656, 2009.

[12] Manolakos, D., Kosmadakis, G., Kyritsis, S. and Papadakis, G., Identification of behaviour and evaluation of performance of small scale, low-temperature organic Rankine cycle system coupled with a RO desalination unit. Energy, vol. 34, pp. 767–774, 2009.

[13] Bruno, J.C., López-Villada, J., Letelier, E., Romera, S. and Coronas, A., Modelling and optimisation of solar organic Rankine cycle engines for reverse osmosis desalination. Applied Thermal Engineering, vol. 28, pp.2212–2226, 2008.

[14] Delgado-Torres, A. and García-Rodríguez, L., Analysis and optimization of the low-temperature solar organic Rankine cycle (ORC) Energy Conversion and Management, vol. 51, pp. 2846–2856, 2010.

[15] Thanche, B.F., Lambrinos, G., Frangoudakis, A. and Papadakis, G., Exergy analysis of micro-organic Rankine power cycles for a small scale solar driven reverse osmosis desalination system. Applied Energy, vol. 87, pp. 1295–1306, 2010.

[16] Schuster, A. and Karl, J., Simulation of an innovative stand-alone solar desalination system using an organic Rankine cycle. Int. J. of Thermodynamics, vol. 10(4), pp. 155-163, 2007.

[17] Karellas, S., Terzis, K. and Manolakos, D., Investigation of an autonomous hybrid solar thermal ORC-PV RO desalination system. The Chalki island case. Renewable Energy, vol. 36, pp. 583-590, 2011.

[18] Kosmadakis, G., Manolakos, D. and Papakakis, G., Parametric theoretical study of a two-stage solar organic Rankine cycle for RO desalination. Renewable Energy, 35, pp. 989–996, 2010.

[19] Franco, A. and Villani, M., Optimal design of binary cycle power plants for water-dominated, medium-temperature geothermal fields. Geothermics, vol. 38, pp. 379–391, 2009.

[20] Aneke, M., Agnew, B. and Underwood, C., Performance analysis of the Chena binary geothermal power plant. Applied Thermal Engineering, vol. 31, pp. 1825-1832, 2011.

[21] Astolfi, M., Xodo, L., Romano, M. and Macchi, E., Technical and economical analysis of a solar–geothermal hybrid plant based on an organic Rankine cycle. Geothermics, vol. 40, pp. 58–68, 2011.

[22] Wang, L.W., R.Z. Wang, R.G. Oliveira. 2009. "A review on adsorption working pairs for refrigeration." Renewable and Sustainable Energy Reviews, 13(3):518 – 534.

[23] Wang, K., O. Abdelaziz, P. Kisari, E.A. Vineyard. 2011. "State-of-the-Art Review on Crystallization Control Technologies for Water/LiBr Absorption Heat Pumps." International Journal of Refrigeration 34(6):1325 – 1337.

[24] Hu, E.J. 1998. "A study of thermal decomposition of methanol in solar powered adsorption refrigeration systems." Solar Energy 62(5):325-329.

[25] Tamainot-Telto, Z., et al. 2009. "Carbon-ammonia pairs for adsorption refrigeration applications: ice making, air conditioning and heat pumping." International Journal of Refrigeration 32(6):1212 – 1229.

[26] http://www.ormat.com

[27] O. Badr, S.D Probert and P.W. O'Callaghan, Selecting a working fluid for a Rankine-cycle engine, Applied Energy 21 (1985) 1-42.

[28] M.J. Lee, D.L. Tien, C.T. Shao, Thermophysical capability of ozone-safe working fluids for anorganicrankine cycle system, Heat Recovery Systems & CHP 13 (1993) 409-418.

[29] Kyoto Protocol to the United Nations Framework Convention on Climate Change, United Nations,1998.

[30] Mahesh A, Kaushik SC, Solar adsorption refrigeration system using different mass ratio. J Therm Anal Calorim 111:897–903,2013.

International Journal of Research in Engineering and Innovation (IJREI)
journal home page: http://www.ijrei.com
ISSN (Online): 2456-6934

Thermodynamic performance of modified collin cryonic system using energy-exergy analysis for liquefaction of helium gas

R. S. Mishra, Devendra Kumar

Department of Mechanical, Production & Industrial and Automobiles Engineering, Delhi Technological University, Delhi, India

Abstract

Cryogenics systems are which are capable of producing temperature below 150. In the Collin cryogenic systems, a detailed thermodynamic second law analysis have not been reported in literature so far , however in the modification of Collin systems , the yields of liquefied mass of gases is very limited available in literature so far. A comprehensive energy and exergy analysis of Collin cryogenic systems for various gases is carried out in this paper by using various properties variables because cycle pressure ratio is very important factor which highly effect the performance parameters of system .Choice of optimum Pressure Ratio PR increases the overall efficiency of Collin cryogenic system. It was observed that the outlet temperature of compressor affect the performance parameters of system. The second law efficiency decreasing with increasing compressor outlet temperature Similarly liquefaction rate is decreasing with increase outlet temperature of compressor and optimum expander flow fraction 0.55 flow ratio and optimum second law efficiency is 3.5 %, while first heat exchanger (HX1) shows highest rate of exergy destruction ranging from 36 % to 24 % with increase in temperature from 200 K to 400 K. The work done requirement is increases up to pressure ratio 13 and then it start decreasing at a very fast rate with increase in pressure ratio of system.
© 2017 ijrei.com. All rights reserved
Keywords: Thermodynamics Analysis, Collin Cryonic System, Energy-Exergy Analysis, First and second Law Analysis

1. Introduction

Normally cryogenics systems are which are capable of producing temperature below -150. According to National Institute of Standard and Technology Boulder, Colorado the temperature of cryogenics is start below from -180 (93.15 K) ,This Temperature consider as the dividing line because boiling point of permanent gases (helium, hydrogen, oxygen, nitrogen and air like gases).Various process are design and invent to achieve cryo temperature at different level of lower temperature Cryogenics is used in various important process at different level with different naming like cryobiology, cryonics, cryo-electronics, cryotrons, cryosurgery etc. Cryogenics is very crucial for aerospace application. This technology is very critical for wind tunnel testing application. High performance wind tunnel required rapid movement of nitrogen gas around the aerodynamic circuit. Cryogenic is required for Frozen Food Industries for preservation of food item depending upon type of food item and whether they are cooked or not before freezing. Cryogenic has got lot of application in medical field. It is wildly used in MRI equipment for diagnosis of diseases. Cryogenic has got a great role in chilled water storage system. The liquefy gases are store in special containers called Dewar flask. To transfer this liquid from carrier to tank the pump which used are called cryogenics transfer pumps. Cryogenic Process to liquefy air which is further extent to extract various particular gases like oxygen, nitrogen, etc. In this process liquefaction and purification of Helium, Nitrogen gases are done. Also using this technique production of inert gases is also be done. Today cryogenics industries are a billionaire industry and lots of research is going on to achieve best one improved process. Various analyses is done to identify the loop hole of process and to rectify it to their upper level.

2. Liquefaction of Helium

Cryogenic Technology is used for production of Gases for industrial and commercial applications. The helium is the most difficult of all gases to liquefy. At atmospheric pressure, it boils at approximately -269oC. Its maximum inversion

Corresponding author: R.S. Mishra
Email Id:rsmishradtu@gmail.com

temperature is about -234oC. The helium was first liquefied by Onnes H.K in the University of Leiden in 1908. It can be liquefied by an arrangement similar to the hydrogen liquefier where both liquid nitrogen and hydrogen are used for pre-cooling. The disadvantages of hydrogen liquefaction system include the higher cost and hazardous nature of liquid hydrogen. Similarly helium may also be liquefied by using Claude principle, where expanders are used for producing refrigeration. Fig-1(a) shows a system developed by Dr. S.C. Collins for liquefaction of helium. In this system, helium at a pressure of approximately 12 atmospheres is supplied to the liquefier by a four stage compressor. The part of helium is pre-cooled by the liquid nitrogen. By using this combination of heat exchangers and expander are shown in Fig-1(a) and T-S-diagram is also shown in Fig-1(b) respectively .The high pressure helium gas may be cooled to about -257^{0}C. The helium gas thus obtained is throttled to atmospheric pressure to product liquid helium at -269oC. Dr. Collins is found that for one such plant, a liquefaction rate of 25 to 32 liters per hour may be obtained with a power requirement of 45kW. Various research and different method are employed to increase efficiency of cryo system. Second law efficiency are very low in all system.

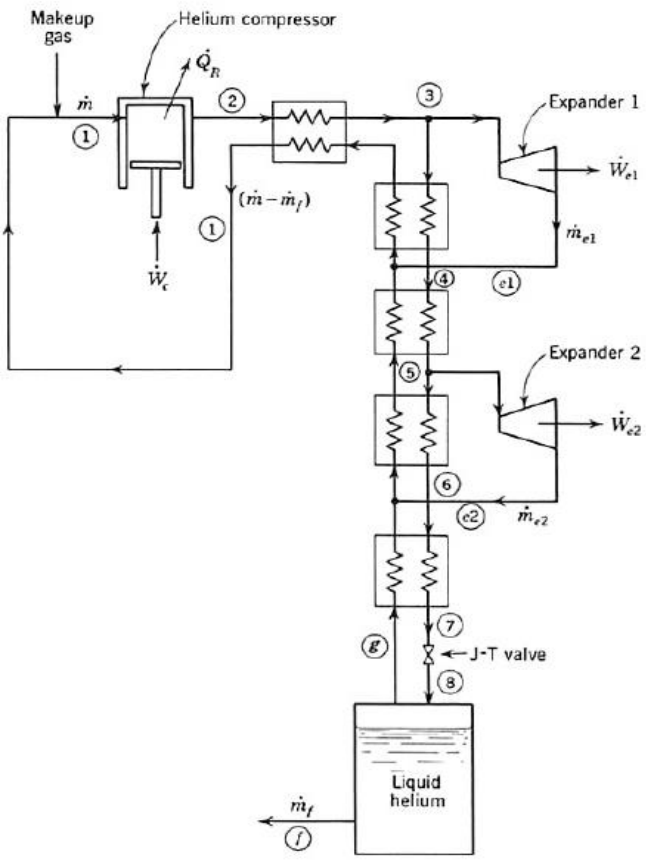


Figure 1(a): Schematic of modified Collin cryonic system

3. Literature Review

Various research and different method are employed to increase efficiency of cryo system. Exergy analysis is a strong method to identified inefficiencies of system and tells which part of system is critical and need to be undertake study. From literature various data collected which help in optimization of cryogenic system.

The Bejan [1] work is basis of all exergetic analysis of heat exchangers. Various problems are studied related to exergy analysis which are mentioning or summarized in [2], from the vast study it noticed that most new methods differ only in the way that entropy generation is non-dimensional [3]. A good exergetic design of a heat exchanger would allow for an increase in the global efficiency of the process, by defining a thermodynamic cycle in which the exergetic losses would be limited [4].

The major cause of exergy loss is the use of compressors and to a lesser extent the use of turbines [5] H. Mahabadipour and H. Ghaebi [6] carried out Thermodynamic (energy –exergy) analysis of and comparison of two expander cycles used in refrigeration system of olefin. Recep Yumrutaş, Mehmet Kunduz, Mehmet Kanoğlu [7] also carried out Exergy analysis of vapor compression refrigeration systems. Gadhiraju Venkatarathnam [8], carried out Simulation of cryogenic processes and compared the performance s of the systems. From literature it noticed that exergy efficiency depend upon mainly upon the inlet condition of the system but which inlet condition best suit for a particular type of the system that is main work of research except to increase the whole system efficiency stress are done on particular parts of system and research are done on that systems. After reviewing literature it conclude that every part of system has its own and equal importance because ones effect on another whether it is small or big create a lot of difference in proper analysis of system. Ignoring one small system due less effect can put gap in complete research analysis of system that why it quite important take all parts of system as one and finding out the every part impact on another to calculate right equation for high output. Air separation unit and compressor, condenser and evaporator of cryo system are the center of research because most of exergy destruction takes place in these parts. Heat exchanger and expansion valve, expander and other addition parts should also properly analyze Advanced technologies are used in very limited way and only on some of system such as Collin cryonic system. Therefore following objectives of present investigation are

(i) energy-exergy analysis of Collin cryogenic systems and to find out optimum exergy destruction in individual component and (ii) Suggestion for reducing exergy destruction losses in whole systems and there components

In this analysis, the effects of pressure ratio and outlet temperature of compressor on various energy- and exergy-based performance parameters are investigated.

4. Mathematical Analysis of Collin system

Fig: 1(b) show the schematic diagram of Collin system along with and T-S diagram in Fig-1(b). The following numerical values have been used for modeling of modified Collins cryogenic system.

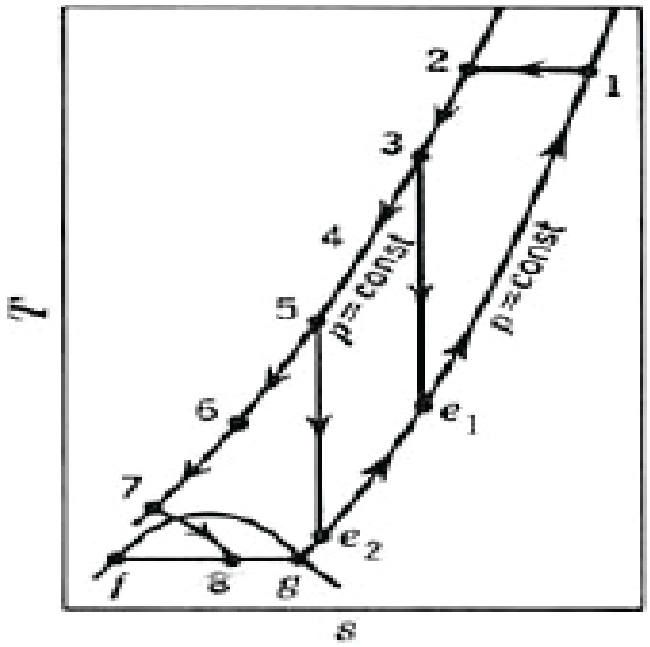


Figure 1(b: T-S Diagram of Collin system

$R\$ =' Helium'$
$P_1 = 1.013, T_2 = 300, T_0 = 298, P_2 = 11, T_1 = T_2, r1 = 0.5$
$r2 = \frac{r1}{2}, r1 = \frac{m_{e1}}{m}, r2 = \frac{m_{e2}}{m}, P_2 = P_3, P_2 = P_5, m = 20$
$T_f = T_g, x_0 = 0$

4.1 Control Vol except compressor

$m * h_2 = W_{e1} + W_{e2} +$
$(m - m_f) * h_1 + m_f * h_f$
$W_{e1} = m_{e1} * (h_3 - h_{e1})$
$W_{e2} = m_{e2} * (h_5 - h_{e2})$
$Ed_{W_{e1}} = (m_{e1} * T_0 * (s_3 - s_{e1}))$
$Ed_{W_{e2}} = (m_{e2} * T_0 * (s_5 - s_{e2}))$
$y = \frac{m_f}{m}$
Compressor
$W_c = m * (T_2 * (s_1 - s_2) - (h_1 - h_2))$
$Q = m * (h_2 - h_1)$
$Ed_{comp} = \begin{pmatrix} m * T_1 * (s_1 - s_2) - \\ \left(Q * \left(\frac{T_0}{T_1}\right)\right) \end{pmatrix}$
$W_{net} = W_c + W_{e1} + W_{e2}$
$-\frac{W_{net}}{m} = Z$ Work done per mass of gas
$-\frac{W_{net}}{m_f} = T$ Work done per mass of liq gas
$COP = \left(\frac{h_1 - h_f}{W_{net}}\right)$
$Eta_{2nd_{\%}} = \left(\left(\frac{(h_f - h_1) - T_0 * (s_f - s_1)}{W_{net}} * m_f\right) * 100\right)$

4.2 First Heat Exchanger(HX_1) analysis

$TypeHX_{1\$} =' counterflow'$
$epsilon_{HX1} = 0.85, T_{h_i} = T_2, T_{15} = T_{c_o}, m_{h_{HX1}} = m$
$m_{c_{HX1}} = m - m_f, T_{h_o} = T_3, T_{c_i} = T_{14},$
$C_{h_{HX1}} = m_{h_{HX1}} * cp_{hot_{fluid_{HX1}}}$
$C_{c_{HX1}} = m_{c_{HX1}} * cp_{cold_{fluid_{HX1}}}$
$q_{HX1} = C_{h_{HX1}} * (T_{h_i} - T_{h_o})$
$q_{HX1} = C_{c_{HX1}} * (T_{c_o} - T_{c_i})$
$q_\max_HX1 = C_\min_HX1 *$
$(T_h_i - T_c_i)$
$epsilon_HX1 = q_HX1 / q\max.$
$Ntu_{HX1} = HX\begin{pmatrix} TypeHX_{1\$}, \\ epsilon_{HX1}, C_{h_{HX1}}, C_{c_{HX1}}, 'Ntu' \end{pmatrix}$
$Ntu_HX1 = (G_HX1)/C\min.$
$Ex_{in_{HX1}} = m * \begin{pmatrix} (h_2 - h_3) - \\ (T_0 * (s_2 - s_3)) \end{pmatrix}$
$Ex_{out_{HX1}} = (m - m_f) * \begin{pmatrix} (h_{14} - h_{15}) - \\ (T_0 * (s_{14} - s_{15})) \end{pmatrix}$
$Ed_{HX1} = \left((Ex_{in_{HX1}}) - (Ex_{out_{HX1}})\right)$

4.3 Second Heat Exchanger(HX_2) analysis

$TypeHX_{2\$} =' counterflow'$
$epsilon_{HX2} = 0.85$
$T_{13} * (m - m_f) = m_{e1} * T_{e1} +$
$(m - m_f - m_e1) * T_12$ "
$m_{h_{HX2}} = m - m_{e1}$
$m_{c_{HX2}} = m - m_f$
$C_{h_{HX2}} = m_{h_{HX2}} * cp_{hot_{fluid_{HX2}}}$
$C_{c_{HX2}} = m_{c_{HX2}} * cp_{cold_{fluid_{HX2}}}$
$q_{HX2} = C_{h_{HX2}} * (T_3 - T_4)$
$q_{HX2} = C_{c_{HX2}} * (T_{14} - T_{13})$
$q_\max_HX2 = C_\min_HX2 *$
$(T_3 - T_13)$
$epsilon_HX2 = q_HX2 / q\max.$
$Ntu_{HX2} = HX\begin{pmatrix} TypeHX_{2\$}, \\ epsilon_{HX2}, C_{h_{HX2}}, C_{c_{HX2}}, 'Ntu' \end{pmatrix}$
$Ntu_HX2 = (G_HX2)/C\min.$
$Ex_{in_{HX2}} = (m - m_{e1}) * \begin{pmatrix} (h_3 - h_4) - \\ (T_0 * (s_3 - s_4)) \end{pmatrix}$
$Ex_{out_{HX2}} = (m - m_f) * \begin{pmatrix} (h_{13} - h_{14}) - \\ (T_0 * (s_{13} - s_{14})) \end{pmatrix}$

$$Ed_{HX2} = \left(\left(Ex_{in_{HX2}}\right) - \left(Ex_{out_{HX2}}\right)\right)$$

4.4 Third Heat Exchanger (HX_3) analysis

$$TypeHX_{3\$} =' counterflow'$$
$$epsilon_{HX3} = 0.85$$
$$m_{h_{HX3}} = m - m_{e1}$$
$$m_{c_{HX3}} = m - m_f - m_{e1}$$
$$C_{h_{HX3}} = m_{h_{HX3}} * cp_{hot_{fluid_{HX3}}}$$
$$C_{c_{HX3}} = m_{c_{HX3}} * cp_{cold_{fluid_{HX3}}}$$
$$q_{HX3} = C_{h_{HX3}} * \ (T_4 - T_5)$$
$$q_{HX3} = C_{c_{HX3}} * \ (T_{12} - T_{11})$$
$$q_\max_HX3 = C_\min_HX3 \ * \ (T_4 - T_11)$$
$$epsilon_HX3 = q_HX3/q\max_{HX3}.$$
$$Ntu_{HX3} = HX\left(\begin{matrix} TypeHX_{3\$}, \\ epsilon_{HX3}, C_{h_{HX3}}, C_{c_{HX3}}, 'Ntu' \end{matrix}\right)$$
$$Ntu_HX3 = (G_HX3)/C\min_{HX3}.$$
$$Ex_{in_{HX3}} = (m - m_{e1}) * \left(\begin{matrix} (h_4 - h_5) - \\ \left(T_0 * (s_4 - s_5)\right) \end{matrix}\right)$$
$$Ex_{out_{HX3}} = \left(m - m_f - m_{e1}\right) * \left(\begin{matrix} (h_{11} - h_{12}) - \\ \left(T_0 * (s_{11} - s_{12})\right) \end{matrix}\right)$$
$$Ed_{HX3} = abs\left(\left(Ex_{in_{HX3}}\right) - \left(Ex_{out_{HX3}}\right)\right)$$

4.5 Fourth Heat Exchanger(HX_4) analysis

$$TypeHX_{4\$} =' counterflow'$$
$$epsilon_{HX4} = 0.85$$
$$T_{10} * \left(m - m_f - m_{e1}\right) = m_{e2} * T_{e2} + \left(m - m_f - m_{e1} - m_{e2}\right) * T_9$$
$$m_{h_{HX4}} = m - m_{e1} - m_{e2}$$
$$m_{c_{HX4}} = m - m_f - m_{e1}$$
$$C_{h_{HX4}} = m_{h_{HX4}} * cp_{hot_{fluid_{HX4}}}$$
$$C_{c_{HX4}} = m_{c_{HX4}} * cp_{cold_{fluid_{HX4}}}$$
$$q_{HX4} = C_{h_{HX4}} * \ (T_5 - T_6)$$
$$q_{HX4} = C_{c_{HX4}} * \ (T_{11} - T_{10})$$
$$q_\max_HX4 = C_\min_HX4 \ * \ (T_5 - T_10)$$
$$epsilon_HX4 = q_HX4/q\max_{HX4}.$$
$$Ntu_{HX4} = HX\left(\begin{matrix} TypeHX_{4\$}, \\ epsilon_{HX4}, C_{h_{HX4}}, C_{c_{HX4}}, \ 'NTU' \end{matrix}\right)$$
$$Ntu_HX4 = (G_HX4)/C\min_{HX4}.$$
$$Ex_{in_{HX4}} = (m - m_{e1} - m_{e2}) * \left(\left(h_5 - h_6\right) - \left(T_0 * (s_5 - s_6)\right)\right)$$
$$Ex_{out_{HX4}} = \left(m - m_f - m_{e1}\right) * \left(\left(h_{10} - h_{11}\right) - \left(T_0 * (s_{10} - s_{11})\right)\right)$$
$$Ed_{HX4} = abs\left(\left(Ex_{in_{HX4}}\right) - \left(Ex_{out_{HX4}}\right)\right)$$

4.6 Fifth Heat Exchanger(HX_5) analysis

$$TypeHX_{5\$} =' counterflow'$$
$$epsilon_{HX5} = 0.90$$
$$c_{p_{fluid_{hot}}} = 5.192 \left[\frac{kj}{kgK}\right]$$
$$c_{p_{fluid_{cold}}} = 5.146$$
$$cp_{hot_{fluid_{HX5}}} = Cp(R\$, T = T_6, P = P_2)$$
$$cp_{cold_{fluid_{HX5}}} = Cp\left(R\$, T = T_f + 1, P = P_1\right)$$
$$m_{dot_{h_{HX5}}} = (m - m_{e1} - m_{e2})$$
$$m_{dot_{c_{HX5}}} = \left(m - m_{e1} - m_{e2} - m_f\right)$$
$$C_{dot_{h_{HX5}}} = m_{dot_{h_{HX5}}} * c_{p_{fluid_{hot}}}$$
$$C_{dot_{c_{HX5}}} = m_{dot_{c_{HX5}}} * c_{p_{fluid_{cold}}}$$
$$q_{HX5} = C_{dot_{h_{HX5}}} * \ (T_6 - T_7)$$
$$q_{HX5} = C_{dot_{c_{HX5}}} * \ \left(T_9 - T_g\right)$$
$$C_dot_\min_HX5 = \min(C_dot_h_HX5, C_dot_c_HX5)$$
$$q_\max_HX5 = C_dot_\min_HX5 \ * \ (T_6 - T_g)$$
$$epsilon_HX5 = q_HX5/q\max_{HX5}.$$
$$Ntu_{HX5} = HX\left(\begin{matrix} TypeHX_{5\$}, epsilon_{HX5}, \\ C_{dot_{h_{HX5}}}, C_{dot_{c_{HX5}}}, 'Ntu' \end{matrix}\right)$$
$$Ntu_HX5 = (G_HX5)/C_dot\min_{HX5}.$$
$$Ex_{in_{HX5}} = (m - m_{e1} - m_{e2}) * \left(\left(h_6 - h_7\right) - \left(T_0 * (s_6 - s_7)\right)\right)$$
$$Ex_{out_{HX5}} = \left(m - m_{e1} - m_{e2} - m_f\right) * \left(\left(h_g - h_9\right) - \left(T_0 * \left(s_g - s_9\right)\right)\right)$$
$$Ed_{HX5} = abs\left(\left(Ex_{in_{HX5}}\right) - \left(Ex_{out_{HX5}}\right)\right)$$

"J-T Valve"

$$h_7 = h_8$$
$$x_1 = 1$$
$$Ex_{in_{Val}} = (m - m_{e1} - m_{e2}) * \left(\left(h_7 - h_0\right) - T_0 * (s_7 - s_0)\right)$$
$$Ex_{out_{val}} = (m - m_{e1} - m_{e2}) * \left(\left(h_8 - h_0\right) - T_0 * (s_8 - s_0)\right)$$
$$Ed_{val} = \left(Ex_{in_{Val}} - Ex_{out_{val}}\right)$$

"Separator"

$$(m - m_{e1} - m_{e2}) * h_8 = m_f * h_f + \left(m - m_{e1} - m_{e2} - m_f\right) * h_g$$
$$m_g = \left(m - m_{e1} - m_{e2} - m_f\right)$$
$$Ed_{sep} = abs\left(T_0 * \left(\begin{matrix} \left(\begin{matrix} m_g * s_g - \\ \left(m_g + m_f\right) * s_8 \end{matrix}\right) + \\ \left(\frac{m_g * h_g - m_f * h_f}{T_0}\right) \end{matrix}\right)\right)$$

$$Ed_{comp_{\%}} = \left(\frac{Ed_{comp}}{Ed_{He_{sys}}}\right) * 100$$

$$Ed_{W_{e1_{\%}}} = \left(\frac{Ed_{W_{e1}}}{Ed_{He_{sys}}}\right) * 100$$

$$Ed_{W_{e2_{\%}}} = \left(\frac{Ed_{W_{e2}}}{Ed_{He_{sys}}}\right) * 100$$

$$Ed_{HX1}\% = \left(\frac{Ed_{HX1}}{Ed_{He_{sys}}}\right) * 100$$

$$Ed_{HX2}\% = \left(\frac{Ed_{HX2}}{Ed_{He_{sys}}}\right) * 100$$

$$Ed_{HX3}\% = \left(\frac{Ed_{HX3}}{Ed_{He_{sys}}}\right) * 100$$

$$Ed_{HX4}\% = \left(\frac{Ed_{HX4}}{Ed_{He_{sys}}}\right) * 100$$

$$Ed_{HX5}\% = \left(\frac{Ed_{HX5}}{Ed_{He_{sys}}}\right) * 100$$

$$Ed_{val}\% = \left(\frac{Ed_{val}}{Ed_{He_{sys}}}\right) * 100$$

$$Ed_{sep}\% = \left(\frac{Ed_{sep}}{Ed_{He_{sys}}}\right) * 100$$

$$Ed_{He_{sys}} = Ed_{comp} + Ed_{W_{e1}} + Ed_{W_{e2}} + Ed_{HX1} + Ed_{HX2} + Ed_{HX3} + Ed_{HX4} + Ed_{HX5} + Ed_{val} + Ed_{sep}$$

Table 1: Variable Table (Collin System)

Variable (a)	Gas	Variable (b)	Variable (c)
h_0	$R\$$	T_0	P_1
h_1	$R\$$	T_1	P_1
h_2	$R\$$	T_2	P_2
s_0	$R\$$	T_0	P_1
s_1	$R\$$	T_1	P_1
s_2	$R\$$	h_2	P_2
s_3	$R\$$	T_3	P_2
h_3	$R\$$	T_3	P_2
s_f	$R\$$	x_0	P_1
h_f	$R\$$	x_0	P_1
s_g	$R\$$	x_1	P_1
h_g	$R\$$	x_1	P_1
T_f	$R\$$	h_f	P_1
T_{e1}	$R\$$	s_3	P_1
h_{e1}	$R\$$	T_{e1}	P_1
s_{e1}	$R\$$	T_{e1}	h_{e1}
T_{e2}	$R\$$	s_5	P_1
h_{e2}	$R\$$	T_{e1}	P_1
s_{e2}	$R\$$	P_1	h_{e1}
$cp(hf)_{HX1}$	$R\$$	T_2	P_2
$cp(cf)_{HX1}$	$R\$$	T_{14}	P_1
C_{min}	-	C_{hot_HX1}	C_{cold_HX1}
$cp(hf)_{HX2}$	$R\$$	T_3	P_2
$cp(cf)_{HX2}$	$R\$$	T_{14}	P_1
C_{min}	$R\$$	C_{hot_HX2}	C_{cold_HX2}
$cp(hf)_{HX3}$	$R\$$	T_4	P_2
$cp(cf)_{HX3}$	$R\$$	T_{13}	P_1
C_{min}	$R\$$	C_{hot_HX3}	C_{cold_HX3}
$cp(hf)_{HX4}$	$R\$$	T_6	P_2
$cp(cf)_{HX4}$	$R\$$	T_{f+1}	P_1
C_{min}	$R\$$	C_{hot_HX4}	C_{cold_HX4}
$cp(hf)_{HX5}$	$R\$$	T_5	P_2
$cp(cf)_{HX5}$	$R\$$	T_{10}	P_1
C_{min}	$R\$$	C_{hot_HX4}	C_{cold_HX4}
h_7	$R\$$	T_6	P_2
s_7	$R\$$	T_6	P_2
h_7	$R\$$	T_7	P_2
s_7	$R\$$	T_7	P_2
s_4	$R\$$	T_4	P_2
h_4	$R\$$	T_4	P_2
s_5	$R\$$	T_5	P_2
h_5	$R\$$	T_5	P_2
s_8	$R\$$	h_8	P_2
h_9	$R\$$	T_9	P_1
s_9	$R\$$	T_9	P_1
h_{10}	$R\$$	T_{10}	P_1
s_{10}	$R\$$	T_{10}	P_1
h_{11}	$R\$$	T_{11}	P_1
s_{11}	$R\$$	T_{11}	P_1
h_{12}	$R\$$	T_{12}	P_1
s_{12}	$R\$$	T_{12}	P_1
h_{13}	$R\$$	T_{13}	P_1
s_{13}	$R\$$	T_{13}	P_1
h_{14}	$R\$$	T_{14}	P_2
s_{14}	$R\$$	T_{14}	P_2
h_{15}	$R\$$	T_{15}	P_1
s_{15}	$R\$$	T_{15}	P_1

5. Results and Discussions

A comprehensive exergy analysis and other analysis of Collin system is carried out by using various different gases with variable properties. Numerical computation is carried out to find out mutually dependency and effect of various properties on other properties and their involvement in exergy destruction. In fig.2, the second law efficiency have maximum value at pressure ratio (PR) 11 and beyond this it start decreasing at very fast rate. COP of the system also decrease with increase in PR of cycle but this decrement is marginal .On entire PR range 5 to 29 the decrement in COP of system is 0.065 to 0.03 so the optimum pressure ratio (PR) is chosen on the basis of highest second law efficiency that is pressure ratio (PR) 11. Similarly, the specific heat of fluid in heat exchanger highly influence the performance of system. Due to change in pressure ratio the specific heat of fluid in different heat

exchanger is effected which turn effect the performance of system.

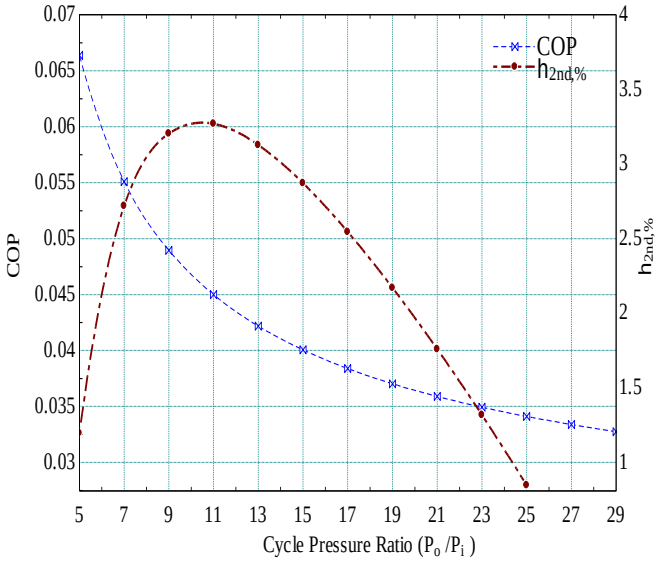


Figure 2: Variation of COP and second law efficiency (%) versus cycle pressure ratio

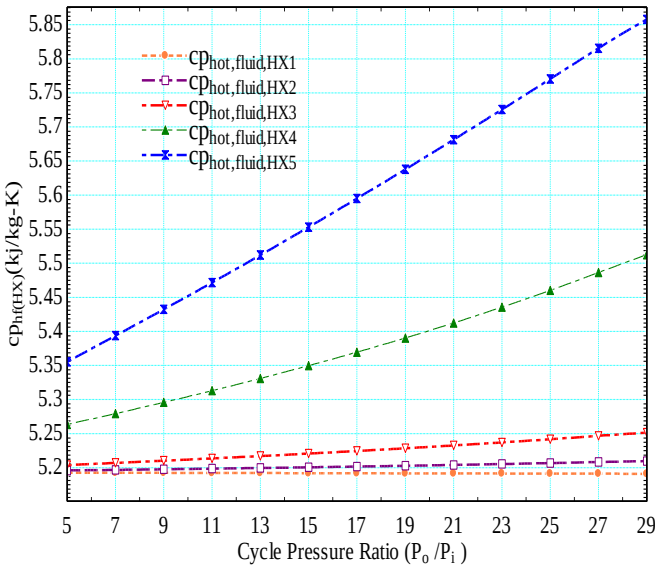


Figure 3: Specific heat of heat exchangers versus cycle pressure ratio

In fig.3, the variation in specific heat of helium gas in different heat exchanger is notice with respect to change in pressure ratio (PR) of the system. From the graph analysis in observed that specific heat in the low temperature heat exchanger (HX4, HX5) are highly influenced by the change in the pressure ratio of system. Lowest heat exchanger five (HX5) show the variation in the specific heat change from 5.35 kJ/kg-K to 5.85 kj/kg-K whereas for fourth heat exchanger (HX4) this change is varies from 5.25 kJ/kg-K to 5.5 kj/kg-K over the cycle pressure ratio range 5 to 29.The high temperature heat exchanger (HX1, HX2, HX3) show very negligible change in specific heat of helium with variation in cyclic pressure ratio of system. From analysis, it observed that low temperature heat exchangers are very crucial as per design consideration. Number of transfer unit value help in design the heat exchanger.

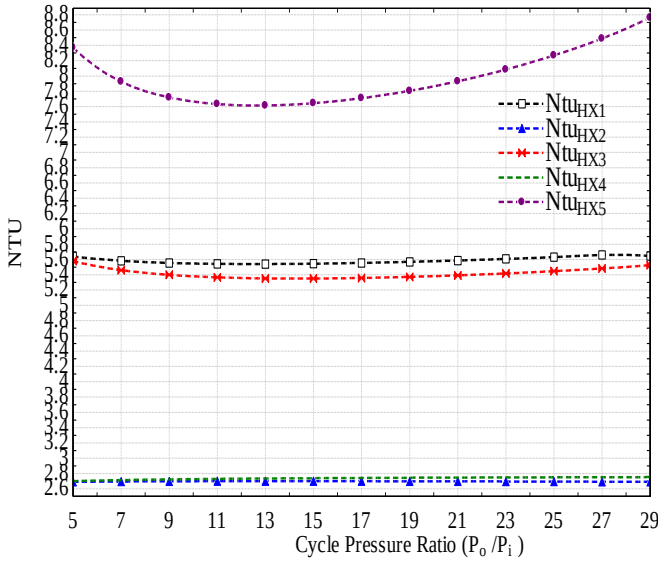


Figure 4: Variation of NTU of heat exchangers versus cycle pressure ratio

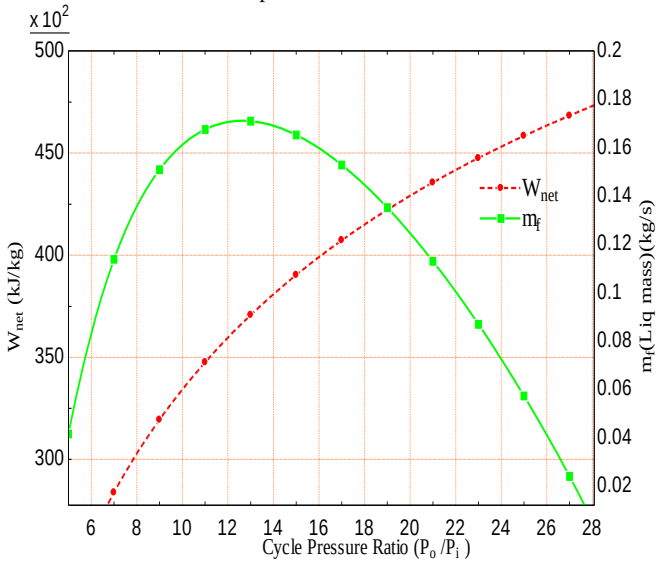


Figure 5: Variation of Net work done and Liquefaction mass rate versus cycle pressure ratio

Fig.4, illustrate the variation in NTU value of heat exchangers with increase in pressure ratio of system. First heat exchanger have the highest value of NTU. Its NTU value first decreases from 8.4 to 7.6 over the PR 5 to 13 .but further increases in PR NTU value of HX1 (First heat exchanger) is increases and it varies from 7.6 to 8.8 up to PR 29.Work done per liquefaction mass and liquefaction rate of system variation with cycle

pressure ratio is shown in fig 5.Liquefaction rate of system is NTU value of HX1 (First heat exchanger) is increases and it varies from 7.6 to 8.8 up to PR 29.Work done per liquefaction mass and liquefaction rate of system variation with cycle pressure ratio is shown in fig 5.Liquefaction rate of system is increases from 0.02 kg/s to 0.18 kg/s over PR range 6 to 28 when input mass flow rate of helium gas is taken as 1 kg/s.

The work done required to liquefy helium gas is very high due to very low liquefaction temperature .The work done requirement is increases up to PR 13 then it start decreasing at a very fast rate with increase in PR of system. Above fig.6 shows exergy destruction (%) in every component of helium liquefaction system with respect to change in pressure ratio. The high temperature heat exchanger show highest rate of destruction in system up 30% while compressor show second highest exergy destruction varies from 15 % to 18 % for pressure ratio range 5 to 29 but at PR 5 and 7 heat exchanger five HX5 show more exergy destruction which gradually decreases over increasing range of PR.

Expansion valve show least exergy destruction among all component followed by separator 3% which gradually decreases with increases in pressure ratio. Exergy destruction in heat exchanger two (HX2) increases with increase in pressure ratio in range of 6 % to 14 % .Heat exchanger four also show decreasing trend of exergy destruction with increase in pressure ratio (PR).

The outlet temperature of compressor affect the performance parameters of system. Fig.7 show the variation in COP and second law efficiency of system with increase in outlet temperature of compressor. COP of system varied from 0.04445 to 0.453 over temperature increasing range of 200 K to 400 K whereas second law efficiency continuously decreasing from 10 % to1 % over this temperature range of compressor. COP of the system is minimum effect of increasing temperature.

Therefore optimum temperature of system is decided by second law efficiency. From graph it is depicted that lowest temperature 200 K is desirable for Collin system and the intersection point of both curve COP and second law efficiency respectively is 270 K.

In fig.8 variation in the total work done required to liquefy helium and liquefaction rate is measured with change in outlet compressor temperature.

Liquefaction rate is varies from 0.35 kg/s to 01 kg/s, a decreasing trend with increase in outlet temperature of compressor.

The net work done is increases with increase in outlet temperature and it varies from 225 kW to 455 kW for overall compressor temperature. Variation in specific heat of helium from 8.4 to 7.6 over the PR 5 to 13, but further increase in PR in heat exchanger with respect to compressor outlet temperature is shown in fig.9.

Low temperature heat exchanger HX5 and HX4 show decreasing value of specific heat that is 5.6 kJ/kg-K to 5.4 kJ/kg-K (HX5) and 5.4 KJ/kg-K to 5.28 KJ/kg-K for (HX4) for compressor outlet temperature increasing range 220 K to 400 K. Other heat exchanger HX3, HX2 and HX1 specific heat variation is decreasing in nature with increasing compressor temperature. The first heat exchanger (HX1) shows the specific heat variation that 5.1.1 KJ/kg-K. For all heat exchangers NTU value is increases with increase in outlet temperature that is shown in fig.10.

It was observed that HX5 show highest increase in its NTU value from 6.8 to 8.2 while HX1 and HX3 show 5.4 to 5.7 and 5.0 to 5.3 with outlet temperature range 200 K to 400 K. Heat exchanger HX2 and HX4 show least value of NTU 2.7 which almost constant for entire compressor temperature range. The exergy destruction (%) of the system with respect to compressor outlet temperature is depicted in fig.11.

From thermodynamic analysis it observed that first heat exchanger (HX1) show highest rate of destruction ranging from 36 % to 24 % with increase in temperature from 200 K to 400 K. heat exchanger five (HX5) show almost constant exergy destruction 15 % at all considered range of temperature of compressor. In compressor the exergy destruction up to 260 K is lower than the exergy destruction of HX5 and then in start increasing again up to 24 % at 400 K .Valve how lowest and destruction in valve is almost negligible because this valve already work at a very low temperature.HX4 followed by separator exergy destruction 4 % and 1 % respectively and constant over considered pressure range.

The variation in expander flow fraction from compressor effect the performance of the system. In Collin system two expander are employed .Second expander ratio is kept constant in one by three ratio with respect to first expander flow fraction .Figure 12 show the variation in COP and second law efficiency (%) with increase in flow ratio of first expander. From study in concluded that COP of system is decreases 0.0457 to 0.0446 with increase in flow ratio while second law efficiency increases up to 0.55 and then it start decreasing with increases in flow fraction. At 0.55 flow ratio the second law efficiency is 3.5 %, so the optimum expander slow fraction for first expander is 0.55. Variation in liquefaction rate with respect first expander flow fraction is shown in fig. 13.

The liquefaction rate is increases with increase in flow fraction up to 0.55 then it start decreasing further more increase in flow fraction. At flow fraction 0.55 the highest liquefaction rate is 0.18 kg/s

.

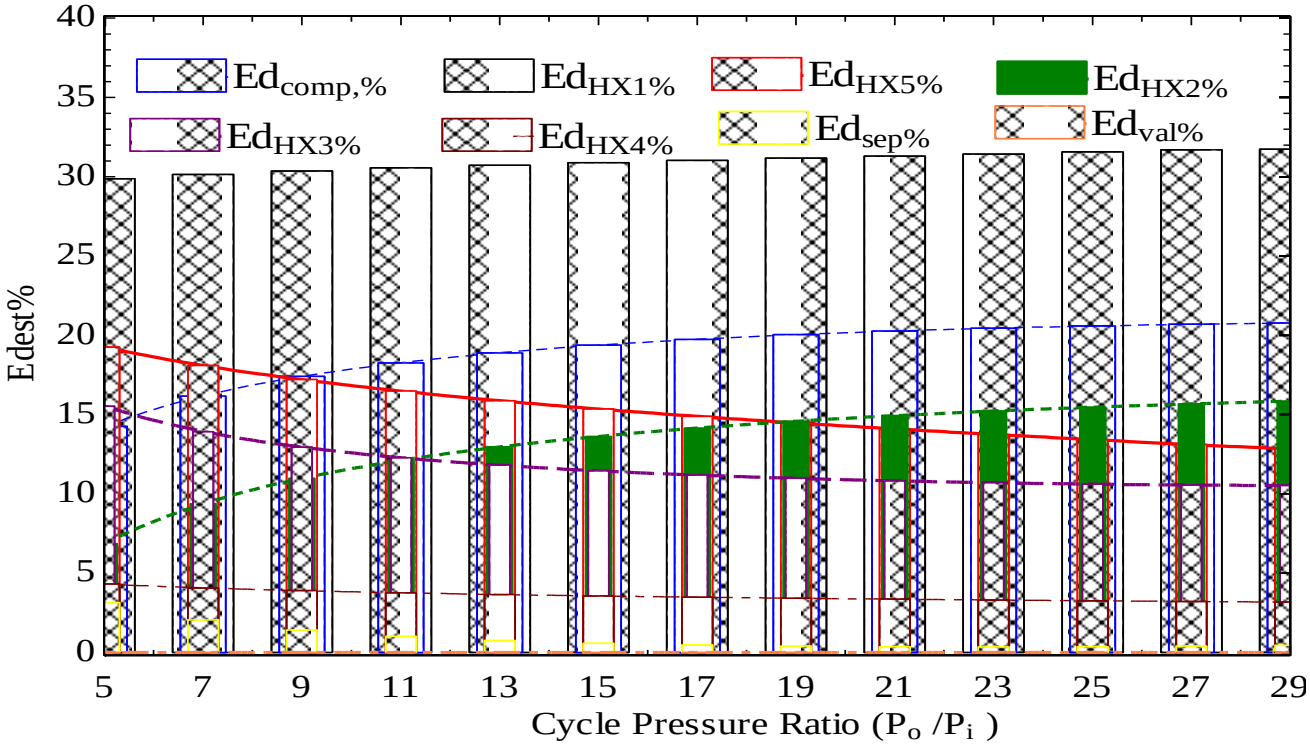


Figure 6: Variation of Exergy destruction (%) versus cycle pressure ratio

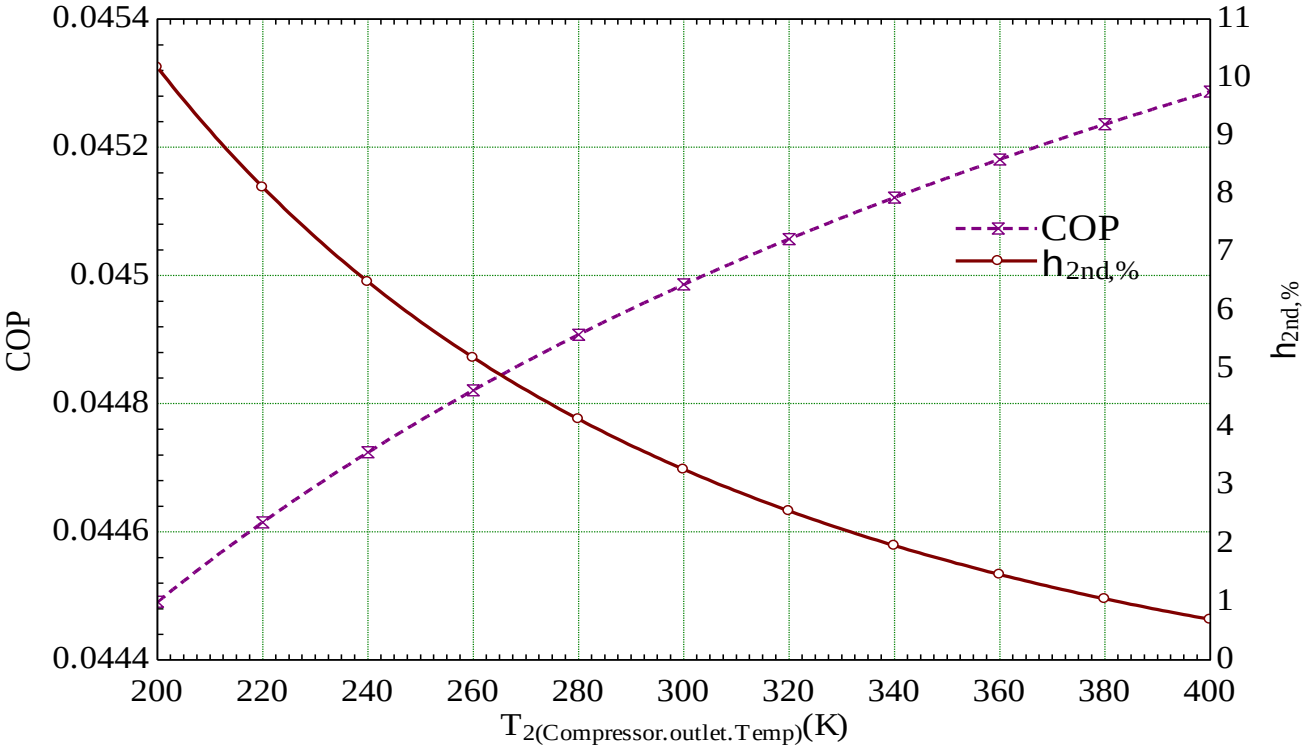


Figure 7: Variation of COP and second law efficiency versus compressor outlet temperature

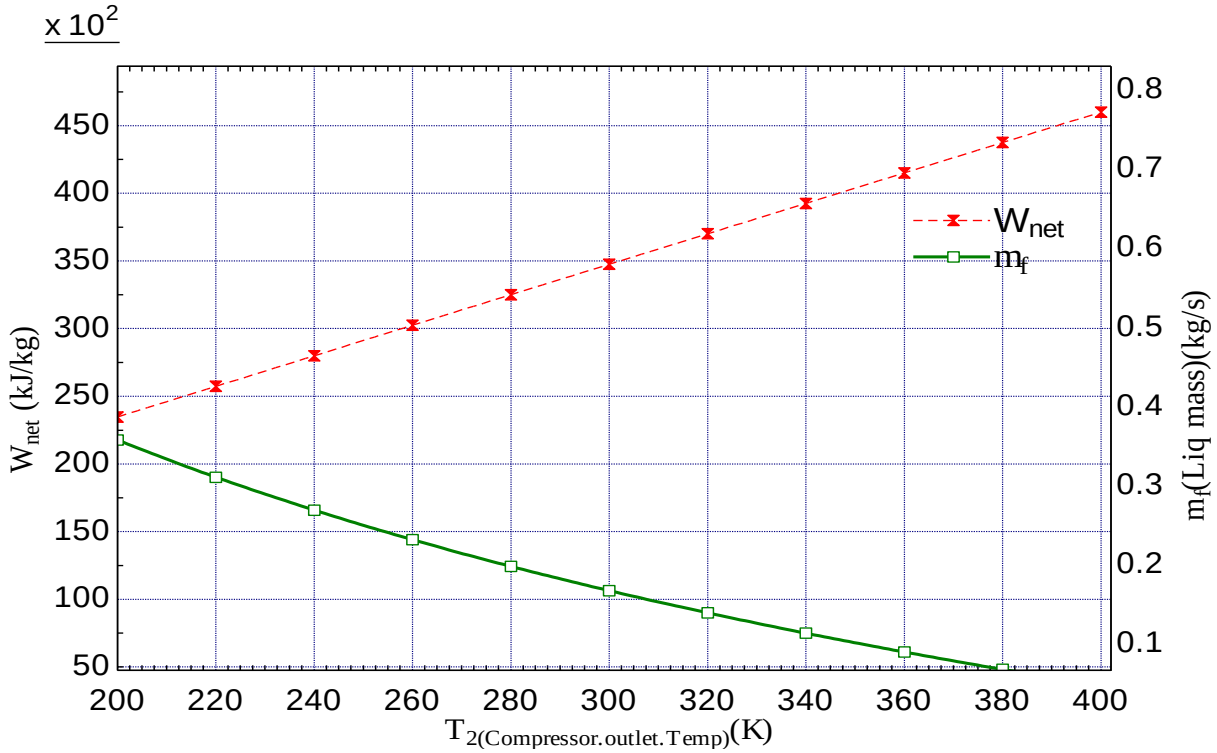


Figure 8: Variation of Net work and liquefaction rate versus compressor outlet temperature

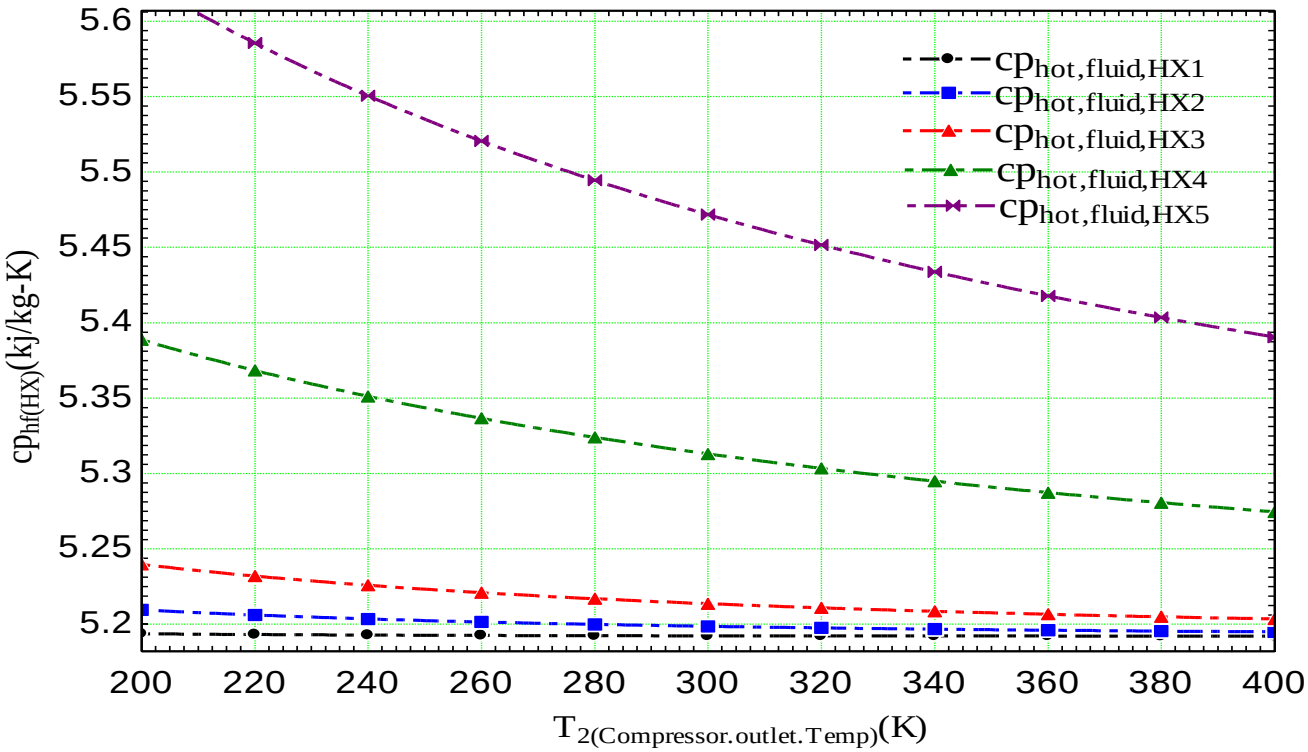


Figure 9: Variation of NTU of heat exchangers versus compressor outlet temperature

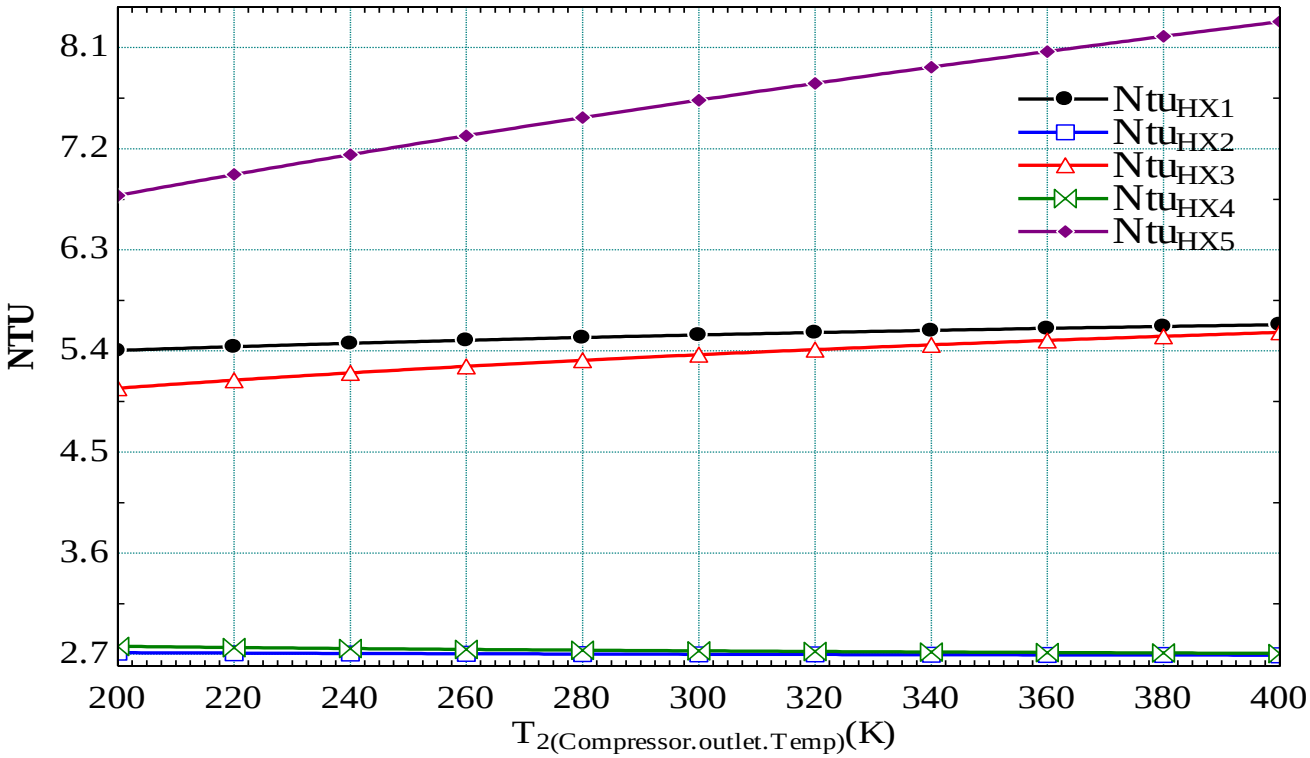


Figure 10: Variation of NTU versus compressor outlet temperature

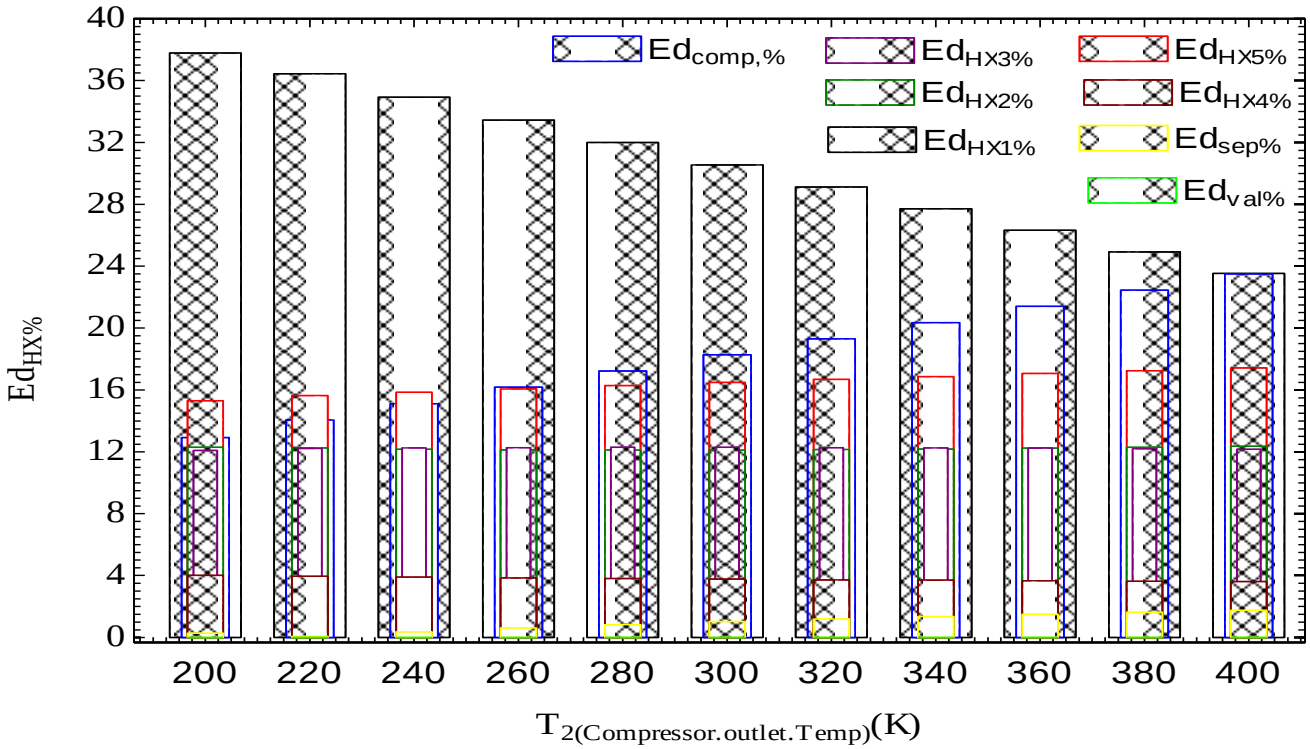


Figure 11: Exergy destruction (%) versus compressor outlet temperature

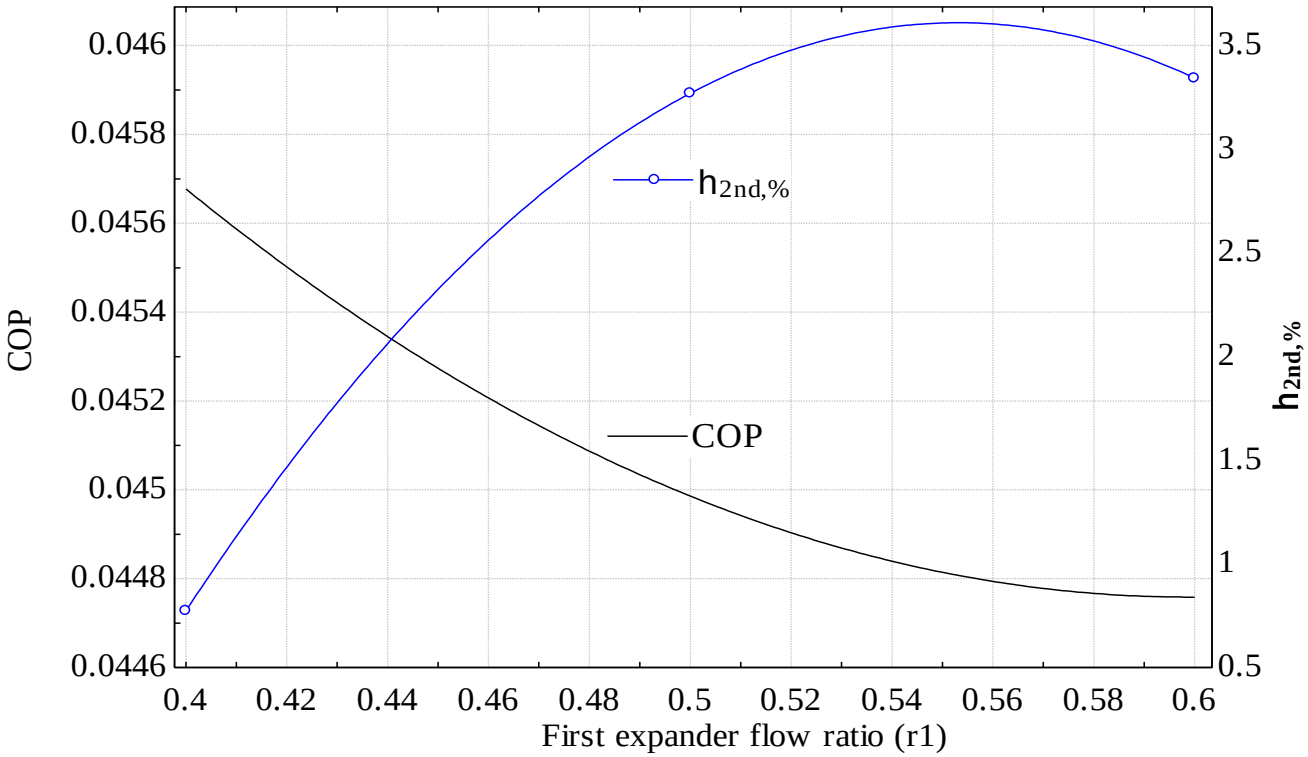


Figure 12: COP and second law efficiency (%) with respect to first expander flow ratio (r1)

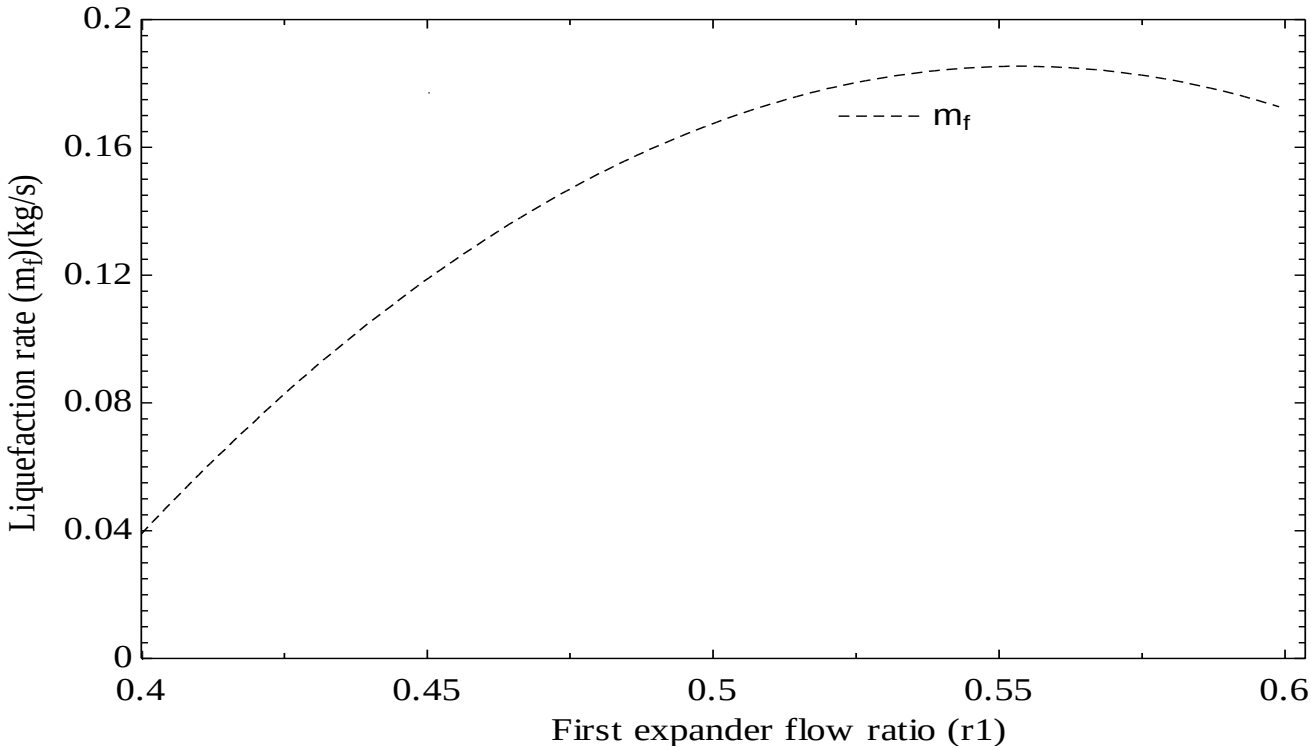


Figure 13: Liquefaction rate versus first expander flow ratio.

6. Conclusions and Recommendations

The following conclusion have been drawn from present investigations.

1. The liquefaction rate is increases with increase in flow fraction to 0.55 then it start decreasing further more increase in flow fraction.
2. At flow fraction0.55 the highest liquefaction rate is 0.18 kg/s.
3. First law efficiency in terms of COP of system is decreases 0.0457 to 0.0446 with increase in flow ratio while second law efficiency increases up to 0.55 and then it start decreasing with increases in flow fraction.
4. First heat exchanger (HX1) shows highest rate of exergy destruction ranging from 36 % to 24 % with increase in temperature from 200 K to 400 K.
5. The specific heat variations in all heat exchangers are decreasing in with increasing compressor temperature.
6. All heat exchangers NTU value is increases with increase in outlet temperature and fifth heat exchanger (HX5) shows highest increase in its NTU value from 6.8 to 8.2 while for other heat exchangers, NTU is remains constant.
7. Liquefaction rate is decreasing with increase outlet temperature of compressor.
8. The high temperature heat exchanger show highest rate of destruction in system up 30% while compressor shows second highest exergy destruction varies from 15 % to 18 % for pressure ratio range 5 to 29 while exergy destruction in the second heat exchanger (HX2) increases with increase in pressure ratio.

References

[1] A. Bejan, General criterion for rating heat-exchanger performance. Int. J. Heat Mass Transf. 1978, 21,pp 655– 658

[2] M. Yilmaz, O. N. Sara, S. Karsli, Performance evaluation criteria for heat exchangers based on second law analysis. Exergy Int. J. 2001, 4,pp 278–294

[3] S. T. Wu, X. F. Yuan, Y. R. Li, L. Xiao, Exergy transfer effectiveness on heat exchanger for finite pressure drop. Energy 2006, 32, pp 2110–2120.

[4] T. J. Kotas, The Exergy Method of Thermal Plant Analysis; 1995 Ed.; Krieger Publishing Company London, UK, 1985

[5] R. L. Cornelissen, G. G. Hirs, Exergy analysis of cryogenic air separation, Energy Conversion and Management, 39, 16–18, 1998, pp 1821-1826.

[6] H. Mahabadipour and H. Ghaebi, "Development and comparison of two expander cycles used in refrigeration system of olefin plant based on exergy analysis", Applied Thermal Engineering 50 (2013), pp 771-780.

[7] Recep Yumrutaş, Mehmet Kunduz, Mehmet Kanoğlu, Exergy analysis of vapor compression refrigeration systems, Exergy, An International Journal, Volume 2, Issue 4, 2002, pp 266-272.

[8] Gadhiraju Venkatarathnam , "Simulation of cryogenic processes", Cryogenic Mixed Refrigerant Processes, International Cryogenics Monograph Series 2008, pp 51-63.

International Journal of Research in Engineering and Innovation (IJREI)
journal home page: http://www.ijrei.com
ISSN (Online): 2456-6934



Thermodynamic performance of vapour compression refrigeration systems using HFO refrigerants for replacing HFC refrigerants

R.S. Mishra

Department of Mechanical & Production Engineering, Delhi Technological University Delhi, India

Abstract

Due to economic growth, population growth and improved living standards the annual energy consumption behavior and demand is steadily increasing. Presently, major demands of cooling and heating applications are met out by the conventional vapor compression systems.The recent global agreement signed in Kigali to limit the use of hydrofluorocarbons (HFCs) as refrigerants, starting *by* 2019, has promoted an active area of research toward the development of low global warming potential (GWP) new refrigerants. Hydro-fluoro-olefins (HFOs) have been proposed as a low GWP alternative to replace third generation HFC refrigerants. The numerical computations for predicting first law and second law performances for two vapour compression refrigeration systems had been carried out using R1234ze and R1234yf as fourth generation low GWP refrigerants for replacing third generation refrigerant (R134a). The comparison were carried out using HFC-134a for two systems (i.e. System-1 : consisting of condenser, evaporator compressor and throttling valve and System-2 consisting of condenser, evaporator compressor and expander, It was found that system-2 using expander gives best thermodynamic performances around 25.65% higher than system-1 using throttle valve . The comparison were made for using eighteen ecofriendly refrigerants and lowest thermal performance were found using R125 and higher thermal performances were observed by using R123. However thermodynamic performance s using hydro carbons are also comparable.
© 2018 ijrei.com. All rights reserved
Keywords: Gas turbine, Retrofitting, EVC, STIG, Exergy

1. Introduction

Refrigeration plays a very important role in industrial, domestic and commercial sectors for cooling, heating and food preserving applications. There are innumerable applications of such systems and they are the major consumer of electricity around the world. Energy consumption is directly proportional to the economic development of any nation, however this area is in great interest now because of increase in the cost of conventional fuels and environmental concerns globally. The scientists are looking for new and renewable sources of energy so as to minimize the costs. Due to the increasing energy demand, degradation of environment, global warming and depletion of ozone layer etc, there is urgent need of efficient energy utilization and waste heat recovery for useful applications. The researchers are concentrating on the alternate and environment friendly refrigerants, especially after the Kyoto and the Montreal protocols. However, in a quest to find out alternate and environment friendly refrigerants, the energy efficiency of the equipment having conventional refrigerants is also very important in the present age of competitive business community. The aim of the scientific community all over the world is to switch to new and renewable energy sources besides, efficient utilization of all conventional sources.

1.1 Use of ecofriendly refrigerants

Currently used third generation hydrofluorocarbon (HFC) refrigerants are known to be Nano zone depleting agents, but are also characterized by their substantial global warming potential (GWP) values. Consequently, the year 2016 marked the launch of a global environmental deal to phase out the production and consumption of HFCs by years 2036 to 2047, starting in 2019. Most of the current effective and proposed regulations target 150 GWP for refrigeration and 750 GWP for air conditioning applications, thus creating an immediate

Corresponding author: R. S. Mishra
Email Address: hod.mechanical.rsm@dtu.ac.in

demand for developing new fourth generation refrigerants with low GWPs. In response to this need, the National Institute of Standards and Technology recommended a list of new classes of refrigerants that would possess low values of GWPs based on estimates done using data on the chemical structure, the radiative efficiency, and the atmospheric lifetime of these molecules. Hydro-fluoro-olefins (HFOs) were included in the NIST list as one of the best candidates found so far, with GWP values comparable to those of hydrocarbon (HC)-based refrigerants. Furthermore, cycle performance tests carried out for HFOs proved their suitability to act as a replacement for HFCs used in mobile air-conditioners, vending machines, and chillers. As a result, a major shift in the automobile industry is planned to start in the year 2017 to replace 1,1,1,2-tetrafluoroethane (HFC-134a) as a working fluid by 2,3,3,3-tetrafluoropropene (HFO-1234yf), a newly introduced fourth generation refrigerant. Vapour compression refrigeration cycles for carrying out these cycles are well known. In theoretical vapour compression refrigeration, saturated vapour refrigerants at low pressure enter a compressor and undergo isentropic compression. The high pressure vapour enters a condenser and heat is rejected from the fluid at constant pressure from the condenser. The working fluid leaves the condenser as a saturated liquid. An isenthalpic throttling process follows across an expansion valve or capillary tube. The working fluid is then evaporated at constant pressure with the working fluid absorbing heat to complete the cycle. Xiaohui et al [1] presented the performance study of vapour compression system where the expander work recovered during the expansion process was also employed for sub cooling of the system and found higher COP of the system while using R12, R32, R22, R134a refrigerants. Victor et al [2] presented a performance study on automobile air-conditioning based on vapor compression refrigeration cycle with R134a as refrigerant by incorporating an expander and predicted reasonable gains in cycle performance. Alison et al [3] did an economic analysis based on thermodynamic performance by using expander in the refrigeration systems of a medium refrigerating load for ambient temperature of 35 °C, evaporating temperature of 7.2 °C and the condensing temperature of 54.4 °C was considered. Bjorn[4]presented a study by compared properties of hydrocarbons, namely propane, propene and isobutene with R134a, R22 and ammonia and predicted the higher performance of hydrocarbons over R134a and R22 in vapour compassion refrigeration system The present investigation relates generally to the vapour compression refrigeration systems, using expander which utilizes the work expended in direct expansion of a refrigerant to power a turbine which drives a compressor of a refrigeration system in compressing gaseous vapours from evaporator pressure to condenser pressure.

2. Results and Discussions

The following two systems have been chosen for numerical computation.

System-1: consisting of condenser, evaporator compressor and throttling valve and
System-2 consisting of condenser, evaporator compressor and expander.

2.1 Effect of ecofriendly refrigerants on thermal performances

The numerical values for both systems are as given below:
Compressor Efficiency=0.80
Expander Efficiency=0.80
Condenser temperature=50^0C
Evaporator temperature=-10^0C
The thermal performance s in terms of first law efficiency (COP) and second law efficiency in terms of exergetic efficiency and exergy destruction ratio are shown in Table-1(a) to Table-1(c) respectively. It was found from Table-1(a) that first law performance in terms of COP of system-2 containing expander gives higher first law efficiency in terms of COP than system-1 and the maximum coefficient of performance is found using R123 and then ecofriendly R245fa refrigerant. However using hydrocarbons in the vapour compression refrigeration systems gives attractive first and second law performance the lowest COP was found using R125 refrigerant. Similarly in system-1, using throttle valve, the maximum COP was observed using R152a and lowest COP was observed using R125 refrigerant. Similarly from table-1(b) & table-1(c) Second law efficiency in terms of exergetic efficiency of system2 containing expander gives better exergetic efficiency and lower exergy destruction ratio than system-1 containing throttle valve. The same trend was also observed in second law performance.

Table-1(a); Comparison of First law efficiency in terms of COP of both systems

Refrigerant	COP_System-I	COP_System-II
R-134a	2.464	3.095
R1234ze	2.42	3.090
R1234yf	2.255	2.981
R-227ea	2.056	2.889
R236fa	2.361	3.052
R245fa	2.634	3.182
R404a	2.009	2.864
R407c	2.084	2.809
R410a	2.259	2.925
R152a	2.652	3.156
R290	2.405	3.067
R600a	2.484	3.11
R600	2.627	3.17
R-125	1.785	2.74
R123	2.744	3.23
R32	2.416	2.917
R717	2.728	2.999
R507a	2.030	2.877

Table-1(b); Comparison of second law efficiency in terms of Exergetic Efficiency of both systems

Refrigerant	ETA_II_System-I	ETA_II_System-II
R-134a	0.328	0.4118
R1234ze	0.3221	0.4113
R1234yf	0.3001	0.3967
R-227ea	0.2737	0.3845
R236fa	0.3142	0.4061
R245fa	0.3505	0.4232
R404a	0.2673	0.3811
R407c	0.2773	0.3739
R410a	0.3007	0.3892
R152a	0.3529	0.420
R290	0.3201	0.4082
R600a	0.3306	0.4138
R600	0.3496	0.4219
R-125	0.2375	0.3646
R-123	0.3652	0.4298
R32	0.3215	0.3882
R717	0.3630	0.3992
R507a	0.2701	0.3838

Table-1(c): Comparison of rational exergy destruction ratio of both systems

Refrigerant	EDR_System_I	EDR_System_II
R-134a	0.6720	0.5882
R1234ze	0.6779	0.5887
R1234yf	0.6999	0.6033
R-227ea	0.7263	0.6155
R236fa	0.6858	0.5939
R245fa	0.6495	0.5766
R404a	0.7327	0.6189
R407c	0.7227	0.6261
R410a	0.6993	0.6108
R152a	0.6471	0.580
R290	0.6799	0.5918
R600a	0.6694	0.5862
R600	0.6504	0.5781
R-125	0.7625	0.6354
R-123	0.6348	0.5702
R32	0.6785	0.6118
R717	0.6370	0.6008
R507a	0.7299	0.6172

2.2 Effect of evaporator temperature on thermal performances using hfo-1234yf refrigerant

Compressor Efficiency=0.80, Expander Efficiency=0.80, Condenser temperature= 50^0C, Refrigerants used: R-1234yf R134a and R-1234yf

The variation of thermal performances in terms of first law efficiency (COP) and II law efficiency in terms of exergetic efficiency and exergy destruction ratio with variation of evaporator temperature using HFO-1234yf, R 134a and HFO-1234ze refrigerants are shown in Table-2(a) to Table-2(c) and using R134a from Table-4(a-c) and also using ecofriendly low GWP and zero ODP HFO -1234ze are shown in Table-6(a-c) respectively. It was found from Table-2(a),Table-(4a) and Table-6(a) that that first law performance in terms of COP of both systems are increased by increasing condenser temperature and exergy destruction ratio is decreased.

Table-2(a); Comparison of First law efficiency in terms of COP of both systems using R1234yf

T_Eva (^{0}C)	COP_System_I	COP_System_II
20	6.179	7.129
15	5.047	5.940
10	4.201	5.049
5	3.547	4.358
0	3.027	3.806
-5	2.604	3.355
-10	2.255	2.981
-15	1.962	2.665
-20	1.714	2.396
-25	1.501	2.163
-30	1.317	1.961

Table-2(b); Comparison of second law efficiency in terms of Exergetic Efficiency of both systems using R1234yf

T_Eva (^{0}C)	ETA_II_System_I	ETA_II_System_II
20	0.1055	0.1217
15	0.1752	0.2062
10	0.2227	0.2676
5	0.2552	0.3135
0	0.2772	0.3485
-5	0.2915	0.3756
-10	0.3001	0.3967
-15	0.3042	0.4132
-20	0.3049	0.4261
-25	0.3026	0.4361
-30	0.2981	0.4438

Table-2(c); Comparison of second law efficiency in terms of Exergetic Efficiency of both systems using R1234yf

T_Eva (^{0}C)	*EDR_System_I*	*EDR_System_II*
20	0.89450.8945	0.8783
15	0.8248	0.7938
10	0.7773	0.7324
5	0.7448	0.6865
0	0.7228	0.6515
-5	0.7085	0.6244
-10	0.6999	0.6033
-15	0.6958	0.5868
-20	0.6951	0.5739
-25	0.6974	0.5639
-30	0.7069	0.5562

Table-3(a); Comparison of First law efficiency in terms of COP of both systems using R1234yf

T_Condenser^{0}C	COP_System_I	COP_System_II
30	4.171	4.814
35	3.551	4.214
40	3.044	3.728
45	2.619	3.324
50	2.255	2.981
55	1.937	2.683
60	1.653	2.42

Table-3(b); Comparison of second law efficiency in terms of Exergetic Efficiency of both systems using R1234yf

T_Condenser ^{0}C	ETA_II_System_I	ETA_II_System_II
30	0.5551	0.6406
35	0.4725	0.5608
40	0.4051	0.4961
45	0.3486	0.4424
50	0.3001	0.3967
55	0.2577	0.3571
60	0.220	0.322

Table-3 (c); Comparison of second law efficiency in terms of Exergetic Efficiency of both systems using R1234yf

T_Condenser ^{0}C	*EDR_System_I*	*EDR_System_II*
30	0.4449	0.3594
35	0.5275	0.4392
40	0.5948	0.5039
45	0.6514	0.5576
50	0.6999	0.6033
55	0.7423	0.6429
60	0.780	0.6780

Table-4(a); Comparison of First law efficiency in terms of COP of both systems using R134a

T_Eva (^{0}C)	COP_System_I	COP_System_II
20	6.429	7.278
15	5.286	6.08
10	4.433	5.182
5	3.772	4.485
0	3.246	3.928
-5	2.819	3.473
-10	2.464	3.095
-15	2.167	2.775
-20	1.914	2.502
-25	1.696	2.267
-30	1.508	2.061

Table-4(b); Comparison of second law efficiency in terms of Exergetic Efficiency of both systems using R134a

T_Eva (^{0}C)	ETA_II_System_I	ETA_II_System_II
20	0.1097	0.122
15	0.1836	0.2111
10	0.2350	0.2747
5	0.2714	0.3226
0	0.2973	0.3597
-5	0.3155	0.3887
-10	0.328	0.4118
-15	0.3359	0.4303
-20	0.340	0.4451
-25	0.3020	0.4570
-30	0.3413	0.4665

Table-4(c); Comparison of second law efficiency in terms of Exergetic Efficiency of both systems using R134a

T_Eva (^{0}C)	*EDR_System_I*	*EDR_System_II*
20	0.8903	0.8758
15	0.8164	0.7889
10	0.765	0.7253
5	0.7286	0.6774
0	0.7027	0.6403
-5	0.6845	0.6113
-10	0.6720	0.5882
-15	0.6641	0.5697
-20	0.6596	0.5549
-25	0.6580	0.5430
-30	0.6587	0.5335

Table-5(a); Comparison of First law efficiency in terms of COP of both systems using R134a

T_Condenser ^{0}C	COP_System_I	COP_System_II
30	4.326	4.904
35	3.718	4.308
40	3.224	3.8270
45	2.814	3.43
50	2.464	3.095
55	2.162	2.807
60	1.895	2.555

Table-5(b); Comparison of second law efficiency in terms of Exergetic Efficiency of both systems using R134a

T_Condenser ^{0}C	ETA_II_System_I	ETA_II_System_II
30	0.5757	0.6526
35	0.4947	0.5733
40	0.4291	0.5093
45	0.3744	0.4565
50	0.3280	0.4118
55	0.2877	0.3735
60	0.2523	0.340

Table-5 (c); Comparison of second law efficiency in terms of Exergetic Efficiency of both systems using R134a

T_Condenser ^{0}C	*EDR_System_I*	*EDR_System_II*
30	0.4243	0.3474
35	0.5053	0.4267
40	0.5709	0.4909
45	0.6255	0.5436
50	0.6720	0.5882
55	0.7123	0.6265
60	0.7477	0.660

Table-6(a); Comparison of First law efficiency in terms of COP of both systems using R1234ze

T_Eva (^{0}C)	COP_System_I	COP_System_II
20	6.446	7.308
15	5.287	6.10
10	4.421	5.196
5	3.75	4.493
0	3.215	3.931
-5	2.78	3.472
-10	2.42	3.09
-15	2.117	2.768
-20	1.860	2.493
-25	1.639	2.255
-30	1.448	2.048

Table-6(b); Comparison of second law efficiency in terms of Exergetic Efficiency of both systems using R1234ze

T_Eva (^{0}C)	ETA_II_System_I	ETA_II_System_II
20	0.110	00.1247
15	0.1836	0.2118
10	0.2349	0.2754
5	0.2697	0.3232
0	0.2944	0.360
-5	0.3112	0.3887
-10	0.3227	0.4113
-15	0.3283	0.4292
-20	0.3308	0.4434
-25	0.3305	0.4546
-30	0.3277	0.4635

Table-6(c); Comparison of second law efficiency in terms of Exergetic Efficiency of both systems using R1234yf

T_Eva (^{0}C)	*EDR_System0.6692_I*	*EDR_System_II*
20	0.890	0.8753
15	0.8164	0.7882
10	0.7657	0.7246
5	0.7303	0.7246
0	0.7056	0.6768
-5	0.6888	0.640
-10	0.6779	0.6113
-15	0.6717	0.5887
-20	0.6692	0.5708
-25	0.6695	0.5566
-30	6723	0.5454

2.3 Effect of condenser temperature on thermal performances using hfo-1234yf refrigerant

Compressor Efficiency=0.80
Expander Efficiency=0.80
Condenser temperature= 50^{0}C
Refrigerants used: R-1234yf, R134a and R1234ze

The variation of thermal performances in terms of first law efficiency (COP) and second law efficiency in terms of exergetic efficiency and exergy destruction ratio with variation of condenser temperature using HFO-1234yf refrigerant are shown in Table-2 (a-c) respectively and using R134a are shown in Table-5(a) to Table-Table-5(c) and using Low GWP and zero ODP are shown in Table-7(a-b) respectively It was found from Table-2(a) that first law performance in terms of COP is reduced by increasing condenser temperature and exergy destruction ratio is also increased.

Table-7(a); Comparison of First law efficiency in terms of COP of both systems using R134a

T_Condenser ^{0}C	COP_System_I	COP_System_II
30	4.308	4.923
35	3.691	4.32
40	3.191	3.833
45	2.774	3.43
50	2.42	3.09
55	2.113	2.798
60	1.843	2.543

Table-7(b); Comparison of second law efficiency in terms of Exergetic Efficiency of both systems using R134a

T_Condenser ^{0}C	ETA_II_System_I	ETA_II_System_II
30	0.5733	0.6551
35	0.4912	0.5749
40	0.4246	0.5101
45	0.3692	0.4565
50	0.3221	0.4113
55	0.2812	0.3724
60	0.2453	0.3384

Table-7 (c); Comparison of second law efficiency in terms of Exergetic Efficiency of both systems using R134a

T_Condenser ^{0}C	EDR_System_I	EDR_System_II
30	0.4267	0.3449
35	0.5088	0.4251
40	0.5754	0.4899
45	0.6308	0.5435
50	0.6779	0.5887
55	0.7188	0.6276
60	0.7547	0.6616

3. Conclusion

(i) The first law performance in terms of COP of system -2 containing expander is higher than system -1 containing throttle valve.
(ii) The higher COP was found usng R123 refrigerant and is higher than R245fa and lower COP is found by using R125.
(iii) Thermal performances in terms of first law efficiency (COP) and second law efficiency in terms of exergetic efficiency decreases with variation of condenser temperature using HFO-1234yf refrigerant. Similarly exergy destruction ratio of both systems are increased with increasing condenser temperature.
(iv) The thermal performances in terms of first law efficiency (COP) and second law efficiency in terms of exergetic efficiency increases with increasing evaporator temperature using HFO-1234yf refrigerant and exergy destruction ratio decreases with increasing evaporator temperature for both systems.
(v) The thermal performances in terms of first law efficiency (COP) and second law efficiency in terms of exergetic efficiency of both systems using R134a is higher than using R1234ze and R1234yf. However first law efficiency of R1234ze is also higher than R1234yf and also slightly lesser than using R134a. It is clear that both HFO refrigerants (i.e. R1234ze and R1234yf) will replace R134a in near future for domestic applications.

References

[1] Xiaohui She, Yonggao Yin, Xiao song Zhang (2014) "A proposed subcooling method for vapor compression refrigeration cycle based on expansion power recovery", International Journal of Refrigeration, Vol 43; pp: 50-61.

[2] Victor A. Gonzalves, Jose A. R. Parise (2008) "A Study on the Reduction of Throttling Losses in Automotive Air Conditioning Systems Through Expansion Work Recovery", International Refrigeration and Air Conditioning Conference, Paper 882; pp: 1-8.

[3] Alison Subiantoro, Kim Tiow Ooi (2013), " Economic analysis of the application of expanders in medium scale air-conditioners with conventional refrigerants, R1234yf and CO2", International Journal of Refrigeration, Vol 36, No. 5; pp: 1472-1482.

[4] Bjorn Palm (2007), "Hydrocarbons as refrigerants in small heat pump and refrigeration systems-A review", International Journal of Refrigeration, 31; pp: 552-563.

Journal of Computational Electronics
https://doi.org/10.1007/s10825-018-1237-2

Ultralow-power dielectric-modulated nanogap-embedded sub-20-nm TGRC-MOSFET for biosensing applications

Ajay Kumar[1] · **M. M. Tripathi**[1] · **Rishu Chaujar**[2]

© Springer Science+Business Media, LLC, part of Springer Nature 2018

Abstract
This work examines a transparent gate recessed channel (TGRC) metal–oxide–semiconductor field-effect transistor (MOSFET) for biosensing, including a nanogap cavity for detection of biomolecules and a transparent gate to enhance the overall current efficiency of the RC-MOSFET. For the detection of neutral biomolecules, electrical characteristics such as I_{ON}/I_{OFF}, shift in threshold voltage and change in surface potential have been studied and thereafter, sensitivity of has been evaluated. The biosensor showed enhanced sensitivity for biomolecules with increase in their dielectric value, due to greater on-current owing to the change in capacitances. The capacitances were therefore also evaluated. In addition, immobilization of biomolecules degrades the noise immunity of MOSFET and thereby their overall biosensing performance, while the noise immunity of the TGRC device was very high even in the presence of biomolecules. Furthermore, modulation of the cavity gap length was also investigated, revealing that its increase (from 8 to 20 nm) significantly enhanced the sensitivity of the proposed biosensor. Overall, the results of this analysis reveal that such TGRC-MOSFET biosensors can exhibit high sensitivity (1.45) at very low drain bias (0.2 V), enabling their use for biosensor applications to diagnose various diseases which require lower noise, high speed, low power, and high density.

Keywords Biosensor · Dielectric constant · ITO · Nanogap · Sensitivity · TGRC-MOSFET

1 Introduction

With the aid of nanotechnology, various kinds of biosensor have been developed for use in medical applications and disease diagnostics, which require high performance. According to medical science, prompt detection of any disease, mainly cancer, favors patient survival. Numerous methods have been developed for detection of biomolecules, e.g., the enzyme-linked immunosorbent assay [1], for Alzheimer's disease, ovarian cancer, and coronary artery disease. However, many of these approaches are complicated and time-consuming due to the requirement for labeling techniques [2]. Field-effect transistor (FET)-based biosensors have attracted much attention over recent years owing to their good scalability, high sensitivity, rapid electrical detection, low power consumption, direct electrical readout, and low-cost mass production in comparison with other methods such as surface plasmon resonance devices [3], microcantilevers [4], and arrays of fluorescence sensors [5]. Low-cost, highly sensitive, reliable, user-friendly, and quick diagnostic biosensing devices are essential for different biological and biomedical applications [6]. For biosensing applications, sensitivity is the key factor for a MOSFET. Over time, various structures such as the nanowire junctionless MOSFET [7] and tunnel FET [8, 9] have been introduced to enhance the sensitivity of FET-based biosensors. Nanotechnology-based biosensor devices have also been used [10–12] to overcome the difficulties of conventional health diagnostic methods.

Moreover, advanced development of semiconductor technology for medical applications has shrunk device dimensions to the nanoscale regime to provide high packing density for high-speed integrated circuits. However, in such ultra-scaled device, the influence of short-channel effects (SCEs)

✉ Rishu Chaujar
chaujar.rishu@dtu.ac.in

Ajay Kumar
ajaykumar@dtu.ac.in

M. M. Tripathi
mmtripathi@dce.ac.in

[1] Department of Electrical Engineering, Delhi Technological University, Delhi 110042, India

[2] Department of Applied Physics, Delhi Technological University, Delhi 110042, India

Published online: 11 September 2018

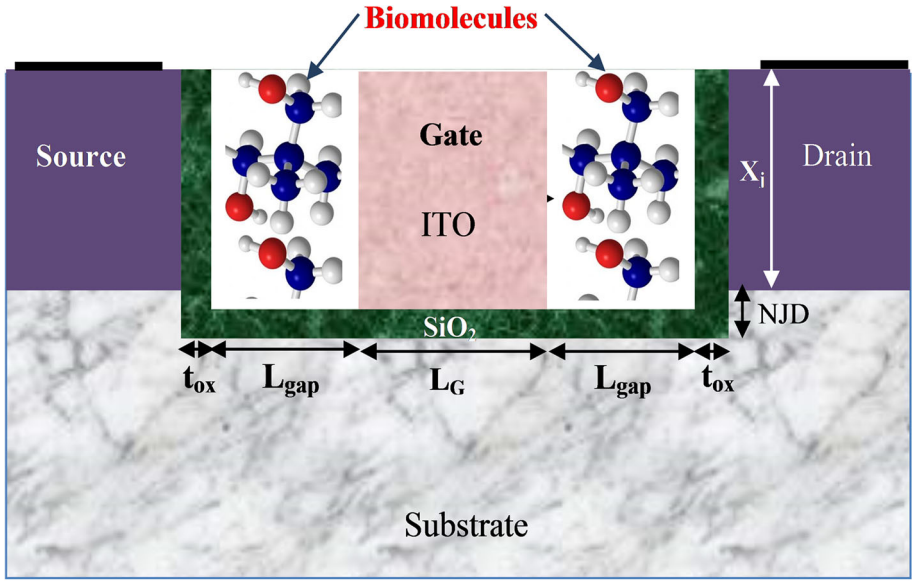


Fig. 1 Schematic structure of the TGRC-MOSFET biosensor

deeply affects device performance [7]. To overcome SCEs, several device engineering schemes and alternative device structures have been reported in literature [13–18]. Among these, the recessed channel (RC) MOSFET is considered to be the most promising, since it overcomes almost all the SCEs and is also compatible with recent complementary metal–oxide–semiconductor (CMOS) technology [19]. Numerous innovative gate materials have been explored recently to enhance the current driving capability of CMOS devices while enhancing their overall performance. In the proposed (TGRC-MOSFET) biosensor device, indium-doped tin oxide (ITO) has been used as a gate material, due to its enhanced electrical properties, as demonstrated in previous work [20–25]. Use of ITO significantly enhances the on-current, due to its very low resistivity (10^{-5} Ω cm) and high mobility (53.5 cm^2 V^{-1} s^{-1}) [26].

In the work presented herein, a TGRC-MOSFET for use as a biosensor was simulated, considering the electrical properties of various biomolecules. The main use of biosensors is to sense biological elements, based on their sensitivity to and binding specificity of biological species such as enzymes, proteins, nucleotides, or antibodies. In the proposed TGRC-MOSFET biosensor, the channel potential of the device is influenced by the electrical properties of the biomolecules, enabling their detection. In a conventional MOSFET, current flows in the channel when the gate voltage exceeds a threshold voltage (V_{TH}). In a biosensor, this effect is modulated by the dielectric constant due to immobilization of biomolecules below the gate electrode, because the threshold voltage depends upon the gate capacitance. Absorption of biomolecules therefore affects the electrical characteristics of the sensor, changing its sensitivity.

2 Device structure, simulation methodology, and calibration

The three-dimensional (3D) structure of the considered biosensor device is shown in Fig. 1. For immobilization of biomolecules, a small nanocavity is created in the gate insulator region, since this is the most important region determining the behavior and characteristics of a CMOS device. Here, L_{gap} is the length of the nanogap cavity (8 nm), t_{ox} is the oxide thickness (2 nm), and the gate length L_G is taken to be 20 nm. The source and drain regions are highly doped with n-type impurity to 5×10^{19} cm^{-3}, while the substrate is doped with p-type impurity to 1×10^{17} cm^{-3}, as shown in Fig. 1. The negative junction depth (NJD) is taken to be 10 nm, while the gate workfunction of ITO (Φ_{ITO}) is 4.7 eV. The gate bias (V_{gs}) is 0.7 V and the drain bias (V_{ds}) is 0.2 V throughout the analysis, unless otherwise stated. Absorption of different biomolecules is modeled by introduction of an insulator having the same dielectric constant as a particular biomolecule into the nanogap cavity. The unfilled cavity (i.e., with no biomolecules present) is modeled by using an insulator with dielectric constant $k = 1$, while the dielectric constant of the different considered biomolecules is as follows: streptavidin ($k = 2.1$) [27], biotin ($k = 2.63$) [28], 3-aminopropyltriethoxysilane (APTES) ($k = 3.57$), and protein ($k = 8$) [29]. Streptavidin–biotin is used to detect Marek's disease virus (MDV) using an enzyme-linked immunosorbent assay (ELISA) method [30], while APTES facilitates immobilization of biomolecules onto the surface for detection of dengue virus [31].

ATLAS is a powerful simulation tool that can be used for extraction of reliability results and figures of merit (FOMs) [32]. Various simulation models were applied in this work, including the Lombardi constant voltage and temperature

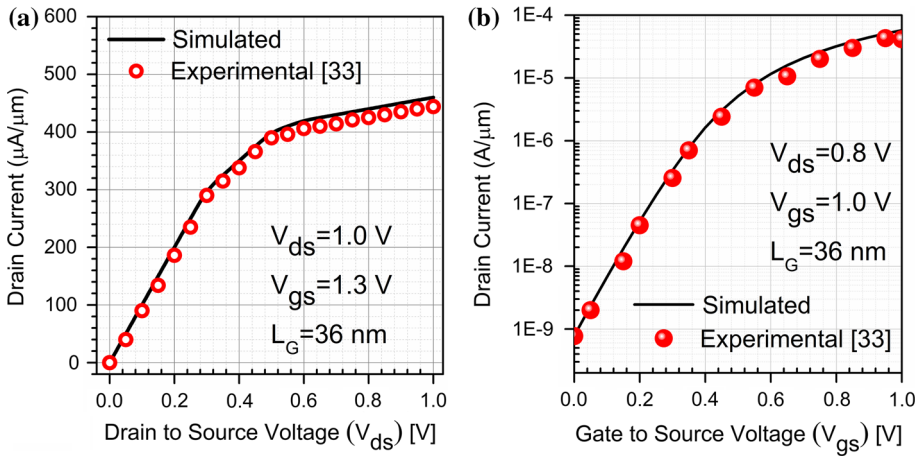


Fig. 2 Calibrated **a** output and **b** transfer characteristics of experimental and simulation data for a recessed channel MOSFET (with 36 nm gate length)

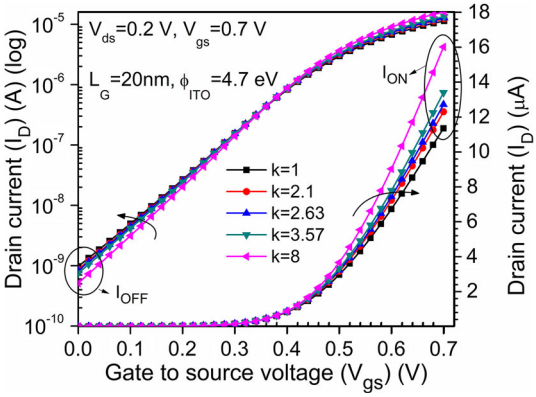


Fig. 3 Transfer characteristics of the nanogap-embedded TGRC-MOSFET in the presence of different biomolecules

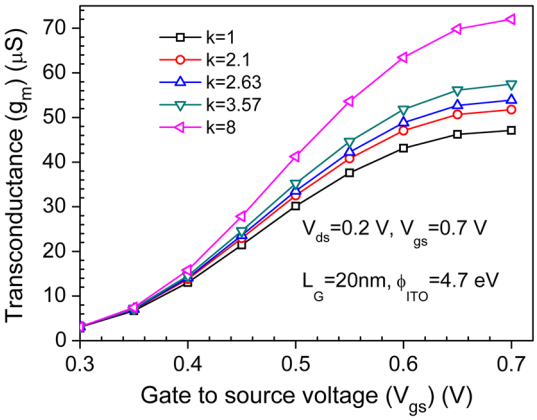


Fig. 4 Transconductance (g_m) of the nanogap-embedded TGRC-MOSFET in the presence of different biomolecules

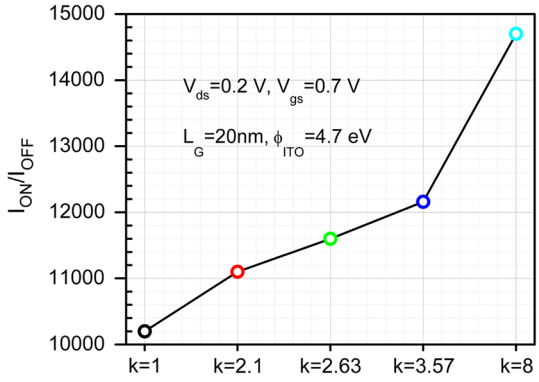


Fig. 5 Switching ratio (I_{on}/I_{off}) of the TGRC-MOSFET at drain voltage of 0.2 V in the presence of different biomolecules

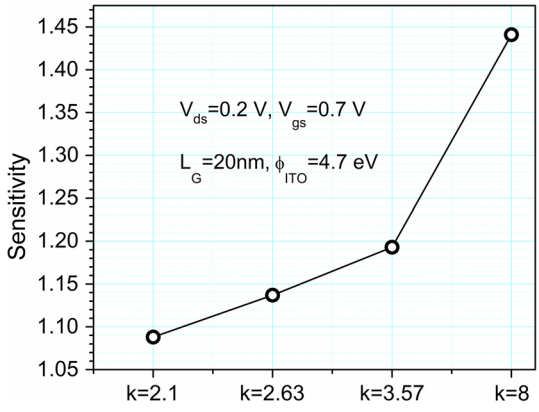


Fig. 6 Sensitivity of the TGRC-MOSFET at drain voltage of 0.2 V to different biomolecules

(CVT) model to consider all the mobilities, e.g., due to scattering caused by the parallel and perpendicular fields applied on the device. For carrier generation–recombination, we used Shockley–Read–Hall (SRH) recombination. Fermi–Dirac statistics were used in case of very highly doped material. To include information about the low energy (temperature) of the carriers, we used the energy balance transport (EBT) model [32]. Calibration of the physical model parameters of the simulated device against experimental results by Appenzeller et al. [33] is shown in Fig. 2. To validate the simulation results, output and transfer characteristic statistics were extracted [33] for a 36-nm RC-MOSFET, as shown in Fig. 2a and b, respectively. The simulation results in Fig. 2a, b almost match with the experimental data for a sub-40-nm RC MOSFET, thus validating the simulation model.

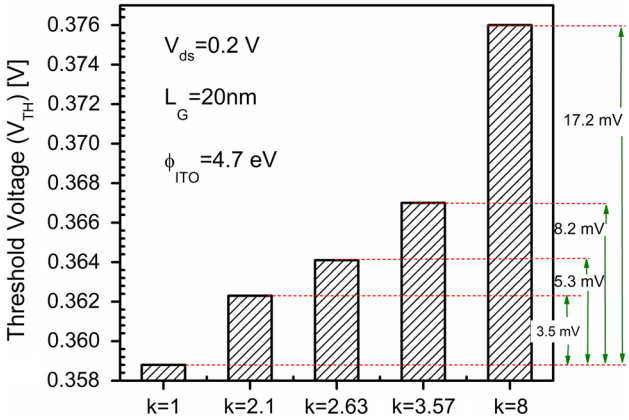


Fig. 7 Threshold voltage shifts for the TGRC-MOSFET in the presence of different biomolecules

3 Results and discussion

It can be observed from the transfer characteristics of the biosensor (Fig. 3) that, when neutral biomolecules are immobilized ($k > 1$) in the cavity, the on-current is significantly enhanced compared with in their absence ($k = 1$), owing to the increase in the dielectric constant and thus transconductance (Fig. 4). Different biomolecules can be detected based on the measured current [5]. Due to the increase in the on-current, the switching ratio (I_{on}/I_{off}) also increases with the dielectric value, as shown in Fig. 5. Thus, the change in the drain current or the enhancement in I_{on} and the switching ratio for a particular biomolecule could be used as key parameters for their detection/sensing. Furthermore, sensitivity is one of the critical parameters for the proposed biosensor device. In this work, the sensitivity (S) is defined as

$$S = \frac{I_{on}(k > 1)}{I_{on}(k = 1)}. \tag{1}$$

Figure 6 presents the sensitivity for the different biomolecules, clearly showing a higher value for protein biomolecules ($k = 8$) compared with streptavidin, biotin, and APTES (2.1, 2.63, and 3.57, respectively); note that the use of a uniform dielectric value implies that the cavity is completely filled by the specific biomolecule.

The threshold voltage was used as a sensing parameter for detection, being directly related to the dielectric constant; in this work, the threshold voltage is defined as the gate voltage at which the drain current is equal to 10^{-7} A/μm. The threshold voltage increases as the dielectric constant of the biomolecule is increased, as shown for the TGRC-MOSFET in Fig. 7. Threshold voltage shifts (ΔV_{TH}) of 3.5 mV, 5.3 mV, 8.2 mV, and 17.2 mV are observed when the dielectric constant changes from the unfilled cavity to a cavity filled with

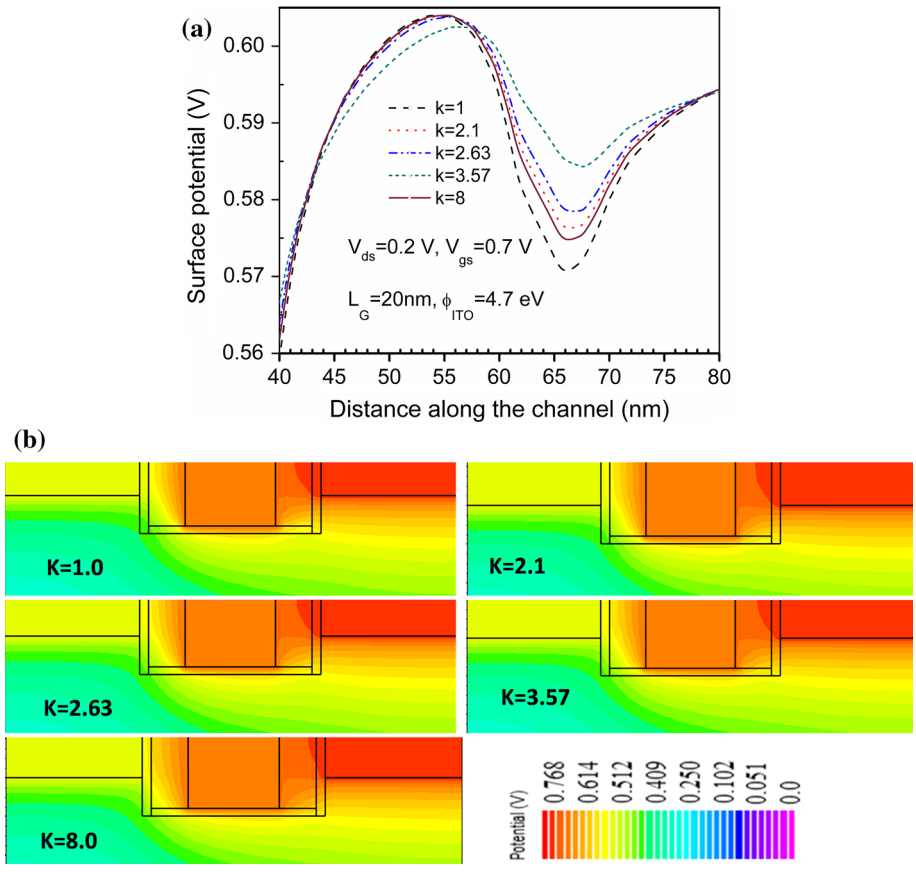


Fig. 8 **a** Surface potential along the channel from the source to drain and **b** corresponding contour plots of the TGRC-MOSFET in the presence of different biomolecules with $k = 1$, 2.1, 2.63, 3.57, and 8

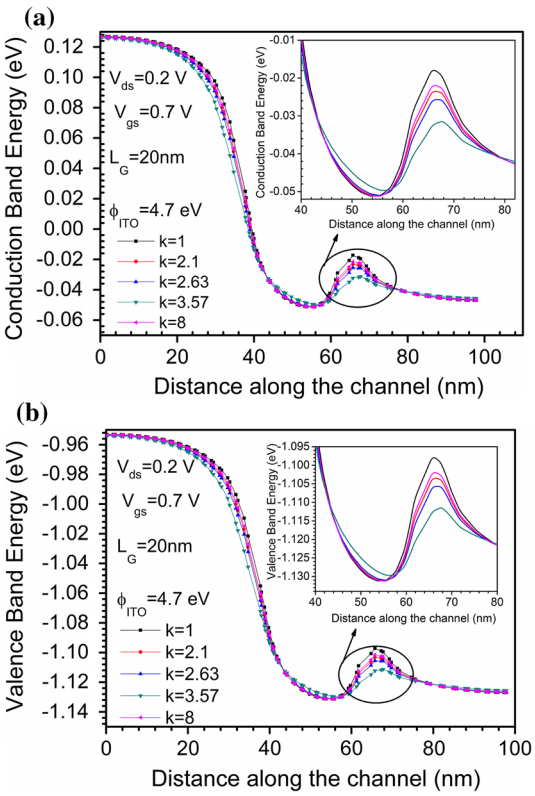


Fig. 9 Effect on **a** conduction band and **b** valence band along the channel of the TGRC-MOSFET in the presence of different biomolecules

biomolecules having $k = 2.1$, 2.63, 3.57, and 8 (Fig. 7). The threshold voltage shift (ΔV_{TH}) can also be used to define the sensitivity of the biosensor as $\Delta V_{TH} = V_{TH}$(after absorption of the molecule) $- V_{TH}$(air-filled cavity) [34, 35]. The threshold voltage shift is directly proportional to the permittivity of the absorbed neutral biomolecule, i.e.,

$$\Delta V_{TH} \propto k_{bio}. \tag{2}$$

Thus, it can be said that, the higher the absolute value of ΔV_{TH}, the better the sensitivity of the biosensor, as ΔV_{TH} also represents the sensitivity of the device and the threshold voltage shifts toward higher gate voltage in the presence of biomolecules in the nanogap cavity [7].

In addition, the electrical performance of the TGRC-MOSFET biosensor was also examined in terms of the surface potential (Fig. 8a). Under the cavity region, deformation of the potential occurs (especially at the drain end). When biomolecules are immobilized in the cavity, a change in potential is observed due to the change in the dielectric constant due to the biomolecules. This shift in potential can also be used to detect the presence of biomolecules in the cavity region. The contour plots of the surface potential in Fig. 8b clearly reveal the change in potential when biomolecules are immobilized in the nanocavity.

Figure 9a, b shows the energy band profile [36] in terms of the conduction- and valence-band energies. When biomolecules are immobilized in the nanogap cavity, these values clearly change. The shift in the energy band is more prominent for the biomolecule with dielectric constant of 3.57 but less prominent for protein, streptavidin, and biotin, in comparison with the case of no biomolecules [37], as reflected in Fig. 9a, b. Thus, the TGRC device can also be used as a low-power sensing device due to this effective change in the energy band profiles at low drain bias (0.2 V) for different biomolecules. Moreover, it is also observed from Fig. 10a that, in the presence of various biomolecules ($k =$

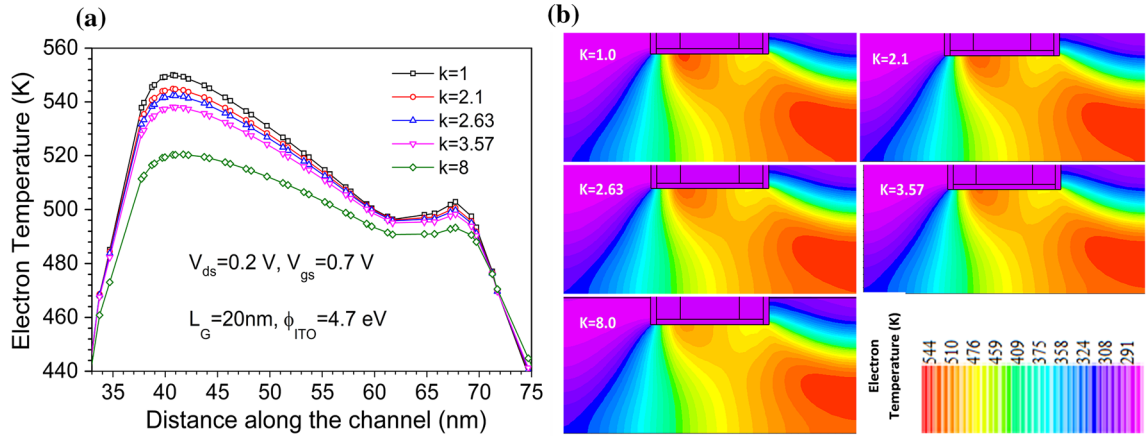


Fig. 10 **a** Electron temperature along the channel from the source to drain and **b** corresponding contour plots for the TGRC-MOSFET in the presence of different biomolecules

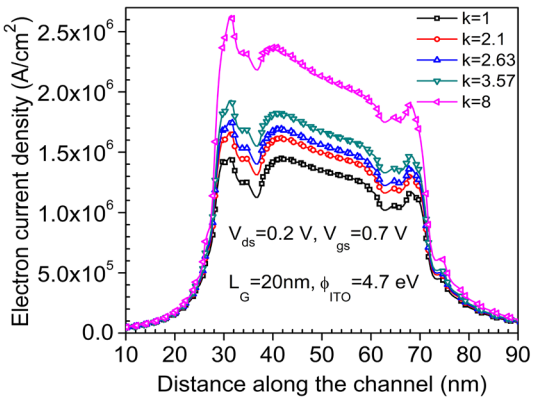


Fig. 11 Electron current density along the channel from the source to drain of the TGRC-MOSFET in the presence of different biomolecules

2.1 to $k = 8$), the electron temperature decreases (~510 K) due to the high-k dielectric (biomolecules) in the nanocavity gap, due to which leakage currents such as hot-electron injected gate current and impact-ionization substrate current are almost eliminated, thereby enhancing the I_{on} (shown in Fig. 2) and sensitivity of the device. The contour plots in Fig. 10b clearly show how the temperature varies when biomolecules are introduced into the nanogap cavity. This change in temperature with the dielectric constant can also be used to detect/sense which biomolecules are present.

Furthermore, the electron current density [38] in the presence and absence of different biomolecules in the nanocavity gap was also investigated (Fig. 11). For the proposed biosensor, it is evident that the electron current density is very low when the nanocavity gap is unfilled (for air, $k = 1$) but increases when the nanocavity gap is filled with different biomolecules, in increasing order of dielectric constant. For higher current density, I_{on} will also be high, due to which the switching ratio is increased. Thus, the device will be more sensitive when the nanocavity gap is filled with biomolecules, and this effect will increase with their dielectric constant (as shown in Fig. 6). It is also observed from Fig. 11 that the electron current density is higher just below the nanocavity gap.

3.1 Effect on parasitic capacitances

The presence of biomolecules can easily be observed via the change in stray capacitances, as the stray (parasitic) capaci-

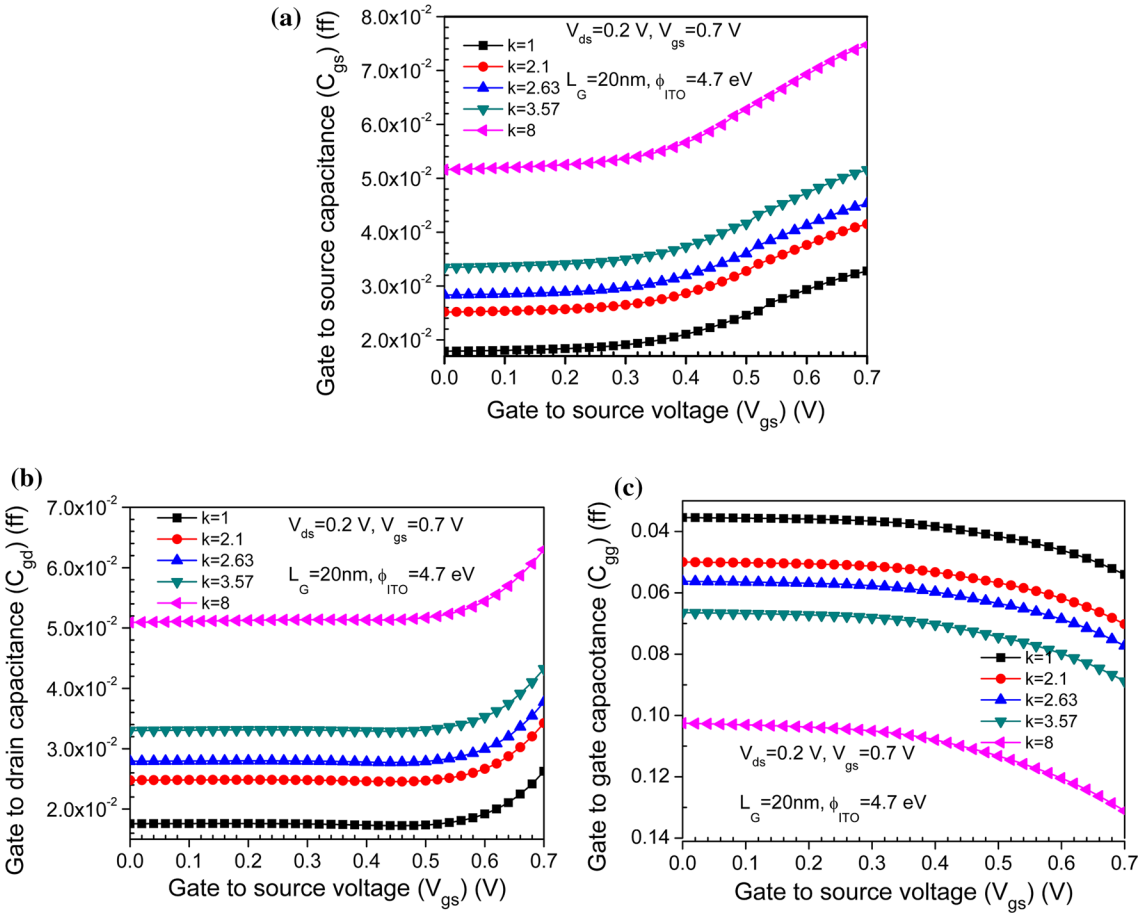


Fig. 12 Effect of different biomolecules on the parasitic capacitances **a** C_{gs}, **b** C_{gd}, and **c** C_{gg} of the TGRC-MOSFET

tances of a field-effect transistor are altered when changing the dielectric constant of the gate oxide. Figure 12a shows that the gate-to-source capacitance (C_{gs}) and gate-to-drain capacitance (C_{gd}) are altered (increased) when changing (increasing) the dielectric constant to $k = 2.1$, 2.63, 3.57, and 8, in comparison with the unfilled nanogap. When V_{gs} increases, the accumulation of charge carriers near the gate increases [39], and as a result, the gate-to-source capacitance and gate-to-drain capacitance also increase. Similarly, the gate capacitance (C_{gg}) is altered in the presence of biomolecules with different dielectric constants, and when V_{gs} increases, the accumulation of charges at the gate increases, and thus so does the gate capacitance [39], as shown in Fig. 12c. When molecules with higher dielectric constant are immobilized, these changes in the capacitances become more prominent, as is evident from Fig. 12a–c. These parasitic capacitances must be as low as possible in semiconductor devices for use in high-performance applications. According to these results, all the parasitic capacitances (C_{gs}, C_{gd}, and C_{gg}) evaluated in the presence of different biomolecules were very low (on femtofarad scale).

3.2 Noise assessment

In the presence of any external agent (e.g., biomolecules) in the channel region of a CMOS device, the electrical behavior in terms of the I–V characteristics is altered. Such shifts in the I–V characteristics and other electrical behaviors can be used as key parameters for detection of biomolecules, as clearly shown above. However, the presence of such agents can also sometimes lead to noise, which degrades biosensor performance. Therefore, to examine the noise immunity of the proposed biosensor, noise FOMs such as the minimum noise figure, noise conductance, etc. were also evaluated w.r.t. frequency [14]. As is clear from Figs. 13, 14, and 15, when biomolecules are immobilized in the cavity, all the noise parameters improved significantly at high frequency. This observation can mainly be attributed to the transparent conducting material (ITO) used in the TGRC-MOSFET architecture, because the random motion of free electrons is decreased in such materials. In a transparent conducting material, the temperature (Fig. 10) does not increase significantly when the concentration of charge carriers is increased, thereby improving the noise immunity of the TGRC biosensor in the presence of biomolecules. Furthermore, Fig. 15 shows another noise parameter, called the optimum source impedance ($Z_{OPT} = R_{OPT} + jX_{OPT}$), with respect to frequency for the different biomolecules, being nearly zero at higher frequencies when the nanocavity gap is empty but increasing with the dielectric constant of the biomolecule. This indicates that the device exhibits very low noise in the presence of biomolecules and is thus suitable for use in biosensing applications.

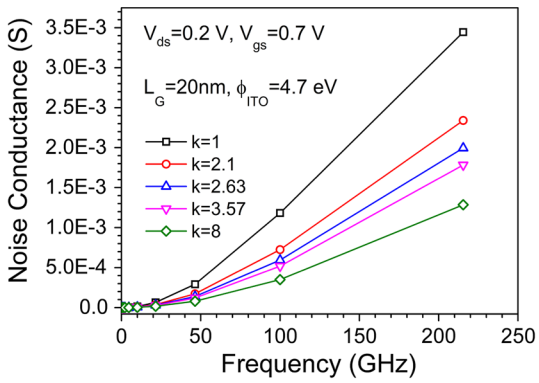


Fig. 13 Noise conductance in the GHz frequency range for the TGRC-MOSFET in the presence of different biomolecules

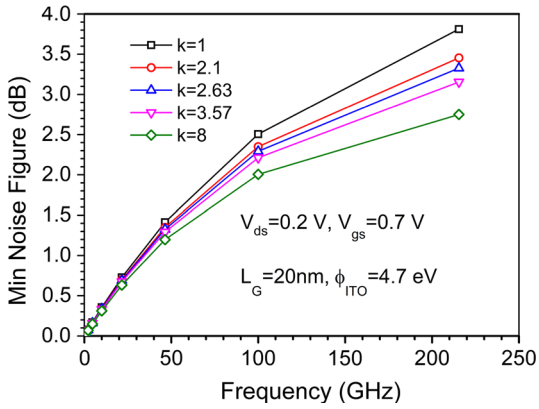


Fig. 14 Minimum noise figure in the GHz frequency range for the TGRC-MOSFET in the presence of different biomolecules

3.3 Effect of the nanogap cavity length

Moreover, the length of the cavity (L_{gap}) [36] was also varied, with the aim of determining its effect on the sensitivity and thereby the performance of the biosensor. Figure 16 shows that, with increase in the cavity gap length, the on/off ratio was evidently reduced due to an increase in the off-current

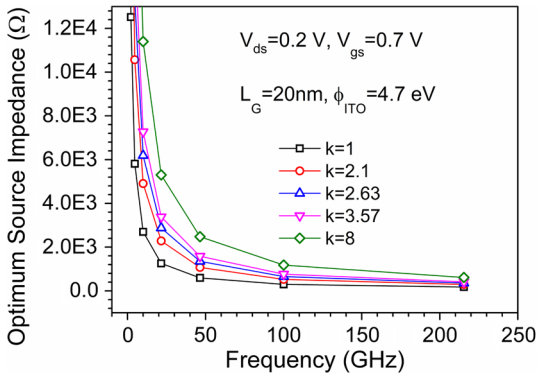


Fig. 15 Optimum source impedance in the GHz frequency range for the TGRC-MOSFET in the presence of different biomolecules

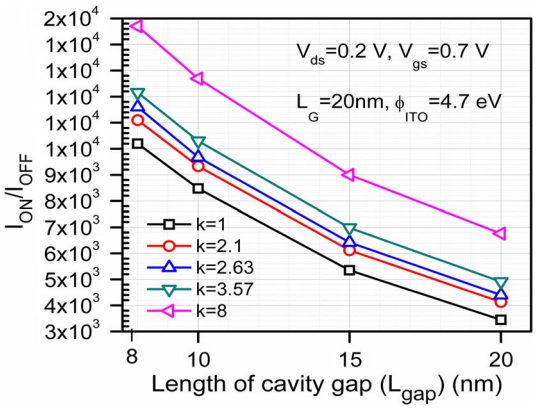


Fig. 16 Effect of varying the cavity gap length in the TGRC-MOSFET on the switching ratio for different biomolecules

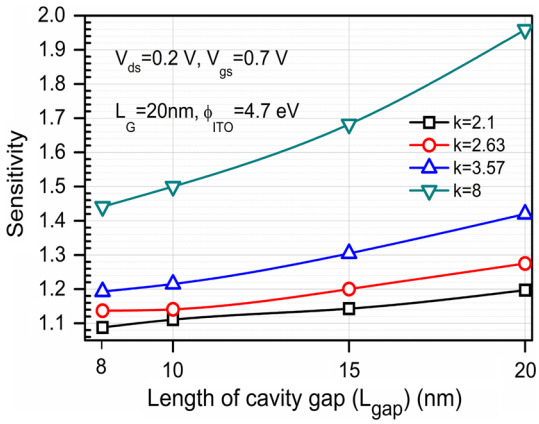


Fig. 17 Effect of varying the cavity gap length in the TGRC-MOSFET on the sensitivity for different biomolecules

resulting from higher capacitance. Moreover, the sensitivity of the TGRC biosensor with different cavity gap lengths was also evaluated, revealing that it increased significantly with increase in L_{gap} (Fig. 17). From this figure, it is observed that the sensitivity increased with k for given L_{gap}. Thus, for $L_{gap} = 20$ nm, the nanogap-embedded TGRC biosensor showed better sensitivity for protein ($k = 8$) in comparison with the other biomolecules. Figure 18 shows the change in the threshold voltage with L_{gap} (from 8 to 20 nm) for the different biomolecules; this noticeable change in the threshold voltage with the dielectric constant can be used as one of the sensing parameters for detection of biomolecules. Thus, the TGRC-MOSFET with cavity gap length of 20 nm showed optimum performance and hence could be employed as a low-power, high-sensitivity biosensor for diagnosis of various associated diseases.

4 Conclusions

The applicability of a nanogap-embedded ITO-gated recessed channel MOSFET as a biosensor was investigated.

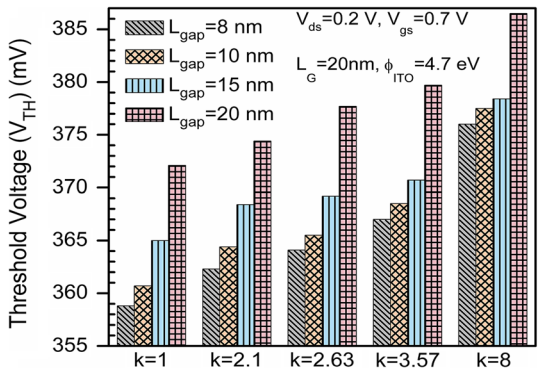


Fig. 18 Effect of varying the cavity gap length in the TGRC-MOSFET on the threshold voltage for different biomolecules

For detection of various biomolecules, the electrical behavior was studied in terms of the threshold voltage shift, sensitivity, switching ratio, surface potential, capacitance, and noise FOMs. The results obtained clearly show that, due to the ITO gate in the nanogap cavity, the electrical performance of the TGRC biosensor was significantly enhanced, showing higher sensitivity for biomolecules with high dielectric value. It was found that the sensitivity was higher for detection of protein ($k \approx 8$) in comparison with the other biomolecules, with higher noise immunity. Such TGRC-MOSFET biosensors are therefore proved to be favorable devices for use in sensing applications, due to their high sensitivity and low-power electrical detection of different biomolecules. Furthermore, the effects of the cavity gap length on the switching ratio, V_{TH}, and sensitivity of the proposed biosensor were also examined, revealing that the sensitivity increased with increase in the cavity length while the overall biosensor performance was slightly degraded. Therefore, the cavity gap length must be optimized for better performance, which will enable use of such sub-20-nm TGRC-MOSFETs as low-noise, high-speed, high-sensitivity biosensors for detection of various associated diseases.

Acknowledgements The authors are grateful to the University Grants Commission (UGC) for provision of financial assistance to carry out this work.

References

1. Comini, E., Baratto, C., Concina, I., Faglia, G., Falasconi, M., Ferroni, M., Galstyan, V., Gobbi, E., Ponzoni, A., Vomiero, A., Zappa, D., Sberveglieri, V., Sberveglieri, G.: Metal oxide nanoscience and nanotechnology for chemical sensors. Sens. Actuators B Chem. **179**, 3–20 (2013)
2. Lee, J., Jang, J., Choi, B., Yoon, J., Kim, J.-Y., Choi, Y.-K., Kim, D.M., Kim, D.H., Choi, S.-J.: A highly responsive silicon nanowire/amplifier MOSFET hybrid biosensor. Sci. Rep. **5**, 12286 (2015)

3. Bergveld, P.: The development and application of FET-based biosensors. Biosensors **2**(1), 15–33 (1986)
4. Sang, S., Wang, Y., Feng, Q., Wei, Y., Ji, J., Zhang, W.: Progress of new label-free techniques for biosensors: a review. Crit. Rev. Biotechnol. **36**(3), 465–481 (2016)
5. Im, H., Huang, X.-J., Gu, B., Choi, Y.-K.: A dielectric-modulated field-effect transistor for biosensing. Nat. Nanotechnol. **2**(7), 430–434 (2007)
6. Vu, X.T., Eschermann, J.F., Stockmann, R., GhoshMoulick, R., Offenhäusser, A., Ingebrandt, S.: Top-down processed silicon nanowire transistor arrays for biosensing. Phys. Status Solidi **206**(3), 426–434 (2009)
7. Ahangari, Z.: Performance assessment of dual material gate dielectric modulated nanowire junctionless MOSFET for ultrasensitive detection of biomolecules. RSC Adv. **6**(92), 89185–89191 (2016)
8. Chandan, B.V., Nigam, K., Sharma, D.: Junctionless based dielectric modulated electrically doped tunnel FET based biosensor for label-free detection. Micro Nano Lett. **13**(4), 452–456 (2018)
9. Kanungo, S., Chattopadhyay, S., Gupta, P.S., Sinha, K., Rahaman, H.: Study and analysis of the effects of SiGe source and pocket-doped channel on sensing performance of dielectrically modulated tunnel FET-based biosensors. IEEE Trans. Electron Devices **63**(6), 2589–2596 (2016)
10. Azmi, M.M., Tehrani, Z., Lewis, R., Walker, K.-A., Jones, D., Daniels, D., Doak, S., Guy, O.: Highly sensitive covalently functionalised integrated silicon nanowire biosensor devices for detection of cancer risk biomarker. Biosens. Bioelectron. **52**, 216–224 (2014)
11. Ahn, J.-H., Choi, S.-J., Han, J.-W., Park, T.J., Lee, S.Y., Choi, Y.-K.: Double-gate nanowire field effect transistor for a biosensor. Nano Lett. **10**(8), 2934–2938 (2010)
12. Gao, A., Lu, N., Dai, P., Li, T., Pei, H., Gao, X., Gong, Y., Wang, Y., Fan, C.: Silicon-nanowire-based CMOS-compatible field-effect transistor nanosensors for ultrasensitive electrical detection of nucleic acids. Nano Lett. **11**(9), 3974–3978 (2011)
13. Barsan, R.M.: Analysis and modeling of dual-gate MOSFET's. IEEE Trans. Electron Devices **28**(5), 523–534 (1981)
14. Gupta, N., Chaujar, R.: Influence of gate metal engineering on small-signal and noise behaviour of silicon nanowire MOSFET for low-noise amplifiers. Appl. Phys. A **122**(8), 1–9 (2016)
15. Gupta, N., Chaujar, R.: Optimization of high-k and gate metal workfunction for improved analog and intermodulation performance of gate stack (GS)-GEWE-SiNW MOSFET. Superlattices Microstruct. **97**, 630–641 (2016)
16. Gupta, N., Chaujar, R.: Investigation of temperature variations on analog/RF and linearity performance of stacked gate GEWE-SiNW MOSFET for improved device reliability. Microelectron. Reliab. **64**, 235–241 (2016)
17. Gupta, N., Kumar, A., Chaujar, R.: Oxide bound impact on hot-carrier degradation for gate electrode workfunction engineered (GEWE) silicon nanowire MOSFET. Microsyst. Technol. **22**, 2655–2664 (2015)
18. Chaujar, R., Kaur, R., Saxena, M., Gupta, M., Gupta, R.: TCAD assessment of gate electrode workfunction engineered recessed channel (GEWE-RC) MOSFET and its multilayered gate architecture—part I: hot-carrier-reliability evaluation. IEEE Trans. Electron Devices **55**(10), 2602–2613 (2008)
19. Chaujar, R., Kaur, R., Saxena, M., Gupta, M., Gupta, R.: Laterally amalgamated DUal material GAte concave (L-DUMGAC) MOSFET for ULSI. Microelectron. Eng. **85**(3), 566–576 (2008)
20. Kumar, A., Gupta, N., Chaujar, R.: Analysis of novel transparent gate recessed channel (TGRC) MOSFET for improved analog behaviour. Microsyst. Technol. **22**(11), 2665–2671 (2016)
21. Kumar, A., Gupta, N., Chaujar, R.: Power gain assessment of ITO based transparent gate recessed channel (TGRC) MOSFET for RF/wireless applications. Superlattices Microstruct. **91**, 290–301 (2016)
22. Kumar, A., Gupta, N., Chaujar, R.: TCAD RF performance investigation of transparent gate recessed channel MOSFET. Microelectron. J. **49**, 36–42 (2016)
23. Kumar, A., Gupta, N., Chaujar, R.: Effect of structured parameters on the hot-carrier immunity of transparent gate recessed channel (TGRC) MOSFET. Microsyst. Technol. **23**, 4057–4064 (2017)
24. Kumar, A., Tripathi, M., Chaujar, R.: Reliability issues of In_2O_5Sn gate electrode recessed channel MOSFET: impact of interface trap charges and temperature. IEEE Trans. Electron Devices **65**, 860–866 (2018)
25. Kumar, A., Tripathi, M., Chaujar, R.: In_2O_5 Sn based transparent gate recessed channel MOSFET: RF small-signal model for microwave applications. AEU-Int. J. Electron. Commun. (2018)
26. Minami, T.: Transparent conducting oxide semiconductors for transparent electrodes. Semicond. Sci. Technol. **20**(4), S35 (2005)
27. Busse, S., Scheumann, V., Menges, B., Mittler, S.: Sensitivity studies for specific binding reactions using the biotin/streptavidin system by evanescent optical methods. Biosens. Bioelectron. **17**(8), 704–710 (2002)
28. Densmore, A., Xu, D.-X., Janz, S., Waldron, P., Mischki, T., Lopinski, G., Delâge, A., Lapointe, J., Cheben, P., Lamontagne, B.: Spiral-path high-sensitivity silicon photonic wire molecular sensor with temperature-independent response. Opt. Lett. **33**(6), 596–598 (2008)
29. Kim, S., Baek, D., Kim, J.-Y., Choi, S.-J., Seol, M.-L., Choi, Y.-K.: A transistor-based biosensor for the extraction of physical properties from biomolecules. Appl. Phys. Lett. **101**(7), 073703 (2012)
30. Davidson, I., Malkinson, M., Strenger, C., Becker, Y.: An improved ELISA method, using a streptavidin-biotin complex, for detecting Marek's disease virus antigens in feather-tips of infected chickens. J. Virol. Methods **14**(3–4), 237–241 (1986)
31. Zhang, G.-J., Zhang, L., Huang, M.J., Luo, Z.H.H., Tay, G.K.I., Lim, E.-J.A., Kang, T.G., Chen, Y.: Silicon nanowire biosensor for highly sensitive and rapid detection of Dengue virus. Sens. Actuators B Chem. **146**(1), 138–144 (2010)
32. Silvaco, I.: ATLAS User's Manual, Santa Clara, CA, Ver 5 (2011)
33. Appenzeller, J., Martel, R., Avouris, P., Knoch, J., Scholvin, J., del Alamo, J.A., Rice, P., Solomon, P.: Sub-40 nm SOI V-groove n-MOSFETs. IEEE Electron Device Lett. **23**(2), 100–102 (2002)
34. Kannan, N., Kumar, M.J.: Dielectric-modulated impact-ionization MOS transistor as a label-free biosensor. IEEE Electron Device Lett. **34**(12), 1575–1577 (2013)
35. Choi, J.-M., Han, J.-W., Choi, S.-J., Choi, Y.-K.: Analytical modeling of a nanogap-embedded FET for application as a biosensor. IEEE Trans. Electron Devices **57**(12), 3477–3484 (2010)
36. Abdi, D.B., Kumar, M.J.: Dielectric modulated overlapping gate-on-drain tunnel-FET as a label-free biosensor. Superlattices Microstruct. **86**, 198–202 (2015)
37. Kranti, A., Armstrong, G.A.: Engineering source/drain extension regions in nanoscale double gate (DG) SOI MOSFETs: analytical model and design considerations. Solid-State Electron. **50**(3), 437–447 (2006)
38. Stern, E., Vacic, A., Reed, M.A.: Semiconducting nanowire field-effect transistor biomolecular sensors. IEEE Trans. Electron Devices **55**(11), 3119–3130 (2008)
39. Kumar, A., Tripathi, M., Chaujar, R.: Investigation of parasitic capacitances of In_2O_5Sn gate electrode recessed channel MOSFET for ULSI switching applications. Microsyst. Technol. **23**, 5867–5874 (2017)